DESIGN, SIMULATION AND OPTIMIZATION OF HYDRAULIC MACHINERY

EDITED BY: Ling Zhou, Jin-Hyuk Kim, Lei Tan and Xiaojun Li
PUBLISHED IN: Frontiers in Energy Research

frontiers Research Topics

ISSN 1664-8714
ISBN 978-2-88976-569-0
DOI 10.3389/978-2-88976-569-0

About Frontiers

Frontiers is more than just an open-access publisher of scholarly articles: it is a pioneering approach to the world of academia, radically improving the way scholarly research is managed. The grand vision of Frontiers is a world where all people have an equal opportunity to seek, share and generate knowledge. Frontiers provides immediate and permanent online open access to all its publications, but this alone is not enough to realize our grand goals.

Frontiers Journal Series

The Frontiers Journal Series is a multi-tier and interdisciplinary set of open-access, online journals, promising a paradigm shift from the current review, selection and dissemination processes in academic publishing. All Frontiers journals are driven by researchers for researchers; therefore, they constitute a service to the scholarly community. At the same time, the Frontiers Journal Series operates on a revolutionary invention, the tiered publishing system, initially addressing specific communities of scholars, and gradually climbing up to broader public understanding, thus serving the interests of the lay society, too.

Dedication to Quality

Each Frontiers article is a landmark of the highest quality, thanks to genuinely collaborative interactions between authors and review editors, who include some of the world's best academicians. Research must be certified by peers before entering a stream of knowledge that may eventually reach the public - and shape society; therefore, Frontiers only applies the most rigorous and unbiased reviews.
Frontiers revolutionizes research publishing by freely delivering the most outstanding research, evaluated with no bias from both the academic and social point of view. By applying the most advanced information technologies, Frontiers is catapulting scholarly publishing into a new generation.

What are Frontiers Research Topics?

Frontiers Research Topics are very popular trademarks of the Frontiers Journals Series: they are collections of at least ten articles, all centered on a particular subject. With their unique mix of varied contributions from Original Research to Review Articles, Frontiers Research Topics unify the most influential researchers, the latest key findings and historical advances in a hot research area! Find out more on how to host your own Frontiers Research Topic or contribute to one as an author by contacting the Frontiers Editorial Office: frontiersin.org/about/contact

DESIGN, SIMULATION AND OPTIMIZATION OF HYDRAULIC MACHINERY

Topic Editors:
Ling Zhou, Jiangsu University, China
Jin-Hyuk Kim, Korea Institute of Industrial Technology, South Korea
Lei Tan, Tsinghua University, China
Xiaojun Li, Zhejiang Sci-Tech University, China

Citation: Zhou, L., Kim, J.-H., Tan, L., Li, X., eds. (2022). Design, Simulation and Optimization of Hydraulic Machinery. Lausanne: Frontiers Media SA.
doi: 10.3389/978-2-88976-569-0

Table of Contents

frontiers | Frontiers in Energy Research

TYPE Editorial
PUBLISHED 26 September 2022
DOI 10.3389/fenrg.2022.971870

OPEN ACCESS

EDITED AND REVIEWED BY
Francois M. A. Marechal,
Swiss Federal Institute of Technology Lausanne, Switzerland

*CORRESPONDENCE
Ling Zhou,
lingzhou@ujs.edu.cn

SPECIALTY SECTION
This article was submitted to Process and Energy Systems Engineering, a section of the journal Frontiers in Energy Research

RECEIVED 17 June 2022
ACCEPTED 08 September 2022
PUBLISHED 26 September 2022

CITATION
Zhou L, Kim J-H, Tan L and Li X (2022), Editorial: Design, simulation and optimization of hydraulic machinery. *Front. Energy Res.* 10:971870. doi: 10.3389/fenrg.2022.971870

Editorial: Design, simulation and optimization of hydraulic machinery

Ling Zhou[1]*, Jin-Hyuk Kim[2], Lei Tan[3] and Xiaojun Li[4]

[1]National Research Center of Pumps, Jiangsu University, Zhenjiang, China, [2]Carbon Neutral Technology R&D Department, Korea Institute of Industrial Technology, Cheonan, South Korea, [3]Department of Energy and Power Engineering, Tsinghua University, Beijing, China, [4]National-Provincial Joint Engineering Laboratory for Fluid Transmission System Technology, Zhejiang Sci-Tech University, Hangzhou, China

KEYWORDS

energy characteristics, energy conversion, hydraulic losses, optimal design, numerical simulation, fluid control, fault diagnosis

Editorial on the Research Topic
Design, simulation and optimization of hydraulic machinery

With the increasing pressure of energy crisis and carbon emission, the energy-saving technology of industrial processes has attracted worldwide attention. Hydraulic machinery and its systems are the key components for the sustainable development of engineering, energy transformation in hydraulic systems, water resources, and chemical industry including various transport of liquids or mixtures. The growing demands for the increase of processes operation efficiency have encouraged and indicated the development and implementation of the optimization at the design stages for pumps and pump systems based on mathematical and physical models, advanced numerical simulation, or data-driven techniques.Recently, an increasing number of papers have discussed the design and optimization for the improvement of pumps, turbines, valves, and other flow components. Many new theories and methods have been proposed and applied to improve hydraulic performance. For more efficient utilization of hydraulic machinery, it is important to collect up-to-date information on this topic.

In the first article, Li et al. simplified the reactor primary circuit system of HPR1000. Meanwhile, the RCP shutdown accident in a single circuit of the reactor is numerically simulated. Results show that the pressure in the pipeline system has changed greatly compared. The torque drops sharply, and then rises slowly to zero. The pressure at the inlet and outlet of the impeller changes dramatically which leads to the change of blade load. The pressure and velocity in the guide vane continue to decrease.

Based on performance test and Pumplinx simulation, Chao et al. investigated the effect of blade inlet width on cavitation performance. The results show that the method of twisting the centrifugal impeller of the suspended forward-extended blade shows a significant effect in preventing cavitation performance under such working conditions

of high speed and negative pressure. Its application in aerospace power systems can significantly improve the cavitation performance.

The third article (Liu et al.) studied the energy loss of bi-directional hydraulic machinery under cavitation conditions, they used high-speed photography combined with six-axis force and torque sensors to collect cavitating flow images and lift signals of S-shaped hydrofoils simultaneously in a cavitation tunnel. The fast Fourier analysis reveals that the fluctuations of the lift signals under cloud cavitation are significantly higher than those under non-cavitation, and the main frequencies of the lift signals under cloud cavitation were all twice the frequency of the cloud cavitation shedding.

The article by Xu et al. proposed a new hard hose traveler with the function of electric drive and self-propelled. A calculation model for the dynamic change of the pulling force and energy consumption of the reel and tube operation is proposed in this study. The difference between the calculated and the measured values of the total winding length of each tube layer was not more than 0.4 m, with the deviation rate being approximately equal to 0.5%. This investigation can help solve the problems of higher energy consumption and lower intelligence of traditional hard hose travelers.

Tian et al. summarized the scientific research results of submersible mixer in recent years from four aspects: structure and energy characteristics of submersible mixer, numerical simulation calculation method, flow field characteristics, and factors affecting the flow field characteristics. Few experimental studies are conducted, and mostly numerical calculations are based on clear water as the medium. Many factors affect the mixing effect of a submersible mixer, such as installation factors and impeller design parameters. Meanwhile, the development and trends of submersible mixer technology are prospected, and the future directions of further research are proposed.

Chen et al. used time-resolved particle image velocimetry (TR-PIV) measurements to investigate the flow structures in the impeller passage under different flow rates. Through the study of the first few proper orthogonal decomposition (POD) modes of the flow field, the coherent flow structures under several flow rates were revealed, consequently, the flow fields were reconstructed by the POD modes. The flow structures that were reflected by the several modes change as the decrease of flow rate, especially, at the extreme part-load condition, not only the shapes of the flow structures changed, but also the flow direction is reversed. This indicates that the generation mechanism of turbulent kinetic energy in the flow passage changed at the extreme part-load conditions.

Lin et al. studied the flow characteristics of the centrifugal pump with different offset angles of inlet guide vanes (IGVs). In terms of external characteristics, the pump with 25°IGVs has the best head and efficiency improvement. Under three small operating points, the pump with 25°IGVs increased the head by 2.11, 0.95, and 0.73% and the efficiency by 2.51, 1.67, and 1. 25%, respectively, compared with the pump with 0°IGVs. The research in this paper contributes to the performance improvement of centrifugal pumps operating at low flow conditions.

Meng et al. adopts the method of experimental and numerical simulation in the pump and studies the variation of the vibration characteristics in the operation process to improve the stability of the pump. The vibration characteristics of the pumps have been significantly improved by adding special trash barriers. In the experiment, the cavitation did occur in the actual operation process. This is the main reason that causes the centrifugal pump performance and pump flow to drop.

The characteristic of steady-state flow force on the cone valve was investigated by Liu et al. the geometric parameters and operating conditions in the steady-state flow force were optimized by the orthogonal test-optimization method. The results show that the greater the pressure differential is, the greater the steady-state flow force is. The steady-state flow force does not increase linearly, but increases first and then decreases with the increase of the opening. The study will lay the foundation to precise axial flow force prediction and reference for design optimization of the valve.

The article by Yan et al. regarded the three fish-type leading-edge structures of mackerel, sturgeon and small yellow croaker as the research objects and use high-precision non-contact 3D scanners to establish three bionic hydrofoils. They used large eddy simulation to simulate the transient cavitating flow of hydrofoils numerically. The numerical simulation results are in good agreement with the experimental results. This study revealed the mechanism of the change in the hydrofoil leading-edge structure in transient cavitating flow and provides a reference for the subsequent optimal design of hydraulic machinery blades.

The transient flow in a new type of dishwasher pump is investigated numerically by Ning et al. The simulation results agree well with the experiment. Three schemes, 0 rpm/30 rpm/ 60 rpm, of volute speeds are investigated. After comparing the three schemes with respect to the radial force, the shape of the vector distribution is most regular for the 30 rpm scheme, which indicates that the stability of the pump is the highest. This paper can be used to improve both the control and selection of volute speeds.

The hydraulic characteristics of vertical axial flow pump devices with different guide vane inlet angles were studied by Xu et al. using computational fluid dynamics (CFD) and model test methods. The results showed that the pump device efficiency under low-head and large-discharge conditions was improved when the guide vane inlet angle was rotated in the clockwise direction. When the operational conditions of the pump device deviate from its high-efficiency zone, the application of these results could improve its hydraulic performance, which is of great

significance to the design and application of low-head pump devices.

Yang et al. fabricated the prototypes of conical tube valveless piezoelectric pump and hyperbolic tubes valveless piezoelectric pump. The size and position of entropy production of the hyperbolic tube and the conical tube were numerically calculated based on entropy production theory. The results show that the entropy production rate of the hyperbolic tube was significantly lower than that of the conical tube, which is consistent with the experimental results. This research provided a new design and research method for improving the output performance of the valveless piezoelectric pump in the future.

Xie et al. established a mathematical model of damping characteristics of the valve-controlled damping adjustable damper and designed the experiment of the damping characteristics of the compression stroke and the recovery stroke. Through simulation and experiment, the accuracy of the mathematical model was verified, and the damping contribution rate of different key parameters under different excitation speeds was analyzed. The research results can screen out the key parameters, improve the development efficiency of the damper, and provide guidance for the damper design and optimization.

Formed with a low-specific-speed centrifugal pump as the study object, unsteady flow calculation and fluid-structure interaction calculation were performed by Jia et al. on centrifugal pumps with different wear-ring clearances. The effect of the incident angle of the wear-ring clearance on the distribution of pressure pulsation and vibration performance of centrifugal pump was analyzed. The results showed that the improved efflux angle of the wear-ring clearance could effectively weaken the impact disturbance of the leakage flow in the wear-ring clearance to the main flow at the inlet. Meanwhile, the efficiency of the centrifugal pump was improved, and the vibration amplitude and vibration energy of the pump were also reduced.

The article by Yu et al. proposed a numerical analysis method based on the computer simulation and the Monte Carlo (MC) method. First, the unit's life simulation values were simulated using the MC method. Next, the CEMS life simulation value can be obtained based on the CEMS reliability model. Then, simulation data were analyzed, and the distribution of the CEMS life was deduced. The goodness-of-fit test, point estimation and confidence interval of the parameters, and reliability measure were estimated. Finally, as a test example of the wind turbine, the practicability and effectiveness of the method proposed in this paper were verified.

Zhao et al. studied the effect of adding non-connected forms of tiny blades with different parameters of radial position, width, and length to the shroud of the impeller on the cavitation performance of a centrifugal pump. A modified SST k-ω turbulence model combined with the Zwart-Gerber-Belamri cavitation model is used for numerical simulation of the model pump. The results show that the numerical prediction of the original pump agrees well with the experimental results. The existence of tiny blades reduces the overall pressure pulsation main frequency amplitude during pump operation, making its operation more stable.

Jia et al. performed external characteristics, dynamic pressure, and vibration tests on the closed impeller model, semi-open type impeller model, and open impeller model to study the influence of the impeller structure on the operational stability of the pump. According to the research findings, the external characteristic curves and the pressure pulsation in the casing tongue area of the three impellers enjoyed the poorest stability can be observed in the open impeller, while the enclosed impeller has the best stability. In addition, the optimum stability of rotor vibration can be observed in the closed impeller, semi-open impeller, and open impeller with similar stability of rotor vibration.

Xi et al. selected four commonly used operating conditions with opening angles to perform simulation calculations on the flow pattern of the water behind the valves at different flow rates. The flow pattern of the water flow is analyzed by three indicators: the streamline of the water flow, the uniformity of the flow velocity, and the head loss in the culvert. The result shows that the larger the opening angle of the flap valve, the less the head loss of the water flow in the outlet culvert, and the flow pattern of the water flow in the culvert gradually becomes better.

Chang et al. employed the Population Balance Model (PBM) to investigate the influence of different air voids and flow conditions on the performance self-priming centrifugal pumps. The result shows that the frequency of bubble coalescence at the shroud is higher. Meanwhile, the increment of flow conditions has a significant effect on reducing the pressure pulsation of the gas-liquid two-phase flow, while the improvement of the air voids destroys the instability and asymmetry of the internal flow of the two-phase flow. Therefore, this article can provide a certain theoretical reference for the study of air-liquid two-phase flow characteristics of self-priming centrifugal pumps.

Zhang et al. use a high-speed camera to visualize the flow field in a rotational hydrodynamic cavitation reactor (RHCR) in a closed cycle test rig, and the numerical simulation is carried out based on the RNG k-ε turbulence model and the Zwart-Gerber-Belamri (ZGB) cavitation model. Influence of hole diameter, hole height and hole cone bottom length on performance of RHCR are comprehensively investigated. The results show that the numerical results are in good agreement with the experimental data, which verifies the accuracy and reliability of the numerical method.

Jinwei et al. analyzes the jet characteristics of the jet mechanism with different openings (20, 40, 60, 80, 100%) under 4.8% eccentricity to study the effect of jet needle eccentricity on the jet, and verify the reliability of the research method. Then the focus is on the jet characteristics of the jet

mechanism at different eccentricities (0, 1, 2.1, 4.8, 8, and 14%) at 40% opening. The results show that as the eccentricity of the nozzle increases, the jet appears to be asymmetrical. The eccentricity of the water jet increases with the increase of the eccentricity of the needle; the efficiency of the injection mechanism gradually decreases, and the energy loss gradually increases.

Li et al. analyzed the internal flow field and particle motion law of a two-stage deep-sea lifting pump at different rotational speeds Through discrete element method-computational fluid dynamics. In addition, the physical phenomena, such as flow field velocity, secondary flow, and particle flow, were studied. The relationship between the rotational speed of the lifting pump and solid–liquid two-phase flow was investigated. An experiment on the hydraulic performance of the lift pump showed that the resulting lift and efficiency were consistent with the numerical simulation data.

Zhou et al. introduce three conventional unit startup processes. Combined with the optimal impulse control strategy, an optimized unit startup method is proposed. Though the CFD simulation and the dynamic stress tests, the equivalent stress characteristics and the peak value of the dynamic and static stresses of the blade under different startup processes is obtained. The validity of the model analysis is proved by the comparison between the simulation calculation and the measured results, and the effectiveness of the startup control strategy is proved. The optimization method of the startup process proposed can provide a basis for long-term stable operation of the hydropower unit.

In conclusion, this Research Topic provides an overview of the design and optimization for the improvement of pumps, turbines, valves, and other flow components. Many new theories and methods have been proposed and applied to improve hydraulic performance under this Research Topic through numerical simulations and experimental studies. We hope readers can find from this Research Topic some useful references for better understanding the research status of design, simulation and optimization of hydraulic machinery. Further development of new energy-saving technologies for hydraulic machinery is an inevitable trend for future industry.

Author contributions

All authors listed have made a substantial, direct, and intellectual contribution to the work and approved it for publication.

Conflict of interest

The authors declare that the research was conducted in the absence of any commercial or financial relationships that could be construed as a potential conflict of interest.

Publisher's note

frontiers in Energy Research

ORIGINAL RESEARCH
published: 16 December 2021
doi: 10.3389/fenrg.2021.813355

Experimental Study on the Relationship Between Cavitation and Lift Fluctuations of S-Shaped Hydrofoil

Haiyu Liu[1], Pengcheng Lin[1], Fangping Tang[1], Ye Chen[2], Wenpeng Zhang[3] and Shikai Yan[4]*

[1]College of Hydraulic Science and Engineering, Yangzhou University, Yangzhou, China, [2]JiangSu TaiHu Planning and Design Institute of Water Resources Co., Ltd, Suzhou, China, [3]Jining Water Conservancy Development Center, Jining, China, [4]Nanjing Water Planning and Designing Institute Corp., Ltd, Nanjing, China

In order to study the energy loss of bi-directional hydraulic machinery under cavitation conditions, this paper uses high-speed photography combined with six-axis force and torque sensors to collect cavitating flow images and lift signals of S-shaped hydrofoils simultaneously in a cavitation tunnel. The experimental results show that the stall angle of attack of the S-shaped hydrofoil is at ±12° and that the lift characteristics are almost symmetrical about +1°. Choosing α = +6° and α = −4° with almost equal average lift for comparison, it was found that both cavitation inception and cloud cavitation inception were earlier at α = −4° than at α = +6°, and that the cavitation length at α = −4° grew significantly faster than at α = +6°. When α = +6°, the cavity around the S-shaped hydrofoil undergoes a typical cavitation stage as the cavitation number decreases: from incipient cavitation to sheet cavitation to cloud cavitation. However, when α = −4°, as the cavitation number decreases, the cavitation phase goes through a developmental process from incipient cavitation to sheet cavitation to cloud cavitation to sheet cavitation to cloud cavitation, mainly because the shape of the S-shaped hydrofoil at the negative angle of attack affects the flow of the cavity tails, which is not sufficient to form re-entrant jets that cuts off the sheet cavitation. The formation mechanism of cloud cavitation at the two different angles of attack (α = +6°、 −4°) is the same, both being due to the movement of the re-entrant jet leading to the unstable shedding of sheet cavity. The fast Fourier analysis reveals that the fluctuations of the lift signals under cloud cavitation are significantly higher than those under non-cavitation, and the main frequencies of the lift signals under cloud cavitation were all twice the frequency of the cloud cavitation shedding.

Keywords: S-shaped hydrofoil, cloud cavitation, high-speed visualization, unsteady lift fluctuations, re-entrant jet

OPEN ACCESS

Edited by:
Lei Tan,
Tsinghua University, China

Reviewed by:
Changchang Wang,
Beijing Institute of Technology, China
Yabin Liu,
University of Edinburgh,
United Kingdom

****Correspondence:***
Fangping Tang
tangfp@yzu.edu.cn

Specialty section:
This article was submitted to Process and Energy Systems Engineering, a section of the journal Frontiers in Energy Research

Received: *11 November 2021*
Accepted: *02 December 2021*
Published: *16 December 2021*

Citation:
Liu H, Lin P, Tang F, Chen Y, Zhang W and Yan S (2021) Experimental Study on the Relationship Between Cavitation and Lift Fluctuations of S-Shaped Hydrofoil. Front. Energy Res. 9:813355. doi: 10.3389/fenrg.2021.813355

INTRODUCTION

The instability and shedding of sheet cavitation will cause noise and performance decline of hydraulic machinery, and severe shedding will cause vibration and material damage (Brennen, 1995; Franc and Michel, 2005; Luo et al., 2016). The evolution of cloud cavitation is not only a complex two-phase flow phenomenon, but also causes unsteady changes in performance of hydraulic machinery (Arndt, 2003; Zwart et al., 2004). In order to provide a theoretical basis for the performance change and efficiency improvement of rotating machinery under cavitation conditions, most of the researches were carried out on the basic unit foil of hydraulic machinery.

The cavitation tunnel experiment is the most direct way to obtain the cavitating flow phenomenon and lift-drag data of the hydrofoil (Foeth et al., 2006; Foeth et al., 2008). Knapp et al. (Knapp, 1955) predicted the existence of the re-entrant jets in cloud cavitation experiments. Kubota et al. (Kubota et al., 1989) used high-speed photography combined with Laser Doppler Anemometry to test that the cloud cavitation shedding is formed by a speed close to the hydrofoil surface that is opposite to the mainstream. Kawanami et al. (Kawanami et al., 1997) successfully prevented the generation of cloud cavitation by installing an obstacle on the surface of the hydrofoil, and verified the existence of the re-entrant jet from cavitating experiments. Wang et al. (Wang et al., 2001) carried out high-speed photography and LDV tests on three different stages of cavitation development, and studied the finger-like structure that accompanies the incipient cavitation, the large-scale shedding of sheet cavitation and the development of super-cavitation. This study provides a basis for understanding the lift variation of hydrofoil in different cavitation stages. The above research provides an experimental basis for understanding cloud cavitation flow and promotes the progress on the role of re-entrant jet in sheet cavitation shedding.

Leroux et al. (Leroux et al., 2004) found through high-speed photography that when the cavity length exceeds 0.5C, the development speed of the cavity length slows down. After the cavity length exceeds 0.7C, partial cavitation instability leads to shedding. Combined with the wall pressure pulsation test, it is found that this phenomenon is related to periodic fluctuations of the re-entrant jet. Leroux et al. (Leroux et al., 2005) further studied the dynamics of two kinds of cloud cavitation movement around 2D hydrofoil through numerical simulation combined with positive pressure fluid model, and found that re-entrant jet was still the main factor of cloud cavitation shedding, and the effect of shock wave could not be ignored. Dular et al. (Dular et al., 2004) used PIV to test the cavitation flow of the hydrofoil with sweeping leading edge, and analyzed the cavitation structure and the re-entrant jet with obvious three-dimensional effect, and verified the hypothesis; Huang et al. (Huang et al., 2014) obtained cavitation flow phenomenon around Clark-y through PIV technology and found that the periodic shedding of attached cavitation has an important influence on the development of vorticity in the flow field. By modifying the ZGB cavitation model, Sun et al. (Sun and Tan, 2020) accurately simulated the cavitation flow of the centrifugal pump under partial load, analyzed the mutual influence of cavitation, vortex and pressure fluctuation, and provided a new perspective for the study of cavitation in the pump. Xiao et al. (Xiao and Tan, 2020) adopted the design method of controllable velocity method to suppress the pressure pulsation in the impeller under different IGVFs, provides a new view for the design of hydraulic machinery under the condition of two-phase flow. These studies provide a reasonable theoretical and experimental basis for understanding the complex dynamic flow in cavitation flow.

Based on a large number of studies on the re-entrant jet and cloud cavitation, researchers began to adopt active/passive control methods to suppress the occurrence of cloud cavitation. In terms of active control, Yu et al. (Yu et al., 2021) studied the interaction between active ventilation and cloud cavitation around the hydrofoil, Kadivar et al. (Kadivar et al., 2018; Kadivar and Javadi, 2018; Kadivar et al., 2019) placed a cylindrical cavitating-bubble generators (CCGS)on the surface of CAV2003 hydrofoil. The CCGS generates a cavitation vortex in the wake flow to counteract the motion of the re-entrant jet, successfully delaying the shedding of cloud cavitation, and provide a three dimensional passive control design method to weaken the strength of re-entrant jet. In the research on TLV (Tip leakage vortex), Liu et al. (Liu and Tan, 2018; Liu and Tan, 2020) innovatively adopted the C groove method on the tip clearance side, and used the groove jet to impact TLV, which successfully weakened the primary and secondary TLV, providing a new idea for inhibiting TLV and improving the performance of the hydrofoil.

The S-shaped hydrofoil is mainly used in the design of bi-directional hydraulic machinery (Li et al., 2017; Ma et al., 2018; Živan et al., 2018; Zhang et al., 2021). Ramachandran et al. (Ramachandran et al., 1986) analyzed the lift-drag characteristics of four different reversible S-shaped foils in tidal power plant. They found that the S-shaped foil with a maximum camber value of 5% has the best cascade performance. Chacko et al. (Chacko et al., 1994) cut off the trailing edge of the foil by 3, 6, and 9% to study the forward and reverse performance. With the increase of the cutting length, the lift coefficient of forward condition increases, but the lift coefficient of reverse condition decreases. At the same time, the sharp trailing edge shape can improve the lift-drag in forward direction of flow. but the lift-drag in the reverse direction of flow will be deteriorated. This study provides a valuable reference for the design of asymmetric S airfoil.

The lift and drag performance of the S-shaped hydrofoil has been partially studied, and it was found that the lift of S-shaped hydrofoil would increase with the development of cavitation (Premkumar et al., 2014), contrary to the influence of cavitation on lift of conventional hydrofoil (Wang et al., 2001). These unusual changes in lift and drag may lead to bi-directional hydraulic machinery with different characteristics from other hydraulic machinery under cavitation conditions. Meanwhile, cavitation is a complex unsteady two-phase flow phenomenon, which requires further study on unsteady lift variation of S-shaped hydrofoil, especially the unsteady fluctuation characteristics of lift under cloud cavitation. In this paper, cavitation tests are performed on a symmetrical S-shaped hydrofoil. Based on the results of high-speed photography, the cavitation map of the S-shaped hydrofoil and the variation of the cavity length with the different cavitation number at two angles of attack ($\alpha = -4^{\circ}$and 6°) are drawn. At the same time, according to the lift-drag signal data, the correlation between lift-drag and cloud cavitation was analyzed, and the main frequency that caused the change of lift-drag around the S-shaped hydrofoil was revealed.

TABLE 1 | The parameters of the cavitation tunnel and the hydrofoil.

Parameter name	Value
Chord length	150 mm
Span length	100 mm
Tip clearance	0.15–0.20 mm
The maximum camber position	23%*C*、77%*C*
The maximum camber value	1.5C%
The maximum thickness position	50%*C*
The maximum thickness value	5%C
The acquisition frequency of cavitation images and lift data	7000 Hz
Angle of attack	-16° - +16°
Flow velocity	9 m/s
Range of cavitation number	0.25–2.00

EXPERIMENT

Experimental Setup

The cavitation study of the S-shaped hydrofoil was carried out in the cavitation tunnel of Yangzhou University. The main part of the cavitation cavern consists of a constriction section, a test section and a diffusion section and each has a length of 2, 1, 1.8 m. The test section has an inlet rectangular section size of 0.1 × 0.22 m^2 (width × height), The maximum inlet velocity of the test section can reach 15 m/s, and a steady running speed of between 4 and 12 m/s; The inlet pressure of the test section is controlled by a vacuum pump connected to the top of the water tank and the minimum inlet pressure can be reduced to 20 kPa. The lift data of the S-shaped hydrofoil is collected by the six-axis force and torque sensors with an acquisition frequency of 7,000 Hz, while the cavitating flow around the hydrofoil is recorded by a high-speed camera with an acquisition frequency of 7,000 Hz, both of which are connected to a computer for simultaneous acquisition. In addition, the cavitation tunnel can also record operating parameters such as water temperature, inlet and outlet pressure and flow rate in real time via corresponding sensors. **Figure 1** is the overall image and partial image of the cavitation tunnel.

The experimental object is a S-shaped hydrofoil commonly used in bi-directional pump design. The S-shaped hydrofoil is centrally symmetrical about the midpoint of the chord and the maximum thickness of the S-shaped hydrofoil is located at 23% C and 77% C respectively. The hydrofoil has a chord length of 150 mm and a span length of 100 mm. The test angle of attack is from −16° to +16° and the inlet cavitation number is from 2.00 to 0.25, The cavitation number σ is calculated as $\sigma = P_{in} - P_V/0.5\rho U_{\infty}^2$. The parameters of the cavitation tunnel and the hydrofoil used in this study are shown in **Table 1**.

Uncertainty Analysis

The total uncertainty of the cavitation tunnel is mainly determined by the uncertainty values of the individual test instruments. During the experiments, the parameters of the cavitation tunnel and the hydrofoil need to be recorded, mainly including: angle of attack, lift-drag signals, inlet and outlet pressure, flow rate and water temperature. The angle of attack of the hydrofoil is precisely adjusted by an in-house designed angle adjustment mechanism, the lift-drag signals is measured by the six-axis force and torque sensors from ATI. The inlet and outlet pressures are recorded by pressure transmitters. The water temperature during the experiment is recorded by a temperature sensor. The electromagnetic flowmeter records the operating flow rate used to calculate the inlet velocity of the test section.

Table 2 shows the uncertainty values for each instrument used in the cavitation tunnel. Based on these uncertainty values, the total uncertainty of the test system for the cavitation tunnel was calculated.

$$E_{\text{Total}} = \sqrt{E_S^2 + E_P^2 + E_A^2 + E_T^2 + E_E^2} = \pm 0.56\% \quad (1)$$

Where E_{Total} represents the total uncertainty of the cavitation tunnel, E_S represents the uncertainty of the six-axis force and torque sensors, E_P represents the uncertainty of the pressure transmitter, E_A represents the uncertainty of the angle adjustment mechanism, E_T represents the uncertainty of the temperature sensor, E_E represents the uncertainty of the electromagnetic flowmeter。

ANALYSIS OF EXPERIMENTAL RESULTS

Lift-Drag Characteristics of S-Shaped Hydrofoil at Different Angles of Attack

Usually when using S-shaped hydrofoil, the design process tends to flow through the convex surface first and then the concave surface. Therefore, the counterclockwise rotation direction is defined as the positive angle of attack. The positions of other geometric parameters of the S-shaped hydrofoil are all marked in **Figure 2**.

Figure 3 shows the lift-drag performance of the S-shaped hydrofoil for angles of attack from −16° to +16°. It should be noted that when the angle of attack is +16° or −16°, there is a distance of 69 mm between the hydrofoil and the upper and lower walls, and the limit of the angle of attack in cavitation test is −12°–12°, which will not cause blocking effect. As can be seen in **Figure 3**: the angle of attack for zero lift is at +1°. When the positive and negative angles of attack reach +12° and −12° respectively, the lift of the hydrofoil starts to decrease and the S-shaped hydrofoil reaches the stall angle of attack. The angle of attack for positive lift ranges from 1° to 11° and for negative lift from −12° to +1°. Negative lift operates at a wider range of angles of attack and has a greater maximum lift value than positive lift, however, the angle

TABLE2 | Uncertainty values for instruments.

Name	Range	Uncertainty
Six-axis force and torque sensors	0–1000 N	±0.1%
Pressure transmitter (inlet outlet)	0–200kPa	±0.1%
Angle adjustment mechanism	-180°–180°	±0.05%
Temperature sensor	-20–80°C	±0.5%
Electromagnetic flowmeter	0–500L/s	±0.2%
Total Uncertainty		±0.56%

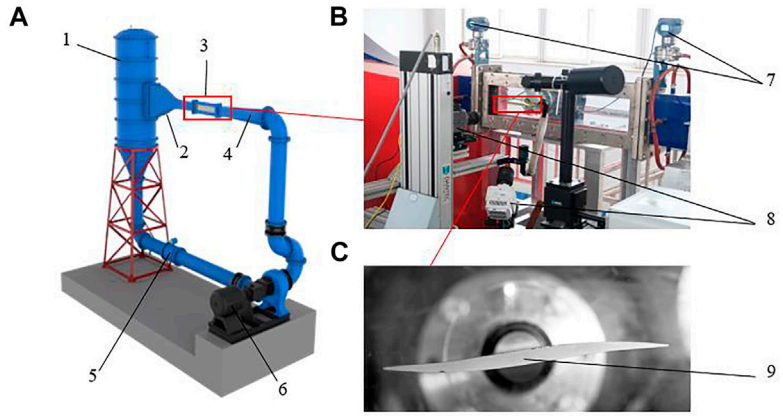

FIGURE 1 | (A) Sketch of the cavitation water tunnel **(B)** image of test section **(C)** the S-shaped hydrofoil. 1. Water tank 2. Shrink section 3. Test section 4. Diffusion section 5. Electromagnetic flowmeter. 6. Pump 7. Pressure sensor 8. High-speed camera 9. S-shaped hydrofoil.

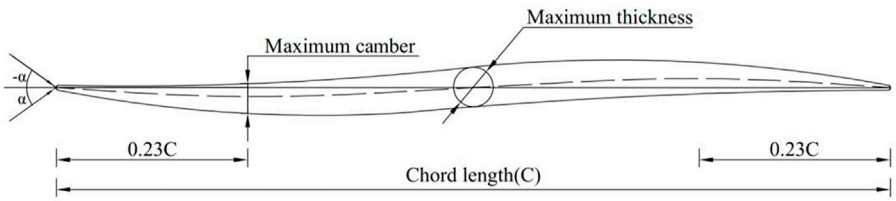

FIGURE 2 | Scheme of S-shaped hydrofoil operation.

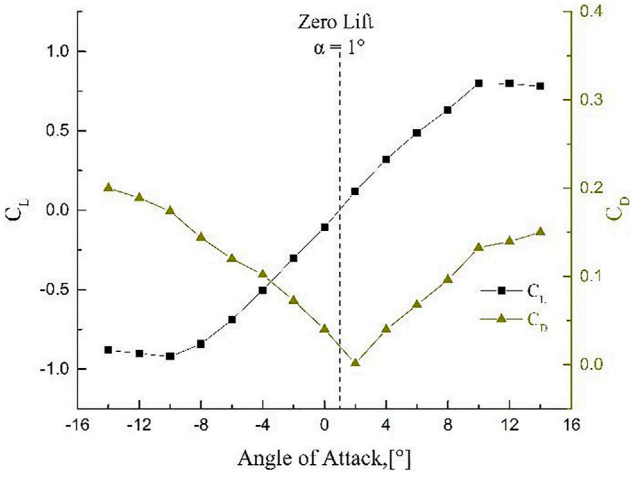

FIGURE 3 | Lift-drag performance of hydrofoil with different angles of attack.

of attack for positive lift corresponds to a lower drag value. For further comparison in this paper, the suction surface and pressure surface shown in **Figure 2** are defined uniformly.

The S-Shaped Hydrofoil Cavitation Mapping Analysis

According to the images measured by the high-speed photography experiment in the cavitation water tunnel, the cavitation maps at different angles of attack and different cavitation numbers as shown in **Figure 4** are drawn. **Figure 4** is mainly consists of cavitation contours with $l/C = 0.25$, $l/C = 0.5$, $l/C = 0.75$, and $l/C = 1$ and the sheet/cloud cavitation area. The shaded part is the region of cloud cavitation, and the blank part is the region of sheet cavitation. As is shown in **Figure 4A**: when $\alpha \in (0^{\circ},4^{\circ})$, the cavitation of S-shaped hydrofoil is always in the stage of sheet cavitation, mainly because the thickness of cavity is not enough to produce cloud cavitation. However, when $\alpha \in (4^{\circ},6^{\circ})$, the cavitation number of cloud cavitation inception increases gradually as the angle of attack increases and the cavity length develops to 0.75–1C. Due to the curvature of the latter part of the S-shaped hydrofoil is larger than that of the conventional hydrofoil, the strength of re-entrant jets at the tail of cavity is strengthened. Although the strength of the re-entrant jets still cannot cut off the cavity from the leading edge of the hydrofoil, it causes the holes from 0.5 to 1C to change into an unstable state, resulting in a periodic change in the cavity length from 0.5C to $l_{\circ}$ When α belongs to (6°, 10°), the sheet cavitation is always

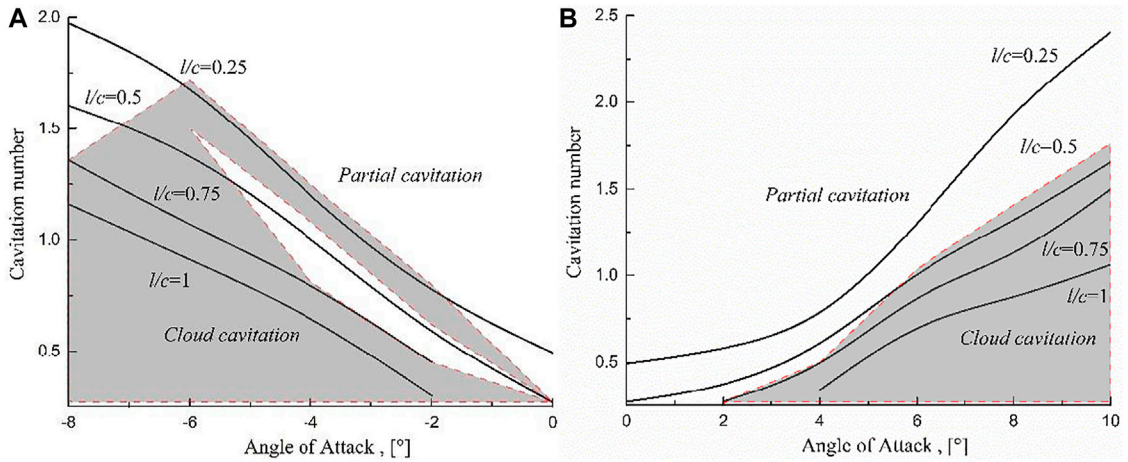

FIGURE 4 | Cavitation map of S-shaped hydrofoil at different angles of attack. (**(A)** negative angle of attack, **(B)** positive angle of attack).

transformed into cloud cavitation near the maximum cavity length developed to 0.25*l*.

As is shown in **Figure 4B**:when $\alpha \in (-6^{\circ},0^{\circ})$ and the cavity length reaches 0.5C, there is a phenomenon that cloud cavitation changes to sheet cavitation, mainly because the re-entrant jets at the tail of the cavity is affected by the S-shaped characteristics of the hydrofoil, and the sheet cavity cannot be cut off to form cloud shedding. Until the cavity length exceeds 0.75C, cloud cavitation can occur again. With the further decrease of the Angle of attack $\alpha \in (-8^{\circ},-6^{\circ})$, the influence of the shape of hydrofoil on the movement of the re-entrant jet weakens, and this phenomenon gradually disappears.

Relationship Between Cavitation Number and Cavity Length

Since $\alpha = +6^{\circ}$ is the common angle of attack designed for pumps, and the lift coefficients of the angles of attack of$+6^{\circ}$ and -4° are almost the same, these two angles of attack are selected for further comparison of cavitation performance. As is shown in **Figure 5** and **Figure 6**, first, the growth rate of the cavity length of $\alpha = -4^{\circ}$ obviously exceeds that of $\alpha = 6^{\circ}$. When the maximum cavity length is $l \in (0,0.5C)$, since the shape characteristics of the front half of the S-shaped hydrofoil are similar to the conventional hydrofoil, the development of cavitation is also similar. When $\alpha = -4^{\circ}$ and the maximum cavity length reaches 0.23 *l*, periodic cloud cavitation will occur. But when $\alpha = +6^{\circ}$ and the maximum cavity length reaches 0.27 *l*, periodic cloud cavitation will occur. The main reason is that at negative angle of attack, the pressure surface is more likely to induce vortex, which intensifies the generation and shedding of cavity and produces cavitation inception and cloud cavitation earlier than that at positive angle of attack. When the cavitation number further decreases, and the maximum cavity length develops between 0.5 and 0.75C, the cavitation has been in the cloud cavitation stage and the cycle time of cloud cavitation gradually increases at $\alpha = +6^{\circ}$. but when $\alpha = -4^{\circ}$, the cavitation stage in **Figures 5C,D** changes from cloud cavitation to "stable" sheet cavitation. Finally, when the maximum cavitation length is between 0.75C and C, The cavitation is still in the cloud cavitation stage at $\alpha = +6^{\circ}$.The cavitation is again transformed from sheet cavitation to periodic cloud cavitation at $\alpha = -4^{\circ}$.

Flow Characteristics of Cloud Cavitation

Two cavitation numbers with obvious periodicity of cloud cavitation were selected for detailed analysis. **Figure 7** is the cloud cavitation images recorded by high-speed photography, in which, the cavitation number in **Figure 7A** is 1.13, and that in **Figure 7B** is 0.98. The cycle time of cloud cavitation in **Figure 7A** is $T_{ref1} = 0.022$s, and the shedding frequency $f_1 = 45.5$ Hz. From $t = t_1$ to $t = t_4$, the cavitation around the hydrofoil is in the stage of sheet cavitation, and the maximum cavity length has developed to $l = 0.4$C, and the fog-like cavitation group of the last shedding period remains at the trailing edge. Under the joint movement of the re-entrant jets from the tail of cavity and the side-entrant jets on both sides of the wall, the vapor-liquid interface begins to become blurred, from the original smooth "mirror surface" with obvious boundaries to the non-smooth vapor-liquid mixture. When the re-entrant jets reach the leading edge of the hydrofoil, the sheet cavity can no longer maintain its maximum cavity length, and the sheet cavity is cut off from the leading edge, resulting in a large scale cloud shedding. From $t = t_5$ to $t = t_6$, after the large-scale cavity that has fallen off quickly leave the surface of the hydrofoil and moves towards the trailing edge of the hydrofoil as a cloud of vapor-liquid mixture. At the same time, the sheet cavity of the suction surface re-grows from the leading edge of the hydrofoil. From $t = t_7$ to $t = t_8$, the shed cloud cavity gradually breaks up after moving to the high pressure region, and the sheet cavity on the hydrofoil surface again reach the maximum cavity length of $l = 0.4$C. The sheet cavity again shows a mirror effect at the vapor-liquid interface and the

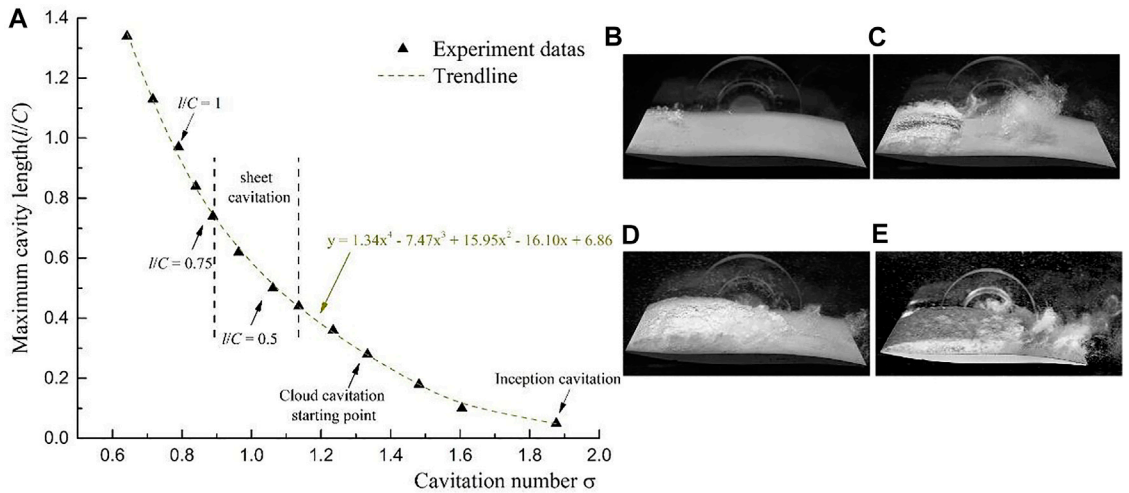

FIGURE 5 | The relationship between cavitation number and cavity length (U_∞ = 9 m/s, α = -4°).

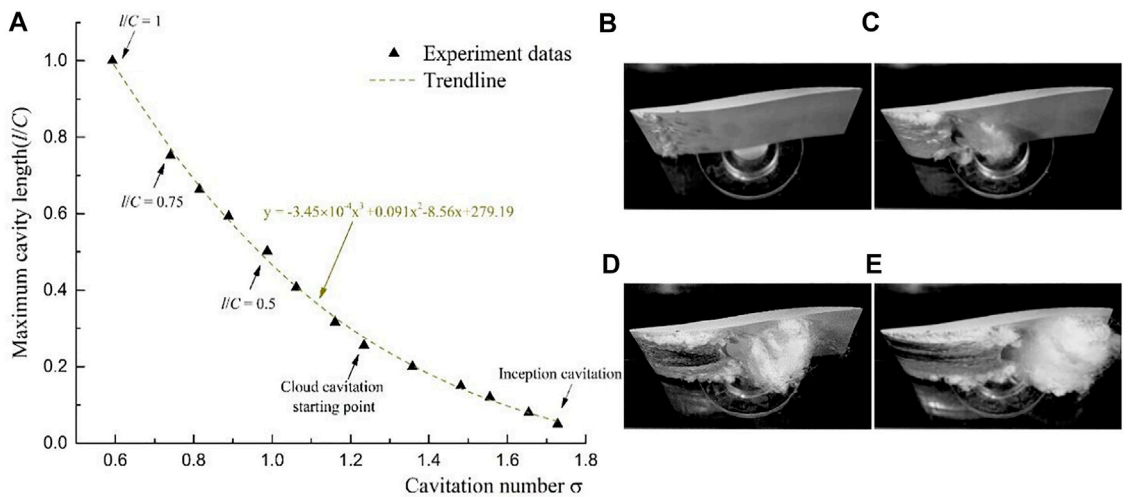

FIGURE 6 | The relationship between cavitation number and cavity length (U_∞ = 9 m/s, α = +6°).

cavitation on the hydrofoil surface is about to enter the next shedding cycle.

When the angle of attack is +6° and the cavitation number decreases to 0.98, the cycle time of cloud cavitation is T_{ref2} = 0.026 s, the shedding frequency of cloud cavitation f_2 = 38.4 Hz, and the maximum cavity length develops to 0.5C. The cloud cavitation phenomena at the two different angles of attack have similar motion characteristics, and both have experienced a cloud cavitation and shedding process from cavity growth to shedding to collapse (regrowth). The shedding of the sheet cavity at two different angles of attack is dominated by the movement of the re-entrant jet. Before the cavity is cut off by the re-entrant jet, the cavity surface will be impacted by the movement of the re-entrant jet from smooth "mirror" to a non-smooth gas-liquid mixture state. During the process of sheet cavity regrowth, smooth interface is formed on the cavity surface.

Evolution of Lift Fluctuations Caused by Cloud Cavitation

While recording the two cloud cavitation phenomena in **Figure 7**, a six-axis force and torque sensors was used to simultaneously collect the evolution in lift signals during a period of T = 1s. In **Figure 8** and **Figure 10**, the fluctuation range of lift signals in the non-cavitation condition is significantly lower than that in the cloud cavitation condition. In addition, the lift signal fluctuations at $\alpha = +6°$ is significantly greater than −4°, which may be caused by more intense flow-induced vortex around the S-shaped hydrofoil.

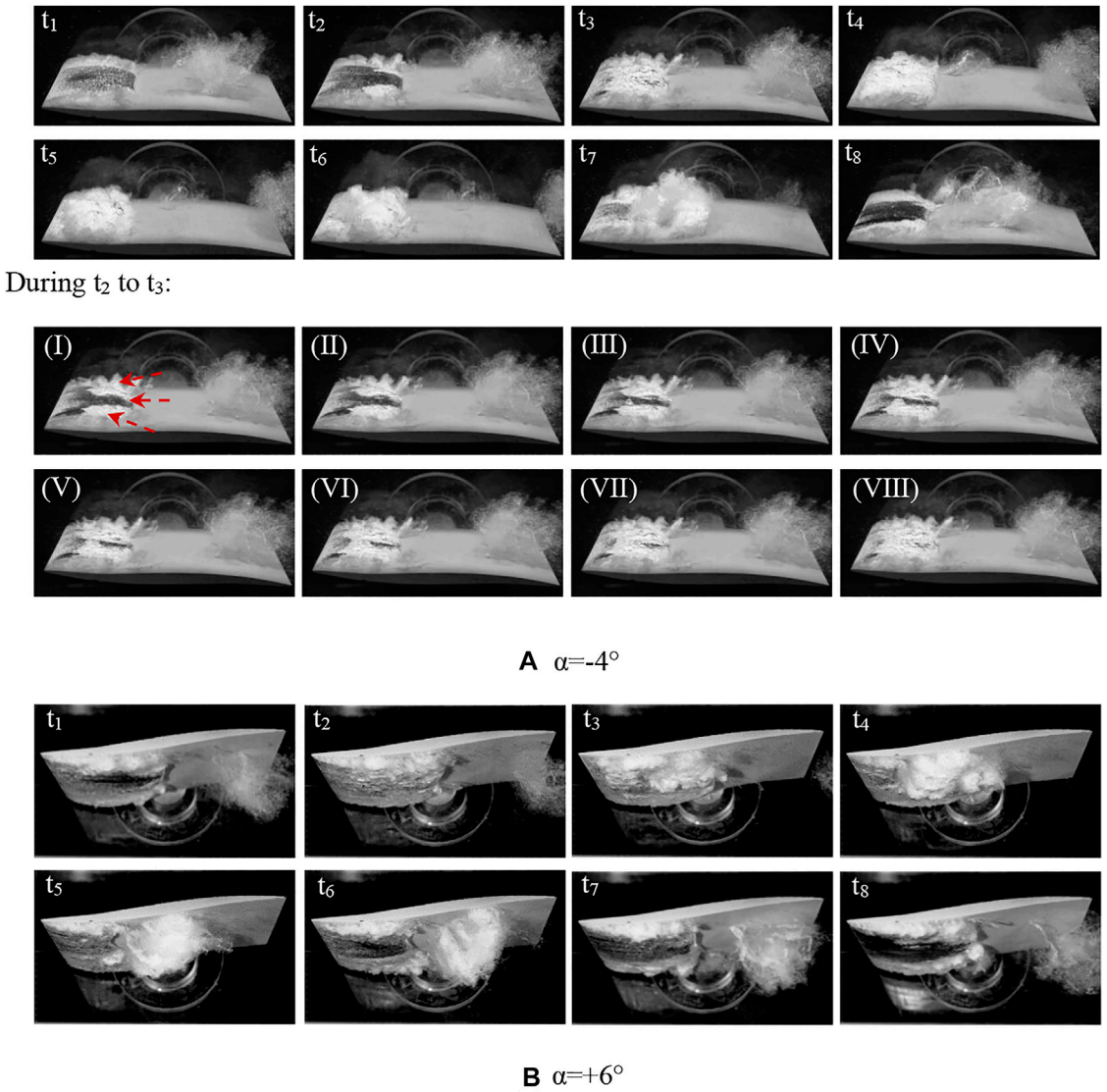

FIGURE 7 | The dynamic evolution of cloud cavitation (U_∞ = 9 m/s).

Apply the fast Fourier transform to process the four different fluctuating lift signals, and obtain the frequency spectra of the lift signals (**Figures 9A,B** and **Figures 11A,B**). As can be seen from **Figure 9**, in the non-cavitation condition, when $\alpha = -4^\circ$, the frequency of lift coefficient is widely distributed within 0–200 Hz and 400–1000 Hz. The amplitude of each frequency is small difference and there is almost no obvious main frequency. When $\alpha = +6^\circ$, the frequency spectra of the lift signals can clearly see that the main frequency is about 200 Hz and there is a lower amplitude distribution in the range of 200–700 Hz. There are obvious differences in the frequency spectra at different in the angle of attack, mainly due to the difference in vortex around S-shaped hydrofoil caused by the changes angles of attack, and it can be seen that the frequency domain distribution of **Figure 9A** is more stable than **Figure 9B**

Figure 10 is the original lift signals during the evolution of cloud cavitation. When cloud cavitation occurs, the lift signals change more dramatically, mainly because the evolution of cloud cavitation causes the change of pressure distribution on the hydrofoil surface, which affects the lift signals. Cloud cavitation is the main flow phenomenon around hydrofoil. The fluctuation of lift signals should be determined by the movement period of cloud cavitation, that is, the main frequency of lift signals is consistent with the frequency of cloud cavitation. The frequency spectra of lift signals (**Figure 10**) are shown in **Figure 11**. As can be seen in **Figure 11**, the main frequency of the lift signals in **Figure 11A** is f_{L1} = 93 Hz ≈ $2f_1$ and the main frequency of the lift signals in **Figure 11B** is f_{L2} = 77 Hz ≈ $2f_2$. The main frequency of the lift coefficient at two different angles of attack is

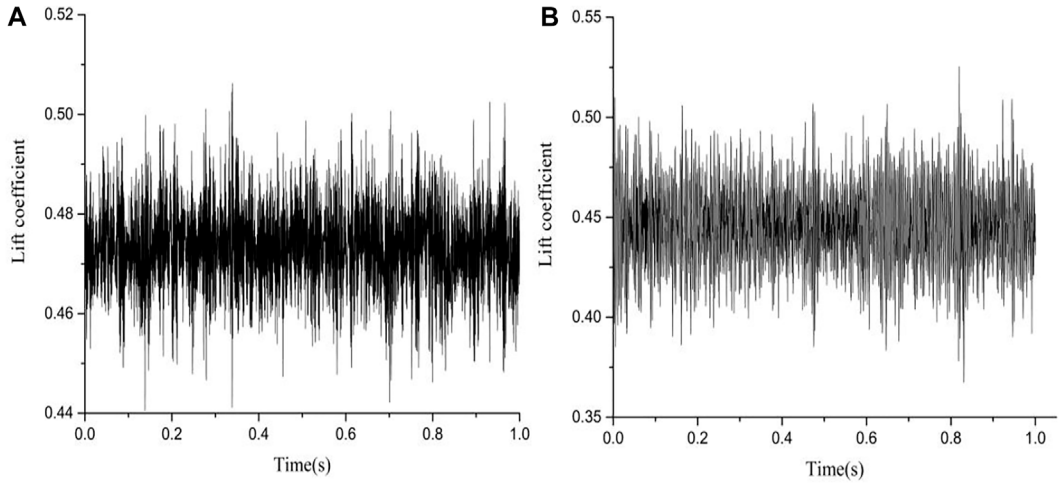

FIGURE 8 | Original lift signals at non-cavitation conditions. (**(A)** α = -4°, σ = 1.95、**(B)** α = 6°, σ = 1.95).

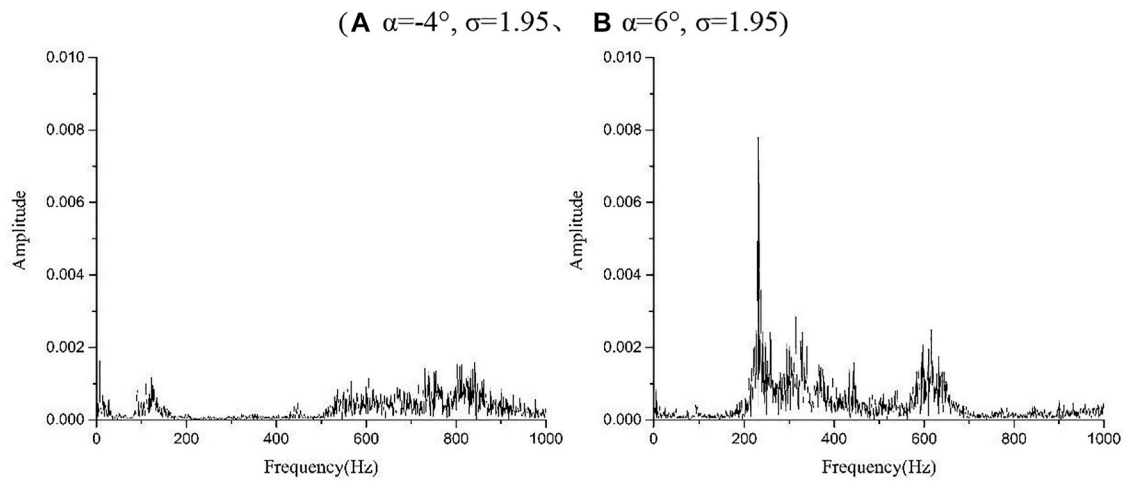

FIGURE 9 | Frequency spectra of the lift signals at non-cavitation conditions. (**(A)** α = -4°, σ = 1.95、**(B)** α = 6°, σ = 1.95).

twice the frequency of the cloud cavitation shedding. It means that in one cycle of cloud cavitation shedding, it causes two periodic fluctuations in the lift signals. At the same time, there are also frequency components of approximately 200–800 Hz in the frequency spectra of the cloud cavitation conditions.

CONCLUSION

In this paper, the lift and drag characteristics of S-shaped hydrofoil at different attack angles are recorded by cavitation tunnel, and the cavitation images at different cavitation numbers are collected by high speed photography. In order to further study the cavitation performance of S-shaped hydrofoil, two angles of attack ($\alpha = -4^{\circ}$ and $\alpha = +6^{\circ}$) were selected to conduct detailed comparison from three aspects: cavity length, cloud cavitation movement and lift signal fluctuation.

(1) Under non-stalling conditions, the angle of attack of negative lift has a wider operation range and the maximum lift value is larger than the angle of attack of positive lift, but the drag corresponding to the angle of attack of positive lift is smaller. If bi-directional hydraulic machinery pursues the highest efficiency, it is recommended to choose a positive angle of attack for design.
(2) The cavitation map of S-shaped hydrofoil shows that regardless of positive or negative angle of attack, cloud cavitation always occurs when the maximum cavity length

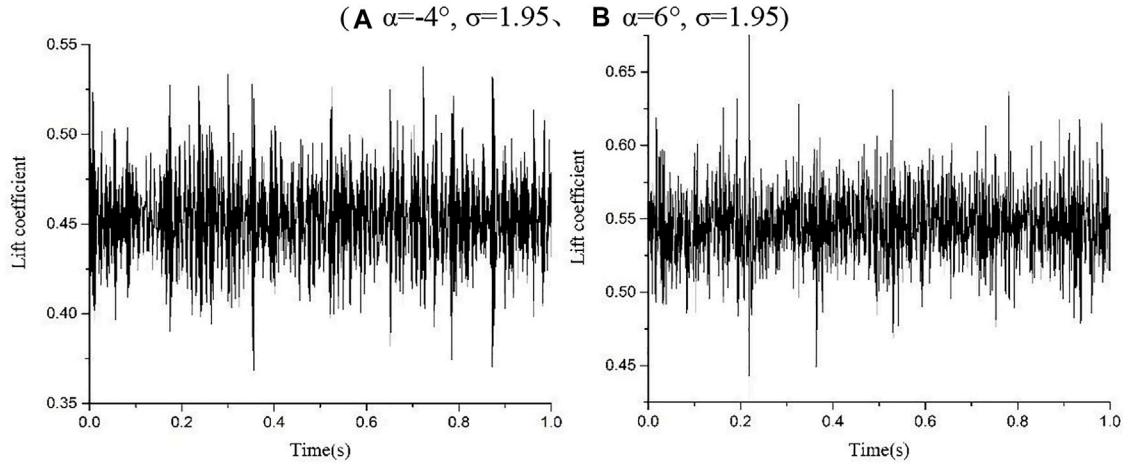

FIGURE 10 | Original lift signals at cloud cavitation conditions.

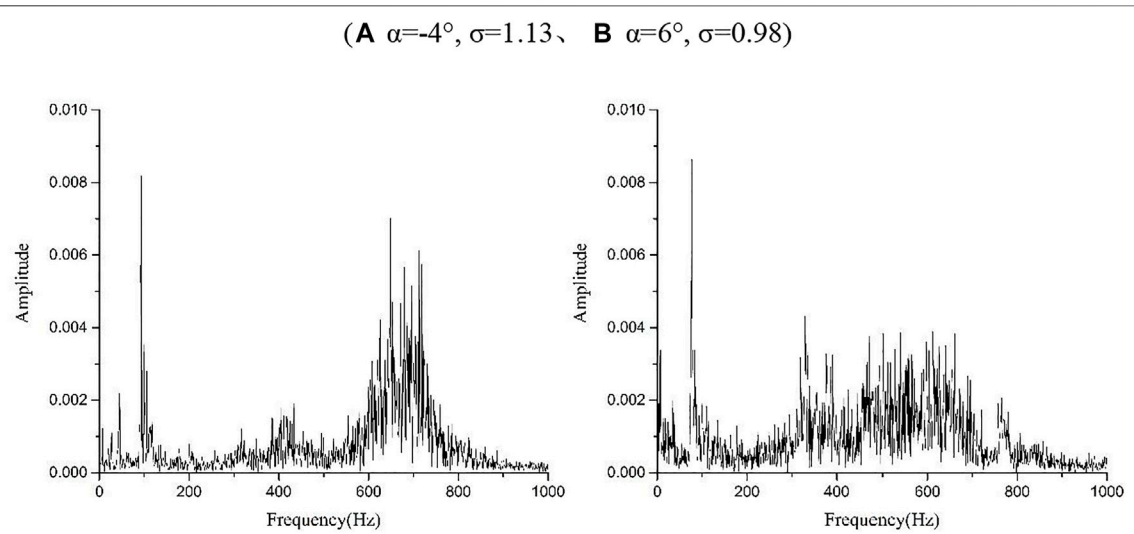

FIGURE 11 | Frequency spectra of the lift signals at cloud cavitation conditions. (**(A)** α = -4°, σ = 1.13、**(B)** α = 6°, σ = 0.98)

develops to about 0.25 *l*, The development of cavitation at the positive angle of attack is similar to that of the conventional hydrofoil, but there is an unconventional phenomenon at negative angle of attack $\alpha \in (-6^{\circ}, 0^{\circ})$: During the process of cavitation number decreases, the cavitation will change from cloud cavitation to sheet cavitation.

(3) Both incipient cavitation and cloud cavitation inception at $\alpha = -4^{\circ}$ are earlier than that at $\alpha = +6^{\circ}$, and the growth rate of cavity length at $\alpha = -4^{\circ}$ is obviously faster than that at $\alpha = +6^{\circ}$. However, when the maximum cavity length $l \in$ (0.5C, 0.75C), cloud cavitation changes to sheet cavitation at $\alpha = -4^{\circ}$. For bi-directional hydraulic machinery that may operate under severe cavitation conditions, the angle of attack of -4° can be considered in the design.

(4) The formation mechanism of cloud cavitation at two different angles of attack is the same, both of which are caused by the instability and shedding of sheet cavity due to the motion of the re-entrant jet. The lift fluctuations of $\alpha = +6^{\circ}$ obviously exceed $\alpha = -4^{\circ}$ at the non-cavitation conditions. After the occurrence of cloud cavitation, the main frequency of lift signals at two angles of attack is half of the shedding frequency of cloud cavitation. This phenomenon means that the unsteady performance of bi-directional hydraulic machinery designed with S-shaped hydrofoil may be different from that designed with conventional hydrofoil under cavitation conditions.

In this paper, the movement details of the re-entrant jet and the reasons for the evolution of the lift signals are still not

very clear. Those phenomena may be related to the change of surface pressure caused by the unique S-shape of hydrofoil, and we will discuss the internal flow through numerical simulation combined with experimental data in future work to provide a basis for the study of cavitation flow in bi-directional hydraulic machinery.

DATA AVAILABILITY STATEMENT

The original contributions presented in the study are included in the article/Supplementary Material, further inquiries can be directed to the corresponding author.

AUTHOR CONTRIBUTIONS

HL completed the writing and experiment part, PL completed the data processing, FT provided theoretical guidance and financial support, Ye chen helped to modify the article, WZ and SY provided the experimental guidance.

FUNDING

A project funded by the Priority Academic Program Development (PAPD) of Jiangsu Higher Education Institutions Support for construction.

REFERENCES

Arndt, R. E. A. (2003). Cavitation in Vortical Flows. *Annu. Rev. Fluid Mech.* 34 (1), 143–175. doi:10.1146/annurev.fluid.34.082301.114957

Brennen, C. E. (1995). *Cavitation and Bubble Dynamics*. New York: Oxford University Press.

Chacko, B., Balabaskaran, V., Tulapurkara, E. G., and Radha Krishna, H. C. (1994). Performance of S-Cambered Profiles with Cut-Off Trailing Edges. *J. Fluids Eng.* 116, 522–527. doi:10.1115/1.2910308

Dular, M., Bachert, R., Stoffel, B., and Širok, B. (2004). Experimental Evaluation of Numerical Simulation of Cavitating Flow Around Hydrofoil. *Eur. J. Mech. B-fluid* 24, 522–538. doi:10.1016/j.euromechflu.2004.10.004

Foeth, E. J., van Doorne, C. W. H., van Terwisga, T., and Wieneke, B. (2006). Time Resolved PIV and Flow Visualization of 3D Sheet Cavitation. *Exp. Fluids* 40, 503–513. doi:10.1007/s00348-005-0082-9

Foeth, E. J., van Terwisga, T., and van Doorne, C. (2008). On the Collapse Structure of an Attached Cavity on a Three-Dimensional Hydrofoil. *J. Fluids Eng.-Trans. ASME* 130, 071303. doi:10.1115/1.2928345

Franc, J. P., and Michel, J. M. (2005). *Fundamentals of Cavitation*. Netherlands: Springer.

Huang, B., Zhao, Y., and Wang, G. (2014). Large Eddy Simulation of Turbulent Vortex-Cavitation Interactions in Transient Sheet/cloud Cavitating Flows. *Comput. Fluids* 92, 113–124. doi:10.1016/j.compfluid.2013.12.024

Kadivar, E., and Javadi, K. "Effect of Cavitating-Bubble Generators on the Dynamics of Unsteady Cloud Cavitation," in Proceedings of the Marine Industries Conference, Edinburgh, September 2018.

Kadivar, E., Moctar, O. E., and Javadi, K. (2018). Investigation of the Effect of Cavitation Passive Control on the Dynamics of Unsteady Cloud Cavitation. *Appl. Math. Model.* 64, 333–356. doi:10.1016/j.apm.2018.07.015

Kadivar, E., Moctar, O. E., and Javadi, K. (2019). Stabilization of Cloud Cavitation Instabilities Using Cylindrical Cavitating-Bubble Generators (CCGs). *Int. J. Multiphase Flow* 115, 108–125. doi:10.1016/j.ijmultiphaseflow.2019.03.019

Kawanami, Y., Kato, H., Yamaguchi, H., Tanimura, M., and Tagaya, Y. (1997). Mechanism and Control of Cloud Cavitation. *J. Fluids Eng.-Trans. ASME* 119, 788–794. doi:10.1115/1.2819499

Knapp, R. T. (1955). Recent Investigations of the Mechanics of Cavitation and Cavitation Damage. *J. Fluids Eng.-Trans. ASME* 77, 1045–1054.

Kubota, A., Kato, H., Yamaguchi, H., and Maeda, M. (1989). Unsteady Structure Measurement of Cloud Cavitation on a Foil Section Using Conditional Sampling Technique. *J. Fluids Eng.-Trans. ASME* 111, 204–210. doi:10.1115/1.3243624

Leroux, J.-B., Astolfi, J. A., and Billard, J. Y. (2004). An Experimental Study of Unsteady Partial Cavitation. *J. Fluids Eng.* 126, 94–101. doi:10.1115/1.1627835

Leroux, J.-B., Coutier-Delgosha, O., and Astolfi, J. A. (2005). A Joint Experimental and Numerical Study of Mechanisms Associated to Instability of Partial Cavitation on Two-Dimensional Hydrofoil. *Phys. Fluids* 17 (5), 052101. doi:10.1063/1.1865692

Li, D., Wang, H., Qin, Y., Han, L., Wei, X., and Qin, D. (2017). Entropy Production Analysis of Hysteresis Characteristic of a Pump-Turbine Model. *Energ. Convers. Manag.* 149, 175–191. doi:10.1016/j.enconman.2017.07.024

Liu, Y., and Tan, L. (2020). Influence of C Groove on Suppressing Vortex and Cavitation for a NACA0009 Hydrofoil with Tip Clearance in Tidal Energy. *Renew. Energ.* 148, 907–922. doi:10.1016/j.renene.2019.10.175

Liu, Y., and Tan, L. (2018). Method of C Groove on Vortex Suppression and Energy Performance Improvement for a NACA0009 Hydrofoil with Tip Clearance in Tidal Energy. *Energy* 155, 448–461. doi:10.1016/j.energy.2018.04.174

Luo, X.-W., Ji, B., and Tsujimoto, Y. (2016). A Review of Cavitation in Hydraulic Machinery. *J. Hydrodyn.* 28, 335–358. doi:10.1016/s1001-6058(16)60638-8

Ma, P., Wang, J., and Wang, H. (2018). Investigation of Performances and Flow Characteristics of Two Bi-directional Pumps with Different Airfoil Blades. *Sci. China Technol. Sci.* 61, 1588–1599. doi:10.1007/s11431-017-9195-x

Premkumar, T. M., Kumar, P., and Chatterjee, D. (2014). Cavitation Characteristics of S-Blade Used in Fully Reversible Pump-Turbine[J]. *J. Fluids Eng.* 136 (5), 051101. doi:10.1115/1.4026441

Ramachandran, R., Krishna, H., and Narayana, P. (1986). Cascade Experiments over "S" Blade Profiles. *J. Energ. Eng.* 112 (1). doi:10.1061/(asce)0733-9402(1986)112:1(37)

Sun, W. H., and Tan, L. (2020). Cavitation-Vortex-Pressure Fluctuation Interaction in a Centrifugal Pump Using Bubble Rotation Modified Cavitation Model under Partial Load[J]. *J. Fluids Eng.* 142, 051206. doi:10.1115/1.4045615

Wang, G., Senocak, I., Shyy, W., Ikohagi, T., and Cao, S. (2001). Dynamics of Attached Turbulent Cavitating Flows. *Prog. Aerospace Sci.* 37, 551–581. doi:10.1016/s0376-0421(01)00014-8

Xiao, W., and Tan, L. (2020). Design Method of Controllable Velocity Moment and Optimization of Pressure Fluctuation Suppression for a Multiphase Pump. *Ocean Eng.* 220 (2), 108402. doi:10.1016/j.oceaneng.2020.108402

Yu, A., Qian, Z., Wang, X., Tang, Q., and Zhou, D. (2021). Large Eddy Simulation of Ventilated Cavitation with an Insight on the Correlation Mechanism between Ventilation and Vortex Evolutions. *Appl. Math. Model.* 89, 1055–1073. doi:10.1016/j.apm.2020.08.011

Zhang, X., Tang, F., Liu, C., Shi, L., Liu, H., Sun, Z., et al. (2021). Numerical Simulation of Transient Characteristics of Start-Up Transition Process of Large Vertical Siphon Axial Flow Pump Station. *Front. Energ. Res.* 9, 706975. doi:10.3389/fenrg.2021.706975

Živan, S., Miloš, J., and Jasmina, B. J. (2018). Design and Performance of Low-Pressure Reversible Axial Fan with Doubly Curved Profiles of Blades. *J. Mech. Sci. Technol.* 32, 3707–3712.

Zwart, P. J., Gerber, A. G., and Belamri, T. "A Two-phase Flow Model for Predicting Cavitation Dynamics," in Proceedings of International Conference on Multiphase Flow, Yokohama, Japan, May-June 2004.

Conflict of Interest: The author YC was employed by the company JiangSu TaiHu Planning and Design Institute of Water Resources Co., Ltd. The author SY was employed by the company Nanjing Water Planning and Designing Institute Corp., Ltd.

The remaining authors declare that the research was conducted in the absence of any commercial or financial relationships that could be construed as a potential conflict of interest.

Publisher's Note: All claims expressed in this article are solely those of the authors and do not necessarily represent those of their affiliated organizations, or those of the publisher, the editors and the reviewers. Any product that may be evaluated in this article, or claim that may be made by its manufacturer, is not guaranteed or endorsed by the publisher.

GLOSSARY

Notation

α = Angle of attack (°)

C = Chord length (m)

l = Cavity length (along the hydrofoil center line) (m)

σ = Cavitation number

f_1, f_2 = Cloud cavitation frequency (Hz)

f_{L1}, f_{L2} = Lift pulsation frequency (Hz)

T_{ref1}, T_{ref2} = The cycle time of cloud cavitation at α = -4°,+6° (s)

t = Different moments in cloud cavitation (s)

C_L, C_D = Lift coefficient, drag coefficient

P_{in} = The inlet pressure (Pa)

P_v = The saturated vapor pressure (Pa)

U_∞ = The inlet velocity (m/s)

E_{Total} = The total uncertainty of the cavitation tunnel

Es = The uncertainty of the six-axis force and torque sensors

E_P = The uncertainty of the temperature sensor

E_A = The uncertainty of the angle adjustment mechanism

E_T = The uncertainty of the temperature sensor

E_E = The uncertainty of the electromagnetic flowmeter

frontiers in Energy Research

ORIGINAL RESEARCH
published: 11 January 2022
doi: 10.3389/fenrg.2021.825159

Numerical Analysis of a New Type of Dishwasher Pump for Different Rotation Speeds of the Volute

Chao Ning[1], *Yalin Li*[1]*, *Ping Huang*[1], *Hui Xu*[2] *and Feng Zheng*[2]

[1]National Research Center of Pumps, Jiangsu University, Zhenjiang, China, [2]Ningbo FOTILE Kitchen Ware Co., Ltd., Ningbo, China

The interaction between impeller and volute produces a complex and unsteady water flow. It involves the interference of the non-uniform flow (such as the impeller's jet wake and a secondary flow). In this paper, the transient flow in a new type of dishwasher pump is investigated numerically. In addition, pressure measurements are used to validate the numerical method, and the simulation results agree well with the experiment. Three schemes, 0 rpm (revolutions per minute)/30 rpm/60 rpm, of volute speeds are investigated. Multiple monitoring points are set at different positions of the new dishwasher pump to record pressure-pulse signals. In addition, frequency signals are obtained using a Fast Fourier Transform, which is then used to analyze the effect of the volute tongue and the outflow of the impeller. The radial force on the principal axis is recorded, and the schemes with different rotation speeds of volute are compared. The results show that the volute speed has only a small effect on the pump performance. In addition, the speed of the volute mainly affects the flow field in the transition section located between impeller and volute. The difference of the flow field in the impeller depends on the relative position between the impeller and the volute. The time domain curve for the pressure pulse is periodic, and there is a deviation between the peak for the schemes in the outflow region. In the frequency domain, the characteristic frequency equals the blade passing frequency. In the outflow region, the effect of the volute speeds increases with increasing volute speed. For the radial force, the rotating volute strengthens the fluctuation of the radial force, which affects the operational stability of the pump. The shape of the vector distribution is most regular for the 30 rpm scheme, which indicates that the stability of the pump is the highest. This paper can be used to improve both the control and selection of volute speeds.

Keywords: dishwasher pump, pressure fluctuation, compound impeller, twin volute, radial force

OPEN ACCESS

Edited by:
Xiaojun Li,
Zhejiang Sci-Tech University, China

Reviewed by:
Denghao Wu,
China Jiliang University, China
Chuan Wang,
Yangzhou University, China

***Correspondence:**
Yalin Li
ylli@ujs.edu.cn

Specialty section:
This article was submitted to Process and Energy Systems Engineering, a section of the journal Frontiers in Energy Research

Received: *30 November 2021*
Accepted: *20 December 2021*
Published: *11 January 2022*

Citation:
Ning C, Li Y, Huang P, Xu H and Zheng F (2022) Numerical Analysis of a New Type of Dishwasher Pump for Different Rotation Speeds of the Volute. Front. Energy Res. 9:825159. doi: 10.3389/fenrg.2021.825159

INTRODUCTION

Electric dishwashers are commonly used in private households as well as commercially. Unfortunately, due to their relatively complex pipe-systems, conventional dishwashers can easily accumulate dirt and often suffer from substantial flow-reduction speeds and poor spray-power. Therefore, the removal of the pipeline (to enable an effective cleaning-function) is an important development goal. Nowadays, the application of computational fluid dynamics (CFD) is commonly used to study and improve dishwashers. Researchers have already carried out several detailed and

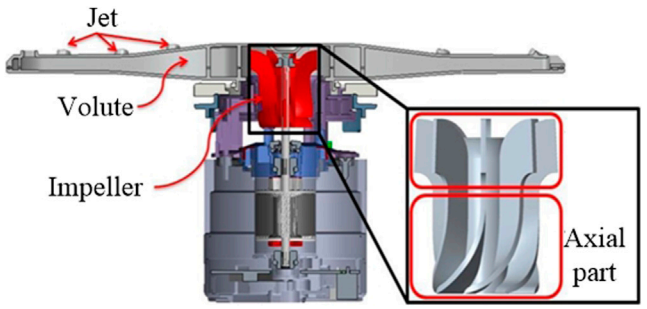

FIGURE 1 | Physical model of new type dishwater pump.

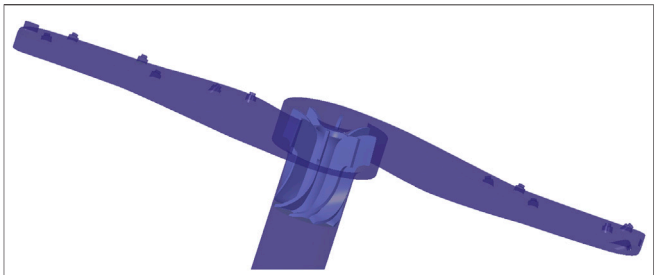

FIGURE 2 | Computational domains of the new type dishwater pump.

systematic studies of the key parts of dishwashers (Dedoussis and Giannatsis, 2004; Santori et al., 2013; Pérez-Mohedano et al., 2015; Minde, 2016; Pérez-Mohedano et al., 2017), and their results indicate that the water-movement analysis plays a very important role in performance studies. The new type of dishwasher pump, which is described in this paper, uses an open cleaning concept to enable cleaning without pipelines in the water tank. As shown in **Figure 1**, the impeller is made of a special composite structure without noticeable front and rear cover-plates, and the volute is a single volute with a long tongue within a 180° array to form twin volute. The pump outlet consists of nozzles that are arranged at different positions and directions on the volute. Driven by the rotating impeller, the fluid flows into the volute and generates a speed torque that causes the volute to rotate. Thanks to the combination of volute flow channel with pipeline spray, the cleaning system has no pipeline, which shortens the cleaning time and saves both water and electricity.

Due to movement between impeller and volute, the outflow of the impeller interacts with the flow in the volute. The unsteady interaction between these components generates pressure pulses, which create unsteady dynamic forces. These unsteady dynamic forces give rise to vibration of the pump components and generate hydraulic noise (Majidi, 2005; Zhou et al., 2021; Zhu et al., 2021). The interaction between these components produces a complex unsteady flow, which involves the interference of non-uniform flow (such as impeller jet wake) with a secondary flow. The dynamic pulses have a strong impact on the internal flow loss as well as operational stability. Many studies focused on the dynamic pulses in pumps (Long et al., 2020; Peng et al., 20212021; Ye et al., 2021; Zhang et al., 2021). Barrio et al. (2008) studied the dynamic pulse mechanism by varying the radial gap of the tongue. Their results show that the gap reduction led to greater pressure-increments. Chen et al. (Chu et al., 1995) investigated the effect of a thick blade on the matching performance of impeller and volute. The group found that the pressure depends on the orientation between the impeller and the tongue. Li et al. (Spence and Amaral-Teixeira, 2008) tested the flow between impeller and volute of a centrifugal pump with large outlet angle. Spence et al. (Spence and Amaral-Teixeira, 2009) analyzed the effect of dynamic pulses on the overall performance using several geometric parameters for the impeller. The cutwater gap and vane arrangement were found to exert the biggest effect. Liu et al. (Liu et al., 2012) used a large-eddy simulation to investigate the effect of the impeller type on the pressure-pulse mechanism of a double suction pump. They found that a staggered arrangement of impellers helped improve the pressure fluctuation for the volute. Solis et al. (2009) changed the clearance between impeller and volute by changing the angle of the tongue, and a k-ω SST model was used to study the dynamic pulse mechanism. Zhu et al. (2011a) conducted a study of the dynamic pulse mechanism by changing the diameter of the volute's base circle and the clearance between impeller and tongue. Guo et al. (Guo and Okamoto, 2003) and González et al. (2003) analyzed the effect of the throat area on the performance and internal flow of a centrifugal pump. This was done by changing the tongue type and the tongue angle. Then, Zhu et al. (2011b) compared the effect of different types of tongues on the dynamic pulses of the pump. Their results show that the pressure fluctuation and the radial forces decrease when middle- and short-tongues were used. Choi (2008) studied the dynamic pulses flow field for an annular volute, a spiral volute, and different types of diffusers using Particle Image Velocimetry (PIV), and they analyzed the vortex and secondary flow that occurs within the impeller passage. Yang et al. (2009) studied the dynamic pulse mechanism in a double volute pump and found that the radial force on the impeller was unsteady—especially at small flow rates.

The above articles help better understand and improve the pulsation mechanism in pumps. However, the blade type of the impeller in these studies was mostly the backward-bending type (Shi et al., 2020; Wang et al., 2021), and there are no relevant studies of the compound impeller at present. Moreover, they mainly focused on the angle of the tongue, the tongue type, and

TABLE 1 | Parameters and corresponding design values.

Parameters	Value
Design flow rate Q (L/min)	55
Number of impeller Blades Z	8
Impeller rotating speed n (rpm)	3,000
Diameter of inlet pipe $D_{1\ (mm)}$	33
Diameter of impeller inlet D_2 (mm)	32
Diameter of impeller outlet b_1 (mm)	43.3
Outlet width of impeller b_2 (mm)	14.15
Inlet width of volute b_3 (mm)	17.8
Angle of tongue (°)	34

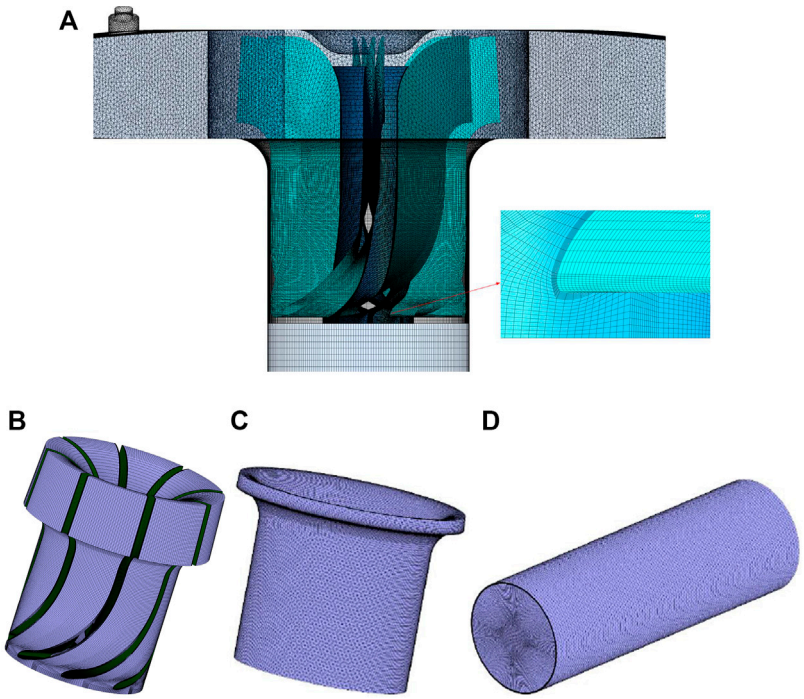

FIGURE 3 | Mesh of the new type dishwater pump **(A)** Computational zone **(B)** Mesh of impeller **(C)** Mesh of tip **(D)** Mesh of inlet pipe.

TABLE 2 | Mesh independence.

	Inlet pipe	Volute	Impeller	Tip	Head
Mesh1	164	448	229	124	1.65
Mesh2	215	448	290	140	1.57
Mesh3	241	448	305	208	1.56

the volute profile in the aspect of the volute. However, the tongue and outlet of the double volute were still one, and the structure of a twin volute is clearly different from a double volute. According to Zheng et al. (2015), the interference between the outflow of impeller and volute is more significant due to increasing number of tongues (in the case of multi-tongue or multi-channel systems). Therefore, the dynamic pulsation of a twin volute should be stronger, theoretically.

In this paper, 3D unsteady numerical simulations were performed to study the secondary flow development (which is due to the interaction between impeller and volute). A change in the circumferential relative positions of impeller and volute is expected to have a clear impact on the fluid. In addition, the upstream- and downstream-flows are affected due to interference with the flow. To reveal both the interference effect of the twin volute and the effect of different volute speeds on the internal flow of the new dishwasher pump, the detailed flow-patterns and radial velocities (for the volute cross-section) were determined via the numerical simulation. In addition, the pressure fluctuation in the tongue region and the outflow of impeller were measured to clarify the effect of volute speed. Finally, the laws for the radial force at different volute speeds were analyzed. The study was organized as follows: The numerical model and setup are clarified in *Numerical Model and Simulation Setup*. *Experimental Setup* describes the experimental detection method, and the effect of volute rotation speed is analyzed in *Results and Discussion*. Conclusions are summarized in *Conclusion*.

NUMERICAL MODEL AND SIMULATION SETUP

Pump Model

Figure 2 shows the computational domains, which consist of suction pipe, impeller, and volute. The complex impeller consists of an axial flow cascade at the bottom, and a centrifugal blade at the top. The key parameters and corresponding target parameters for this pump are listed in **Table 1**.

A clearance of 0.5 mm was set between the axial flow cascade and the end wall at the axial part of the compound impeller. The inlet was simplified to a straight pipe, and the diameter of the end wall D_3 was equal to the inlet pipe diameter D_2.

Governing Equations

The commercial finite-volume solver ANSYS Fluent 19.0 was used to simulate the incompressible flow for the new dishwasher pump. The continuity equation was solved using the k-ω based Shear-Stress-Transport (SST) model published by Menter (Menter, 1994) because it can accurately predict the flow pattern near wall-regions. The turbulence model was used as a closure for the Reynolds-averaged Navier-Stokes solver to enable

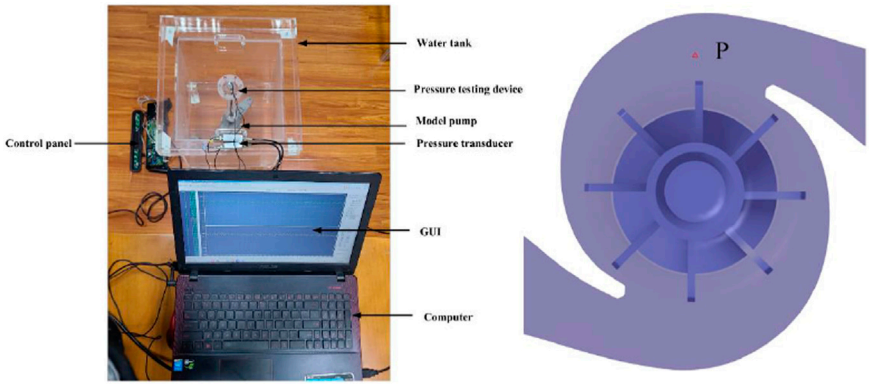

FIGURE 4 | Pressure measurements system setup and position of monitoring point P.

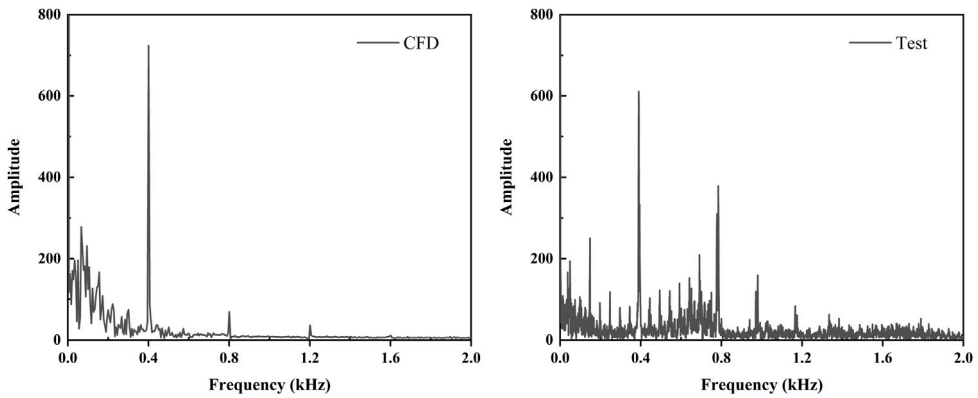

FIGURE 5 | Frequency domain diagram of pressure fluctuation obtained from the numerical simulation and test at the monitoring point P under rated conditions.

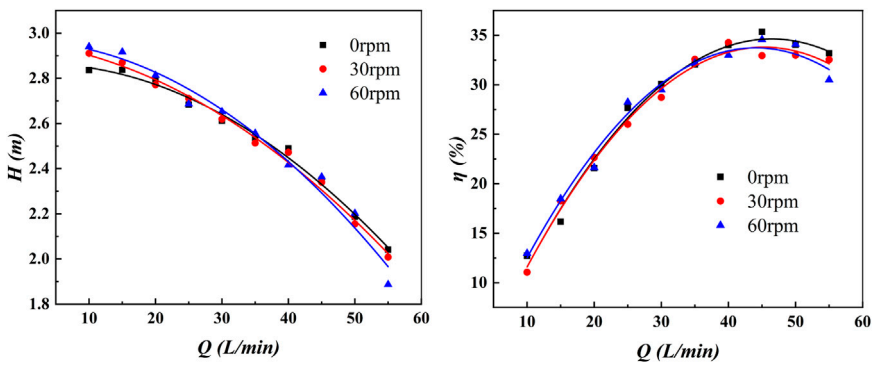

FIGURE 6 | Performance curves *Q-H* and *Q-η* obtained by simulation.

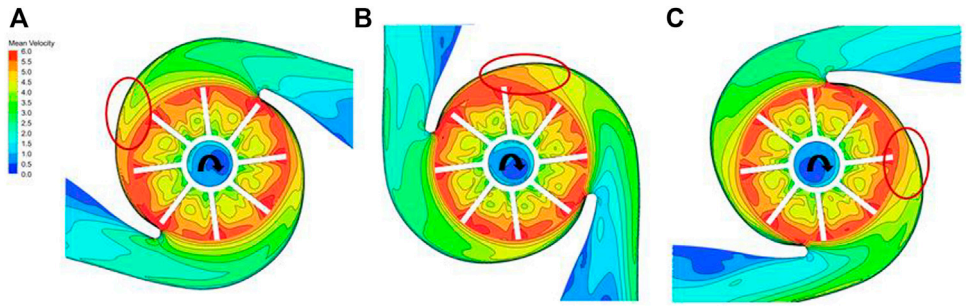

FIGURE 7 | Time average velocity distribution of different volute rotating speeds at the same time **(A)** 0 rpm **(B)** 30 rpm **(C)** 60 rpm.

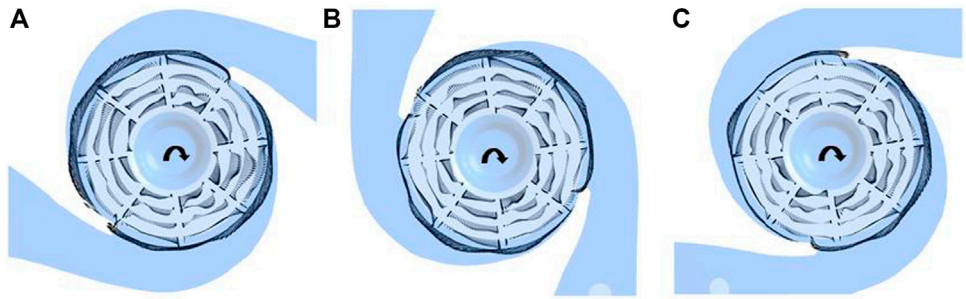

FIGURE 8 | Vector diagram of different volute rotating speeds at the same time **(A)** 0 rpm **(B)** 30 rpm **(C)** 60 rpm.

a more-accurate prediction of flow separation. The transport equations for the turbulent kinetic energy and the specific dissipation rate were given by **Eqs 1**, **2**:

$$\frac{\partial}{\partial t}(\rho k) + \frac{\partial}{\partial x_i}(\rho k u_i) = \frac{\partial}{\partial x_j}\left[\Gamma_k \frac{\partial k}{\partial x_j}\right] + G_k - Y_k + S_k \quad (1)$$

$$\frac{\partial}{\partial t}(\rho \omega) + \frac{\partial}{\partial x_i}(\rho \omega u_i) = \frac{\partial}{\partial x_j}\left[\Gamma_\omega \frac{\partial \omega}{\partial x_j}\right] + G_\omega - Y_\omega + D_\omega + S_\omega \quad (2)$$

In the above equations, ω represents the specific dissipation rate, D_ω was the cross-diffusion term, G_k and G_ω represent the generation of the turbulence variables k and ω, while Y_k and Y_ω represent the dissipation of the turbulence variables k and ω, respectively. The effective diffusivities Γ_k and Γ_ω are given by:

$$\Gamma_k = \mu + \frac{\mu_t}{\sigma_k} \quad (3)$$

$$\Gamma_\omega = \mu + \frac{\mu_t}{\sigma_\omega} \quad (4)$$

Here, σ_k and σ_ω are the turbulent Prandtl numbers for k and ω. μ_t denotes the turbulent viscosity.

Mesh Independence

To discretize the whole computation domain, a structured hexahedral mesh was generated for the impeller domain using the software ANSYS ICEM. **Figure 3A** shows the computational domain grids. The impeller domain was used using the J/O method, when the topological structure was selected. For the periodic structure of the impeller, the grid could be generated via circumference duplication according to the number of blades, and the mesh near the blade surface was well (locally) refined—see **Figure 3B**. Because of the small tip-clearance in the impeller, the grid was more refined within that region—see **Figure 3C, D**.

To ensure that the calculation result was not affected by the mesh density, three sets of meshes were selected. Moreover, a grid-independence test was carried out, and the difference for the predicted head between Mesh 2 and Mesh 3 was less than 1%. The ultimate optimal grid, with 1,203 million cells (Mesh 3), was checked thoroughly. The results were shown in **Table 2**.

Numerical Setup and Boundary Setting

In Fluent, the turbulent kinetic energy k and turbulent dissipation rate ω were 1.0 and 1.3 respectively. The four fluid-domains were connected by pairs of interfaces, and all walls were set as no-slip boundary condition to be consistent with a viscous fluid. The water temperature was 25°C. To analyze the internal flow-fields, a transient simulation was conducted which was initialized using the steady results. As for boundary conditions, the mass flow rate inlet boundary-condition was used at the pump inlet, and the pressure outlet was set at the distal cross section of outlet all the time. For the transient simulation, the SIMPLEC algorithm was chosen to deal with velocity–pressure coupling. Furthermore, a second-order upwind scheme was used for the discretization of

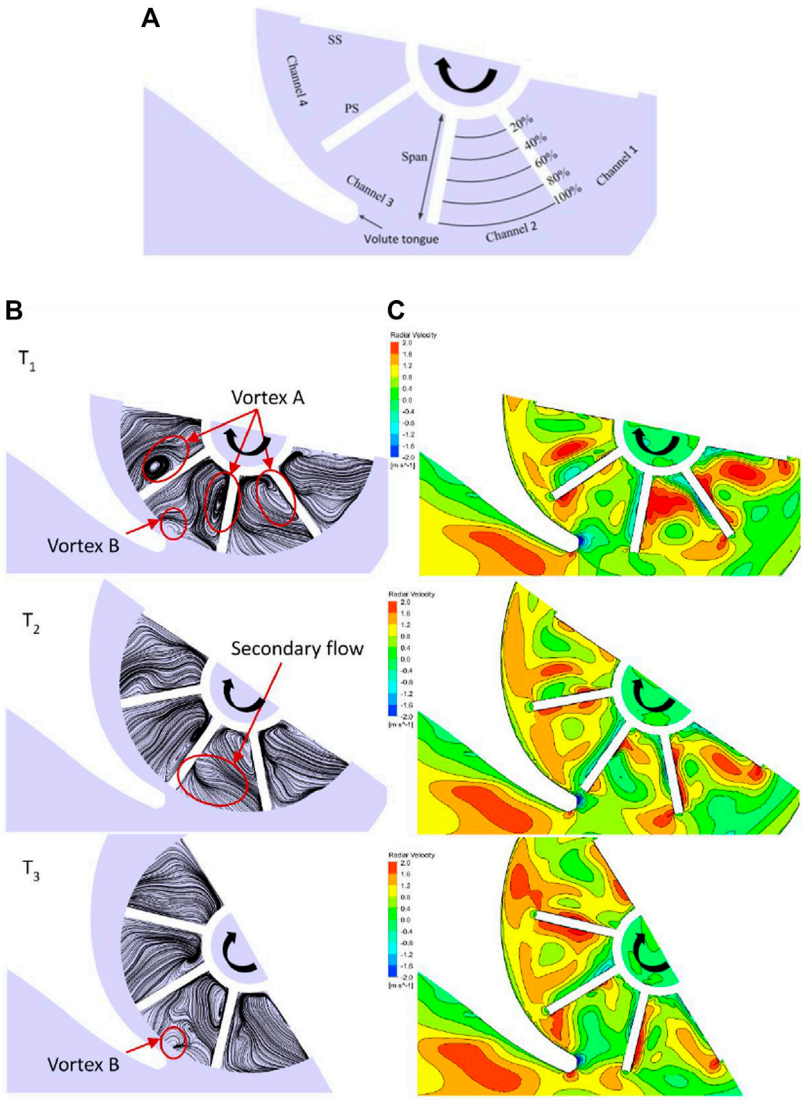

FIGURE 9 | Streamline and distribution of radial velocity at the middle cross-sectional plane of volute **(A)** View of section **(B)** Streamline **(C)** Radial velocity.

the convection terms of momentum, turbulent kinetic energy, and the turbulent dissipation rate equations. A second-order implicit scheme was used for transient formulation. The boundary conditions were the same as for the steady simulation. The solution accuracy was set to second order, the residual convergence accuracy of the scheme was 10^{-4}. In addition, the time step in the calculation was set to 2.22×10^{-4} according to the impeller's rotating period T, which was equal to 1/90 T.

EXPERIMENTAL SETUP

To compare the pressure fluctuation between the numerical and the test results, a pressure pulse monitoring point *P* was set inside the volute—see **Figure 4**. The monitoring point was at the same position as in the prototype test. Considering the rotation of the spray arm in the test, a set of pressure-pulsation test devices, which can rotate with the spray arm, was designed. The sensor was installed on the cover of the test-bed and fastened on the test-bed with bolts. At this time, it was ensured that the sensor was suspended above the volute, and we placed the probe of the sensor in the preset installation hole of the volute. The line was connected to the connecting groove to ensure that the sensor probe can rotate with the volute. This test device could effectively avoid the problem of wire-winding during the rotation of the spray arm and ensure normal operation. A sampling frequency of 10 kHz was used to collect the data, and the measuring accuracy of the pressure sensors was 0.2%.

Comparisons of the amplitude between CFD and experimental data at the monitoring point *P* under the rated conditions are shown in **Figure 5**. The transient pressure was

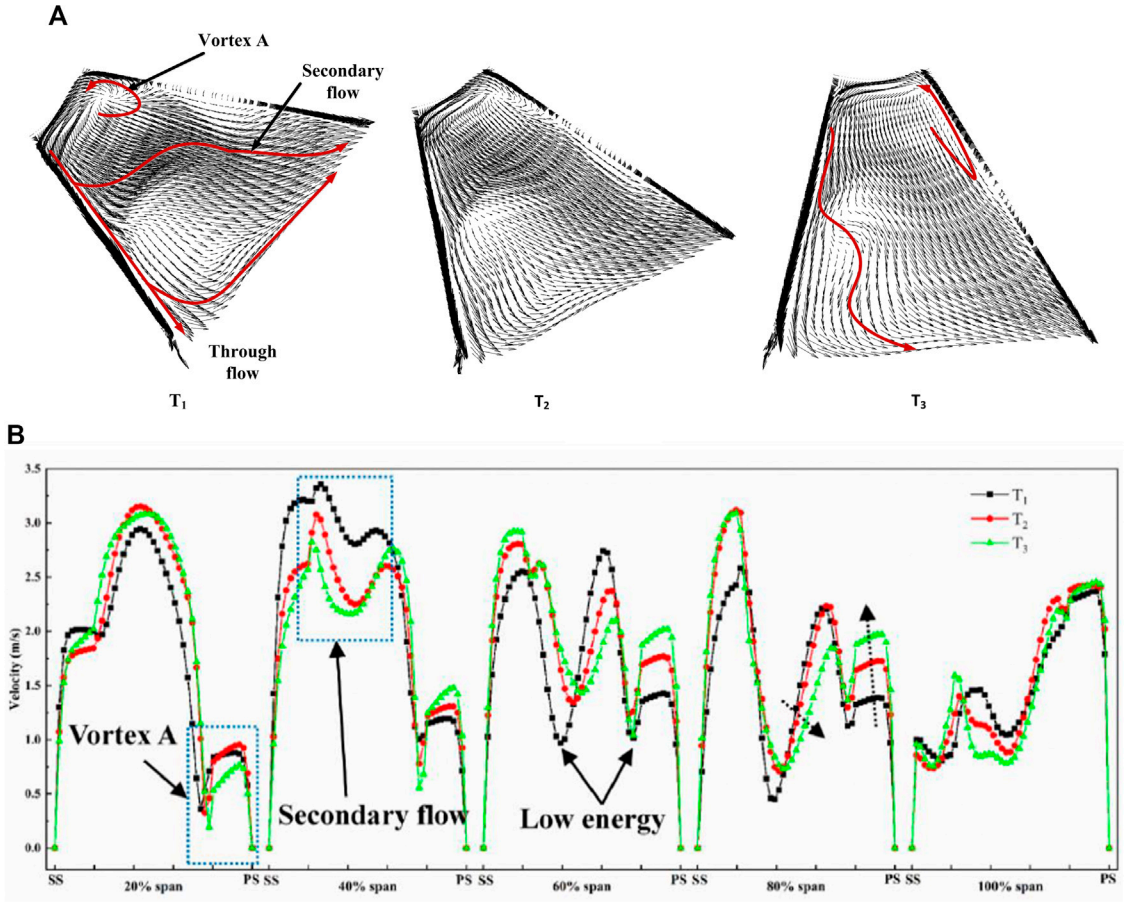

FIGURE 10 | Vectors and velocity distribution of T_1, T_2 and T_3 in channel 1 **(A)** Vector distribution **(B)** Velocity distribution.

processed using a fast Fourier transform (FFT). Based on the impeller speed, the shaft frequency $f_N = n/60 = 50$ Hz and the blade passing frequency $f_{BPF} = Z \times f_N = 400$ Hz. This result is in good agreement with the experiment which verifies the accuracy of the numerical simulation. Both the experimental and the numerical dominant frequencies of pressure fluctuation at the monitoring point were 1 times the blade passing frequency. Compared with the experimental results, the amplitude of the dominant frequency in numerical simulation was higher. The experimentally obtained amplitudes for the two- and three-times blade-frequency components were higher than the numerical results. Interestingly, there were more high frequencies in the experimental results. The difference between measurement and simulation may be because of environmental factors that affected the measurements but were not considered in the numerical simulation.

RESULTS AND DISCUSSION

Performance of Pump

Because the new dishwasher pump had no pipeline, its head was difficult to measure. The numerical simulation was carried out under several different conditions. The volute speeds were set to 0, 30, and 60 rpm. The main hydraulic performance curves were calculated, including head, and efficiency.

The performance of the pump was characterized by the head rise, H, and the efficiency, η, curves of **Figure 6** versus the flow rate, Q. The Q-H data show that the head slightly decreases with increasing flow rate. The results for the three schemes are consistent. For the small flow rate, the head and efficiency of the 60 rpm scheme were 3.88 and 1.89% higher, respectively, than for the 0 rpm scheme. For the operating condition, the head and efficiency of the static volute scheme exceed the respective values for the rotating volute schemes. The curve fluctuates less, which means the rotation speed of the volute has only a small effect on the pump performance.

Flow Development

At the flow rate of 55 L/min, the speed of the impeller was 3,000 rpm. Hence, the impeller rotation period T = 0.02 s. After the impeller rotated for 20 cycles, the volute of the 30 rpm scheme rotated 72°, and the volute of 60 rpm scheme rotated 144°. **Figure 7** shows the time-averaged velocity distribution for different rotation speeds at the same time. It can be seen that the time-averaged velocity

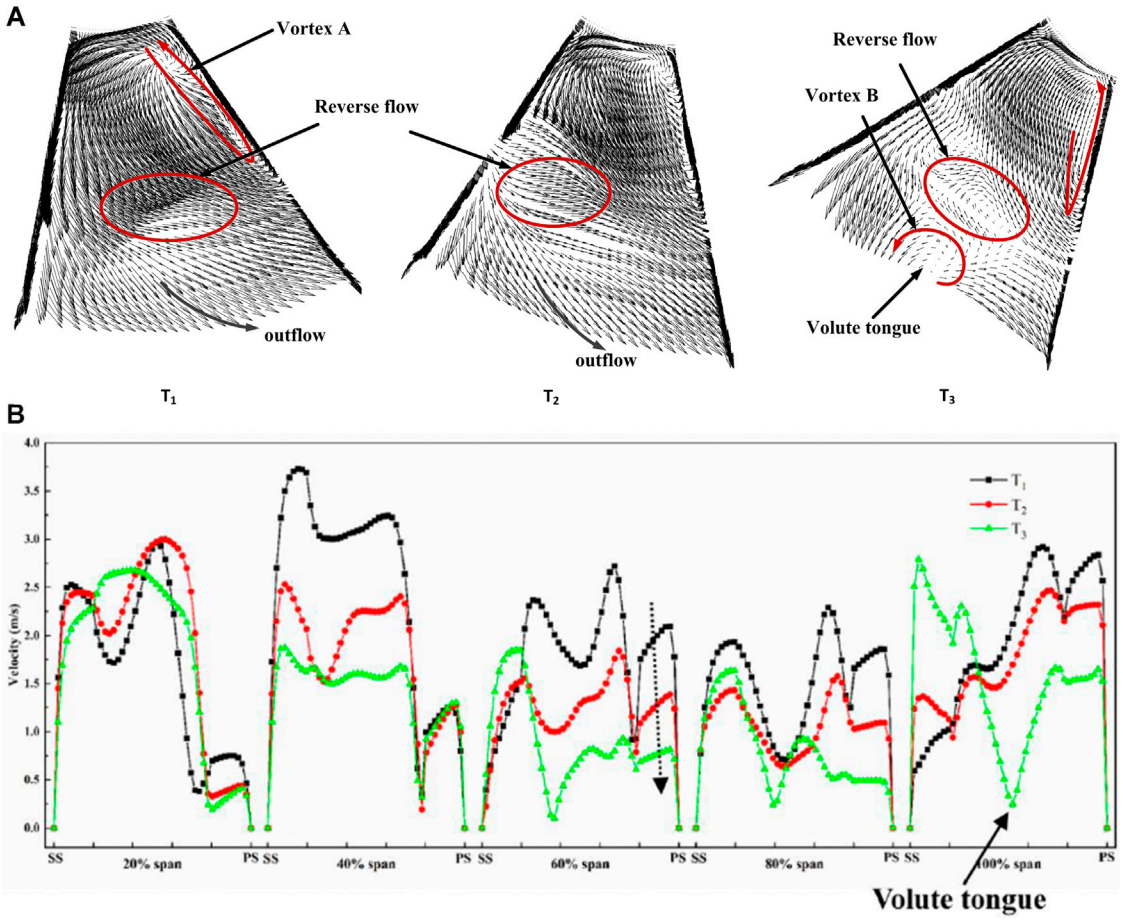

FIGURE 11 | Vectors and velocity distribution of T_1, T_2, and T_3 in channel 2 **(A)** Vector distribution **(B)** Velocity distribution.

distribution for each channel was basically the same within a rotation cycle. This indicates that the flow law for each channel was the same, and the velocity in the volute also reveals the characteristics of axial symmetry. Compared to different rotation speed schemes, the distribution of time-averaged velocity inside the impeller shows the same law, and the same distribution law is valid for the tongue part. However, with increasing rotation speed of the volute, the transition of the flow field in the transition section between the impeller and the volute becomes smoother. This indicates that the rotation of the volute has a significant effect on the interference between the impeller and the volute.

The vector diagram of the different volute speeds (at the same time) is shown in **Figure 8**. It can be seen that the velocity distribution for schemes with different volute speeds is basically the same in the flow channel when they are not passing the tongue. This also shows that the speed of the volute does not affect the velocity distribution in the impeller but the position of the tongue was the main factor that determined the velocity distribution in the impeller. A reflux phenomenon at the tongue region can be clearly seen in **Figure 8**. In each flow channel, the velocity vector opposite to the mainstream direction also appears (mostly at the pressure surface of the blade close to the hub), which is also consistent with the position of the vortex generation.

To investigate the flow development under the effect of the tongue, the detailed velocity profiles of the 0 rpm scheme were selected. In this way it becomes possible to explain the interaction between impeller and volute. Because the twin volute was formed by a single volute with a long tongue using a 180° array, only half of the flow field need to be studied instead of all flow channels. **Figure 9** shows the streamline and distribution of the radial velocity for the central cross-section of the volute. As shown in **Figure 9A**, four channels are shown and the tongue is located at channel 3. The rotation of the impeller occurred in the clockwise direction. The three moments of the 21st cycle of the impeller were recorded as T_1, T_2, and T_3 respectively. The following relations are valid: $T_1 = T$, $T_2 = T_1+1/15T$ and $T_3 = T_1+2/15T$. The streamline of the impeller is shown in **Figure 9B**, and the radial velocity of the impeller was subtracted from the local fluid velocities to obtain their relative component, see **Figure 9C**. There were two main vortex structures at the central plane, vortices A and B. Vortex A was a passage vortex near the hub, which was growing and attaching gradually to the pressure side as

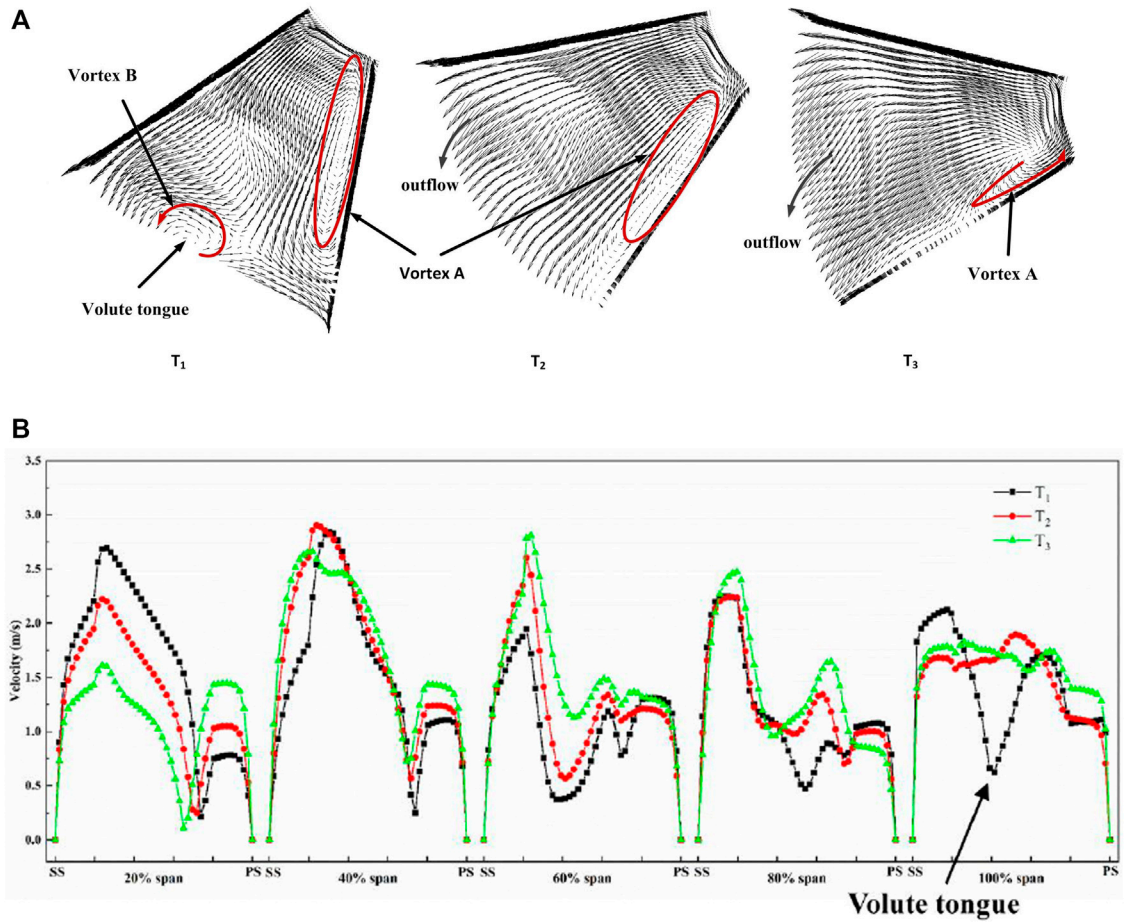

FIGURE 12 | Vectors and velocity distribution of T_1, T_2, and T_3 in channel 3 **(A)** Vector distribution **(B)** Velocity distribution.

the outflow pressure increased. Vortex B was generated by the volute tongue and the interacting flow. The low-energy fluid accumulated at the volute tongue. **Figure 9B** shows that the flow pattern in the impeller passage was very complex, exhibiting both reverse flow and secondary flow. The secondary flow was the cross flow, which was perpendicular to the radial flow of the impeller passage. Common features observed in channels are the presence of a strong outward through-flow along the suction side of each blade as well as the presence of a strong localized outflow at the pressure side of each blade. When the channel reached the volute tongue region, the flow started to reverse back to the impeller, and the direction of vortex B was opposite to the rotation of the impeller. The intensity of vortex A at the hub corner increased and moved to the middle of the pressure surface. After the channel passed the tongue region, the vortex B disappeared immediately, and the radial velocity, particularly along the blade suction side, increased. However, the secondary flow still exists in the impeller passage, which was found to be a common feature for all channels. The radial velocity along the blade pressure side increased, which reduced the intensity of vortex A, then vortex A back to the hub corner. To investigate the vortex structure in the channels, a detailed analysis of the vector and the velocity distribution in the channels is shown in **Figure 10** to **Figure 13**.

As shown in **Figure 10A**, the outward flow region generates the complex secondary flow in the region between the blades and the vortex at the hub corner. In addition, there is a strong through-flow along the blade suction side. The flow direction at the impeller outlet is important because it determines the overall performance of the impeller considered. According to Choi et al. (2004), when the impeller rotates clockwise with angular velocity, the Coriolis force works perpendicularly to the angular velocity and the relative tangential velocity. In the (radial) outward-flow region of the impeller passage, the Coriolis force acts in the direction from the suction side to the pressure side. Thus, a large cross-flow region is located within the impeller channel. **Figure 10B** illustrates the location of the secondary flow. There are two low-energy areas in the channel: one was located at the center of the passage (caused by the secondary flow), while the other one was caused by the vortex A. After rotation by 24°, the area of secondary flow moved towards the pressure surface and the velocity at the pressure side increased.

As shown in **Figure 11A**, in channel 2, the secondary flow increased. There was a strong relative tangential velocity in the

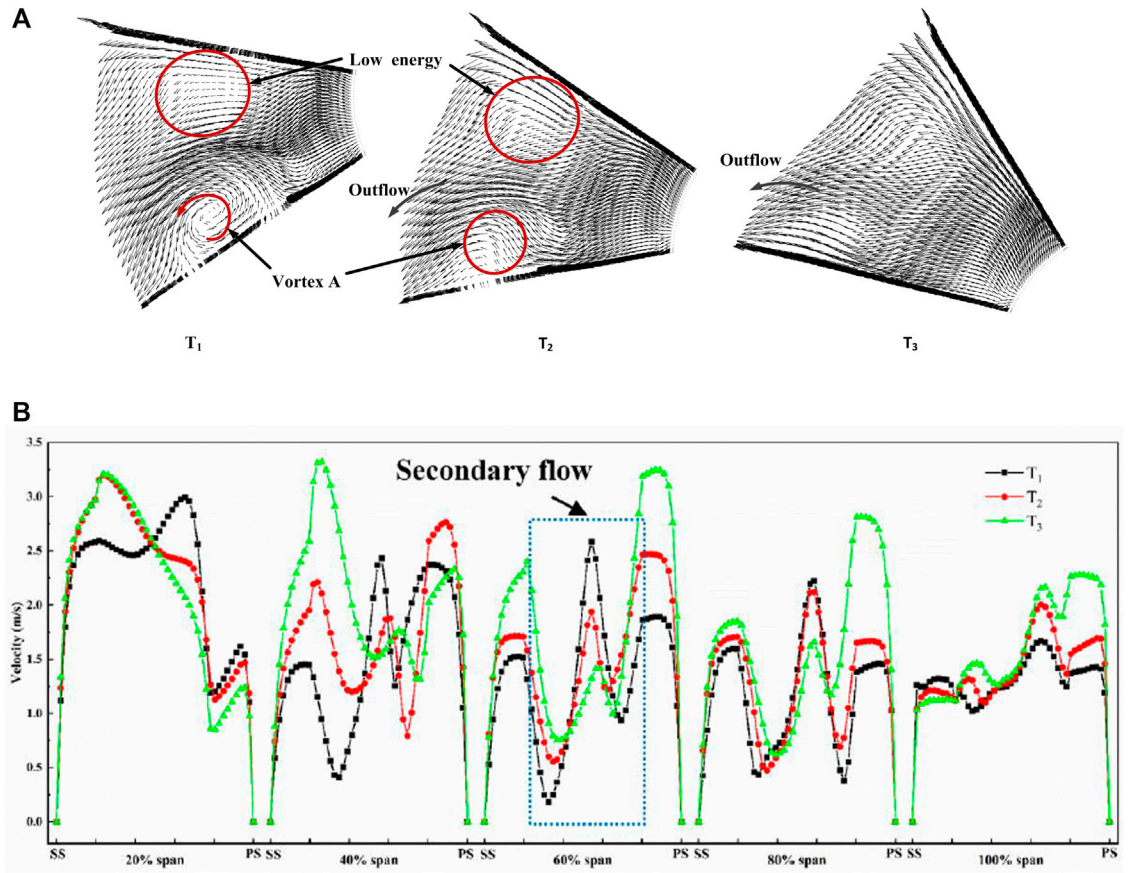

FIGURE 13 | Vectors and velocity distribution of T_1, T_2 and T_3 in channel 4 **(A)** Vector distribution **(B)** Velocity distribution.

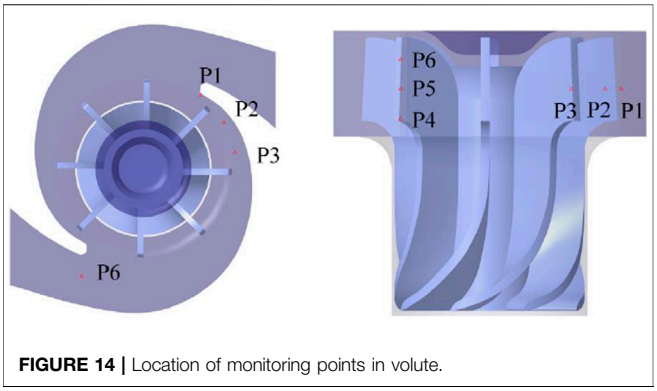

FIGURE 14 | Location of monitoring points in volute.

vicinity of the impeller outlet, which generated a strong Coriolis force acting in the direction toward the impeller center. This induced reverse flow within the impeller channel. The flow direction at the impeller outlet was mostly outward, except for the weak and small reverse flows marked in the figure. When the channel was close to the volute tongue, the velocity decreased, and a low-velocity area appeared at the side shroud of the channel—see **Figure 11B**. After the appearance of vortex B, the reverse flow in the channel increased. As the flow channel approached the tongue, the strength of vortex A gradually decreased, and the velocity in the flow channel also decreased.

While the first two channels rotated towards the tongue, channels 3 and 4 rotated away from the tongue. **Figure 12A** shows the vectors in channel 3. After the channel passed the volute tongue, the outflow became more stable, and the velocity in the secondary flow area increased. The intensity of vortex A decreased such that vortex A moved back to the hub corner. As shown in **Figure 12B**, the velocity change was largest in the hub area. With the rotation of the impeller, the fluid velocity near the suction surface decreased but the fluid velocity near the pressure surface increased. The intensity of the secondary flow decreased gradually, and the flow field in the channel became uniform.

Figure 13 shows the flow development for channel 4. The two low-energy regions are clearly shown in **Figure 13A**. The region of vortex A reached a maximum at T_1, and the velocity started to increase sharply under the effect of outflow pressure. As shown in **Figure 13B**, the lowest velocity in channel four was at about 60% span (caused by the secondary flow). With the rotation of the impeller, the velocity changed dramatically and the intensity of the secondary flow decreased substantially. The flow field was most uniform at T_3.

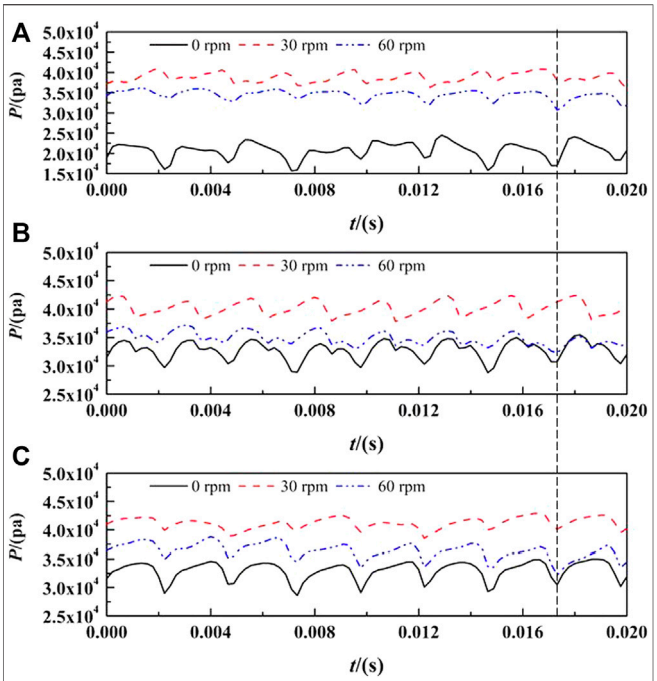

FIGURE 15 | Time domain diagram of static pressure fluctuation at different monitoring points in transition section **(A)** P1 **(B)** P2 **(C)** P3.

Pressure Field

In the new dishwasher type, the strong interaction between the flow leaving the impeller and entering the volute casing generates pulsating pressure. To analyze the pressure fluctuation of the flow field in the complete cycle, three monitoring points were introduced along the circumferential direction in the transition section of the tongue position. In addition, three radial monitoring points were added at the outlet of the impeller for analysis. The locations of the monitoring points are shown in **Figure 14**. The static pressure value was obtained every 4° of the time steps, and the pressure fluctuation (obtained by a complete rotation cycle) was analyzed. The monitoring point P1 was located in the tongue region.

Figure 15 shows the time-domain diagram for the static pressure fluctuation at the monitoring points in the transition section. The abscissa represents the time, and the ordinate refers to the static pressure value. During a complete cycle, the pressure fluctuations have eight peaks. The peak of the scheme with a volute speed of 0 rpm was the smallest at the monitoring point P1. The pressure of the 30 rpm scheme was greater than that of the 60 rpm scheme, while the pressure of the other two schemes (30 and 60 rpm) changed little from P1 to P3.

FFT was conducted to investigate the amplitude of the dominant frequency, and the data of the last 3 cycles were used for the frequency characteristics. **Figure 16** shows the frequency spectra for different monitoring points of the transition section of the volute along the circumferential direction. The results show that the characteristic frequency was the blade passing frequency (BPF) for all three schemes, and the dominant frequency was one time the BPF. On the other hand, the secondary frequency was an integral multiple of the BPF. The results also indicate that the dominant frequency was closely related to the rotor/stator interaction between the impeller and volute. Furthermore, the frequency-domain curve of the pressure fluctuation in the transition section was smooth, and there was practically no harmonic. A comparison of the amplitudes of the monitoring points P1 to P3 indicates that the frequency-domain amplitudes of the 0 rpm scheme were the highest and weakened in turn. They are mainly associated with the blade passage frequency, which represent high amplitudes near the tongue and at impeller discharge locations. The amplitude of the 30 rpm scheme first increased and then decreased, while the amplitude-change for the 60 rpm scheme was exactly opposite to the 30 rpm scheme (which first decreased and then increased).

Figure 17 shows the time domain of the static pressure fluctuation at the monitoring point in the impeller outflow section. P4 is at the bottom of the volute, while P6 is located at the top of the volute. The peak value from the bottom to the top of each scheme decreases slightly. The scheme with the volute speed of 0 rpm shows almost no fluctuation and the peak value for the 30 rpm scheme was slightly higher than for the 60 rpm scheme. Due to the effect of volute speed, there can be a

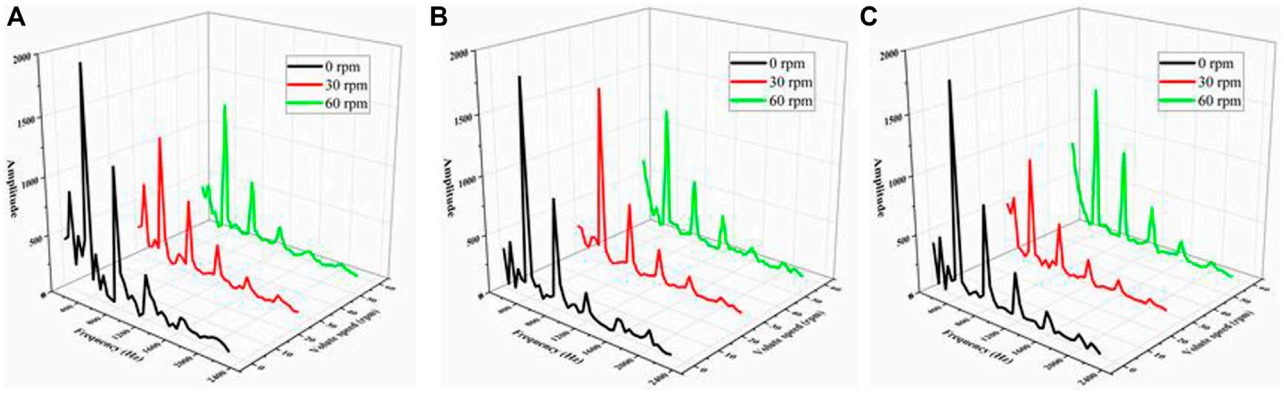

FIGURE 16 | Frequency spectrum of pressure fluctuation at different monitoring points in the transition section **(A)** P1 **(B)** P2 **(C)** P3.

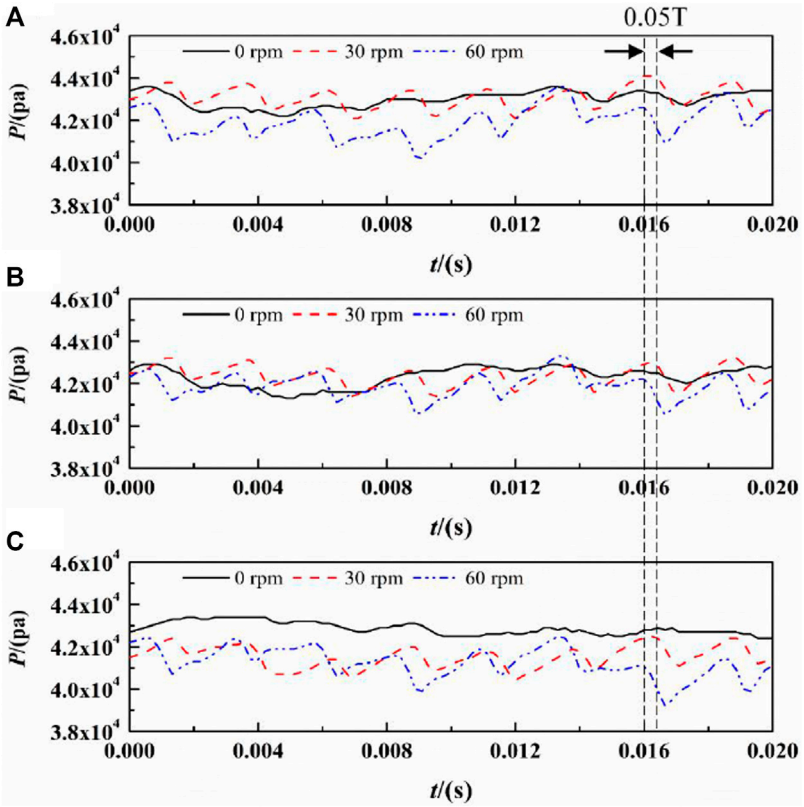

FIGURE 17 | Time domain of static pressure fluctuation at monitoring points in outflow section **(A)** P4 **(B)** P5 **(C)** P6.

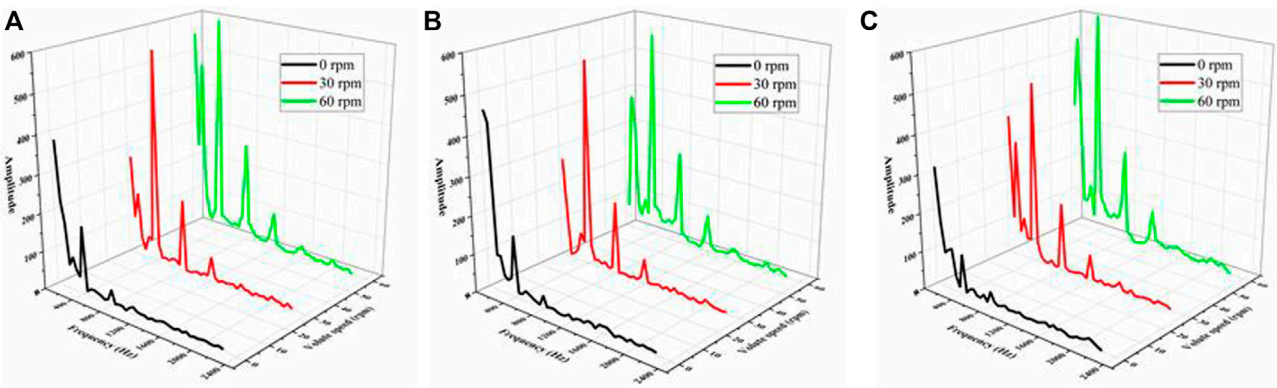

FIGURE 18 | Frequency of pressure fluctuation at different monitoring points in outflow section**(A)** P4 **(B)** P5 **(C)** P6.

deviation between the different schemes. The deviation between the two peaks (30 and 60 rpm) was 0.05 T, which indicates that the volute speed had a strong effect on the flow field in the volute outflow section.

Figure 18 shows the pressure fluctuation spectrum at different monitoring points for the outflow section of the impeller. The characteristic frequency was the BPF, and the dominant frequency was one times the BPF (which is the same as for the transition section). The effect of the shaft frequency on the outflow section of was larger. From P4 to P6, the frequency-domain amplitude of the 0 rpm scheme was the smallest and weakens in turn, while the amplitude of the

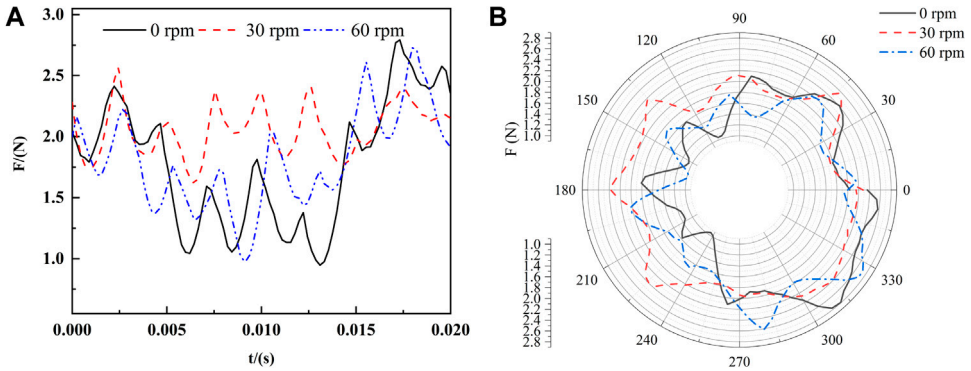

FIGURE 19 | Time domain and vector distribution of radial force of impeller **(A)** Time domain **(B)** Vector distribution.

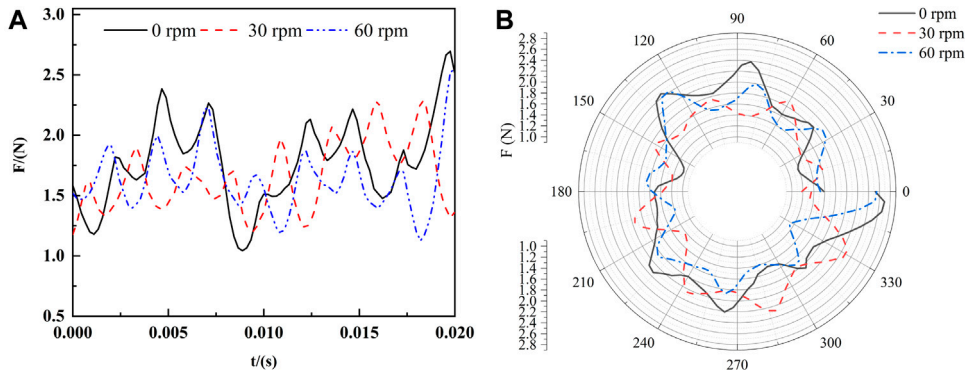

FIGURE 20 | Time domain and vector distribution of radial force of volute **(A)** Time domain **(B)** Vector distribution.

60 rpm scheme was highest at three monitoring points. This indicates that, with increasing volute speed, the effect on the outflow section increases.

Radial Force

The radial force on the principal axis of a pump mainly originates from the flow field in the impeller (Yue et al., 2017; Wang et al., 2020). Thus, the distribution of the radial force was analyzed to better understand the relationship between flow characteristic and radial force. Given that the time step was set to 1/90 of the period of the impeller revolution in the transient calculation, 90 data point were recorded during one impeller revolution. **Figure 19A** shows the time revolution of the radial force. The horizontal axis is the time, and the vertical axis is the magnitude of the resultant force. The magnitude of the radial force was computed at each time step using a full integration of the pressure and shear stress on the surfaces of both hub and blades. The results show that there were eight peaks and troughs in a complete cycle but the distribution of force shows great differences between the schemes. The radial force of the impeller was in the range 1N–3 N. The deviation between the 30 rpm peak and the 0 rpm peak was 0.02 T, while the deviation between the peaks for 60 and 30 rpm was also 0.02 T. Due to the rotor/stator interaction, the radial force vector on the principal axis completed a full trace with a closed circle. From the macro perspective, the vector diagrams of impeller appear irregular, octagonal, and they were essentially closed—see **Figure 19B**. There were obvious differences in the peak-to-peak values, which shows that the force on the blade was very non-uniform, and the bearing can be greatly affected. When the volute rotated at 30 rpm, the shape of the vector distribution on the impeller was more regular. In other words, the speed of the volute strengthens the fluctuation of the radial force and affects the operational stability of the new dishwasher pump.

Figure 20 shows the time-domain diagram and vector distribution for the radial force of the volute. Similar to the impeller, the radial force on the volute was non-uniform. The vector diagram of the volute was not closed because the data were obtained during one period of impeller revolution. The maximum radial forces for 0, 30, and 60 rpm were 2.69, 2.28, and 2.54 N, respectively. There was also a deviation between the peaks of the schemes with different rotation speeds of the volute. The deviation was 0.05 T, which was the same as for the pressure deviation in the outflow section. The deviation was larger compared to the impeller radial force.

CONCLUSION

Both performance and flow development of a new type of dishwasher pump were investigated. The pressure fluctuation and radial force, which are associated with the rotor stator interaction, were determined. The simulation with an SST k-ω turbulence model produced results that were in good agreement with the experimental values. Based on the numerical simulation and theoretical analysis, the following conclusions can be drawn:

1) The rotation speed of volute had only a small effect on both the head and efficiency of pump. The flow field in the impeller shows symmetry due to the twin volute. The speed of the volute mainly affected the flow field in the transition section between impeller and volute. Therefore, the volute speed can be set as static condition to study the flow field in the impeller.
2) The flow development in the channels indicates that the differences in flow fields in the impeller were related to the relative positions of the impeller and the volute. A passage vortex A was located at the corner between the pressure surface and the hub. The intensity of vortex A increased, when the channel rotated towards the tongue. It then decreased when the channel moved away from the tongue. A secondary flow occurred in the impeller passage, which was found to be a common feature of all channels. The intensity of the secondary flow follows the same rules as vortex A. Another vortex (B) was generated by the low-energy flow in the tongue region when the channel moved through the volute tongue.
3) The time-domain curve for the pressure pulses was periodic. In the transition section of the volute, the characteristic frequency was the blade passing frequency, while the dominant frequency was one times the BPF, i.e., 400 Hz. After comparing 3 schemes of different volute speed, it was found that the static scheme had the lowest pressure but the highest amplitude in the tongue region (which reduced the stability of the pump). Rotating the volute increased the pressure in the tongue region but the pressure did not always increase with increasing volute speed. The 30 rpm scheme showed the best stability. In the outflow section, the pressure was higher than in the transition section, and the pressure decreased slightly from the bottom to the top of the volute. A deviation in the tongue region was not clearly observed, while the deviation for the outflow section was 0.05 T. This indicates that the rotating volute affects the pressure pulse via the rotor/stator interaction. In the frequency domain, the shaft frequency affected the outflow of the impeller. In addition, this effect increased with increasing volute speed.
4) After comparing the 3 schemes with respect to the radial force, a deviation between the peaks for the different rotation-speed schemes was found. The deviation for the radial force in the volute was larger compared to the impeller. When the volute rotated 30 rpm, the shape of the vector distribution was more regular, which indicates that the stability of the pump was the highest.

DATA AVAILABILITY STATEMENT

The raw data supporting the conclusion of this article will be made available by the authors, without undue reservation.

AUTHOR CONTRIBUTIONS

CN: Literature search, Figures, Study design, Investigation, data analysis, Writing. YL: Conceptualization, Methodology, Data collection, Formal analysis, Funding acquisition. PH: Figures, Data interpretation, Reviewing and Editing. HX: Reviewing and Editing. FZ: Reviewing and Editing.

FUNDING

The National Natural Science Foundation of China (No. 51809120), the Natural Science Foundation of Jiangsu Province (No. BK20180871), the Project Funded by China Postdoctoral Science Foundation (No. 2018M640462) and the Natural Science Foundation of the Jiangsu Higher Education Institutions of China (No. 18KJB470005), Key Research and Development Plan Project of Jiangsu Province (No. BE2019009).

REFERENCES

Barrio, R., Blanco, E., Parrondo, J., GonzáLez, J., and FernáNdez, J. (2008). The Effect of Impeller Cutback on the Fluid-Dynamic Pulsations and Load at the Blade-Passing Frequency in a Centrifugal Pump. *J. Fluid Eng.* 130 (11), 1349–1357. doi:10.1115/1.2969273

Choi, Y.-D. (2008). Investigation on the Internal Flow Characteristics of the Low Specific Speed Centrifugal Pump with Circular Casing. *J. Korean Soc. Mar. Eng.* 32 (3), 404–412. doi:10.5916/jkosme.2008.32.3.404

Choi, Y.-D., Nishino, K., Kurokawa, J., and Matsui, J. (2004). PIV Measurement of Internal Flow Characteristics of Very Low Specific Speed Semi-open Impeller. *Exp. Fluids* 37 (5), 617–630. doi:10.1007/s00348-004-0838-7

Chu, S., Dong, R., and Katz, J. (1995). Relationship between Unsteady Flow, Pressure Fluctuations, and Noise in a Centrifugal Pump-Part B: Effects of Blade-Tongue Interactions. *J. Fluids Eng. Trans. ASME* 117 (1), 30–35. doi:10.1115/1.2816814

Dedoussis, V., and Giannatsis, J. (2004). Stereolithography Assisted Redesign and Optimisation of a Dishwasher Spraying Arm. *Rapid Prototyping J.* 10 (4), 255–260. doi:10.1108/13552540410551388

Guo, S., and Okamoto, H. (2003). An Experimental Study on the Fluid Forces Induced by Rotor-Stator Interaction in a Centrifugal Pump. *Int. J. Rotating Machinery* 9 (2), 135–144. doi:10.1155/s1023621x03000125

Gonzáles, J., Santolaria, C., Parrondo, J. L., Fernández, J., and Blanco, E. (2003). "Unsteady Radial Forces on the Impeller of a Centrifugal Pump with Radial gap Variation," Proceeding of 4th ASME/JSME Joint Fluids Engineering Conference 1173–1181.

Liu, M. Q., Li, Q. W., Bai, Y. H., Liu, Z. Y., and He, P. J. (2012). Efficiency and Pressure Pulsation Analysis of a Double Suction Centrifugal Pump with Different Arrangement Impellers. *Amr* 433-440, 709–715. doi:10.4028/www.scientific.net/amr.433-440.709

Long, Y., Lin, B., Fang, J., Zhu, R., and Fu, Q. (2020). Research on the Transient Hydraulic Characteristics of Multistage Centrifugal Pump during Start-Up Process. *Front. Energ. Res.* 8, 76. doi:10.3389/fenrg.2020.00186

Majidi, K. (2005). Numerical Study of Unsteady Flow in a Centrifugal Pump. *J. Turbo machinery* 127 (2), 805–812. doi:10.1115/1.1776587

Menter, F. R. (1994). Two-equation Eddy-Viscosity Turbulence Models for Engineering Applications. *Aiaa J.* 32, 1598–1605. doi:10.2514/3.12149

Minde, M. (2016). *"Validation of Dishwasher CFD Model Using PIV"*. Master thesis. Lulea, Sweden: Lulea University of Technology.

Peng, G., Du, J., Chang, H., Chen, Q., Li, J., Pan, C., et al. (2021). Numerical and Experimental Analysis of Influence of Impeller Structures on Slurry Pump Performance. *Front. Energ. Res.* 9, 762159. doi:10.3389/fenrg.2021.762159

Pérez-Mohedano, R., Letzelter, N., Amador, C., Vanderroest, C. T., and Bakalis, S. (2015). Positron Emission Particle Tracking (Pept) for the Analysis of Water Motion in a Domestic Dishwasher. *Chem. Eng. J.* 259 (259), 724–736. doi:10.1016/j.cej.2014.08.033

Pérez-Mohedano, R., Letzelter, N., and Bakalis, S. (2017). Integrated Model for the Prediction of Cleaning Profiles inside an Automatic Dishwasher. *J. Food Eng.* 196, 101–112. doi:10.1016/j.jfoodeng.2016.09.031)

Santori, G., Frazzica, A., Freni, A., Galieni, M., Bonaccorsi, L., Polonara, F., et al. (2013). Optimization and Testing on an Adsorption Dishwasher. *Energy* 50 (1), 170–176. doi:10.1016/j.energy.2012.11.031

Shi, L., Zhu, J., Tang, F., and Wang, C. (2020). Multi-Disciplinary Optimization Design of Axial-Flow Pump Impellers Based on the Approximation Model. *Energies* 13 (4), 779. doi:10.3390/en13040779

Solis, M., Bakir, F., and Khelladi, S. (2009). ""Pressure Fluctuations Reduction in Centrifugal Pumps: Influence of Impeller Geometry and Radial Gap,"," in ASME 2009 Fluids Engineering Division Summer Meeting, 253–265. doi:10.1115/fedsm2009-78240

Spence, R., and Amaral-Teixeira, J. (2009). A CFD Parametric Study of Geometrical Variations on the Pressure Pulsations and Performance Characteristics of a Centrifugal Pump. *Comput. Fluids* 38 (6), 1243–1257. doi:10.1016/j.compfluid.2008.11.013

Spence, R., and Amaral-Teixeira, J. (2008). Investigation into Pressure Pulsations in a Centrifugal Pump Using Numerical Methods Supported by Industrial Tests. *Comput. Fluids* 37 (6), 690–704. doi:10.1016/j.compfluid.2007.10.001

Wang, H. L., Hu, Q. X., Yang, Y., and Wang, C. (2021). Performance Differences of Electrical Submersible Pump under Variable Speed Schemes. *Int. J. Simul. Model.* 20 (1), 76–86. doi:10.2507/ijsimm20-1-544

Wang, H., Long, B., Wang, C., Han, C., and Li, L. (2020). Effects of the impeller blade with a slot structure on the centrifugal pump performance. *Energies* 13, 1628. doi:10.3390/en13071628

Yang, M., Min, S. M., and Wang, F. J. (2009). Numerical Simulation of Pressure Fluctuation and Radial Force in a Double Volute Pump. *Trans. Chin. Soc. Agric. Machinery* 40 (11), 83–88.

Ye, D., Liu, A., Luo, Y., Yu, B., and Lai, X. (2021). Research Progress of Reactor Coolant Pump Pressure Fluctuation and its Improvement Methods. *J. drainage irrigation machinery Eng.* 39 (8), 770–776. doi:10.3969/j.issn.1674-8530.19.0307

Yue, H., Lei, T., Liu, Y., Yun, X., Zhang, J., and Zhu, B. (2017). Energy Performance and Radial Force of a Mixed-Flow Pump with Symmetrical and Unsymmetrical Tip Clearances. *Energies* 10 (1), 57. doi:10.3390/en10010057

Zhang, L., Wang, C., Zhang, Y., Xiang, W., He, Z., and Shi, W. (2021). Numerical Study of Coupled Flow in Blocking Pulsed Jet Impinging on a Rotating wall. *J. Braz. Soc. Mech. Sci. Eng.* 43, 508. doi:10.1007/s40430-021-03212-0

Zheng, S. H., Qian, H., Mou, J. G., Wu, B., Gu, Y. Q., and Chen, Y. (2015). Influences of Staggered Blades on Hydrodynamic Performance of Three-Channel Volute Centrifugal Pump. *Trans. CSAE* 31 (23), 51–59. doi:10.11975/j.issn.1002-6819.2015.23.007

Zhou, J., Zhao, M., Wang, C., and Gao, Z. (2021). Optimal Design of Diversion Piers of Lateral Intake Pumping Station Based on Orthogonal Test. *Shock and Vibration*, 6616456. doi:10.1155/2021/6616456

Zhu, L., Yuan, S. Q., Yuan, J. P., and Pei, J. (2011). Numerical Simulation on Rotor-Stator Interaction in a Centrifugal Pump with Different Gaps between Impeller and Tongue. *Trans. Chin. Soc. Agric. Machinery* 42 (5), 49–55. doi:10.3969/j.issn.1002-6819.2011.10.009

Zhu, L., Yuan, S. Q., Yuan, J. P., Zhou, J. J., Jin, R., and Wang, H. (2011). Numerical Simulation for Rotor-Stator Interaction of Centrifugal Pump with Different Tongues. *Trans. CSAE* 27 (10), 50–55. doi:10.3969/j.issn.1002-6819.2011.10.009

Zhu, Y., Li, G., Wang, R., Tang, S., Su, H., and Cao, K. (2021). Intelligent Fault Diagnosis of Hydraulic Piston Pump Combining Improved Lenet-5 and Pso Hyperparameter Optimization. *Appl. Acoust.* 183, 108336. doi:10.1016/j.apacoust.2021.108336

Conflict of Interest: HX and FZ were employed by the company Ningbo FOTILE Kitchen Ware Co., Ltd.

The remaining authors declare that the research was conducted in the absence of any commercial or financial relationships that could be construed as a potential conflict of interest.

Publisher's Note: All claims expressed in this article are solely those of the authors and do not necessarily represent those of their affiliated organizations, or those of the publisher, the editors and the reviewers. Any product that may be evaluated in this article, or claim that may be made by its manufacturer, is not guaranteed or endorsed by the publisher.

frontiers in Energy Research

ORIGINAL RESEARCH
published: 13 January 2022
doi: 10.3389/fenrg.2021.817262

Operation Energy Consumption Study on Reel and Polyethylene Tube of a New Hard Hose Traveler

Zhengdian Xu, Hong Li, Yue Jiang, Qingjiang Xiang and Pan Tang*

Research Center of Fluid Machinery Engineering and Technology, Jiangsu University, Zhenjiang, China

To solve the problems of higher energy consumption and lower intelligence of traditional hard hose travelers, a new hard hose traveler with the function of electric drive and self-propelled is developed in this paper. The operational energy consumption of a reel and a polyethylene tube is an important part of hard-hose traveler energy consumption. In this paper, based on the JP50-180 hard hose traveler, the required pulling force and energy consumption at the reel and tube operation are theoretically and experimentally obtained. The aforementioned provides support for reducing energy consumption in the future. The influencing factor that affects the energy consumption of the reel rotation is the tube length, and the influencing factors that affect the energy consumption of the tube sliding are the ground slope, soil moisture content, and tube length. A calculation model for the dynamic change of the pulling force and energy consumption of the reel and tube operation is proposed in this study. Through theoretical analysis, maximum pulling tension and cumulative energy consumption requirements for the for reel rotation are 278.6 N and 15120.83 J, respectively. Furthermore, the requirements for the tube sliding are 1372.86 N and 123,456.96 J. Through test analysis, the maximum pulling tension for the tube sliding is between 1258.3 N and 1773.3 N, while the maximum pulling tension for reel rotation is 285.05 N. Under the same influencing factors, the deviation rates between theoretical and testable energy consumption for the reel rotation and tube sliding are 2.3 and 8.3%, respectively. The pulling force and cumulative energy consumption required for the reel rotation and tube sliding both increase with an increase in their influencing factors. The operating costs of the tube one-time unrolled are approximately 0.0185 CNY. Combined with the mobile resistance of the electric tracked vehicle, the power configuration of this new hard hose traveler is provided by two servo motors with a power of 5500 W each.

Keywords: hard hose traveler, reel rotation, polyethylene tube sliding, energy consumption, soil moisture content, power configuration

OPEN ACCESS

Edited by:
Xiaojun Li,
Zhejiang Sci-Tech University, China

Reviewed by:
Jinjing Sun,
University of Shanghai for Science and Technology, China
Quan Hui,
Lanzhou University of Technology, China

****Correspondence:***
Hong Li
hli@ujs.edu.cn

Specialty section:
This article was submitted to Process and Energy Systems Engineering, a section of the journal Frontiers in Energy Research

Received: *17 November 2021*
Accepted: *27 December 2021*
Published: *13 January 2022*

Citation:
Xu Z, Li H, Jiang Y, Xiang Q and Tang P (2022) Operation Energy Consumption Study on Reel and Polyethylene Tube of a New Hard Hose Traveler. Front. Energy Res. 9:817262. doi: 10.3389/fenrg.2021.817262

INTRODUCTION

The traditional hard hose traveler is a continuous mobile irrigation machine (Ge, 2018), that is driven by a water turbine and has the highest energy consumption of all irrigation machines (Keller and Bliesner, 1990; Burt et al., 1999). Its operational energy consumption is mainly composed of the driving energy consumption, sprinkler irrigation energy consumption (Rochester and Hackwell, 1991), pressure loss in the polyethylene tube (Rochester et al., 1990; Tang et al, 2017). Under typical working conditions, it is found that the former two account for 7–12% and 50–70% of [1]operational

energy consumption, respectively. The latter approximately accounts for 18–43% of energy consumption (Oakes and Rochester, 1980). The driving energy is mainly consumed by the water turbine, gearbox transmission, reel rotation, friction between polyethylene tube and the ground and friction between the irrigation cart and the ground (Ge, 2018), which has a lower energy conversion efficiency (Li et al., 2019). Both numerical simulation (Biolan et al., 2012) and actual measurement (Tang Y et al., 2014; Yuan et al., 2014) results showed that the energy conversion efficiency of the water turbine is only 1.5–20.0%. Although the driving energy consumption accounts for a relatively lower proportion of the operating energy consumption of traditional hard hose travelers, the long-term operating costs are affected by the driving energy consumption of the water turbine (Ge et al., 2020). Therefore, studying the reduction of driving energy consumption is still a significant for the hard hose traveler.

In addition to the water turbine driven by the traditional hard hose traveler, electric motors (Yang, et al., 2018) and hydraulic motors (Pan, 2019) can also be used. Among them, the highest energy conversion efficiency is obtained for driven electric motors. The driving efficiency of ordinary motors is generally 70–80%. However, brushless DC motors can reach more than 80% of energy through batteries or solar energy (Tang et al., 2018). To directly reduce operating costs, energy consumption should be lowered. In addition, achieving the applicability of the hard hose traveler in a variety of fields (such as mountain slopes and small and medium-sized irregular fields) and more application functions (such as fertilization, spraying and short distance transport) is also an effective way. In other words, a variety of agricultural machinery or more models of the hard hose traveler can be used to reduce early purchasing costs. Consequently, a design concept of the new hard hose traveler is proposed in this paper. Within the model, the electric tracked vehicle is used to load the sprinkler for irrigation. Moreover, part of the structural design and the principle of retracting and placing polyethylene tubes are based on the traditional hard hose traveler. The electric tracked vehicle is characterized by fiercer climbing and more flexible maneuvering. The aforementioned could solve the irrigation problems of the sloping field mountain area and irregular fields. Moreover, it could improve the applicability of the hard hose traveler in a variety of fields. In addition, the electric tracked vehicle could also achieve multi-functional applications of fruit and vegetable management in the greenhouse (Cui et al., 2019; Xu et al., 2022), picking (Zhang, 2016), and short distance transport (Li, 2018).

In this paper, to reduce the energy consumption of traditional hard hose traveler and develop a new hard hose traveler, exploring the energy consumption of reel and polyethylene tube operation is one of the key parameters. This is of particular importance since not many investigations exist on the topic. Currently, the study on energy consumption of traditional hard hose travelers is mainly focused on the pressure loss in the tube. Under the wound state of the tube, the additional value of the pressure loss is shown in **Eq. 1** (Rochester et al., 1990). Within a certain flow range, the pressure loss of the curved polyethylene tube under a specific pipe diameter and different curvature radii were measured, and the obtained specific law is shown in **Eq. 2** (Zhang and Wang, 2005). Characteristics of secondary flow in the polyethylene tube wound were numerically analyzed by multiple schemes. The regression equation of the friction coefficient in the wound tube was then established (**Eq. 3**) (Tang L et al., 2014).

$$h_b = \frac{K_b V^2}{2g} \tag{1}$$

$$h_{bzw} = f_b S Q^m \tag{2}$$

$$f_{CT} = \frac{0.07}{\mathrm{Re}^{0.25}} + 0.006\sqrt{\frac{r}{R_0}} \tag{3}$$

where h_b is the additional value of the pressure loss in the tube, mm; K_b is the coefficient of the wound tube; V is the liquid flow velocity in the tube, m s^{-1}; g is the acceleration due to gravity, m s^{-2}; h_{bzw} is the pressure loss in the tube, mm; f_b is the coefficient of the pressure loss in the tube; S is the length of the tube, m; Q is the flow rate in the tube, m^3 h^{-1}; m is the index of flow rate; f_{CT} is the friction coefficient in the wound tube; Re is Reynolds number in the tube; r is the inner radius of the tube, mm; R_0 is the radius of the reel, mm.

The energy consumption of reel rotation is affected by the length of the tube and the friction coefficient between the machines (Zhang et al., 2015). The energy consumption of the tube sliding is affected by factors such as the ground slope, soil moisture content, and tube length (GB/T 21400.1- 2008, 2008). The aforementioned two types of energy consumption are one of the foundations of power configuration in the proposed hard hose traveler. Moreover, power configuration is the core of electric tracked vehicles (Fan, 2017). Therefore, energy consumption analysis is a very important parameter for the design of a new hard hose traveler.

In this paper, the required pulling force and energy consumption of reel and polyethylene tube operation are analyzed theoretically and experimentally. Furthermore, the aforementioned is combined with the running energy consumption of the electric tracked vehicle. Together, these parameters represent a basis for power configuration design and optimization of a new hard hose traveler.

COMPOSITION AND ENERGY CONSUMPTION OF A NEW HARD HOSE TRAVELER

Composition and Working Principle of a New Hard Hose Traveler

The new hard hose traveler is based on the structure design of the traditional hard hose traveler. Moreover, it is controlled and operated by a remote terminal. Its structure mainly includes a reel, polyethylene tube, electric tracked vehicle, sprinkler and motor-gearbox system, as shown in **Figure 1**. The reel is used to store the polyethylene tubes. The electric tracked vehicle is used to pull out the tubes in the reel and load the sprinkler. The motor-gearbox system is used to recycle the tubes, which are used to

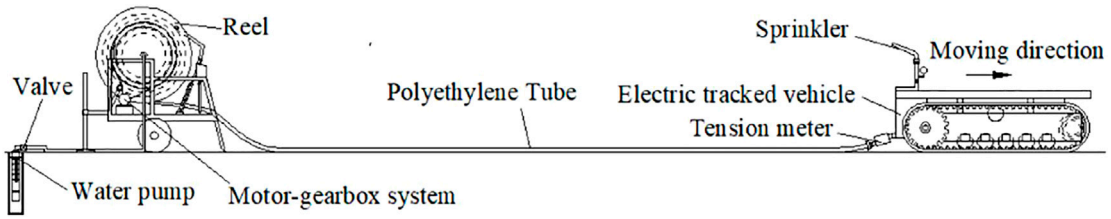

FIGURE 1 | Composition of new hard hose traveler and test method.

TABLE 1 | Factors and parameters.

Serial number	Factors	Parameters
1	The moving velocity of the sprinkler (m h^{-1})	15, 20, 25, 30, 35, 40, 45, 50
2	Soil moisture content (%)	20.8, 47.7, 70.3
3	Ground slope (°)	0, 15, 30
4	Tube length (m)	10, 20, 30, 40, 50, . . . , 170, 180

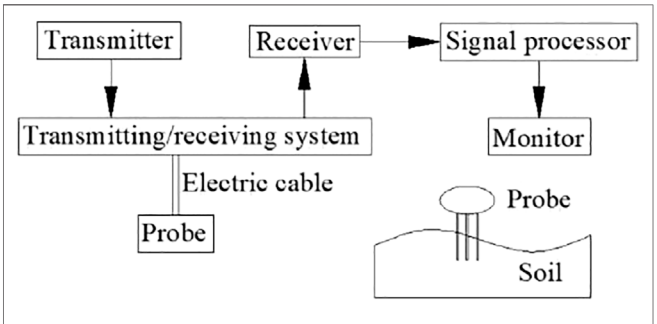

FIGURE 2 | The operating principle and Time-domain reflectometry method.

replace the water turbine and turbine gearbox of the traditional hard hose traveler. During the sprinkler irrigation operation, the reel is stored at the water source, and an electric tracked vehicle is located relatively far from the reel. Furthermore, the tubes are pulled out to achieve mobile sprinkler irrigation. At the end of the sprinkler irrigation operation, the tubes are separated from the electric tracked vehicle. The motor-gearbox system rotates the reel which recycles the tubes. Consequently, the electric tracked vehicle is transferred to the next sprinkling point.

Energy Consumption Composition and Influencing Factors

Energy consumption of a new hard hose traveler mainly consists of driving energy consumption, sprinkler irrigation energy consumption, and tube pressure loss. The driving energy consumption is mainly the energy consumption of the electric tracked vehicle and the operating energy consumption of the reel as well as the tube. The power configuration of the electric tracked vehicle is affected by the operation energy consumption of the reel and the tube. Based on the JP50-180 model of a traditional hard hose traveler, the operation process of the reel and the tube can be divided into two dynamic processes: reel rotation and tube sliding. The tube is unrolled during reel rotation, and the reel load is reduced. During the sliding process of the tube, the unfolded length increases. The pulling tension and energy consumption required for the reel and tube operation are the total tension and total energy consumption. When reel rotation or tube sliding is studied, the superimposed energy consumption from the start to the end of the operation is denoted as cumulative energy consumption of the reel rotation or the tube sliding. The aforementioned is shown in **Eqs 4**, **5**.

In this paper, the unfolded tube length is employed to represent parameter x, which is related to the reel load change and modified quality of the tube sliding. The friction coefficient between the tube and the soil is designated as μ_2, which mainly covers the soil surface flatness and soil moisture content. Some influencing factors and parameters are shown in **Table 1**. The tube is filled with water, and the mobile velocity of the sprinkler, i.e., the velocity of the electric tracked vehicle has no effect on the operation energy consumption of the reel and the tube at a constant velocity, which is used as a reference in this paper. In this paper, the soil moisture content is referred to as the volumetric moisture content of the soil and is measured by the Time Domain Reflectometry method, which is shown in **Figure 2**. Here, 20.8% was the value before the new hard hose traveler operation in the experiment. The remaining values were the measured during sprinkler irrigation. The ground slope represents the sprinkler angle as it moves upwards. During theoretical analysis, the soil moisture content remains unchanged. During experimental analysis, the ground slope remains unchanged.

$$W_1 = f(\mu_1, x) \tag{4}$$

$$W_2 = g(\mu_2, x, \theta) \tag{5}$$

where W_1 and W_2 are the accumulated energy consumption for reel rotation and tube sliding, respectively, J; μ_1 is the constant friction coefficient between the machines during rotation; θ is the slope of the ground, °.

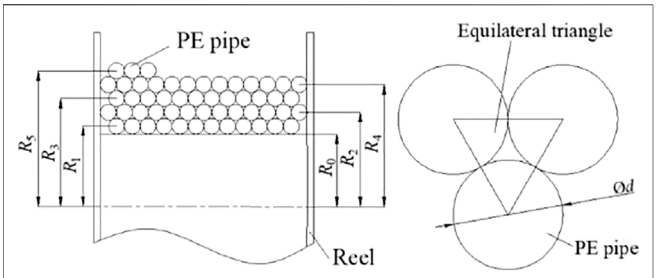

FIGURE 3 | The stacking method of the reel winding tube.

THEORETICAL ANALYSIS OF OPERATION PULLING FORCE AND ENERGY CONSUMPTION

Calculation Model

In this paper, the pulling tension and energy consumption are analyzed through the calculation model. Changes in the operating state of the new hard hose traveler are discussed. These changes provide a basis for power configuration design. Based on the above-provided information, four hypotheses are proposed: 1) During unwinding of the reel wound tube, the reel is regarded as a cylindrical rigid body. 2) When reel wound tube layers are changed, the fluctuation process of the required pulling force is neglected. 3) Under a specific working condition, it is assumed that the friction coefficient between the reel and the tube is constant. 4) The suspended length between the part of the tube close to the ground and the winding part on the reel is assumed as negligible.

Reel Rotation

The winding method of the tube is shown in **Figure 3**. This method is designated as 1 - n layers from the inside to the outside (the number of tube layers is represented by *n*, which is a positive integer). In this paper, the distance from the reel center line to the circle point of the tube section is defined as the winding radius. Tube circles are superimposed and three adjacent centers of tube circle are connected to form equilateral triangles, as shown in **Figure 3**. By combining the unloaded radius of the reel and the diameter of the tube, the winding radius of the *n*th tube layer can be obtained according to **Eq. 6**. This method is suitable for any type of traditional hard hose traveler. The calculation method of the reel rotation angle is shown in **Eq. 7**. The total length of the tube is represented by S, and the length of the tube wound on the reel is designated as (S-x). When the length of the reel tube wound is reduced, the pulling force required for the reel to rotate at a constant speed is significantly lowered, as shown in **Eq. 8**. Kinetic and cumulative energy consumptions of the reel at a constant speed are shown in **Eqs 9**, **10**.

$$R_n = R_0 + \frac{d}{2} + \frac{\sqrt{3}d}{2}\sum_{n=2}^{i}(n-1) \tag{6}$$

$$\alpha_n = 2\pi\frac{x - \sum_{n+1}^{i} j_{n+1}L_{n+1}}{L_n} \tag{7}$$

$$F_1 = \mu_1 g[m_0 + \Delta m_{PE}(S-x)] \tag{8}$$

$$T_n = F_1 R_n = \mu_1 g[m_0 + \Delta m_{PE}(S-x)]\left[R_0 + \frac{d}{2} + \frac{\sqrt{3}}{2}\sum_{n=2}^{i}(n-1)\right] \tag{9}$$

$$W_1 = \sum_{n=1}^{i}\int T_n d\alpha = \frac{2\pi\mu_1 g}{L_n}\left[R_0 + \frac{d}{2} + \frac{\sqrt{3}}{2}\sum_{n=2}^{i}(n-1)\right]\int [m_0 + \Delta m_{PE}(S-x)]dx \tag{10}$$

where R_n is the winding radius of the *n*th tube layer, m; R_0 is the unloaded reel radius, m; d is the tube diameter, m; α_n is the rotation angle of the *n*th tube layer of when the reel is unrolled, rad; i is the total number of PE layers; j_{n+1} is the total number of tube wounds at the (n+1)-th layer of the reel; L_n is the winding perimeter of each tube in the *n*th layer, m; F_1 is the pulling force required for the reel to rotate at a constant speed, N; m_0 is the unloaded weight of the reel, kg; Δm_{PE} is the weight of a tube full of water per unit length, kg m^{-1}; T_n is the kinetic energy of the reel required to rotate at a constant speed, N m^{-1}.

Tube Sliding

The pulling force required for the tube to slide at a constant ground velocity is gradually increased, as shown in **Eq. 11**. The cumulative energy consumption of the tube required to slide at a constant speed is shown by **Eq. 12**:

$$F_2 = \frac{\mu_2 \Delta m_{PE} g x}{\cos\theta} \tag{11}$$

$$W_2 = \int F_2 dx = \frac{\mu_2 m_{PE} g}{\cos\theta}\int x dx \tag{12}$$

where F_2 is the required pulling force for the tube to slide at a constant ground velocity, N.

Dynamic Total Energy Consumption of Reel Rotation and Tube Sliding

Total dynamic pulling force F and operation total energy consumption W of the reel and the tube are shown by **Eqs 13**, **14**, respectively:

$$F = F_1 + F_2 = \mu_1 g[m_0 + \Delta m_{PE}(S-x)] + \mu_2 \Delta m_{PE} g x \tag{13}$$

$$W = W_1 + W_2 = \int T_n d\alpha + \int F_2 dx \tag{14}$$

Model Parameters

The model JP50-180 of the traditional hard hose traveler is chosen in this paper. The inner diameter, outer diameter, and tube length are 40 mm, 50 mm, and 180 m, respectively, while the weight of the reel is 102 kg. The weight of 1 m of the waterless tube is measured by the weighing method. Combined with the amount of water that can be contained in the tube, the full water weight of the tube is approximately 2.592 kg/m. Since most of the soil has a certain viscosity and cannot be completely dried, it is assumed that the soil moisture content under natural drying conditions is 20.7%. The minimum friction coefficient between the tube and the soil is 0.3 (GB/T 21400.1-2008, 2008). Therefore, in this paper, the friction

TABLE 2 | Reel and tube parameters.

Number of tube layers	Winding radius (m)	Number of winding turns	Winding circumference per turn (m)	Total winding length (m)		Deviation
				Calculated value a	Rate (%)	
1	0.479	12.0	3.025	36.30	36.12	0.50
2	0.522	13.0	3.292	42.80	42.66	0.33
3	0.566	12.0	3.533	42.40	42.65	-0.59
4	0.609	13.0	3.846	50.00	49.74	0.52
5	0.652	Approximately 2.1	4.099	8.50	8.83	-3.74

*Note: The deviation is calculated as [(a-b)/b]*100%.*

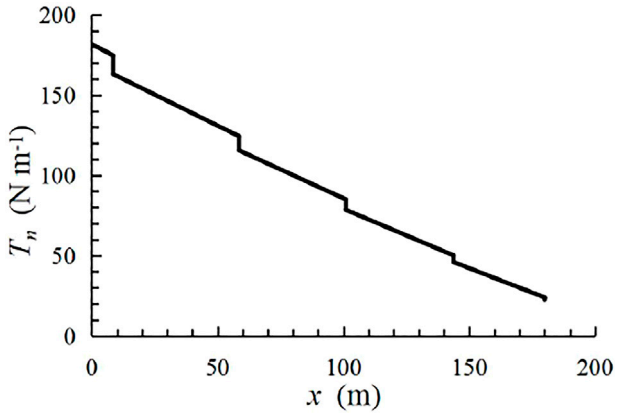

FIGURE 4 | The kinetic energy of reel rotation.

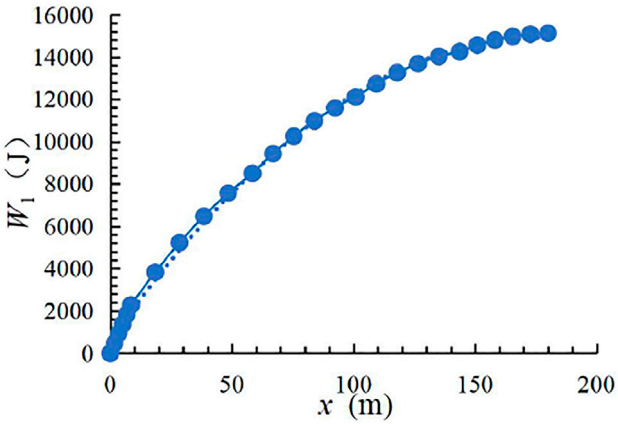

FIGURE 5 | Accumulated energy consumption of reel rotation.

coefficient for a certain soil surface flatness and soil moisture content of 20.7% is also 0.3. After removing the water turbine and turbine gearbox of a traditional hard hose traveler, the friction coefficient of the reel rotation is taken according to the general friction coefficient of metal lubrication, i.e., 0.05. By measuring the circumference of the unloaded reel, the radius is calculated as 0.454 m. After employing **Eq. 6**, the remaining reel and tube parameters are shown in **Table 2**. The difference between the calculated and the measured value of the total winding length of each tube layer is not more than 0.4 m, and the deviation rate is approximately equal to 0.5%. Therefore, the calculation method according to **Eq. 6** is more accurate. Hence, more effective support for the calculation of the cumulative energy consumption of the reel can be provided.

Calculation Results

During the operation process of the reel from the full load tube to the no-load tube, according to **Eq. 8**, the function of the pulling force required for the reel to rotate at a constant speed is shown in **Eq. 15**, and its maximum value is 278.6 N. The change process of kinetic energy calculation value of the reel rotation is shown in **Figure 4**. As the tube length on the reel gradually decreases, the kinetic energy demonstrates a stepped downward trend. This step is caused by the tube switching the number of winding layers. Gradual step decrease is mainly caused by the reduction of the wound tube quality. Calculation of the cumulative energy consumption of reel rotation is shown in **Figure 5**. The maximum value is obtained as 15120.83 J. According to **Eq. 10**, the curve is divided into five sections, and each segment is represented by a quadratic function. Therefore, the curve is fitted into a quadratic function according to **Eq. 16** with a fitting coefficient of 0.998. As the expansion length of the tube increases, the amount of cumulative energy consumption change is gradually reduced reduce. The change parameters of kinetic energy and accumulated energy consumption of the reel are shown in **Table 3**.

$$F_1 = -1.2701x + 278.6 \tag{15}$$

$$W_1 = -0.4533x^2 + 160.94x + 643.3 \tag{16}$$

During the tube pulling process, according to **Eqs 11**, **12**, when θ is not substituted into a specific value, the functions of the required pulling force and cumulative energy consumption of the tube are shown in **Eqs 17**, **18**, respectively. As previously demonstrated, with a continuous increase of the ground slope from 0°, 15°, and 30°, the required tensile force, and energy consumption of the tube are also increased. When the ground slope is 0°, maximum values of the tensile force and maximum cumulative energy consumption are 1372.86 N and 123 456.96 J, respectively. The change process of cumulative energy consumption for tube sliding is shown in **Figure 6**.

$$F_2 = \frac{7.627}{\cos\theta}x \tag{17}$$

$$W_2 = \frac{1}{\cos\theta}\left(3.8104x^2 - 2.067 \times 10^{-3}x\right) \tag{18}$$

TABLE 3 | Change parameters of reel energy consumption.

Number of tube layers	The expanded length of the tube (m)	Kinetic energy (N m^{-1})	Accumulated energy consumption (J)
5	0	181.70	0
	1.7	180.29	469.94
	3.4	178.88	932.54
	5.1	177.47	1,387.80
	6.8	176.07	1,835.71
	8.5	174.66	2,276.29
4	8.5	163.06	2,276.29
	18.5	155.33	3,829.58
	28.5	147.60	5,228.20
	38.5	139.86	6,472.15
	48.5	132.13	7,561.43
	58.5	124.40	8,496.04
3	58.5	115.55	8,496.04
	66.98	109.46	9,424.24
	75.46	103.37	10,249.13
	83.94	97.27	10,970.69
	92.42	91.18	11,588.95
	100.9	85.09	12,103.89
2	100.9	78.58	12,103.89
	109.46	72.90	12,727.90
	118.02	67.22	13,254.69
	126.58	61.54	13,684.27
	135.14	55.86	14,016.64
	143.7	50.18	14,251.79
1	143.7	46.02	14,251.79
	150.96	41.61	14,553.86
	158.22	37.19	14,791.80
	165.48	32.77	14,965.61
	172.74	28.36	15,075.28
	180	23.94	15,120.83

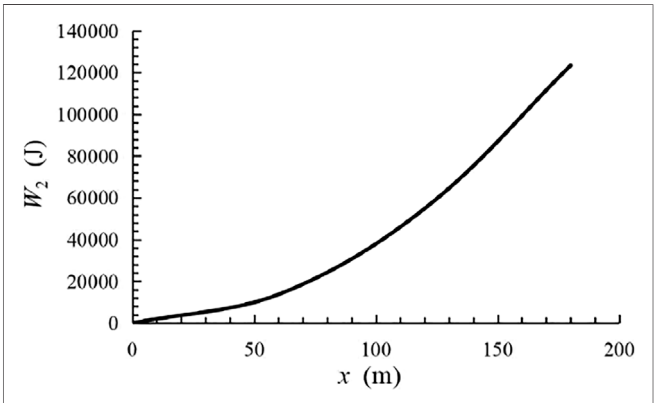

FIGURE 6 | Cumulative energy consumption of tube sliding.

According to **Eqs 17**, **18**, the dynamic function of the total tensile force and total reel and tube energy consumption can be determined. With an increase in the length of the pulled-out tube, the required pulling force and accumulated energy consumption for reel rotation are gradually reduced. Cumulative energy consumption of reel rotation and tube sliding accounts for 10.91 and 89.09% of the total energy consumption, respectively. Moreover, tube sliding accounts for the highest proportion.

OPERATION PULLING FORCE AND ENERGY CONSUMPTION TEST ANALYSIS

During the test, calculating energy consumption *via* pulling force is the same as the calculation model. Therefore, the test research will only focus on the pulling force. First, the pulling force of the tube sliding is investigated. Second, the total pulling force of the reel and tube operation is analyzed. By observing the difference between the two, the pulling force of the reel rotation during the test is obtained. The test assumes fixed soil surface flatness, and the effect of soil moisture content and tube length on tube sliding will be considered.

Test Method

In this paper, the tube is pulled out by a small machine and moved along a straight line. A measuring bucket, which is used to calibrate the position of the tension meter and measure the pulling force, is placed every 10 m from the reeling car. The test operation process of the reel and the tube is shown in **Figure 7**. The test site is in Zibo City, Shandong Province, China. The terrain is relatively flat, and the

FIGURE 7 | The test process of dragging the tube with water.

ground slope is within ±1°. Therefore, the default value is set as 0°. The pulling force of the tube is measured by a tension meter (a range of 0.1–10 kN), and the data is acquired at multiple velocities and the average value is taken. The schematic diagram of the test method is shown in **Figure 1**. After the tube is filled with water, the valve is closed and the pump is cut out. Lastly, the tension meter is connected between the small machine and the tube.

During the test, due to the local unevenness of the field roads, the soil of the field roads is leveled to improve the accuracy of the measured pulling tension between the tube and the soil. The aforementioned provides a reference for power configuration design and future research. The soil surface flatness is measured by the chain measurement method (Zhang et al., 2016), which is shown in **Figure 8**. The calculation method of soil surface flatness is shown in **Eq. 19**. Within the leveling method, the bumps are drawn, filled with soil, and compacted by the movement of small machine, repeatedly. The leveled soil surface is shown in **Figure 9**. The soil surface flatness after treatment was 99.6%.

$$C = \left(1 - \frac{H_2}{H_1}\right) \times 100\% \tag{19}$$

where C is soil surface flatness, %; H_1 is the length of chain, m; H_2 is the length of a tape measure when the chain is relatively close to the measured soil, m.

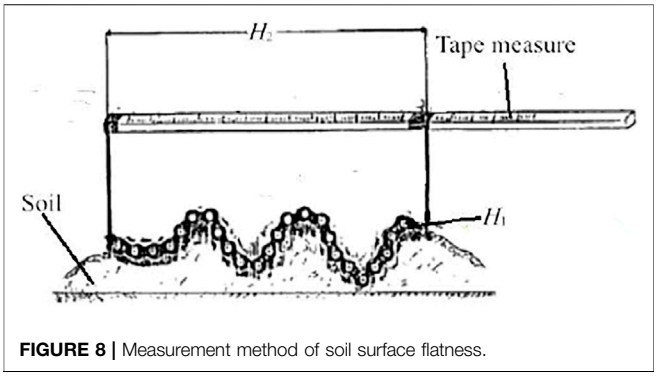

FIGURE 8 | Measurement method of soil surface flatness.

FIGURE 9 | The leveled soil surface.

Tube Sliding

The test was carried out on a road with three soil moisture contents. An 18 m closed tube with water is pulled by a motor at a constant speed. The weight of an 18 m tube with water per unit length is 443.6 N. A tension meter with a range of 0–500 N and an accuracy of 0.1 N pulls the tube at a constant speed, and the average value of multiple measurements is taken. The friction data of different soil moisture contents are shown in **Table 4**, while the friction coefficient between the tube and the ground is shown in **Eq. 20**.

$$\mu_2 = \frac{F'}{m'g} \tag{20}$$

Where F' is the average value of friction for 18 m tube, N; m' is the quality of 18 m tube with water, kg.

According to **Table 4**, with an increase in the soil moisture content, the friction coefficient between the tube and the soil increases. The coefficient value is approximately in the range of 0.275–0.388. After proportional conversion, the minimum and maximum friction force between the 180 m tube and the soil is 1258.3 N and 1773.3 N, respectively. Therefore, the required pulling force and energy consumption for tube sliding increase with an increase in the soil moisture content.

Reel and Tube Operation

During reel and tube operation, the linear relationship between the unfolded tube length and the average value of the total pulling force is shown in **Figure 10**. The fitting equation and fitting coefficient R^2 of each soil moisture contents are shown in **Eq. 21** and **Table 5**,

TABLE 4 | Friction data of different soil moisture contents.

Soil moisture content (%)	The average value of friction of 18 m tube (N)	The friction coefficient between the tube and the ground	The friction force between a 180 m tube and the ground (N)
20.8	125.8	0.275	1258.3
47.7	148.7	0.325	1487.5
70.3	177.3	0.388	1773.3

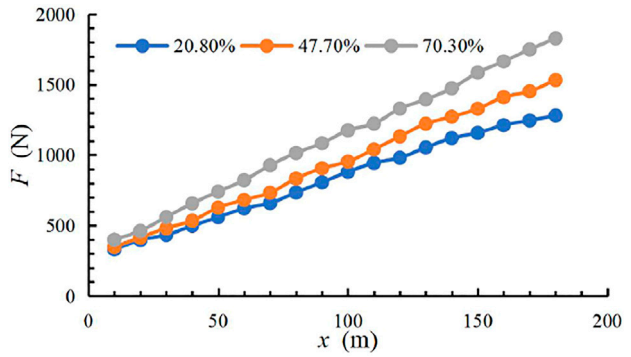

FIGURE 10 | The total pulling force of the reel and the tube.

respectively. It can be observed that the combined effect is the most optimal. With an increase in the soil moisture content, the total pulling force and the slope of the fitted curve are both increased. As the length of the expanded tube increases, the total pulling force increases linearly. As the soil moisture content becomes higher and the length of the tube increases, the superposition of dual factors causes the cumulative amount of the total pulling force to continuously increase. Therefore, the slope of the fitting curve gradually increases. The maximum pulling forces of three types of soil moisture contents are 1280.73, 1532.49, and 1828.24 N, respectively.

$$U(x) = Dx + E \tag{21}$$

where $U(x)$ is the universal pulling force which represents the operation pulling force of the reel and the tube or the pulling force required for the reel rotation, N; Parameters D and E are the equation coefficients.

According to the conducted pulling force analysis, when the reel is fully loaded with the tube, the maximum pulling force of the reel rotating at a constant speed is 317.17, 264.98, and 272.99 N, respectively, and the average value is 285.02 N. The equation coefficients are also shown in **Table 5**.

DISCUSSION

Comparison of Theoretical and Experimental Analysis

Since the weight of the reel in a fully loaded tube is 548.58 kg, the theoretical and tested values of the maximum reel rotation pulling force are 278.6 and 285.02 N, respectively. The deviation rate of the pulling force is 2.3%. The deviation rate equation is shown in **Eq. 22**.

$$p_1 = \frac{(F'_1 - F_1)}{F'_1} \times 100\% \tag{22}$$

where p_1 is the deviation rate of the reel rotation pulling force, %; F_1' is the tested value of the reel rotation pulling force, N.

When the soil moisture content and flatness are 20.7 and 99.6%, respectively, and the tube is dragged, the pulling force and the friction coefficient are 1258.3 N and 0.275, respectively. These values deviate from theoretical ones by 8.3%. The calculation equation is shown in **Eq. 23**. The friction coefficients of other soil moisture content are 0.325 and 0.388, respectively. These values belong to the category of the national standard regarding friction coefficient reference range of 0.3–1.0. Therefore, the measured friction coefficient between the tube and the soil in the test is more reliable.

$$p_1 = \frac{(F_2 - F'_2)}{F_2} \times 100\% \tag{23}$$

where p_2 is the deviation rate of the tube sliding pulling force, %; F_2' is the tested value of the tube sliding pulling force, N.

Analysis of the Tube One-Time Unrolled Time and Operating Costs

The operating costs of the one-time unrolled tube are one of the key parameters of the traditional or new hard hose travelers. During the unwinding of the tube, the reel rotates. By combining the parameters of the moving velocity of the sprinkler and the tube length, the one-time unrolled tube time is shown in **Table 6**. Since the energy consumption of expanding the tube is not affected by the moving velocity of the sprinkler, the longer it takes to expand the tube, the higher are the operating costs. When the new hard hose traveler is designed, under the condition that the same precipitation depth is met, shortening of the one-time unrolled tube time is beneficial to reducing expenses. Chinese electric power transmission and distribution for well-facilitated farmland construction is taken as an example. Under certain conditions, when the maximum cumulative energy consumption of the unrolled tube is 123456.96 J, its operating cost is 0.0185 CNY, as shown in **Table 7**.

According to the presented data, the energy consumption of the new hard hose traveler can be reduced by increasing the

TABLE 5 | Coefficient of the fitting equation for the reel and the tube.

Soil moisture content (%)	The operation pulling force of reel and tube			Pulling force required for reel rotation	
	D	*E*	R_2	*D*	*E*
20.8	5.8567	272.99	0.9963	−1.1334	272.99
47.7	7.0974	264.98	0.9984	−1.1665	264.98
70.3	8.4111	317.17	0.9991	−1.4496	317.17

TABLE 6 | The one-time unrolled tube time.

The moving velocity of the sprinkler (m h^{-1})	15	20	25	30	35	40	45	50
The tube one-time unrolled time (h)	12.00	9.00	7.20	6.00	5.14	4.50	4.00	3.60

TABLE 7 | The operating costs of the one-time unrolled tube.

Project		Parameters
Conditions of the unrolled tube	Ground slope (°)	0°
	Soil moisture content (%)	20.8%
	Tube length (m)	180
Electric power transmission and distribution	AC voltage level (kV)	<1
	Unit price (CNY)	0.54
Total price (CNY)		0.0185

moving velocity of the sprinkler (i.e., the moving velocity of the tube) and reducing the driving mechanism energy consumption of the sprinkler radial movement. Thus, the operating costs will be reduced.

Power Configuration

Design Scheme of an Electric Tracked Vehicle

The power configuration of an electric tracked vehicle is the power source for the reel and tube operation of a new hard hose traveler. Since the maximum friction coefficient between the tube and the soil is 1.0 (GB/T 21400.1-2008, 2008), the electric tracked vehicle needs to overcome a frictional force between the reel and the tube of approximately 4851 N (**Eq. 13**). Performance design parameters of the electric tracked vehicle are shown in **Table 8**. Considering the operation start and some accidental factors, the external pulling force that has to be overcome is set to 6500 N. To achieve remote control of new hard hose traveler and more flexible anti-friction ability, the rubber crawler chassis is driven by the battery power supply and an AC380V servo motor. Power configuration plays a decisive role in overcoming the resistance of the electric tracked vehicle, as well as operation resistance between the reel and the tube. Resistance of the electric tracked vehicle is divided into operation resistance and internal rolling friction resistance. The sprinkler gear and the transfer gear are set for the sprinkler irrigation operation and the transformation of the new hard hose traveler.

Motor Power Selection

Driving resistance includes rolling friction of the crawler and the soil, adhesion, and slant downward static friction. All of them are caused by driving straight, turning, side-slip, and climbing the slope upward of the crawler. The coefficients of rolling friction and adhesion of electric tracked vehicles in normal operation on the soil are 0.07 and 1.0, respectively (Chen and Gu, 1965). The internal rolling friction resistance mainly includes the meshing friction between the driving wheel and the crawler and the rolling friction between the guide wheel and the crawler. The friction coefficient is generally between 0.05 and 0.07 (Chen and Gu, 1965). Therefore, the mean value of 0.06 is taken in this paper.

The AC380V servo motor has three times the overload capacity than the rated power and some overload time. During sprinkler irrigation operation and transfer, possible extreme operating states of new hard hose traveler electric tracked vehicles are divided into a long and short time. The friction coefficient of various operating states is defined as μ_3 (including the rolling friction between the crawler and the soil, and the internal rolling friction of the electric tracked vehicle). The power of these states is converted by **Eq. 24** and shown in **Table 9**.

$$P_0 = \frac{F_3 v}{3600\eta_1\eta_2} = \frac{\mu_3 M g v}{3600\eta_1\eta_2} \tag{24}$$

where P_0 is the limit power, W; F_3 is the force that needs to be overcome in various extreme states of the electric tracked vehicle, N; v is the traveling speed of the electric tracked vehicle, m h^{-1}; η_1 is the

TABLE 8 | Performance parameter design of electric tracked vehicle.

Design project	External pulling force (N)	Weight (kg)	Climbing ability (°)	Speeds of sprinkler gear (m h^{-1})	Speed of transfer gear (m h^{-1})
Parameters	6,500	1400	30	15/20/25/30/35/40/45/50	5,000

TABLE 9 | The extreme power of the new hard hose traveler in different operating states.

Work content of the new hard hose traveler	Different extreme operating states				Extreme power (W)
	Climbing 30°	Speed (m h^{-1})	Turn	Overcome pulling force 6,500 N	
Short-term, sprinkler irrigation	Yes	5,000	No	Yes	24,599.74
Short-term, transfer	No	5,000	Yes	No	25,184.54
Long-term, sprinkler irrigation	Yes	50	No	Yes	246.00
Long-term, transfer	No	5,000	No	No	2,893.34

efficiency of the transmission device of the electric tracked vehicle which is generally in the range of 0.95–0.98, i.e., it is taken as η_1 = 0.95 in this paper; M is the weight of the electric tracked vehicle, kg.

If the motor power reserve coefficient is selected as 1.2, the maximum short-term and long-term limit power required of the electric tracked vehicle is 30221.45 and 3476.80 W, respectively. Since the electric tracked vehicle achieves normal movement and steering *via* forward and reverse rotation of the two motors and different speeds and reduces costs, when choosing two AC380V servo motors with a power of 5500 W, all working requirements of the electric tracked vehicle can be met.

CONCLUSION

In this paper, a new hard hose traveler with the function of electric drive and self-propelled was developed to reduce the energy consumption of traditional hard hose travelers and achieve intelligent operation. The operational energy consumption of reel and polyethylene tubes is an important part of the energy consumption of the proposed hard hose traveler. Therefore, the traditional JP50-180 reel sprinkler was selected. The required pulling force and operation energy consumption of the reel and the tube were theoretically and experimentally analyzed. A reasonable power configuration of the new hard hose traveler was designed. The following conclusions are drawn:

A calculation model for the dynamic change of the pulling force and energy consumption of reel and tube operation was constructed. The difference between the calculated and the measured values of the total winding length of each tube layer was not more than 0.4 m, with the deviation rate being approximately equal to 0.5%. The reel was fully loaded to no-load tubes. The maximum value of the pulling force and cumulative energy consumption of reel rotation were 278.6 N and 15 120.83 J, respectively. When the ground slope was 0° and the friction coefficient between the tube and the soil was 0.3, the maximum value of the pulling force and cumulative energy consumption of the tube sliding were 1372.86 N and 123 456.96 J, respectively. These values account for 10.91 and 89.09% of the total energy consumption, respectively. As the length of the tube increased, the kinetic energy of reel rotation showed a stepwise downward trend. Moreover, the pulling force and cumulative energy consumption showed an upward trend in the form of a quadratic function. With an increase in the ground slope, the required pulling force and energy consumption of the tube were also increased.

For three soil moisture contents of 20.8, 47.7, and 70.3%, the friction coefficient of the drag tube was 0.275, 0.325, and 0.388, respectively, and the maximum pulling force were 1258.3, 1487.5, and 1773.3 N, respectively. The required pulling force and energy consumption for tube sliding increased with an increase in the soil moisture content. The maximum test value of the reel rotation was 285.05 N, and the deviation rate from the theoretical value was 2.3%. When the soil surface had the same flatness and the soil moisture content was 20.8%, the theoretical and experimental value of the pulling force had a deviation rate of 8.3%. The operating costs of the one-time unrolled tube are approximately 0.0185 CNY.

The conducted study shows that the required pulling force of the reel and the tube under the working conditions of the new hard hose traveler was 6500 N. The power configuration of the electric tracked vehicle is the power source for the operation of the hard hose traveler reel and the tube. The design plan and power configuration were provided according to the working mode of the electric tracked vehicle. The power of two AC380V servo motors was 5500 W each.

The other energy consumption of the new hard hose traveler and other parts design on electric tracked vehicle will be studied in future works.

DATA AVAILABILITY STATEMENT

The original contributions presented in the study are included in the article/supplementary material, further inquiries can be directed to the corresponding author.

AUTHOR CONTRIBUTIONS

ZX conceived and designed the study and completed the paper in English. HL and QX revised it critically for important intellectual content and gave good research advice and revised the manuscript. All authors have read and agreed to the published version of the manuscript.

FUNDING

This research was supported by the following grants: the National Natural Science Foundation of China (51939005, 51809119), Postgraduate Research & Practice Innovation Program of Jiangsu Province (KYCX19_1602).

REFERENCES

Biolan, I., Sovaiala, G., and Visan, A. L. (2012). Optimization of the Hydraulic Bellows Engine Parameters Used to Drive Irrigation Reel Hose Machine - IATF 300. *Adv. Mater. Res.* 463-464, 1137–1140. doi:10.4028/www.scientific.net/amr.463-464.1137

Burt, C. M., Clemmens, A. J., Bliesner, R., Hardy, L., and Merriam, J. L. (1999). *Selection of Irrigation Methods for agriculture[M]*. San Luis Obispo: American Society of Civil Engineers.

Chen, B., and Gu, P. (1965). *Tractor theory[M]*. Beijin: China Industry Press.

Cui, Z., Guan, C., and Chen, Y. (2019). Design of Small Multi-Functional Electric Crawler Platform for Greenhouse. *Trans. Chin. Soc. Agric. Eng. (Transactions CSAE)* 35 (9), 4857 (in Chinese with English abstract). doi:10.11975/j.issn.1002-6819.2019.09.006

Fan, S. (2017). *Lightweight Design and Dynamics Research of Chassis Frame for Orchard Electric Tracked Vehicle [D]*. Guangzhou: South China Agricultural University.

GB/T 21400.1-2008 (2008). *Traveller Irrigation Machines-Part1:Operational Characteristics and Laboratory and Field Test methods[S]*. Beijing: Standards Press of China.

Ge, M. (2018). *Study on Irrigation Quality and Optimal Design of Solar Driven Hard Hose Traveler[D]*. Yang ling, China.: Yang ling: Northwest A&F University.

Ge, M., Wu, P., Zhu, D., Zhang, L., and Cai, Y. (2020). Optimized Configuration of a Hose Reel Traveling Irrigator. *Agric. Water Manage.* 240, 106302. doi:10.1016/j.agwat.2020.106302

Keller, J., and Bliesner, R. D. (1990). *Sprinkle and Trickle irrigation[J]*. US: Springer.

Li, D., Zhu, D., Ge, M., Wu, S., Wang, R., Wang, B., et al. (2019). Optimal Configuration and Field Experiments for the Photovoltaic System of a Solar-Powered Hose-Drawn Traveler. *Trans. ASABE (American Soc. Agric. Biol. Engineers)* 62 (6), 1789–1801. doi:10.13031/trans.13298

Li, H. (2018). *Design and Research of Tracked Electric Bamboo and Wood Pruning Tip Cutting and Transportation Machine[D]*. Hangzhou: Zhejiang Agriculture & Forestry University.

Oakes, P. L., and Rochester, E. W. (1980). Energy Utilization of Hose Towed Traveler Irrigators. *Trans. ASAE* 23 (5), 1131–1134. doi:10.13031/2013.34733

Pan, J. (2019). *Design and Study of Large Scale Hydraulic Drive Reel Sprinkler Irrigation Machine and its Control System[D]*. Xuzhou, China.: China University of Mining and Technology.

Rochester, E. W., Flood, C. A., and Hackwell, S. G. (1990). Pressure Losses from Hose Coiling on Hard-Hose Travelers[J]. *Trans. ASAE* 33 (3), 834–0838. doi:10.13031/2013.31408

Rochester, E. W., and Hackwell, S. G. (1991). Power and Energy Requirements of Small Hard-Hose Travelers. *Appl. Eng. Agric.* 7 (5), 551–556. doi:10.13031/2013.26267

Tang, L., Yuan, S., Malin, M., and Parameswaran, S. (2017). Secondary Vortex-Based Analysis of Flow Characteristics and Pressure Drop in Helically Coiled Pipe. *Adv. Mech. Eng.* 9 (4), 1. doi:10.1177/1687814017700059

Tang, L., Yuan, S., and Tang, Y. (2018). Analysis on Research Progress and Development Trend of Hose Reel Hard Hose Traveler [J]. *Trans. Chin. Soc. Agric. Machinery* 49 (10), 1–15. doi:10.6041/j.issn.1000-1298.2018.10.001

Tang, L., Yuan, S., and Tang, Y. (2014). *Flow Resistance Study of Helically Coiled Pipe for A Hose Reel Hard Hose Traveler Based on CFD Analysis [J]*. ASABE.

Tang, Y., Zhu, X., and Mei, X. (2014). Performance Test of Water Turbine of JP50 Reel Sprinkler[J]. *China Rural Water and Hydropower* 2014 (02), 26–29.

Xu, G., Song, Y., and Qiu, X. (2022). Matching Design and Test of Power System for Electric Self-Propelled Crawler Chassis of Orchard[J]. *J. Agric. Mechanization Res.* 44 (04), 251–255. doi:10.13427/j.cnki.njyi.2022.04.045

Yang, L., Tang, Y., and Tang, L. (2018). Brushless DC Motor Drive Characteristics and System for Reel-Type Hard Hose Traveler. *J. Drainage Irrigation Machinery Eng.* 36 (08), 690–695. doi:10.3969/j.issn.1674-8530.18.1159

Yuan, S., Niu, G., Tang, Y., Lingdi, T., and Xiangyuan, Z. (2014). Experiment and Numerical Estimation of Performance of Hydraulic Turbine of JP50 Reel Sprinkle. *J. Drainage Irrigation Machinery Engineering(JDIME)* 32 (7), 553557+562. (in Chinese). doi:10.3969/j.issn.1674-8530.13.0187

Zhang, C., Tang, Y., and Tang, L. (2015). Efficiency Analysis and Experimental of the Type JP75 Hose Reel Hard Hose Traveler[J]. *J. Agric. Mechanization Res.* 37 (09), 37–40.

Zhang, H. (2016). *Design of Multifunctional Orchard Lifting Platform in Electric Crawler Type [D]*. Guangzhou: South China Agricultural University.

Zhang, M., and Wang, H. (2005). Experimental Study of the Pressure Loss of Hoses of Hard Hose Traveler[J]. *Chin. Agric. Mechanization* 2005 (03), 58–59. doi:10.3969/j.issn.1006-7205.2005.03.019

Zhang, S., Huang, P., and Zhao, Z. (2016). A Research on Soil Surface Roughness Measurment-Methods[J]. *J. Agric. Mechanization Res.* 38 (11), 257–262. doi:10.3969/j.issn.1003-188X.2016.11.051

Conflict of Interest: The authors declare that the research was conducted in the absence of any commercial or financial relationships that could be construed as a potential conflict of interest.

Publisher's Note: All claims expressed in this article are solely those of the authors and do not necessarily represent those of their affiliated organizations, or those of the publisher, the editors and the reviewers. Any product that may be evaluated in this article, or claim that may be made by its manufacturer, is not guaranteed or endorsed by the publisher.

frontiers in Energy Research

ORIGINAL RESEARCH
published: 14 January 2022
doi: 10.3389/fenrg.2021.821925

The Leading-Edge Structure Based on Geometric Bionics Affects the Transient Cavitating Flow and Vortex Evolution of Hydrofoils

Hao Yan[1], *Haozhou Zhang*[1]*, *Junhua Wang*[2], *Tianya Song*[3] *and Fenglei Qi*[1]

[1]School of Mechanical Engineering, Hefei University of Technology, Hefei, China, [2]Hefei Kaiquan Electric Motor Pump Co., Ltd., Hefei, China, [3]Hefei Hengda Jianghai Pump Co., Ltd., Hefei, China

A hydrofoil is a fundamental structure in fluid machinery, and it is widely applied to the fields of propellers, blades of axial flow pumps and underwater machinery. To reveal that the geometric structure of the leading-edge of a hydrofoil is the mechanism that affects the transient cavitating flow, we regard the three fish-type leading-edge structures of mackerel, sturgeon and small yellow croaker as the research objects and use high-precision non-contact 3D scanners to establish three bionic hydrofoils (Mac./Stu./Cro.). We use large eddy simulation to simulate the transient cavitating flow of hydrofoils numerically and compare and analyze their lift–drag characteristics, the transient behavior of unsteady cavitation and the vortex evolution. The numerical simulation results are in good agreement with the experimental results. The warping of leading-edge structure will cause a change in lift–drag characteristics, and the Cro. hydrofoil has a good lift-to-drag ratio. When the leading-edge structure is tilted upward (Cro. hydrofoil), the position of the attached cavity will move forward, which will accelerate the cavitation evolution and improve the velocity fluctuation of the trailing edge. When the leading-edge structure is tilted downward (Stu. hydrofoil), the change in the vortex stretching and dilatation terms will be complex, and the influence area of the vortex will widen.

Keywords: bionic hydrofoil, large eddy simulation, cavitation, lift-drag characteristic, vortex evolution

OPEN ACCESS

Edited by:
Jin-Hyuk Kim,
Korea Institute of Industrial Technology, South Korea

Reviewed by:
Bin Huang,
Zhejiang University, China
Jiang Lai,
Nuclear Power Institute of China (NPIC), China
Man-Woong Heo,
Korea Institute of Ocean Science and Technology (KIOST), South Korea

***Correspondence:**
Haozhou Zhang
haozhouzhang@mail.hfut.edu.cn

Specialty section:
This article was submitted to Process and Energy Systems Engineering, a section of the journal Frontiers in Energy Research

Received: *25 November 2021*
Accepted: *27 December 2021*
Published: *14 January 2022*

Citation:
Yan H, Zhang H, Wang J, Song T and Qi F (2022) The Leading-Edge Structure Based on Geometric Bionics Affects the Transient Cavitating Flow and Vortex Evolution of Hydrofoils. Front. Energy Res. 9:821925. doi: 10.3389/fenrg.2021.821925

INTRODUCTION

Cavitation is a typical vapor-liquid flow, and mass transmission is determined using the bypass pressure and the local vaporisation pressure of the fluid. The fluid bypassing a hydrofoil will generate lift. In accordance with this principle, hydrofoils are widely used in the field of hydraulic machinery. However, cavitating flow is prone to occur in the application process, and a long-term operation under cavitation will cause cavitation erosion, which will seriously affect the performance of hydraulic machinery. In-depth research has found that the leading-edge geometry of a hydrofoil is the key factor affecting the aerofoil cavitating flow (Arabnejad et al., 2019; Liu and Tan, 2020; Garg et al., 2019). Most aerofoils used in hydraulic machinery are still based on aerodynamics. The fluid flow state will inevitably be changed by the difference in physical properties, such as density and viscosity, between air and water and other liquid fluids, thereby affecting the cavitation performance of hydraulic machinery. Therefore, changing the structure of the leading-edge of a hydrofoil and developing a new type of aerofoil suitable for hydraulic machinery are particularly important. A large number of fishes are living in oceans and

freshwater lakes. These fishes have excellent hydraulic properties and provide basic materials for changing the structure of the leading-edge of a hydrofoil.

Researchers have conducted considerable basic research on the cavitating flow of different hydrofoils. For example, Zhang et al. (2020) used numerical simulation to study the hydrodynamic characteristics of the Clark-y hydrofoil and found that the cavitation of the leading-edge promotes the formation of a counterclockwise vortex at the trailing edge and weakens the fluctuation in hydrodynamic load. Rajaram and Srikanth (2020) optimised the geometry of a basic hydrofoil to obtain a superior hydrofoil under specific flow conditions. Marimon et al. (2018) evaluated a simplified hydrofoil geometry and used a performance prediction method for flexible foils to prove that distortion will reduce the effective angle of attack by approximately 30% and substantially reduce the lift and drag of the hydrofoil at high flow rates. Antoine et al. (2009) analysed the structural characteristics of a deformable hydrofoil in a forced pitching motion and showed that structural changes are closely related to the phenomenon of fluid mechanics. Fujii et al. (2007) also studied the influence of hydrofoil geometry on cavitation dynamic characteristics, and found that the change of hydrofoil geometry only affects the oscillation intensity of some cavities. Custodio et al. (2018) defined different hydrofoil leading-edge structures to study the cavitation and hydrodynamic characteristics of hydrofoils. The results showed that the cavitation of the hydrofoil with a large amplitude is mainly confined to the area behind a convex groove, whereas the hydrofoil with a flat leading-edge and small amplitude shows flaky cavitation in the whole span direction. Oller and Nallim (2016) designed the geometric structure of a hydrofoil blade by using an appropriate aerofoil shape to check its hydrodynamic characteristics and determine the streamline velocity and pressure field. Amini et al. (2019) used an ellipse as the contour of the hydrofoil and studied its suppression effect on tip vortex cavitation by bending the hydrofoil. For the hydrofoil (10%-bent 90 degrees-downward), the tangential velocity of the leading-edge vortex is improved. Zhou et al. (2016) studied the effect of the wingtip clearance on the flow characteristics of the hydrofoil. The sharp-tip foil has a small amount of vortex leakage, and the tip separation vortex makes the gap cavitation more serious. Recent studies have confirmed that the hydrodynamic and lift–drag characteristics of a blade can be significantly improved by changing the shape of the leading-edge of a hydrofoil.

Bionics is a comprehensive cross-discipline that applies the laws and mechanisms discovered in the biological world to the engineering application field to solve problems. Many methods for solving problems have been found using biological geometry, physiological functions or life processes in engineering practice (Hong et al., 2009). Huang et al. (2020) designed three new dolphin-type hydrofoils based on the contour curve of a dolphin and compared them with NACA0018 aerofoils. They found that the hydrofoils have the best lift–drag characteristics when the deflection angle is 24°. You et al. (2020) designed two bionic tools based on the surface structure of a dung beetle head, which effectively reduced the main cutting force of the tools and the average friction coefficient of the chip interface. Liu and Liu (2014) constructed a bionic hydrofoil based on the geometric characteristics of an owl, which effectively improved the lift and drag characteristics of the hydrofoil and revealed the characteristics of the sound source. Xue et al. (2016) regarded fish as imitation organisms and designed a fin–peduncle propulsion mechanism in accordance with their shape, which improved the propulsion efficiency of hydrofoil propellers. In the above research report, when obtaining the surface information of an organism, acquiring an accurate bionic physical model through curve-fitting technology is a critical step. In the aspect of bionic hydrofoil design, the Hicks–Henne shape function method with a strong hydrofoil shape control capability (Hicks and Henne, 1978), the CST aerofoil parameterisation method with a large design space description (Kulfan, 2008) and the spline parameterisation method using a non-uniform rational B-spline (NURBS) curve (Masters et al., 2017) to describe aerofoils are the commonly used modeling methods. These methods can provide theoretical support for this paper.

With the development of CFD technology, the numerical simulation technology based on large eddy simulation (LES) has been widely used in capturing complex cavitating flows and vortex evolution. Wang et al. (2019) simulated the cavitating flow of liquid nitrogen on a hydrofoil on the basis of a homogeneous mixture model with LES and found that the strong re-entrant jet initiated in the cavity tail is the main reason causing the cavity shedding. Huang et al. (2010) proposed a cavitating flow calculation model based on density correction to calculate the cavitating flow of a hydrofoil and found that this model has a significant improvement in the numerical calculation results of cavitating flow. Zhang et al. (2015) studied the unstable cavitation desorption of the Clark-y hydrofoil by increasing the maximum density ratio, which improved the accuracy of numerical simulation. Li et al. (2016) used the LES method to simulate the transient spatiotemporal flow of the Clark-y hydrofoil, which provided an effective numerical simulation framework for the study of cavitating flow. Ji et al. (2015) used the LES method to numerically simulate the cavitating flow around the NACA66 hydrofoil to study the evolution of cavitation. Sun et al. (2020) used the Schnerr–Sauer cavitation model to simulate hydrofoil cavitation and used the LES method to calculate an unsteady natural ventilation cavitation flow. Huang et al. (2017) proposed an improved partially averaged Navier–Stokes turbulence model to study the transient cavitation turbulence of the Clark-y hydrofoil. Kim and Lee (2015) used LES to study the cloud cavitation behaviour of the Clark-y hydrofoil under different slip conditions.

In summary, the research on hydrofoil hydrodynamics has mainly focused on the lift–drag characteristics and cavitating flow of existing aerofoils (NACA, Clark-y series hydrofoils). However, on the basis of different fishes, the basic research on using geometric bionic principles to change the geometric structure of the traditional hydrofoil leading-edge and analyse the 3D vortex structure and cavitating flow evolution is inadequately deep. Therefore, we select three fishes (mackerel/sturgeon/small yellow croaker) with evident leading-edge differences as the

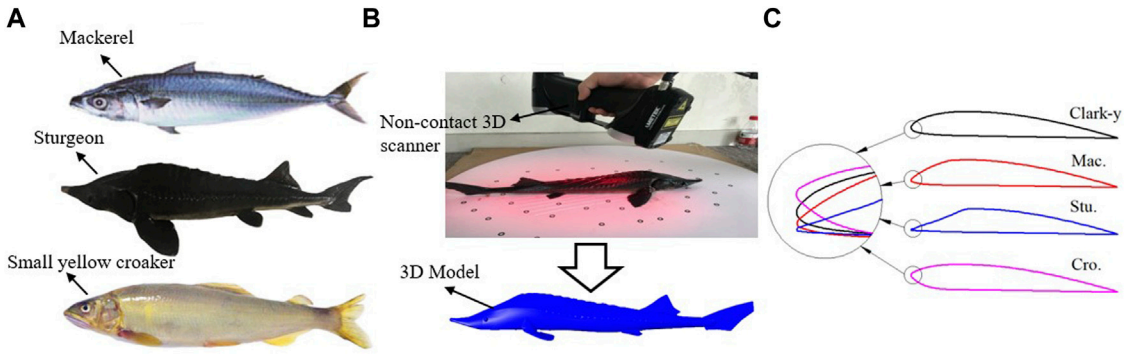

FIGURE 1 | Physical model construction of bionic hydrofoils. **(A)** Three types of fishes. **(B)** 3D reverse engineerin. **(C)** contour curves of four hydrofoils.

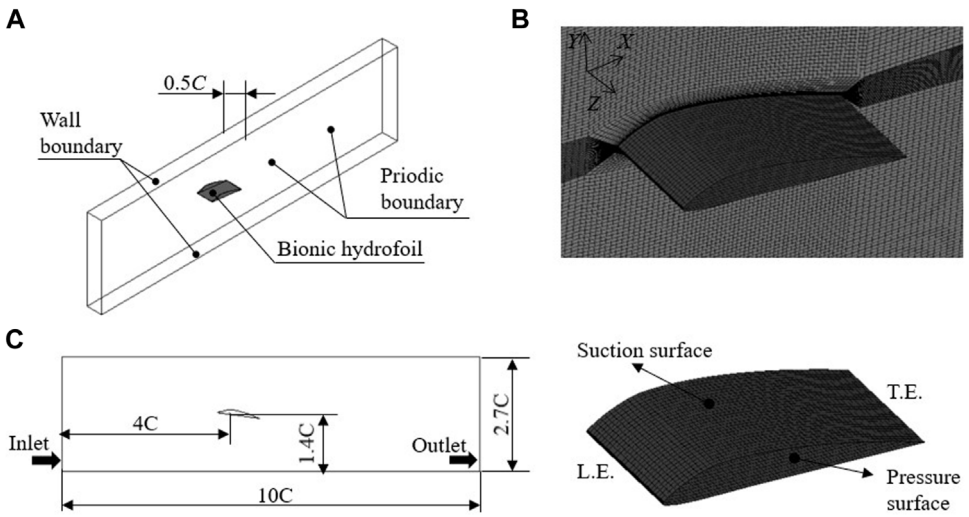

FIGURE 2 | Computational domain and grids. **(A)** Computational area. **(B)** 3D mesh. **(C)** hydrofoil.

research objects to construct a bionic hydrofoil physical model. The lift–drag characteristics, vortex evolution and cavitating flow evolution under different schemes are compared and analysed through the combination of LES and typical hydrofoil model experiments to reveal the mechanism of the change in the hydrofoil leading-edge structure in transient cavitating flow. This study provides a reference for the subsequent optimisation design of hydraulic machinery blades.

NUMERICAL METHOD AND SETUP

Establishment of the Physical Model of Bionic Hydrofoils

Through measurement, we found that mackerel, sturgeon, and small yellow croaker have different leading edge structures. We take these three kinds of fish as the research objects, as shown in **Figure 1A**. Ten fish are selected for each type of fish, and the average value is collected several times to avoid the error caused by the different body sizes of fish. High-precision non-contact 3D scanners are used to perform 3D reverse engineering modeling of all types of fish surface functional surfaces, and Geomagic Design X software is used to reverse the process of obtaining point cloud data to acquire a 3D physical model of fish, as shown in **Figure 1B**. The geometric profile curves of different hydrofoils are obtained and combined with the contours of the Clark-y hydrofoil via the NURBS curve-fitting technology. Four hydrofoils with different leading-edge structures are obtained, as shown in **Figure 1C**.

Simulation Setup

In this study, the commercial software FLUENT is used for numerical simulation. LES is used to calculate the transient cavitating flow of the above four hydrofoils numerically, and the setting of the calculation domain is shown in **Figure 2A** (Hu et al., 2018). The chord length of all hydrofoils is set to C = 70 mm, the angle of attack is 8°, the calculated area length is 10 C, the height is 2.7 C, and the width is 0.5 C. The distance from the

hydrofoils to the inlet is 4 *C*, and the distance to the bottom is 1.4 *C*. The finite volume method is used to discretize the governing equation, and the diffusion term of the equation is in central difference format. The equations are solved using the separation and semi-implicit pressure coupling algorithm. The inlet is set to imposed velocity, the flow rate is 10 m/s, the outlet is set as fixed static pressure, and the pressure is 43,540 Pa. It can be obtained that the cavitation number is 0.8 and the Reynolds number is 700,000. The hydrofoil walls adopt the no-slip boundary condition, the upper and lower walls are set as the free slip walls, and the sidewall boundary is arranged as a periodicity interface. The time step is set to 0.1 ms, and the number of calculation steps is set to 6,000 steps (Zhang et al., 2017).

For LES, the basic governing equations of mass conservation and momentum conservation are as follows:

$$\frac{\partial \rho_m}{\partial t} + \frac{\partial (\rho_m u_i)}{\partial x_i} = 0 \tag{1}$$

$$\frac{\partial (\rho_m u_i)}{\partial t} + \frac{\partial (\rho_m u_i u_j)}{\partial x_j} = -\frac{\partial p}{\partial x_i} + \frac{\partial}{\partial x_j}\left(\mu \frac{\partial u_i}{\partial x_j}\right) \tag{2}$$

Among them, p represents the pressure, and u_i and u_j represent the velocity components on i and j respectively. μ is the laminar viscosity of the mixture, ρ_m is the density of the mixture, which is defined as follows:

$$\mu = \alpha_v \mu_v + (1 - \alpha_v)\mu_l \tag{3}$$

$$\rho_m = \alpha_v \mu_v + (1 - \alpha_v)\mu_l \tag{4}$$

After filtering the above equation, the large eddy equation is obtained:

$$\frac{\partial p}{\partial t} + \frac{\partial (\rho_m \bar{u}_i)}{\partial x_i} = 0 \tag{5}$$

$$\frac{\partial (\rho_m \bar{u}_i)}{\partial t} + \frac{\partial (\rho_m \bar{u}_i \bar{u}_j)}{\partial x_j} = \frac{\partial}{\partial x_j}\left(\mu_m \frac{\partial \bar{u}_i}{\partial x_j}\right) - \frac{\partial \bar{p}}{\partial x_i} - \frac{\partial \tau_{ij}}{\partial x_j} \tag{6}$$

where τ_{ij} is the subgrid scaled stress, which is defined as

$$\tau_{ij} = \rho_m\left(\overline{u_i u_j} - \overline{u_i u_j}\right) \tag{7}$$

The ZGB cavitation model is based on the simplified Rayleigh-Plesset equation, and its accuracy has been widely verified (Cheng et al., 2019). The cavitation model in this paper also adopts the ZGB model, and its mass transfer equation is as follows:

$$\frac{\partial}{\partial t}(\alpha_v \rho_v) + \nabla \cdot \left(\alpha_v \rho_v \vec{V}\right) = S^+ + S^- \tag{8}$$

where α_v is the volume fraction of the vapor, ρ_v is the density of the vapor, and S^+ and S^- represent the mass transfer rates of evaporation and condensation, respectively.

When $P \le P_v$,

$$S^+ = C_{vap}\frac{3(1 - \alpha_v)\alpha_{nuc}\rho_v}{R_B}\sqrt{\frac{2}{3}\frac{(P_v - P)}{\rho_l}} \tag{9}$$

When $P > P_v$,

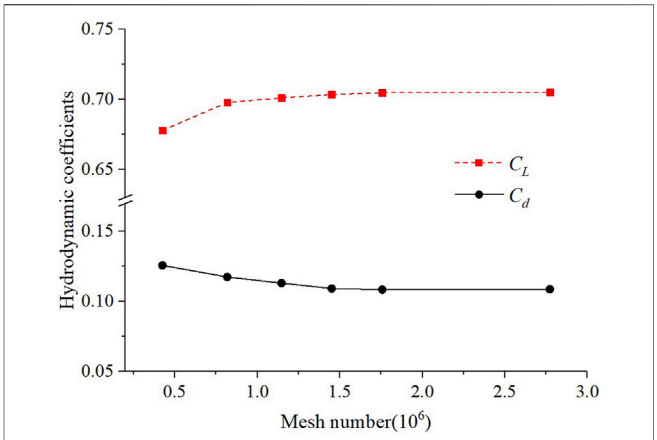

FIGURE 3 | Time-averaged lift and draft coefficients against mesh number.

$$S^- = C_{cond}\frac{3\alpha_v \rho_v}{R_B}\sqrt{\frac{2}{3}\frac{(P - P_v)}{\rho_l}} \tag{10}$$

P_v is the vapor pressure, α_{nuc} is the proportion of noncondensable gas in the liquid, ρ_l is the density of the liquid, and C_{vap} and C_{cond} represent the evaporation and condensation coefficients, respectively. According to reference Ji et al. (2017), we take $\alpha_{nuc} = 5 \times 10^{-4}$, $R_B = 10^{-6}$, C_{vap} is set to 50, and C_{cond} is set to 0.01.

Grid Generation and Independence Verification

ICEM software is used to divide the computational area into structured grids. **Figure 2B** shows the 3D grids, and the hydrofoil structure is shown in **Figure 2C**. The periphery of the hydrofoils is densified to ensure that the grid size near the hydrofoil bone lines is less than or equal to 1.9e-4m in the flow direction, less than or equal to 1.9e-4m in the normal direction of the walls and less than or equal to 2e-5m in the spanwise direction. The calculated $Y+<1$. Before the transient calculation, a sufficient steady-state calculation is performed to ensure the accuracy of the numerical simulation calculation results.

The Mac. bionic hydrofoil is regarded as an example to verify the grid independence. We verify the grid independence by testing the average lift and drag coefficients, which are defined as follows:

$$C_L = \frac{F_L}{0.5\rho \times U_\infty^2 \times A}, C_L = \frac{F_d}{0.5\rho \times U_\infty^2 \times A} \tag{11}$$

Amongst them, F_L and F_d, respectively represent the lift and drag of the hydrofoil, ρ is the density of the medium, U_∞ is the velocity at infinity from the hydrofoil, and A is generally regarded as the chord length of the hydrofoil multiplied by the span.

Figure 3 shows the lift and drag coefficients of the six grid types under the test conditions. When the number of grids increases from case1 (420545) to case 4 (1450464), the lift

TABLE 1 | Verification of grid independence.

Case	Nodes	C_l	C_d	P_1(Pa)	P_2(Pa)
Case 1	420545	0.6779	0.1257	60,339	26581
Case 2	819720	0.6978	0.1174	60,889	27166
Case 3	1146458	0.7011	0.1113	60,955	28086
Case 4	1450464	0.7035	0.1092	61,106	28479
Case 5	1757400	0.7048	0.1084	61,761	28725
Case 6	2772392	0.7052	0.1086	61,825	28832

coefficient rises obviously, and the drag coefficient decreases fast, which shows that the number of grids significantly affects the test results. From case 4 (1450464) to case 6 (2772392), the lift and drag coefficients change minimally. When the coarse grid is refined, the coefficient fluctuation becomes small; when the number of grids is sufficiently high, the coefficient tends to a constant.

Table 1 summarises the six test grids under the test conditions to verify the grid independence. It includes the average pressure value P_1 on the suction surface at $x/C = 0.4$, and the average pressure value P_2 on the pressure surface at $x/C = 0.32$. The table presents that case 5 and case 6 have similar characteristics, and both can meet the grid requirements for LES. We choose case 5 as the final grid to reduce the computational workload, and the number of grids is approximately 1.7 million.

RESULTS AND DISCUSSIONS

Verification of Numerical Simulation Methods

Figure 4 shows the numerical simulation results of the transient cavitating flow distribution of the three types of bionic hydrofoils and the Clark-y hydrofoil. The setting of numerical conditions is completely consistent with experimental setting (Huang et al., 2012; Roohi et al., 2013). The figure presents that the cavitation circumfluence in a cycle can be roughly divided into four stages. In the first stage, an attached cavity forms at the leading-edge, and the cavity at the trailing edge begins to fall off. In the second stage, the attached cavity gradually increases and forms a sheet cavity, and the influence range of cavitation is the largest. In the third stage, the sheet cavitation breaks up gradually, separates and falls off, forming cloud cavitation, and the influence range of cavitation becomes small. In the fourth stage, the cavity gradually moves from the leading-edge to the trailing edge. At this time, the cavity of the hydrofoil is mainly concentrated at its trailing edge, and the influence range of cavitation is the smallest. Afterwards, the attached cavity is generated again at the leading-edge, which represents the beginning of the next cycle. **Figure 4** depicts that the numerical simulation can accurately observe the transient cavitating flow change process under different hydrofoil schemes. Comparison of the results of the four-stage numerical simulation with experimental results shows a high degree of agreement, which proves the correctness of the numerical calculation method in this paper. The numerical simulation and experimental values of clark-y hydrofoil are given on the right side of **Table 2** [numerical simulation is carried out under the same experimental conditions as Wei et al. (2011)]. It can be seen that both the lift coefficient and the drag coefficient are very close to the experimental value, and the maximum error is 1.68%, which is within the allowable error range. Further, according to the formula $Sr = lf/v$, the experimental Strouhal number is 0.169 and the numerical simulation Strouhal number is 0.176. The relative error between them is 3.98%, which can meet the similarity criterion of flow unsteady. This further verifies the accuracy of the numerical simulation in this paper.

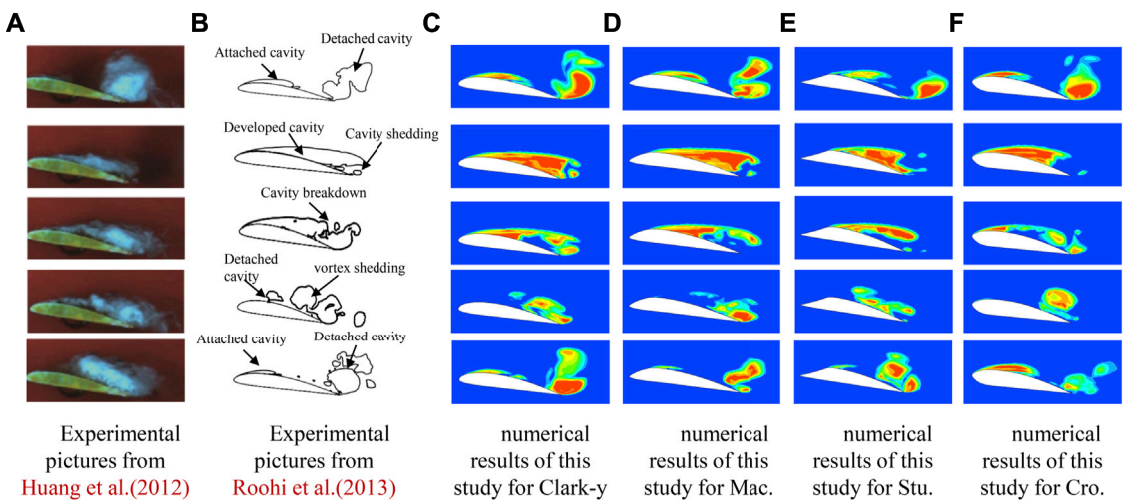

FIGURE 4 | Cavitation experimental results and numerical simulation results of different hydrofoils in a single cycle. **(A)** Experimental pictures from Huang et al. (2012) **(B)** Experimental pictures from Roohi et al. (2013) **(C)** Numerical results of this study for Clark-y **(D)** Numerical results of this study for Mac. **(E)** Numerical results of this study for Stu. **(F)** Numerical results of this study for Cro.

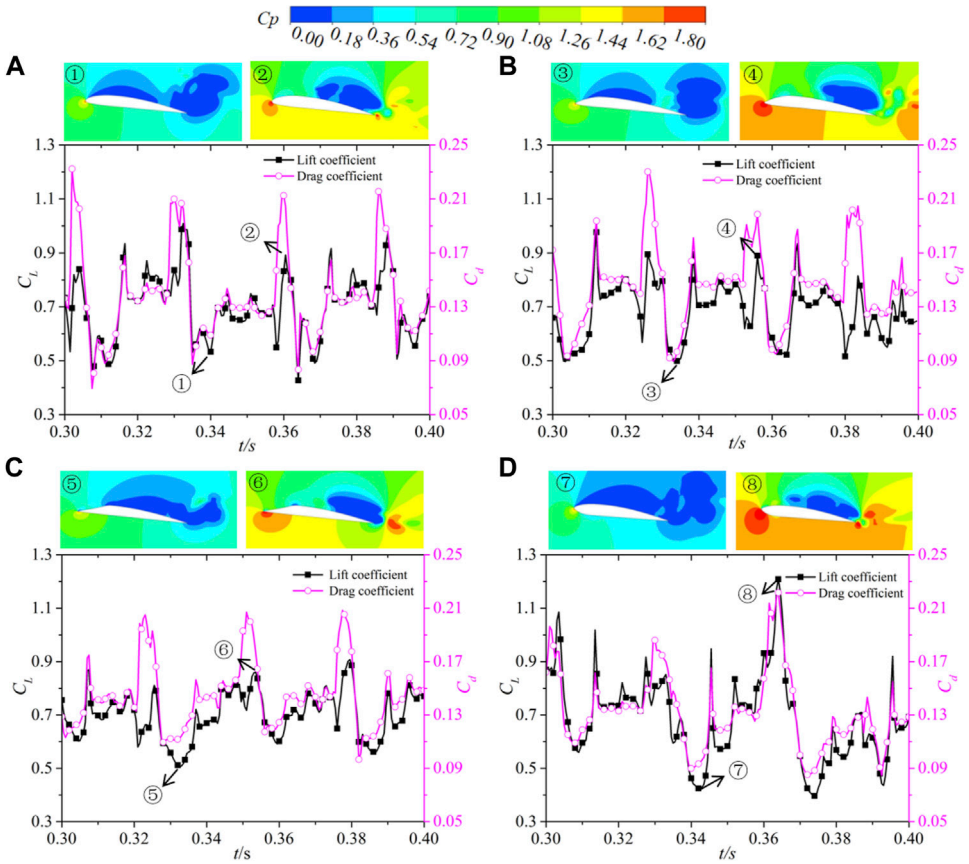

FIGURE 5 | Transient lift–drag coefficient curves and pressure coefficient Cp cloud diagrams of the four hydrofoils. **(A)** Clark-y **(B)** Mac. **(C)** Stu. **(D)** Cro.

TABLE 2 | Average lift–drag coefficient and lift-to-drag ratio and cavitation cycle (*T*) of each hydrofoil.

Hydrofoil	Mac	Stu	Cro	Clark-y	
				LES	Exp
C_L	0.765	0.770	0.754	0.768	0.760
C_d	0.131	0.130	0.117	0.121	0.119
C_L/C_d	5.840	5.923	6.444	6.347	6.387
T (ms)	42.10	40.72	39.43	39.68	–

Comparison of Lift and Drag Characteristics

Figure 5 shows the transient change curves of the lift coefficient C_L and drag coefficient C_d of the four hydrofoils over a while. The left side of the coordinate axis represents the value of C_L, and the right side represents the value of C_d. C_L and C_d of the four hydrofoils fluctuate periodically over time, and the value of C_L is always greater than the value of C_d. Their fluctuations are also always synchronised, that is, crests and troughs appear at the same time. Depending on the scheme, the period and amplitude of the fluctuations in the values of C_L and C_d differ, which shows that a change in the leading-edge structure will have a certain effect on the lift and drag characteristics of the hydrofoils. The Cro. scheme has the largest amplitude, whereas the Stu. scheme has the smallest amplitude. The average values of C_L and C_d for each scheme in **Table 2** indicate that the average lift coefficients of the four hydrofoils are relatively close, but the lift coefficient of the Stu. hydrofoil is relatively larger. For the average drag coefficient, the four hydrofoils have small differences, but the average drag coefficient of the Cro. hydrofoil is the smallest. **Table 2** also provides the lift-to-drag ratios of the four hydrofoils to measure their lift–drag characteristics clearly. The lift-to-drag ratio of the Cro. hydrofoil is significantly greater than those of the two other bionic hydrofoils, and it is also slightly higher than that of the traditional Clark-y hydrofoil.

The upper part of each curve in **Figure 5** shows the pressure coefficient C_p cloud diagram of the four hydrofoils at the peak and trough of the C_L curve. The expression is

$$C_p = \frac{p}{0.5\rho U_0^2} \tag{12}$$

p represents the pressure value in space coordinates. The figure demonstrates that the C_p value of the pressure surface of the hydrofoils is always higher than that of the suction surface regardless of when the lift coefficient is the largest or smallest,

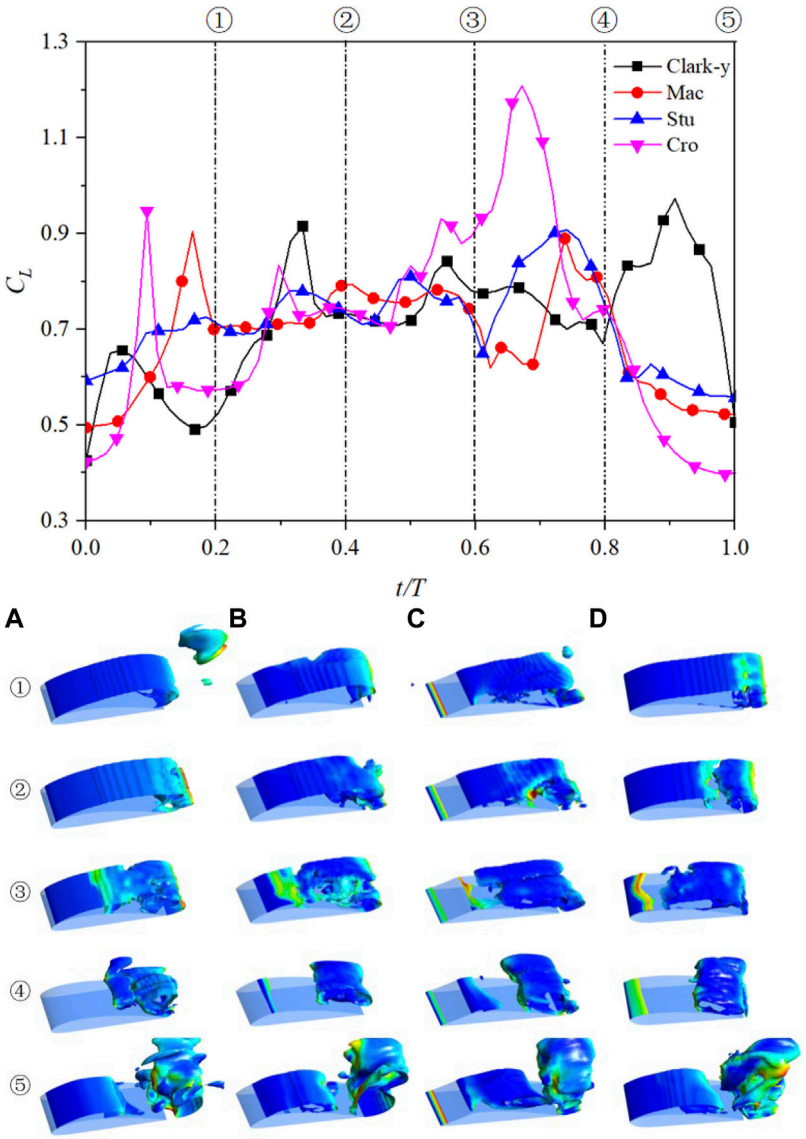

FIGURE 6 | Transient evolution process of the cavitating flow of the four hydrofoils in one cycle. (10% vapor volume fraction iso-surface) **(A)** Clark-y **(B)** Mac. **(C)** Stu. **(D)** Cro.

and the value reaches the maximum at the front and trailing edges of the pressure surface. When the lift coefficient changes from the trough to the crest, the low-pressure area on the suction surface of the hydrofoils gradually decreases and moves to the trailing edge. On the contrary, the high-pressure area on the pressure surface of the hydrofoils gradually expands and mainly concentrates on the leading and trailing edges. The pressure difference between the suction and pressure surface is the fundamental reason for the lift of hydrofoils. When the low-pressure area of the hydrofoils is large, the pressure difference of hydrofoil is also great which can obtain a good lift. Comparison of C_p cloud images of the four hydrofoils at the wave crests shows that the pressure surface of the Cro. hydrofoil has the widest high-pressure area, and the lift coefficient is also the largest. From the C_p cloud picture at the trough, the low-pressure area on the suction surface of the Cro. hydrofoil is the widest. On the basis of the lift–drag ratios in **Table 2**, the Cro. hydrofoil has a better lift–drag characteristics than the others.

Evolution of Transient Cavitating Flow

We use the C_L curve as a basis, regard one wave trough to the next wave trough as a cycle and provide the cavitation evolution diagram of the four hydrofoils in one cycle, as shown in **Figure 6**. The cavitation process of the four hydrofoils changes periodically with the change in C_L. When C_L is in the trough position, a thin attached cavity is produced at the leading-edge of the hydrofoils, and the cloud cavity generated in the previous cycle at the trailing edge is gradually falling off. At

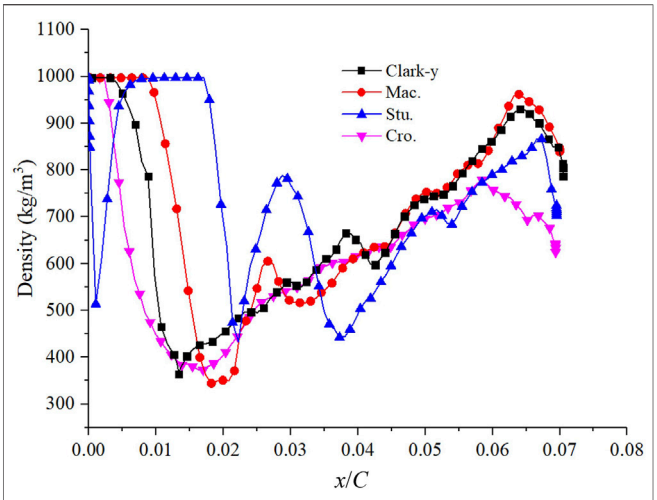

FIGURE 7 | Average density distribution on the suction surface of the four hydrofoils, $\sigma = 0.8$.

moment ①, the cloud cavitation at the trailing edge falls off and leaves the hydrofoil surface, whilst the attached cavity at the leading-edge gradually extends backward until the cavity covers the suction surface to form sheet cavitation. At time ②, the sheet cavitation continues to move to the trailing edge of the hydrofoils, the cavity begins to break in the middle and rear parts, and the volume of the cavity reaches the maximum at this time. At time ③, the sheet cavitation is breaking down, the cavitation of the leading-edge is gradually reduced, and the cavitation area of the hydrofoils is gradually divided into two parts. When time ④ is reached, the cavitation at the leading-edge disappears, the cavity is mainly concentrated near the trailing edge, and the influence range of cavitation is the smallest. Time ⑤ is another trough. The attached cavity reappears, and the cloud cavitation at the trailing edge begins to fall off. This phenomenon indicates that the evolution of the hydrofoil cavitation begins to enter the next cycle.

The figure illustrates that the cavitation evolution of the four hydrofoils is similar, but some differences exist. The cavitation of the Stu. hydrofoil is slightly different from that of the three other types of hydrofoils. The Stu. hydrofoil always has a thin attached cavity at the leading-edge, and the subsequent series of cavitation evolution occurs close to the maximum thickness of the hydrofoil (approximately $x/C = 0.25$). The cavitation evolution of the other three hydrofoils starts from the leading-edge. The Cro. hydrofoil cavitation occurs more forward than the others, whereas the Mac. hydrofoil cavitation occurs more rearward. At time ②, the sheet cavitation of the Cro. hydrofoil has been basically broken, whilst the remaining three hydrofoils have just started to break. This condition may be due to the upturning of the leading-edge, resulting in the early break of its sheet cavitation. The last line of **Table 2** shows the average cavitation cycle of the four hydrofoils. It can be seen from the table that the cavitation cycle of the Cro. hydrofoil (T = 39.43 ms) is the shortest and that of the Mac. Hydrofoil (T = 42.10 ms) is the longest. This further shows that the change of hydrofoil leading-edge will affect the evolution of cavitation. When the characteristic curve of the hydrofoil leading-edge is Cro. model, the hydrofoil can have a shorter cavitation evolution cycle.

Figure 7 shows the curves of the density distribution (averaged in one cycle) on the suction surface of the four hydrofoils to consider the cavitation evolution of the hydrofoils. The position of the Cro. hydrofoil cavitation occurs earlier (approximately $x/C = 0.03$) than that of the others, whereas the position of the Mac. hydrofoil cavitation occurs later (approximately $x/C = 0.124$). For the Stu. hydrofoil, cavitation has already appeared at the forefront of the hydrofoil, and the cavitation range ends at $x/C = 0.099$. The subsequent evolution of cavitation starts at $x/C = 0.241$. This is consistent with the results observed in the 3D cavitation evolution of the hydrofoil in **Figure 6**. The cavitation of the hydrofoils is mainly concentrated in their middle section, and it is the most serious at approximately $x/C = 0.21$–0.23. As the cavity stretches along the hydrofoils, the density fields of the hydrofoils rise. After the trailing edge is approached, the density fields of the four hydrofoils drop again slightly.

The occurrence of cavitation will inevitably lead to changes in the cavity velocity. **Figure 8** shows the time-averaged x-velocity distribution of the four types of hydrofoils. The upper part of **Figure 8** shows the location of the selected area (taking Clark-y hydrofoil as an example, the other hydrofoils are the same). The figure indicates that the velocity fluctuation is related to the selected position of the hydrofoil sections. From the Y-axis direction, the velocity near the walls of the hydrofoils shows great fluctuations; the higher the upward tilt is, the more the velocity fluctuations tend to be stable. As the fluid particle moves towards the trailing edge of the hydrofoils, the influence range of the velocity fluctuation in the Y-axis direction gradually increases. Especially at $x/C = 1.2$, velocity fluctuations exist in the Y-axis direction, indicating that the cavity will continue to move backward after falling off the surface of the hydrofoils. The size of the velocity fluctuation is related to the thickness of the cavity, and the velocity fluctuation of the Cro. hydrofoil is the smallest. The figure also shows the experimental results of Li et al. (2017). The velocity fluctuations of the four hydrofoils tend to be in good agreement with the experimental results.

Vortex Evolution

The transient cavitating flow of the hydrofoils is closely related to the vortex structure. We use the Q criterion to study the structure of the vortex, which is an important method to study the vortex in transient cavitation flow (Yu et al., 2020). It is defined as follows:

$$Q = \frac{(\Omega^2 - S^2)}{2} \tag{13}$$

Amongst them, Q is the second invariant of the velocity gradient tensor, Ω represents the vorticity amplitude, and S represents the strain rate tensor. The magnitude of its value can be used to identify the relationship between vorticity and strain rate. When $Q > 0$, the rotation effect is dominant; when $Q < 0$, the shearing effect is dominant.

Figure 9 shows Q distribution of the four hydrofoils. It can be seen from the figure that the Q distribution of Clark-y hydrofoil is significantly different from that of the three bionic hydrofoils. In

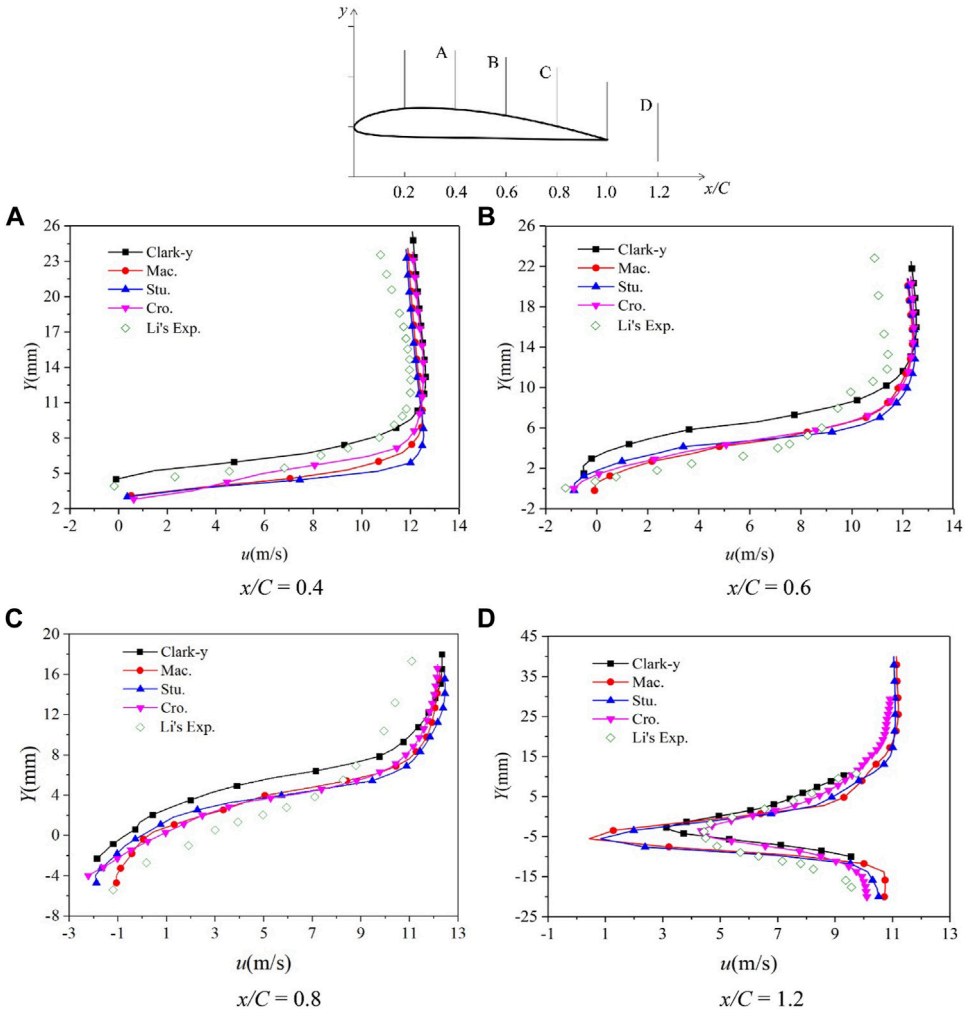

FIGURE 8 | Time-averaged velocity fluctuation curve along the flow direction around the four hydrofoils.

the whole cycle, the negative Q area of Clark-y hydrofoil is always larger than that of the other three bionic hydrofoils, which shows that the shear effect of Clark-y hydrofoil is dominant when cavitation shedding. The vortex evolution of the three bionic hydrofoils is similar. Take Mac. hydrofoil as an example, in the initial stage (1/5T), Q of the leading-edge is mainly negative, and Q towards the trailing edge becomes positive. The rotation effect of the hydrofoil at the trailing edge is dominant at this time. When the sheet cavitation begins to break (2/5T), the negative Q area near the trailing edge begins to increase gradually, and the shear effect begins to become evident. When the break of the hydrofoil cavity intensifies (3/5T), the negative Q area appears widely. At this time, the positive Q and negative Q areas alternately appear, and the rotation and shear effects jointly dominate the cavitation flow. When the cavity moves further back (4/5T), cavitation is mainly concentrated at the trailing edge. Q value is mainly positive at this time given no shedding of the cavity, and the rotation effect is dominant. With continuous development, an attached cavity is formed at the leading-edge, and the cavitation at the trailing edge begins to fall off the hydrofoil surface (5/5T). At this time, the cavitating flow becomes unstable, and rotation- and shear-dominant areas appear on the cavity surface.

However, there are still differences among the three bionic hydrofoils. In the initial stage, the negative Q area of the front edge of the Mac. hydrofoil is more obvious; when the sheet cavitation breaks, the shear effect of the Mac. hydrofoil is more significant. The positive Q area of the leading-edge of the Cro. hydrofoil is significantly wider, indicating that the rotation effect of the Cro. hydrofoil is more obvious. This result shows that in unsteady cavitating flow, rotation and shear jointly control the cavitation evolution. When the leading-edge structure is changed, the evolution of the hydrofoil vortex will also be affected.

The vorticity transport equation is used to compare and analyse the vorticity on the three bionic hydrofoils to study the cavitation–vortex interaction. The equation is as follows:

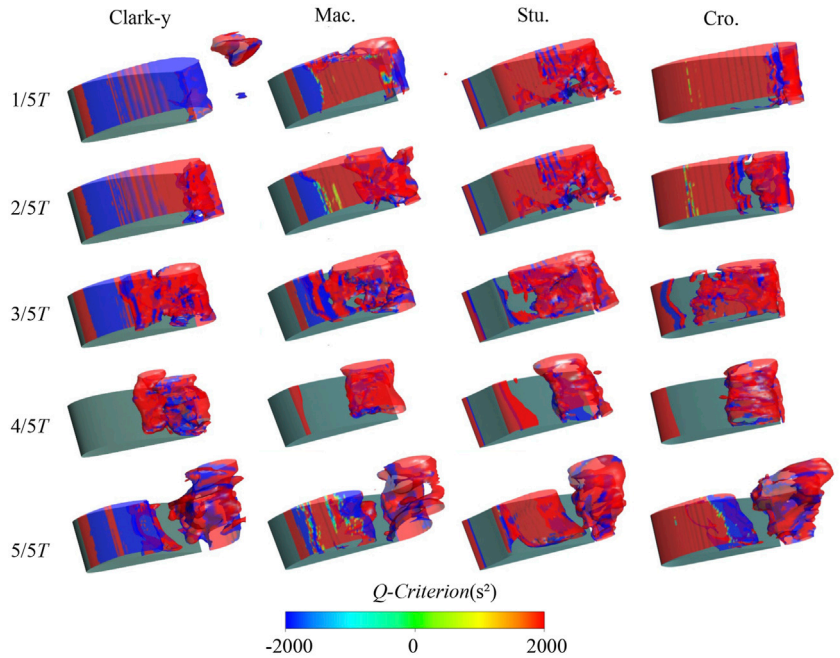

FIGURE 9 | Comparison of the vortex structures around the four hydrofoils based on *Q* criterion.

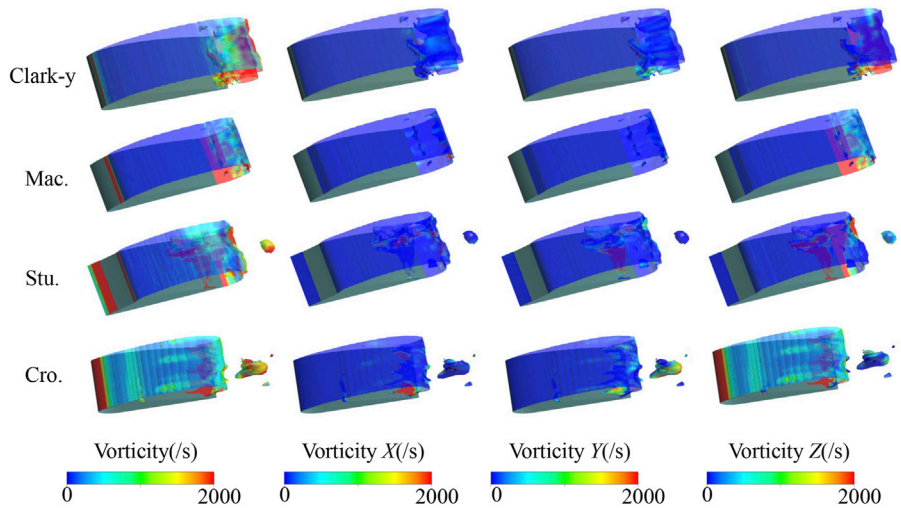

FIGURE 10 | Distribution of total vorticity, vorticity X, vorticity Y and vorticity Z of the four hydrofoils at the same time (*t* = 60 ms).

$$\frac{D\vec{\omega}}{Dt} = \left(\vec{\omega}\cdot\nabla\right)\vec{V} - \vec{\omega}\left(\nabla\cdot\vec{V}\right) + \frac{\nabla\rho_m\times\nabla p}{\nabla\rho_m^2} + (\nu_m+\nu_t)\nabla^2\vec{\omega} \quad (14)$$

The vortex-stretching term $(\vec{\omega}\cdot\nabla)\vec{V}$ reveals the stretching and tilting of the vortex caused by the velocity gradient. The vortex dilatation term $\vec{\omega}(\nabla\cdot\vec{V})$ is affected by volume expansion or contraction. $\frac{\nabla\rho_m\times\nabla p}{\nabla\rho_m^2}$ is the vortex baroclinic term, which describes the effect of the baroclinic moment on the vorticity due to the nonparallel pressure gradient and density gradient. $(\nu_m+\nu_t)\nabla^2\vec{\omega}$ of different bionic hydrofoils slightly changes, but this change is minimal and is thus usually ignored.

Figure 10 shows the distribution of total vorticity and the three directional vorticities of the four hydrofoils on the cavity surface at the same time (t = 0.4 s). Vorticity distribution in the Z direction is similar to the total vorticity, and the vorticity in the Z direction is much larger than the vorticity distribution in the other two directions. Therefore, the vorticity dynamics of the three bionic hydrofoils are evaluated by analyzing the vorticity Z.

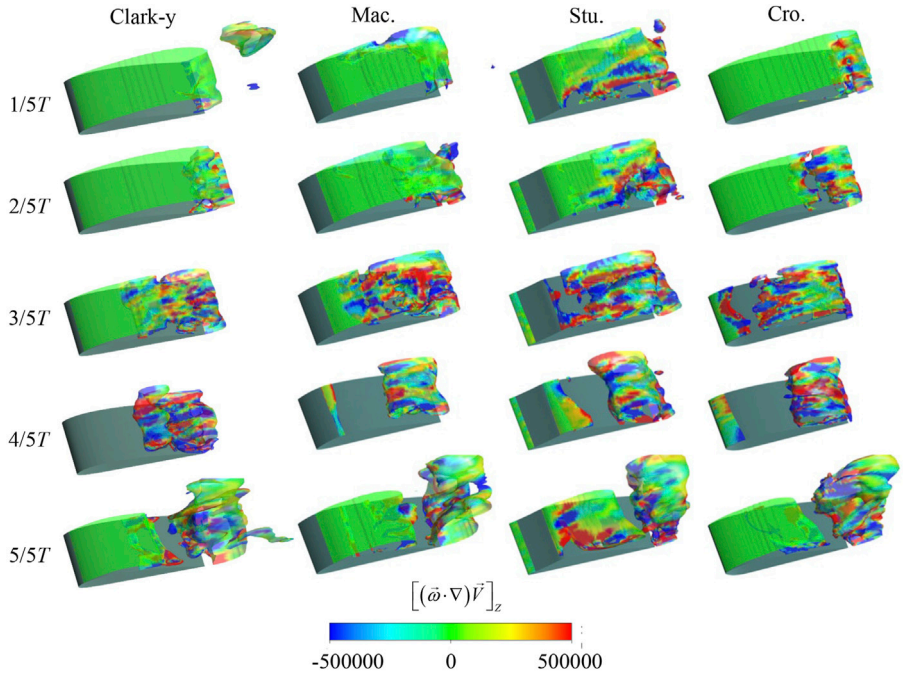

FIGURE 11 | Comparison of the Z-direction vortex-stretching term evolution of the four hydrofoils in a typical cycle.

The vortex-stretching term is related to the velocity gradient, and cavitation will have a significant effect on the velocity gradient in the transient flow. As shown in **Figure 11**, in the initial stage (1/5*T*), only a small range of vortex stretching is evident. Cavitation is in the developing stage, and the velocity gradient does not change much. With the development of cavitation (2/5*T*), a re-entrant flow gradually forms and develops, causing the velocity gradient of the hydrofoil surface to change. At this time, the influence range of the vortex-stretching term gradually increases. When the sheet cavitation gradually breaks (3/5*T*), the scope of influence of this item further increases and gradually extends to the entire surface of the hydrofoils. When the sheet cavitation is completely broken, the cavitation begins to move to the trailing edge of the hydrofoils, and the leading-edge cavitation begins gradually (4/5*T*–5/5*T*). At this time, the growth of the cavity slows down, the velocity gradient change is small, and the influence range of the vortex-stretching term gradually decreases.

The change trends of the vortex-stretching term of the four hydrofoils are generally similar. However, there are still differences. Compared with the bionic hydrofoil, the variation area of the vortex-stretching term of Clark-y hydrofoil in the initial stage of cavitation is smaller, but when the cavity begins to shedding from the living cavity, the vortex stretching term begins to change dramatically. The stretching term of vortices of the three bionic hydrofoils changes gently in the whole cycle, and the change of the velocity gradient of the Stu. hydrofoil in each stage is more obvious, especially near the leading-edge. This is because the flat structure of the leading-edge is more conducive to the formation and development of re-entrant flow, resulting in greater changes in velocity gradient. When the attached cavitation of Cro. hydrofoil is formed, the area with zero vortex-stretching term accounts for a larger proportion, and the change of velocity gradient is the smallest.

The vortex dilatation term mainly refers to the change in fluid volume that affects the vortex. Due to cavitation, the volume of the fluid will change, causing the vorticity to also change. **Figure 12** shows the distribution of the vortex dilatation term of the four hydrofoils in a typical period. In the 1/5*T* stage, the vortex expansion is concentrated near the trailing edge, and the vortex dilatation term of the leading-edge is small. When the cavitation develops to the 2/5*T* stage, an attached cavity gradually develops, and the volume change rate gradually increases. When the sheet cavitation begins to break (3/5*T*), the volume changes drastically, and the value of the vortex dilatation term reaches the maximum at the break of the cavity. When the sheet cavitation is completely broken to form cloud cavitation (4/5*T*), the positive and negative values of the vortex dilatation term appear alternately. Afterwards, the value of the vortex dilatation term gradually decreases due to the slow formation of the attached cavity (5/5*T*).

In the initial stage of the cavitation evolution cycle, the fluid volume change rate of Clark-y hydrofoil and Mac. hydrofoil is low, and the dilatation term of the vortex is mainly zero. However, at 3/5*T*, due to the shedding of sheet cavitation, the fluid volume changes sharply, resulting in a sharp decrease in the zero value region of the dilatation term. The zero value area of the vortex dilatation term of the Stu. hydrofoil in the whole cavitation

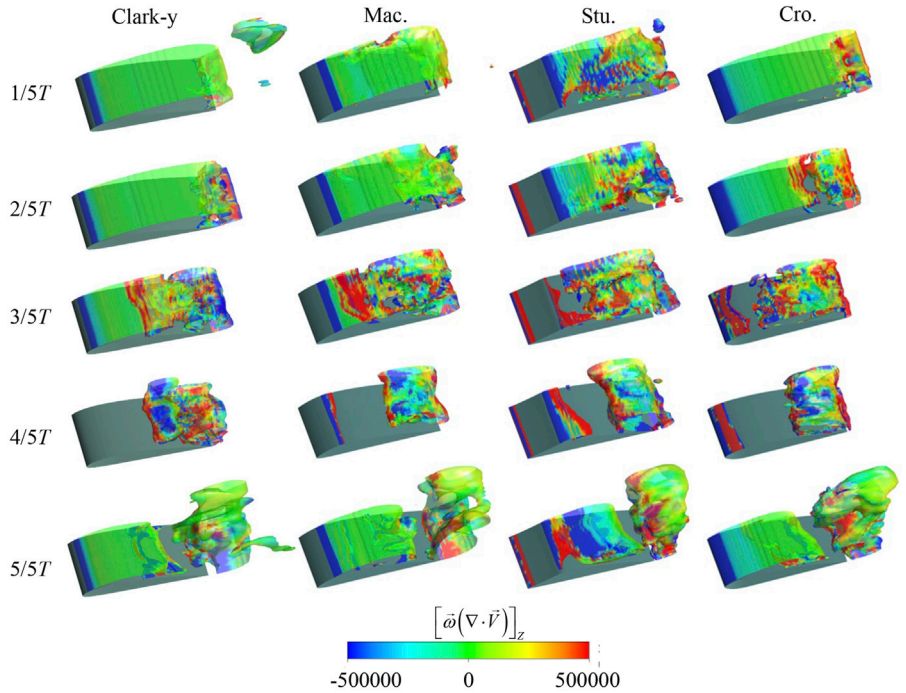

FIGURE 12 | Comparison of the Z-direction vortex dilatation term evolution of the four hydrofoils in a typical cycle.

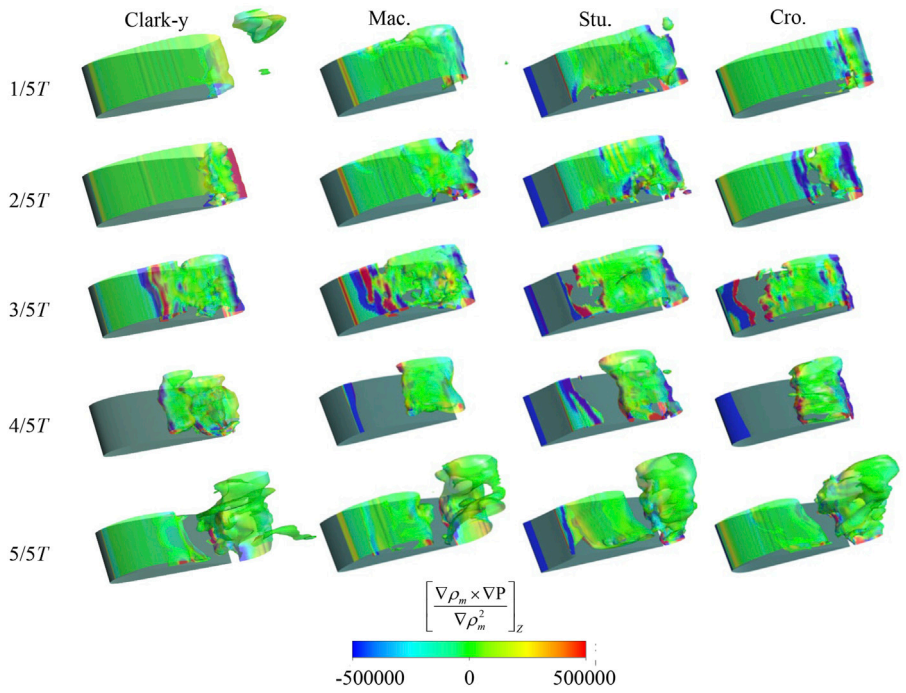

FIGURE 13 | Comparison of the Z-direction vortex baroclinic term evolution of the four hydrofoils in a typical cycle.

evolution cycle is low, indicating that its fluid volume changes most dramatically. The warping of hydrofoil leading-edge structure will affect the change of vortex dilatation rate.

The vortex baroclinic term is related to the variation of nonparallel pressure and density. For a general positive pressure fluid, pressure and density have the same gradient,

that is, zero. For an unsteady cavitating flow, these two items are not always the same, which will cause the change of the vorticity. **Figure 13** shows the distribution of vortex baroclinic terms for the four hydrofoils. The vortex baroclinic terms mainly exist in the leading-edge of the hydrofoils and the area where the sheet cavitation is broken. The occurrence of the attached cavity or the break of the cavity will cause a gas-liquid two-phase transition, which in turn will change the density gradient of the flow field. Although the influence range of this term is smaller than those of the above two terms, it plays an important role in the generation of vortices. The baroclinic term of the Mac. hydrofoil and Clark-y hydrofoil are more complex when cavitation breaks (3/5T). When attached cavitation occurs (5/5T), the baroclinic term of the Cro. hydrofoil is more stable. The change in the vortex of the flow field will also change due to the influence of cavitation, and the change in the leading-edge structure will affect the evolution of the hydrofoil vortex.

CONCLUSION

This study uses geometrical bionic principles to establish three bionic hydrofoils with evident leading-edge structural differences and calculates the lift and drag coefficients, transient cavitating flow and vortex evolution of the hydrofoils by using the LES method. On the basis of comparison and analysis, the conclusions are as follows:

1) From the comparison of the numerical simulation and experimental results of the transient cavitating flow of four hydrofoils in a period, their cavitation evolution process is always similar. Regardless of the location where the attached cavity occurs, the size of the sheet cavitation and the location of its break and the shape of the cloud cavitation, the numerical simulation and experimental results show a high degree of agreement. This agreement verifies the accuracy of the numerical simulation method in this paper.
2) The lift and drag coefficients of the three bionic hydrofoils and the Clark-y hydrofoil are inconsiderably different in general, but the lift–drag ratio of the Cro. hydrofoil is better. Comparison of C_p cloud images of the four hydrofoils shows that when C_L reaches the peak, the pressure surface of the Cro. hydrofoil has the widest high-pressure area. When C_L is in the trough, the low-pressure area of the Cro. hydrofoil is the widest. The Cro. hydrofoil has better lift and drag characteristics than the others.
3) The position of the attached cavity of a hydrofoil will change due to the change in the leading-edge structure. When the leading-edge structure is upturned, the position of the attached cavity will move forward. The position where the attached cavity of the Stu. hydrofoil occurs is the rearmost (approximately x = 16.9 mm). The position where the attached cavity of the Cro. Hydrofoil occurs is the most forward (approximately x = 2.9 mm), and the velocity fluctuation at its trailing edge is the smallest. From the perspective of the cavitation evolution period, the cavitation evolution period of the Cro. hydrofoil is shorter (approximately T = 27 ms) than that of the others, whereas the cavitation period of the Mac. hydrofoil is longer (approximately T = 31 ms).
4) The warping of leading-edge structure will cause significant changes in the vortex evolution of hydrofoils. The Mac. hydrofoil has a wider negative Q area at the leading-edge compared with others, whereas the rotation effect of the Cro. hydrofoil is more obvious than that of the others. When the leading-edge structure is tilted downward, the changes in the vortex stretching and dilatation terms of the hydrofoils, particularly the Stu. hydrofoil, are complicated, and their vortex has a wide range of influence.

DATA AVAILABILITY STATEMENT

The original contributions presented in the study are included in the article/Supplementary Material, further inquiries can be directed to the corresponding author.

AUTHOR CONTRIBUTIONS

All authors contributed to this research. HZ conducted the experiments, performed the experiments, and wrote the draft of this paper. HY, JW, TS, and FQ suggested the study idea and shared in writing and revising the paper.

FUNDING

This work was supported by the University Synergy Innovation Program of Anhui Province under Grant No. GXXT-2019-004, the Fundamental Research Funds for the Central Universities (NO: JZ2021HGTB0090), the financial support provided by the National Natural Science Foundation of China (51806053) and Anhui Provincial Key Research and Development Program (Grant No. 201904a05020070, 1804a09020012 and 1804a09020007).

REFERENCES

Amini, A., Reclari, M., Sano, T., Iino, M., and Farhat, M. (2019). Suppressing Tip Vortex Cavitation by Winglets. *Exp. Fluids* 60, 159. doi:10.1007/s00348-019-2809-z

Antoine, D., Jacques, A. A., François, D., and Sigrist, J. F. (2009). Fluid Structure Interaction Analysis on a Transient Pitching Hydrofoil. *Am. Soc. Mech. Eng.* 4, 665–671. doi:10.1115/pvp2009-78082

Arabnejad, M. H., Amini, A., Farhat, M., and Bensow, R. E. (2019). Numerical and Experimental Investigation of Shedding Mechanisms from Leading-Edge Cavitation. *Int. J. Multiphase Flow* 119, 123–143. doi:10.1016/j.ijmultiphaseflow.2019.06.010

Cheng, H., Long, X., Ji, B., Peng, X., and Farhat, M. (2019). LES Investigation of the Influence of Cavitation on Flow Patterns in a Confined Tip-Leakage Flow. *Ocean Eng.* 186, 106115. doi:10.1016/j.oceaneng.2019.106115

Custodio, D., Henoch, C., and Johari, H. (2018). Cavitation on Hydrofoils with Leading Edge Protuberances. *Ocean Eng.* 162, 196–208. doi:10.1016/j.oceaneng.2018.05.033

Fujii, A., Kawakami, D. T., Tsujimoto, Y., and Arndt, R. E. (2007). Effect of Hydrofoil Shapes on Partial and Transitional Cavity Oscillations. *J. Fluids Eng.* 129, 669–673. doi:10.1115/1.2734183

Garg, N., Pearce, B. W., Brandner, P. A., Phillips, A. W., Martins, J. R. R. A., and Young, Y. L. (2019). Experimental Investigation of a Hydrofoil Designed via Hydrostructural Optimization. *J. Fluids Structures* 84, 243–262. doi:10.1016/j.jfluidstructs.2018.10.010

Hicks, R. M., and Henne, P. A. (1978). Wing Design by Numerical Optimization. *J. Aircraft* 15, 407–412. doi:10.2514/3.58379

Hong, J., Qian, Z. H., and Ren, L. Q. (2009). Extensive Model of Multi-Factor Coupling Bionics and Analysis of Coupling Elements. *J. Jilin University(Engineering Tech. Edition)* 39, 726–731. doi:10.1061/41039(345)45

Hu, C., Chen, G., Yang, L., and Wang, G. (2018). Large Eddy Simulation of Turbulent Attached Cavitating Flows Around Different Twisted Hydrofoils. *Energies* 11, 2768. doi:10.3390/en11102768

Huang, B., Wang, G., Yu, Z., and Shi, S. (2012). Detached-eddy Simulation for Time-dependent Turbulent Cavitating Flows. *Chin. J. Mech. Eng.* 25, 484–490. doi:10.3901/cjme.2012.03.484

Huang, B., Wang, G. Y., and Yuan, H. T. (2010). A Cavitation Model for Cavtating Flow Simulations. *J. Hydrodynamics, Ser.B.* 22, 798–804. doi:10.1016/s1001-6058(10)60033-9

Huang, R., Luo, X., and Ji, B. (2017). Numerical Simulation of the Transient Cavitating Turbulent Flows Around the Clark-Y Hydrofoil Using Modified Partially Averaged Navier-Stokes Method. *J. Mech. Sci. Technol.* 31, 2849–2859. doi:10.1007/s12206-017-0528-z

Huang, S. X., Hu, Y., and Wang, Y. (2020). Research on Aerodynamic Performance of a New Dolphin Head-Based Bionic Airfoil. *Energy* 11, 118179. doi:10.1016/j.energy.2020.118179

Ji, B., Long, Y., Long, X.-p., Qian, Z.-D., and Zhou, J.-j. (2017). Large Eddy Simulation of Turbulent Attached Cavitating Flow with Special Emphasis on Large Scale Structures of the Hydrofoil Wake and Turbulence-Cavitation Interactions. *J. Hydrodyn* 29, 27–39. doi:10.1016/s1001-6058(16)60715-1

Ji, B., Luo, X. W., Arndt, R. E. A., Peng, X., and Wu, Y. (2015). Large Eddy Simulation and Theoretical Investigations of the Transient Cavitating Vortical Flow Structure Around a NACA66 Hydrofoil. *Int. J. Multiphase Flow* 68, 121–134. doi:10.1016/j.ijmultiphaseflow.2014.10.008

Kim, J., and Lee, J. S. (2015). Numerical Study of Cloud Cavitation Effects on Hydrophobic Hydrofoils. *Int. J. Heat Mass Transfer* 83, 591–603. doi:10.1016/j.ijheatmasstransfer.2014.12.051

Kulfan, B. M. (2008). Universal Parametric Geometry Representation Method. *J. Aircraft* 45, 142–158. doi:10.2514/1.29958

Li, L., Li, B., Hu, Z., Lin, Y., and Cheung, S. C. P. (2016). Large Eddy Simulation of Unsteady Shedding Behavior in Cavitating Flows with Time-Average Validation. *Ocean Eng.* 125, 1–11. doi:10.1016/j.oceaneng.2016.07.065

Li, Z., Zheng, D., Hong, F., and Ni, D. (2017). Numerical Simulation of the Sheet/cloud Cavitation Around a Two-Dimensional Hydrofoil Using a Modified URANS Approach. *J. Mech. Sci. Technol.* 31, 215–224. doi:10.1007/s12206-016-1224-0

Liu, X., and Liu, X. (2014). A Numerical Study of Aerodynamic Performance and Noise of a Bionic Airfoil Based on Owl wing. *Adv. Mech. Eng.* 6, 859308. doi:10.1155/2014/859308

Liu, Y., and Tan, L. (2020). Method of T Shape Tip on Energy Improvement of a Hydrofoil with Tip Clearance in Tidal Energy. *Renew. Energ.* 149, 42–54. doi:10.1016/j.renene.2019.12.017

Marimon Giovannetti, L., Banks, J., Ledri, M., Turnock, S. R., and Boyd, S. W. (2018). Toward the Development of a Hydrofoil Tailored to Passively Reduce its Lift Response to Fluid Load. *Ocean Eng.* 167, 1–10. doi:10.1016/j.oceaneng.2018.08.018

Masters, D. A., Poole, D. J., Taylor, N. J., Rendall, T. C. S., and Allen, C. B. (2017). Influence of Shape Parameterization on a Benchmark Aerodynamic Optimization Problem. *J. Aircraft* 54, 1–15. doi:10.2514/1.c034006

Oller, S., Nallim, L., and Oller, S. (2016). Usability of the Selig S1223 Profile Airfoil as a High Lift Hydrofoil for Hydrokinetic Application. *J. Appl. Fluid Mech.* 9, 537–542. doi:10.18869/acadpub.jafm.68.225.24302

Rajaram, A. N., and Srikanth, N. (2020). Multi-objective Optimization of Hydrofoil Geometry Used in Horizontal axis Tidal Turbine Blade Designed for Operation in Tropical Conditions of South East Asia. *Renew. Energ.* 146, 166–180. doi:10.1016/j.renene.2019.05.111

Roohi, E., Zahiri, A. P., and Passandideh-Fard, M. (2013). Numerical Simulation of Cavitation Around a Two-Dimensional Hydrofoil Using VOF Method and LES Turbulence Model. *Appl. Math. Model.* 37, 6469–6488. doi:10.1016/j.apm.2012.09.002

Sun, T., Wang, Z., Zou, L., and Wang, H. (2020). Numerical Investigation of Positive Effects of Ventilated Cavitation Around a NACA66 Hydrofoil. *Ocean Eng.* 197, 106831. doi:10.1016/j.oceaneng.2019.106831

Wang, S., Zhu, J., Xie, H., Zhang, F., and Zhang, X. (2019). Studies on thermal Effects of Cavitation in LN2 Flow over a Twisted Hydrofoil Based on Large Eddy Simulation. *Cryogenics* 97, 40–49. doi:10.1016/j.cryogenics.2018.11.007

Wei, Y.-J., Tseng, C.-C., and Wang, G.-Y. (2011). Turbulence and Cavitation Models for Time-dependent Turbulent Cavitating Flows. *Acta Mech. Sin.* 27, 473–487. doi:10.1007/s10409-011-0475-3

Xue, G., Liu, Y., Zhang, M., Zhang, W., Zhang, J., Luo, H., et al. (2016). Optimal Design and Numerical Simulation on Fish-like Flexible Hydrofoil Propeller. *Polish Maritime Res.* 23, 59–66. doi:10.1515/pomr-2016-0070

You, C., Zhao, G., Chu, X., Zhou, W., Long, Y., and Lian, Y. (2020). Design, Preparation and Cutting Performance of Bionic Cutting Tools Based on Head Microstructures of Dung Beetle. *J. Manufacturing Process.* 58, 129–135. doi:10.1016/j.jmapro.2020.07.057

Yu, A., Qian, Z. H., Wang, X. C., Tang, Q. H., and Zhou, D. Q. (2020). Large Eddy Simulation of Ventilated Cavitation with an Insight on the Correlation Mechanism between Ventilation and Vortex Evolutions. *Appl. Math. Model.* 89, 1055–1073. doi:10.1016/j.apm.2020.08.011

Zhang, D.-s., Shi, W.-d., Zhang, G.-j., Chen, J., and van Esch, B. P. M. B. (2017). Numerical Analysis of Cavitation Shedding Flow Around a Three-Dimensional Hydrofoil Using an Improved Filter-Based Model. *J. Hydrodyn* 29, 361–375. doi:10.1016/s1001-6058(16)60746-1

Zhang, D., Shi, W., Pan, D., and Zhang, G. (2015). Numerical Simulation of Cavitation Shedding Flow Around a Hydrofoil Using Partially-Averaged Navier-Stokes Model. *Int. J. Numer. Methods Heat Fluid Flow* 25, 825–830. doi:10.1108/hff-05-2014-0150

Zhang, M. J., Huang, B., Qian, Z. D., Liu, T. T., Wu, Q., Zhang, H. Z., et al. (2020). Cavitating Flow Structures and Corresponding Hydrodynamics of a Transient Pitching Hydrofoil in Different Cavitation Regimes. *Int. J. Multiphase Flow* 132, 103408. doi:10.1016/j.ijmultiphaseflow.2020.103408

Zhou, L. J., Guo, Q., and Wang, Z. W. (2016). Numerical Evaluation of the Clearance Geometries Effect on the Flow Field and Performance of a Hydrofoil. *Renew. Energ.* 99, 390–397. doi:10.1016/j.renene.2016.06.064

Conflict of Interest: Author JW is employed by Hefei Kaiquan Electric Motor Pump Co., Ltd. Author TS is employed by Hefei Hengda Jianghai Pump Co., Ltd.

The remaining authors declare that the research was conducted in the absence of any commercial or financial relationships that could be construed as a potential conflict of interest.

frontiers in Energy Research

ORIGINAL RESEARCH
published: 26 January 2022
doi: 10.3389/fenrg.2022.818244

Influence of Different Offset Angles of Inlet Guide Vanes on Flow Characteristics of Centrifugal Pump

Peifeng Lin, Tao Yang, Wenbin Xu and Zuchao Zhu*

Key Laboratory of Fluid Transmission Technology of Zhejiang Province, Zhejiang Sci-Tech University, Hangzhou, China

The efficiency of the impeller machinery can be improved by the inlet guide vanes, but the relationship between the external characteristics of the centrifugal pump and the internal flow state needs further study. In this paper, the flow characteristics of the centrifugal pump with different offset angles of inlet guide vanes (IGVs) are simulated based on the SST k-ω turbulence model. The influence of the offset angle of the IGV on the internal flow and energy dissipation of the centrifugal pump is analyzed by using the entropy generation theory and Q-criterion. The research results show that the increase of the offset angle is beneficial to reducing the intensity of vortex in the volute and impeller, while the energy loss is reduced by 21.12 and 17.82% at $0.6Q_d$ and $0.8Q_d$, respectively. However, the excessive offset angle of the IGV tends to cause greater energy loss in the inlet pipe, thus reducing the head and efficiency of the centrifugal pump. In terms of external characteristics, the pump with 25° IGVs has the best head and efficiency improvement. Under three small operating points, the pump with 25° IGVs increased the head by 2.11, 0.95, and 0.73% and the efficiency by 2.51, 1.67, and 1.25%, respectively, compared with the pump with 0° IGVs. The research in this paper contributes to the performance improvement of centrifugal pumps operating at low flow conditions.

Keywords: centrifugal pump, inlet guide vanes, offset angle, internal flow, energy loss

OPEN ACCESS

Edited by:
Ling Zhou,
Jiangsu University, China

Reviewed by:
Fubing Bao,
China Jiliang University, China
Jinjing Sun,
University of Shanghai for Science and Technology, China
Peijian Zhou,
China Jiliang University, China

****Correspondence:***
Peifeng Lin
linpf@zstu.edu.cn

Specialty section:
This article was submitted to Process and Energy Systems Engineering, a section of the journal Frontiers in Energy Research

Received: *19 November 2021*
Accepted: *03 January 2022*
Published: *26 January 2022*

Citation:
Lin P, Yang T, Xu W and Zhu Z (2022) Influence of Different Offset Angles of Inlet Guide Vanes on Flow Characteristics of Centrifugal Pump. Front. Energy Res. 10:818244. doi: 10.3389/fenrg.2022.818244

INTRODUCTION

Pumps, a machine for converting energy, are widely used in social production practices (Martinich, 1990; Aaronson et al., 2012). The internal flow of a centrifugal pump is turbulent, which is very different from the laminar flow in some straight channels. Therefore, its internal flow is more complicated (Hu et al., 2020; Hu et al., 2021). Due to the complexity of the flow in the pump, it may have an unstable working operation. For improving the operational performance of centrifugal pumps, researchers have done a lot of research studies in improving the energy conversion efficiency of pumps (Xiong, 1996; Dou et al., 2014; Wang et al., 2018). A common study of pumps includes regulating the intrinsic parameters such as the size structure of the pump and the shape and number of blades. With the continuous development of research, researchers are increasingly interested in the study of adding guide vanes inside various fluid machinery. And some experiments and numerical simulations also prove that IGVs can improve the operating performance of fluid machinery (Dou, 2006; Liu et al., 2011; Shi et al., 2012; Kim et al., 2013).

As early as the 1950s, the method of adjusting working conditions of the impeller machinery such as centrifugal compressors, fans, and turbines by adding IGVs had been widely used. Coppinger and

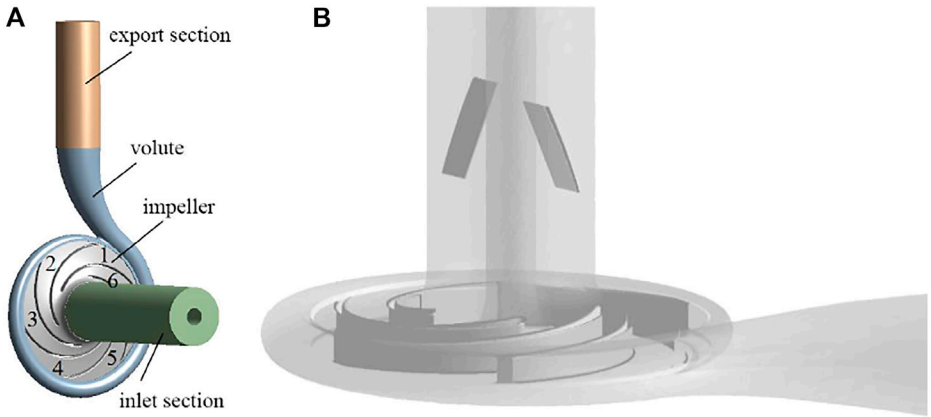

FIGURE 1 | Three-dimensional model of the centrifugal pump: **(A)** geometric model; **(B)** overall perspective view of the centrifugal pump with IGVs.

TABLE 1 | Main design parameters of the centrifugal pump.

Parameters	Sign	Value
Design flow rate (kg/s)	Q_d	16.637
Head (m)	H	60
Rotating speed (rpm)	n	2900
Effectiveness (%)	η	80
Specific speed	n_s	19.9
Inlet diameter (mm)	D_1	94
Inlet of the impeller (mm)	D_2	220
Outlet width of the impeller (mm)	b_1	15
Outlet diameter of the volute (mm)	D_3	70

Swain (2000) investigated the effect of guide vanes with an angle ranging from −20° to +80° on industrial centrifugal compressors through experiments and simulations. They found that an excessively large setting angle led to a larger pressure loss, which resulted in a reduction of the overall system efficiency. A suitable angle of guide vanes had a significant effect on extending the stable operating range of the compressor. The performance of centrifugal compressors with IGVs was also studied by Xiao et al. (2006). He demonstrated that the performance curve of centrifugal pumps moved toward the low flow region when guide vanes were positively offset. The opposite result was obtained when they were negatively offset. In the low flow region, the optimal efficiency operating point of the centrifugal pump decreased faster. Fukutomi and Nakamura (2005) investigated the effect of angle and length of IGVs on the performance of cross-flow turbines. By installing guide vanes in the inlet region, the cross-flow turbines had higher pressure and higher efficiency compared to the case without guide vanes. In the high flow condition, the turbines obtained higher pressure and efficiency. But in the low flow condition, the presence of the guide vanes had an inhibiting effect on the circulating flow in the rotor inlet. To address the flow inhomogeneities in centrifugal turbines, Junaidi et al. (2015) installed guide vanes at the impeller inlet of the turbine to eliminate the vortex flow due to internal deformation. Comparing the internal static pressure and axial power of centrifugal fans with and without IGVs, they noticed that the stable operating range of centrifugal fans was extended and the power consumption was reduced under off-design conditions. Based on the above research, the purpose of this article is to understand the effect of the law of inlet guide vanes on the flow field and external characteristics of the centrifugal pump.

In this paper, the flow characteristics of the centrifugal pump with IGVs are simulated. The influence of the law of inlet guide vanes on the pressure, velocity, and other physical quantities of the internal flow field of the centrifugal pump is studied by a steady calculation method. Combined with the energy dissipation in the impeller, the influence of guide vanes with an angle ranging from 0° to 35° on the performance of centrifugal pumps is revealed. The reasons why the offset angle of guide vanes

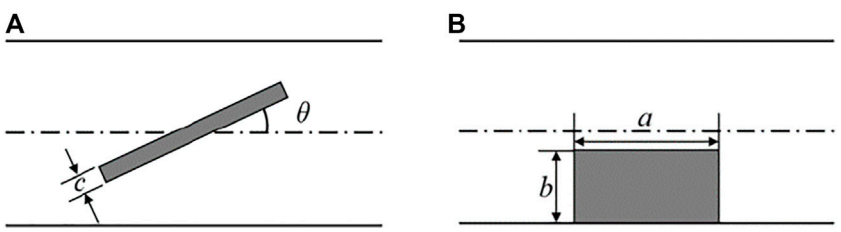

FIGURE 2 | Schematic diagram of inlet guide vanes: **(A)** side view; **(B)** radial view.

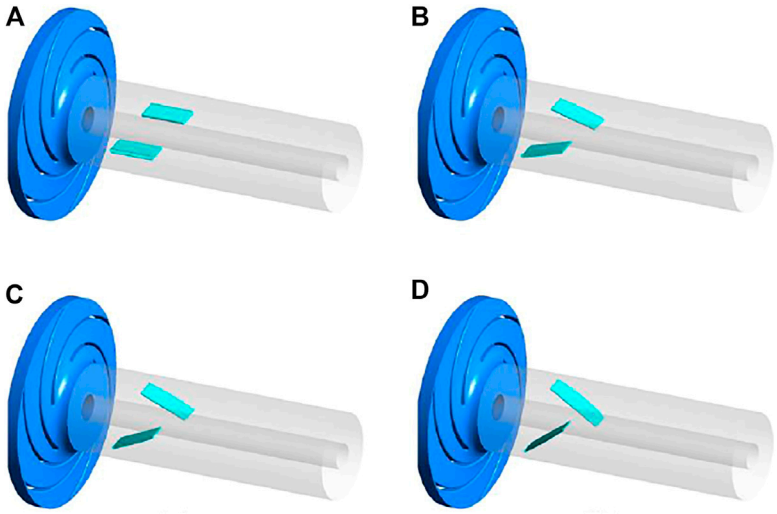

FIGURE 3 | IGVs at different offset angles: **(A)** 0°; **(B)** 15°; **(C)** 25°; **(D)** 35°.

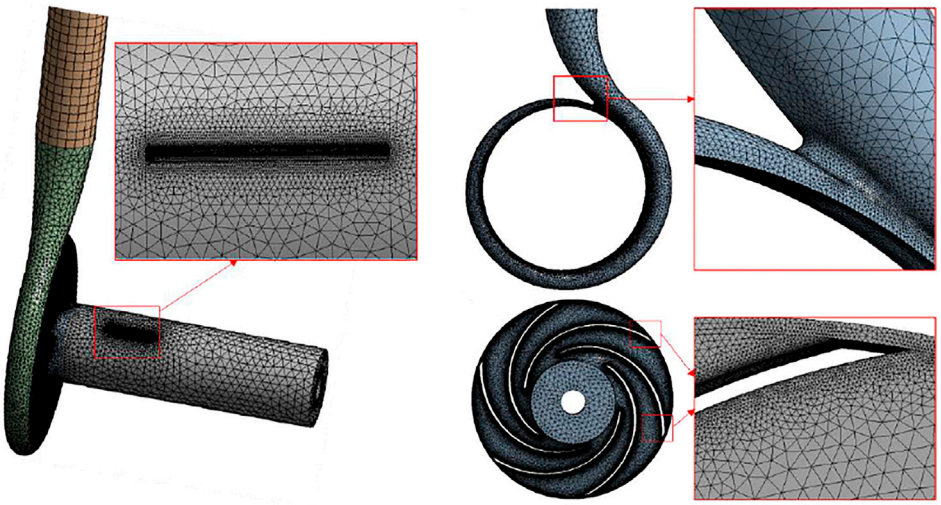

FIGURE 4 | Mesh of IGVs, volute, and impeller.

should not be too large are specifically analyzed, and the microscopic mechanism of external characteristics is elucidated. This study provides a certain reference for the selection of the pre-selection angle of the inlet guide vane of the centrifugal pump, and it is of great practical significance to guarantee the long-term and efficient operation of the centrifugal pump.

TABLE 2 | Grid independence check for the simulation.

Grid	Grid 1	Grid 2	Grid 3	Grid 4
Number of grids	1220844	1831266	2746899	4120348
Predicted head (m)	61.43	61.63	61.28	61.03

MODEL DESCRIPTION AND NUMERICAL CONSIDERATIONS

Geometric Model

The centrifugal pump can be divided into four parts according to the overall flow (Li et al., 2018; Li et al., 2020): impeller flow channel, inlet flow channel, outlet flow channel, and volute flow channel. In consideration of reducing the disturbance and stabilizing the flow, a cylindrical extension of four times the diameter is added to the impeller inlet and volute outlet, respectively, in the computational domain model. Pro/Engineer software is used to model the full flow channel of the centrifugal pump, and the 3D model obtained is shown in

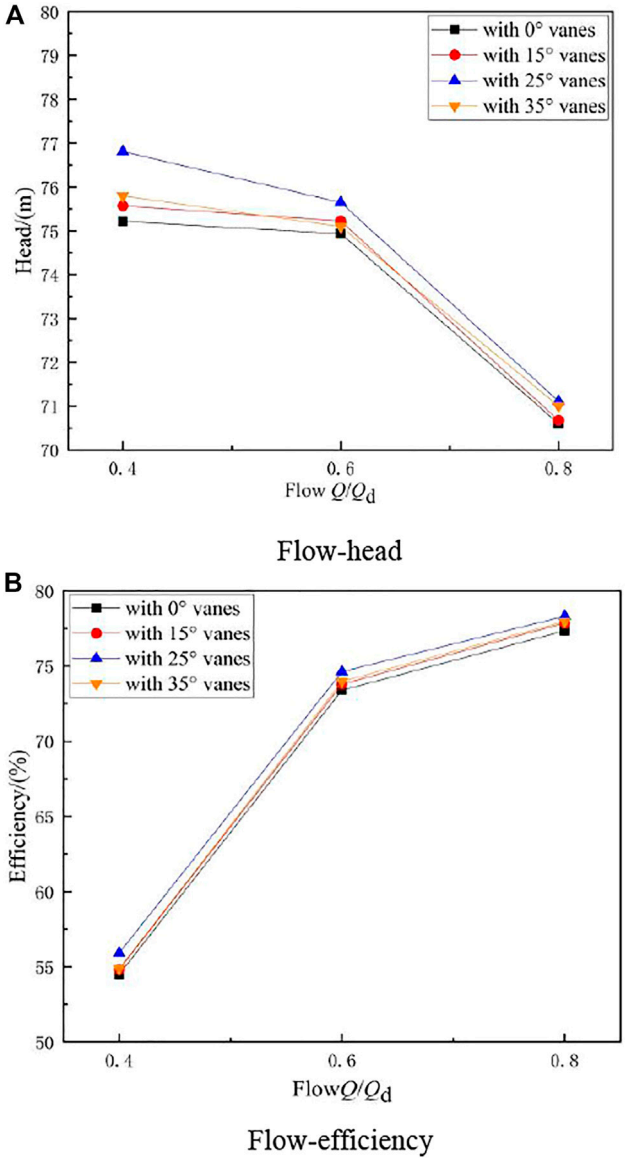

FIGURE 5 | External characteristics of centrifugal pumps: **(A)** flow-head; **(B)** flow-efficiency.

Figure 1. The structural design parameters of the pump are shown in **Table 1**.

Two symmetrical inlet straight thick guide vanes were arranged in the inlet section of the centrifugal pump, and the schematic diagram of the guide vane is shown in **Figure 2**. The length of the vane a is 40 mm, the width b is 50 mm, the thickness c is 2 mm, the distance of the vane from the impeller inlet is 60 mm, and the offset angle between the vane and the axial direction is θ. The geometric shapes of IGVs at different offset angles are demonstrated in **Figure 3**.

Computational Mesh

The multiple reference frame (MRF) method is used for data transfer between dynamic and static computational domains. The meshes are generated for impellers and IGVs with ANSYS ICEM, and the meshes of IGVs and impellers are exhibited in **Figure 4**. Local refinement is used to improve the simulation accuracy.

Numerical Methods

The shear stress transport (SST) k-ω turbulence model was applied to solve the flow equations in this study. It has the capability to predict the flow within a side channel pump after evaluating the effects of different turbulence models. And the k-ω model can better simulate turbulent flow away from the wall and has a wider application for solving boundary layer problems under various pressure gradients (Wang, He, Shi et al., 2019; Li et al., 2019; Pei et al., 2019). The boundary condition at the pump inlet and outlet is set to the mass flow rate and pressure, respectively. And the no-slip condition is applied on pump walls, and the scalable wall function is used for near-wall regions. The control equations are as follows.

k equation:

$$\frac{\partial(\rho k)}{\partial t}+\frac{\partial}{\partial x_j}\left(\rho U_j k\right)=\frac{\partial}{\partial x_j}\left[\left(\mu+\frac{\mu_t}{\sigma_k}\right)\frac{\partial k}{\partial x_j}\right]+P_k-\beta'\rho k\omega+P_{kb} \tag{1}$$

ω equation:

$$\frac{\partial(\rho\omega)}{\partial t}+\frac{\partial}{\partial x_j}\left(\rho U_j \omega\right)=\frac{\partial}{\partial x_j}\left[\left(\mu+\frac{\mu_t}{\sigma_\omega}\right)\frac{\partial \omega}{\partial x_j}\right]+\alpha\frac{\omega}{k}P_k-\beta\rho\omega^2+P_{\omega b} \tag{2}$$

The turbulent viscosity is calculated using

$$\mu_t=\frac{\alpha_1 k\rho}{\max\left(\alpha_1\omega, SF_2\right)} \tag{3}$$

Here, β', α, β, σ_k, and σ_ω are empirical model parameters: β' = 0.09, α = 5/9, β = 0.075, and $\sigma_k = \sigma_\omega$ = 2.

The second law of thermodynamics states that the entropy of an isolated system does not decrease, also known as the principle of entropy increase. Fluid flow in centrifugal pump is complex and vortex currents are created. Fluid-fluid interactions and fluid-wall interactions result in fluid energy loss. The entropy generation rate (EGR) in turbulent flow consists of two terms: the first part caused by the dissipation in the averaged flow (direct or viscous dissipation) and the other part due to the dissipation in the fluctuating terms of the flow (turbulent dissipation). The unit volume entropy generation is defined as

$$S'''_D=S'''_{\bar{D}}+S'''_{D'} \tag{4}$$

where $S'''_{\bar{D}}$ is the direct dissipation term:

$$S'''_{\bar{D}}=\frac{\mu}{T}\left[\left(\frac{\partial\bar{u}}{\partial y}+\frac{\partial\bar{v}}{\partial x}\right)^2+\left(\frac{\partial\bar{u}}{\partial z}+\frac{\partial\bar{w}}{\partial x}\right)^2+\left(\frac{\partial\bar{v}}{\partial z}+\frac{\partial\bar{w}}{\partial y}\right)^2\right]+2\frac{\mu}{T}\left[\left(\frac{\partial\bar{u}}{\partial x}\right)^2+\left(\frac{\partial\bar{v}}{\partial y}\right)^2+\left(\frac{\partial\bar{w}}{\partial z}\right)^2\right] \tag{5}$$

where $\bar{u}$, $\bar{v}$, $\bar{w}$ denote the time-averaged velocities in the x, y, and z directions, respectively, T is the temperature, and μ is

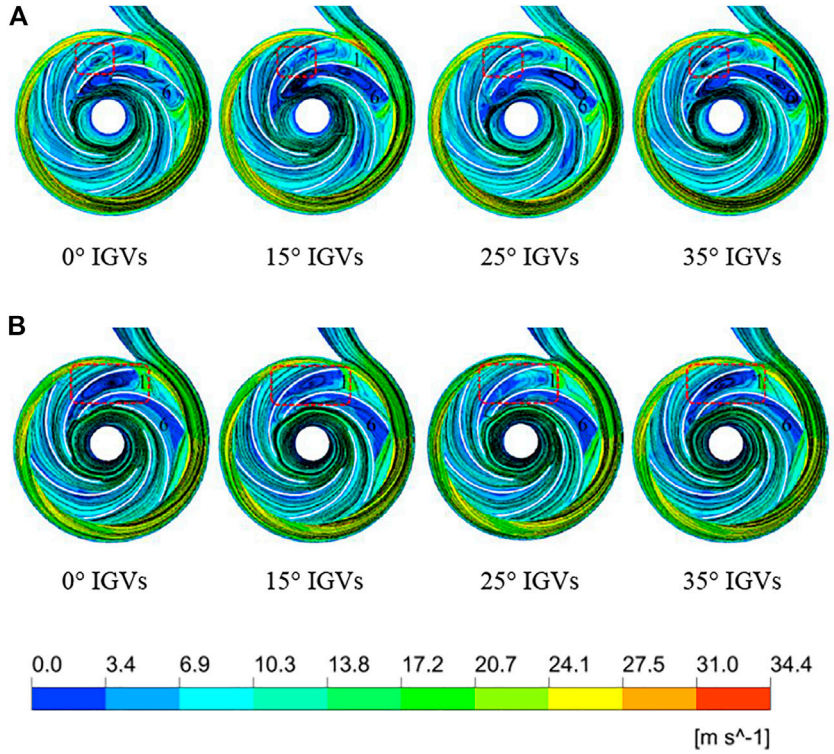

FIGURE 6 | Streamlines of relative velocity at the cross-section: **(A)** $0.6Q_d$ and **(B)** $0.8Q_d$.

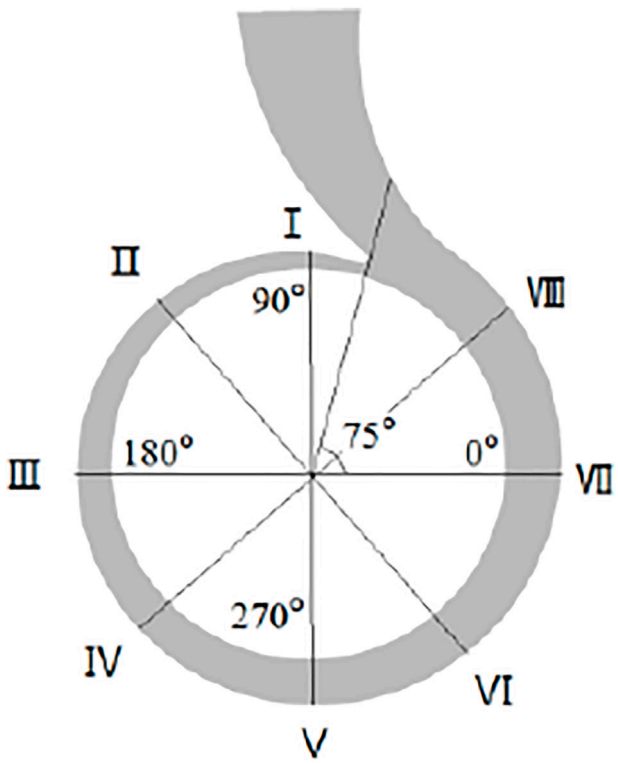

FIGURE 7 | Circumferential angle and cross-section distribution of the volute.

the kinetic viscosity. And $S'''_{D'}$ is the turbulent dissipation term:

$$S'''_{D'} = \frac{\mu}{T}\left[\left(\frac{\partial u'}{\partial y}+\frac{\partial v'}{\partial x}\right)^2+\left(\frac{\partial u'}{\partial z}+\frac{\partial v'}{\partial x}\right)^2+\left(\frac{\partial v'}{\partial z}+\frac{\partial w'}{\partial y}\right)^2\right] + 2\frac{\mu}{T}\left[\left(\frac{\partial u'}{\partial x}\right)^2+\left(\frac{\partial v'}{\partial y}\right)^2+\left(\frac{\partial w'}{\partial z}\right)^2\right] \quad (6)$$

Based on investigations by Kock and Herwig (2004), Herwig and Kock (2006), and Eliezer and Cohen (2001), the specific entropy generation rate due to the turbulent dissipation $S'''_{D'}$ is to be calculated through the proposed models. These models describe the relationship between the turbulent entropy generation rate and the parameters obtained from the solution of turbulence model equations. These models are accurate for flows with high Reynolds number, and as $Re\rightarrow\infty$, they lead to an exact solution:

$$S'''_{D} = \frac{\rho\varepsilon}{T} \quad (7)$$

Furthermore, **Eq. 7** can be approximately given by the following expression:

$$S_{D'} = C\frac{\rho\omega k}{T} \quad (8)$$

where k and ω are the turbulence kinetic energy and characteristic frequency in the shear stress transport (SST) model, respectively. C is an empirical constant and equals 0.09 (Menter, 1994).

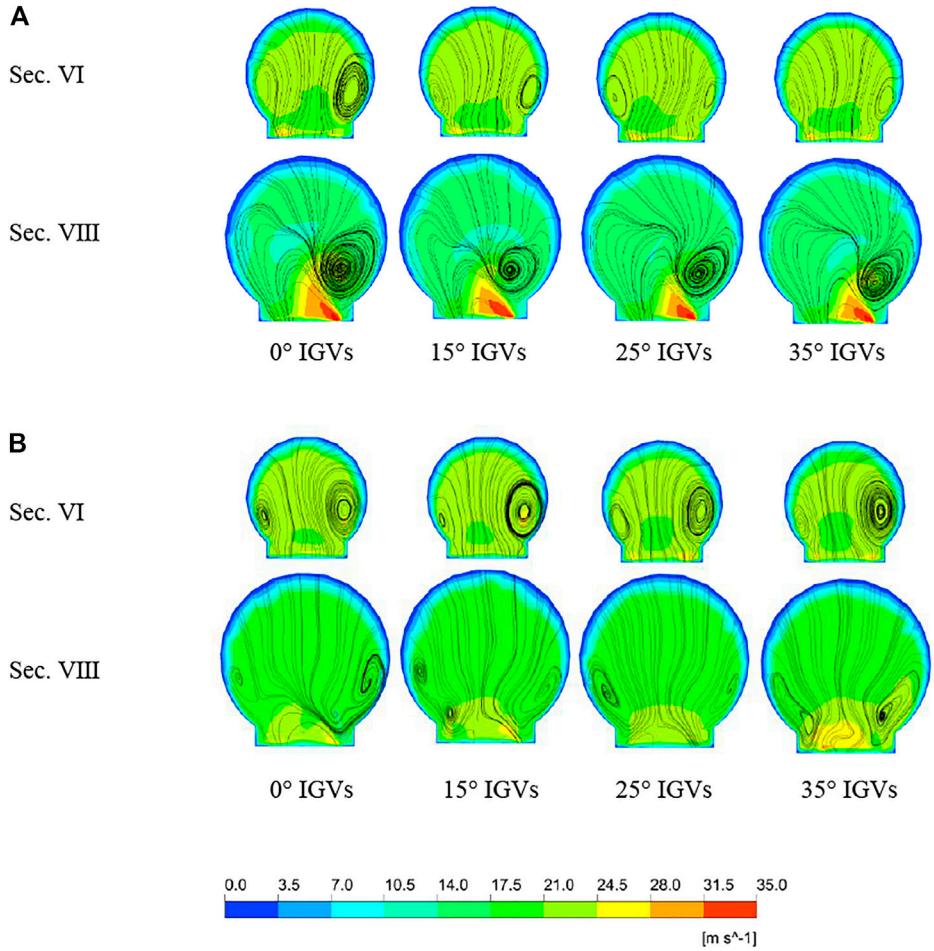

FIGURE 8 | Velocity contours and streamlines of four pump sections under two operating points. **(A)** 0.6Qd and **(B)** 0.8Qd.

A reasonable selection of the number of meshes can both speed up the calculation and ensure the accuracy and reliability of the simulation results (Li et al., 2017; Wang, He, Cheng et al., 2019). Four groups of computational models with different grid numbers were used for numerical simulations, and their heads were obtained separately, as shown in **Table 2**. The result shows that all the deviations are within 0.5%. Taking the factors such as saving computing resources and computing time into account, the third grid was finally selected. The accuracy and reliability of the numerical method were verified as well by comparing the simulation pump head and efficiency with experiment results under different flow rates (Lin et al., 2020).

RESULTS AND DISCUSSION

The Results of External Characteristics

The results of the external characteristic curves of the pump with IGVs of different offset angles at small operating conditions are shown in **Figure 5**. From **Figure 5**, it can be seen that the head and efficiency of the pump with 15°, 25°, and 35° IGVs are higher than those of the pump with 0° IGVs at each small operating condition, and the pump with 25° IGVs has the greatest increase in head and efficiency. Comparing the differences of the head and efficiency of the pump with 0° IGVs and the pump with 25° IGVs under different flow conditions, the head increased by 2.11, 0.95, and 0.73% at the three small flow conditions of $0.4Q_d$, $0.6Q_d$, and $0.8Q_d$, respectively, and the efficiency increased by 2.51, 1.67, and 1.25%, respectively. In order to study the intrinsic microscopic mechanism of the above external results, the internal flow of the centrifugal pump was analyzed. Considering the actual operating environment of the centrifugal pump and the range of operating conditions studied in this paper, we selected the $0.6Q_d$ operating point and the $0.8Q_d$ operating point for the internal flow study.

Internal Flow Characteristics

Figure 6 shows the streamlines of relative velocity at mid-section (the location of each flow path is shown in **Figure 1A**). When the centrifugal pump is operated under low flow conditions, different degrees of vortices appeared in both

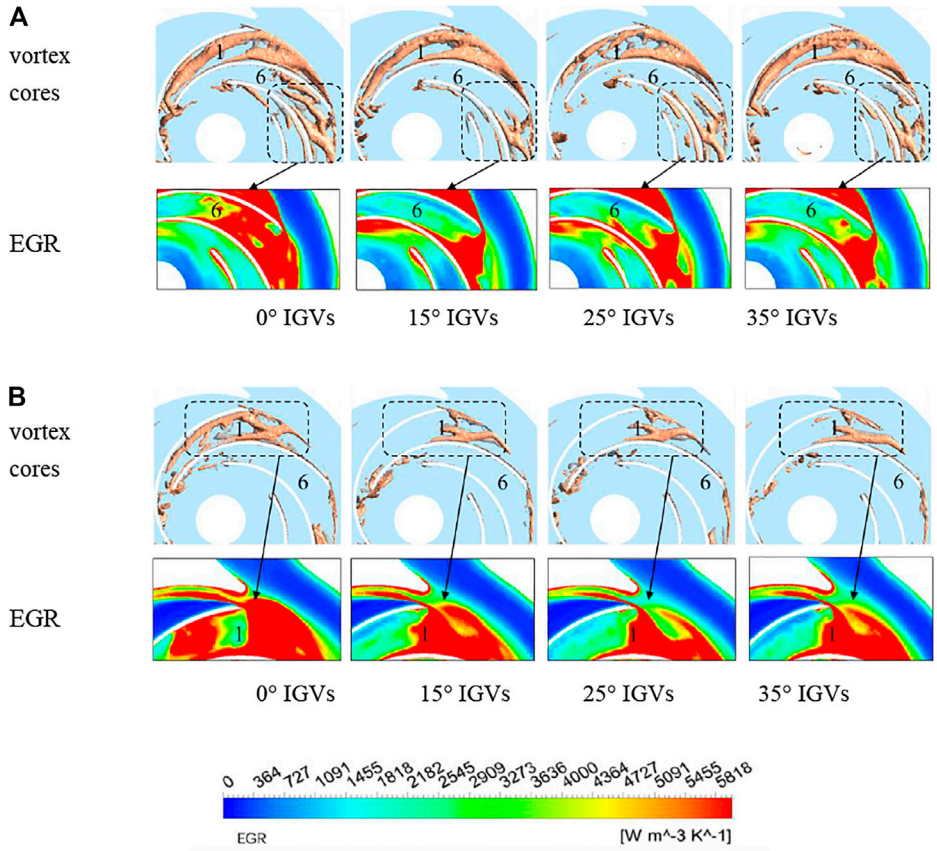

FIGURE 9 | Local EGRs and vortex cores of the centrifugal pump with vanes of different offset angles: **(A)** $0.6Q_d$ and **(B)** $0.8Q_d$.

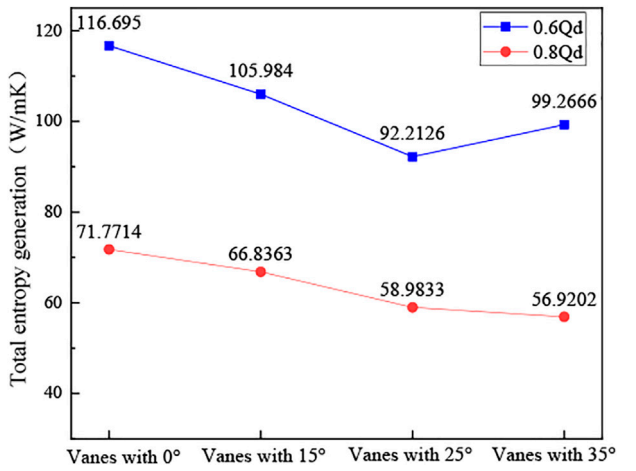

FIGURE 10 | Entropy generation rate at $0.6Q_d$ and $0.8Q_d$ operating points.

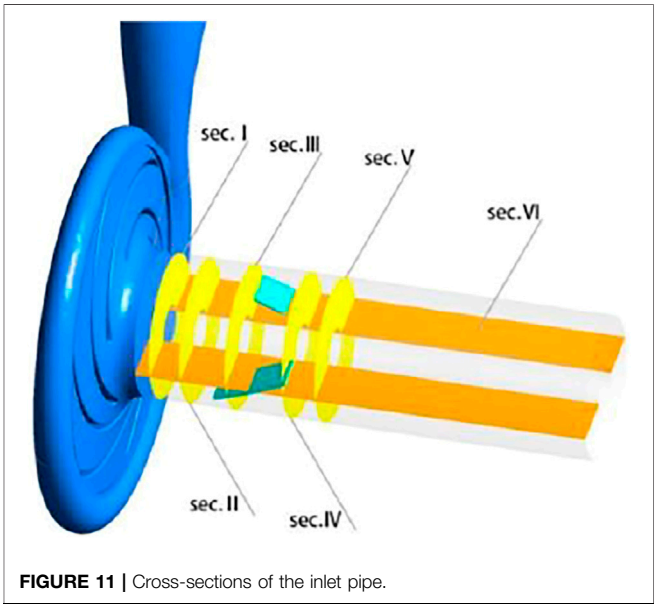

FIGURE 11 | Cross-sections of the inlet pipe.

TABLE 3 | Relative percentage reduction of energy loss at $0.6Q_d$ and $0.8Q_d$ operating points.

Q_d	15° IGV	25° IGV	35° IGV
0.6	−9.17%	−21.12%	−14.91%
0.8	−6.88%	−17.82%	−20.69%

path 1 and path 6 near the tongue, and the vortices resulted in large vortex cores in the impeller path. Compared with the $0.8Q_d$ operating point, the dynamic and static interference between the tongue and the impeller is more obvious at the

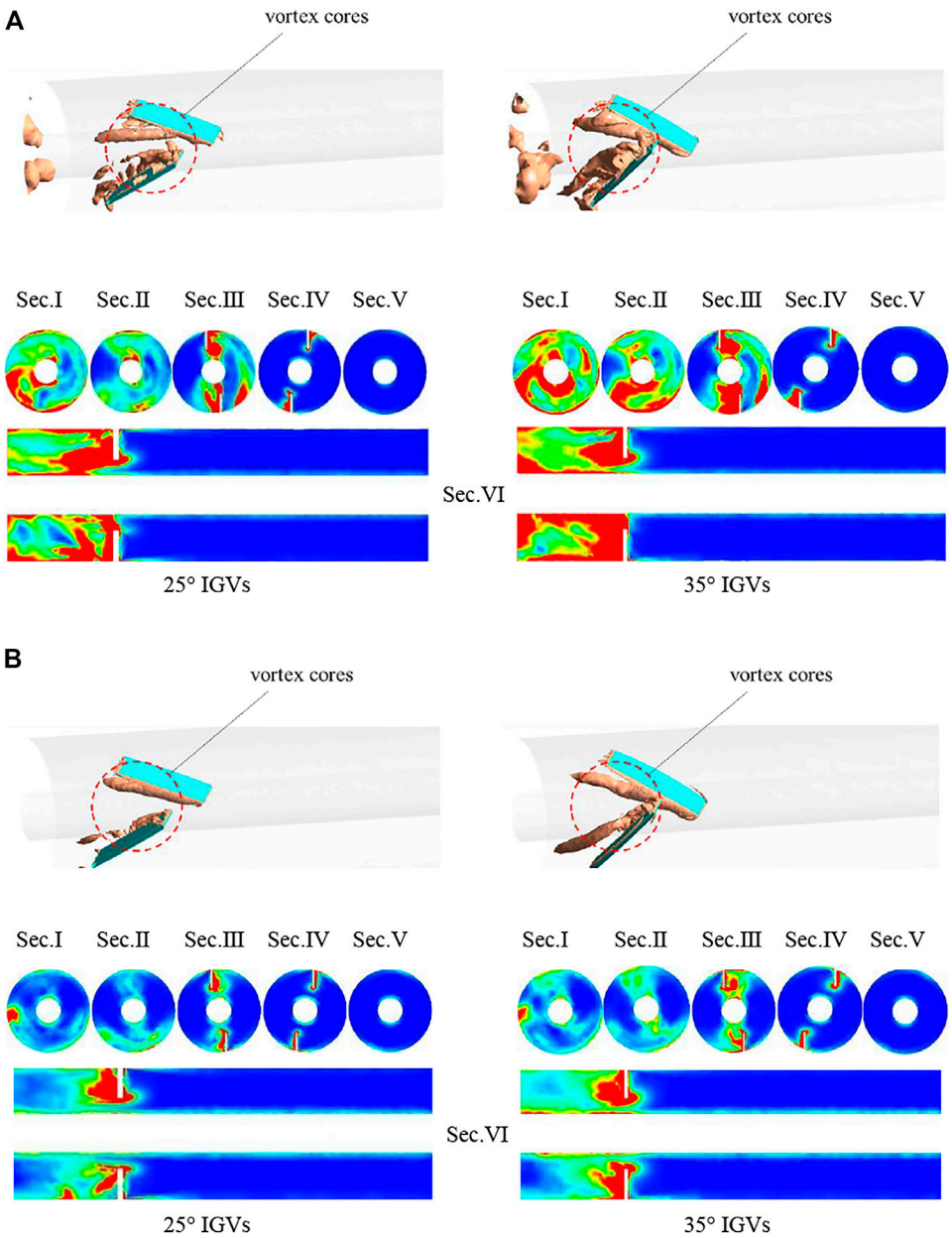

FIGURE 12 | Contours of the entropy generation rate at different cross-sections and vortex cores of the inlet pipe: **(A)** $0.6Q_d$ and **(B)** $0.8Q_d$.

$0.6Q_d$ operating point, and the flow pattern in path 1 and path 6 is more turbulent. At the $0.6Q_d$ operating point, the increase of the vane angle is beneficial to reducing the scale of vortices in the flow path. Besides, the area of the vortex core in flow path 1 is the smallest, and there is no large-area agglomeration. At the $0.8Q_d$ operating point, there are almost no vortices in flow path 1 and the area of the low velocity region is minimal.

The volute is divided into zones, as shown in **Figure 7**. The VI and VIII sections of the volute shown in **Figure 7** are selected, and their flow is analyzed. The velocity contour and streamlines of the mid-sections under two operating conditions are shown in **Figure 8**. The offset angle of the guide vane has a certain influence on the size and position of the vortex in the volute section, and the pump with 25° IGVs is the most effective in reducing the size of the vortex. At $0.8Q_d$ operating conditions, the 25° IGV pump has a more stable flow in Section VIII near the spacer tongue. The above results indicate that the increase of the angle has a certain effect on improving the flow pattern near the tongue. The $0.8Q_d$ operating point is closer to the design point, and its scale of vortices is reduced compared with that of $0.6Q_d$.

Local Entropy Generation Analysis

The relationship between the flow inside the centrifugal pump and the energy loss can be visualized in **Figure 9**. The vortex in

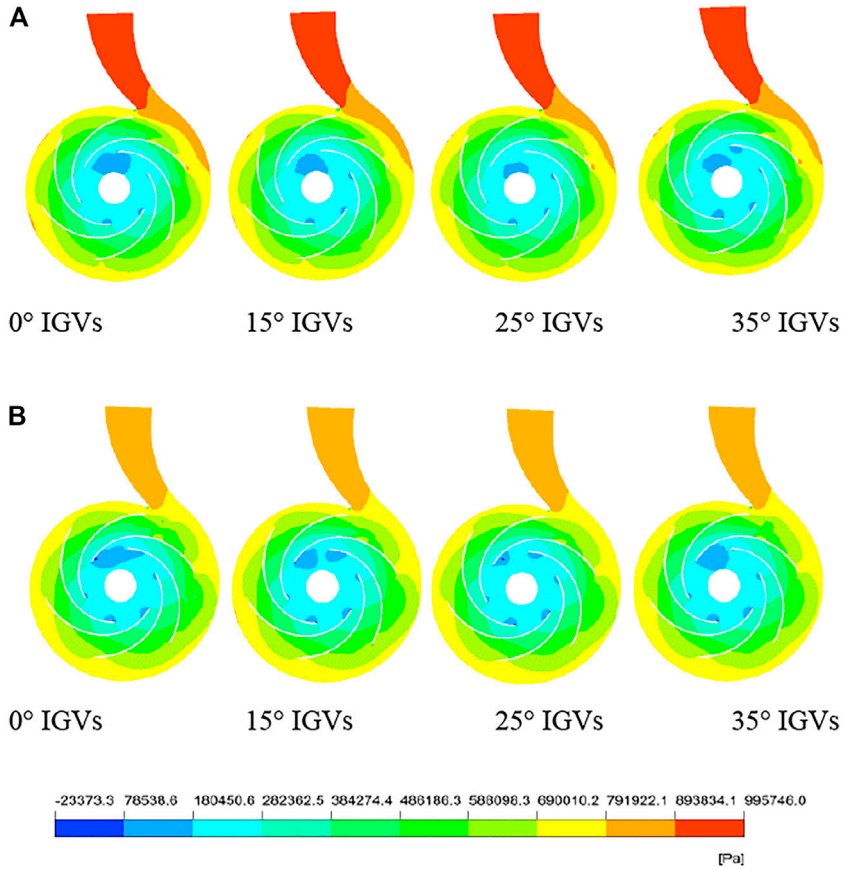

FIGURE 13 | Contours of static pressure at the cross-section: **(A)** $0.6Q_d$ and **(B)** $0.8Q_d$.

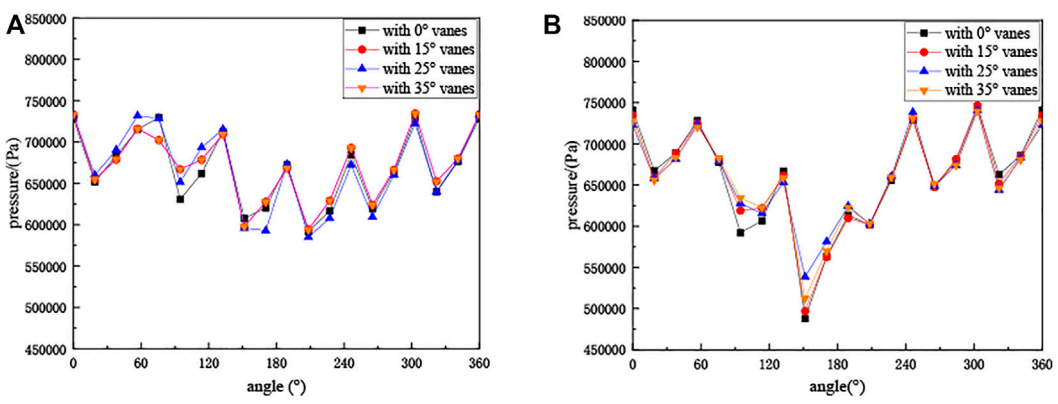

FIGURE 14 | Pressure distribution at the intersection of the volute and impeller: **(A)** $0.6Q_d$ and **(B)** $0.8Q_d$.

the impeller is represented by the Q-criterion, and the actual value of the Q-criterion is 3.6×10^5 s^{-2}. At the $0.6Q_d$ operating point, a larger range of high Q regions appears in flow path 1 of four pumps due to the stronger dynamic and static interference near the tongue. Since the flow of the pump with 25° IGVs is more stable, the area of vortex core in flow path 1 is the smallest. From **Figure 9**, it can be obtained that the increase in the vane's angle is conducive to reducing the intensity of the vortex and the local entropy generation rate (EGR) in the flow path. At the operating point of $0.8Q_d$, the effect of increasing the offset angle on reducing the area of vortex core in the flow path is more obvious, indicating that 15°, 25°, and 35° offset angles can effectively suppress the flow turbulence.

The local entropy generation rate for the pump with vanes of different angles at $0.6Q_d$ and $0.8Q_d$ operating points is

illustrated in **Figure 10**. And the percentage reduction of energy loss in the cross-section for the four pumps is shown in **Table 3** (percentage represents the relative ratio of energy loss to that of the pump with 0° IGVs). The energy loss in the section tends to decrease with the increase of the guide vane angle. Compared with that of the pump with 0° IGVs, the energy loss of the pump with 25° IGVs in the cross-section is reduced by 21.12 and 17.82% for the two operating conditions, respectively. The influence of the offset angle on the internal flow of the centrifugal pump is shown as follows: the 25° IGV has the best improvement impact on flow path 1 near the tongue, and the pump's head and efficiency have improved the most. The larger vortex core area of flow path 1 in the pump with 0° IGVs indicates a much more complex vortex structure in flow path 1, which results in more energy dissipation during energy transport.

From the above analysis results and combined with the efficiency and head curves, it can be seen that the increase of the vane angle can improve the flow pattern of fluid in the volute and impeller, increasing the head and efficiency of the centrifugal pump. In order to further reveal the reason why the offset angle of the IGV should not be too large, we subjected the inlet of the centrifugal pump with 25° and 35° IGVs to flow and loss analysis. The contour of the entropy generation rate is depicted in **Figure 11** for five different cross-sections of the inlet, and the inlet vortex core of two pumps is characterized in **Figure 12**. The actual value of the Q-criterion is $9 \times 10^4\ s^{-2}$. Compared with the $0.6Q_d$ operating point, the $0.8Q_d$ operating point which is closer to the design point has a lower entropy generation rate under the same condition. In both operating conditions, the loss of energy near the inlet increases with the increase of the offset angle.

The distribution of vortex core in the inlet pipe is more consistent with the variation of energy loss: the higher Q value of the region corresponds to the larger energy loss, which indicates that the energy loss near the vanes is mainly caused by vortices. It is obvious from **Figure 12** that the core is mainly distributed in the suction side of the guide vane, which means that the fluid flowing around the guide vanes will produce vortex in the suction side of the guide vane. The above analysis can be summarized as follows: it can be concluded that, for the same operating point, the 35° IGV causes a larger vortex compared to the 25° IGV. Excessive offset angle of the IGV increases the flow turbulence near the inlet, intensifying the hydraulic losses and making the head and efficiency smaller.

Pressure Characteristics at the Cross-Section

Figure 13 shows the static pressure distribution at the cross-section in the centrifugal pump. The static pressure distribution pattern in the pump is basically the same in both operating points. As the flow rate increases, the pressure at the outlet of the volute gradually decreases, but the area of higher pressure remains in the volute. At the $0.8Q_d$ operating point, the pressure at the volute outlet is the lowest. In the impeller flow path, the pressure value increases continuously from the impeller inlet to the outlet. But in the flow path near the tongue, the pressure value distribution is different from that in the other flow paths due to the influence of the tongue, and the pressure gradient is more uneven. At the impeller inlet, due to the energy loss, low-pressure areas appear in both operating conditions, and the low-pressure area is not uniformly distributed. In both operating points, the low-pressure area of the impeller inlet of pumps with 15°, 25°, and 35° IGVs is smaller than that of the pump with 0° IGVs, indicating that the increase in the offset angle of IGVs can reduce the energy loss at the impeller inlet. Of the four pumps studied, the pump with 25° IGVs has the best effect on the pump's impeller inlet pressure improvement: the low-pressure area is smaller and the distribution of the low-pressure area is more uniform.

The pressure distribution at the interface between the volute and the impeller is shown in **Figure 14**, and the pressure is distributed periodically. In the vicinity of the tongue, the pressure fluctuation is more violent. As the flow rate decreases, the pressure fluctuation near the tongue becomes more and more violent. The pump with 0° IGVs has the lowest pressure at the impeller outlet near the tongue, while the pump with 25° IGVs has the most significant pressure boost. At the position away from the tongue, the pressure distribution at the intersection of the volute and impeller is basically the same for all four pumps, which indicates that the offset angle has no significant effect on the flow at locations away from the tongue.

CONCLUSION

The flow characteristics of the centrifugal pump with IGVs of different offset angles were numerically simulated, and the effects of offset angle on the impeller flow, volute flow, and inlet flow were compared and analyzed. Some conclusions are as follows:

1) At $0.4Q_d$, $0.6Q_d$, and $0.8Q_d$ operating points, the head and efficiency of pumps with 15°, 25°, and 35° IGVs are higher than those of the pump with 0° IGVs. Among the studied pumps, the head and efficiency of the pump with 25° IGVs have improved the most. The pump with 25° IGVs increased the head by 2.11, 0.95, and 0.73% and the efficiency by 2.51, 1.67, and 1.25%, respectively, compared with that with 0° IGVs.
2) The angle of the IGV has a more pronounced effect on the flow in the flow path near the tongue. The pump with 0° IGVs has a strong vortex in the impeller and a complex flow near the tongue, which always has the largest energy loss. On the contrary, when the IGV is installed at an angle of 25°, the impeller inlet low-pressure area is weakened and the turbulent kinetic energy near the tongue is smaller. It can better reduce the hydraulic loss caused by inlet shock, flow separation, and vortex, thus increasing the pump head and efficiency.
3) Fluid flow around the guide vane will produce vortex on the suction side of the vane, making the energy loss on the suction

side greater than that on the pressure side. And the larger the angle of the guide vane, the greater the energy loss on the suction side of the vane. The energy loss of the inlet is the reason why the external characteristics of the centrifugal pump are not proportional to the angle of the IGV.

4) Setting a certain offset angle of the inlet guide vane can inhibit the backflow and separation flow of the impeller inlet and improve the internal flow state of the impeller. And it is beneficial to reducing the energy loss in the impeller so that the centrifugal pump exhibits a higher head and efficiency.

DATA AVAILABILITY STATEMENT

The original contributions presented in the study are included in the article/supplementary material, and further inquiries can be directed to the corresponding author.

AUTHOR CONTRIBUTIONS

PL and ZZ contributed with conceptualization and writing original draft preparation. TY and WX carried out the experiment validation. All authors have read and agreed to the published version of the manuscript.

FUNDING

This work was financially supported by the Key R&D Program of Zhejiang Province (Grant No. 2020C03081), the Joint Funds of the National Natural Science Foundation of China (Grant No. U2006221), the National Natural Science Foundation of China (Grant No. 51676173), and the Top-notch Talent Support Program of Zhejiang Province (Grant No. 2019R51002). The supports are gratefully acknowledged.

REFERENCES

Aaronson, K. D., Slaughter, M. S., Miller, L. W., McGee, E. C., Cotts, W. G., Acker, M. A., et al. (2012). Use of an Intrapericardial, Continuous-Flow, Centrifugal Pump in Patients Awaiting Heart Transplantation. *Circulation* 125 (25), 3191–3200. doi:10.1161/CIRCULATIONAHA.111.058412

Coppinger, M., and Swain, E. (2000). Performance Prediction of an Industrial Centrifugal Compressor Inlet Guide Vane System. *Proc. Inst. Mech. Eng. A: J. Power Energ.* 214 (2), 153–164. doi:10.1243/0957650001538254

Dou, H.-S. (2006). Mechanism of Flow Instability and Transition to Turbulence. *Int. J. Non-Linear Mech.* 41 (4), 512–517. doi:10.1016/j.ijnonlinmec.2005.12.002

Dou, H., Jiang, W., Zhang, Y., Zhu, Z., Cui, B., and Li, Y. (2014). Flow Instability in Centrifugal Pump Based on Energy Gradient Theory. *Trans. Chin. Soc. Agric. machinery* 45 (12), 88–92. doi:10.6041/j.issn.1000-1298.2014.12.014

Eliezer, K., and Cohen, J. (2001). An Introduction to Turbulent Flow by Jean Mathieu and Julian Scott, Cambridge University Press, 2000, ISBN 0521570662. *Int. J. Multiphase Flow* 27 (9), 1655–1656. doi:10.1016/S0301-9322(01)00020-9

Fukutomi, J., and Nakamura, R. (2005). Performance and Internal Flow of Cross-Flow Fan with Inlet Guide Vane. *JSME International Journal. Ser. B, Fluids Thermal Engineering* 48 (4), 763–769. doi:10.1299/jsmeb.48.763

Herwig, H., and Kock, F. (2006). Direct and Indirect Methods of Calculating Entropy Generation Rates in Turbulent Convective Heat Transfer Problems. *Heat Mass. Transfer* 43 (3), 207–215. doi:10.1007/s00231-006-0086-x

Hu, X., Lin, J., Chen, D., and Ku, X. (2020). Stability Condition of Self-Organizing Staggered Particle Trains in Channel Flow. *Microfluidics and Nanofluidics* 24 (25), 1–12. doi:10.1007/s10404-020-2329-4

Hu, X., Lin, J., Guo, Y., and Ku, X. (2021). Motion and Equilibrium Position of Elliptical and Rectangular Particles in a Channel Flow of a Power-Law Fluid. *Powder Technol.* 377, 585–596. doi:10.1016/j.powtec.2020.09.028

Junaidi, M. A. R., Kumari, N. B. V. L., Samad, M. A., and Ahmed, G. M. S. (2015). CFD Simulation to Enhance the Efficiency of Centrifugal Pump by Application of Inner Guide Vanes. *Mater. Today Proc.* 2 (4-5), 2073–2082. doi:10.1016/j.matpr.2015.07.200

Kim, S., Heo, S., Cheong, C., and Kim, T.-H. (2013). Numerical and Experimental Investigation of the Bell-mouth Inlet Design of a Centrifugal Fan for Higher Internal Flow Rate. *J. Mech. Sci. Technol.* 27 (8), 2263–2273. doi:10.1007/s12206-013-0609-6

Kock, F., and Herwig, H. (2004). Local Entropy Production in Turbulent Shear Flows: A High-Reynolds Number Model with Wall Functions. *Int. J. Heat Mass Transfer* 47 (10), 2205–2215. doi:10.1016/j.ijheatmasstransfer.2003.11.025

Li, B., Li, X., Jia, X., Chen, F., and Fang, H. (2019). The Role of Blade Sinusoidal Tubercle Trailing Edge in a Centrifugal Pump with Low Specific Speed. *Processes* 7 (9), 625. doi:10.3390/pr7090625

Li, X., Chen, B., Luo, X., and Zhu, Z. (2020). Effects of Flow Pattern on Hydraulic Performance and Energy Conversion Characterisation in a Centrifugal Pump. *Renew. Energ.* 151, 475–487. doi:10.1016/j.renene.2019.11.049

Li, X., Jiang, Z., Zhu, Z., Si, Q., and Li, Y. (2018). Entropy Generation Analysis for the Cavitating Head-Drop Characteristic of a Centrifugal Pump. *Proc. Inst. Mech. Eng. C: J. Mech. Eng. Sci.* 232 (24), 4637–4646. doi:10.1177/0954406217753458

Li, X., Yu, B., Ji, Y., Lu, J., and Yuan, S. (2017). Statistical Characteristics of Suction Pressure Signals for a Centrifugal Pump under Cavitating Conditions. *J. Therm. Sci.* 26 (01), 47–53. doi:10.1007/s11630-017-0908-9

Lin, P., Li, Y., Xu, W., Chen, H., and Zhu, Z. (2020). Numerical Study on the Influence of Inlet Guide Vanes on the Internal Flow Characteristics of Centrifugal Pump. *Processes* 8 (1), 122. doi:10.3390/pr8010122

Liu, T., Qi, D., and Tan, J. W, R. (2011). Influence of the Equivalent Precession Radius of the Guide Vane Passage on the Performance of Centrifugal Compressors. *J. Xian Jiaotong Univ.* 45 (03), 91–94.

Martinich, A. (1990). Leviathan and the Air-Pump, Hobbes, Boyle, and the Experimental Life. *Rev. Hist. Sci.* 43 (1), 109–116. doi:10.1353/hph.1989.0025

Menter, F. R. (1994). Two-equation Eddy-Viscosity Turbulence Models for Engineering Applications. *AIAA J.* 32, 1598–1605. doi:10.2514/3.12149

Pei, J., Zhang, F., Appiah, D., Hu, B., Yuan, S., Chen, K., et al. (2019). Performance Prediction Based on Effects of Wrapping Angle of a Side Channel Pump. *Energies* 12 (1), 139. doi:10.3390/en12010139

Shi, F. X., Yang, J. H., Wang, X. H., Zhang, R. H., and Li, C. E. (2012). The Impact of Inlet Angle and Outlet Angle of Guide Vane on Pump in Reversal Based Hydraulic Turbine Performance. *IOP Conf. Ser. Earth Environ. Sci.* 15, 042030. doi:10.1088/1755-1315/15/4/042030

Wang, C., He, X., Cheng, L., Luo, C., Xu, J., Chen, K., et al. (2019). Numerical Simulation on Hydraulic Characteristics of Nozzle in Waterjet Propulsion System. *Processes* 7 (12), 915. doi:10.3390/pr7120915

Wang, C., He, X., Shi, W., Wang, X., Wang, X., and Qiu, N. (2019). Numerical Study on Pressure Fluctuation of a Multistage Centrifugal Pump Based on Whole Flow Field. *AIP Adv.* 9 (3), 035118. doi:10.1063/1.5049196

Wang, J., Yan, J., Liu, H., Shao, C., and Wang, Y. (2018). Influence on Unsteady Characteristics of Suction Chamber with Built-In Baffles in Low Specific Speed Centrifugal Pump. *Fluid Mach* 46 (11), 28–33.

Xiao, J., Gu, C., Shu, X., and Gao, C. (2006). Performance Analysis of a Centrifugal Compressor with Adjustable Inlet Guide Vanes. *J. Chin. Soc. Power Eng.* 2006 (06), 804–807. doi:10.3321/j.issn:1000-6761.2006.06.009

Xiong, T. (1996). Operating Characteristics of Francis Turbine under Partial Load Conditions. *Hydropower Inf.* 1996 (15), 1–5.

Conflict of Interest: The authors declare that the research was conducted in the absence of any commercial or financial relationships that could be construed as a potential conflict of interest.

Publisher's Note: All claims expressed in this article are solely those of the authors and do not necessarily represent those of their affiliated organizations, or those of the publisher, the editors, and the reviewers. Any product that may be evaluated in this article, or claim that may be made by its manufacturer, is not guaranteed or endorsed by the publisher.

frontiers in Energy Research

ORIGINAL RESEARCH
published: 31 January 2022
doi: 10.3389/fenrg.2021.818232

Time-Resolved Particle Image Velocimetry Measurements and Proper Orthogonal Decomposition Analysis of Unsteady Flow in a Centrifugal Impeller Passage

Bo Chen, Xiaojun Li and Zuchao Zhu*

State-Province Joint Engineering Lab of Fluid Transmission System Technology, Zhejiang Sci-Tech University, Hangzhou, China

Time-resolved particle image velocimetry (TR-PIV) measurements were conducted to analyze the unsteady flow field developing in a centrifugal pump. The flow structures in the impeller passage under different flow rates were investigated. The overall statistical characteristics of the flow were obtained with the study of relative phase-averaged flow field, phase-averaged turbulent kinetic energy (TKE), and the analysis of frequency. Through the study of the first few proper orthogonal decomposition (POD) modes of the flow field, the coherent flow structures under several flow rates were revealed, consequently, the flow fields were reconstructed by the POD modes. Results show that the main flow structures could be reflected by the first few modes of the flow field: when the fluid follows the blade contour well, the first few modes corresponded to the "jet-wake" structures; when the large-scale flow structures appear in the passage, the 1st and 2nd modes were associated in pairs and corresponded to the stall cells, the 3rd and 4th modes corresponded to the "jet-wake" structures, and the 5th and 6th modes corresponded to the passage vortexes or the "jet-wake" structures (for the extreme part-load conditions). The flow structures that were reflected by the first few modes change as the decrease of flow rate, especially, at the extreme part-load condition, not only the shapes of the flow structures changed, but also the flow direction is reversed. This indicates that the generation mechanism of turbulent kinetic energy in the flow passage changed at the extreme part-load conditions.

Keywords: TR-PIV, centrifugal pump, POD, coherent structure, energy loss

OPEN ACCESS

Edited by:
Enhua Wang,
Beijing Institute of Technology, China

Reviewed by:
Sq Yang,
Tianjin University, China
Xiangyuan Zhu,
Shandong Jianzhu University, China

****Correspondence:***
Xiaojun Li
lixj@zstu.edu.cn

Specialty section:
This article was submitted to Process and Energy Systems Engineering, a section of the journal Frontiers in Energy Research

Received: *19 November 2021*
Accepted: *21 December 2021*
Published: *31 January 2022*

Citation:
Chen B, Li X and Zhu Z (2022) Time-Resolved Particle Image Velocimetry Measurements and Proper Orthogonal Decomposition Analysis of Unsteady Flow in a Centrifugal Impeller Passage. Front. Energy Res. 9:818232. doi: 10.3389/fenrg.2021.818232

1 INTRODUCTION

Centrifugal pumps consume about 20% of the total generated energy in the world due to their extensive usage in petrochemical, chemical, coal, chemical, pharmaceutical, and other process fields (Arun Shankar et al., 2016; Bozorgasareh et al., 2021). Improving the efficiency and stability of centrifugal pumps is an urgent request for sustainable development (Krause et al., 2005; Keller et al., 2014; Zhang et al., 2020; Zhang et al., 2021). While unsteady flow structures is the core technical problem to centrifugal pumps' improvement.

Numerous studies have revealed the relationship between the pump operation instability and the unsteady flow structures. Tan et al. (2017) investigated the role of blade rotational angle in the energy

performance and pressure fluctuation of a mixed flow pump and found that the maximum amplitude of pressure fluctuation in the impeller at a blade rotational angle of 4° is greater than that of a blade rotational angle at 0°and 4°, the performance was caused by the strong vortex intensity. Santolaria Morros et al. (2011) explored operation characteristics of a pump in reverse mode involved in unsteady flow pattern and forces. These results demonstrated that fluctuations derived from blade-tongue interactions possess up to 25% of steady component, constituting a serious risk of fatigue failure. Xia et al. (2014) investigated the rotating stall of a pump-turbine in pump mode, and they concluded that under rotating stall condition, the enforced rotating non-uniform pressure distribution on the circumference acting on the impellers can result in a stronger sub-synchronous fluctuation of radial force, which leads to rotor-dynamic instabilities and strong vibrations. Moreover, the difference of pressure fluctuations on both sides of the guide vanes induces torque variations, which may have adverse influence on the machine operation. Kaupert (1999) and Kaupert and Staubli (1999) investigated the unsteady pressure field within a high specific speed centrifugal pump impeller, and they found that the hysteresis loop of the pump may be caused by the backflow at the runner outlet and recirculation at the runner inlet.

The analysis of energy loss within a pump reveals that turbulent dissipation could cause the energy loss. Ghorani et al. (2020) studied the irreversible energy losses within the pump as turbine (PAT), and they found that the blade inlet shock, flow deviation at the blade outlet, flow separation, backflow, and vortices in flow passages were categorized as the main reasons for irreversible hydraulic losses within the PAT components. Their results indicate that the turbulent entropy generation is the dominant mechanism for hydraulic losses. Shi et al. (2020) investigated the velocity distribution in the tip clearance of a multiphase pump, their results show that the flow separation phenomenon occurred at the radial coefficient of 0.97 and led to the increase of the turbulent energy loss of the pump. Li et al. (2018a) analyzed the hydraulic loss and flow field in a PAT, their results show that the increase in hydraulic loss in the runner is caused by the backflow and accompanying vortices at the runner inlet near the shroud. On the other hand, the increase in hydraulic loss in the stay/guide vanes is caused by the flow separation and separation vortices near the hub or the shroud. In order to further enrich the theory of rotational stall, Li et al. (2020a) and Li et al. (2020b) explored the mechanism of internal energy loss in the mixed-flow pump under stall conditions. They found that the high-value region of turbulent kinetic energy was basically corresponding to the backflow region of the impeller outlet and the separation region of the boundary layer near the suction surface, which led to a great increase of energy loss in the impeller.

The aforementioned investigations reveal that unsteady flow structures are responsible for the operation stability and energy loss. The flow structures inside the turbomachines are very complicated, including stall sell, flow deviation, flow separation, backflow, and vortices in flow passages, etc. These flow structures overlap and interact with each other, and it is difficult to obtain the characteristics of a single flow structure and the losses. However, when designing the pump, structural optimization is mainly to suppress the main flow structure that produces instability and loss. Therefore, it is necessary to extract these main flow structures from the flow field and analyze their characteristics. Nowadays, the POD method has been widely used to identify the most important and energetic structures dominated in the flow field. Li et al. (2018b) analyzed the airflow characteristics of thermal plumes inside a small space with POD, and the spatial and temporal characteristics of thermal plumes were identified. Lim et al. (2019) extracted POD modes of flow field about the free jets issued from V-notched nozzles, and the results showed that there was energy redistribution from low-order modes to higher-order modes along both PP- and TT-planes of both notched nozzles. Zhou et al. (2021) implemented the POD analysis to reveal the dominant modes of the flow field near the trailing edge of a pitching NACA 0012 airfoil. Tang et al. (2020) used a POD method to decompose the flow structures downstream of a dynamic cylindrical element in a turbulent boundary layer. Yang et al. (2019) applied the POD method to uncover the relation of the instantaneous energetic large-scale turbulent structures to the dominant POD modes. Moreover, POD has also been used to analyze the coherent structures in turbomachines. Han and Tan (2020) used a POD method to decompose the tip leakage vortex in a mixed flow pump as turbine at pump mode and found that POD could capture the main coherent structures of tip leakage vortex. Semlitsch and Mihăescu (2016) applied POD on the analysis of the flow structures appearing in a centrifugal turbocharger compressor. However, the focus of all recent studies has been made on the volute or diffuser, and little research has been done on the flow field characteristics inside the impeller.

In the present work, a TR-PIV system was utilized to measure the flow fields in a special voluteless centrifugal pump. The phase-averaged relative velocities, TKE, and frequency analysis were obtained to analyze the overall statistical characteristics of the flow. The POD method was used to decompose and reconstruct the passage flow. The contributions to the overall energy and the spatial/temporal behavior of the large-scale flow structures were analyzed in detail, and the dynamic and kinematic energy characteristics of the coherent flow structures that were in the impeller were revealed. Understanding the dynamic and energy dissipation characteristics of the unstable flow structure in the pump would allow inventing improved design methods for delaying or suppressing the unstable flow structures.

2 METHODOLOGY

2.1 Experimental Setup

The pump was subjected to a closed loop (containing a variable frequency drive system, two pressure sensors, three discharge valves, and an electronic flowmeter), which have been already described by Li et al. (2020c). The test pump is a special voluteless centrifugal pump. The impeller and pump casing are made of transparent plexiglass to visualize the flow. **Figure 1** shows the test rig and test pump. The main characteristics of the impeller

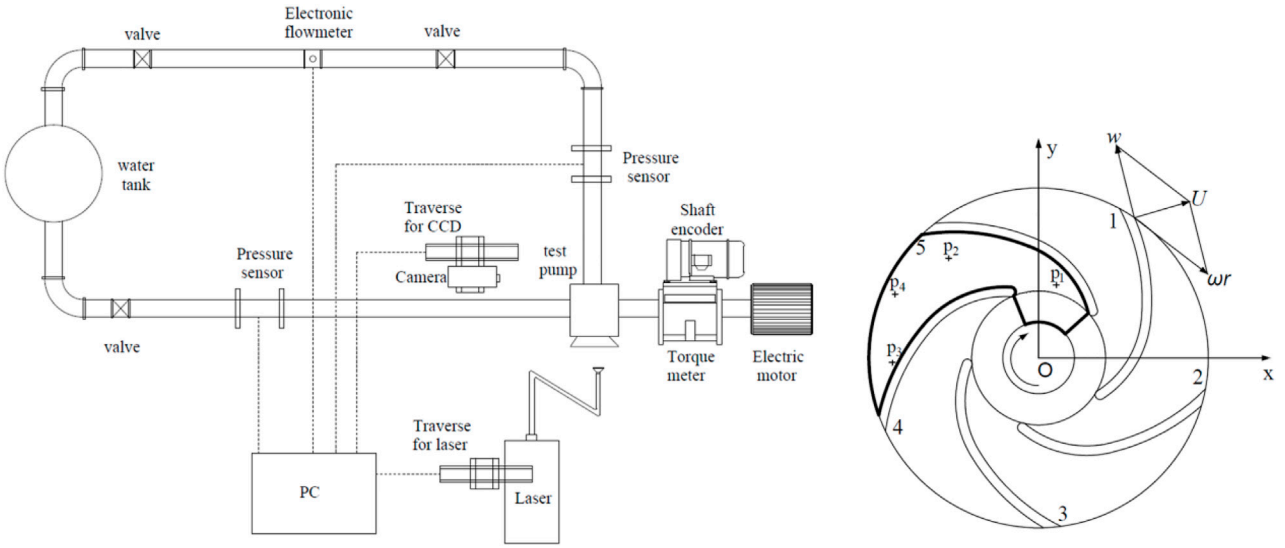

FIGURE 1 | Test impeller.

TABLE 1 | Impeller geometry.

Parameter name	Symbol	Value
Inlet diameter (mm)	D_1	71
Outlet diameter (mm)	D_2	142
Blade height at inlet (mm)	b_1	7
Blade height at outlet (mm)	b_2	7
Blade number	Z	5
Inlet angle of blade (°)	β_1	28
Outlet angle of blade (°)	β_2	34

are listed in **Table 1**. Water was used as working fluid in the pump.

2.2 Time-Resolved Particle Image Velocimetry

A TR-PIV system from Lavision was used to obtain a 2D velocity field. The main components are a laser, a laser guiding arm, a high-speed CMOS camera (Phantom Miro 320), and a synchronizer. A commercial software package (DaVis 10.1.2, LaVision) was used to control the image acquisition timing and obtain the velocity fields. The flow was seeded with glass hollow spheres, the diameters ranged from 9–13 μm, and the density is 1050 kg/m^3. During the test, the particles were scattered well in the pump. The laser guiding arm and light sheet optics system forms a light sheet of 1 mm thickness and directed along the mid-plane of the impeller. The CMOS camera with 1920 × 1200 pixels was used to acquire images, a Nikkor f = 50 mm, f/1.4 objective from Nikon Corporation was used and an optical filter with a 527-nm high pass filter was installed in front of the camera in order to increase signal-to-noise ratios. The camera was aligned perpendicularly to the laser sheet. The acquisition area contains a complete flow path with a resolution of 0.13 mm/pixel. The maximum frame rate of the camera is 1380 Hz at full resolution, and the minimum frame interval is 1.4 μs. A triggering system (shaft encoder) was used on the rotating shaft, and images were acquired in the same phase of each cycle. The images were processed by the LaVision Davis 10.1.2 software. The multiple interrogation method was used to process the images. The interrogation windows decrease in size in successive iterations: 64 × 64 pixels with 50% overlap, and 32 × 32 pixels with 75% overlap. According to Wernet (2000) the associated uncertainty in the instantaneous PIV velocity estimates was of 1% of the measured velocity, and the remaining particle lag errors arising from non-uniform particle seeding or particle lag are also assumed to be less than 1%, so the relative uncertainty in particle displacement was estimated as 2%.

2.3 Proper Orthogonal Decomposition

The idea of the POD approach is to find the maximized projection of the collected velocity fields onto an orthogonal basis. Moreover, it was introduced into turbulence analysis by Lumley (1967) and Holmes et al. (1997). In the present study, implementation of the POD analysis was based on the mathematical procedure described by Sirovich (1987). A summary of the method is reported here. In the 2D measurement plane, the instantaneous PIV snapshots are arranged into a matrix $\boldsymbol{V}$:

$$V = \begin{bmatrix} u_1^1 & u_1^2 & \cdots & u_1^N \\ \vdots & \vdots & \vdots & \vdots \\ u_M^1 & u_M^2 & \cdots & u_M^N \\ v_1^1 & v_1^2 & \cdots & v_1^N \\ \vdots & \vdots & \vdots & \vdots \\ v_M^1 & v_M^2 & \cdots & v_M^N \end{bmatrix} \tag{1}$$

where M is the number of spatial nodes in a single snapshot, N is the total number of time steps, u denotes the horizontal velocity component, and v is the vertical velocity component. The fluctuating matrix, V', is then calculated by subtracting the mean velocity field, $\bar{V}$, from V.

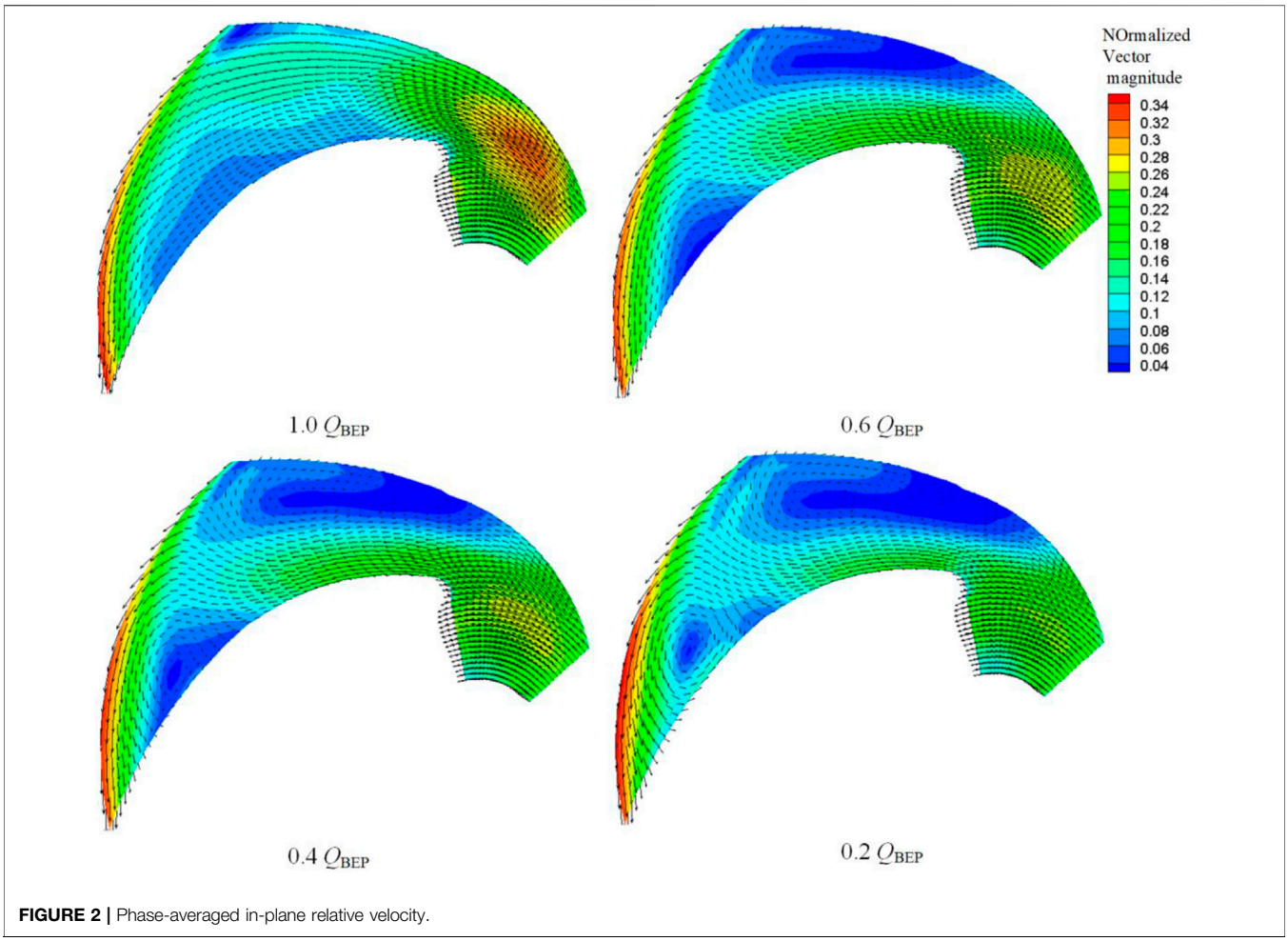

FIGURE 2 | Phase-averaged in-plane relative velocity.

Next, the auto-covariance matrix is formed as follows:

$$C_{NXN} = V'^{T}V' \tag{2}$$

The eigenvector A^i and eigenvalue λ^i can be solved as follows:

$$CA^i = \lambda^i A^i \tag{3}$$

The solutions are ordered according to the magnitude of the eigenvalues:

$$\lambda^1 > \lambda^2 > \cdots > \lambda^N \geq 0 \tag{4}$$

The spatially orthogonal POD mode may be obtained by:

$$\phi^i = V'A^i \tag{5}$$

The fluctuating part of the instantaneous velocity field can be calculated with the POD modes by:

$$V'_{recon} = \phi a^T \tag{6}$$

where a is the corresponding temporal coefficient.

2.4 Measurements Conditions

The measurements were carried out at a pump rotation speed of 1200 rpm, which corresponds to f_{BP} = 20 Hz and a blade tip speed U_{tip} of 8.92 m/s. The best efficiency point (BEP) was observed at a flow rate of Q_{BEP} = 2.4 m^3/h. In addition, the experiments were carried out at four flow rates: 0.2 Q_{BEP}, 0.4 Q_{BEP}, 0.6 Q_{BEP}, and 1.0 Q_{BEP}. For each flow rate, successive double images were taken every impeller rotation. Therefore, the image collection frequency is 20 Hz. The passages have been numbered from 1 to 5 as presented in **Figure 1B**. A convergence analysis at four reference points (**Figure 1B**) showed that convergence starts at about 150 double images (results not shown). Nevertheless, at least 200 double images were obtained for all the results reported herein. Since the development trend of the fluid inside each flow passage is relatively similar with the change of flow rate, the study focuses on the passage 1 shown in **Figure 1B**. Since the state of the fluid before entering the impeller directly affects the flow state inside the impeller, the study area includes the flow area between the impeller and the shaft, as shown in **Figure 1B**.

3 RELATIVE PHASE-AVERAGED FLOW FIELD AND STATISTICS

3.1 Relative Phase-Averaged Flow Field

A preliminary view of the influence of flow rate on the impeller passage can be gained by the time averaged flow field. The

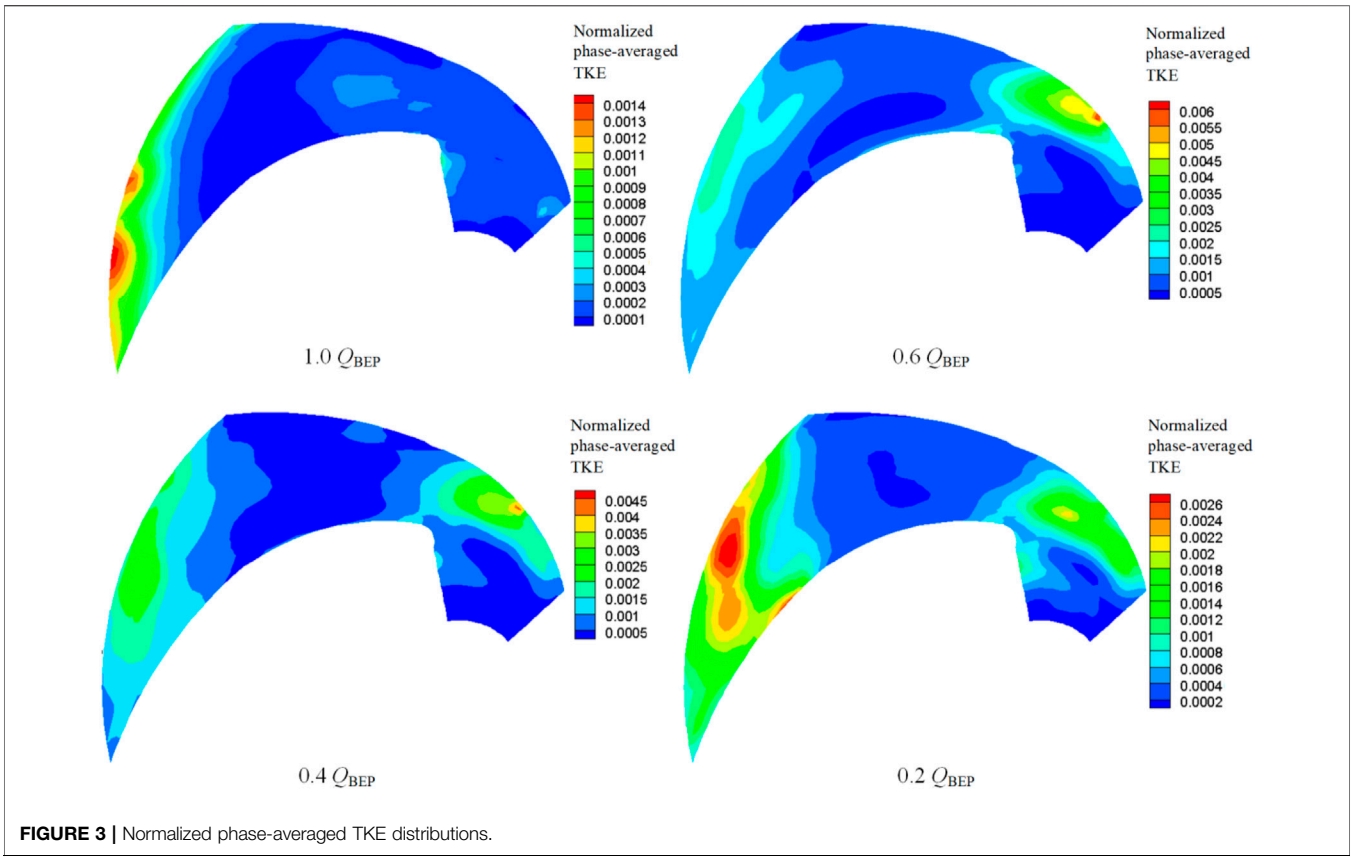

FIGURE 3 | Normalized phase-averaged TKE distributions.

relative phase-averaged flow field of an impeller passage has been widely described in previous publications (Westra et al., 2010; Li et al., 2020d). **Figure 2** shows the phase-averaged relative velocity maps for different flow rates. The contour maps are colored by the vector magnitude, which is normalized by U_{tip}. The relative velocity is obtained by $W = U - \omega r$, where U is the absolute velocity and ωr is the local velocity of the impeller. When the flow rate is 1.0 Q_{BEP}, the fluid at the inlet near the suction side enters the flow passage along the blades with a high velocity, and the fluid follows the blade contour very well. Nevertheless, 'jet-wake' phenomenon is still present. When the flow rate is 0.6 Q_{BEP}, the fluid near the suction side deviates from the suction side due to the increase of the attack angle, resulting in blockage. Then the fluid entering the passage is greatly reduced, its velocity is also significantly reduced, resulting in the appearance of a vortex at the suction side. When the flow rate is 0.4 Q_{BEP}, the inlet fluid deviates from the suction surface more severely, causing the suction side of the vortex to increase in size, and a smaller vortex appears at the pressure side. When the flow is further reduced to 0.2 Q_{BEP}, the scales of the two vortexes are further increased. From the average relative velocity field, the deviation of the inlet fluid is a key factor that causes the instability of the flow in the passage. In addition, for all flow rates, the 'jet-wake' phenomenon at the outlet intensifies as the flow rate decreases.

3.2 Phase-Averaged TKE Distribution

It is of particular interest to observe the mean TKE distribution of the velocity field as it is the component responsible for the total energy distribution of injected momentum over the flow field. **Figure 3** shows the normalized phase-averaged TKE distributions for different flow rates. Because of the limitations of 2-D measurements, the phase-averaged TKE is calculated through fluctuating components of velocity as shown below:

$$K_{2D}^{*} = \frac{1}{2} \cdot \frac{\overline{u'u'} + \overline{v'v'}}{U_{tip}^{2}} \tag{7}$$

As shown in **Figure 3**, a global view on the flow field shows that the high TKE values are observed at the passage inlet and outlet, which is consistent with Pedersen (2000). For the flow rate 1.0 Q_{BEP}, the high TKE area is located at the passage outlet, which is probably due to the "jet-wake" phenomenon. In addition, compared with other flow rates, the maximum value of TKE is the smallest when the flow rate is 1.0 Q_{BEP} due to the relatively uniform flow in the flow channel. For the part load flow rates, high TKE values at the passage inlet near the suction side become maximum, and the other turbulence sheet with less TKE can be observed at the middle of the passage outlet. For the flow rate 0.6 Q_{BEP}, flow instability causes blockage at the inlet, making the inlet fluid accelerate, causing a larger shock effect at the inlet, and therefore, generating the maximum turbulent energy. As the flow rate decreases, the flow velocity at the inlet decreases gradually

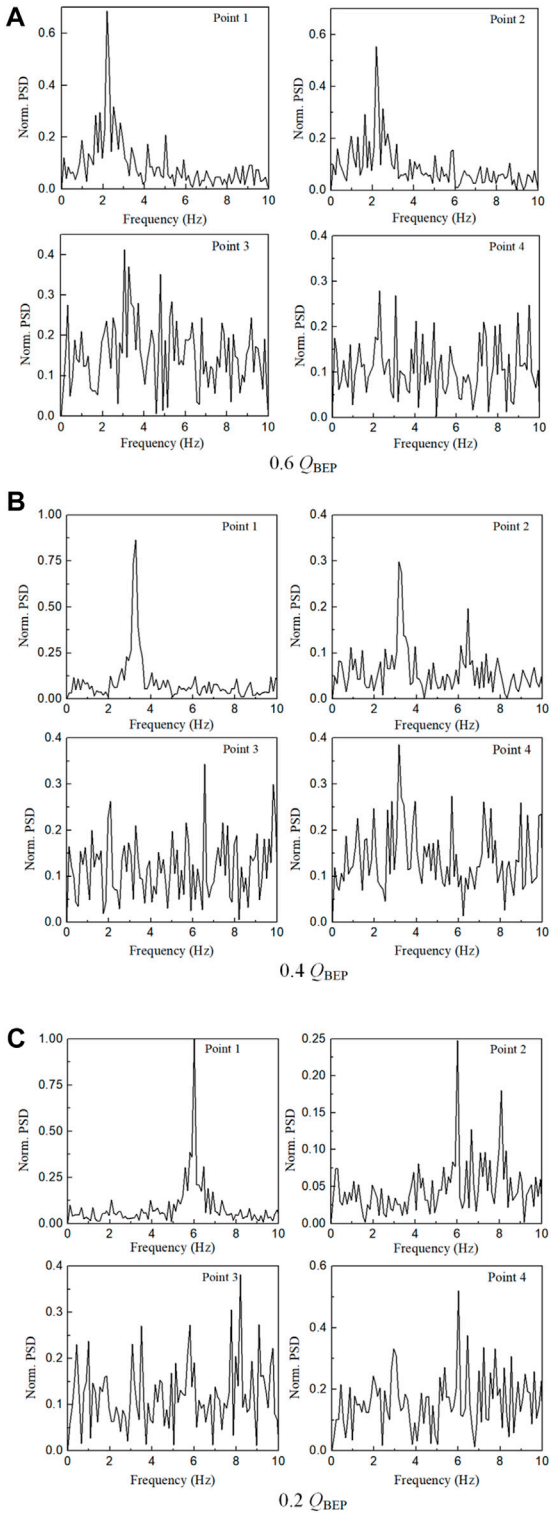

FIGURE 4 | Spectra of the velocity fluctuations measured at three points, **(A)** 0.6 Q_{BEP}, **(B)** 0.4 Q_{BEP}, and **(C)** 0.2 Q_{BEP}.

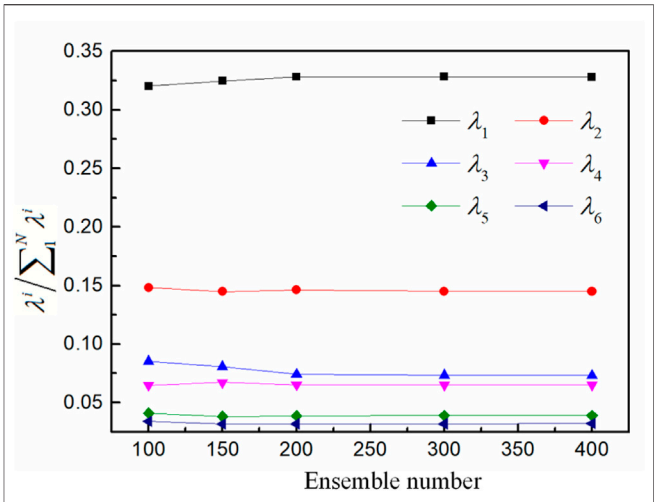

FIGURE 5 | Eigenvalue convergence as a function of ensemble size.

due to the increase of the inlet blockage. Therefore, the maximum value of TKE in the passage decreases gradually. In addition, the deterioration of the internal flow field causes a gradual increase in the area with high TKE values. The high value area located at the inlet extends toward the pressure side, and the high value area located at the outlet extends toward the pressure side, the suction side, and the inlet direction, respectively.

3.3 Velocity Spectra

According to the distribution characteristics of the relative phase-averaged velocity and TKE field, four points (marked with a black dot in **Figure 1B**) are selected for velocity spectrum analysis. Points 1 and 3 are located in the high TKE values area, and points 2 and 4 are located in the core area of the two vortexes, respectively. For this analysis the fast Fourier transformation (FFT) was used within a MATLAB 2014 algorithm. Because there is no unsteady flow generated at the flow rate of 1.0 Q_{BEP}, the spectral analysis is only performed for the flow fields of 0.2 Q_{BEP}, 0.4 Q_{BEP}, and 0.6 Q_{BEP}. **Figure 4** reveals that the dominant frequencies at flow rates of 0.6 Q_{BEP}, 0.4 Q_{BEP}, and 0.2 Q_{BEP} are 2.2, 3.3, and 6 Hz, respectively. All PSDs were normalized by the maximum peak amplitude value (for the point 1, at the flow rate of 0.2 Q_{BEP}). These frequencies lie in the range of 11–30% of the rotor speed, which is known as a typical propagation speed of a stall cell (Pedersen et al., 2003; Krause et al., 2007). As shown in **Figure 4A**, for the flow rate of 0.6 Q_{BEP}, the second and third peaks at point 2 are at 5.0 and 5.9 Hz, respectively. At point 4, the second peak is at 3.1 Hz, and some other peaks are at 4.0 Hz, 5.0 Hz, and so on, meaning the existence of other second flow structures in the vortex region near the suction and pressure side. The highest peak at point 3 is at 3.1 Hz, the second and third peaks are at 3.28 and 4.8 Hz, respectively. These frequencies do not coincide with the main frequencies but are equal or close to the other frequencies at points 2 and 4, probably due to the mixing of the upstream flow at the outlet. As shown in **Figure 4B**, for the flow rate of 0.4 Q_{BEP}, the second peak at point 2 is at 6.5 Hz. At point 3, the highest peak is at 6.5 Hz, which is consistent with the second peak at point 2. At point 4, the second and third peaks are at 5.7 and

TABLE 2 | Specific values for the first 10 modes.

	Mode 1 (%)	Mode 2 (%)	Mode 3 (%)	Mode 4 (%)	Mode 5 (%)	Mode 6 (%)	Mode 7 (%)	Mode 8 (%)	Mode 9 (%)	Mode 10 (%)
0.2 Q_{BEP}	32.82	14.63	7.4	6.52	3.86	3.19	2.61	2.34	2.0	1.69
0.4 Q_{BEP}	41.32	14.26	7.03	5.57	2.97	2.68	2.32	1.94	1.57	1.52
0.6 Q_{BEP}	49.50	13.48	5.35	4.96	2.48	2.33	1.68	1.5	1.37	1.29
1.0 Q_{BEP}	13.83	7.98	5.73	4.74	4.49	4.07	3.47	3.22	3.05	2.77

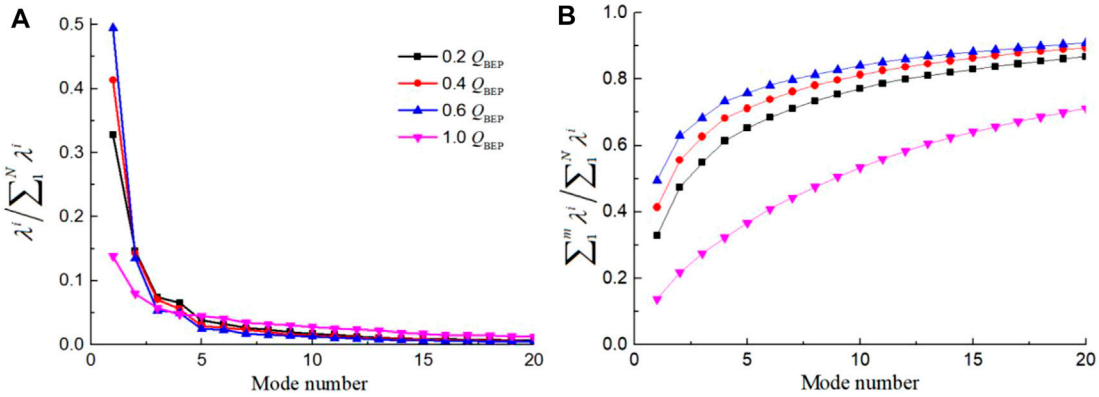

FIGURE 6 | (A) Energy contribution of each mode and **(B)** cumulative energy contents.

4.0 Hz, respectively. As shown in **Figure 4C**, for the flow rate of 0.2 Q_{BEP}, the highest peaks are at 6.0 Hz at points 1, 2, and 4. But the highest peak for point 3 is at 8.2 Hz. Point 2 has a second peak at 8.1 Hz and a third peak at 6.7 Hz, indicating that the suction side appears to have the small-scale structures.

4 PROPER ORTHOGONAL DECOMPOSITION RESULTS

For each flow rate, 200 instantaneous vector fields are used to perform the POD analysis by the POD code in MATLAB. The sensitivity of the POD analysis in relation to the number of the vector fields is studied for the flow rate of 0.4 Q_{BEP}. The results obtained for the first six eigenvalues are plotted in **Figure 5**. The magnitude of the first four largest eigenvalues does not change significantly when the number is larger than 150. This indicates that the number of velocity fields 200 is sufficiently large for providing statistically converged results.

4.1 Flow Energy Distributions

The distribution of the relative TKE content ($\lambda^i/\sum_1^N \lambda^i$) associated with the individual mode is shown in **Figure 6A**, and the values for the first 10 modes are shown in **Table 2**. The cumulative energy contents ($\sum_1^m \lambda^i/\sum_1^N \lambda^i$) for different numbers of the POD modes are shown in **Figure 6B**. For the flow rate of 1.0 Q_{BEP}, the cumulative energy content is 53.35% for the first 10 modes and 21.8% for the first 2 modes. As for the other flow rates of 0.2–0.6 Q_{BEP}, their cumulative energy content for the first 10 modes is 77.09, 81.2, and 83.98%, respectively. For the first two modes, it is 47.45, 55.58, and 62.98%, respectively. These distributions indicate that there is significant energy redistribution to POD modes for different flow rates. It suggests that for the flow rate of 1.0 Q_{BEP}, the large-scale and coherent flow structures that are associated with lower POD modes are the most incoherent and minimum. For the other flow rates, the large-scale and coherent flow structures are being rendered more incoherent and smaller scale as the decrease of flow rates. Which indicates the energy is redistributed to the higher POD modes and the flow structures are more complex as the flow rate decreases. This trend is consistent with the mean flow characteristics described earlier. For all the flow rates, the energy content does not show classical distribution: the energy content for the first mode is much higher than that for the second mode, and also the following modes do not look like they are in pairs. Furthermore, the largest energy content reduction occurs for the first mode as the decrease of flow rate, which would correspond to the change of the large-scale coherent flow structures.

4.2 Analysis of POD Modes 1 and 2

4.2.1 Vector Plots

Figure 7 shows the vector plots for the first two modes, the contour maps are colored by the vector magnitude which is normalized by U_{tip}. For the flow rate of 1.0 Q_{BEP}, the large flow structures are detected at the passage outlet that is near the pressure side for both modes. In addition, the area is consistent with the high TKE area that is shown in **Figure 3**. Both modes display similar structures as shown in **Figure 7**, which illustrates the presence of alternate counter-rotating vortexes, reflecting the

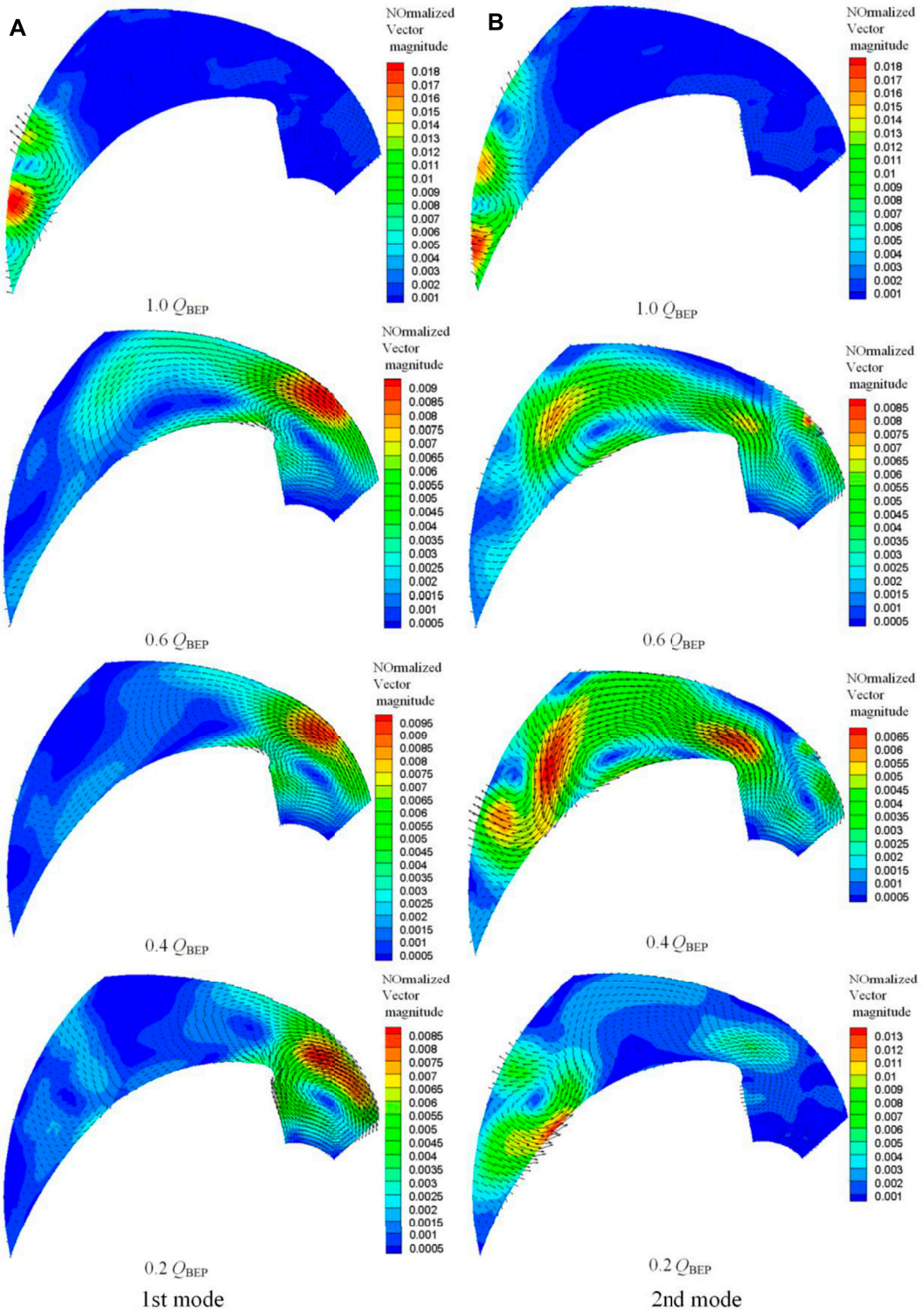

FIGURE 7 | The vector plots of the first and second modes for different flow rates. **(A)** First mode, **(B)** second mode.

mutual interaction process occurring between the backflow and the outflow. As for the flow rate of 1.0 Q_{BEP}, the fluid in the passage follows the blade very well, thus no large-scale coherent structures in the passage have been observed. However, due to the complexity of the flow in the passage, the low energy fluid has been swept toward the suction side, and the high-energy fluid has

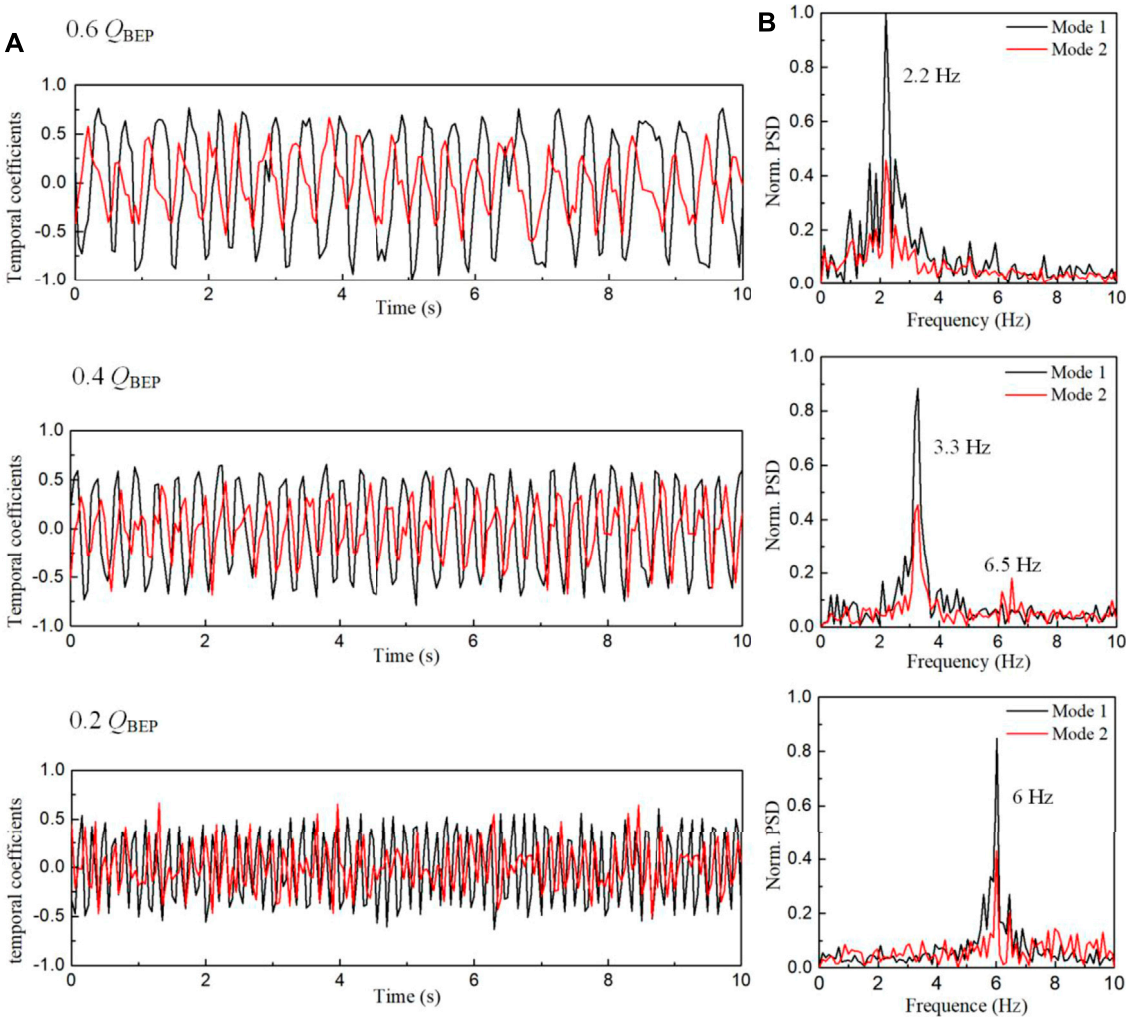

FIGURE 8 | Temporal characteristics of mode 1 and mode 2. **(A)** Temporal coefficients of the first two modes; **(B)** FFT distribution of the first two modes.

been forced toward the pressure side. Therefore, the "jet-wake" structure is taken place at the outlet of the impeller, and the high-energy fluid near the pressure side results in a jet region (Pedersen et al., 2003). The first two modes are the reflection of the mixing of the "jet-wake" (Pedersen et al., 2003), which means that the energy losses are mainly from the "jet-wake" structure for the flow rate of 1.0 Q_{BEP}.

As for the flow rates of 0.2 Q_{BEP} to 0.6 Q_{BEP}, large flow structures are detected in the passage. For the first mode, at the flow rate of 0.6 Q_{BEP}, the kinetic energy is concentrated near the suction side along the passage, a large-scaled anticlockwise vortex structure near the pressure side is observed at the impeller inlet, and an anticlockwise vortex with the same scale is downstream this vortex. The upstream vortex blocks the passage inlet, since the vortex is closer to the pressure side, the fluid near the suction side is accelerated. As the fluid flows downstream, the accelerated fluid bends and forms the second vortex at the leading edge of the pressure side. As the flow rate further decreases to 0.4 Q_{BEP}, the kinetic energy is concentrated at the passage inlet, and the downstream vortex disappears, the scale and strength of the upstream vortex increase, due to the stronger blocking effect. When the flow rate decreases to 0.2 Q_{BEP}, the upstream vortex turns rotating clockwise, and the flow direction in the passage begins to reverse. Indicating the vortex dynamics is different from that at 0.4 Q_{BEP}, and the turbulent kinetic energy is mainly caused by reverse flow. For the flow rates of 0.2 Q_{BEP} to 0.6 Q_{BEP}, the position of accelerated area is consistent with the high TKE area that is near the passage inlet.

For the second mode, at the flow rate of 0.6 Q_{BEP}, the kinetic energy is concentrated at the middle of the passage, a large-scaled clockwise vortex structure near the suction side is observed at the impeller inlet. In addition, an anticlockwise vortex with the same scale near the pressure side downstream the vortex is observed. Both vortexes are induced by the inlet fluid that is near the pressure side. At the passage outlet, a small-scaled vortex is observed downstream the anticlockwise vortex. At the flow rate of 0.4 Q_{BEP}, the scales of the two large-

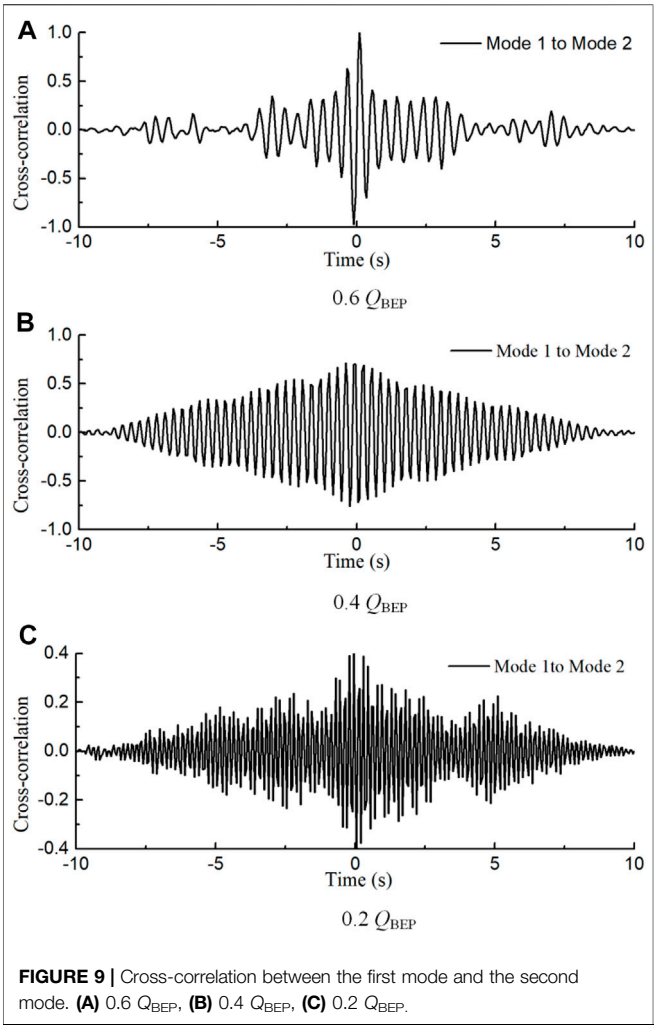

FIGURE 9 | Cross-correlation between the first mode and the second mode. **(A)** 0.6 Q_{BEP}, **(B)** 0.4 Q_{BEP}, **(C)** 0.2 Q_{BEP}.

scaled vortexes are smaller than that at 0.6 Q_{BEP}, but the scale of the vortex near the passage outlet is much larger than that at 0.6 Q_{BEP}. At the flow rate of 0.2 Q_{BEP}, the kinetic energy is concentrated near the pressure side at the outlet of the passage, and an anticlockwise vortex is detected. For the flow rates of 0.2 Q_{BEP} to 0.6 Q_{BEP}, the positions of the vortexes that near the outlet are consistent with the high TKE area that nears the passage outlet.

4.2.2 Temporal Characteristics

Although there is no classical paired distribution between the first and second modes from the energy content distribution, the flow structures for the first two modes are complementary. To further investigate this observation, the corresponding temporal characteristics are determined. The normalized temporal coefficients (normalized by the maximum value for 0.6 Q_{BEP}) of the first two modes are shown in **Figure 8A**, their normalized frequency spectra (normalized by the maximum peak amplitude value for 0.6 Q_{BEP}) are shown in **Figure 8B**. The cross-correlations between the coefficients are shown in **Figure 9**. All cross-correlation values are normalized by the same peak amplitude value of cross-correlation values. At the flow rate of 1.0 Q_{BEP}, the temporal coefficient for both modes does not exhibit regular variation, and no prominent spectral peak has been found, meaning that no regular vortex shedding persists. Therefore, the structures in the "jet" region might be small-scale fluctuations, or the vortex shedding processes could not be resolved due to the limited time resolution. For the sake of simplicity, the temporal coefficients, the frequency, and the spectra cross-correlations are not shown in the figures.

At the flow rate of 0.6 Q_{BEP}, the temporal coefficients for the first two modes have the same variation properties except that the variation strength for the second mode is smaller than that for the first mode, and the cross-spectrum showed that the two modes have 0.2 s time lag led by the second mode. Furthermore, a well-defined peak frequency for both modes corresponding to 2.2 Hz is identified. This is consistent with the frequency of stall cell described in **Section 3.1**. The distinct single peak indicates that there is a single flow phenomenon described by the first two modes at the flow rate of 0.6 Q_{BEP}. All the above temporal characteristics for the first and second modes display excellent matches, indicating that the first two modes are different phases of the stall phenomenon.

At the flow rate of 0.4 Q_{BEP}, the matching degree for the two modes is smaller than that at 0.6 Q_{BEP}. The variation properties of temporal coefficient for the two modes are different; a distinct single peak is identified at 3.3 Hz for the first mode, whereas for the second mode, two peaks are identified, the dominant peak occurs at 3.3 Hz and the other peak occurs at 6.5 Hz with a small amplitude. Furthermore, the cross-spectrum showed less correlation between the two modes. The frequency 3.3 Hz is consistent with the frequency of the stall cell described in **Section 3.1**. In addition the frequency of 6.5 Hz is consistent with the frequency corresponding to the highest peak of point 3 in **Section 3.1**. From the vector plots of mode 2 as shown in **Figure 7B**, the position of point 3 is exactly in the small-scale vortex area at the outlet. Therefore, it can be concluded that the frequency of this small-scale vortex structure is 6.5 Hz. In addition, the second peak of point 2 is also at 6.5 Hz, so it can be inferred that this small-scale vortex is caused by the backflow structure that is induced by the suction side vortex at the outlet. It is precisely because of this small-scale vortex structure that the correlation between the first mode and the second mode is reduced. However, they still mainly reflect the characteristics of the stall phenomenon.

At the flow rate of 0.2 Q_{BEP}, the flow structures become more complex, the vector plots and temporal coefficients do not show obvious correlation between the two modes. But the spectral peaks for the two modes both correspond to 6 Hz, the cross-spectrum also shows some correlations between the two modes, suggesting the possibility of limited matches between the two modes.

4.2.3 Analysis of Higher POD Modes

Figure 10 shows the vector plots for the third and fourth modes. The kinetic energy at different flow rates is concentrated at the passage outlet, and the flow structures are very similar to the first and second modes at 1.0 Q_{BEP}, indicating that both the third and fourth modes mainly reflect

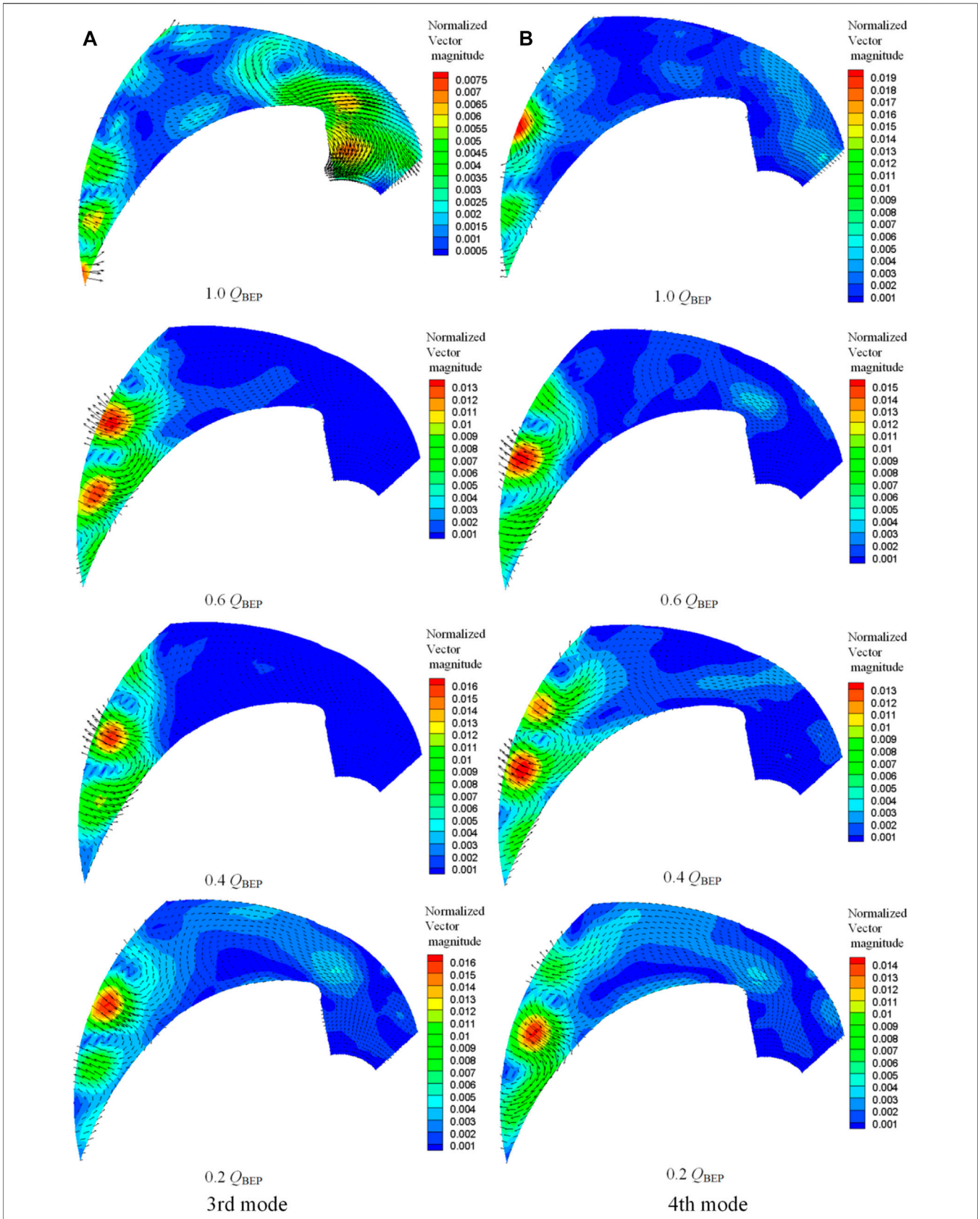

FIGURE 10 | The vector plots of the third and fourth modes for different flow rates. **(A)** Third mode, **(B)** fourth mode.

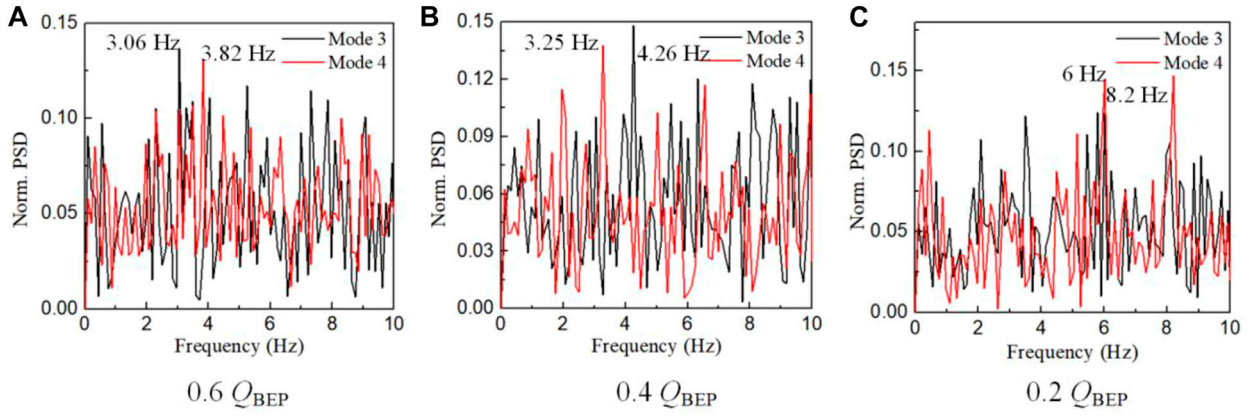

FIGURE 11 | FFT distribution of the third mode and the fourth mode. **(A)** 0.6 Q_{BEP}, **(B)** 0.4 Q_{BEP}, **(C)** 0.2 Q_{BEP}.

the characteristics of the 'jet-wake' structures. The flow structures extend toward the suction side along the outlet with the decrease of flow rate. For all the flow rates, the distributions of temporal coefficients and cross-spectrum between the third and fourth modes show that there is no obvious correlation between them. Therefore, only the frequency spectra are presented in **Figure 11**. The frequency spectra distributions are very noisy and multiple peaks at relatively low amplitudes can be observed. The peak frequency situations are also very intriguing. At the flow rate of 0.6 Q_{BEP}, the peak frequencies ranked in terms of amplitudes are detected at 3.06, 5.24, 7.32, and 4.0 Hz for the third mode, and 3.82, 8.4, 5.4, and 3.06 Hz for the fourth mode. At the flow rate of 0.4 Q_{BEP}, the peak frequencies occur at 4.26, 6.33, and 8.1 Hz for the third mode and 3.25, 2, 6.5, and 5.5 Hz for the fourth mode. While at the flow rate of 0.2 Q_{BEP}, the peak frequencies ranked in terms of amplitudes are detected at 6.0, 3.5, 8.1, and 2.1 Hz for the third mode, 6.0 and 8.2 Hz for the fourth mode. In addition, some of these frequencies coincide with those detected in **Section 3.1**. This suggests that at the outlet, the interaction between the upstream flow structure and the outlet flow structure creates the 'jet-wake' structures.

Figures 12–14 show the vector plots, the temporal frequency spectra, and the cross-correlations between the coefficients for the fifth and sixth modes. At the flow rates of 1.0 Q_{BEP} and 0.2 Q_{BEP}, the kinetic energy is concentrated at the outlet of the passage, very similar to the "jet-wake" structures, and no obvious peak can be identified for their frequency spectra. Therefore, the results for the flow rates of 0.6 Q_{BEP} and 0.4 Q_{BEP} are analyzed. At the flow rate of 0.6 Q_{BEP}, the kinetic energy for both modes is almost evenly distributed in the whole passage, and three large-scale vortexes can be seen for both modes. In addition, there are some other small-scale structures. For the frequency spectra, the maximum amplitude peaks are distinct and occur at 5.0 Hz for both the fifth and sixth modes. The cross-spectrum shows that the two modes have 0.1 s time lag led by the sixth mode. So that the dominant structures that are described by the two modes represent the same flow phenomenon, we introduce the passage vortexes. The frequency about 5.0 Hz is consistent with the frequency corresponding to the second peak of point 1 and the third peak of points 2 and 4 that were detected in **Section 3.1**, indicating that the passage vortexes are induced by the stall cell. At the flow rate of 0.4 Q_{BEP}, the main flow structures for both modes are also passage vortexes in the passage, but the energy in the outlet area is more concentrated. The frequency spectrum for both modes is also very similar. The maximum amplitude peaks for both modes occur at 6.5 Hz, which is also consistent with the frequency corresponding to the second peak of point 2 and the highest peak of point 3 that were detected in **Section 3.1**. But their cross-spectrum shows that their correlation decreases a lot. This is due to the appearance of the flow structures corresponding to the next highest peaks: 6.45 and 6.78 Hz correspond to the fifth and sixth modes. This means that the dominance of passage vortexes has been affected by the passage outlet structures. For the seventh mode, the vector plots exhibit smaller and irregular structures. In addition, no obvious peak can be identified for their frequency spectra, too. After the seventh mode, the structures of the higher modes become increasingly random and irregular; the details will not be repeated for the sake of brevity.

4.2.4 Mode Reconstruction

Figure 15 shows the reconstructed vector plots using mean velocity and a few lower modes at an arbitrary time at 0.6 Q_{BEP} and 1.0 Q_{BEP}. At the flow rate of 0.6 Q_{BEP}, it is evident that the first two modes are sufficient to capture the largest-scale vortex which has been marked with a red rectangle in **Figure 15A**. The general structure of the other two vortexes (also marked with a red rectangle) can also be described, but their shapes and scales are significantly different from the raw flow field. As the number of modes considered in POD flow reconstruction increases, the structure of the two vortexes is closer to the raw flow field. When the first seven modes are used, the other two vortexes are basically the same in scale as those in the raw flow field, except for their different shapes. In addition, the flow reconstructed from 20 modes appears identical to the raw data in terms of vector plots. At this time, the energy occupied by the first 20 modes is more than 90% of the total energy. This is

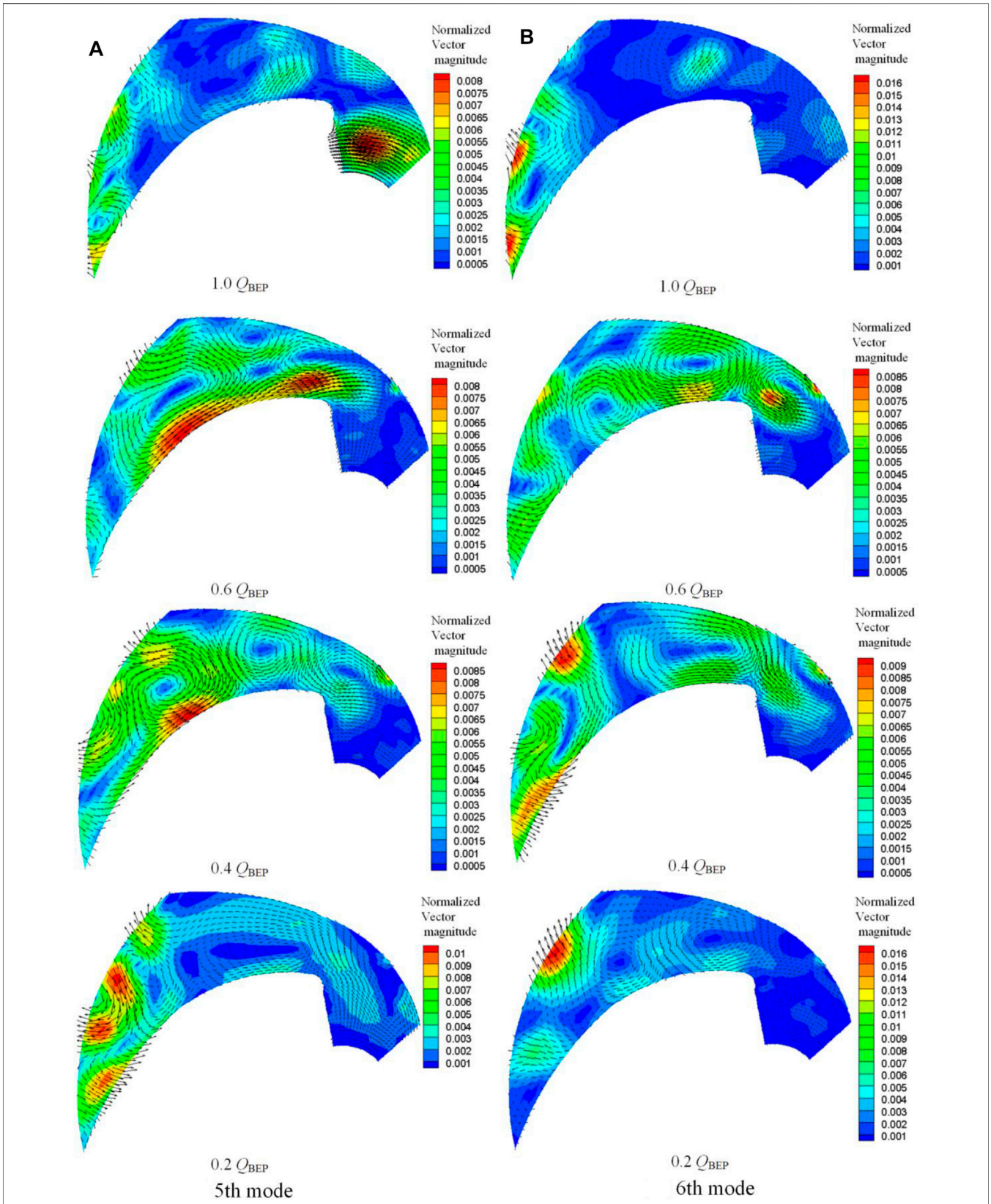

FIGURE 12 | The vector plots of the fifth and sixth modes for different flow rates. **(A)** Fifth mode, **(B)** sixth mode.

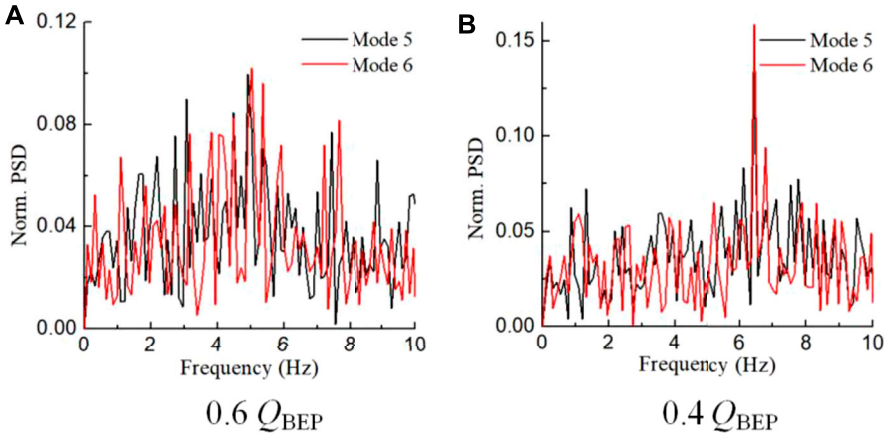

FIGURE 13 | FFT distribution of the fifth mode and the sixth mode. **(A)** 0.6 Q_{BEP}, **(B)** 0.4 Q_{BEP}.

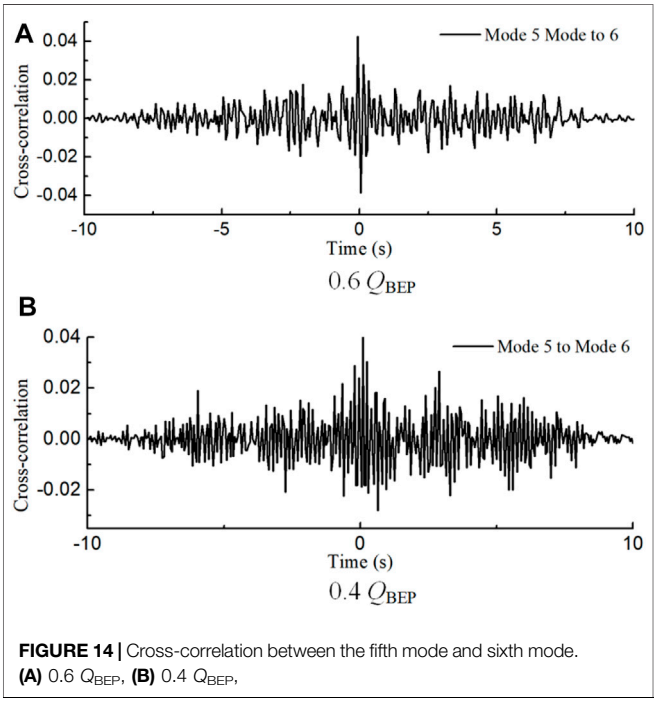

FIGURE 14 | Cross-correlation between the fifth mode and sixth mode. **(A)** 0.6 Q_{BEP}, **(B)** 0.4 Q_{BEP},

another indication that the chosen sample size for the number of flow fields is adequate. In addition, the large-scale structure in the flow field can be well displayed by the first seven modes, which means that the coherent structures in the flow field are mainly composed of the stall structure at the inlet, the "jet wake" structure at the outlet, and the passage vortex structure in the passage. Therefore, during the design of centrifugal pumps, it is suggested to consider suppressing these three types of flow structures, especially the stall structure caused by inlet blockage. This can provide guidance for the design of centrifugal pumps.

At the flow rate of 1.0 Q_{BEP}, the deviation trend of the fluid from the pressure blade near the outlet is captured by the first two modes. As the number of modes considered in POD flow reconstruction increases, the deviation degree of the fluid increases slowly (the deviation area has been marked with a red rectangle in **Figure 15B**), and the flow structure is closer to the raw flow field. When the flow is reconstructed from 20 modes, the deviation degree is obviously smaller than that of the raw field. At this time, the energy occupied by the first 20 modes is 71.2% of the total energy. This means that more energy is allocated to higher-order modes when the flow field is without a large-scale flow structure. Therefore, the flow field reconstructed from the first few modes is not enough to express the flow characteristics.

5 CONCLUSION

The unsteady behavior of flow structures in a centrifugal pump is investigated by means of TR-PIV measurements. Four cases with different flow rates, e.g., 0.2 Q_{BEP}, 0.4 Q_{BEP}, 0.6 Q_{BEP}, 1.0 Q_{BEP}, are chosen for investigation. The POD method is employed to decouple and reconstruct the coherent structures of flow fields. The main conclusions can be drawn as follows:

1) The mean results show that the decrease of the relative velocity and the deviation to the suction side of the inlet fluid are the main causes of unstable flow. The TKE statistical results show that at the flow rate of 1.0 Q_{BEP}, the highest TKE value area is located at the passage outlet due to the "jet-wake" phenomenon; for the part load flow rates, the highest TKE values are concentrated at the passage inlet near the suction side due to the larger shock effect of the inlet flow. The velocity spectra results show that the dominant frequencies for part load flow rates reveal a typical propagation speed of a stall cell.
2) For the best efficiency point (1.0 Q_{BEP}), the fluid follows the blade contour very well. In addition, the main POD modes show that the coherent structures are located at the passage outlet and are shown as alternate counter-rotating vortexes, which is due to the mixing of the "jet-wake" structures.

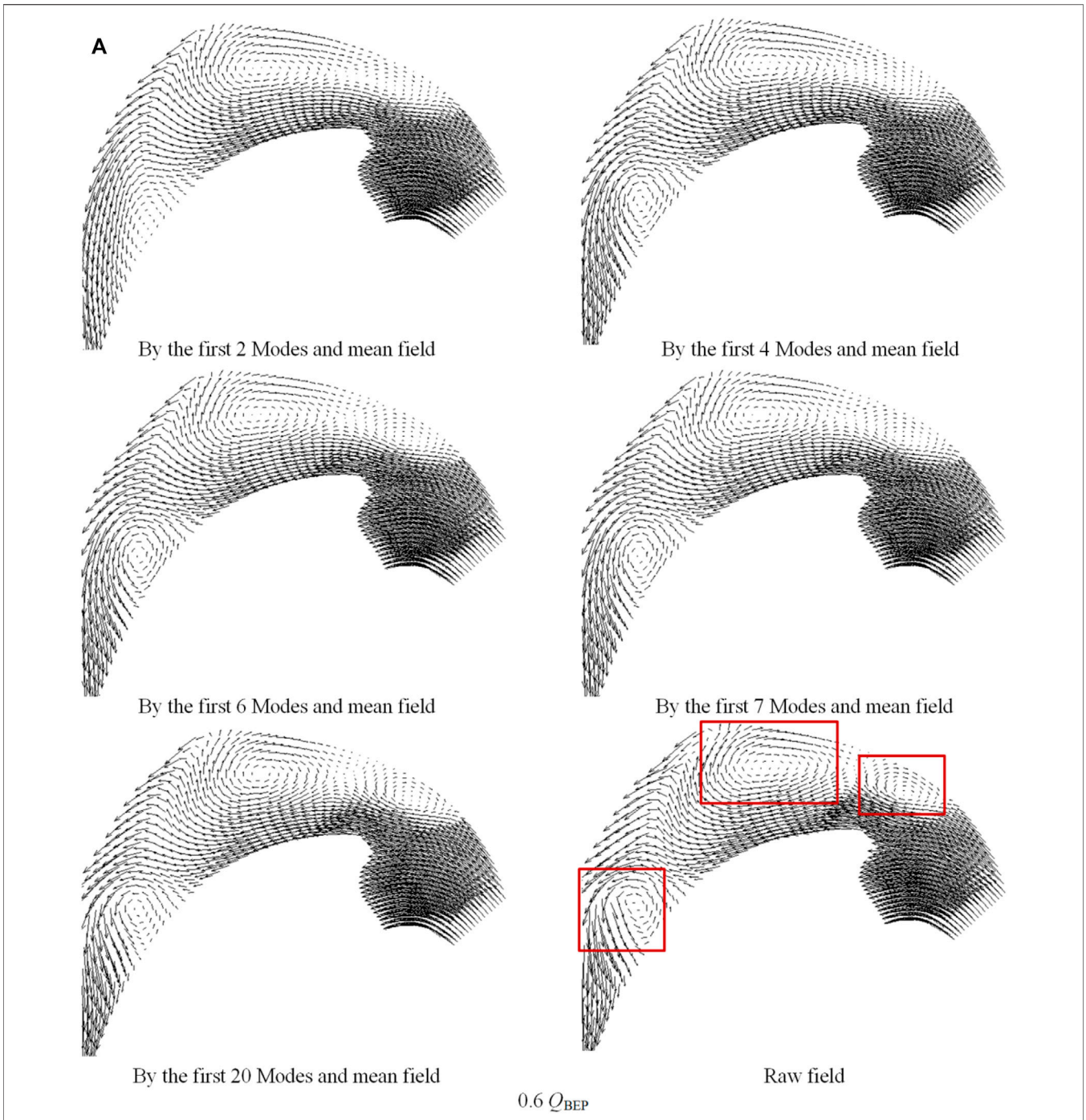

FIGURE 15 | Comparison of vector plots between the raw and reconstructed fields. **(A)** 0.6 Q_{BEP}, **(B)** 1.0 Q_{BEP}.

3) For the medium part-load condition (0.4 Q_{BEP} to 0.6 Q_{BEP}), the first and second modes are found to be associated in pairs corresponding to the stall cells. However, the flow structures of the first two modes change as the flow rate decreases, resulting in the weakening of the correlation between the first and second modes, and the increase of stall cell frequency. The third and fourth modes are found to be associated with the 'jet-wake' structures; some of the frequencies for the third and fourth modes are consistent with the frequencies of the velocity spectrums, indicating that the interaction between the upstream flow structure and the outlet flow structure creates the "jet-wake" structures. The fifth and sixth modes are found to be associated with the passage vortexes, and the passage vortexes are induced by the stall cell.

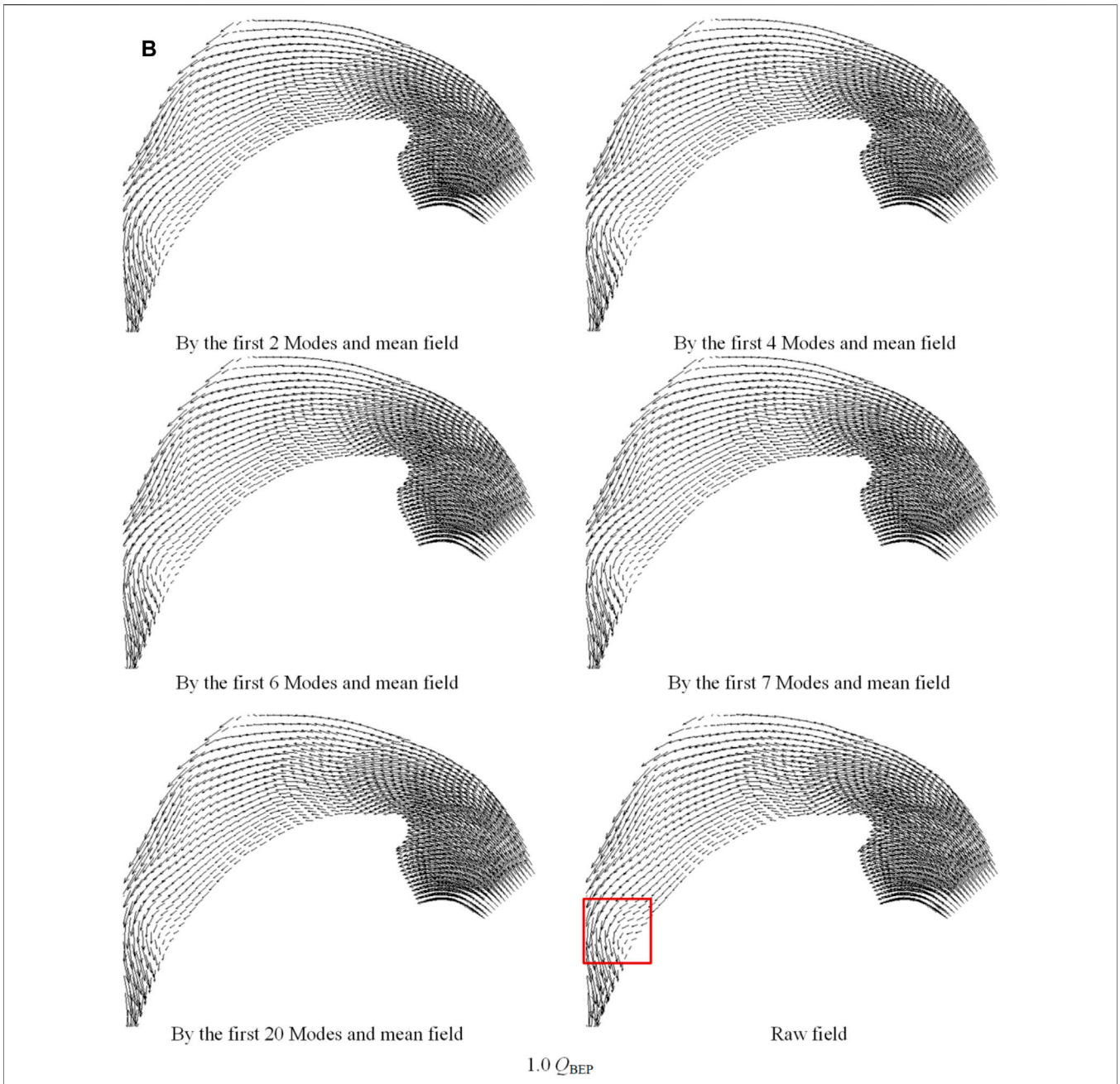

FIGURE 15 | (Continued)

4) For the extreme part-load condition (0.2 Q_{BEP}), the characteristics of the stall cells are different from that at medium part-load condition: the stall cells shown in the first and second modes are reverse flow, the rotation directions of the stall cells are opposite to that of the medium part-load condition, indicating the turbulent kinetic energy of the internal flow is mainly caused by the reverse flow; furthermore, the third to sixth modes are all displayed as jet-wake characteristics.

5) POD can reconstruct the flow structures when large-scale flow structures appear in the flow field. The large-scale structures can be reconstructed by the first two high-energy modes and the phase-averaged approach; the reconstruction of the smaller scale structures required at least six POD modes when a large-scale coherent structure appears. This suggests that most of the turbulent kinetic energy is manifested in the first few modes; therefore, the inlet

region and outlet region should be optimized to suppress the generation of stall cells and "jet-wake" structures.

DATA AVAILABILITY STATEMENT

The original contributions presented in the study are included in the article/Supplementary Material, Further inquiries can be directed to the corresponding author.

AUTHOR CONTRIBUTIONS

B.C.: Writing-original draft preparation, MATLAB programming, visualization. X.L.: Conceptualization, data curation, investigation, methodology. Z.Z.: Conceptualization, supervision, writing—review and editing.

FUNDING

This work was supported by the National Natural Science Foundation of China (Grant Nos. 51806197, U1709209), the Natural Science Foundation of Zhejiang Province (No. LY20E060006). Key Research and Development Program of Zhejiang Province (Grant No. 2021C05006). Top-notch Talent Support Program of Zhejiang Province (Grant No. 2019R51002). The Fundamental Research Funds of Zhejiang Sci-Tech University (Grant No. 2021Q017). The supports are gratefully acknowledged.

ACKNOWLEDGMENTS

The supports are gratefully acknowledged.

REFERENCES

Arun Shankar, V. K., Umashankar, S., Paramasivam, S., and Hanigovszki, N. (2016). A Comprehensive Review on Energy Efficiency Enhancement Initiatives in Centrifugal Pumping System. *Appl. Energ.* 181, 495–513. doi:10.1016/j.apenergy.2016.08.070

Bozorgasareh, H., Khalesi, J., Jafari, M., and Gazori, H. O. (2021). Performance Improvement of Mixed-Flow Centrifugal Pumps with New Impeller Shrouds: Numerical and Experimental Investigations. *Renew. Energ.* 163, 635–648. doi:10.1016/j.renene.2020.08.104

Ghorani, M. M., Sotoude Haghighi, M. H., Maleki, A., and Riasi, A. (2020). A Numerical Study on Mechanisms of Energy Dissipation in a Pump as Turbine (PAT) Using Entropy Generation Theory. *Renew. Energ.* 162, 1036–1053. doi:10.1016/j.renene.2020.08.102

Han, Y., and Tan, L. (2020). Dynamic Mode Decomposition and Reconstruction of Tip Leakage Vortex in a Mixed Flow Pump as Turbine at Pump Mode. *Renew. Energ.* 155, 725–734. doi:10.1016/j.renene.2020.03.142

Holmes, P. J., Lumley, J. L., Berkooz, G., Mattingly, J. C., and Wittenberg, R. W. (1997). Low-dimensional Models of Coherent Structures in Turbulence. *Phys. Rep.* 287, 337–384. doi:10.1016/s0370-1573(97)00017-3

Kaupert, K. A., and Staubli, T. (1999). The Unsteady Pressure Field in a High Specific Speed Centrifugal Pump Impeller-Part I: Influence of the Volute. *J. Fluid Eng.* 121 (3), 621–626. doi:10.1115/1.2823514

Kaupert, K. A. (1999). The Unsteady Pressure Field in a High Specific Speed Centrifugal Pump Impeller—Part II: Transient Hysteresis in the Characteristic. *J. Fluid Eng.* 121 (3), 3558–3565. doi:10.1115/1.2823515

Keller, J., Blanco, E., Barrio, R., and Parrondo, J. (2014). PIV Measurements of the Unsteady Flow Structures in a Volute Centrifugal Pump at a High Flow Rate. *Exp. Fluids* 55 (10), 1820. doi:10.1007/s00348-014-1820-7

Krause, N., Pap, E., and Thevenin, D. (2007). Influence of the Blade Geometry on Flow Instabilities in a Radial Pump Elucidated by Time-Resolved Particle-Image Velocimetry. *Proc. ASME Turbo Expopower Land, Sea, Air* 6, 1659–1668. doi:10.1115/gt2007-27455

Krause, N., Zähringer, K., and Pap, E. (2005). Time-resolved Particle Imaging Velocimetry for the Investigation of Rotating Stall in a Radial Pump. *Exp. Fluids* 39 (2), 192–201. doi:10.1007/s00348-005-0935-2

Li, D., Wang, H., Qin, Y., Wei, X., and Qin, D. (2018). Numerical Simulation of Hysteresis Characteristic in the Hump Region of a Pump-Turbine Model. *Renew. Energ.* 115, 433–447. doi:10.1016/j.renene.2017.08.081

Li, J., Liu, J., Pei, J., Mohanarangam, K., and Yang, W. (2018). Experimental Study of Human thermal Plumes in a Small Space via Large-Scale TR PIV System. *Int. J. Heat Mass Transfer* 127, 970–980. doi:10.1016/j.ijheatmasstransfer.2018.07.138

Li, W., Ji, L., Li, E., Ramesh, A., and Zhou, L. (2020). Numerical Investigation of Energy Loss Mechanism of Mixed-Flow Pump under Stall Condition. *Renew. Energ.* 167 (9), 740–760. doi:10.1016/j.renene.2020.11.146

Li, W., Li, E., Ji, L., Zhou, L., Shi, W., and Zhu, Y. (2020). Mechanism and Propagation Characteristics of Rotating Stall in a Mixed-Flow Pump. *Renew. Energ.* 153, 74–92. doi:10.1016/j.renene.2020.02.003

Li, X., Chen, B., Luo, X., and Zhu, Z. (2020). Effects of Flow Pattern on Hydraulic Performance and Energy Conversion Characterisation in a Centrifugal Pump. *Renew. Energ.* 151 (5), 475–487. doi:10.1016/j.renene.2019.11.049

Li, X., Chen, H., Chen, B., Luo, X., Yang, B., and Zhu, Z. (2020). Investigation of Flow Pattern and Hydraulic Performance of a Centrifugal Pump Impeller through the PIV Method. *Renew. Energ.* 162, 561–574. doi:10.1016/j.renene.2020.08.103

Lim, H. D., Ding, J., Shi, S., and New, T. H. (2019). Proper Orthogonal Decomposition Analysis of Near-Field Coherent Structures Associated with V-Notched Nozzle Jets. *Exp. Therm. Fluid Sci.* 112, 109972.

Lumley, J. L. (1967). The Structure of Inhomogeneous Turbulent Flows. *J. Comput. Chem.* 790, 166–178.

Pedersen, N. (2000). *Experimental Investigation of Flow Structures in a Centrifugal Pump Impeller Using Particle Image Velocimetry Technical University of Denmark*. Technical University of Denmark.

Pedersen, N., Larsen, P. S., and Jacobsen, C. B. (2003). Flow in a Centrifugal Pump Impeller at Design and Off-Design Conditions-Part I: Particle Image Velocimetry (PIV) and Laser Doppler Velocimetry (LDV) Measurements. *J. Fluid Eng.* 125, 61–72. doi:10.1115/1.1524585

Santolaria Morros, C., Fernández Oro, J. M., and Argüelles Díaz, K. M. (2011). Numerical Modelling and Flow Analysis of a Centrifugal Pump Running as a Turbine: Unsteady Flow Structures and its Effects on the Global Performance. *Int. J. Numer. Meth. Fluids* 65 (5), 542–562. doi:10.1002/fld.2201

Semlitsch, B., and Mihăescu, M. (2016). Flow Phenomena Leading to Surge in a Centrifugal Compressor. *Energy* 103 (C), 572–587. doi:10.1016/j.energy.2016.03.032

Shi, G., Liu, Z., Xiao, Y., Li, H., and Liu, X. (2020). Tip Leakage Vortex Trajectory and Dynamics in a Multiphase Pump at Off-Design Condition. *Renew. Energ.* 150, 703–711. doi:10.1016/j.renene.2020.01.024

Sirovich, L. (1987). Turbulence and the Dynamics of Coherent Structures. I. Coherent Structures. *Quart. Appl. Math.* 45, 561–571. doi:10.1090/qam/910462

Tan, L., Yu, Z., Xu, Y., Liu, Y., and Cao, S. (2017). Role of Blade Rotational Angle on Energy Performance and Pressure Fluctuation of a Mixed-Flow Pump. *Proc. Inst. Mech. Eng. Part. A. J. Power Energ.* 231, 227–238. doi:10.1177/0957650917689948

Tang, Z., Fan, Z., Ma, X., Jiang, N., Wang, B., Huang, Y., et al. (2020). Tomographic Particle Image Velocimetry Flow Structures Downstream of a Dynamic Cylindrical Element in a Turbulent Boundary Layer by Multi-Scale Proper Orthogonal Decomposition. *Phys. Fluids* 32 (12), 125109. doi:10.1063/5.0026955

Wernet, M. P. (2000). Application of DPIV to Study Both Steady State and Transient Turbomachinery Flows. *Opt. Laser Technol.* 32 (7-8), 497–525. doi:10.1016/s0030-3992(00)00090-6

Westra, R. W., Broersma, L., Andel, K. V., and Kruyt, P. (2010). PIV Measurements and CFD Computations of Secondary Flow in a Centrifugal Pump Impeller. *ASME J. Fluids Eng.* 132 (6), 061104. doi:10.1115/1.4001803

Xia, L. S., Cheng, Y. G., Zhang, X. X., and Yang, J. D. (2014). Numerical Analysis of Rotating Stall Instabilities of a Pump- Turbine in Pump Mode. *IOP Conf. Ser. Earth Environ. Sci.* 22 (3), 032020. doi:10.1088/1755-1315/22/3/032020

Yang, S. Q., Wang, Y. H., Yang, M., Song, Y. W., and Yan, H. (2019). POD-based Data Mining of Turbulent Flows in Front of and on Top of Smooth and Roughness-Resolved Forward-Facing Steps. *IEEE Access.* 7 (1), 18234–18255.

Zhang, L., Wang, C., Zhang, Y., Xiang, W., He, Z., and Shi, W. (2021). Numerical Study of Coupled Flow in Blocking Pulsed Jet Impinging on a Rotating wall. *J. Braz. Soc. Mech. Sci. Eng.* 43, 508. doi:10.1007/s40430-021-03212-0

Zhang, N., Zheng, F., and Liu, X. (2020). Unsteady Flow Fluctuations in a Centrifugal Pump Measured by Laser Doppler Anemometry and Pressure Pulsation. *Phys. Fluids* 32 (12), 108–125. doi:10.1063/5.0029124

Zhou, T., Zhong, S., and Fang, Y. (2021). Trailing-edge Boundary Layer Characteristics of a Pitching Airfoil at a Low Reynolds Number. *Phys. Fluids* 33 (3), 033605. doi:10.1063/5.0039416

Conflict of Interest: The authors declare that the research was conducted in the absence of any commercial or financial relationships that could be construed as a potential conflict of interest.

NOMENCLATURE

$\boldsymbol{\omega}$ Impeller rotation angular velocity

$\boldsymbol{K_{2D}^{*}}$ phase-averaged turbulent kinetic energy

$\boldsymbol{\phi}$ spatially orthogonal POD mode

$\boldsymbol{A}$ eigenvector

$\boldsymbol{b}$ blade height, mm

$\boldsymbol{D}$ diameter, mm

$\boldsymbol{f_{BP}}$ rotation frequency of the impeller

$\boldsymbol{M}$ the number of spatial nodes in a single snapshot

$\boldsymbol{Q_{BEP}}$ design flow rate, m^3/h

$\boldsymbol{r}$ radius, mm

$\boldsymbol{U}$ absolute velocity, m/s

$\boldsymbol{u}$ horizontal velocity component

$\boldsymbol{U_{tip}}$ blade tip speed

$\boldsymbol{V}$ the matrix of velocity

$\boldsymbol{v}$ vertical velocity component

$\boldsymbol{W}$ relative velocity, m/s

$\boldsymbol{Z}$ number of blades

$\boldsymbol{\beta}$ blade angle, °

$\boldsymbol{\lambda}$ eigenvalue

$^{\mathbf{1}}$ parameters are related to fluctuating valueimpeller inlet

Subscripts

1 parameters are related to fluctuating valueimpeller inlet

2 impeller outlet

frontiers in Energy Research

REVIEW
published: 01 February 2022
doi: 10.3389/fenrg.2021.818211

Review of Numerical Simulation Research on Submersible Mixer for Sewage

Tian Fei[1], *Zhang Erfeng*[1]*, *Yang Chen*[1], *Shi Weidong*[2]* *and Zhang Chenghua*[3]

[1]School of Energy and Power Engineering, Jiangsu University, Zhenjiang, China, [2]School of Mechanical Engineering, Nantong University, Nantong, China, [3]Yatai Pump & Valve Co. Ltd., Taixing, China

Submersible mixer is the core machinery of sewage treatment, which has a profound effect on the efficiency and performance of the submersible mixing system of sewage treatment. This paper summarizes the scientific research results of submersible mixer in recent years from four aspects: structure and energy characteristics of submersible mixer, numerical simulation calculation method, flow field characteristics, and factors affecting the flow field characteristics. The existing published literature indicates that the structure of submersible mixer for sewage is complicated and the parameters of energy characteristics are special. Few experimental studies are conducted, and mostly numerical calculations are based on clear water as the medium. The mixture model based on the Euler–Euler method is the multiphase flow model currently applied in the field of submersible mixer research. Many factors affect the mixing effect of a submersible mixer, such as installation factors (the location and angle of installation) and impeller design parameters (blade gap, hub-tip ratio, blade angle, etc.), all having a significant impact on the mixing performance. Meanwhile, the development and trends of submersible mixer technology are prospected, and the future directions of further research are proposed: establishing a more suitable numerical calculation method for submersible mixer based on the Euler–Lagrange model; constructing the calculation model with real fluid—solid-liquid two-phase flow as the medium; exploring the influence of various parameters on flow field characteristics of mixing fluid; getting the mixing mechanism of submersible mixer; promoting the development of submersible mixer; and realizing the efficient and stable operation of submerged mixing system.

Keywords: submersible mixer, numerical simulation, flow field characteristics, multiphase flow, CFD

OPEN ACCESS

Edited by:
Xiaojun Li,
Zhejiang Sci-Tech University, China

Reviewed by:
Daoxing Ye,
Xihua University, China
Yu-Liang Zhang,
Quzhou University, China

***Correspondence:**
Zhang Erfeng
1603073043@qq.com
Shi Weidong
wdshi@ujs.edu.cn

Specialty section:
This article was submitted to Process and Energy Systems Engineering, a section of the journal Frontiers in Energy Research

Received: *19 November 2021*
Accepted: *22 December 2021*
Published: *01 February 2022*

Citation:
Fei T, Erfeng Z, Chen Y, Weidong S and Chenghua Z (2022) Review of Numerical Simulation Research on Submersible Mixer for Sewage. Front. Energy Res. 9:818211. doi: 10.3389/fenrg.2021.818211

INTRODUCTION

Environmental protection is a prerequisite for the coordinated development of economy, society, and environment, an important social and economic development strategy of all countries and an important and arduous task facing national construction. Water pollution has caused serious water loss in China, and the harmless treatment of sewage is an important measure to protect the environment and maintain green mountains on Earth. Therefore, it is important to study and develop efficient submersible agitators for wastewater (Li et al., 2007).

Submersible mixer for sewage (hereinafter referred to as submersible mixer (as shown in **Figure 1**) is a submerged device of mixing and pushing flow, is suitable for mixing various

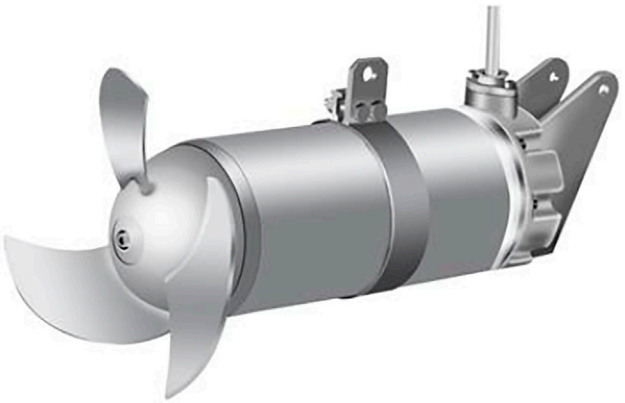

FIGURE 1 | Submersible mixer.

types of sewage treatment, which can mix and stir the surrounding water to improve the efficiency of sewage treatment (Gu et al., 2015), and is the core machinery in sewage treatment, with the advantages of small size, high efficiency, and strong turbulence (Yi and Zhai, 2003). In the treatment process, its power consumption accounts for more than 50% of the total power consumption of the whole wastewater treatment process (Kissel and Effenberger, 2010; Brehmer and Kraume, 2012). Its performance directly affects the efficiency, effectiveness, and stability of the whole wastewater treatment system (Qiu, 2021).

The study of the submersible mixer not only aims at the structure and performance of the submersible mixer itself but also includes the flow characteristics in the impeller of the submersible mixer and the movement of fluid in the mixing pool of the submersible mixer. As the whole fluid is continuous and interacts with each other, the mixing effect and efficiency are affected by the combination of mixer and pool wall. The research on mixers is complicated.

Scholars from various countries have carried out much research on the working mechanism, flow field characteristics, and other aspects of submersible mixers and achieved certain research results. This paper summarizes the structural characteristics of submersible mixers. It reviews and analyses the current status and progress of domestic and international research in terms of the structure and energy characteristics of submersible mixers, numerical simulation research methods of submersible mixers, flow field characteristics and key factors affecting the flow field characteristics, respectively. It also points out the shortcomings in the research on submersible mixers and the areas that need further in-depth research. It provides a technical reference for relevant personnel to carry out research on submersible mixers.

STRUCTURE AND ENERGY CHARACTERISTICS OF SUBMERSIBLE MIXERS

The submersible mixer is mainly composed of a submerged motor, sealing mechanism, runner, hand hoist mechanism, electrical control, and so on (as shown in **Figure 2**). The impeller of the submersible mixer rotates the agitated liquid under the drive of the electric motor to generate a rotating jet and mixes it with shear stress along the jet surface so that liquids other than the jet can be agitated by friction. Volume flow is formed during extreme mixing. A mass flow mode is applied to obtain the agitated and pushed conveyance of controlled fluid (Xu, 2006; Yan et al., 2009; Weixing and Shouqi, 2010b).

The rotational speed of submersible mixers is generally 100–1,500 r/min, which is divided into three types according to the impeller speed and the main function: low speed, medium speed, and high speed. The rotating speed of a low-speed submersible mixer is lower than 120r/min, which is mainly used to form long-distance flow pushing, improve fluid flow rate, and prevent sedimentation. The impeller speed range of the medium speed submersible mixer is 120 r/min ~350 r/min, which mainly focuses on pushing the flow between far and near distances to improve the fluid flow rate and prevent deposition. The rotating speed of the impeller of the high-speed submersible mixer is higher than 350 r/min, which mainly focuses on the short-distance push flow to improve the fluid mixing effect and prevent deposition (GB/T 33566-2017, 2017).

During the operation of the submersible mixer, the fluid in the pool is subjected to the action of convection and vortex splitting, and the effect of uniform mixing is achieved by mixing, which is usually in a turbulent state (Tian et al., 2014a). In the turbulent flow field, there are vortices of different sizes, and the fluid energy is stored in these vortices. Shear forces are formed at the boundary of large-scale vortices to split the large-scale vortices into multiple small-scale vortices. At the same time, the energy of large-scale vortices is transferred to small vortices, and there is energy loss in the process of energy transfer in the meantime. The vortex phenomenon has a significant impact on the effect of pushing the flow. The fewer the number of vortices, the larger the scale of individual vortices, the steadier the flow regime, the lower the energy consumption of vortices, and the better the effect of pushing the flow and mixing (Zhang et al., 2020a). Therefore, the design and the installation of submersible mixers and the matching of the pool should be fully considered to reduce the vortex energy consumption.

Wastewater contains a large amount of suspended organic matter, sediment, mineral fertilizers, and microorganisms with a complex composition (Yan et al., 2009; GB 18918-2002, 2002; Jishui Paishui Sheji Shouce (Disanban), 2016; GB 50318-2017, 2017; Ma and He, 2003); the volume of the pool being agitated is typically large (Chen et al., 2016; Gong et al., 2017; Shi et al., 2019; Chen et al., 2020a); and the development of the flow field is also influenced by factors such as boundaries (Peng et al., 2009; Tian, 2012), making the flow field situation highly complex. Generally, the velocity flow field distribution diagram and axial effective propelled distance, effective disturbance radius of water section, operating power, efficiency, and so on are used to express the conversion characteristics of submersible mixers to the water flow energy. These are the external manifestations of the internal flow law of submersible mixer (CJ/T 109-2007, 2007; GB 37485-2019, 2019).

The velocity flow field distribution diagram can indicate the velocity distribution in the flow field and show the effective range of the fluid stirred by the submersible mixer (**Figure 3**).

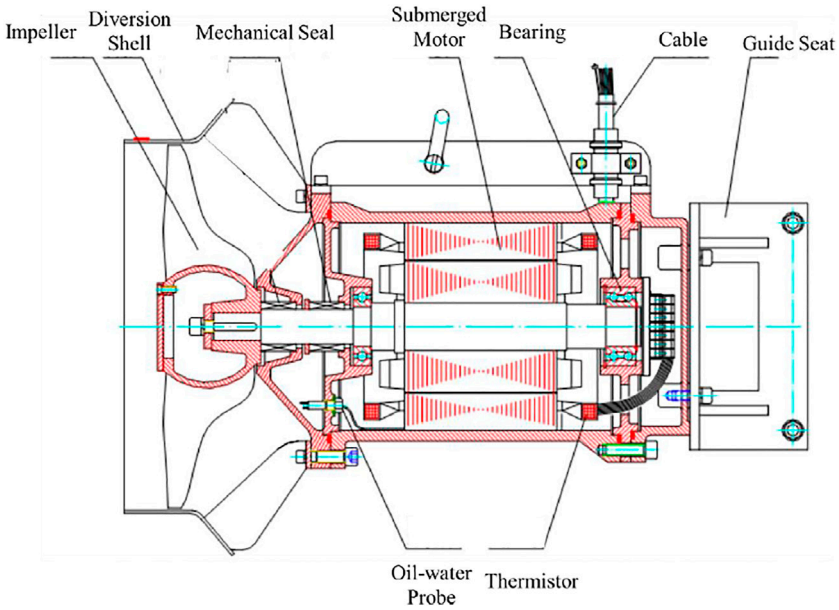

FIGURE 2 | Structural diagram of submersible mixer.

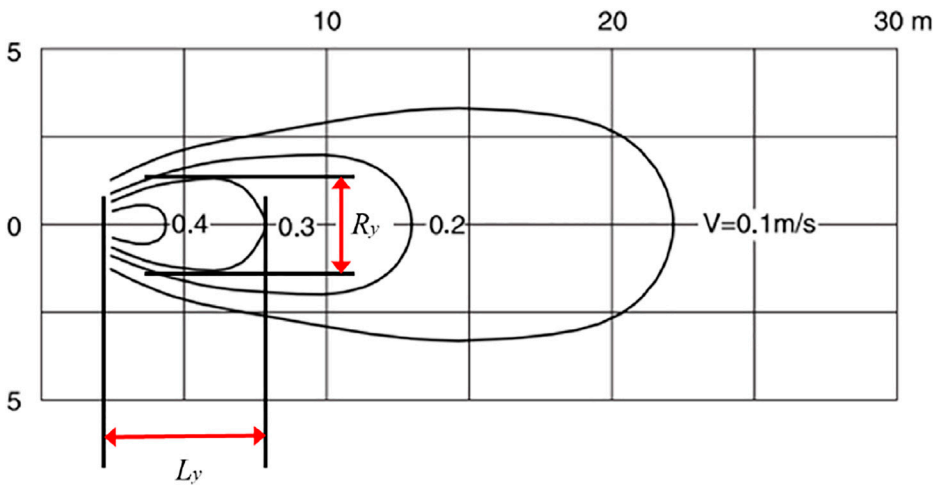

FIGURE 3 | Velocity flow field distribution.

Axial effective propelled distance refers to the effective distance that submersible mixer pushes the water along the axial direction in the effective area of the water body's push-flow mixing work (maintaining the flow velocity greater than or equal to 0.3 m/s), expressed by the symbol L_y (CJ/T 109-2007, 2007).

Effective Disturbance Radius of Water Section

The effective radius of the submersible mixer that disturbs the cross section of the water body in the effective working area of the water body's push-flow mixing (maintaining the flow rate greater than or equal to 0.3 m/s) is expressed by the symbol R_y (CJ/T 109-2007, 2007). These two parameters investigate the mixing effect of submersible mixers from a macro perspective.

Operating power was proposed in 2019, which refers to the input power acting on each cubic meter of water when the water velocity is not less than 0.3 m/s under the specified test conditions, expressed by symbol *E*. The calculation formula is as follows (GB 37485-2019, 2019):

$$E = \frac{P}{V}, \tag{1}$$

where E is the operating power, P is the input power of the motor, and V is the equivalent effective volume.

Efficiency

In 2012, Tian Fei and other scholars used the power definition and momentum conservation to deduce the efficiency calculation formula of the submersible mixer. It is concluded that the mixer's efficiency is directly proportional to the 3/2 power of the water thrust and inversely proportional to the impeller diameter and shaft power of the submersible mixer. The calculation formula is as follows (Tian et al., 2012a):

$$\eta = \frac{kF^{\frac{3}{2}}}{30DP_1} \times 100\% \quad (2)$$

where η is the efficiency, F is the water thrust of the submersible mixer, D is the impeller diameter, P_1 is the shaft power, and k is the coefficient, deduced by scholars as different.

The special working environment and matching conditions determine that the design of a submersible mixer is different from other fluid machineries such as water pumps and turbines.

NUMERICAL SIMULATION CALCULATION METHOD

The experimental study of submersible mixer is difficult to conduct due to the large size of the pool, the complex internal flow field, the difficulty of measurement, and the high cost.Therefore, experimental research on submersible mixers is not well conducted. Currently, the numerical simulation method is applied to study the characteristics of the flow field. It can analyze the flow field and predict the performance of the flow field inside the impeller of the submersible mixer and the pool, with a short period, high efficiency, and low cost, and provide guidance for engineering applications and optimization of the design (Tian et al., 2013a).

In 1982, Harvey first introduced computational fluid dynamics to the prediction of two-dimensional flow fields in stirred tanks (Harvey and Greaves, 1982a; Harvey and Greaves, 1982b). Numerical simulation studies then developed rapidly, from two-dimensional to three-dimensional numerical simulations and from single-phase to multiphase flows. Research tools were no longer limited to experimental schemes, and the theoretical data no longer depended on experimental empirical data. Recently, as the development of grid technology has enabled the numerical study of more complicated geometric models, computational fluid dynamics functions have become more complete and powerful.

Treatment Method of Mixing Area

In the numerical simulation of the mixing field, for solving the problem of relative motion in the stationary and rotating regions, research scholars have proposed some different solutions, which are primarily black box model method, inner-outer iterative procedure, multiple reference frame method, sliding grid method, and so on (Zhou et al., 2004).

Black Box Model Method

Also known as the impeller boundary condition method, this method deducts the blade area from the calculation domain during calculation. The blade's effect is virtualized, and the time-averaged velocity and turbulence parameters are used to replace the actual effect of the blade on the fluid. The data of boundary conditions are generally obtained by experimental methods. The model method does not need to consider the grid of the impeller part and has a small amount of computation, which is suitable for the calculation of the steady-state flow field. Harvey verified the feasibility of this method for the first time (Harvey and Greaves, 1982a). However, its boundary conditions need to rely on the support of experimental data, and it is difficult to carry out numerical calculations in complex situations.

Inner-Outer Iterative Procedure

The inner and outer iterative procedure adopts the method of considering the calculation domain separately and divides the calculation domain into two overlapping parts of the inner ring and the outer ring. The calculation of the inner ring is carried out in the reference system rotating at the speed of the impeller, and the calculation of the outer ring is carried out in the static coordinate system. Through the alternating iterative calculation of the two regions, a convergence result is finally obtained. Compared with the black box model method, the inner and outer iterative procedure does not require experimental data, can realize the simulation of the whole mixing area, and has succeeded in calculating some mixing fields. Wang Weijing et al. used an improved internal and external iteration procedure to perform an overall numerical simulation of the Rushton turbine baffled stirred pool. The results are basically consistent with the experimental values (Wang and Mao, 2002). However, this method is not popularly used in commercial software because it requires trial-and-error iterations in the calculation, and the convergence speed is slow.

Multiple Reference Frame Method

The multiple reference frame method (MRF) was proposed by Issa et al. (Issa et al., 1994), which is a calculation method applied to steady-state flow fields. This method divides the mixing area into the impeller area and the mixing pool area. Each area uses an independent reference system for calculation: the impeller area uses the coordinate system of the impeller rotation, and the mixing pool uses the static coordinate system. MRF can simulate the whole flow field of submersible mixer with small amount of calculation and is widely used in many commercial software. At present, the numerical simulation of steady flow field of submersible mixer is mainly based on MRF method. Peng Zhenzhen et al. used FLUENT software to numerically simulate the three-dimensional flow field of a submersible mixing pool with the MRF method and achieved good results (Peng et al., 2009). Tian Fei et al. used the MRF method to perform numerical simulation of the three-blade submersible mixer and verified the matching between submersible mixer and the sewage treatment pool (Tian et al., 2012b). Zhang Haisheng et al. conducted numerical simulations using the MRF method to study the hydraulic performance of submersible mixers at different placement angles and arrived at the optimal placement angle (Zhang et al., 2021). Chen Yunfan et al. used the MRF method for numerical simulation to verify the feasibility of the streamline

method and the loop quantity distribution method applied to the design of submersible mixer blades (Chen et al., 2020b).

Sliding Grid Method

The flow field generated by the impeller of the submersible mixer is a periodic flow field (Van't Riet et al., 1976), and the steady-state calculation method cannot completely reflect this flow field. In 1993, Luo proposed the sliding grid method (Luo et al., 1993). The division method of this method is the same as the MRF method, and it is also divided into the impeller area and the mixing pool area. The sliding grid method is an unsteady calculation method. In this method, the grid of the impeller part rotates with time, so there is mutual sliding of the grid at the interface between the impeller and the mixing pool. At present, this method is widely adopted by general commercial software. Zhou Guozhong et al. used the sliding grid method to numerically simulate the flow field near the paddle in a stirred pool (Zhou et al., 2002). Jin Jianhua et al. used the sliding grid method to numerically simulate the three-dimensional two-phase flow of a submersible mixer (Jin and Zhang, 2014). Tian Fei et al. used the sliding grid method to analyze the internal pressure pulsation characteristics of the submersible mixer and achieved good results (Tian et al., 2014b).

Numerical Calculation Method of Turbulence Model

The fluid ejected from the impeller of the submersible mixer has not only an axial velocity and radial velocity but also a certain tangential velocity (rotational velocity). Rotational velocity makes the radial and axial pressure gradient and affects the entire flow field. So, this jet is a rotating jet. The rotational jet is a composite flow of free jet plus rotation, and its flow situation is relatively sophisticated, mostly in a turbulent state (Tian, 2012). Currently, three types of numerical simulation of turbulence are used in engineering: direct numerical simulation (DNS); Reynolds-averaged equation (RANS), and large eddy simulation (LES) (Liang, 2012). DNS is used to solve the N-S equations directly without introducing any closed model within the grid size at the turbulent scale (Wang, 2016). DNS method would require high computational tools, and thus the DNS method is presently not directly applied to engineering numerical calculations to solve practical problems in engineering. RANS is used to solve the time-averaged Reynolds equation. The controlling equation for the time-averaged physical quantities is obtained by averaging the time of the non-stationary N-S equation. This control equation contains the unknown quantity of the time average of the pulsation, so the number of equations obtained will be less than the number of unknown quantities. Then, it is necessary to assume a closed model, using the lower-order time average to represent the unknown higher order to determine the function of some quantity to make the equation closed. At present, the RANS method has become the most widely used numerical simulation method of turbulence, which is also applied extensively in the numerical simulation of submersible mixers (Wang et al., 2016). LES is a direct solution of the N-S equation. Its basic idea is to accurately solve the motion at all turbulence scales above a certain scale, which enables capturing many large-scale effects and anthropomorphic structures that occur in non-stationary and non-equilibrium processes that the RANS method is unable to do while overcoming the huge computational overhead of DNS method due to the requirement to solve for all turbulence scales. Thus, it is considered the most promising direction for developing a numerical simulation of turbulence. Nevertheless, LES has not been widely used in engineering because the computational overhead is still substantial (Zhang et al., 2008).

Boundary Conditions

For delineating boundary conditions in the numerical simulation of the submersible mixer, the contact surface between pool and atmosphere is relatively unusual. The liquid surface is a free liquid surface. The more popular setting of the free liquid surface boundary conditions has three treatments: no-slip wall, VOF, and rigid-lid assumption. Wang Li et al. used the VOF method, but this method is more cumbersome, and human factors are particularly critical when dealing with function problems (Wang et al., 2007). He Zigan et al. applied simple rigid-lid assumption to the setting of free liquid level in large eddy simulation. By comparing the numerical simulation results with the test results, the limitation of the benchwork assumption near the solid wall was revealed (He et al., 2000).

Tian Fei et al. used FLUENT software to study the numerical simulation of the free liquid surface of the pool set to wall, VOF model, and rigid-lid assumption for three cases, respectively. They found that, in these three models, only the flow field near the pool surface has a significant effect. Among the three models, the numerical simulation of the pool surface as no-slip wall surface was the most difficult to converge, and the computational time was longer. The calculation of the free liquid surface treatment of pool surface using the VOF model required a higher computer configuration and accounted for more computational memory. The rigid-lid assumption was closer to the actual situation and easier to converge, with lower requirements for the computer. Nevertheless, the authors also suggested that the rigid-lid assumption is not realistic for liquid surfaces with relatively large free surface undulations (Fei et al., 2013).

Multiphase Flow Model

Practical application scenarios of submersible mixers are mainly for the movement of multiphase flows. The role of a submersible mixer in the wastewater treatment process is to provide the required circulating flow rate to keep the mixture in the pool in suspension (Liu et al., 2010), where the flow is relatively complex. Compared to the study of single-phase flow, the study of multiphase flow is more difficult. Currently, two major treatments are used in the study of numerical simulation of solid-liquid two-phase flow: Euler–Euler model and Euler–Lagrange model (Liu and Liu, 2018).

Euler–Euler Model

In the Euler–Euler model, the solid and liquid phases are treated as a continuous medium mixed. The solid and liquid phases are placed in the Euler coordinate system for solution (Bao et al.,

2005). The Euler–Euler model contains a variety of calculation models. The mixture model is commonly used when studying solid-liquid two-phase flow in FLUENT. The mixture model is a simplified multiphase flow model. The model assumes that the velocity is locally balanced on a short time and space scale. An interphase interaction model must be added to calculate the homogeneous multiphase flow with strong coupling. Jin Jianhua et al. investigated the flow field characteristics of submersible mixers in solid-liquid two-phase flow based on the mixture model (Jin and Zhang, 2014). Tian Fei et al. studied the three-dimensional flow field of submersible mixers based on the rigid-lid assumption using the mixture model (Tian et al., 2014c).

Euler–Lagrange Model

The Euler–Lagrange model regards the fluid as a continuous phase and uses the continuity equation, momentum equation, and energy equation of the Euler method to establish the governing equation. The solid is regarded as a discrete phase, and the Lagrange equation of the discrete phase is established. Momentum, energy, and mass are exchanged between the discrete phase and the continuous phase. Typical Euler–Lagrange models include discrete phase model (DPM) and discrete element model (DEM). Lang Tao et al. investigated the flow characteristics of a sewage pump with a front-mounted stirring device using a DPM model (Lang et al., 2015). Shao Ting et al. used the CFD-DEM method to simulate the solid-liquid suspension system in the stirred kettle (Shao et al., 2013). Shao Wenbo, Shi Weidong, and Xia Cheng et al. conducted a numerical simulation study based on the fully coupled CFD-DEM method for multistage mixed-flow and cyclonic pumps and compared it with the experimental results to verify the accuracy of the computational model (Shao et al., 2020; Shi et al., 2020; Cheng et al., 2021).

The Euler–Euler model has the advantages of shorter solution time and simpler operation (Yang and Zhou, 2017) but ignores the interaction between the solid and liquid phases, which weakens the realism of the non-homogeneous structure in the solid-liquid two-phase flow and is not able to characterize the various properties at the particle level. In contrast, the Euler–Lagrange model takes into account the effects of components of different particle sizes on turbulent diffusion and the effects of turbulent diffusion and pulsation on the motion of the particle population and can trace the complex motion of the particle population and visualize the motion and changes of solid-phase particles in a visual form. Nevertheless, tracking the particle population by the Euler–Lagrange model requires many computer resources and a long solution time (Liu and Liu, 2018).

RESEARCH ON FLOW FIELD CHARACTERISTICS

The research on the flow field characteristics of submersible mixers can be divided into research on the flow field characteristics inside the impeller and research on the flow field characteristics inside the mixing pool.

Flow Field Characteristics Inside the Impeller

The research on the characteristics of the flow field inside the impeller is mainly to analyze and study the speed field and pressure field inside the impeller. The research in this area is of great significance to the performance analysis and structural design of the impeller. Tian Fei et al. studied the internal flow field characteristics of the 2-blade submersible mixer and the internal pressure pulsation characteristics by numerical simulation using FLUENT as the calculation software. It is found that the fluid flow velocity near the blade working surface is low and the pressure is high, the back of the blade will form a high-speed zone and a negative pressure zone, and the fluid velocity and pressure gradient from the blade working surface to the back of the blade is apparent. Impeller import and export axis surface velocity is parabolic distribution, import and export velocity ring volume value is small, and the change is smoother. The blade exit axis surface velocity changes gently, approximately equal axial velocity distribution, blade inlet axis surface velocity is linear distribution, and blade import and export velocity ring volume is linear, regular distribution (Tian et al., 2013a).

The fluid inside and near the impeller is greatly affected by the periodic rotation of the impeller. Both the high-pressure low-speed zone and the low-pressure high-speed zone periodically change with the rotation of the impeller. The frequency of pressure pulsation at the inlet and outlet of the impeller and its interior is dominated by the rotation frequency of the impeller, and the pressure pulsation amplitude difference at the inlet of the impeller is greater than the pressure pulsation amplitude difference at the outlet of the impeller (Tian et al., 2014b).

Characteristics of the Flow Field Inside the Pool

The research on the internal flow field characteristics of the submersible mixing pool is of great significance for the design optimization of the submersible mixer and the evaluation of the mixing effect. At present, there is much research on the single-phase flow of submersible mixers but few studies on multiphase flow.

Single-Phase Flow

Peng Zhenzhen et al. used the effective axial advancing distance and the effective diffusion radius to judge the hydraulic performance of submersible mixers. The numerical simulation results show that the rotating impeller produces a high-speed jet, which is pushed forward and divided into two streams. One stream flows to the liquid level and returns to the back of the impeller to form a circulating vortex. The other stream is pushed forward until it hits the pool wall and turns back to form a large circulating vortex. The effective diffusion radius near the blade area is ≥ 2 m. The fluid away from the blade area to the pool wall also rotates around the x-axis but with smaller velocity values

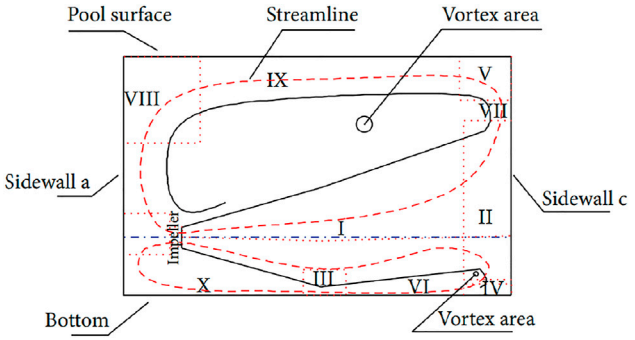

FIGURE 4 | Flow diagram in pool. (I) Free jet region; (II) the region impacting with sidewall c; (III) the region impacting with the bottom of the pool; (IV) the region impacting with the bottom of the pool; (V) the region impacting with the surface of the pool; (VI) the region of the bottom of the pool wall jet; (VIII) the region of radial wall jetting with the sidewall c; (IX) the region of radial wall jetting with the pool surface.

(Peng et al., 2009). Xu Qiao et al. used numerical simulation methods to compare the mixing flow fields of the axial flow pump impeller and submersible mixer impeller and found that the flow fields in the two pools are basically similar, showing the characteristics of axial thrust and radial diffusion. However, there are also certain differences. The submersible mixer impeller works better than the axial flow pump impeller in the area where the flow rate is less than 0, and the mixing effect is better (Qiao, 2018). Xu Weixing and others used FLUENT software to analyze the stirred flow field. It was found that the liquid is thrown out by the high-speed rotating impeller on the one hand and compressed by the impeller on the other hand, which forms a high-speed flow area near the impeller with a strong axial component and forms a rotating jet. It advances forward in accordance with an elliptical isovelocity line. The velocity along the centerline is faster than that in other directions. The liquid is conveyed by volume flow (Weixing and Shouqi, 2010a; Weixing and Shouqi, 2010b; Xu and Yuan, 2011a; Xu and Fan, 2011). Tian Fei and others studied the flow field characteristics of the conventional submersible mixer, new-type two-way submersible mixer, and new-type two-impeller submersible mixer. They found that the mixing performance of the two new-type submersible mixers is obviously better than that of the conventional submersible mixer with the same impeller, and the axial effective propelled distance is larger, which is suitable for mixing in a large water pool (Tian et al., 2019). Zhang Xiaoning et al. used the dynamic grid module and UDF module in FLUENT software to numerically simulate the mixing flow field of the swing submersible mixer. They found that the mixing effect of the swing submersible mixer is better than that of the non-swing submersible mixer (Zhang et al., 2017).

Tian Fei et al. summarized and further studied the jet characteristics of submersible mixers on the basis of previous studies. By analyzing and comparing the velocity flow field diagrams in the pools stirred by the four submersible mixers, it is concluded that the jet of the submersible mixer belongs to the submerged non-free turbulent circular cross section rotating jet.

As shown in **Figure 4**, the fluid in the pool flows under the combined action of the submersible mixer and the pool wall. The fluid flows from the suction surface of submersible mixer blades and is pushed out from the impeller working surface after the action of the impeller. As the fluid flows downstream, the perturbation radius of the jet of the submersible mixer increases, the range of the mixing area becomes wider, and the flow velocity at the center of the jet of the mixer gradually decreases. When the fluid moved to the pool wall, the fluid spread to both sides to form a backflow, and two obvious large vortices appeared between the backflow fluid and the jet. Most of the fluid is sucked back into the working area of the impeller due to the backflow, forming the circulation of the fluid in the stirred pool. The fluid flow in the pool is more complicated, and there are three phenomena of entrainment, wall attachment, and vortex (Tian, 2012; Fei et al., 2014).

Błoński conducted a comparative study on the performance of submersible mixers under three methods (experiment, numerical simulation, and theoretical calculation) and found that the jet of a submersible mixer was divided into three areas. As shown in **Figure 5**, the first area is the core area. In this area, the streamline is similar to the shape of a cone, the bottom diameter is equal to the diameter of the impeller, and the length of the area is 4–5 times the diameter of the impeller. The second zone is the transition zone, which is responsible for stronger mixing. The cone angle is approximately $2\pi/15$ radians. The third area is the diffusion area, where momentum loss occurs and the velocity field tends to be unified (Błoński et al., 2021).

Solid-Liquid Two-Phase Flow

The mixing fluid of the submersible mixer is usually clear water-sludge solid-liquid two-phase flow. Compared with the flow field of single-phase flow, the study of solid-liquid two-phase flow will focus on the distribution, velocity, trajectory, and suspension characteristics of the solid phase inside the pool.

Jin Jianhua et al. used FLUENT software as a tool to study the flow field under two conditions: single-phase flow with clean water and two-phase flow with sewage-sludge as media. The results show that the overall flow law of the flow field is roughly the same under both conditions, and the mixing radius increases with the advance distance of the flow. However, the

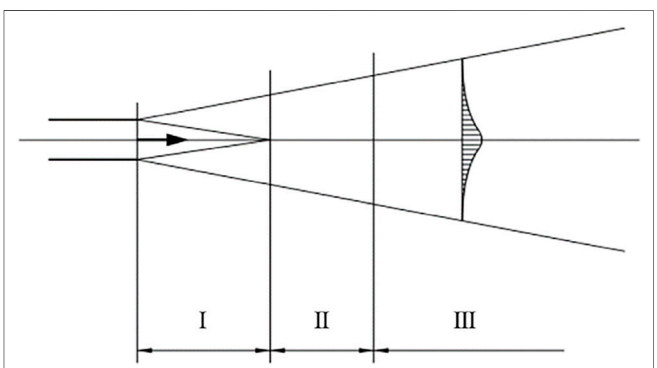

FIGURE 5 | Immersed free stream.

axial push-flow velocity of the sewage-sludge two-phase flow is less than the flow velocity of the clean water single-phase flow, and the high-velocity area above 1 m/s is also small. At a certain distance downstream of the mixing flow field, the mixing radius is small, and precipitation is formed at the bottom of the pool. In addition, there are obvious deposits directly under the mixer (Jin and Zhang, 2014). Tian Fei et al. used FLUENT software to compare and study the flow field characteristics in the two cases of clear water flow and solid-liquid two-phase flow. The study found that the velocity distribution of the flow field in the two cases is similar. However, in the solid-liquid two-phase flow, due to the influence of solid particles, the velocity of the flow field will increase in the low-velocity zone. In contrast, in the high-speed zone, the velocity of the flow field will decrease. The concentration of solid particles near the pressure surface of the blade is greater than that near the suction surface. Moreover, it was found that, in the dead zone inside the pool, the concentration of solid particles in the dead zone near the pool was higher than that in the upper dead zone of the pool (Tian et al., 2014c).

RESEARCH ON KEY FACTORS AFFECTING FLOW FIELD CHARACTERISTICS

In practical engineering applications, fluid movement is relatively complicated. The jet will collide with the wall of the pool and produce rebound, backflow, vortex, and other phenomena (Tian et al., 2012a). The flow field characteristics of the mixing tank are influenced by several factors, including installation factors of installation position and angle of submersible mixer and impeller design parameters of hub-tip ratio, blade angle, impeller diameter, number of blades, and so on. These factors directly affect the mixing effect and have intuitive guidance for the engineering application of submersible mixers.

Installation Factors

Installation Position

The distance between the installation position and the bottom of the pool stipulated in the measurement of the specific power of the submersible mixer is 1/3 of the effective water depth (GB/T 33566-2017, 2017). However, in practical application, the installation position of the submersible mixer needs to be adjusted according to the actual situation, and various positions have a different impact on the characteristics of the flow field. Xu Weixing et al. used the method of numerical simulation. They used clean water as the medium to compare the flow field distribution in the pool when the installation depth of the submersible mixer was 3 and 5.72 m. It was found that when a submersible mixer is installed near the bottom of the pool, a high-speed flow zone can be formed on the bottom of the pool, which will flush it with jets. This will help prevent the deposition of solid particles at the bottom of the pool so that the medium in the pool can be averaged (Xu and Yuan, 2011b). Tian Fei et al. used numerical simulation methods to study the external characteristics of submersible mixers at four different positions in the pool and analyzed the velocity cloud diagram inside the pool. The results show that when the center axis of submersible mixer impeller is 600 mm from the bottom of the pool, the blade is at least 200 mm from the bottom of the pool, the distance ratio between the left and right walls is 4 : 3, the mixing efficiency and the average velocity of the pool are the highest, and the fluid is stirred the most stable (Tian et al., 2013b). Jin Jianhua used numerical simulation methods to numerically simulate the three-dimensional flow in a two-phase environment of sewage and sludge. It is concluded that reducing the installation position of the mixer can increase the flow rate at the bottom of the pool and reduce the sedimentation of sludge. Moreover, it was found that when the central axis of the impeller is 0.4 m away from the bottom of the pool, there is no obvious sludge deposition, and the density distribution is uniform (Jin and Zhang, 2014).

Installation Angle

Tian Fei et al. used numerical simulation to study the flow field distribution in the pool at different installation angles for two submersible mixers at the same depth and concluded that the installation position and angle of submersible mixers have a great influence on the flow field in the pool and the average flow velocity of the whole pool (Tian et al., 2012c). Based on Star-ccm + virtual simulation platform, Chen Yunfan et al. carried out numerical simulation of the full flow field with water as the research medium and studied the impact of the layout on the mixing effect of the hypoxic pool mixtures when using two submersible mixers. Analyzing the flow field, it was found that the mixing effect of the overall pushing was better than that of the distributed pushing, and the area of the low-speed area was smaller. On the basis of the overall pushing flow, the mixing flow field under three installation angles was studied, and combined with the actual situation of the pool, it was finally determined that the mixer with 45° installation angle would run more safely and stably (Chen et al., 2020a). Zhang Xiaoning et al. studied the velocity distribution of the flow field in the mixing pool with water as the medium and horizontal installation angles of 30°, 45°, 60°, and 90°. It is concluded that the different horizontal installation angles of submersible mixer have a great influence on the flow field in the pool. Among the four schemes studied, the layout angle of 45° has the best effect. In addition, a new method for evaluating the performance of submersible mixer, effective mixing domain method, is presented; that is, the hydraulic performance of submersible mixer can be evaluated by calculating the effective mixing volume (≥0.1 m/s) of water pushing mixing (Zhang et al., 2014). Zhang Zhi et al. used FLUENT software to numerically simulate and theoretically analyze the flow field of the submersible mixer at different installation angles to obtain the effect of different installation angles on the push-flow effect and found that adjusting the installation angle of the submersible mixer can improve the flow state inside the pool, increase the average flow velocity, and reduce the dead zone rate at the bottom, while reasonably changing the installation angle can also reduce the vortex energy consumption. They proposed that the analysis of the dead zone rate using the grayscale correlation method is more accurate than the average velocity method (Zhang et al., 2020a).

Impeller Design Parameters

Blade Gap

Xu Shun et al. found that the blade gap has some influence on the mixing effect of the submersible mixer. Through numerical simulation, the flow field under six working conditions with blade gap of 1, 3, 6, 8, 10, 14 mm was studied and analyzed. It was found that the shaft power and outlet flow were not affected by the blade gap, and the effective mixing ratio increased first and then decreased with the increase in blade gap. The maximum effective mixing ratio, maximum thrust, and minimum effective energy consumption per unit were achieved when the blade gap was 6 mm (Xu et al., 2017).

Hub-Tip Ratio

The hub-tip ratio is the ratio of the diameter of the hub to the diameter of the impeller. It is an important parameter in the design of the impeller of the submersible mixer and has an important influence on the hydraulic performance of the submersible mixer. Xu Weixing et al. used numerical simulation methods to compare the flow fields when the hub-tip ratio was 0.2, 0.3, and 0.4. It is concluded that the impeller with a smaller hub has higher speed, more uniform speed distribution, and better mixing effect (Xu and Yuan, 2010; Xu and Yuan, 2011b; Weixing and Jianping, 2011).

Blade Angle

Blade angle is an important parameter in the impeller design, which has a significant influence on the stirring effect and pressure distribution on the impeller surface. Xu Shun and Ren Xiangxuan used numerical simulation to analyze the flow field under three models with a blade angle of −4°, 0°, and 4°. The results show that, with the increase of blade angle, the area of effective mixing area increases, and the mixing effect is better. The shaft power and thrust of the submersible mixer are continuously increased, and the area of high pressure on the pressure surface of the blade is constantly increased when the blade angle is increased from −4° to 4° degrees. In addition, with the increase of blade angle, the effective energy consumption per unit also increases (Xu et al., 2017; Ren et al., 2021).

Impeller Diameter

The impeller diameter is a fundamental parameter of the impeller, and the optimal matching relationship exists between the outer diameter of the impeller and the rotational speed under the same power. Chen Bin et al. used STAR-CCM + simulation software to conduct a full flow field constant numerical simulation of the submersible mixer and analyzed the average flow velocity in the pool with various impeller diameters in the operation of the circular inspection pool and the square pool. It was found that, in the circular inspection pool, the larger the impeller diameter of the submersible mixer at the same power, the better the effect of push flow, as shown in **Figure 6A**. In the square pool, the average fluid flow velocity in the pool would first increase and then decrease with the increase of impeller diameter, as shown in **Figure 6B**. It means that in a square pool, the increase of impeller diameter may deteriorate the mixing effect of submersible mixer. As the impeller diameter is excessive, the cross section of the mainstream is large, the return channel area is reduced, and the total resistance is increased. Thus, the efficiency of the submersible mixer will be declined. Therefore, it is necessary to conduct a more detailed analysis when selecting a submersible mixer in a square pool (Chen et al., 2018).

Number of Blades

The number of blades of submersible mixer is usually 2–3 blades. Zhuang Yufang et al. used numerical simulation to study the effect of the number of blades on the push-flow performance of the submersible mixer. It was found that the push-flow effect of the three-blade submersible mixer and two-blade submersible mixer is basically the same in the circular pool, but there are certain discrepancies as shown in **Figure 7A**. When the impeller diameter is 1.1–3.1 m, under the same power, the three-blade submersible mixer pushes the flow better than the two-blade effect. When the impeller diameter is greater than 3.1 m later, the two-blade submersible mixer has a better effect of push flow. In the square pool, two-blade and three-blade submersible mixer impeller diameter and speed curve trend are identical. The effect of push flow is enhanced with the increase in impeller diameter and then weakened, as shown in **Figure 7B**. However, while the impeller diameter is from 1.7 to 4.3 m, the two-blade submersible mixer has a better push-flow effect. When the impeller diameter is in the range of 1.1–1.7 m or greater than 4.3 m, the three-blade submersible mixer has a better push-flow effect (Zhuang, 2018).

Impeller Speed

Tian Fei et al. conducted a three-dimensional numerical simulation of the flow field inside the stirred wastewater treatment pool with the same submersible mixer under various rotational speeds using the RNG k -ε turbulence model and SIMPLE algorithm with FLUENT software. By analyzing the velocity field at different cross sections in the pool, it was obtained that, with the increase in impeller speed, the fluid stirred more and more sufficiently in the whole pool, and the effective disturbance radius of the water body cross section became increasingly large. Moreover, it was found that the power of the mixer was proportional to the third power of the mixer speed for the same pool with the same mixer (Tian et al., 2011).

Other Factors

Pool Structure

Column structures are commonly found in large underground sewage mixing pools. The shape and distribution of the column and the shape of the pool have a great influence on the mixing effect. Shi Shuzhou et al. studied the flow field when the columns are square and cylindrical by numerical simulation. It was found that the overall flow velocity of the cylinder was higher, and the flow field distribution was more uniform. The shape resistance of the square column near the column was significantly higher than that of the cylinder, and the fluid flow around the column was poor. The distribution of the column should be well-coordinated with the installation position of the submersible mixer to avoid the loss of the thrust caused by the direct jet network of the mixer. In addition, the simulation analysis on the corner of the pool with

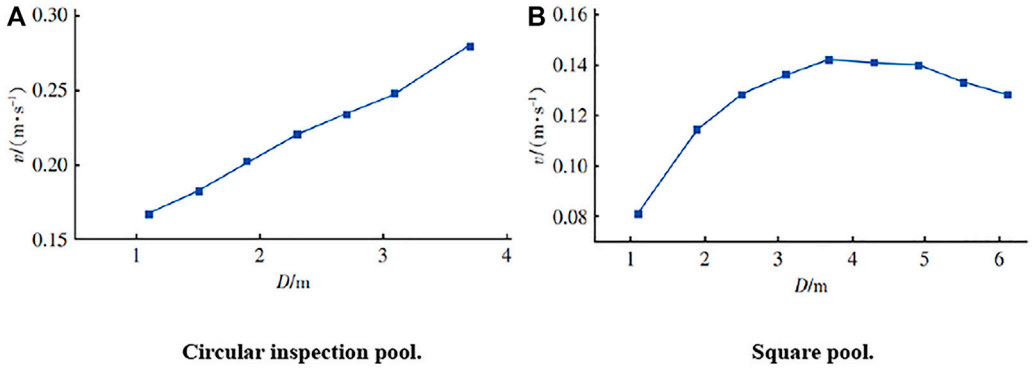

FIGURE 6 | Average flow velocity in two kinds of pools with different impeller diameters.

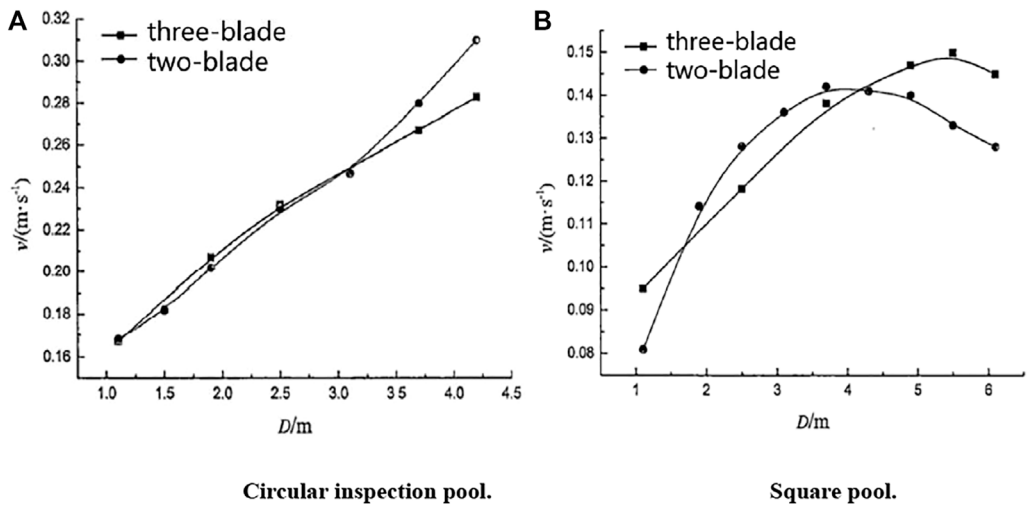

FIGURE 7 | Comparison of the average velocity in the pool of three-blade and two-blade submersible mixer.

right and round corners was carried out. The results show that the smooth transition can minimize the generation of vortices. The flow state in the pool with round corners was more uniform, the overall flow rate was higher, the dead zone area was smaller, and sludge was not easy to deposit (Shi et al., 2019).

Pool Shape

Shi Weidong et al. used the numerical simulation method to simulate the operation of the same submersible mixer in rectangular, straight circular tube, progressive circular tube, and abrupt circular tube four pool types of pools to compare the different power consumption. It was found that the fluid flow in the straight circular tube pool is relatively stable, the effect of fluid flow in the progressive circular tube pool is the second, and the fluid flow in the abrupt circular tube pool is the worst. In the power consumption, the abrupt change circular tube pool within the submersible mixer consumes the most power, the smallest power consumption within the progressive circular tube pool. The authors recommended the application of progressive circular tube pools and circular straight tube pools in the engineering design (Shi et al., 2009).

Diversion Shell

A diversion shell is widely used in fluid machinery and is a device for diversion. After installing the diversion shell, a submersible mixer can produce stable axial flow, reduce the shaft power, and improve efficiency. Using FLUENT as the fluid calculation software, Shi Weidong et al. simulated and analyzed the flow of submersible mixer with diversion shell by combining numerical simulation with experimental verification. It was found that the fluid velocity of submersible mixer with a diversion shell was obviously transferred along the axis, and the radial diffusion was relatively small, which had obvious axial diversion and reduced the effect of the boundary of the pool wall on the fluid in the pool (Shi et al., 2011). Using CFX as the fluid calculation software, Xu Qiao et al. compared the flow field of the submersible mixer with and without the diversion shell by numerical simulation. It was found that the trend of the

axial flow velocity is the same in both cases, manifesting as the phenomenon of axial push flow and radial diffusion. However, the model with a diversion shell had a higher axial flow velocity, and the model without a diversion shell had a higher velocity in the reflux zone and a better reflux effect (Qiao, 2018). Using ANSYS-CFX as the fluid calculation software, Xiao Xia et al. studied the flow field distribution of diversion shells at the front and back ends of large and small pools, respectively, by combining numerical simulation with experimental verification. It was found that adjusting the diversion shell to the front can increase the effective advancing distance of the mixer and increase the mixer's efficiency. In small pools, adjusting the diversion shell to the back can increase the effective advancing distance and overall mixing volume and increase the efficiency of the submersible mixer in the pool (Xia et al., 2019).

OUTLOOK

In recent years, domestic numerical simulation of submersible mixer research has been a significant development. In the future, the following directions deserve attention in the research on submersible mixers:

1) Application of numerical calculation method based on the Euler–Lagrange model to numerical simulation of solid-liquid two-phase flow in the submersible mixer. At present, there are few studies on numerical simulation of submersible mixer in solid-liquid two-phase flow, and the main application is the Euler–Euler model. The numerical simulation method based on the Euler–Lagrange model is more suitable for the practical application of submersible mixer and has been widely used and verified by experiments in the field of water pump, mixing sink (Sun, 2015; Zhang et al., 2020b; Cao et al., 2020; Chen et al., 2021; Li et al., 2021; Quan et al., 2021; Shi et al., 2021). Referring to other research methods of hydro-machinery and combining with the characteristics of the submersible mixer itself, the development of a numerical simulation model suitable for the study of multiphase flow in the submersible mixer will become the main research content in the future.
2) Flow field characteristics of submersible mixer with the solid-liquid two-phase flow as a medium. The flow field characteristics of submersible mixers in water medium have been studied maturely. However, there are some deficiencies in the study of the flow field characteristics of submersible mixer with the solid-liquid two-phase flow as the medium, especially the distribution of solid phase, motion track, and velocity characteristics in two-phase flow. In practical application, the sewage tank usually contains unfiltered small sediment, microorganisms, and other objects. The solid medium will affect the flow field characteristics of the submersible mixer, such as the wear, oscillation, and unstable operation of the impeller of the submersible mixer. For the mixing flow field, there are also effects such as sludge deposition in the mixing dead zone and poor mixing effect.
3) The calculation model based on real fluid—solid-liquid multiphase flow is built to explore the influence of various parameters on the flow field characteristics of mixing fluid in a submersible mixer. At present, the research on the factors influencing the flow field characteristics of submersible mixers in single-phase flow is mature. However, there are few studies on the factors influencing the flow field characteristics in solid-liquid two-phase flow. In the case of two-phase flow, the influence of various parameters of solid phase, such as density, hardness, and volume, on the flow field characteristics should be the focus of future research.

AUTHOR CONTRIBUTIONS

TF and ZE contributed to the conception and design of this paper. YC collated and collected the literature. TF wrote the first draft of the manuscript. TF, ZE, and YC wrote all parts of the manuscript. SW was responsible for the calibration and modification of the manuscript. All authors participated in the revision, reading, and approval of the submitted version of the manuscript.

FUNDING

The authors would like to acknowledge the support received from the National Key R&D Program Project (no. 2020YFC1512405), the National Natural Science Foundation of China (no. 51979125), and Six Talent Peaks Project of Jiangsu province (JNHB-192).

REFERENCES

Bao, Y., Gao, Z., and Shi, L. (2005). Recent Research Progress of Multiphase Stirred Reactors [J]. *Chemical Industry and Engineering Progress* 24 (10), 1124–1130.

Błoński, D., Szulc, P., Machalski, A., and Rogula, J. (2021). Numerical Simulation and Experimental Investigation of Submersible Sewage Mixer Performance [J]. *J. Phys. Conf. Ser.* 1741 (1), 012007.

Brehmer, M. E. T., and Kraume, M. (2012). *Fluid Dynamik in Biogas Reaktoren [J].*

Cao, W., Xu, Y., Zhang, H., and Wang, X. (2020). Analysis of Gas-Liquid Two-phase Flow Characteristics of Mining Multistage Emergency Drainage Pump. *J. Drainage Irrigation Machinery Eng.* 38 (12), 1189–1195.

Chen, B., Chen, Y, Zhang, H., Wang, Y., and Xia, C. (2021). Cavitation Characteristics of High-Speed Submersible Axial-Flow Pump[J]. *J. Drainage Irrigation Machinery Eng.* 39 (2), 109–115.

Chen, B., Wang, B., Zhang, H., Wang, Q., and Wang, Z. (2016). Effects of Propeller Layout Position on Flow Characteristics in Oxidation Ditch [J]. *J. Drainage Irrigation Machinery Eng. (Jdime)* 34 (3), 227–231.

Chen, B., Zhuang, Y., Chen, K., Chen, X., and Yang, J. (2018). Influence of Impeller Diameter on Hydraulic Characteristics of Submersible Propeller [J]. *China Water & Wastewater* 34 (5), 57–60.

Chen, Y., Cai, X., Zhang, H., Chen, Y., Wang, Y., and Xu, Y. (2020). Calculation and Analysis of Airfoil Optimization in Artificial Flow[J]. *J. Drainage Irrigation Machinery Eng.* 38 (2), 170–175.

Chen, Y., Chen, Y., Zhang, H., Wang, Y., and Xia, C. (2020). Influence and Optimization of Mixer's Arrangement of Flow Field of Anoxic Pool [J]. *J. Drainage Irrigation Machinery Eng.* 38 (10), 1045–1050.

Cheng, X., Zhao, R., Shi, W., Zhang, D., and Gao, X. (2021). Numerical Investigation of Particle Induced Erosion in a Mixed Pump by CFD-DEM Coupled Method [J]. *J. Eng. Thermophys.* 42 (2), 357–369.

Cj/T 109-2007 (2007). *Submersible Agitator: [S]*.

Fei, T., Shi, W., and Hua, J. (2014). Matching Criterion of Submersible Mixer and Pool [J]. *Adv. Mech. Eng.* 2014, 1–5.

Fei, T., Wei-Dong, S., and Hua, J. (2013). "Comparison of Sewage Treatment Mixer in Three Pool Face Boundary Conditions [Z]," in Frontiers of mechanical engineering and materials engineering II : Part 2, Hong Kong, 979–983.

Gb 18918-2002 (2002). *Discharge Standard of Pollutants for Municipal Waste-Water Treatment Plant: [S]*.

Gb 37485-2019 (2019). *Minimum Allowable Values of Energy Efficiency and Energy Efficiency Grades for Submersible Mixers of Wastewater: [S]*.

Gb 50318-2017 (2017). *Code for Urban Wastewater and Stormwater Engineering Planning: [S]*.

Gb/T 33566-2017 (2017). *Pusher Submersible Agaiter: [S]*.

Gong, F., Pan, M., and Tang, L. (2017). Numerical Simulation of Submersible Agitator inside Two-Dimensional Flow Field [J]. *J. Hubei Univ. Technol.* 32 (1), 93–96.

Gu, Y., Gaoxiao, Q., Jiaobanqi, De. Y., and Yu, Y. (2015). "Research and Application of High-Efficiency Submerged Agitator [Z]." in Proceedings of the First Cross-Straits (Fujian-Taiwan) Water Technology Exchange Conference. Fujian: Quanzhou, 72–73.

Harvey, P. S., and Greaves, M. (1982). *Turbulent Flow in An Agitated Vessel - 1. A Predictive Model [J]*.

Harvey, P. S., and Greaves, M. (1982). *Turbulent Flow in An Agitated Vessel - 2. Numerical Solution and Model Predictions [J]*.

He, Z., Rodi, W., and Frohlich, J. (2000). Large Eddy Simulation of Turbulent Flows in Smooth and Rough Open Channels [J]. *Journal of Hydrodynamics* 15 (2), 191–201.

Issa, R., Luo, J. Y., and Gosman, D. (1994). "Prediction of Impeller Induced Flows in Mixing Vessels Using Multiple Frames of Reference," in Proceedings of the 4th European Conf on Mixing, IMechE Symposium Series No 136, F.

Jin, J., and Zhang, H. (2014). A Numerical Simulation of Submersible Mixer in Three-Dimensional Flow with Sewage-Sludge Two-phase [J]. *China Rural Water and Hydropower* (10), 159–162.

Jishui Paishui Sheji Shouce (Disanban) (2016). Water Supply and Drainage Design Manual (Third Edition)] [J]. *Water Wastewater Inf.* 2016 (1).

Kissel, R., and Effenberger, M. (2010). *Empfehlungen für die Auswahl von Rührwerken für Gärbehälter [J]*.

Lang, T., Shi, W., Chen, K., Li, W., and Cheng, C. (2015). Research on the Flow Field and Abrasion Characteristics in Sewage Pump with Pre-mixing Device [J]. *Fluid Machinery* 43 (11), 29–33.

Li, W., Wang, L., Shi, W., Chang, H., and Wu, P. (2021). Numerical Simulation and Performance Prediction of Solid-Liquid Two-phase Flow of Alkaline Pump Based on Full Factor Test[J]. *J. Drainage Irrigation Machinery Eng.* 39 (9), 865–870.

Li, W., Liu, X., and Wu, C. (2007). Application and Summary of Biologic Disposal High Efficiency Blender [J]. *Journal of Agricultural Mechanization Research* (7), 181–182.

Liang, T. (2012). *Numerical Simulation on Agitated Flow Field of Submersible Mixer and Study on Impeller Optimization Design [D]*. Shandong: Shandong University.

Liu, H., and Liu, Y. (2018). Guyebeng Liangxiangliu Ji Mosun Yanjiu Xianzhuang Ji Zhanwang [Research Status and Prospect of Two-phase Flow and Wear of Solid-Liquid Pump] [J]. *South Agric. Machinery* 49 (23), 8–11.

Liu, X., Wang, W., Zhao, J., and Chang, J. (2010). "The Numerical and Experimental Study on the Hydraulic Characteristics of Submersible Mixer [Z]," in 2010 International Conference on E-Product E-Service and E-Entertainment [v7], Henan, China, 6007–6011.

Luo, J. Y., Gosman, A. D., Issa, R. I., Middleton, J. C., and Fitzgerald, M. K. (1993). Full Flow Field Computation of Mixing in Baffled Stirred Vessels [J]. *Chem. Eng. Res. Des.* 71, 342–344.

Ma, S., and He, X. (2003). Brief on the Pollutant Discharge Standard of Municipal Wastewater Treatment Plant [J]. *Water and Wastewater Engineering* 29 (9), 89–94.

Peng, Z., Zhao, H., Guo, C., Wang, W., and Zeng, D. (2009). Qianshuijiaobanji Sanwei Liuchang de Shuzhi Moni. Numerical Simulation of 3-Dimensional Flow Field in Submersible Mixer [J]. *Water Wastewater Eng.* 35 (z2), 340–342.

Qiao, X. (2018). *Design of Impeller of Submersible Mixer Based on Characteristics of Stirring Flow Field [D]*. Yangzhou: Yangzhou University.

Qiu, S. P. (2021). Qianshuijiaobanji zai Shuichuli Lingyude Yingyong Yanjiu. [Research on Application of Submerged Agitator in Water Treatment Field] [J]. *Shandong Water Resour.* (5), 23–25.

Quan, H., Kang, L., Guo, Y., Cheng, J., Yu, X., and Quan, S. (2021). Effect of Solid Concentration on Circulation Flow and Hydralic Characteristics in Vortex Pump[J]. *J. Drainage Irrigation Machinery Eng.* 39 (6), 555–561.

Ren, X., Tang, F., Xu, Y., Shi, L., and Shang, X. (2021). Performance Analysis of Blade Angle of Submersible Agitator [J]. *South-to-North Water Transfers Water Sci. Technol.* 19 (4), 805–813.

Shao, T., Hu, Y., Wang, W., Jin, Y., and Cheng, Y. (2013). Simulation of Solid Suspension in a Stirred Tank Using CFD-DEM Coupled Approach [J]. *Chin. J. Chem. Eng.* 10, 1069–1081.

Shao, W., Zhao, R., and Zhang, D. (2020). Erosion of Multistage Mixed Flow Pump Based on Fully Coupled CFD-DEM Method [J]. *J. Hydrodynamics* 35 (5), 640–648.

Shi, G., Liu, Z., Li, H., and Yang, X. (2021). Pressure Fluctuation Characteristics of Gas-Liquid Two-phase Flow in Multiphase Pump[J]. *J. Drainage Irrigation Machinery Eng.* (1), 23–29.

Shi, S., Wang, Y., Xie, J., and Liu, Y. (2019). Application of CFD Simulation in Submersible Agitator Layout and Optimization of Operating Conditions [J]. *Water Wastewater Eng.* 45 (9), 36–40.

Shi, W., Shi, Y., Gao, X., Zhang, D., Lang, T., and Zhao, T. (2020). Simulation and Experiment on Flow Characteristics of Large Particles in Vortex Pump Based on DEM-CFD [J]. *Trans. Chin. Soc. Agric. Machinery* 51 (10), 176–185.

Shi, W., Tian, F., Cao, W., Chen, B., and Zhang, D. (2009). Numerical Simulation of Mixer Power Consumptions in Different Ponds [J]. *J. Drainage Irrigation Machinery Eng.* 27 (3), 140–144.

Shi, W., Tian, F., and Chen, B. (2011). Flow Analysis and Measurement of Wastewater Treatment Mixer with Dome [J]. *Transactions of the Chinese Society for Agricultural Machinery* 42 (3), 96–99.

Sun, Y. (2015). *Numerical Simulation and Analysis of Flow Field and Solid—Liquid Suspension in Stirred Tanks [D]*. Ma'anshan, China: Anhui University of Technology.

Tian, F., Shi, W. D., He, X. H., Jiang, H., and Xu, Y. H. (2013). Study on Installation of Submersible Mixer [J]. *IOP Conf. Ser. Mater. Sci. Eng.* 52 (2). doi:10.1088/1757-899x/52/2/022024

Tian, F., Shi, W. D., Jiang, H., Lu, X. N., and Chen, B. (2012). Study on Velocity Distribution in a Pool by Submersible Mixers [J]. *IOP Conf. Ser. Earth Environ. Sci.* 15 (5). doi:10.1088/1755-1315/15/5/052031

Tian, F., Shi, W., Jiang, H., and Zhang, Q. (2014). A Study on Two-phase Flow of Multiple Submersible Mixers Based on Rigid-Lid Assumption [J]. *Adv. Mech. Eng.* 2014 (Pt.2), 531234.

Tian, F. (2012). *Jet Characteristics and Experimental Research of Submersible Mixer [D]*. Jiangsu: Jiangsu University.

Tian, F., Shi, W., Chen, B., and Cao, W. (2011). "Mixing Performance Investigation of Sewage Treatment Mixer under Multi-Rotational Speed [Z]," in Proceedings of the Fourth National Conference on Hydraulic Machinery and Systems, Lanzhou, 494–497.

Tian, F., Shi, W., Lu, X., Zhang, D., and Lang, T. (2014). Analysis of Characteristics of Pressure Fluctuation inside Submersible Mixer [J]. *J. Drainage Irrigation Machinery Eng.* (7), 606–610.

Tian, F., Shi, W., Lu, X., Chen, B., and Ou, M. (2012). Numerical Simulation of Submersible Mixer with Three Blades [J]. *J. Drainage Irrigation Machinery Eng.* 30 (1), 11–14.

Tian, F., Shi, W., Xu, L., and Shao, P. (2014). Jet Characteristics of Submersible Mixer [J]. *J. Ningxia Univ. (Natural Sci. Edition)* (3), 221–228.

Tian, F., Shi, W., Zhang, D., Cao, W., and Zhou, Q. (2019). Flow Filed Characteristics of New-type Multi-Impeller Submersible Mixer [J]. *J. Drainage Irrigation Machinery Eng.* 37 (3), 232–236.

Tian, F., Shi, W., Zhang, Q., Zhang, D., and Zhang, G. (2013). Inner Flow Characteristics at Impeller of Submersible Mixer with Two Blades [J]. *J. Jiangsu University(Natural Sci. Edition)* 34 (4), 395.

Tian, F., Shi, W., Lu, X., Chen, B., and Xu, Y. (2012). Theoretical Calculation and Simulation Analysis of Submersible Mixer Effciency for Wastewater Treatment [J]. *Trans. Chin. Soc. Agric. Eng.* 28 (12), 50–54.

Van't Riet, K., Bruijn, W., and Smith, J. M. (1976). Real and Pseudo-turbulence in the Discharge Stream from a Rushton Turbine. *Chem. Eng. Sci.* 31 (6), 407–412. doi:10.1016/0009-2509(76)80024-3

Wang, C., Yuan, L., Li, Z., and Gao, Z. (2016). Recent Progress in the Numerical Simulation of Solid-Liquid Suspensions in Stirred Reactors [J]. *J. Beijing Univ. Chem. Technology(Natural Sci. Edition)* 43 (1), 1–12.

Wang, F. (2016). Research Progress of Computational Model for Rotating Turbulent Flow in Fluid Machinery [J]. *Trans. Chin. Soc. Agric. Machinery* 47 (2), 1–14.

Wang, L., Changyong, T., and Moxing Shiyongxing Fenxi ji Yixing Vof Shuzhimoni (2007). *Applicability Analysis of Commonly Used Turbulence Models and VOF Numerical Simulation of Airfoils [D]*. Huazhong: Huazhong University of Science and Technology.

Wang, W., and Mao, Z. (2002). Numerical Simulation of the Whole Flow Field in a Stirred Tank with a Rushton Turbine Using the Improved Inner-Outer Iterative Procedure [J]. *The Chinese Journal of Process Engineering* 2 (3), 193–198.

Weixing, X., and Jianping, Y. (2011). "Optimization Design of Submersible Mixer Based on Simulation Study of AgitatedFlow Field [Z]," in 2011 Third International Conference on Measuring Technology and Mechatronics Automation [v2B], Shanghai, China, 807–810.

Weixing, X., and Shouqi, Y. (2010a). "CFD Analysis on Agitated Flow Field of Submersible Mixer [Z]," in 2010 ASME International Mechanical Engineering Congress and Exposition, Vancouver, British Columbia, Canada, 8890–8894.

Weixing, X., and Shouqi, Y. (2010b). "Numerical Simulation of Agitated Flow Field of Submersible Mixer Based on Computational Fluid Dynamics [Z]." in Mechanical Engineering and Green Manufacturing, Xiangtan, China, 1543–1546.

Xia, X., Lan, F., and Liu, X. (2019). Influences of Diversion Hood Position on Working Efficiency of a Push-Flow Submersible Agitator Based on CFX. *[J]. Machinery* 46 (7), 71–75.

Xu, S., Tang, F., Wang, W., Liu, Y., and Xu, Q. (2017). Influence of Different Blade Gaps on Flow Field of Submersible Mixer [J]. *China Water & Wastewater* 33 (1), 106–109.

Xu, W. (2006). *Qianshuijiaobanqi Yelun Sheji ji Jiaoban Liuchang Shuzhi Moni. [Design Theory of Submerged Agitator Impeller and Numerical Simulation of Agitation Flow Field] [D]*. Zhenjiang: Jiangsu University.

Xu, W., and Fan, M. (2011). "Structure Reverse Design and CFD Analysis on Agitated Flow Field of Submersible Mixer [Z]," in Manufacturing Science and Technology, Singapore, 23–29.

Xu, W., and Yuan, S. (2011). Optimization Design of Submersible Mixer Based on a Simulation Study of Agitated and Engineering Application [J]. *China Rural Water and Hydropower* 2011(6), 32–35.

Xu, W., and Yuan, S. (2011). Simulation Study on Agitated Flow Field of Submersible Mixer Based on Fluent [J]. *Machinery Des. Manufacture* 2011(9), 155–157.

Xu, W. X., and Yuan, S. Q. (2010). Numerical Analysis of Agitated Flow Field of Submersible Mixer. *Amr* 139-141, 2681–2684. doi:10.4028/www.scientific.net/amr.139-141.2681

Yan, J., Huang, D., and Teng, G. (2009). Research on Rural Domestic Sewage Disposal of Biologic Disposal High Efficiency Blender [J]. *Journal of Anhui Agricultural Sciences* 37 (20), 9606.

Yang, F., and Zhou, S. (2017). Progress of Solid-Liquid Suspension in Stirred Vessel [J]. *CIESC Jorunal* 68 (6), 2233–2248.

Yi, C. L., and Zhai, H. W. (2003). The Application of Submersible Agitator in Sewage Treatment [J]. *J. Luohe Vocational Tech. Coll.* 2 (2), 17–18.

Zhang, D., Mei, J., Zhao, R., Huang, J., and Jin, Y. (2020). Response Surface Method-Based Optimization of Impeller of Fluoroplastic Two-phase Flow Centrifugal Pump. *J. Drainage Irrigation Machinery Eng.* 38 (9), 898–903.

Zhang, H., Zheng, Y., Zhang, Z., Kan, K., and Xuying, M. O. (2021). Influence of Placement Angle of Sewage Mixer on its Hydraulic Characteristics[J]. *J. Drainage Irrigation Machinery Eng.* 39 (5), 483–487.

Zhang, X., Wang, Y., and Zhao, G. (2017). Yaobaixing Qianshui Jiaobanqi de Shuzhi Moni Yanjiu. Numerical Simulation Research of Swing Submersible Mixer [J]. *China Sci. Technol. Inf.* (17), 837.

Zhang, X., Zhao, J., and Wang, W. (2014). Influence of Submersible Mixer Installation Angle with the Mixing Effect [J]. *J. Beijing Inst. Civil Eng. Architecture* (4), 48–51.

Zhang, Z., Cui, G., and Xu, C. (2008). *Tuanliu Dawo Shuzhimoni de Lilun yu Yingyong. [Theory and Application of Large Eddy Simulation of Turbulence] [M]*. Beijing, China: Tsinghua University Press.

Zhang, Z., Yuan, Z., Jiang, J., and Li, C. (2020). Influence of Wastewater Mixer Setting Angle on Flow Field in Sewage Treatment Pool. *J. Drainage Irrigation Machinery Eng.* 38 (3), 272–276.

Zhou, G., Shi, L., and Wang, Y. (2002). CFD Prediction of Flow Near the Agitator in Stirred Tank [J]. *Journal of Chemical Engineering of Chinese Universities* 16 (1), 17–22.

Zhou, G., Shi, L., and Wang, Y. (2004). Computational Fluid Dynamics Progress in Stirred Tank Reactors [J]. *Chemical Engineering* 32 (3), 28–32.

Zhuang, Y. (2018). *Qianshuituiliuqi Zai Shengwufa Wushuichuli Gongyizhong Shuilitexing de Yanjiu. [Research on Hydraulic Characteristics of Submerged Pusher in Biological Sewage Treatment Process] [D]*. Hefei, China: Hefei University of Technology.

Conflict of Interest: Author ZC is employed by Yatai Pump and Valve Co. Ltd.

The remaining authors declare that the research was conducted in the absence of any commercial or financial relationships that could be construed as a potential conflict of interest.

frontiers in Energy Research

ORIGINAL RESEARCH
published: 02 February 2022
doi: 10.3389/fenrg.2021.808393

Study on Hydraulic Characteristics of Reactor Coolant Pump Shutdown Transition Process Based on Primary Circuit Closed System

Dong-hao Li, Yi-bin Li, Fan Zhang, Yan-lei Guo, Cong-xin Yang and Xiu-yong Wang*

College of Energy and Power Engineering, Lanzhou University of Technology, Lanzhou, China

According to the structural characteristics of a steam generator and a reactor pressure vessel, the reactor primary circuit system of HPR1000 is simplified to make the reactor coolant pump (RCP) characteristics match the resistance characteristics of the system pipeline, so a simplified model of reactor primary circuit closed system is formed. On this basis, the RCP shutdown accident in a single circuit of the reactor is numerically simulated. Results show that the pressure in the pipeline system has changed greatly compared. The flow rate drops rapidly and decreases to 1.7% of stable operation at 10s. The torque drops sharply to –51.89% of stable operation, and then rises slowly to zero. The pressure at the inlet and outlet of the impeller changes dramatically which leads to the change of blade load and the velocity in the impeller passage decreases gradually. The pressure and velocity in the guide vane continue to decrease.

Keywords: reactor coolant pump, reactor primary circuit closed system, shutdown, transition process, computational fluid dynamics

OPEN ACCESS

Edited by:
Ling Zhou,
Jiangsu University, China

Reviewed by:
Dong Liu,
Jiangsu Second Normal University, China
Hao Yan,
Hefei University of Technology, China

****Correspondence:***
Yi-bin Li
liyibin58@163.com

Specialty section:
This article was submitted to Process and Energy Systems Engineering, a section of the journal Frontiers in Energy Research

Received: *03 November 2021*
Accepted: *13 December 2021*
Published: *02 February 2022*

Citation:
Li D-h, Li Y-b, Zhang F, Guo Y-l, Yang C-x and Wang X-y (2022) Study on Hydraulic Characteristics of Reactor Coolant Pump Shutdown Transition Process Based on Primary Circuit Closed System. Front. Energy Res. 9:808393. doi: 10.3389/fenrg.2021.808393

INTRODUCTION

Nuclear power is a kind of efficient environmental protection energy, HPR1000 is China's independent third generation nuclear power technology (Long et al., 2020), and the reactor primary system is mainly a closed energy generation and exchange system composed of reactor pressure vessel, RCP, pressurizer, steam generator, and pipeline. It is the most basic core part of all reactor systems. **Figure 1** is a schematic diagram of the primary circuit of the reactor. Safe and stable operation is the most important for nuclear power plants, so it is of great significance to study the transient process of emergency shutdown of reactor primary circuit closed system. Many scholars have done a lot of research on different transient processes of pumps. Kim et al. (2014) analyzed the transient characteristics of pump-rising pipeline system with an air chamber using the method of characteristics. Wang et al., (2020) studied the transient characteristic of RCP under the condition of the rotor seizure accident by experiment. Fu et al. (2020) conducted experimental and numerical studies of the transient characteristics during the start-up process of the axial flow pump. Lu et al. (2019) used different models of RCP to carry out transient performance test research of RCP during shutdown coasting transition. Zhong (2018) built the transient test system of RCP shaft sticking accident, and calculated the transient flow of RCP shaft sticking accident by bidirectional fluid structure coupling. Gao et al. (2013) and Su et al. (2017) studied the RCP transient performance in primary coolant system during the start-up period and mathematically solved and elucidated the RCP start-up mechanism. Tang et al. (2021) carried out transient three-dimensional numerical simulation of CEFR primary circuit pump shaft sticking accident, and obtained three-dimensional

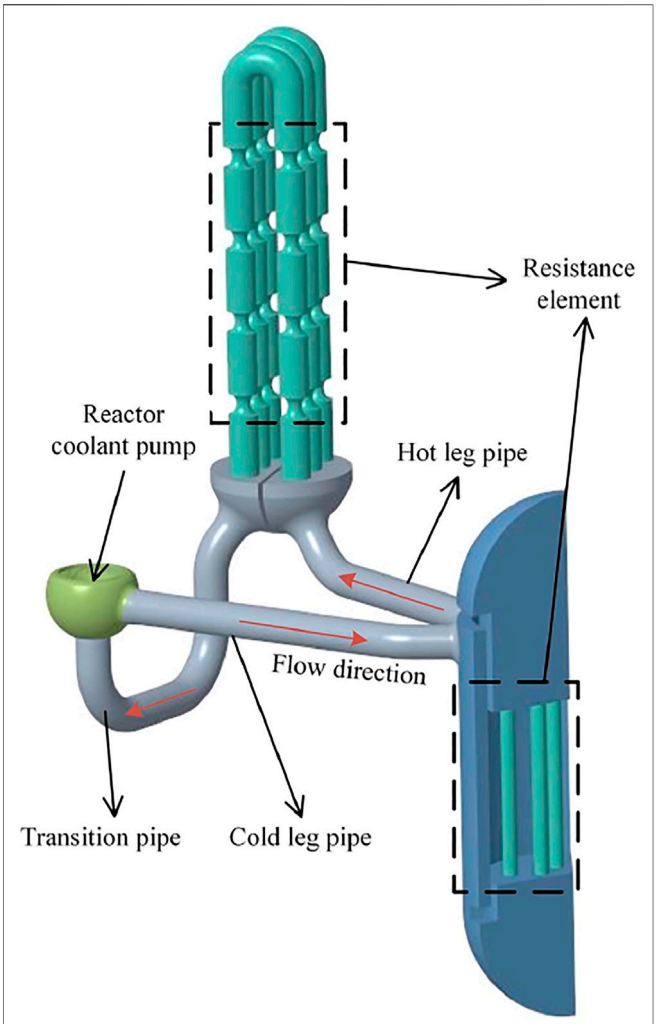

FIGURE 1 | HPR1000 reactor primary circuit simplification.

thermal hydraulic characteristics of key structures and components during shaft sticking accident. Liu et al. (2009) has carried out experimental research on the transient hydraulic characteristics of the RCP during the shutdown and idling process, and found that the instantaneous flow and rotation speed of power failure rapidly decreased, the vibration of bearing seat suddenly increases at the moment of power failure. Wu et al. (2010) reported the transient flow of the RCP in the transient process of rapid valve opening. Azzoune et al. (2019) took the main pump of AP1000 reactor as the research object, studied the transient transition process under the condition of a stuck rotor, and carried out two-way fluid structure coupling calculation. Sabotinov and Srivastava (2010) simulated and analyzed the large break loss of coolant accident of VVER-1000 reactor. A large number of researchers have also calculated and analyzed the influence of some transient processes of pump shutdown on the system in multi-pump system (Farhadi, 2010; Liu et al., 2021). In the study of pump shutdown transition process, most numerical calculations need to give boundary conditions, but in this paper, the reactor primary circuit closed system model of the RCP is adopted, so the boundary conditions of the RCP inlet and outlet cannot be given, and the transient process of the RCP shutdown can be simulated more accurately.

TABLE 1 | Nominal parameters of the RCP

Parameters	Value
Nominal flow rate coefficient, φ_a	0.289
Nominal head coefficient, ψ_a	0.247
Nominal rotation speed, n_d (r/min)	1,485
Density of medium, ρ (kg/m^3)	745
Dynamic viscosity, μ(kg/m•s)	0.000745
Reference pressure, p (MPa)	15.5
Impeller blade number, Z_l	4
Diffuser blade number, Z_d	11

MODEL SIMPLIFICATION

The primary circuit system of HPR1000 includes three circuits. It is assumed that the circuit in the reactor three circuits are independent of each other and do not affect each other, and the probability that the RCP rotor accident occurs in the reactor three circuit systems is extremely low, so it is assumed when a pump shutdown accident occurs in a single circuit of the reactor, the other two circuits are in normal operating conditions at this time, which can simplify the reactor's three circuits power system to a single circuit power system. If the pipeline performance curve is superimposed with curve of the pump performance, the meeting point will be the operating point of the pump for that system. The pipe resistance can be controlled by regulating the pipe diameter of the resistance element. The local resistance loss formula is as follows and changing the diameter of the resistance element can change the resistance.

Due to the complicated internal structure of the steam generator and the reactor pressure vessel, the steam generator in the reactor single circuit system needs to be simplified in structure. Use CREO software to model the water body of the RCP suction section, impeller, guide vane, and pressurized water chamber (Li et al., 2020), the rated parameters of the main pump are shown in **Table 1**. According to the structural characteristics of large number of heat transfer tubes, small diameter, and thin tube wall in the ZH-65 steam generator (He et al., 2021) of HPR1000. Therefore, it is difficult to carry out numerical simulation for all heat transfer tubes, so the heat transfer tubes can only be simplified. Based on the equal flow cross-section method for heat transfer tubes, the equal area of heat transfer tubes is further simplified to three inverted U-bends. Similarly, the cold leg pipe, heat leg pipe, transition pipe, and reactor pressure vessel of single circuit reactor are simplified, and resistance characteristic elements are added into the simplified structure of inverted U-bend and reactor pressure vessel. By adjusting the resistance values of each part and comparing with the theoretical resistance values, it shows that the simplification is reasonable as shown in **Figure 1**.

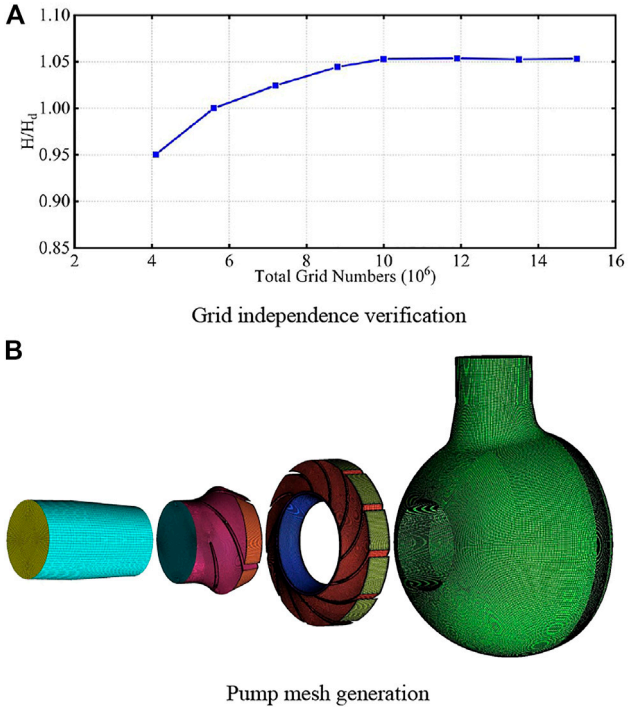

FIGURE 2 | Grid independence verification **(A)** and pump mesh generation **(B)**.

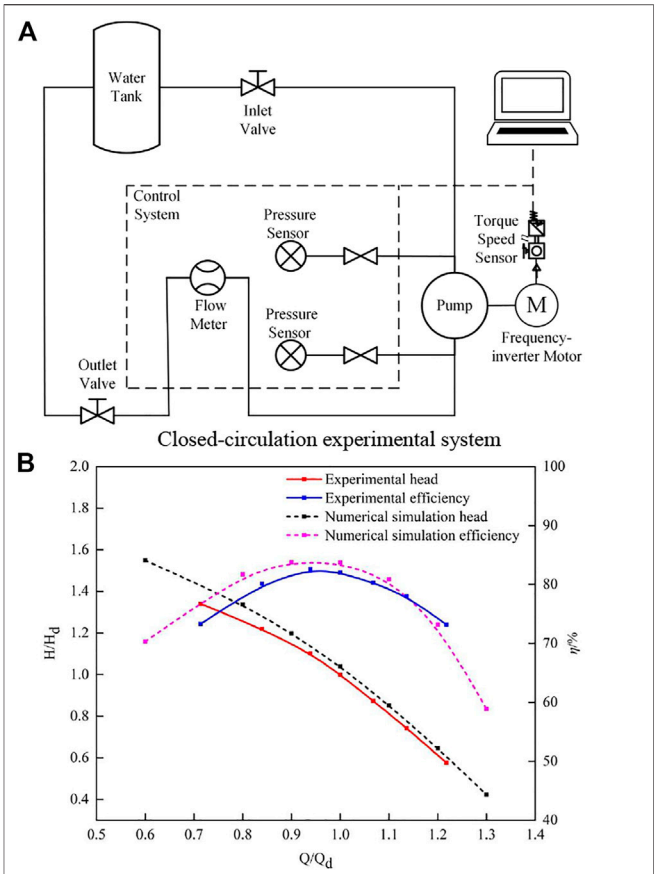

FIGURE 3 | Experimental system **(A)** and hydraulic performance comparison **(B)**.

CONDITION MATCHING OF REACTOR PRIMARY CIRCUIT SYSTEM

According to the principle of determining the operating point of the closed pump system, the resistance performance curve of the reactor primary circuit pipeline can only be adjusted by controlling the flow radius of the resistance element, so that the reactor single circuit system can operate at the rated operating condition. By adjusting and controlling the resistance characteristics of the heat transfer tube and the reactor pressure vessel, the resistance characteristics of the simplified three inverted U-bends are in line with the resistance characteristics of the original heat transfer tube, and the resistance characteristics of the reactor pressure vessel are in line with the actual situation.

Mesh Generation

Use ANSYS ICEM software to divide the water body of the pump with high-quality hexahedral meshes and encrypt the wall meshes. The distance between the first layer of mesh and the wall is 0.3–0.4 mm to meet the requirements of the turbulence model y^+ = 30–300. In order to ensure the reliability of numerical calculation and reduce the cost of the calculation, the grid independence test is performed with the head of the RCP as a verification index. When the number of grids reached 8.8 million, the head of the RCP stabilized. Therefore, the total number of grids of each flow-through component reaches 9.0305 million to meet the requirements. Among them, the number of grid units of the impeller is 2.7978 million, the guide vane is 2.5503 million, the pressurized water chamber is 2.896 million, and the suction section is 786,400. The grid of each part of the pump is shown in **Figure 2**. Tetrahedral grids with good adaptability are used in the pipeline system, and the total number of pipeline grids is 24.3372 million. The total grid number of the whole system is about 33 million.

Experimental Verification of Calculation Model and Condition Adjustment

The reliability of the numerical calculation is verified by the external characteristic experiment of the RCP. Test the change of RCP head and efficiency under different flow conditions, draw the external characteristic curve. The hydraulic performance test device included the console, motor, closed water tank, pump, control system, and valves, as shown in **Figure 3A**. The comparison between the experimental results and the steady-state calculation results is shown in **Figure 3B**. The curve of numerical calculation results and the curve of experimental results have the same change trend, and the consistency of each point is high under the full condition. At rated flow, the error between the calculated head of RCP and the experimental value is 4.0% and the error between the calculated efficiency of RCP and the experimental value is 1.73%, the maximum error is

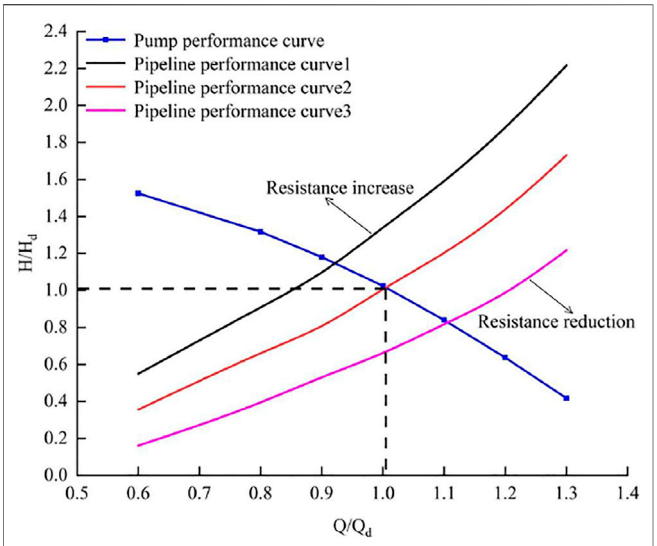

FIGURE 4 | Pump performance curve and pipeline performance curve.

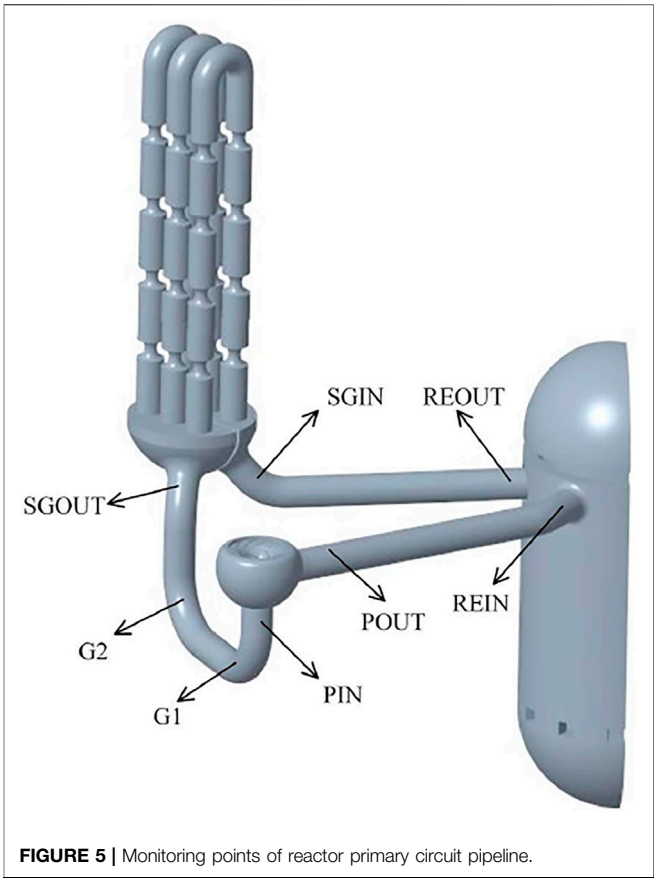

FIGURE 5 | Monitoring points of reactor primary circuit pipeline.

less than 5%. The calculation model of the RCP meets the requirements of the engineering calculation.

If the pipeline performance curve is superimposed with the curve of the pump performance, the meeting point will be the operating point of the pump for that system. The pipe resistance can be controlled by regulating the pipe diameter of the resistance element. The local resistance loss formula is as follows and changing the diameter of the resistance element can change the resistance.

$$\Delta P = K\frac{\rho v^2}{2} = K\frac{\rho Q^2}{2A^2} \tag{1}$$

In this formula, ΔP is the pressure drop, K is the resistance coefficient, A is the cross-sectional area of the pipeline, and Q is fluid volume flow rate.

As shown in **Figure 4**, if the resistance is too small, the position of the pipeline performance curve 1 deviates from the rated operating point of the pump. Currently, it is necessary to reduce the pipe diameter. If the resistance is too large, it will reach the position of pipeline performance curve 2. Currently, it is necessary to increase the pipe diameter. After several adjustments, the pipeline performance curve 3 is finally obtained. Currently, the error of the steam generator resistance is 3.3%, the error of the reactor pressure vessel resistance is 2.9%, the error between the pump flow of the closed system and that of the rated condition is 0.998%, the error between the pump head of the closed system and that of the rated condition is 3.76%. The error of the two methods is small, which meets the requirements of overall simplification.

NUMERICAL SIMULATION OF TRANSITION PROCESS

For the transient process of pump stop, according to the above parameters, the commercial ANSYS-CFX software platform was used to calculate, and the RNG κ-ε turbulence model was selected to consider the influence of curved wall on the flow as much as possible. The near wall area is treated by the standard wall function. The pressure and velocity are coupled by SIMPLEC algorithm. The second-order central difference scheme is used to discretize the diffusion term, the second-order upwind scheme is used to discretize the diffusion term, and the second-order discrete scheme is used to discretize the governing equations, which can reduce the influence of truncation error and improve the calculation accuracy. The time step of transient calculation is 1.122×10^{-4}s, the starting time of shutdown is 0.404 s (the pump rotates for 10 turns). Refer to the experimental data of literature (Zhong, 2018), and the pump stop time is selected as 0.6 s. Since the primary circuit system of RCP is a closed system, the transition process of stopping the pump can be realized only by changing the speed of the pump. The function of the pump speed n changing with time is shown below, the unit is r/min, and the transient calculation lasts for a total of 10 s.

$$\begin{cases} n = 1485\,(t \le 0.404s) \\ n = -2475t + 2484.9\,(0.404s \le t \le 1.004s) \\ n = 0\,(1.004s \le t \le 10s) \end{cases} \tag{2}$$

In this formula, n is rotation speed, t is time.

Eight monitoring points: PIN, REIN, REOUT, SGIN, SGOUT, G1, G2, and POUT located in the middle of the pipeline section as shown in **Figure 5** are arranged in the primary circuit pipeline

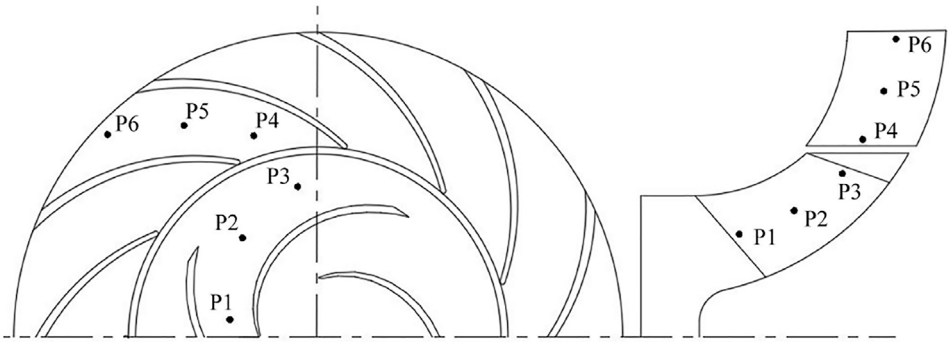

FIGURE 6 | Monitoring points of impeller and guide vane.

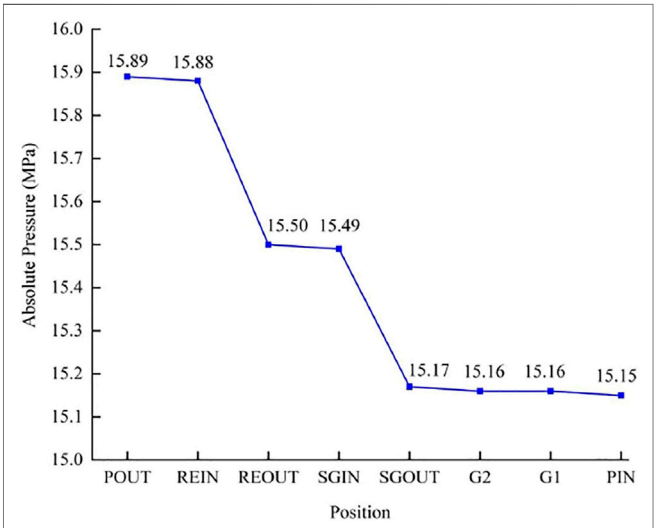

FIGURE 7 | Average absolute pressure of pipeline monitoring points.

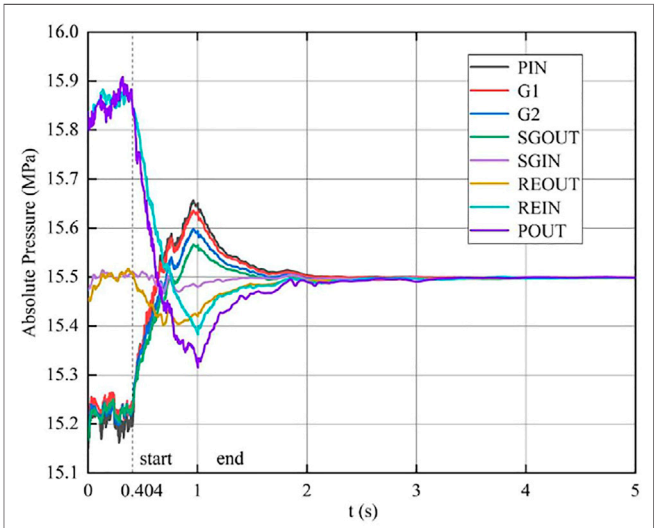

FIGURE 8 | Absolute pressure change of pipeline monitoring points during the transition process.

system of the pump to monitor the change of instantaneous pressure with time in the pipeline system during the shutdown transition of the pump. In the impeller passage of the pump, 6 monitoring points are arranged along the direction of fluid flow as shown in **Figure 6** which are P1, P2, and P3 in the impeller passage, and 3 monitoring points in the guide vane passage are P4, P5, and P6, respectively, to monitor the instantaneous changes of pressure and velocity in the pump.

NUMERICAL SIMULATION OF TRANSITION PROCESS

Pressure Change in Piping System

Figure 7 shows the average transient absolute pressure value at each position of the reactor primary circuit when the RCP operates normally. The calculation results show that the pressure distribution in the whole closed primary system is not uniform under the stable operation of the reactor primary system. Because of pipeline resistance, the pressure in all parts of the system decreases from the outlet of RCP along the direction of transition pipe, reactor pressure vessel, hot leg pipe, steam generator, cold leg pipe, and RCP inlet.

Figure 8 is the absolute pressure change diagram of each monitoring point in the pipeline system during the pump shutdown transition process. After the start of the pump shutdown transition process, due to the rapid stop of the impeller hindering the fluid flow, the fluid in the pipeline system generates pressure wave due to inertia, and strong oscillation occurs in the pipeline system. The pressure wave is transmitted along the direction of the transition pipe, steam generator, and hot leg pipe, and the peak point of the transient pressure wave gradually presents a downward trend. The maximum peak pressure is located at the PIN monitoring point at the inlet pipeline of the pump, and the value is 15.65 MPa at the end of pump shutdown. The minimum value is located at the POUT monitoring point at the outlet section, and the time is also at the end of the pump stop, and the value is 15.31 MPa.

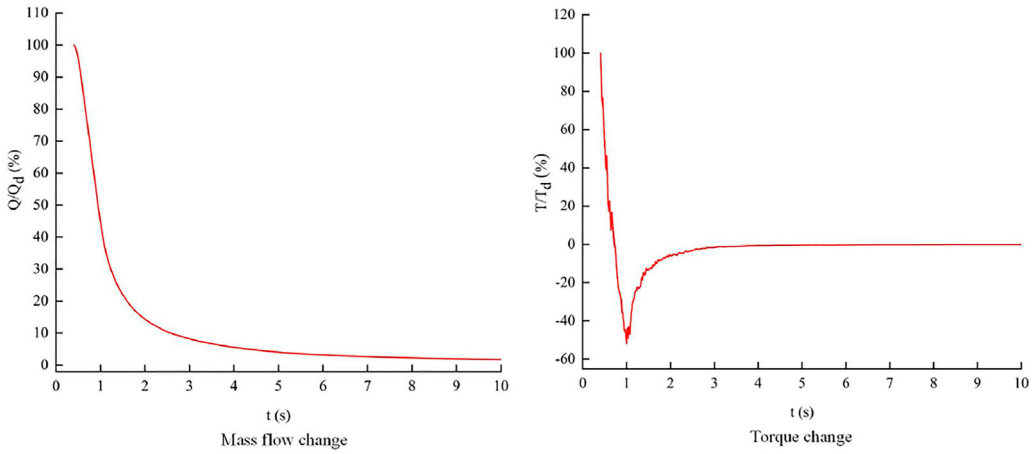

FIGURE 9 | Change of mass flow and torque during the transition process.

The pressure values at the monitoring points of PIN, G1, G2, and SGOUT all rose rapidly to the end of the clamping shaft and reached the peak value, and then decreased slowly. They were close to stable around 2 s and finally reached the reference pressure of 15.5 MPa. In addition, due to the dissipation effect of pressure wave propagation in the pipeline, the closer to the pump inlet, the greater the peak value, and the smaller the peak value away from the pump inlet. The pressure values at SGIN, REOUT, REIN, and POUT monitoring points all rapidly decrease to the end of pump shutdown and reach the minimum value, then slowly rise. The closer to the pump outlet, the greater the decrease value will be, and it is close to stable around 2 s, finally reaching the reference pressure of 15.5 MPa.

Analysis of External Characteristics of RCP

The change of flow rate and torque with time during pump shutdown is shown in **Figure 9**. It can be seen from the figure that when the pump rotation speed drops to 0r/min, due to the inertia effect of the fluid in the pipeline system, the mass flow rate does not immediately drop to 0 m^3/h, but rapidly decreases before the time point when the rotation speed of the pump decreases to 0r/min, and then slowly decreases. The overall trend shows an exponential function, and by 10 s, the mass flow rate decreases to 1.7% of the stable operation. The torque decreased sharply with the transition process of pump stopping. The torque decreases sharply at first and becomes 0N•m at 0.68 s. When the pump speed drops to 0r/min, it drops to −51.89% of the stable operation. Then it rises slowly and becomes flat at 2.2 s, close to 0N•m.

Flow Analysis in Impeller Passage

Figure 10A shows the pressure change in the impeller passage during the pump stop transition. The pressure from impeller inlet to outlet presents obvious gradient change in the stable operation state. As a result of rapid stop blocking of impeller flow and fluid inertia, the transition process stopped after the start in the pump, the impeller import part of the fluid to the impeller flow in inlet pressure increases first and then, within the impeller outlet outside part of the fluid to the impeller flow in inlet pressure increases after the first decreases, and export pressure decreases then increases first. **Figure 11A** shows the pressure change at the monitoring point in the impeller passage of the pump during the pump shutdown transition process, which is consistent with the trend of change in **Figure 10A**. When the monitoring point P1 runs smoothly, the pressure value is the smallest in the monitoring points P1, P2, and P3. In the process of pump shutdown transition, the pressure value rises sharply to the maximum value of 15.64 MPa and then decreases slowly. The next monitoring point, P2, dropped sharply to 15.27 MPa and then rose. When the pressure value of P3 is the largest in stable operation, the pressure value drops sharply to the minimum value of 15.19 MPa and then rises. With the process of pump shutdown transition, the pressure values in the impeller flow passage tend to be stable and close to the reference pressure of 15.5 MPa.

Figure 10B shows the velocity changes in the impeller during the pump shutdown transition process. After the pump shutdown transition process starts, the velocity in the flow passage gradually decreases compared with the stable operation state of the pump. **Figure 11B** shows the velocity changes at the monitoring points in the impeller passage of the pump during the transition process of pump shutdown. The velocity at P1 gently decreases during the transition process, while the velocity at P2 and P3 gradually decreases and is accompanied by oscillation. At 5s, the speed of each monitoring point was close to 0 m/s.

Load Analysis of Blade

Figure 12 shows the pressure distribution on different spans of blades along the flow direction during the pump shutdown transition process. The variation trend of blade load along with the transition process is relatively consistent on the span of 0.1, 0.5, and 0.9. At 0.5 s, the pump shutdown transition process has begun, the pressure on the pressure surface is greater than the pressure on the suction surface, and the pressure difference becomes smaller compared with the stable operation. The torque is smaller than that of smooth operation. All these make the torque relatively stable and the

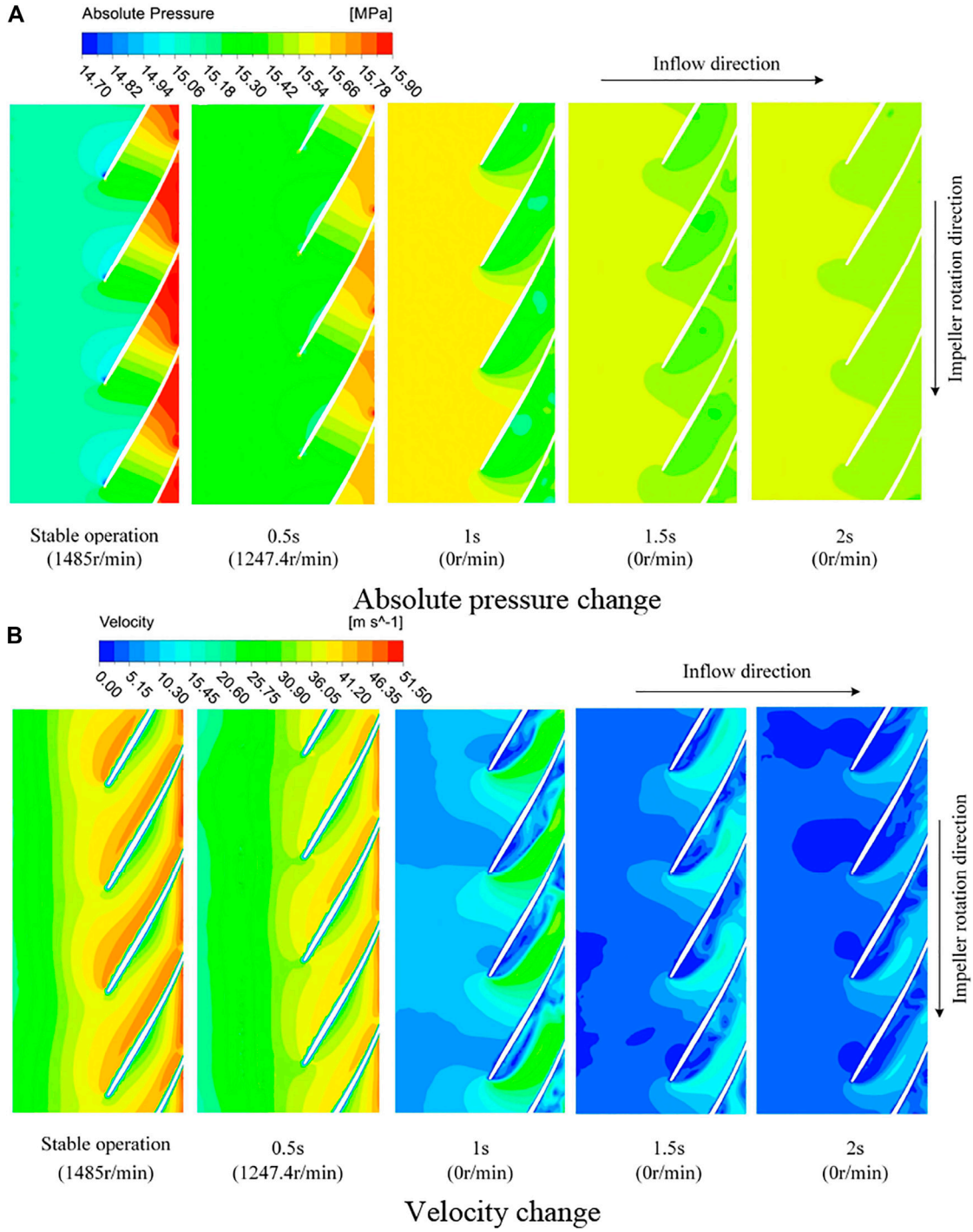

FIGURE 10 | Change of absolute pressure **(A)** and velocity **(B)** in impeller passage during the transition process.

operating value smaller. Currently, the torque of the impeller to the fluid is active. In the transition process of pump shutdown, the pressure on the pressure surface gradually decreases, and the pressure on the suction surface gradually increases. The pressure on the suction surface begins to become larger than the pressure surface, leading to the negative torque, and the torque of the fluid on the impeller gradually becomes active. At 1 s, the pressure difference between the suction surface and the working pressure surface reaches the maximum, resulting in reverse peak torque. At 1.5 s, the pressure on the suction surface is still greater than that on the pressure surface, but less than the pressure difference at 1 s, so the torque value is still negative, but the value decreases

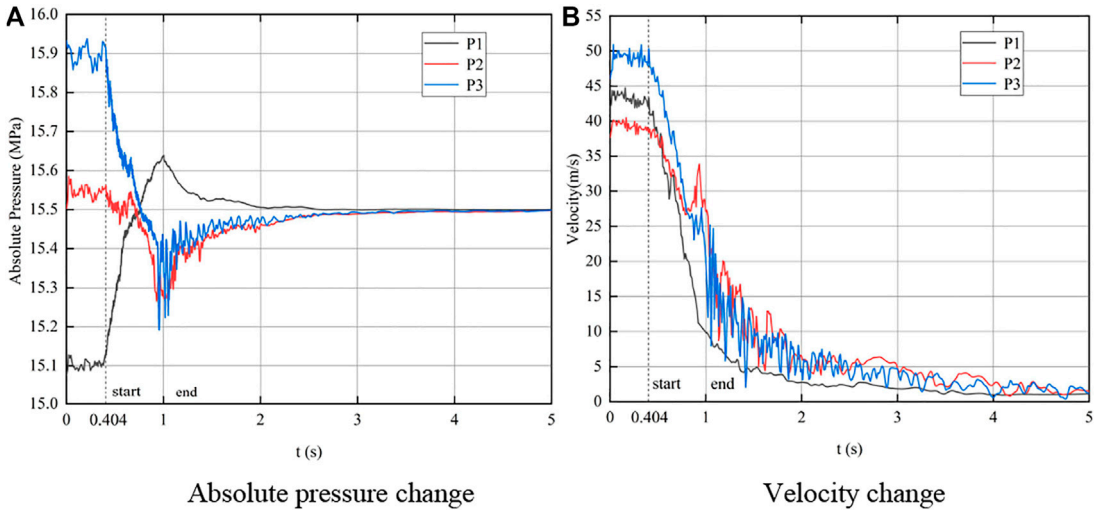

FIGURE 11 | Change of absolute pressure **(A)** and velocity **(B)** at monitoring points in impeller passage during the transition process.

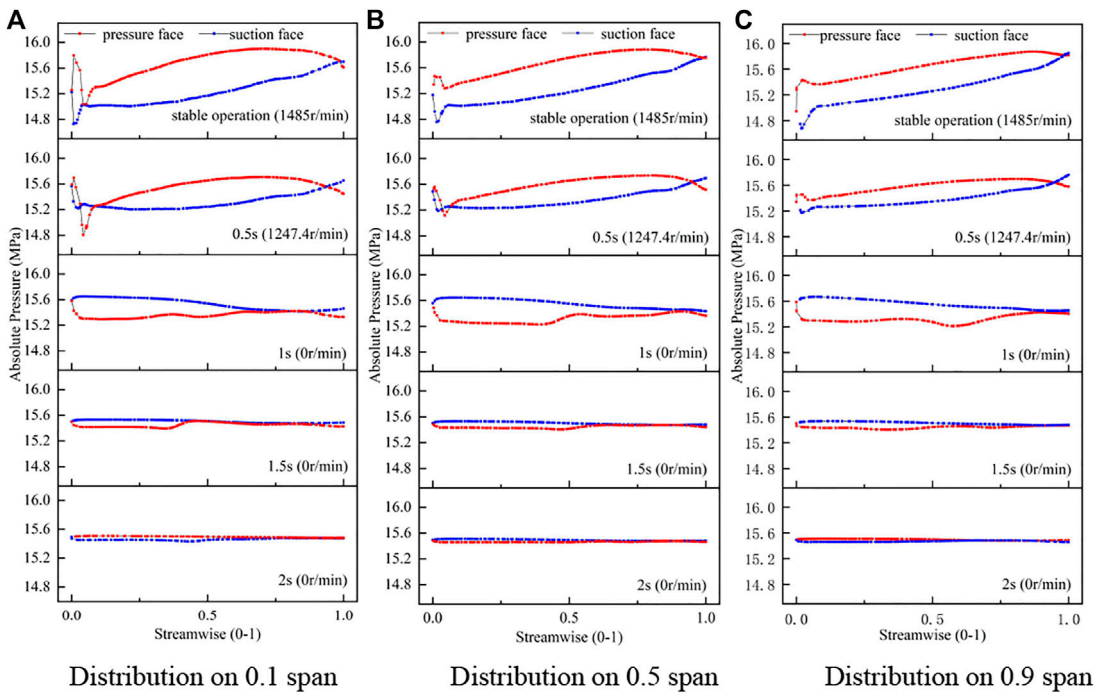

FIGURE 12 | Absolute pressure distribution on one blade 0.1 span **(A)** 0.5 span **(B)** and 0.9 span **(C)** during the transition process.

somewhat. When it reaches 2 s, the pressure of the pressure surface is close to that of the suction surface, and the torque is close to 0N•m. The overall trend of torque is consistent with **Figure 9**.

Flow Analysis in Guide Vane Passage

Figure 13A shows the pressure changes in the guide vane during the pump stop transition process. After the start of the pump shutdown transition process, the fluid continues to flow to the outlet of the pump because the impeller stops fast and hinders the flow and the inertia of the fluid, leading to the pressure in the guide vane dropping first and then rising slowly. **Figure 13A** shows the change diagram of the pressure monitoring points during the pump stop transition process. The pressure values of the monitoring points P4, P5, and P6 inside the guide vane flow passage all drop sharply. The pressure value of P5 point decreases

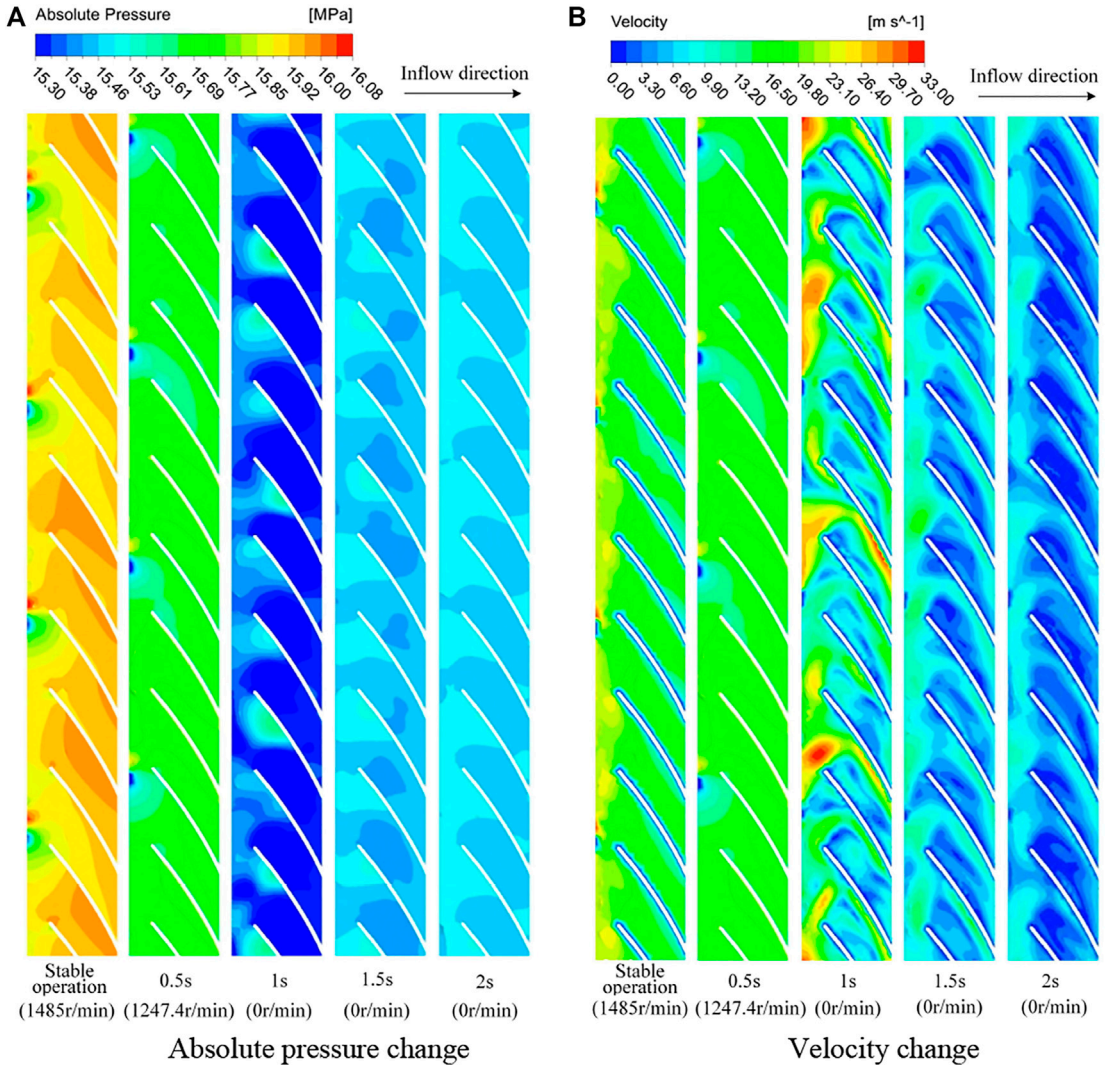

FIGURE 13 | Change of absolute pressure **(A)** and velocity **(B)** in guide vane passage during the transition process.

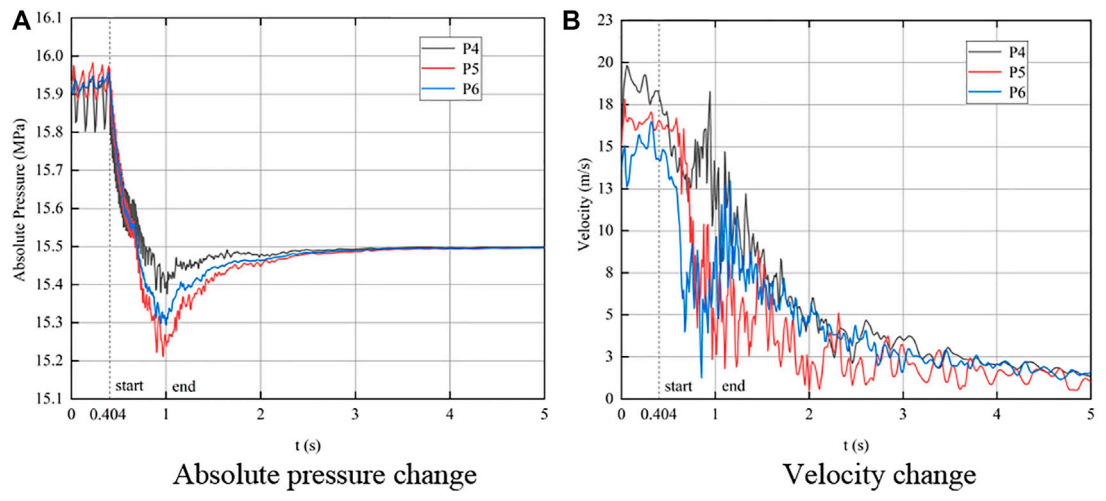

FIGURE 14 | Change of absolute pressure **(A)** and velocity **(B)** at monitoring points in the guide vane passage during the transition process.

most sharply, reaching 15.21 MPa. Then there is the pressure value at P6, which drops to 15.29 MPa. The pressure value of P4 drops slightly, which is 15.38 MPa. With the progress of the pump shutdown transition process, the final pressure values in the guide vane passage are close to the reference pressure of 15.5 MPa and tend to be stable.

Figure 14B shows the velocity changes in guide vane passage during the pump stop transition process. After the start of the pump shutdown transition process, the velocity in the flow passage first decreases, then increases, and then decreases. **Figure 14B** shows the change diagram of velocity monitoring points in guide vane passage during the pump stop transition process. The speed of the monitoring point in the guide vane channel increases suddenly and then decreases slowly at about 1 s. At 5 s, the velocity of the monitoring point in the guide vane passage is close to 0 m/s.

CONCLUSION

1) In the pump under the shutdown accident shows obvious transient effect, the pressure near the RCP inlet in the pipeline system increases and then decreases, and the pressure near the RCP outlet first decreases and then increases. The maximum pressure is at the pump inlet and the minimum pressure is at the pump outlet.
2) With the process of pump shutdown, the flow rate decreases rapidly. The torque curve first drops sharply to zero and continues to decrease to the negative extreme when the pump rotation speed drops to zero, finally the torque rises slowly and then tends to zero.
3) During the transition process of pump shutdown, the work capacity of the impeller decreases gradually. The pressure at the inlet of the impeller passage first increases and then decreases, the pressure the outlet of the impeller passage first decreases and then increases, and the velocity in the impeller channel gradually decreases to zero. The load of the impeller blade changes from the pressure on the pressure surface is greater than that on the suction surface during stable operation to the pressure on the suction surface is greater than that on the pressure surface, after reaching the peak value, the pressure difference gradually decreases to zero.
4) The pressure in the guide vane passage decreases rapidly at first and then increases slowly during the transition process of pump shutdown. When the velocity in the guide vane channel decreases, the velocity rises suddenly when the pump rotation speed drops to 0r/min, and then continues to drop to zero.

DATA AVAILABILITY STATEMENT

The original contributions presented in the study are included in the article/Supplementary Material. Further inquiries can be directed to the corresponding author.

AUTHOR CONTRIBUTIONS

D-HL: Data curation, software, formal analysis, writing-original draft. Y-BL: Resources, formal analysis, supervision, funding acquisition. FZ: Formal analysis, validation. Y-LG: Visualization, investigation. C-XY: Methodology. X-YW: Resources, data curation.

FUNDING

The work in this paper is supported by the National Defense Basic Scientific Research Program of China (Grant No. JCKY2019427D001) and the National Natural Science Foundation of China (Grant No. 51866009).

REFERENCES

Azzoune, M., Boumedien, A., Lababsa, D., Boulheouchat, M. E.-H., and Ameur, A. (2019). Analysis of a Loss-Of-Flow Accident Resulting from the Primary Pump Shaft Break Transient of the NUR Research Reactor. *J. Nucl. Sci. Tech.* 56 (1), 130–145. doi:10.1080/00223131.2018.1532845

Farhadi, K. (2011). Transient Behaviour of a Parallel Pump in Nuclear Research Reactors. *Prog. Nucl. Energ.* 53 (2), 195–199. doi:10.1016/j.pnucene.2010.05.001

Fu, S., Zheng, Y., Kan, K., Chen, H., Han, X., Liang, X., et al. (2020). Numerical Simulation and Experimental Study of Transient Characteristics in an Axial Flow Pump during Start-Up. *Renew. Energ.* 146, 1879–1887. doi:10.1016/j.renene.2019.07.123

Gao, H., Gao, F., Zhao, X., Chen, J., and Cao, X. (2013). Analysis of Reactor Coolant Pump Transient Performance in Primary Coolant System during Start-Up Period. *Ann. Nucl. Energ.* 54, 202–208. doi:10.1016/j.anucene.2012.11.020

He, G. N., Zhang, F. Y., Li, D. H., Wu, G., Hu, Y., and Lu, J. (2021). Design Research and Performance Tests of HPR1000 Model ZH-65 Steam Generator. *Press. Vessel Tech.* 38 (4), 48–52.

Kim, S.-G., Lee, K.-B., and Kim, K.-Y. (2014). Water Hammer in the Pump-Rising Pipeline System with an Air Chamber. *J. Hydrodyn* 26 (6), 960–964. doi:10.1016/S1001-6058(14)60105-0

Li, Y.-b., Fan, Z.-j., Guo, D.-s., and Li, X.-b. (2020). Dynamic Flow Behavior and Performance of a Reactor Coolant Pump with Distorted Inflow. *Eng. Appl. Comput. Fluid Mech.* 14 (1), 683–699. doi:10.1080/19942060.2020.1748720

Liu, X. J., Liu, J. S., Wang, D. Z., and Yang, Z. (2009). Test Study on Safety Features of Station Black-Out Accident for Nuclear Main Pump. *At. Energ. Sci. Tech.* 43 (05), 448–451.

Liu, Y.-f., Zhou, J.-x., Guo, Q., Shen, A.-l., and Zhang, J. (2021). 3-D CFD Simulation of Transients in Multiple Pump System with Some Pumps Being Stopped. *J. Hydrodyn* 33 (3), 583–592. doi:10.1007/S42241-021-0042-8

Long, Y., Yuan, S. Q., Zhu, R. S., Qiang, F. U., and Tianbin, L. I. (2020). Review on Research Status of Internal Flow and Technological Development of Reactor Coolant Pump. *J. Drainage Irrigation Machinery Eng.* 38 (11), 1081–1097. doi:10.3969/j.issn.1674-8530.20.0238

Lu, Y., Zhu, R., Wang, X., An, C., Zhao, Y., and Fu, Q. (2019). Experimental Study on Transient Performance in the Coasting Transition Process of Shutdown for Reactor Coolant Pump. *Nucl. Eng. Des.* 346 (4), 192–199. doi:10.1016/j.nucengdes.2019.03.007

Sabotinov, L., and Srivastava, A. (2010). Large Break Loss-Of-Coolant Accident Analysis of VVER-1000 Reactor Using CATHARE Code. *Nucl. Tech.* 170 (1), 123–132. doi:10.13182/NT10-A9451

Su, S. Z., Wang, P. F., Xu, Z. B., Ruan, X. D., and Kong, W. J. (2017). Study on Pressure Fluctuation and Radial Force during Startup of Reactor Coolant Pump. *Nucl. Power Eng.* 38 (3), 110–114.

Tang, J., Lu, D., Liang, J., Ma, X., Liu, Y., Ye, S., et al. (2021). Numerical Simulation on Asymmetrical Three-Dimensional Thermal and Hydraulic Characteristics of the Primary Sodium Pool under the Pump Stuck Accident in CEFR. *Nucl. Sci. Eng.* 195 (5), 478–495. doi:10.1080/00295639.2020.1834314

Wang, X., Lu, Y., Zhu, R., Fu, Q., Chen, Y., and Zhong, W. (2020). Experimental Study on Transient Characteristics of Reactor Coolant Pump under Rotor Seizure Accident. *Ann. Nucl. Energ.* 136, 107039. doi:10.1016/j.anucene.2019.107039

Wu, D., Wu, P., Li, Z., and Wang, L. (2010). The Transient Flow in a Centrifugal Pump during the Discharge Valve Rapid Opening Process. *Nucl. Eng. Des.* 240 (12), 4061–4068. doi:10.1016/j.nucengdes.2010.08.024

Zhong, W. Y. (2018). *Study on Fluid-Solid Interaction Transient Characteristics of Nuclear Reactor Coolant Pump under Shaft-Stuck Accident Condition*. Jiangsu: Jiangsu University.

Conflict of Interest: The authors declare that the research was conducted in the absence of any commercial or financial relationships that could be construed as a potential conflict of interest.

NOMENCLATURE

RCP reactor coolant pump

Q mass flow rate

$\mathbf{Q_d}$ nominal mass rate flow

H pump head

$\mathbf{H_d}$ pump head under nominal rate flow

$\boldsymbol{t}$ time

T torque

$\mathbf{T_d}$ torque under rated condition

$\boldsymbol{n}$ pump speed

K resistance coefficient

$\boldsymbol{\Delta P}$ pressure drop

A cross-sectional area of the pipeline

Greek

$\boldsymbol{\eta}$ efficiency

$\boldsymbol{\rho}$ density

frontiers in Energy Research

ORIGINAL RESEARCH
published: 14 February 2022
doi: 10.3389/fenrg.2022.841730

Entropy Analysis of a Valveless Piezoelectric Pump With Hyperbolic Tubes

*Qing Yang and Jun Chen**

School of Computer Engineering, Nanjing Institute of Technology, Nanjing, China

In order to solve the problems of large reflux and low output performance of the valveless piezoelectric pump with conical tubes, the valveless piezoelectric pump with hyperbolic tubes was proposed. However, the previous research only paid attention to the difference of forward and reverse flow resistance inside the tubes. For this reason, the prototypes of conical tube valveless piezoelectric pump and hyperbolic tubes valveless piezoelectric pump were fabricated in this paper. The maximum output flow rate of the valveless piezoelectric pump with hyperbolic tubes was 54 ml/min. Subsequently, the size and position of entropy production of the hyperbolic tube and the conical tube were numerically calculated based on entropy production theory in this paper. The results show that the entropy production rate of the hyperbolic tube was significantly lower than that of the conical tube, which is consistent with the experimental results. This research analyzed the energy loss inside the valveless piezoelectric pump by using the entropy generation theory, and provided a new design and research method for improving the output performance of the valveless piezoelectric pump in the future.

Keywords: hyperbolic tube, conical tube, valveless piezoelectric pump, entropy generation, output flow

OPEN ACCESS

Edited by:
Ling Zhou,
Jiangsu University, China

Reviewed by:
Weidong Liu,
Hohai University, China
Quan Zhang,
Shanghai University, China

****Correspondence:***
Jun Chen
chenj@njit.edu.cn

Specialty section:
This article was submitted to Process and Energy Systems Engineering, a section of the journal Frontiers in Energy Research

Received: *22 December 2021*
Accepted: *12 January 2022*
Published: *14 February 2022*

Citation:
Yang Q and Chen J (2022) Entropy Analysis of a Valveless Piezoelectric Pump With Hyperbolic Tubes. Front. Energy Res. 10:841730. doi: 10.3389/fenrg.2022.841730

INTRODUCTION

As the core component of the micro-fluid control system, the output performance of the micro pump determines the characteristics of the entire system. According to different driving methods, micro pumps can be divided into electromagnetic pumps (Mi et al., 2020; Rusli et al., 2018) heat pumps (Feng et al., 2021; Skye and Wu, 2021), pneumatic pumps (Hamid et al., 2017; Ma et al., 2019), shape memory pumps (Robertson et al., 2016) and piezoelectric pumps (Huang et al., 2020; Ma et al., 2016; Ma et al., 2015). Among them, piezoelectric pumps have attracted more and more attention for their outstanding advantages such as high energy density, fast response speed, large driving force, and easy integration. According to whether there are valves inside, piezoelectric pumps can be divided into valve piezoelectric pumps and valveless piezoelectric pumps (Singhal et al., 2004; Li et al., 2021). The valve piezoelectric pump has a movable valve, which can avoid backflow and generate a larger output pressure. However, due to the existence of micro-valves, processing and assembly are difficult. In addition, the valve is easy to wear and there is a risk of fatigue damage, which greatly reduces the reliability of the valve piezoelectric pump. Compared with the former, the valveless piezoelectric pump uses a fluid diode to replace the active valve, which simplifies the structure of the valveless piezoelectric pump, makes it easy to miniaturize, and improves the system integration (Zhang et al., 2017).

The valveless piezoelectric micropump is usually composed of a piezoelectric vibrator, a pump body and a fluid diode. The fluid diode has the characteristics of unequal flow resistance between the

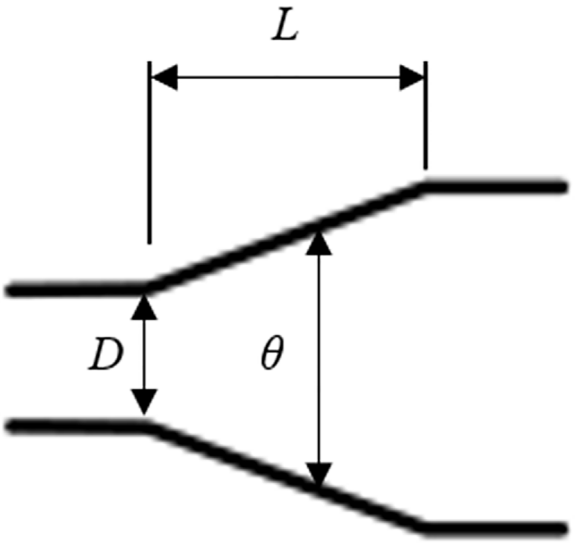

FIGURE 1 | Schematic diagram of conical tube structure.

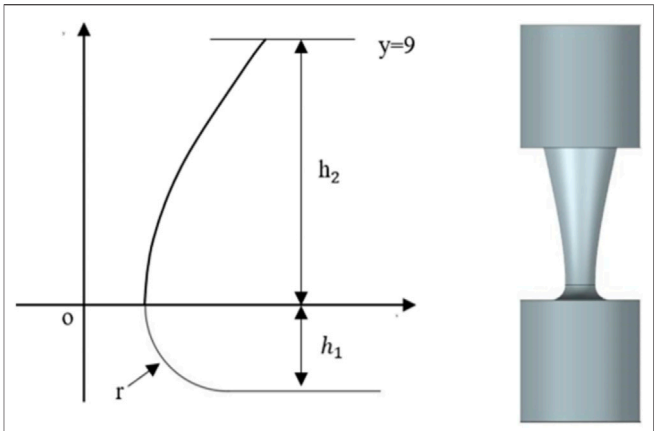

FIGURE 2 | Schematic diagram of hyperbolic structure.

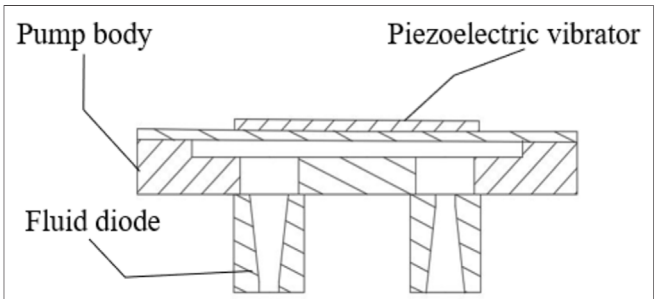

FIGURE 3 | Structure diagram of valveless piezoelectric pump.

forward and reverse directions, so it is the most important part of the valveless pump. Among them, the cone tube, as the most classic fluid diode, was first used in valveless piezoelectric pumps (Stemme and Stemme, 1993; Olsson et al., 1997). Because there is no movable valve, there are shortcomings of large output return and low output performance for the valveless piezoelectric pump. To this end, many researchers have proposed valveless piezoelectric pumps such as Tesla tube (Morris and Forster, 2003; Gamboa et al., 2005), Y-shaped tube (Zhang et al., 2008), multi-stage bifurcated tube0 (Fadl et al., 2010; Huang et al., 2014), spiral tube (Leng et al., 2013), and vortex tube (Huang et al., 2019; Huang et al., 2021) to reduce backflow and increase output flow.

However, the conical tubes valveless piezoelectric pump is still widely studied due to its simple structure. Among them, Zhang et al. (Bian et al., 2020) proposed the hyperbolic tubes valveless piezoelectric pump based on the conical tube, aiming to improve the output performance of the valveless piezoelectric pump by reducing the vortex during the flow of the piezoelectric pump. However, this study only used software simulation (Tang et al., 2021) and combined with experimental research on the internal flow field distribution of the hyperbolic tubes to illustrate the flow characteristics of the pump (Wang et al., 2020). Therefore, this article will analyze minutely the internal flow and energy loss of the hyperbolic tubes valveless piezoelectric pump based on the entropy generation theory. Subsequently, the size and position of entropy generation in the conical tube and the hyperbolic tube are obtained by numerical calculation. Finally, the output performance experiments of the prototypes are carried out. The calculation and analysis of fluid diodes using entropy generation theory can provide new ideas for improving the output performance of valveless piezoelectric pumps.

STRUCTURAL DESIGN AND WORKING PRINCIPLE

Design of Hyperbolic Tube

Figure 1 shows a schematic diagram of the conical tube structure, in which L is the length of the conical tube, D is the diameter of the throat of the conical tube, and θ is the cone angle. The hyperbolic tube is made by changing the structure of the conical tube, that is, the gradually expanding straight wall of the conical tube is changed to a hyperbolic wall, and the throat of the conical tube is changed to a circular arc transition section. The left side of **Figure 2** shows the wall curve of the hyperbolic tubes, where h_1 is the height of the arc section, h_2 is the height of the hyperbola section, and r is the minimum radius of the flow channel of the tube. The hyperbolic function is:

$$\frac{x^2}{a^2} - \frac{y^2}{b^2} = 1 \tag{1}$$

Among them, a is equal to r, and b is the only variable in **Formula (1)**. Constrain the hyperbola with two straight lines $y = 0$ and $y = 9$. The arc part at the throat is constructed by **Formula (2)**:

$$(x - c)^2 + (y - d)^2 = r \tag{2}$$

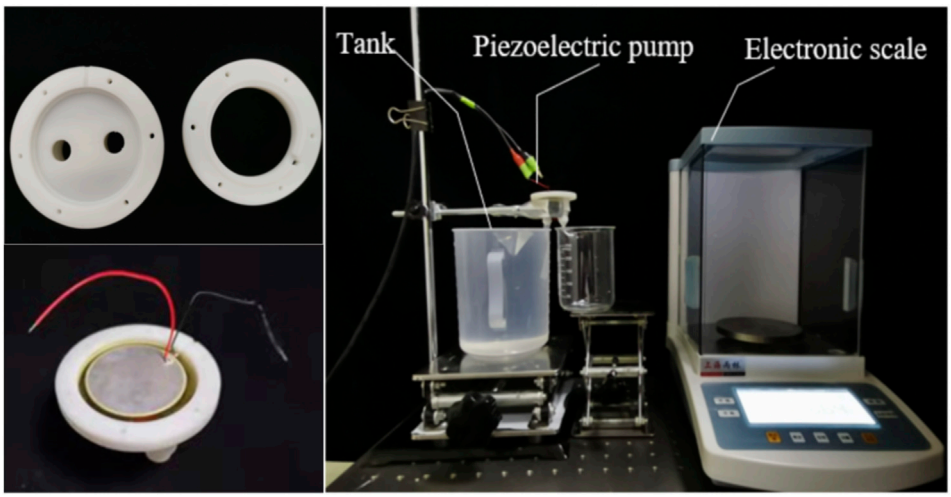

FIGURE 4 | Experimental setup and piezoelectric pump body model.

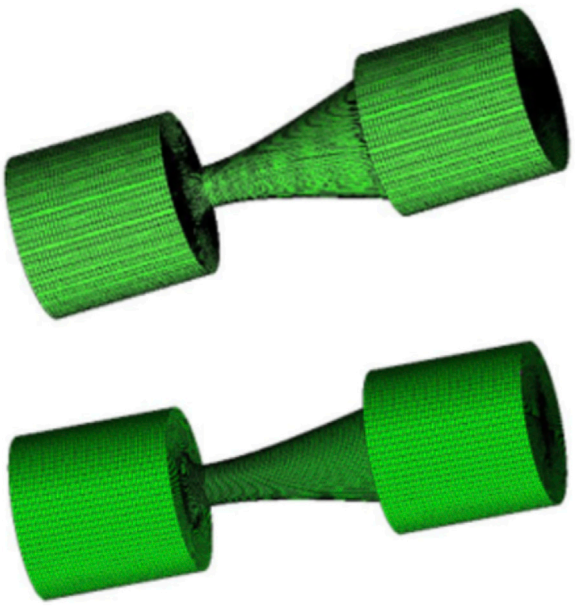

FIGURE 5 | Finite element models of conical tube and hyperbolic tube.

Finally, the obtained hyperbolic arc streamline is rotated 360° around the axis to obtain the inner flow passage of the hyperbolic tube as shown in the right side of **Figure 2**.

Working Principle

The valveless piezoelectric pump with hyperbolic tubes is composed of a piezoelectric vibrator, a pump body containing two hyperbolic tubes, and a pump cover, as shown in **Figure 3**. In this study, the fluid flowing from the arc section into the hyperbola is defined as the forward flow, and the fluid flowing from the hyperbolic section into the arc section is defined as the reverse flow. The piezoelectric vibrator receives the current voltage signal to generate up and down vibrations to change the volume of the pump cavity and change the pressure inside the pump cavity, so as to realize the unidirectional transportation of the fluid on the macroscopic level.

TABLE 1 | Analysis of grid independent.

Tube1			Tube2		
$N/10^5$	$Q/kg{\cdot}s^{-1}$	r/%	$N/10^5$	$Q/kg{\cdot}s^{-1}$	r/%
1.35	14285.7	—	2.62	13454.4	—
1.84	14416.4	0.91	3.03	13539.9	0.63
2.8	14532.2	0.8	3.76	13594.6	0.4
4.0	14644.9	0.77	3.54	13625.7	0.23

The circular piezoelectric vibrator is fixed by adhering its periphery to the pump body, and AC voltage is applied to generate periodic vibration, and its vibration shape is approximately parabolic. By establishing a polar coordinate system, the origin of the coordinate system is the center of the piezoelectric vibrator, then the polar coordinate equation of the parabola:

$$W(r) = \omega_0\left(1 - \frac{r_2}{R_2}\right) \tag{3}$$

In the formula, $\Omega_0$is the maximum amplitude, R is the radius of the piezoelectric vibrator, and the maximum volume change of the pump cavity is:

$$\Delta V = 2\pi \int_0^R \omega_0\left(1 - \frac{r^2}{R^2}\right) = \pi\omega_0\frac{R^2}{2} \tag{4}$$

The flow resistance experienced by the fluid in the hyperbolic tube is mainly local resistance and friction resistance, as shown below:

$$\gamma_+ = \gamma_{\tau+} + \gamma_{D+} \tag{5}$$

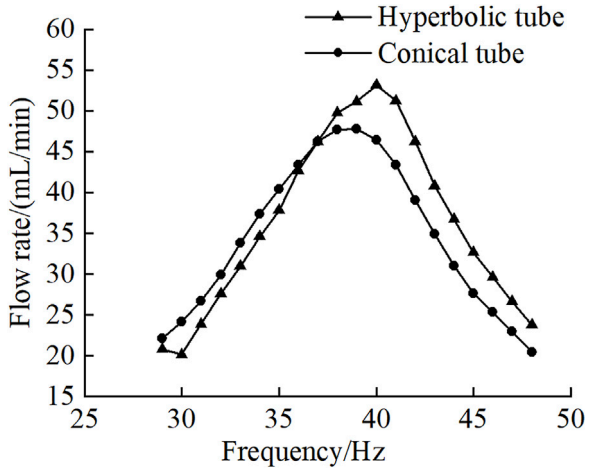

FIGURE 6 | Flow rate of the piezoelectric pumps.

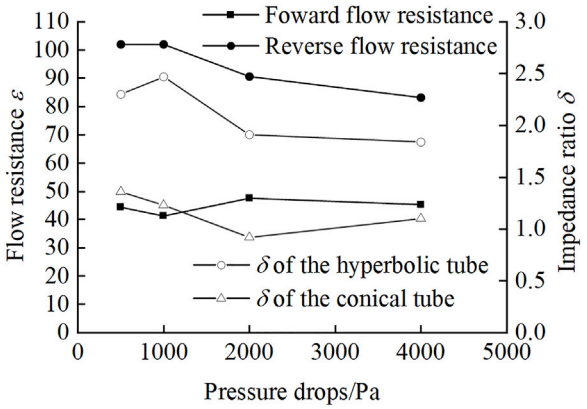

FIGURE 7 | Flow resistance and impedance ratio.

TABLE 2 | Entropy production of conical tube under different pressure difference.

Differential pressure (Pa)	Viscous entropy generation (10^{-4})	Turbulent entropy production
500	12.66	9.97
1,000	23.66	20.08
2,000	46.79	40.93
4,000	85.47	107.55

$$\gamma_{-} = \gamma_{\tau-} + \gamma_{D-} \tag{6}$$

In the formula, γ_{+} is the total forward flow resistance coefficient of the hyperbolic tube, and γ_{-} is the total reverse flow resistance coefficient of the tube. The output flow of the pump can be expressed as:

$$Q = \nabla V f \frac{(\gamma_{+} - \gamma_{-})}{(2 + \gamma_{+} + \gamma_{-})} \tag{7}$$

Where f is the driving frequency of the piezoelectric vibrator.

EXPERIMENTAL SETUP

In this paper, a stereolithography machine (SLA) was used to fabricate the valveless piezoelectric pump with conical tubes and the valveless piezoelectric pump with hyperbolic tubes. As shown in the left of **Figure 4**, the pump body is made of photosensitive resin. The tube parameters are shown in **Table 1**, the pump cavity diameter is 41 mm, the pump cavity depth is 0.8 mm, and the vibrator radius is 41 mm.

The experimental setup of the piezoelectric pumps with two tubes is shown in the right of **Figure 4**. The input AC voltage of the piezoelectric pump is set to 200 Vpp (peak-to-peak voltage). The reservoir contained a certain amount of deionized water. Take the small radius of the flow tube as the inlet and the flow tube with joints as the outlet, and the liquid level of the inlet and outlet are the same during the experiment. The analytical balance is used to measure the output flow of the piezoelectric pump per unit time under different frequencies. The accuracy of the analytical balance is 0.001 g.

SIMULATION ANALYSIS

Entropy Generation Theory

During the operation of the valveless piezoelectric pump, due to the viscosity of the working fluid and Reynolds stress, the consumed mechanical energy is irreversibly converted into internal energy. According to the second law of thermodynamics, the entropy generation theory is used to calculate the energy loss.

For turbulent flow, based on the Reynolds time-average equation, the entropy generation rate can be divided into two parts, the one is caused by the average velocity, called the direct dissipation term; the other is caused by the pulsating velocity, called the turbulent dissipation term. So, define the local total entropy production rate S_D per unit volume as:

$$S_D = S_{D1} + S_{D2} \tag{8}$$

In the formula, S_{D1} is the entropy production rate caused by the average speed, W/(m3·K); S_{D2} is the entropy production rate caused by the pulsating velocity, W/(m3·K).

TABLE 3 | Entropy production of hyperbolic tubes under different pressure difference.

Differential pressure (Pa)	Viscous entropy generation (10^{-4})	Turbulent entropy production
500	5.11	5.43
1,000	14.42	14.2
2,000	29.07	31.59
4,000	72.13	85.11

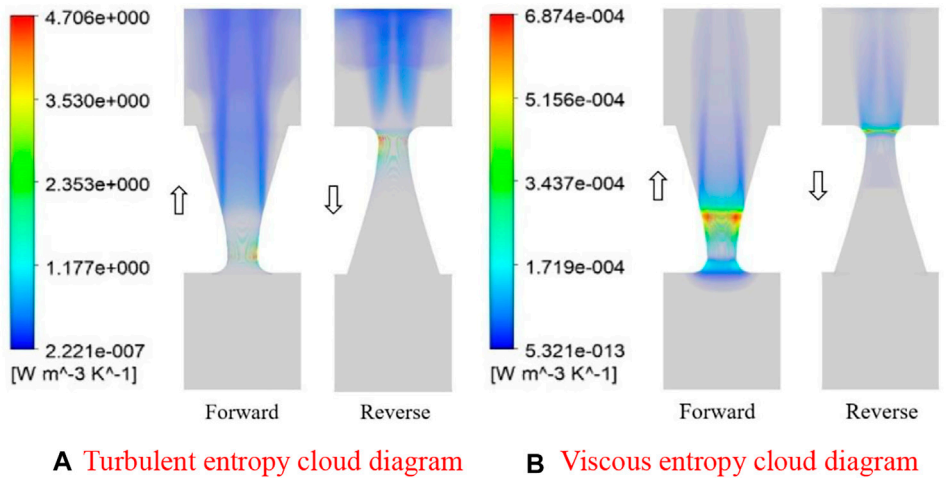

FIGURE 8 | Entropy cloud diagram of the conical tube. **(A)** Turbulent entropy cloud diagram **(B)** Viscous entropy cloud diagram.

The entropy production rate caused by the average speed is:

$$S_{D1} = \frac{\mu}{T}\left[\left(\frac{\partial \bar{u}}{\partial y}+\frac{\partial \bar{v}}{\partial x}\right)^2+\left(\frac{\partial \bar{u}}{\partial z}+\frac{\partial \bar{\omega}}{\partial x}\right)^2+\left(\frac{\partial \bar{\mu}}{\partial y}+\frac{\partial \bar{\omega}}{\partial y}\right)^2\right] + 2\frac{\mu}{T}\left[\left(\frac{\partial \bar{u}}{\partial x}\right)^2+\left(\frac{\partial \bar{v}}{\partial y}\right)^2+\left(\frac{\partial \bar{\omega}}{\partial z}\right)^2\right] \quad (9)$$

The entropy production rate caused by the pulsating velocity is

$$S_{D2} = \frac{\mu_{eff}}{T}\left[\left(\frac{\partial \mu'}{\partial y}+\frac{\partial v'}{\partial x}\right)^2+\left(\frac{\partial u'}{\partial z}+\frac{\partial v'}{\partial x}\right)^2+\left(\frac{\partial u'}{\partial y}+\frac{\partial \omega'}{\partial y}\right)^2\right] + 2\frac{\mu}{T}\left[\left(\frac{\partial u'}{\partial x}\right)^2+\left(\frac{\partial v'}{\partial y}\right)^2+\left(\frac{\partial \omega'}{\partial z}\right)^2\right] \quad (10)$$

Where $\bar{u}$, $\bar{v}$, $\bar{w}$, are the components of the average velocity in the x, y, and z directions, m/s; u', v', w' are the components of the pulsating velocity in the x, y, and z directions, m/s; T is the temperature, K; μ is the hydrodynamic viscosity, Pa·s; μ_{eff} is the effective dynamic viscosity of the fluid, Pa·s, which can be calculated by **Formula (11)**, where μ_t is the turbulent flow viscosity, Pa·s.

$$\mu_{eff} = \mu + \mu_t \quad (11)$$

However, the pulsating velocity component cannot be calculated in the Reynolds average equation. This paper adopts the k-epsilon turbulence (Shi et al., 2020; Han et al., 2021) model. Therefore, the entropy generation rate produced by the pulsating velocity can be approximated by the following formula.

$$S_{D2'} = \beta\frac{\rho f k}{T} \quad (12)$$

In the formula, the empirical coefficient β = 0.09, f is the characteristic frequency of turbulent pulsation, s^{-1}, k is turbulent kinetic energy, m^2/s^2; ρ is the density, kg/cm^3.

Integrating the above-mentioned parts of the entropy production rate in the integration area, the direct dissipation entropy production S'_{D1}(W/k) and the turbulent dissipation entropy production S'_{D2}(W/k) can be obtained respectively.

$$S'_{D1'} = \int S_{D1} dV \quad (13)$$

$$S'_{D2'} = \int S_{D2'} dV \quad (14)$$

Therefore, the entropy production of the mainstream area in the entire computational domain is:

$$S_D = S'_{D1'} + S'_{D2'} \quad (15)$$

According to the entropy generation calculation results of the conical tube and the hyperbolic tube, the resistance coefficient ε is used to describe the flow performance and defined in **Eq. 16**. the impedance ratio is defined in **Eq. 17**, which is adopted to describe the unidirectional transport performance of the tube.

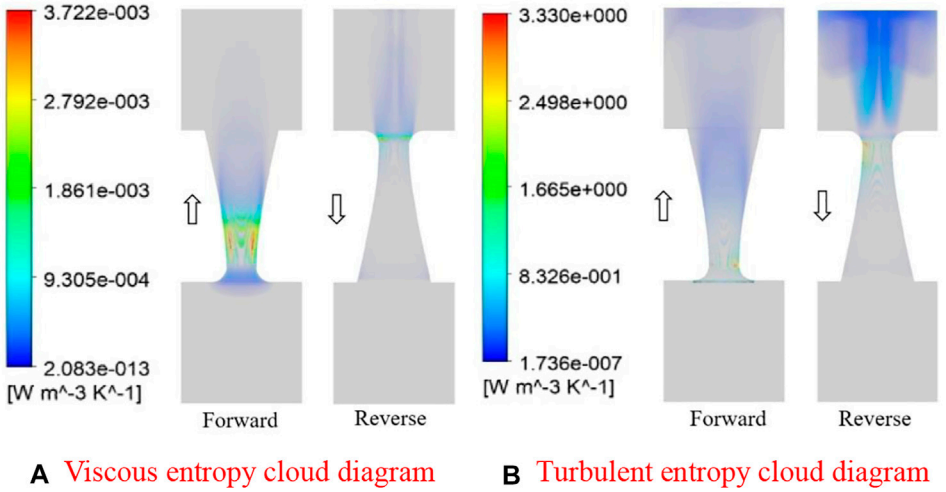

FIGURE 9 | Entropy cloud diagram of the hyperbolic tube. **(A)** Viscous entropy cloud diagram **(B)** Turbulent entropy cloud diagram.

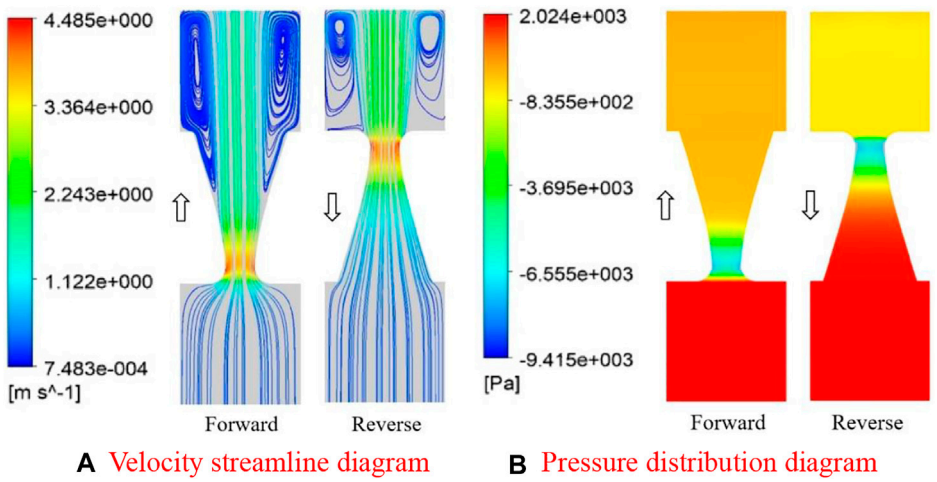

FIGURE 10 | Flow distribution simulation results of the conical tube. **(A)** Velocity streamline diagram **(B)** Pressure distribution diagram.

$$\varepsilon = \frac{2\nabla P}{\rho v^2} \tag{16}$$

$$\delta = \frac{\varepsilon_R}{\varepsilon_F} \tag{17}$$

Hyperbolic Tube Grid Establishment

The finite element models of the tubes are shown in **Figure 5** (the conical tube on the top and the hyperbolic tube on the bottom). The *k*-epsilon turbulence model is adopted, because there is small turbulence in tubes. The wall is a non-slip boundary, the pressure applied to the inlet is 500, 1,000, 2,000, and 4,000 Pa, the outlet of the tube is defined as 0 Pa, and the numerical convergence residual is set to 10^{-4}.

The grid independence of the model is verified. **Table 1** shows the calculation results of grid independence, where N is the number of grids, Q is the flow rate (kg/s), and r is the relative error. When the mesh numbers of the conical tube and the hyperbolic tube are 375,700 and 279,000 respectively, the error is less than 1%, so the finite element model is used to calculate the entropy generation.

RESULTS AND DISCUSSION

The experimental result of the pump flow rate is shown in **Figure 6**. The output flow rate of the piezoelectric pump with hyperbolic tubes is finally measured at a frequency of 40 Hz, which is 54 ml/min. The maximum output flow rate of the piezoelectric pump with conical tube is 47 ml/min. Therefore, the output performance of the piezoelectric pump with hyperbolic tubes is greater than that of the piezoelectric pump with conical tubes.

Calculate the viscous entropy production and turbulent entropy production under different pressure differences

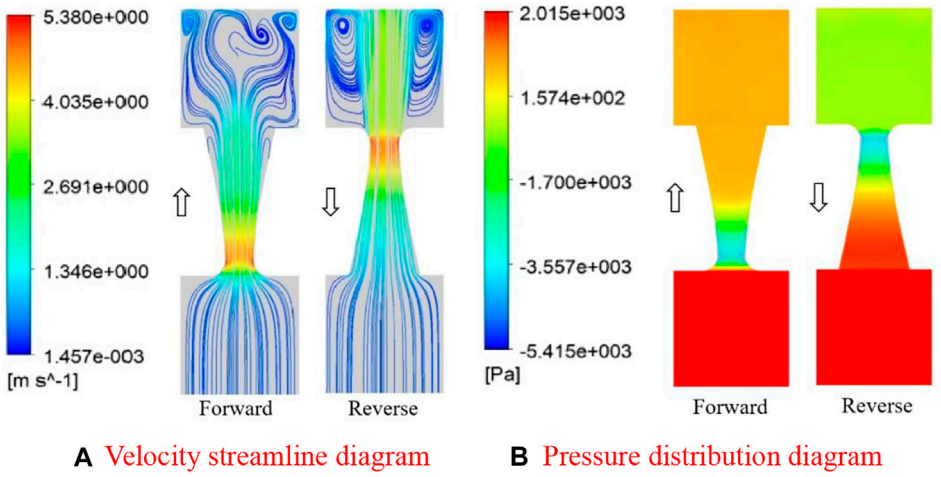

FIGURE 11 | Flow distribution simulation results of the hyperbolic tube. **(A)** Velocity streamline diagram **(B)** Pressure distribution diagram.

when the two tubes are flowing in the forward direction, as shown in **Table 2** and **Table 3**. It can be seen that under the same working conditions, the turbulent entropy production and viscous entropy production of the hyperbolic tube are smaller than that of the conical tube. Therefore, the output performance of the piezoelectric pump with hyperbolic tubes is better than that of the piezoelectric pump with conical tubes.

The difference between the forward and reverse flow resistance of the hyperbolic tube directly affects the cut-off performance, which in turn affects the output performance of the valveless piezoelectric pump with hyperbolic tubes.

Figure 7 shows that the forward flow resistance of the hyperbolic tube is smaller than the reverse flow resistance, indicating that unidirectional transport of fluid can be achieved. Moreover, the impedance ratio of the hyperbolic tube is larger than that of the conical tube, indicating that the unidirectional transport performance of the hyperbolic tube is better than that of the conical tube.

Figure 8A shows the turbulent entropy production of the conical tube. The turbulent entropy production is mainly caused by turbulent dissipation. It can be seen that the turbulent entropy production is symmetrically distributed on the axis of the conical tube, and it is greater in the reverse flow than that in the forward flow. **Figure 8B** shows the viscous entropy production of the conical tube. Compared with the turbulent entropy production, the viscous entropy production is smaller. The viscous entropy production is mainly caused by the dissipation of the irreversible viscous entropy production. The viscous entropy production is at the smallest radius of the tube. The maximum, decreases as the tube spreads.

Figure 9A shows the viscous entropy production of the hyperbolic tube. Compared with the conical tube, the viscous entropy production area of the hyperbolic tube in the forward and reverse flow is smaller than that of the conical tube. **Figure 9B** shows the turbulent entropy production of the hyperbolic tube. Compared with the conical tube, the turbulent entropy production of the hyperbolic tube is much smaller than that of the conical tube, and the viscous entropy production is less dissipated. In summary, the entropy production at the smallest channel diameter of the tube is larger, and both viscous entropy production and turbulent entropy production are positively correlated with the pressure difference, but the turbulent entropy production and viscous entropy production of the hyperbolic tube are both smaller than those of the conical tube.

Figure 10A and **Figure 11A**respectively show the velocity cloud diagrams of the conical tube and the hyperbolic tube. It can be seen that the flow velocity of the fluid in the hyperbolic tube is greater than that in the conical tube. In addition, there is a larger vortex in the conical tube, which is larger than the hyperbolic tube, which has a greater impact on the flow of fluid in the tube. **Figure 10B** and **Figure 11B** respectively show the pressure cloud diagrams of the conical tube and the hyperbolic tube. It can be seen that the reverse cut-off performance of the hyperbolic tube is better than that of the conical tube.

Therefore, under the same working conditions, the energy loss of the hyperbolic tube is smaller than that of the conical tube, and the output performance of the hyperbolic tube piezoelectric pump is better than that of the conical tube piezoelectric pump.

CONCLUSION

In order to improve the flow characteristics of the valveless piezoelectric pump, two valveless piezoelectric pumps with tubes with different curves as the inlet and outlet pipes were developed. The prototypes of the piezoelectric pumps were fabricated, and the experimental results showed that the hyperbolic tubes had the largest flow rate, and the corresponding valveless piezoelectric pump had better output performance. The entropy generation theory was used to analyze the energy loss of the tube, and the entropy production values of the tubes were calculated. The results show that the total entropy produced by the hyperbolic curve

tube is smaller than the entropy produced by the conical tube. The entropy generation theory can effectively predict and analyze the energy loss of the tubes, and provide a reference for the structural design and performance optimization of the piezoelectric pump.

DATA AVAILABILITY STATEMENT

The datasets presented in this study can be found in online repositories. The names of the repository/repositories and accession number(s) can be found in the article/supplementary material.

AUTHOR CONTRIBUTIONS

QY and JC contributed to conception and design of the study. QY and JC performed the simulation analysis. QY wrote the first draft of the manuscript. JC wrote sections of the manuscript. All authors contributed to manuscript revision, read, and approved the submitted version.

REFERENCES

Bian, K., Huang, Z., Bao, Q. B., Zhang, J. H., Lai, L., Chen, X. S., et al. (2020). Design and experiment of Streamlined Piezoelectric Pump with Low Vortex and Large Flow Rate. *Trans. Nanjing Univ. Aeronautics Astronautics* 37 (01), 155–163. doi:10.16356/j.1005-1120.2020.01.014

Fadl, A., Demming, S., Zhang, Z., Büttgenbach, S., Krafczyk, M., and Meyer, D. M. L. (2010). A Multifunction and Bidirectional Valve-Less Rectification Micropump Based on Bifurcation Geometry. *Microfluid Nanofluid* 9, 267–280. doi:10.1007/s10404-009-0544-0

Feng, L., Jin, Z., Zhou, R., Xu, M., Qin, L., and Li, S. (2021). Thermodynamic Analysis of an Ammonia-Water Solution Cross-type Absorption-Resorption Heat Pump System. *Appl. Therm. Eng.* 198, 117460. doi:10.1016/j.applthermaleng.2021.117460

Gamboa, A. R., Morris, C. J., and Forster, F. K. (2005). Improvements in Fixed-Valve Micropump Performance through Shape Optimization of Valves. *J. Fluids Eng.* 127, 339–346. doi:10.1115/1.1891151

Hamid, N. A., Majlis, B. Y., Yunas, J., Syafeeza, A. R., Wong, Y. C., and Ibrahim, M. (2017). A Stack Bonded Thermo-Pneumatic Micro-pump Utilizing Polyimide Based Actuator Membrane for Biomedical Applications. *Microsyst Technol.* 23, 4037–4043. doi:10.1007/s00542-016-2951-y

Han, Y., Zhou, L., Bai, L., Shi, W., and Agarwal, R. (2021). Comparison and Validation of Various Turbulence Models for U-bend Flow with a Magnetic Resonance Velocimetry experiment. *Phys. Fluids* 33, 125117. doi:10.1063/5.0073910

Huang, J., Li, K., Chen, G., Gong, J., Zhang, Q., and Wang, Y. (2021). Design and Experimental Verification of Variable-Structure Vortex Tubes for Valveless Piezoelectric Pump Translating High-Viscosity Liquid Based on the Entropy Generation. *Sensors Actuators A: Phys.* 331, 112973. doi:10.1016/j.sna.2021.112973

Huang, J., Zhang, J., Wang, S., and Liu, W. (2014). Analysis of the Flow Rate Characteristics of Valveless Piezoelectric Pump with Fractal-like Y-Shape Branching Tubes. *Chin. J. Mech. Eng.* 27, 628–634. doi:10.3901/cjme.2014.03.628

Huang, J., Zou, L., Li, Z., Wang, X., Zhang, Q., and Wang, Y. (2020). Development and Performance Comparison of Valveless Piezoelectric Pumps with Asymmetrical Channels. *Sensors Actuators A: Phys.* 314, 112241. doi:10.1016/j.sna.2020.112241

Huang, J., Zou, L., Tian, P., Wang, Y., and Zhang, Q. (2019). Development of a Valveless Piezoelectric Pump with Vortex Diodes. *J. Micromech. Microeng.* 29 (12), 125006. doi:10.1088/1361-6439/ab4852

Leng, X.-f., Zhang, J.-h., Jiang, Y., Zhang, J.-Y., Sun, X.-c., and Lin, X.-g. (2013). Theory and Experimental Verification of Spiral Flow Tube-type Valveless Piezoelectric Pump with Gyroscopic Effect. *Sensors Actuators A: Phys.* 195, 1–6. doi:10.1016/j.sna.2013.02.026

Li, H., Liu, J., Li, K., and Liu, Y. (2021). A Review of Recent Studies on Piezoelectric Pumps and Their Applications. *Mech. Syst. Signal Process.* 151, 107393. doi:10.1016/j.ymssp.2020.107393

Ma, H.-K., Luo, W.-F., and Lin, J.-Y. (2015). Development of a Piezoelectric Micropump with Novel Separable Design for Medical Applications. *Sensors Actuators A: Phys.* 236, 57–66. doi:10.1016/j.sna.2015.10.010

Ma, H. K., Chen, R. H., Yu, N. S., and Hsu, Y. H. (2016). A Miniature Circular Pump with a Piezoelectric Bimorph and a Disposable Chamber for Biomedical Applications. *Sensors Actuators A: Phys.* 251, 108–118. doi:10.1016/j.sna.2016.10.010

Ma, T., Sun, S., Li, B., and Chu, J. (2019). Piezoelectric Peristaltic Micropump Integrated on a Microfluidic Chip. *Sensors Actuators A: Phys.* 292, 90–96. doi:10.1016/j.sna.2019.04.005

Mi, S., Pu, H., Xia, S., and Sun, W. (2020). A Minimized Valveless Electromagnetic Micropump for Microfluidic Actuation on Organ Chips. *Sensors Actuators A: Phys.* 301, 111704. doi:10.1016/j.sna.2019.111704

Morris, C. J., and Forster, F. K. (2003). Low-order Modeling of Resonance for Fixed-Valve Micropumps Based on First Principles. *J. Microelectromech. Syst.* 12, 325–334. doi:10.1109/jmems.2003.809965

Olsson, A., Enoksson, P., Stemme, G., and Stemme, E. (1997). Micromachined Flat-Walled Valveless Diffuser Pumps. *J. Microelectromech. Syst.* 6, 161–166. doi:10.1109/84.585794

Robertson, J. M., Rodriguez, R. X., Holmes, L. R., Mather, P. T., and Wetzel, E. D. (2016). Thermally Driven Microfluidic Pumping via Reversible Shape Memory Polymers. *Smart Mater. Struct.* 25 (8), 085043. doi:10.1088/0964-1726/25/8/085043

Rusli, M., Chee, P. S., Arsat, R., Lau, K. X., and Leow, P. L. (2018). Electromagnetic Actuation Dual-Chamber Bidirectional Flow Micropump. *Sensors Actuators A: Phys.* 282, 17–27. doi:10.1016/j.sna.2018.08.047

Shi, L., Zhu, J., Tang, F., and Wang, C. (2020). Multi-Disciplinary Optimization Design of Axial-Flow Pump Impellers Based on the Approximation Model. *Energies* 13 (4), 779. doi:10.3390/en13040779

Singhal, V., Garimella, S. V., and Raman, A. (20042004). Microscale Pumping Technologies for Microchannel Cooling Systems. *Appl. Mech. Rev.* 57 (1), 191. doi:10.1115/1.1695401

Skye, H. M., and Wu, W. (2021). Experiments and Exergy Analysis for a Carbon Dioxide Ground-Source Heat Pump in Cooling Mode. *Int. J. Refrigeration* 131, 920–937. doi:10.1016/j.ijrefrig.2021.08.018

Stemme, E., and Stemme, G. (1993). A Valveless Diffuser/nozzle-Based Fluid Pump. *Sensors Actuators A: Phys.* 39, 159–167. doi:10.1016/0924-4247(93)80213-z

Tang, S., Zhu, Y., and Yuan, S. (2021). An Improved Convolutional Neural Network with an Adaptable Learning Rate towards Multi-Signal Fault Diagnosis of Hydraulic Piston Pump. *Adv. Eng. Inform.* 50, 101406. doi:10.1016/j.aei.2021.101406

Wang, H., Long, B., Wang, C., Han, C., and Li, L. (2020). Effects of the Impeller Blade with a Slot Structure on the Centrifugal Pump Performance. *Energies* 13 (7), 1628. doi:10.3390/en13071628

Zhang, J.-H., Wang, Y., and Huang, J. (2017). Advances in Valveless Piezoelectric Pump with Cone-Shaped Tubes. *Chin. J. Mech. Eng.* 30 (4), 766–781. doi:10.1007/s10033-017-0151-z

Zhang, J., Lu, J., Xia, Q-X., Kou, J., and Ren, G. (2008). Working Principle and Flux Characteristics of Valve-Less Piezoelectric Pump with Y-Shape Tubes for Transporting Cells and Macromolecule. *Jme* 44, 92–99. doi:10.3901/jme.2008.09.092

Conflict of Interest: The authors declare that the research was conducted in the absence of any commercial or financial relationships that could be construed as a potential conflict of interest.

frontiers in Energy Research

ORIGINAL RESEARCH
published: 17 March 2022
doi: 10.3389/fenrg.2022.866037

Experimental Study on Operational Stability of Centrifugal Pumps of Varying Impeller Types Based on External Characteristic, Pressure Pulsation and Vibration Characteristic Tests

XiaoQi Jia[1], *Qingyang Chu*[1], *Li Zhang*[2] *and ZuChao Zhu*[1]*

[1]*Key Laboratory of Fluid Transmission Technology of Zhejiang Province, Zhejiang Sci-Tech University, Hangzhou, China,*
[2]*Department of Application and Engineering, Zhejiang Economic and Trade Polytechnical, Hangzhou, China*

This study performed external characteristics, dynamic pressure, and vibration tests on the closed impeller model, semi-open type impeller model, and open impeller model in order to study the influence of the impeller structure on the operational stability of the pump. According to the research findings, the external characteristics of the three impellers enjoyed favorable stability with flat curves under low flow rates. As the flow increases, the stability of the external characteristics weakens, and the poorest stability can be observed in the open impeller, while the enclosed impeller has the best stability under a large flow rate. In addition, intense pressure fluctuations arise near the casing tongue due to the dynamic and static interference between the blade and the casing tongue, causing a large amplitude of pressure pulsation near the casing tongue and the pump outlet. It can be seen that the stability of pressure pulsation of the closed impeller in the casing tongue area was the best, whereas the stability of pressure pulsation of the open impeller was the poorest. The minimum casing vibration can be found in the closed impeller, followed by the semi-open impeller, and the open impeller, with the maximum vibration. In addition, the optimum stability of rotor vibration can be observed in the closed impeller, semi-open impeller, and open impeller with similar stability of rotor vibration.

Keywords: external characteristic, pressure pulsation, vibration characteristic, stability, centrifugal pump

OPEN ACCESS

Edited by:
Ling Zhou,
Jiangsu University, China

Reviewed by:
Ivan Pavlenko,
Sumy State University, Ukraine
Alin Bosioc,
Politehnica University of Timişoara, Romania

****Correspondence:***
ZuChao Zhu
zhuzuchao01@163.com

Specialty section:
This article was submitted to Process and Energy Systems Engineering, a section of the journal Frontiers in Energy Research

Received: *30 January 2022*
Accepted: *21 February 2022*
Published: *17 March 2022*

Citation:
Jia X, Chu Q, Zhang L and Zhu Z (2022) Experimental Study on Operational Stability of Centrifugal Pumps of Varying Impeller Types Based on External Characteristic, Pressure Pulsation and Vibration Characteristic Tests. Front. Energy Res. 10:866037. doi: 10.3389/fenrg.2022.866037

INTRODUCTION

The centrifugal pump should be of high security and reliability during operation; otherwise, it might affect the normal operation. Hence, the stability of the operating condition of the centrifugal pumps has become a hotspot issue of high concern. Centrifugal pumps are widely used in the oil and gas industry (Bellary and Samad, 2016), aerospace engineering (Hong et al., 2013), marine engineering (Wang. et al., 2020), and other fields. Centrifugal pumps, in general, are equipped with varying types of impellers for different pumped mediums. An open impeller is suitable for conveying materials containing a large amount of suspended matter, a semi-open impeller is suitable for conveying easy precipitation or containing particles of material, and a closed impeller is suitable for conveying clean liquid without impurities (Gulich, 2010). Different impeller types have significant impacts on the

operational stability and reliability of the centrifugal pump, mainly stable performance and vibration stability of the pump. To be specific, the stable performance of the pump involves a flat lift curve and equally distributed pressure, while vibration stability consists of satisfactory vibration characteristics of the rotor system and casing vibration characteristics. Stable operation of the centrifugal pump is normally affected by many complex flows in the operation of centrifugal pumps, such as interstitial flow (Wood et al., 1965), secondary flow (Klaus and Rainer, 2005), eddy current (Zhu and Kamemoto., 2005), and backflow (Yamamoto and Tsujimoto, 2009), as well as a variety of unstable phenomena occurring in the operation, such as rotating stall (Sano et al., 2002), rotor-stator interaction (Zheng et al., 2016), cavitation (Zhang et al., 2015), and vibration (Jia et al., 2015). Chen et al. (2022a) utilized a TR-PIV system to measure the flow fields in a special voluteless centrifugal pump. The contributions to the overall energy and the spatial/temporal behavior of the large-scale flow structures were analyzed in detail, and the dynamic and kinematic energy characteristics of the coherent flow structures that were in the impeller were revealed. Chen et al. (2022b) explored a method to directly describe the loss distribution trend of the flow field through the PIV

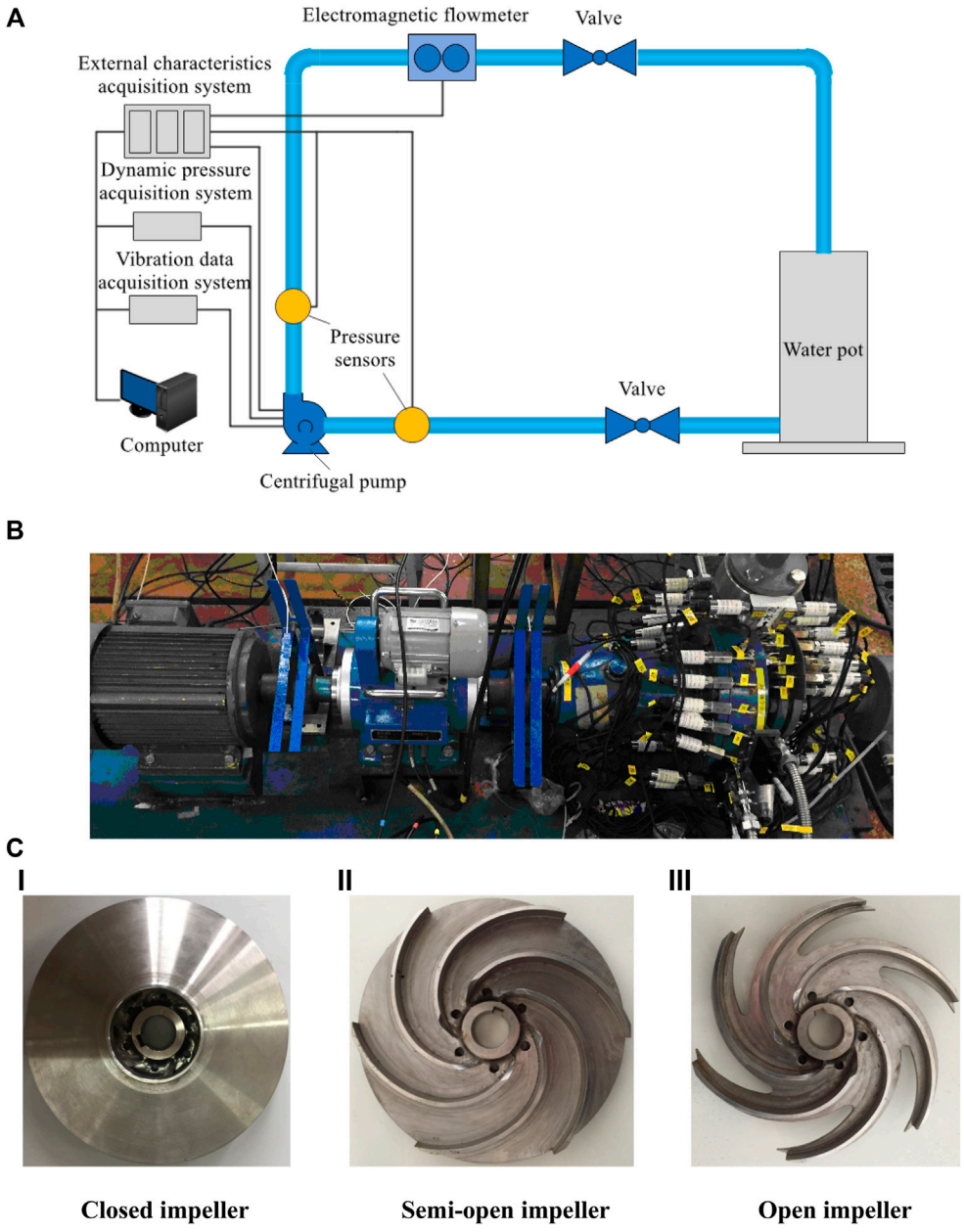

FIGURE 1 | Experimental apparatus: **(A)** testing system of the centrifugal pump and **(B)** testing centrifugal pump (b): (I) closed impeller, (II) semi-open impeller, and (III) open impeller **(C)** Testing centrifugal impellers.

TABLE 1 | Performance parameters and geometric parameters of the centrifugal pump.

Parameter/symbol	Value	Parameter/symbol	Value
Head/H_{des}	39 m	Rotate speed/n_{des}	3,000 rpm
Flow rate/Q_{des}	10 m^3/h	Specific speed/n_s	41.91
Pump outlet diameter/D_d	40 mm	Impeller inlet diameter/D_1	50 mm
Blade thickness/δ	3 mm	Impeller outlet diameter/D_2	160 mm
Blade inlet angle/β_1	25°	Volute inlet diameter/D_3	165 mm
Blade outlet angle/β_2	25°	Blade outlet width/b_1	10 mm
Blade number/Z	6	Volute inlet width/b_2	15 mm

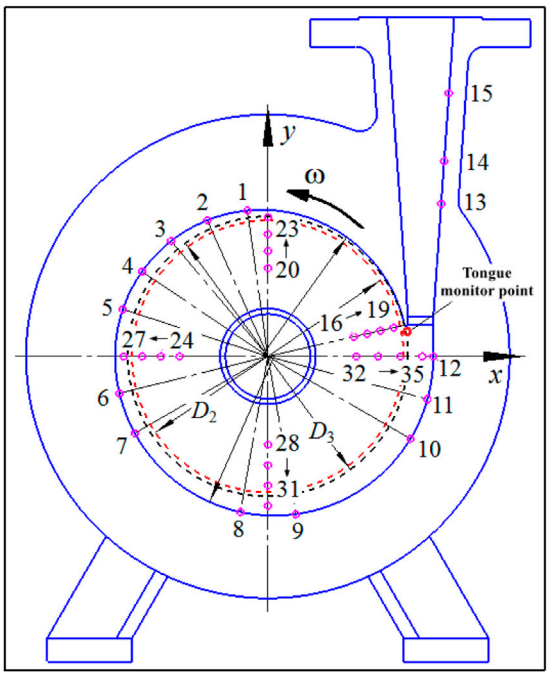

FIGURE 2 | Locations of the pressure testing points.

experiment. Results show the distribution of local pressure head increase (H_{pr}) is affected mainly by the inlet flow field of the impeller passage, while the maximum value region of local velocity head increase (H_{vr}) along the radial direction is located at the downstream of the unstable region on the blade suction side and at the center of the unstable region on the pressure side. A vast number of numerical and experimental studies have been performed on the pressure pulsation and vibration characteristics of centrifugal pumps under unsteady conditions. He (1996) studied the mechanism of pressure pulsation of the pump and indicated that vibration and noise of the pump are related to the pressure pulsation of the pump. Pressure pulsation mainly consists of axial frequency and blade frequency pressure pulsations. Yuan et al. (2010) pointed out that no evident high-frequency component was found in the pressure pulsation of the volute under design flow rate. The dominant frequency at the same monitoring point was constant, but its amplitude varied under different flow rates. Specifically, the amplitude was large under low flow rate, reaching the minimum under design flow rate, according to Zhu and Hu (2010). Moreover, the centrifugal pump is also affected by the rotor–stator interaction and unsteady internal flow apart from the abovementioned influence of different hydraulic conditions on pressure pulsation, since asymmetry of pressure distribution and pressure pulsation are inevitable. Jia et al. (2019) studied the pressure distributions of the volute and the front sleeving wall under different flow rates, with the results showing that the asymmetry of the pressure distribution and the magnitude of the pressure decrease with the rising flow rate. The rotor–stator interaction between the rotating impeller and the fixed volute might lead to high-frequency unsteady pulsation inside the volute and low-frequency unsteady pressure pulsation inside the impeller. Yang et al. (2014) studied the influence of radial clearance between the blade tip of the impeller and the casing tongue on the performance and pressure pulsation of the pump as a turbine, showing that the high-frequency unsteady amplitude will be increased and the pressure pulsation in the volute will be decreased with the increase in radial clearance. Cui et al. (2015) studied the unsteady flow characteristics of the low specific speed centrifugal pump under varied flow rates, indicating that the flow instability resulted from the interaction of the impeller and the volute, thereby leading to the instability in the circumferential direction. As the impeller and the volute are essential for the generation of pressure pulsation inside the pump, their geometric parameters were modified in some studies to lower the pressure pulsation and vibration. Zhu et al. (2007) proved that the geometrical shape of the impeller blades exerted an impact on the unstable pressure pulsation. Tao et al. (2016) studied the effect of blade thickness on the transient flow characteristics of a centrifugal slurry pump with semi-open impellers. According to the result, the greater the blade thickness, the larger the pressure pulsation at the impeller outlet. This article studied closed, semi-open, and open impellers through performing external characteristics, dynamic pressure, and vibration characteristics tests under full flow rates, as well as comparatively analyzed the external characteristics, pressure pulsation, and vibration characteristics of the three impellers.

To sum up, most of the current centrifugal pump impeller structures are for a single type, and comparing the flow characteristics of different types of centrifugal pump impeller is impossible. Therefore, studying the influence of different impellers structures on the stability and reliability of centrifugal pumps is very important. In this article, the performance stability and vibration stability of centrifugal pumps with three typical impeller models (closed, semi-open, and open) are studied through external characteristic tests, dynamic pressure tests, and vibration tests.

EXPERIMENTAL APPARATUS

The test bench designed for the operational stability of the centrifugal pump described in this study is composed of data acquisition systems, such as dynamic pressure, vibration characteristics, and external characteristics, as well as

TABLE 2 | Locations of the pressure testing points.

Circumferential pressure hole		Radial pressure hole	
Point	θ (°)		Location dimension
1	8	A (16–19)	R_1 = 52 mm、Δ = 10 mm
2	24		
3	40		
4	56	B (20–23)	R_2 = 52 mm、Δ = 11 mm
5	72		
6	104		
7	120	C (24–27)	R_3 = 52 mm、Δ = 12 mm
8	170		
9	190		
10	240	D (28–31)	R_4 = 52 mm、Δ = 13 mm
11	255		
12	270		
13	h = 90 mm	E (32–35)	R_5 = 52 mm、Δ = 8 mm
14	h = 115 mm		
15	h = 130 mm		

centrifugal pump, water tank, high-precision electromagnetic flowmeter, valves, water inlet and outlet pipelines, and motors. The circuits of the test system are shown in **Figure 1A**. A low specific speed centrifugal pump with three impeller types at a rotational speed of 3,000 r/min was tested. Specific performance parameters and geometric parameters are shown in **Table 1**. The physical diagram of the model centrifugal pump test bench is demonstrated in **Figure 1B**, and the physical diagrams of the three impellers of the model pump are presented in **Figure 1C**. Note that three impellers with the same molded lines have six blades. Clearwater is used as the experimental medium in this study.

The centrifugal pump dynamic pressure test system is composed of a pump, pressure sensor, and dynamic pressure data acquisition system. The locations of pressure measuring points of the centrifugal pump body are given in **Figure 2** and **Table 2**.

(The layout of monitoring points should reflect the pressure value of the centrifugal pump and its changing trend as far as possible. Therefore, on the premise of ensuring that effective data can be obtained, monitoring points should be arranged as much as possible in key positions with large pressure changes in order to ensure the performance stability of the centrifugal pump to make accurate judgment. This explains why the pressure testing points are not symmetrical on the casing. Due to the large unstable flow in the impeller runner, tongue area, and pump outlet, the monitoring points in these locations are properly encrypted, so as to more accurately reflect the pressure change of the centrifugal pump.)

The centrifugal pump vibration test system comprised an acceleration sensor, an eddy current displacement sensor, and a data acquisition system. The acceleration sensor is a piezoelectric triaxial acceleration sensor that can simultaneously measure the vibration acceleration in the directions of x, y, and z, with a sensitivity of 10 mV/g, a measuring range of 500 g, and a response frequency ranging from 0.5 to 10 kHz. Acceleration sensors are installed at the pump inlet, pump outlet, casing tongue area, and pump body. As can be seen from the installation position of the acceleration sensor in **Figure 3**, measuring point 1 is installed at the position near the volute tongue, measuring point 2 is installed on the pump outlet flange, measuring point 3 is installed on the pump body, and measuring point 4 is installed on the inlet flange. The sensitivity of the eddy current vibration displacement sensor used is 4 mV/μm, with the effective measuring distance ranging from 0 to 2 mm, and the frequency response ranging from 0 to 10 kHz. The installed position of the eddy current vibration displacement sensor is shown in **Figure 3**, with the horizontal direction defined as direction x and the vertical direction as direction y.

External characteristics, pressure pulsation, and vibration data are collected synchronously *via* 64-channel data collectors with a maximum sampling frequency of 204.8 kHz. Sampling can be performed by each channel in a simultaneous and parallel manner with an amplitude accuracy of 0.1% FS (1 V input, ≤10 kHz) and a frequency accuracy of 0.001%.

RESULTS AND DISCUSSION

External Characteristics

External characteristic curves of the three impeller model pumps under full flow rates are presented in **Figure 4**. Evidently, the closed impeller has the highest lift and efficiency, whereas the open impeller has the smallest lift and efficiency. The lift curves of the three impellers are relatively stable and flat at small flow rates. When the flow rate increased from $1.0Q_{des}$ to $1.4Q_{des}$, the lifts of the three impellers dropped significantly. Specifically, the lifts of the closed impeller, the semi-open impeller, and the open impeller were dropped by 19.05%, 29.86%, and 38.95%, respectively. Evidently, the lifts of the three impellers are relatively stable under small flow rates, which become less stable with rising flow rates. In addition, the closed impeller has the best lift stability, while the open impeller has the worst lift stability.

Circumferential pressure distribution profiles of the three impeller volute walls under different flow rates are shown in **Figure 5**. Apparently, the pressures of the three impellers are progressively decreased with the increasing flow rate as the strengthening degree of pressure declines. The pressure change of the closed impeller is less affected by the flow rate, followed by the semi-open impeller, and the wall pressure of the volute of the open impeller is most sensitive to flow change. The pressure drop of the closed impeller near the pump outlet is smaller than that of the other two impellers with the rising flow rate, and the open impeller has the most obvious pressure drop.

When the flow rate is small (ranging from 0 to $0.8Q_{des}$), the pressure will be increased from the circumferential position of 0° to the pump outlet, and the maximum will be reached at the impeller outlet. The pressure increase gradient is increased near the casing tongue of the volute, and the pressure increase trend becomes more significant with the rising flow rate. The pressure increase near the volute reaches 40 kPa at $0–0.4Q_{des}$, while the pressure increase is only 10 kPa at $0.8Q_{des}$ for the closed impeller. The pressure increase trend becomes gentle from the volute

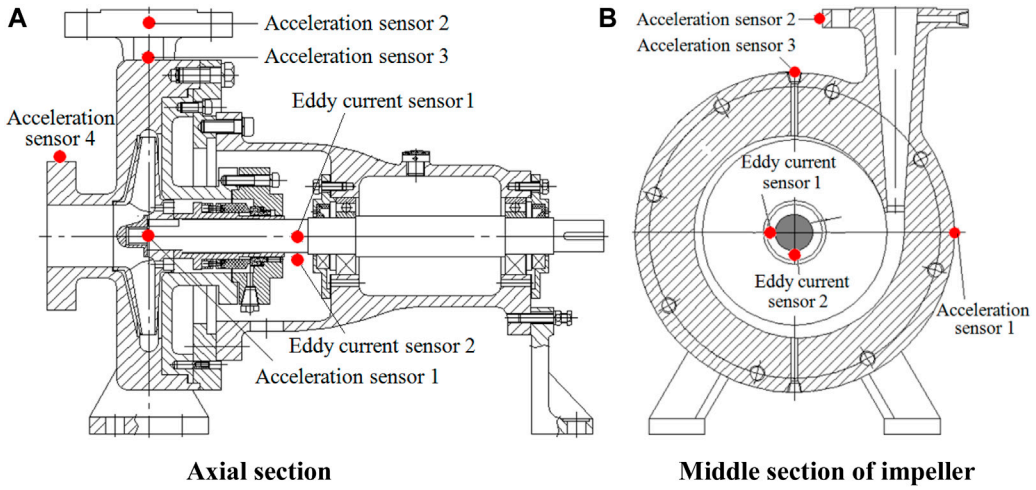

FIGURE 3 | Install locations of acceleration sensors and eddy current sensors: **(A)** axial section and **(B)** middle section of impeller.

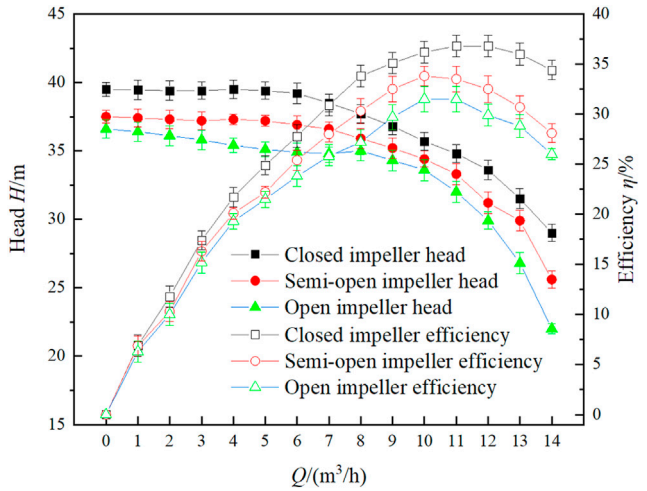

FIGURE 4 | External characteristics of the centrifugal pump with three impellers.

tongue to the pump outlet, and the pressure increase for the open impeller reaches only 15 kPa. When the flow rate is large, the pressure at the casing tongue of the volute will suddenly decrease, and the pressure drop range will become more severe with the further increasing flow rate with the pressure drop gradient reaching its maximum at $1.4Q_{des}$. The closed impeller, semi-open impeller, and open impeller reached the maximum pressure drop amplitudes of 39 kPa, 45 kPa, and 51 kPa, respectively, at the separation tongue, and the pressure is rising quickly from the casing tongue of the volute to the pump outlet, with their pressure rise amplitudes reaching 60 kPa, 46 kPa, and 25 kPa, respectively. This showed that the closed impeller has the strongest pressure recovery capability with good pressure distribution stability, while the open impeller has the weakest pressure recovery capability with the worst pressure distribution stability at large flow rates from the volute tongue to the pump outlet.

Radial static pressure distribution profiles of the three impeller front cover walls under different flow rates are shown in **Figure 6**. As can be observed from the figure, the closed impeller has the largest pressure value, followed by the semi-open impeller, and the open impeller has the smallest pressure value. The pressure is on the rise along the direction from the impeller inlet to the outlet. The maximum pressure increase gradient is found in group D, and then pressure drops rapidly in group E. The closed impeller has the smallest degree of pressure drop in group E, followed by the semi-open impeller, and the open impeller has the greatest degree of pressure drop. As group E is located near the volute tongue area, the quick drop in static pressure might lead to a sharp increase in the fluid speed of the tongue area. As a consequence, energy loss caused by the collision between fluids as well as between fluid and wall might increase, conveying slanted against fluids. This shows that the stable pressure distribution of the closed impeller in the tongue area is most conducive to fluid conveying, whereas the excessive pressure drop of the open impeller in the tongue area is least conducive to fluid conveying.

Pressure Pulsation Characteristic

Pressure fluctuation distribution profiles of the three impeller volute walls under design flow rates in the frequency domain are shown in **Figure 7**. Apparently, the axial frequency and the blade frequency of the closed impeller test are 49.85 Hz and 298.16 Hz, respectively; the axial frequency and the blade frequency of the semi-open impeller test are 49.79 Hz and 298.03 Hz, respectively; and the axial frequency and the blade frequency of the open impeller test are 49.73 Hz and 297.52 Hz, respectively. As can be observed from **Figure 9**, the degree of pressure pulsation is strengthened along the rotating direction of the impeller from the pressure measuring point 1 to 15, reaching the maximum at the pump outlet. The dominant frequency of pressure pulsation is concentrated at the shaft frequency at measuring points 1 to 12,

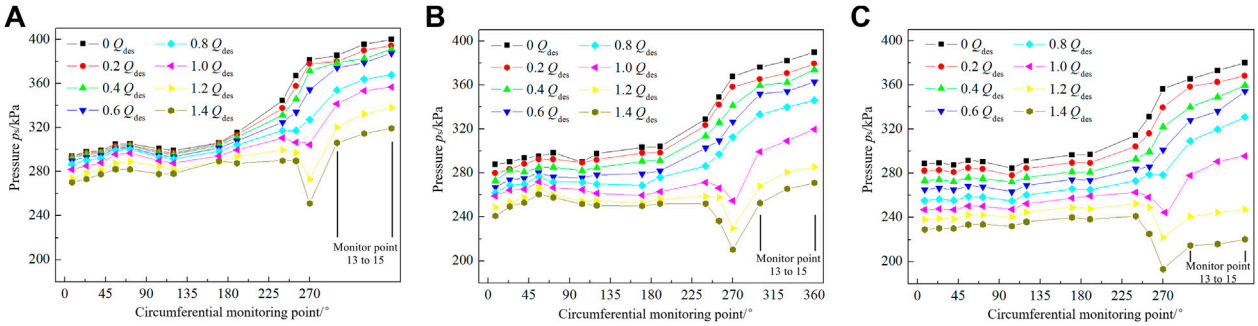

FIGURE 5 | Static pressure on volute casing of the centrifugal pump with three impellers: **(A)** closed impeller, **(B)** semi-open impeller, and **(C)** open impeller.

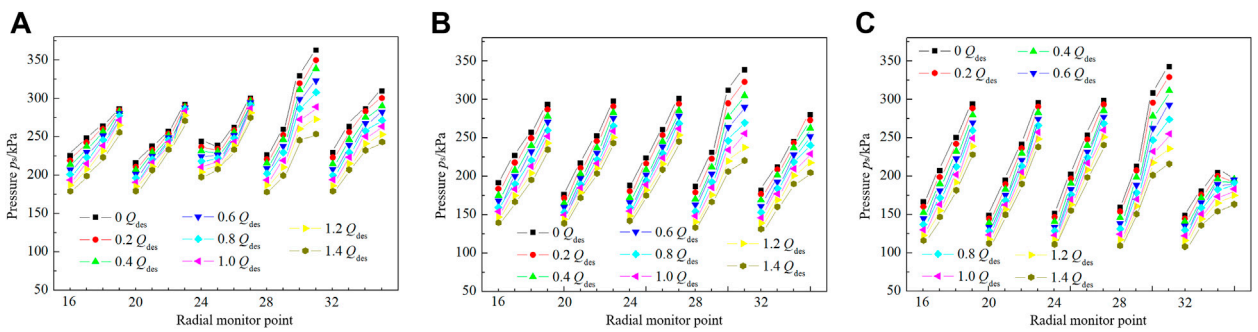

FIGURE 6 | Static pressure on front casing of the centrifugal pump with three impellers: **(A)** closed impeller, **(B)** semi-open impeller, and **(C)** open impeller.

while the dominant frequency of pressure pulsation is concentrated at the blade frequency at the pressure measuring points (measuring points 13–15) of the pump outlet. A frequency range of broadband pulsation exists at all pressure measuring points. So the position of the broadband pulsation moves gradually from near the shaft frequency to near the blade frequency from measuring points 1 to 15. The broadband pulsation is concentrated at the blade frequency or above at the pump outlet. The open impeller has the largest pressure pulsation amplitude, and conversely, the closed impeller has the smallest amplitude at the same measuring point. In the model pump, pressure pulsation at varying positions in the volute has different effects on the operational stability of the pump; the effect degree gradually increases from the starting point of the volute spiral to the outlet along the rotation direction, and the operational stability of the pump is dependent on pressure pulsations at the pump outlet and the casing tongue of the volute.

Pressure fluctuation distribution profiles of the three impeller volute walls under design flow rates in the frequency domain are shown in **Figure 8**. Apparently, the axial frequency and the blade frequency of the closed impeller test are 49.85 Hz and 298.16 Hz, respectively; the axial frequency and the blade frequency of the semi-open impeller test are 49.79 Hz and 298.03 Hz, respectively; and the axial frequency and the blade frequency of the open impeller test are 49.73 Hz and 297.52 Hz, respectively. As can be observed from **Figure 8**, the maximum pressure pulsation amplitude appeared in group D, and the maximum pressure pulsation of the closed impeller was the smallest in group D, followed by the open-plate impeller, and the open-type impeller was the largest. The amplitude of pressure pulsation in group E is small. Because group E is close to the tongue region, pressure pulsation here will cause a large energy loss. In the model pump, the effect degree on the operational stability of the pump gradually increases from the inlet of the impeller to the outlet.

To obtain the relationship between the pressure pulsation intensity and the flow rate at different circumferential positions of the volute in a rotation cycle, the dimensionless coefficient of the event-related pressure pulsation intensity is defined as Cpsd, which can be expressed as

$$C_{\mathrm{psd}} = \frac{\sqrt{\frac{1}{N}\sum_{i=0}^{N-1}\left(p(x,y,z,t_i) - \frac{1}{N}\sum_{i=1}^{N}p(x,y,z,t_i)\right)^2}}{\frac{1}{2}\rho u_2^2} = \frac{\sqrt{\frac{1}{N}\sum_{i=0}^{N-1}(p-\bar{p})^2}}{\frac{1}{2}\rho u_2^2}, \quad (1)$$

where N is the number of time steps in a stable rotation cycle (it is 360 in this paper), $p(x, y, z, t_i)$ is the static pressure value of the node (x, y, z) at the ith time step, ρ is the fluid density, and u_2 is the peripheral speed of the impeller outlet.

The pressure pulsation intensity at monitoring points 1–15 of the three impellers under design flow rate is presented in **Figure 9**. Pressure pulsation amplitudes at measuring points 1

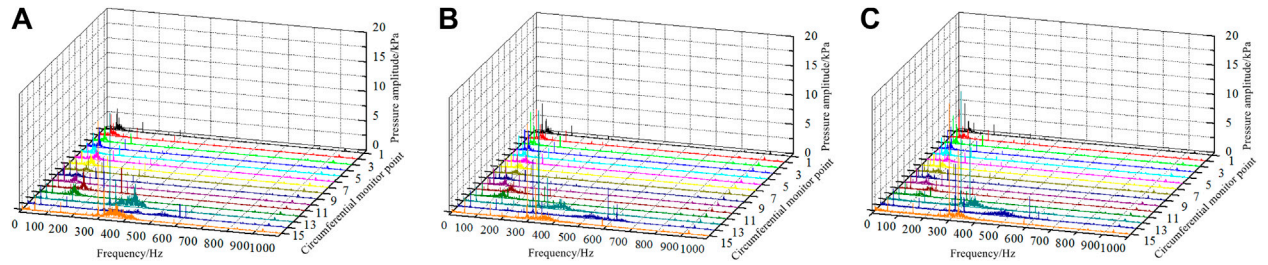

FIGURE 7 | Pressure pulsations on volute casing of three impellers at design point: **(A)** closed impeller, **(B)** semi-open impeller, and **(C)** open impeller.

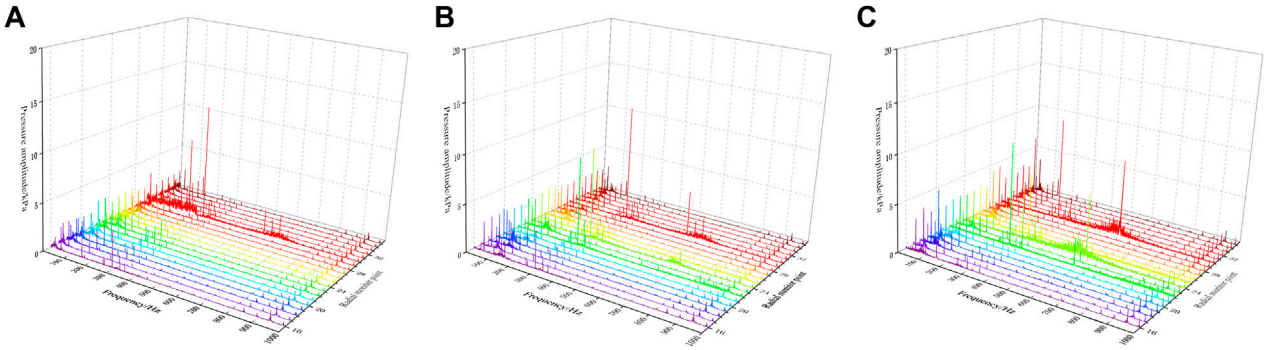

FIGURE 8 | Pressure pulsations on volute casing of three impellers at design point: **(A)** closed impeller, **(B)** semi-open impeller, and **(C)** open impeller.

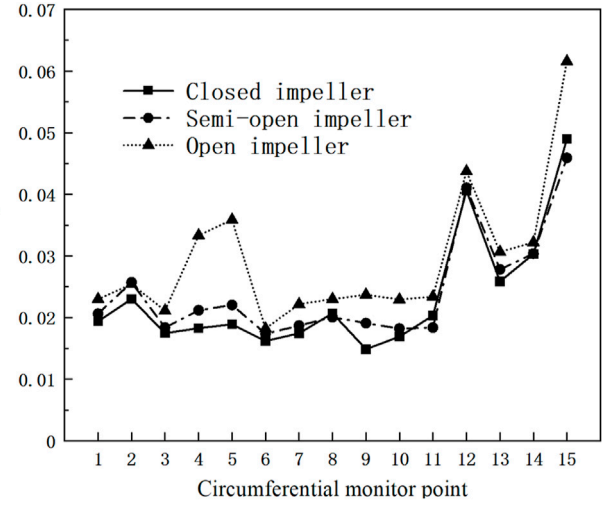

FIGURE 9 | Pressure pulsation intensity with three impellers.

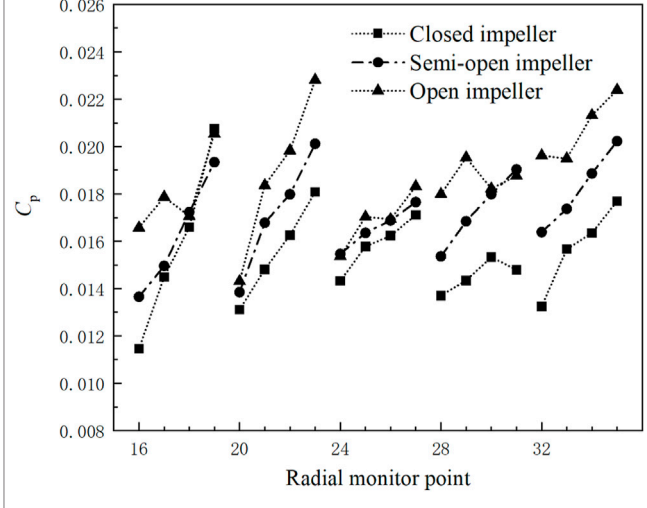

FIGURE 10 | Pressure pulsation intensity with three impellers.

to 11 fluctuate gently for the three impeller types. Pressure pulsation amplitudes near the casing tongue (at the measuring point 12) and the pump outlet (at the measuring 13 to the measuring 15) are significantly greater than those of other measuring points, and the pulsation amplitudes of the open impeller and the semi-open impeller are 7.7% and 3.5% greater than those of the closed impeller, respectively. The open impeller has the largest pressure pulsation amplitude, while the closed impeller has the smallest amplitude at the same measuring point. It indicates that intense pressure fluctuations arise near the casing tongue due to the dynamic and static interference between the blade and the casing tongue, causing a large amplitude of pressure pulsation near the casing tongue and the pump outlet. At the same time, the closed impeller

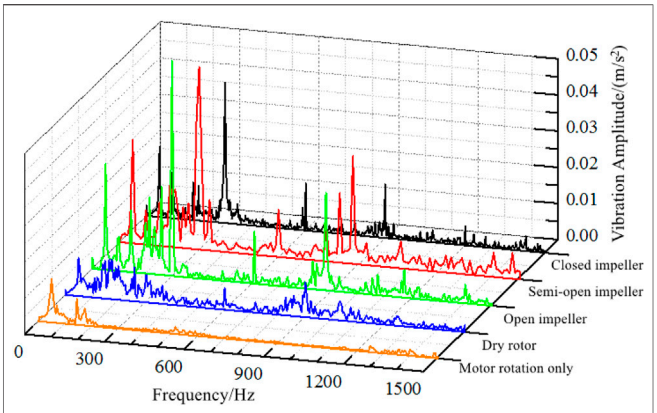

FIGURE 11 | Frequency distribution of vibrating acceleration of different impellers at design flow rate.

has the best stability under pressure pulsation and the open impeller has the poorest stability under pressure pulsation.

The pressure pulsation intensity at monitoring points 16–35 of the three impellers under design flow rate is presented in **Figure 10**. The pressure pulsation intensity increases gradually along the direction from the impeller inlet to the impeller outlet, and reaches its maximum at the impeller outlet. As group E is located near the volute tongue area, the static pressure drops rapidly here, so the pressure pulsation intensity is greater than that in other positions.

Vibration Characteristics

The distribution profile of vibration acceleration in domain frequency at the casing tongue of the volute of varying impellers under design flow rates is shown in **Figure 11**. According to **Figure 5**, the dominant frequency of vibration acceleration is at the shaft frequency only when the motor is rotating. At the same time, certain vibration acceleration pulsations can be found at the multiplier of the shaft frequency. Moreover, a certain degree of vibration can also be observed at the shaft frequency and its multiplier when the pump is idling. The dominant frequencies of vibration acceleration of the centrifugal pumps with three impeller types are the blade frequencies, with distinct pulsation amplitudes at the shaft frequency and its multiplier. Among them, the open impeller has the maximum pulsation of vibration acceleration, followed by the semi-open impeller, and the closed impeller has the smallest acceleration pulsating amplitude. The maximum vibration acceleration pulsation amplitudes of the open, semi-open, and closed impellers at the blade frequency are 0.046 m/s^2, 0.039 m/s^2, and 0.035 m/s^2, respectively, with 0.026 m/s^2, 0.025 m/s^2, and 0.015 m/s^2, respectively, at the shaft frequency. It can be seen that vibration acceleration in the tongue area is larger than that in other areas, demonstrating that internal flow in the area is unstable. The dynamic and static interference between the impeller in the pump and the casing tongue has the maximum impact on the vibration of the pump case. Comparatively speaking, the flow in the casing tongue area of the closed impeller is more stable than that of the other two impellers.

The distribution profile of radical vibration displacement of the pump shaft of the centrifugal pump with different impeller types under design flow rates in a rotation cycle is shown in **Figure 12**. Vibration displacements in the x and y directions share similar distribution patterns, with a phase difference of 90°. Displacement components of the rotating shaft in the x and y directions fluctuate slightly, from−0.008 mm to 0.012 mm when the motor is idling. Evidently, the model pump motor shaft has favorable dynamic balance performance. When the pump is idling, the model pump shaft fluctuates from−0.025 mm to 0.045 mm in direction x, and from−0.041 mm to 0.028 mm in direction y. It can be seen that a certain range of shaft vibration displacement deviation can be witnessed between the model pump shaft and the motor shaft due to rotor centering. As a result, the vibration displacement when the pump is idling is greater than that when the motor is idling. Components of vibration displacement in the x and y directions have similar distribution patterns for three impellers. The rotation center of the closed impeller rotor system is much closer to that when the pump is idling, and both are closer to the shaft center. On the contrary, the rotation centers of the centrifugal pumps with semi-open and open impellers greatly deviate from the shaft center. In combination with **Figure 5**, it can be found that the circumferential pressure of the volute of the closed impeller is uniformly distributed, showing a slowly rising trend; and the circumferential pressures of the volutes of the open impeller and semi-open impeller are dropping suddenly near the casing tongue, which might be caused by the shape of the decline in the fluid force acting on the impeller in the area. Furthermore, it leads to the shifted center of rotation of the pump shaft.

The distribution profile of radical vibration displacement of the pump shaft of the centrifugal pump with different impeller types under design flow rates in the frequency domain is shown in **Figure 13**. Evidently, the dominant frequency of pulsation of vibration displacement of the model pump in the x and y direction components is at the shaft frequency when the motor and pump are idling, and the pulsating amplitude of vibration displacement at the dominant frequency when the pump is idling is greater than that when the motor is idling. The pulsating amplitude of idling vibration displacement at the dominant frequency is roughly 0.013 mm, whereas the pulsating amplitude of vibration displacement when the motor is idling is only 0.004 mm. The dominant frequencies of vibration displacement pulsation for three impeller types are at the shaft frequency, with the pulsation amplitude far greater than that of the idled pump. Therefore, the excitation force of the unsteady fluid in the pump has a remarkable impact on the vibration of the pump rotor system. Meanwhile, the pulsating amplitude of the closed impeller at the dominant frequency is smaller than that of the other two impellers, and the open impeller has the maximum pulsating amplitude. According to the research on rotor vibration of varying impeller types, the closed impeller rotor system has the optimum vibration stability, and the semi-open and open impellers have similar rotor vibration stability. In addition, pressure pulsation and fluid exciting force are dominant factors affecting the vibration stability of the pump rotor.

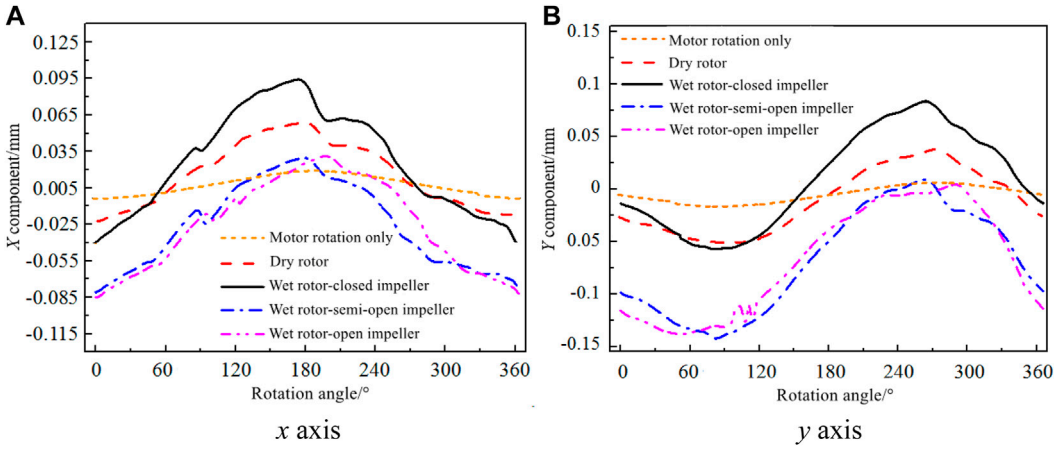

FIGURE 12 | Vibration displacements of different impellers at design flow rate: **(A)** *x* axis and **(B)** *y* axis.

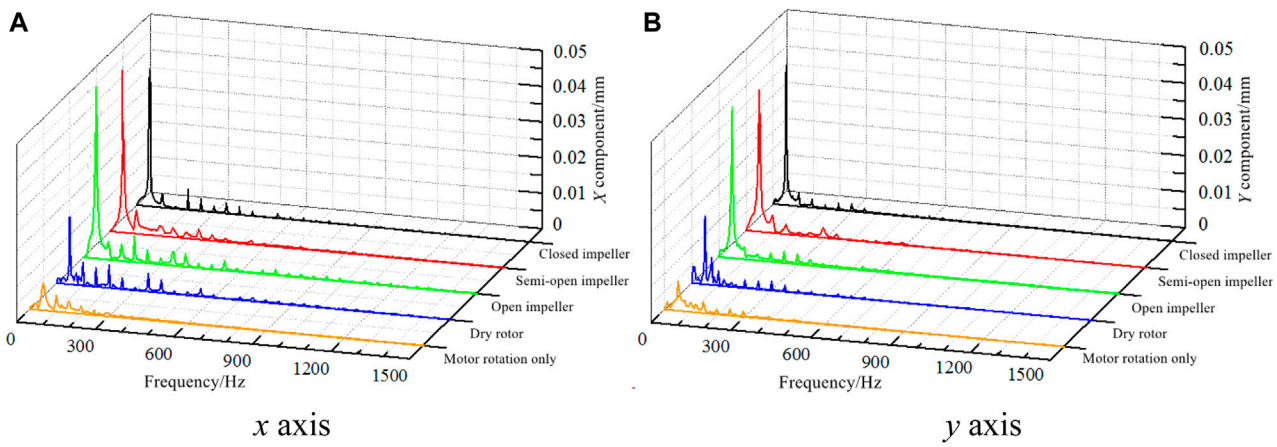

FIGURE 13 | Frequency distribution of vibration displacements of different impellers: **(A)** *x* axis and **(B)** *y* axis.

Furthermore, the rotor vibration stability is less affected by the motor vibration, and more affected by the rotor centering problem between the pump and the motor.

Simonovskiy et al. (2021) introduced the method of linear and nonlinear parameter identification for vibration mathematical models of centrifugal pumps and turbocharger rotors to ensure vibration reliability of the centrifuge rotor system. As an example of using the proposed methodology, the analysis of forced oscillations and stability of the rotor's rotation of a centrifugal compressor for underground gas storage with 25 MW power is considered. In solving the nonlinear differential equations, the time characteristics, the spectrum, and the orbit of rotor oscillations for 2nd mass in the directions of the *X*-axis and *Y*-axis in the case of stable and unstable rotation are obtained. The vibration results obtained in my experiment have similar distribution patterns. The vibration displacement of the rotor system in the *X*-axis and *Y*-axis directions is periodic. In the same period, the deviation degree between the rotation center and the axis center is also different at different times. The reliability of my test results has been verified.

CONCLUSION

This study analyzed the lift and efficiency, the circumferential pressure distribution of the volute wall, the dynamic pressure of the volute wall and the front cover wall, the vibration acceleration, the radial vibration displacement of the pump shaft, and the vibration energy for model pumps with three varying impellers under different flow rates. Conclusions are presented as follows:

1) The closed impeller enjoys the best performance stability, whereas the open impeller has the poorest performance stability, particularly when the flow rate is large. The closed impeller has the maximum radial static pressure value of the

front cover wall, followed by the semi-open impeller, and the open impeller shows the least static pressure value. The stable pressure distribution of the closed impeller in the casing tongue area is most favorable to fluid conveying, whereas the excessive pressure drop in the casing tongue area of the open impeller is least conducive to fluid conveying.

2) In the model pump, pressure pulsation at varying positions in the volute has different effect degrees on the operational stability of the pump; the effect degree gradually increases from the starting point of the volute spiral to the outlet along the rotation direction. Also, intense pressure fluctuations arise near the casing tongue due to the dynamic and static interference between the blade and the casing tongue, causing a large amplitude of pressure pulsation near the casing tongue and the pump outlet. The pulsation amplitudes near the casing tongue of the open impeller and the semi-open impeller are 7.7% and 3.5% greater than those of the closed impeller, respectively. At the same time, the closed impeller has the best stability under pressure pulsation and the open impeller has the poorest stability under pressure pulsation.
3) Based on the findings of vibration acceleration, tongue vibration has the greatest proportion, and the flow in the volute tongue area is the least stable among the vibrations of the pump case. The maximum vibration acceleration pulsation amplitudes of the open, semi-open, and closed impellers at the blade frequency are 0.046 m/s^2, 0.039 m/s^2, and 0.035 m/s^2, respectively, with 0.026 m/s^2, 0.025 m/s^2, and 0.015 m/s^2, respectively, at the shaft frequency. The minimum casing vibration can be found in the closed impeller, followed by the semi-open impeller, and the open impeller has the maximum vibration. The optimum stability of rotor vibration can be observed in the closed impeller, semi-open impeller, and open impeller with similar stability of rotor vibration.

Overall, it can be proven that the centrifugal pump equipped with a closed impeller has the best performance stability and vibration stability, followed by the semi-open impeller, and the open impeller is the worst.

DATA AVAILABILITY STATEMENT

The raw data supporting the conclusions of this article will be made available by the authors, without undue reservation.

AUTHOR CONTRIBUTIONS

XJ: conceptualization, methodology, investigation, writing—original draft, writing—review and editing. QC: formal analysis and data curation. LZ: investigation. ZZ: validation.

FUNDING

This work was supported by the National Natural Science Foundation of China (Grant No. 51906221) and the Joint Fund of the Zhejiang Natural Science Foundation (Grant No. LZY21E060002).

REFERENCES

Bellary, S. A. I., and Samad, A. (2016). Pumping Crude Oil by Centrifugal Impeller Having Different Blade Angles and Surface Roughness. *J. Petrol. Explor Prod. Technol.* 6, 117–127. doi:10.1007/s13202-015-0173-y

Chen, B., Li, X., and Zhu, Z. (2022). Investigations of Energy Distribution and Loss Characterization in a Centrifugal Impeller through PIV experiment. *Ocean Eng.* 247 (2022), 110773. doi:10.1016/j.oceaneng.2022.110773

Chen, B., Li, X., and Zhu, Z. (2022). Time-Resolved Particle Image Velocimetry Measurements and Proper Orthogonal Decomposition Analysis of Unsteady Flow in a Centrifugal Impeller Passage. *Front. Energ. Res.* 9, 818232. doi:10.3389/fenrg.2021.818232

Cui, B., Chen, D., Xu, W., Jin, Y., and Zhu, Z. (2015). Unsteady Flow Characteristic of Low-Specific-Speed Centrifugal Pump under Different Flow-Rate Conditions. *J. Therm. Sci.* 24 (1), 17–23. doi:10.1007/s11630-015-0750-x

Gulich, J. F. (2010). *Centrifugal pumps[M]*. Springer.

He, X. (1996). The Mechanism on Forming of the Pressure Pulse in Vane Pump. *Mech. Sci. Technol. Aerosp Eng.* 25 (6), 38–42.

Hong, S.-S., Kim, D.-J., Kim, J.-S., Choi, C.-H., and Kim, J. (2013). Study on Inducer and Impeller of a Centrifugal Pump for a Rocket Engine Turbopump. *Proc. Inst. Mech. Eng. C: J. Mech. Eng. Sci.* 227, 311–319. doi:10.1177/0954406212449939

Jia, X.-Q., Cui, B.-L., Zhang, Y.-L., and Zhu, Z.-C. (2015). Study on Internal Flow and External Performance of a Semi-open Impeller Centrifugal Pump with Different Tip Clearances. *Int. J. Turbo Jet-Engines* 32, 1–12. doi:10.1515/tjj-2014-0010

Jia, X.-Q., Cui, B.-L., Zhu, Z.-C., and Zhang, Y.-L. (2019). Experimental Investigation of Pressure Fluctuations on Inner Wall of a Centrifugal Pump. *Int. J. Turbo Jet-Engines* 36, 401–410. doi:10.1515/tjj-2016-0078

Klaus, B., and Rainer, K. (2005). Analysis of Secondary Flows in Centrifugal Impellers. [*J*]. *Int. J. Rotating Machinery* 1, 45–52. doi:10.1155/IJRM.2005.45

Sano, T., Yoshida, Y., Tsujimoto, Y., Nakamura, Y., and Matsushima, T. (2002). Numerical Study of Rotating Stall in a Pump Vaned Diffuser. *Engineering* 124, 363–370. doi:10.1115/1.1459076

Simonovskiy, V., Pavlenko, I., Pitel, J., Stremoukhov, D., and Ivanov, V. (2021). *Methods and Algorithms for Calculating Nonlinear Oscillations of Rotor Systems*. Springer International Publishing.

Tao, Y., Yuan, S., Liu, J., Zhang, F., and Tao, J. (2016). Influence of Blade Thickness on Transient Flow Characteristics of Centrifugal Slurry Pump with Semi-open Impeller. *Chin. J. Mech. Eng.* 29, 1209–1217. doi:10.3901/cjme.2016.0824.098

Wang., K., Luo., G., Li, Y., Xia., R., and Liu., H. (2020). Multi-condition Optimization and Experimental Verification of Impeller for a marine Centrifugal Pump. *Int. J. Naval Architecture Ocean Eng.* 12, 71–84. doi:10.1016/j.ijnaoe.2019.07.002

Wood, G. M., Welna, H., and Lamers, R. P. (1965). Tip-clearance Effects in Centrifugal Pumps. *J. Basic Eng.* 87, 932–939. doi:10.1115/1.3650846

Yamamoto, K., and Tsujimoto, Y. (2009). Backflow Vortex Cavitation and its Effects on Cavitation Instabilities. *Int. J. Fluid Machinery Syst.* 2 (1), 40–54. doi:10.5293/ijfms.2009.2.1.040

Yang, S. S., Liu, H. L., Kong, F. Y., Xia, B., and Tan, L. W. (2014). Effects of the Radial Gap between Impeller Tips and V O-Lute Tongue Influencing the Performance and Pressure Pulsations of Pump as Turbine. *J. Fluids Eng.* 136, 054501. doi:10.1115/1.4026544

Yuan, J., Fu, Y., Yang, L., Zhang, J., and Pei, J. (2010). Analysis on Pressure Fluctuation within Volute of Centrifugal Pump Based on Large Eddy Simulation. *J. Drainage Irrig Mach Eng* 28, 310–314.

Zhang, D. S., Shi, W. D., Pan, D. Z., and Dubuisson, M. (2015). Numerical and Experimental Investigation of Tip Leakage Vortex Cavitation Patterns and

Mechanisms in an Axial Flow Pump. *J. Fluids Eng.* 137, 121103. doi:10.1115/1.4030914

Zheng, L. L., Dou, H.-S., Jiang, W., Chen, X. P., Zhu, Z. C., and Cui, B. L. (2016). Influence of Rotor-Stator Interaction on Flow Stability in Centrifugal Pump Based on Energy Gradient Method. *Int. J. Turbo Jet- Engines* 33, 413–419. doi:10.1515/tjj-2015-0046

Zhu, B., and Kamemoto., K. (2005). Numerical Simulation of Unsteady Interaction of Centrifugal Impeller with its Diffuser Using Lagrangian Discrete Vortex Method. *Acta Mech. Sinica* 21 (1), 40–46. doi:10.1007/s10409-004-0005-7

Zhu, B., Lei, J., and Cao, S. (2007). Numerical Simulation of Vortex Shedding and Lock-In Characteristics for a Thin Cambered Blade. *ASME J. Fluids Eng.* 129 (10), 1297–1305. doi:10.1115/1.2776964

Zhu, R. S., and Hu, Z. Q. (2010). Numerical Simulation of Pressure Fluctuation in Double-Blade Pump. *Trans. Chin. Soc. Agric. Eng.* 26 (6), 129–134. doi:10.3969/j.issn.1002-6819.2010.06.023

Conflict of Interest: The authors declare that the research was conducted in the absence of any commercial or financial relationships that could be construed as a potential conflict of interest.

frontiers in Energy Research

ORIGINAL RESEARCH
published: 24 March 2022
doi: 10.3389/fenrg.2022.821282

Characteristic of Steady-State Flow Force on the Cone Valve Based on Orthogonal Test Method

Xiumei Liu[1], Jie He[2], Jichao Ma[1], Beibei Li[1], Shaobin Xiang[1], Yujia Zhang[1], Qihang Liu[1] and Fangwei Xie[1]*

[1]School of Mechatronic Engineering, China University of Mining and Technology, Xuzhou, China, [2]School of Electrical and Control Engineering, Xuzhou Institute of Technology, Xuzhou, China

The steady-state flow force is the fundamental reason that affects the pressure stability, which will reduce the control performance of a hydraulic valve. A mathematical model of the axial steady-state flow force on the valve core is proposed to master the principle and characteristics of steady-state flow force. For understanding the dynamic changes of the steady-state flow force, a two-dimensional axisymmetric model is built to discuss the value of flow force. Different geometric parameters and operating conditions have different effects on the performance of the valve, and analyzing a variety of parameters is difficult because of the complexity of the test. Therefore, the geometric parameters and operating conditions in the steady-state flow force were optimized by the orthogonal test-optimization method. The main significant factors affecting the performance of steady-state flow force on the cone valve core are determined by extreme difference analysis, which are the opening and pressure differential, respectively. Furthermore, a test ring is built to measure the steady-state flow force. The results show that the greater the pressure differential is, the greater the steady-state flow force is. The steady-state flow force does not increase linearly, but increases first and then decreases with the increase of the opening. The study will lay the foundation to precise axial flow force prediction and reference for design optimization of the valve.

Keywords: steady-state flow force, cone valve, orthogonal test method, opening, pressure differential

OPEN ACCESS

Edited by:
Ling Zhou,
Jiangsu University, China

Reviewed by:
Hui Zhang,
Nanjing University of Science and Technology, China
Jiang Lai,
Nuclear Power Institute of China (NPIC), China

****Correspondence:***
Jie He
hejie794@163.com

Specialty section:
This article was submitted to Process and Energy Systems Engineering, a section of the journal Frontiers in Energy Research

Received: *24 November 2021*
Accepted: *31 January 2022*
Published: *24 March 2022*

Citation:
Liu X, He J, Ma J, Li B, Xiang S, Zhang Y, Liu Q and Xie F (2022) Characteristic of Steady-State Flow Force on the Cone Valve Based on Orthogonal Test Method. Front. Energy Res. 10:821282. doi: 10.3389/fenrg.2022.821282

INTRODUCTION

Cone valve is the main control component of the hydraulic systems, which is widely used due to their advantages of fast dynamic response, high control accuracy, and simple structure. The flow force is one of the most important reasons for the vibration of the cone valve, which has a significant influence on the stability and accuracy of the hydraulic system (Li et al., 2018). In the working process of the cone valve, the flow force will impede the spool displacement, cause the vibration of the cone valve, and reduce the reliability of valve, so far as to shorten the service life of the cone valve. A comprehensive understanding of the flow force is rather complicated, which is closely related to complex flow fields in the valve. Due to the complex flow channel structure of the valve, there may be complex turbulence phenomenon. Because of this complexity and uncertainty in the turbulence flow, it is difficult to effectively estimate the precise information caused by the flow force. Therefore, it is very necessary to fully investigate the reason, influencing factors, and variation characteristics of flow force in conical valve, which is of great significance to improve the control performance of the hydraulic system.

Many scholars have carried out the research on the flow field characteristics of the valve and deepened the research on the flow force (Kang et al., 2020). Jia et al. (2019) studied the fluctuation of the pressure in the cone valve to obtain the L/D parameter, which had the greatest impact on the stability of the system and could be used to predict the more stable flow force output of the system. Gao et al. (2019) took the influence of flow force into account and developed a nonlinear mathematical model to improve the valve's performance. Han et al. (2017) investigated unsteady cavitation process inside a water hydraulic poppet valve, and pointed that the flow force will increase with the increase of cone angles, and cavitation could slightly decrease the flow force. Zong et al. (2020) got the steady-state flow forces exerted on the valve disk at different valve openings numerically and experimentally. However, it is hard to get how flow force works on different types of valves because of the turbulent flow in the valve. Lei et al. (2018) discussed the flow model of the poppet valve orifice with a novel function of flow discharge coefficient, and the flow force caused by the valve body motion and the flowrate variation are also considered; CFD method (Computational Fluid Dynamics) and experimental evaluation are combined together, predicting the flow force more accurately. Zhang et al. (2019) studied the opening characteristics of the dynamic relief valve by combining numerical calculation and experimental research, and then obtained the correlation between operating parameters and variation characteristics of the flow force. Filo et al. (2019) proposed a new core head geometry to improve the valve's performance by analyzing the flow force of differential switch valve installed in throttle check valve body. Tan et al. (2019) analyzed the force of the split proportion valve core numerically and got the influence of the valve core structure parameters on the force. Yang et al. (2019a, 2019b) compared and analyzed the continuous micro-jet control flapper nozzle pilot valves with traditional nozzle and micro-nozzle, then obtained the influence of different structural parameters on the flow force. Lin et al. (2018) presented a novel method to reduce the overflow loss using an energy recovery unit and pointed that the steady-state flow force decreases dramatically with increasing return line pressure. Scuro et al. (2018) pointed that average normal disc force is about 19% lower than theoretical ASME force, which could prevent the valve oversizing. Kang et al. (2020) pointed that the fluctuation of the flow force of the pilot stage will affect the output stability of the servo valve. However, most research focus on flow force in the slide valve rather than the cone valve, and a single control volume is used to calculate the flow force and the influence of wall surface is not considered. There are many factors affecting the flow force, such as opening, the inlet and outlet pressure, the cone angle of the conical valve core, the diameter of valve core, the radius of flow channel, and the density of the fluid, not only the geometric parameters but also operating conditions. Different parameters have different effects on the control accuracy of valve, so analyzing a variety of parameters on the flow force is difficult because of the complexity of the test. Although some literature discussed the effect of pressure differential and opening on the flow force, their findings were not comprehensive enough and did not apply the influence degree of each factor.

In this paper, a mathematical model of axial steady-state flow force based on the momentum theorem and Bernoulli equation is derived to perform a detailed force analysis of the control volume in the upstream and downstream flow channels of cone valve. A test ring is used to measure axial steady-state flow force at different conditions to validate the model. In addition, for the comprehensive consideration of geometric parameters and operating conditions, an orthogonal test combined with extreme difference analysis is used to examine factors affecting flow force. The weight between geometric parameters and operating conditions is discussed, and the most significant influence parameters on the flow force are presented. Then the value of flow force on the variation of pressure and opening of the cone valve are investigated. The paper will provide theoretical guidance for the calculation of flow force, give reference for design optimization, and control accuracy improvement of the valve.

THEORETICAL ANALYSIS OF STEADY-STATE FLOW FORCE

As shown in **Figure 1A**, the flow area of the internal flow cone valve is divided into two control volumes taking the orifice as the interface; the upper valve abcd-a′b′c′d′ is defined as control volume *I*, the lower valve efghijk is defined as control volume *II*, and the upward direction is used as the positive direction. The momentum theorem is applied to analyze the force in control bodies *I* and *II*, which are shown as follows:

$$-mv_f - (-mv\sin\alpha) = -F_{\mathrm{I}} + P_s\Delta A \tag{1}$$

$$-mv_2 - \left(-mv_f\right) = -F_{\mathrm{II}} + P_2A_2 \tag{2}$$

where m is the mass of fluid passing through flow section per unit time, v_f is the velocity of fluid flowing through the orifice, v is the velocity of fluid flowing into control volume *I*, α is the angle of horizontal velocity direction in the control volume *I*, F_{II} is the axial force acting on control volume *I* by valve core, *Ps* is the pressure on the ring *ad-a′d′* at the valve seat in control volume *I*, ΔA is the area on the ring *ad-a′d′*in control volume *I*, v_2 is the velocity of fluid flowing out of the control volume *II*, F_{II} is the axial force acting on control volume *II* by valve core, P_2 is the outlet pressure, and A_2 is the cross-sectional area of the downstream channel. Combined with **Eqs 1**, **2**, the total axial force F_{axis} acting on control volume by valve core could be obtained, which is defined as follows:

$$F_{axis} = F_{\mathrm{I}} + F_{\mathrm{II}} \tag{3}$$

According to Newton's third law of motion, action and reaction are equal and opposite. The force F on the cone valve core could be obtained, which is shown as

$$F = -F_{axis} = \rho Qv\sin\alpha - \rho Qv_2 - P_s\Delta A - P_2A_2 \tag{4}$$

where ρ is the fluid density and Q is the fluid flow. When the fluid flows into and out of control volume *I*, the velocity of fluid will change with the position of the flow area. According to the

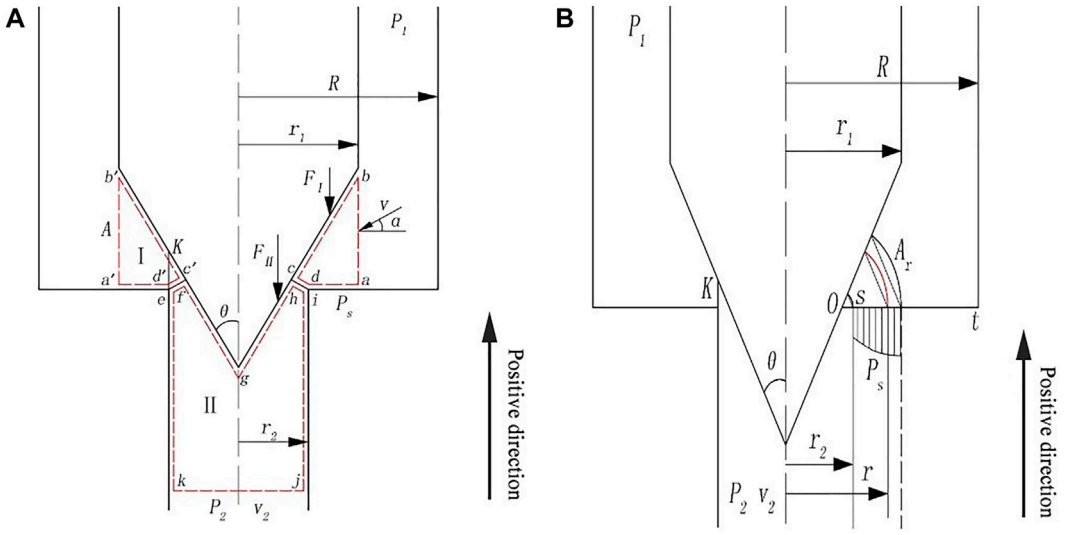

FIGURE 1 | Schematic diagram of control valve: **(A)** control volume; **(B)** pressure distribution at the shoulder.

Bernoulli equation, the pressure of fluid from the inlet to the outlet will also change.

As shown in **Figure 1B**, the control volumes *I* and *II* have good symmetry. By using the axisymmetric theoretical model, we usually can get good effect in solving problems. Point *O* could be obtained by extending the line *ad* to intersect with the valve core, and then a few equally spaced nodes are set in the line *ad* to divide it into several smaller segments. Some different length segments could be obtained by connecting each node with the point *O*, and then the isobaric surfaces at different positions in the line *ad* could be obtained by drawing an arc with each small segment, which is the radius, and the point *O*, which is the center of the circle. Therefore, the PsΔA is defined as follows:

$$P_s \Delta A = \int_{r_2}^{r_1} 2\pi r \left[P_1 - \frac{\rho}{2} \left(\frac{Q}{A_r} \right)^2 \right] dr \tag{5}$$

$$A_r = 2\pi r \frac{(r - r_2 + K \tan\theta)\cos\theta}{\cos\left(\frac{\pi}{4} - \frac{\theta}{2}\right)} \tag{6}$$

where r_1 is the radius of valve core, r_2 is the radius of the flow channel downstream, P_1 is the inlet pressure, A_r is the area of isobaric surface, K is the opening of the valve core, and θ is the half cone angle of the valve core.

Combining **Eqs. 4–6**, the hydrostatic pressure F_P could be obtained. The mathematical model of the axial steady-state flow force on the internal flow cone valve core is listed as follows:

$$F_s = \rho Q v \sin\alpha - \rho Q v_2 - \int_{r_2}^{r_1} 2\pi r P_s dr - P_2 A_2 - F_p \tag{7}$$

As shown in **Eq. 7**, the axial steady-state flow force is not only influenced by geometric parameters but also influenced by operating conditions, such as opening, inlet and outlet pressure, the angle and radius of the valve core, the radius of the flow channel downstream, and the density of the fluid. While other physical conditions all remain unchanged except the opening, the axial steady-state flow force does not simply change linearly with the increase of the opening. In fact, it is a nonlinear process.

NUMERICAL MODELLING

Governing Equations and Boundary Conditions

Continuity equation for the mixture is

$$\frac{\partial}{\partial t}(\rho_m) + \nabla\left(\rho_m \vec{v}_m\right) = 0 \tag{8}$$

The momentum equation for the mixture is

$$\frac{\partial}{\partial t}\left(\rho_m \vec{v}_m\right) + \nabla \cdot \left(\rho_m \vec{v}_m \vec{v}_m\right) = -\nabla p + \nabla \cdot \left[\mu_m \left(\nabla \vec{v}_m + \nabla \vec{v}_m^T\right)\right] \tag{9}$$

The net mass transfer from liquid to vapor is often described by Schnerr and Sauer model:

$$\frac{\partial}{\partial t}(\alpha \rho_v) + \nabla \cdot \left(\alpha \rho_v \vec{v}\right) = \frac{\rho_v \rho_l}{\rho_m} \frac{D\alpha}{Dt} \tag{10}$$

Here,

$$R_e = \frac{\rho_l \rho_v}{\rho_m} \alpha(1-\alpha) \frac{3}{R_B} \left(\frac{2}{3} \frac{P_v - P}{\rho_l} \right)^{1/2}; P \le P_v \tag{11}$$

$$R_c = \frac{\rho_l \rho_v}{\rho_m} \alpha(1-\alpha) \frac{3}{R_B} \left(\frac{2}{3} \frac{P - P_v}{\rho_l} \right)^{1/2}; P \ge P_v \tag{12}$$

where ρ_m is the mixture density; α_v is the vapor volume fraction; $\vec{v}_m$ and μ_m are the velocity and viscosity of the mixture, respectively; and R_e and R_C are the mass transfer between the vapor and liquid phases in cavitation.

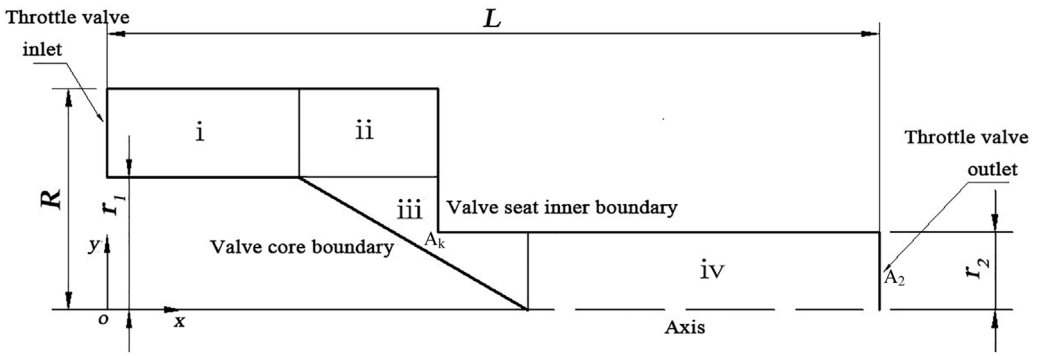

FIGURE 2 | Geometric structure of the cone valve.

The internal fluid's flow state is turbulent because the Reynolds number in the cone valve is much greater than the critical Reynolds number. Based on the results of Park and Rhee (2012) and Lain et al. (2002), the *RNG* k–ε model in turbulent flow is used to study the flow force, which is shown as follows:

$$\frac{\partial}{\partial t}(\rho k) + \frac{\partial}{\partial x_i}(\rho k u_i) = \frac{\partial}{\partial x_j}\left(\alpha_k \mu_{eff} \frac{\partial k}{\partial x_j}\right) + G_k - \rho\varepsilon + S_k \quad (13)$$

$$\frac{\partial}{\partial t}(\rho\varepsilon) + \frac{\partial}{\partial x_i}(\rho\varepsilon u_i) = \frac{\partial}{\partial x_j}\left(\alpha_\varepsilon u_{eff} \frac{\partial \varepsilon}{\partial x_j}\right) + \frac{C_{1\varepsilon}}{k}\varepsilon G_k - C_{2\varepsilon}\rho\frac{\varepsilon^2}{k} - R_\varepsilon + S_\varepsilon \quad (14)$$

where G_k is the generation of turbulence kinetic energy due to the mean velocity gradients and ε is the fluid's turbulent dissipation rate. σ_k and σ_ε are the turbulent Prandtl numbers for k and ε, respectively. $C_{1\varepsilon}$, $C_{2\varepsilon}$, and $C_{3\varepsilon}$ are constants. S_k and S_ε are user-defined source terms.

The inlet and the outlet pressure are chosen as the boundary conditions in this paper. No.46 antiwear hydraulic oil is used for the hydraulic fluid, whose density is 889 kg/m^3 and viscosity is 4.6 $\times$ 10^{-5} m^2/s. In CFD simulation, according to the study of Han et al. (2017), the force could be expressed as follows:

$$F_s = F_p - F_{x-axis} = F_p - \int P_{dynamics} S_c \quad (15)$$

where F_s is the flow force acting on the cone, F_p is the force that generated by the static pressure, $P_{dynamics}$ is the dynamics pressure distributed on the surface of the spool, and S_c is the axial area of the conical surface.

Geometry and Mesh of the Cone Valve

Considering the axisymmetric structure of the valve, the computational domain could be simplified to a two-dimensional axisymmetric geometric model (Liang et al., 2016; Han et al., 2017). To save calculation time and reduce the complexity of numerical simulation, a two-dimensional axisymmetric model is adopted, as shown in **Figure 2**. The flow channel in the cone valve is divided into four regions. The structural grid is used in regions i, ii, and iv, while the unstructured grid and local encryption are used in region iii because the flow field is complex due to the large variation of fluid velocities and pressures at the orifice. R is the radius of the flow channel upstream and L is the total length of flow channel.

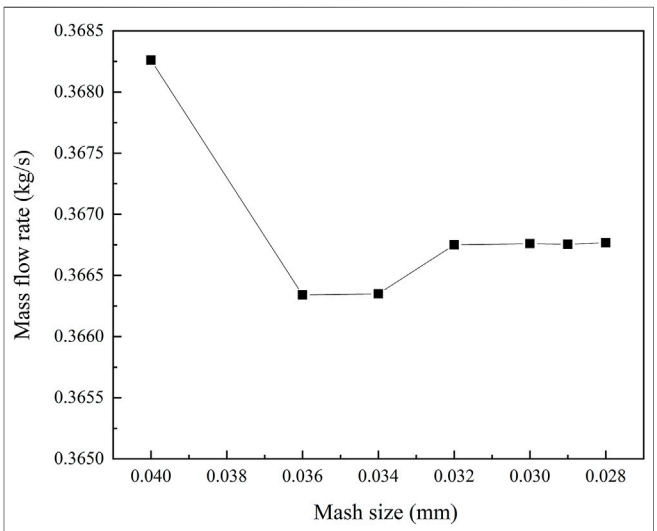

FIGURE 3 | Verification of grid size independence at orifice.

Figure 3 is the grid independence verification in region iii because of local encryption of the grid under the same operating conditions. It could be found that the grid size gradually reduced in region iii, while the corresponding mass flow rate reduced first, and then increase later, and finally it remains stable. Therefore, the mesh size of 0.032 mm is chosen for the simulation, to maintain the calculation accuracy and save the calculation time. The detailed of meshing near the orifice and partial enlarged drawing are shown in **Figure 4**, and the final grid number of the whole flow channels is about 80,000.

EXPERIMENTAL METHODS

Orthogonal Tests and Analyses

Different geometric parameters and operating conditions have different effects on the performance of steady-state flow force on the internal flow cone valve core, so analyzing their respective

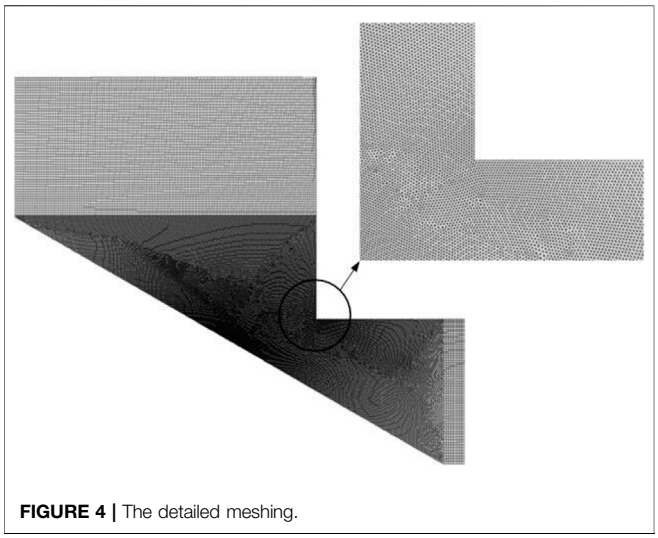

FIGURE 4 | The detailed meshing.

roles for flow force needs a tremendous amount of work. Therefore, the orthogonal test-optimization method is designed to study the combined effect of geometric parameters and operating conditions on the flow force. **Table 1** shows the factors affecting the flow force and their levels. In this paper, four factors and four levels are selected for the orthogonal analysis of the flow force.

According to the factor level numbers and data processing software SPSS, a suitable orthogonal test table $L_{19}(4^4)$ is developed and its header is also designed as shown in **Table 2**. The target of this analysis is to estimate the value of the flow force. According the test scheme shown in **Table 2**, a numerical simulation could be used to calculate the flow force (Xie et al., 2018), which is $F_s = F_{axis} - F_p$, $F_p = P_1A_1 + P_2A_2 = \pi(P_1 + P_2)(r_1^2 + r_2^2)$.

In **Table 2**, K_{ij} is the sum of all test factors in column j and the level number i, $\bar{K}_{ij}$ is the average value of K_{ij}, and the optimal level and combination of factors in column j could be determined by the value of K_{ij}. R_j is the extreme difference analysis of factor in column j, $R_j = \max\{\bar{K}_{ij}\} - \min\{\bar{K}_{ij}\}$, which could reflect their variable range if there are fluctuations of the factors in column j. The larger R_j is, the greater effect of this factor on this extreme difference analysis process is. According to the value of R_j, we could rank these factors in order of importance. It could been seen from the orthogonal test results in **Table 2** that

TABLE 1 | Table of factor levels

Factor	(A) Opening	(B) Differential pressure	(C) Cone angle	(D) Valve core diameter
Level	**1**	**2**	**3**	**4**
1	1 mm	1 MPa	30°	8 mm
2	1.5 mm	2 MPa	60°	10 mm
3	2 mm	3 MPa	90°	12 mm
4	2.5 mm	4 MPa	120°	—

TABLE 2 | Orthogonal test table

Test No.	Factor				Results		Analysis				
	A	B	C	D	C_q	F_s (N)	—	A	B	C	D
	1	2	3	4				1	2	3	4
1	1 (1)	1 (1)	1 (30)	1 (8)	0.918	3.3743	$K_{1j}C_q$	4.226	3.39	3.2	3.042
2	2 (1.5)	2 (2)	2 (60)	1	0.817	9.8371	$K_{2j}C_q$	3.156	3.236	3.939	3.143
3	3 (2)	3 (3)	3 (90)	1	0.732	61.5612	$K_{3j}C_q$	3.035	4.632	3.793	8.534
4	4 (2.5)	4 (4)	4 (120)	1	0.575	113.47	$K_{4j}C_q$	4.302	3.461	3.787	
5	4	3	2	2 (10)	0.746	54.649	$K_{1j}F_s$	61.67	40.74	51.89	188.2
6	3	2	1	2	0.791	10.987	$K_{2j}F_s$	73.19	68.55	154.7	104.0
7	2	1	4	2	0.825	9.0517	$K_{3j}F_s$	166.4	199.8	192.1	337.7
8	1	4	3	2	0.781	29.308	$K_{4j}F_s$	328.6	320.8	231.1	
9	1	3	4	3 (12)	0.848	18.776	$\overline{K_{1j}}C_q$	0.845	0.847	0.8	0.760
10	2	4	1	3	0.74	16.496	$\overline{K_{2j}}C_q$	0.789	0.809	0.787	0.785
11	3	1	2	3	0.871	8.3029	$\overline{K_{3j}}C_q$	0.758	0.772	0.758	0.775
12	4	2	3	3	0.73	43.485	$\overline{K_{4j}}C_q$	0.717	0.692	0.757	
13	4	1	3	3	0.776	20.018	$\overline{K_{1j}}F_s$	12.33	10.18	12.97	47.06
14	3	4	4	3	0.641	85.573	$\overline{K_{2j}}F_s$	18.29	17.13	30.95	25.99
15	2	3	3	3	0.774	37.812	$\overline{K_{3j}}F_s$	41.60	33.30	38.43	30.70
16	1	2	4	3	0.898	4.2415	$\overline{K_{4j}}F_s$	54.77	64.16	46.22	
17	1	3	2	3	0.781	5.9765					
18	4	3	1	3	0.751	21.039	R_jC_q	0.128	0.155	0.042	0.025
19	4	4	2	3	0.724	75.997	R_jF_s	42.44	53.98	33.24	21.06

Factor (primary→secondary): BACD

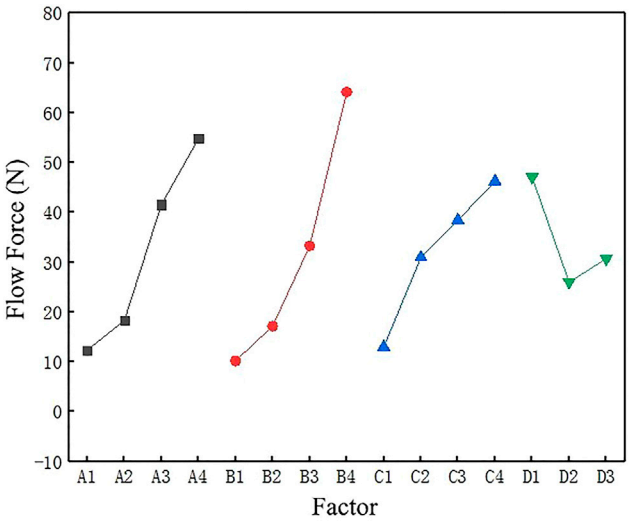

FIGURE 5 | Comparison of experimental results of various factors.

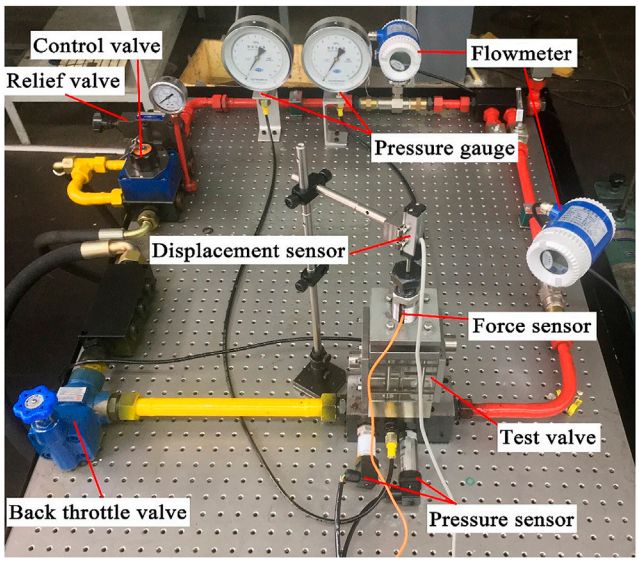

FIGURE 6 | Experimental system.

$R_2 > R_1 > R_3 > R_4$. It points out some primary factors affecting the flow force and their important orders are pressure differential > opening > cone angle of valve core > the diameter of valve core. Therefore, these two factors, pressure differential and opening, have the most important influences on the flow force. This orthogonal test-optimization method provides a theoretical basis for the following flow force and its influencing factors.

Figure 5 shows the relationship between influencing factors and indicators, which helps us to better understand the influence of various factors on flow force at the unlimited and given level, so as to better assist the experimental work and save time. It could be found from **Figure 5** that the flow force is the minimum when the opening reduces to the minimum A_1 and other conditions, such as the pressure differential, remain the same. When the pressure differential reduces to the minimum B_1 and other conditions, such as the opening, remain the same, the flow force is the minimum.

Experimental System

The experimental device is shown in **Figure 6**, which consisted of a hydraulic system and a flow force measuring system. The hydraulic system contains a pump, an air-cooling device, an accumulator, a relief valve, a control valve, two flowmeters, a transparent test valve, a back throttle valve, two pressure gauges, and two pressure sensors. They are all connected by oil tubes. The hydraulic pump is used to provide power for this system. The air-cooling device is used to keep the oil at constant temperature, and the accumulator is used to reduce the pressure pulsation of this system. The relief valve, control valve, and back throttle valve are used to control the pressure and flow of the system. The inlet and outlet pressure of the transparent test valve are displayed by two pressure gauges. Two pressure sensors are used to monitor the inlet and outlet pressure of the test valve in real time. The flow force measuring system consisted of a displacement sensor and a micro-force sensor. The transparent valve is self-designed for installing this flow force measuring system. The opening of this test valve is measured by the displacement sensor, and the micro-force sensor is used to measure the flow force. The measured signals are collected and transmitted to the computer via a data acquisition card. All these components and parts are mounted on a self-designed optical platform to reduce vibration and improve the accuracy of the results.

RESULTS AND DISCUSSION

As discussed in the aforementioned orthogonal tests, the pressure differential and the opening are the most important factors influencing the characteristics of steady-state flow force. The relationship between the pressure differential, the opening, and steady-state flow force is discussed theoretically, numerically, and experimentally in this section.

Effects of Pressure on Steady-State Flow Force Characteristics of the Valve

Figure 7 shows the relationship among the A_k, A_2 and the valve core's opening K. The cross-sectional area A_k of the cone valve orifice is defined in **Figure 2**, which is the minimum flow area. A_2 is defined as the maximum area A_{max} (Ye et al., 2014) when K_{max} is 5 mm. It could be seen that A_k increases with the increasing opening of the valve, while the opening is less than 5 mm.A_k is equal to the area of the channel downstream A_2 while $k = 5$ mm. If the opening continues to increase, A_2 will be smaller than A_k, and the throttling effect of the cone valve will disappear. Therefore, the range of the opening in this paper varies from 0 to 5 mm.

To interpret the change of steady-state flow force in the valve, the nephogram of pressure and velocity in the flow channel under different inlet and outlet pressures is shown in **Figure 8**; at this

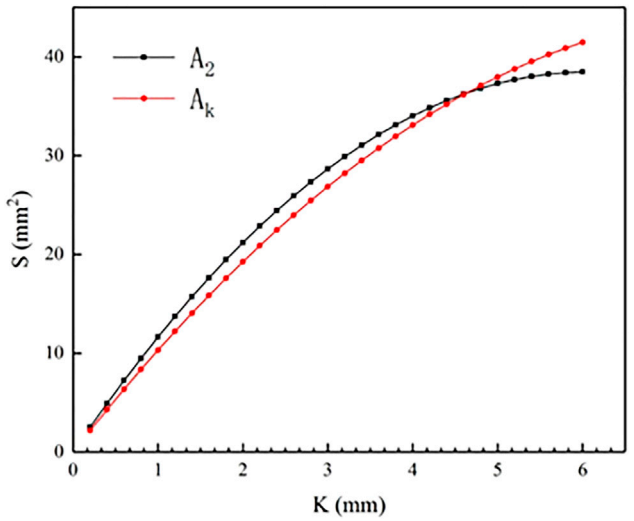

FIGURE 7 | The relationship among the cross-sectional area of the orifice and downstream channel and the opening.

time, the opening is 1 mm. There is one low-pressure area located near the tip of the valve core, while the other low-pressure area is located at the orifice. When the pressure differential increases gradually, greater pressure variation happens near the orifice. The greater pressure differential is, the larger pressure downstream is. In addition, the size of low pressure area at the orifice gradually increases with the increasing pressure differential. If the low pressure is lower than the saturated vapor pressure of liquid, cavitation will occur (Yuan et al., 2019). Furthermore, the velocity nephogram shows that both the maximum velocity and the average velocity at orifice increase with the increasing pressure differential. The larger pressure differential is, the larger range of high-speed zone is. The high-speed zone is corresponding to the low pressure range. The increment of pressure differential enhances the variation gradient of velocity, and the result is that the variation of pressure gradient near the orifice becomes more obvious. These changes of pressure and velocity in the flow field satisfied Bernoulli equation ignoring the energy loss and gravity potential energy.

To better understand the influence of pressure differential on the flow force, the numerical calculation results of the local pressure distribution along the outline of the valve core tip is shown in **Figure 9**. The opening and the outlet pressure remain the same, while the inlet pressure increases gradually, that is to say, the pressure differential increases gradually. From **Figure 9**, we could find that the abscissa of the minimum pressure along the outline of the valve core tip increases gradually with increasing pressure differential, and the position where pressure changes dramatically gradually moved to the valve core tip. The value of this minimum pressure decreases with increasing pressure differential. The changes of the minimum pressure are more obvious under a larger pressure differential.

The experimental data, calculation, and simulation results of the axial steady-state flow force under different pressure differentials are shown in **Figure 10**. The value of axial steady-state flow force increases with the increasing pressure differential at the same opening of the valve. When the differential pressure is 0.3 MPa, the value of flow force is 2.8 N. When the differential pressure increases to 1.4 MPa, the value of flow force reaches 14.1 N. When the pressure difference is small, the flow rate

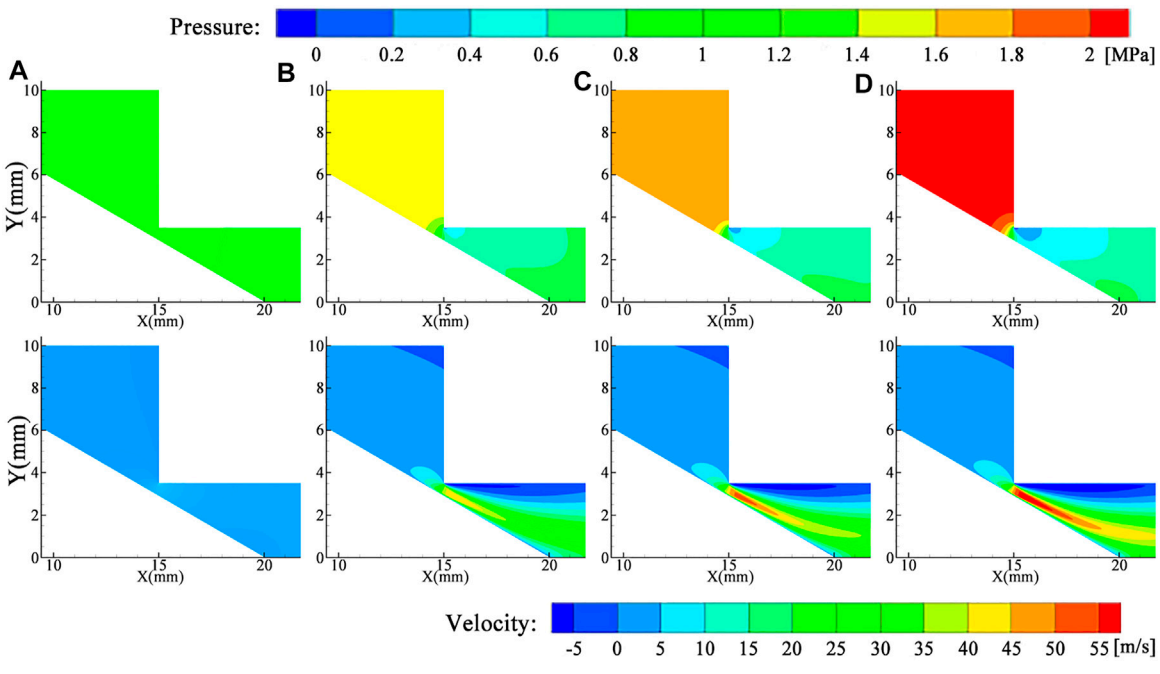

FIGURE 8 | Pressure and velocity nephogram with different pressure differentials: **(A)** Δp = 0.5 MPa; **(B)** Δp = 0.8 MPa; **(C)** Δp = 1.1 MPa; **(D)** Δp = 1. 4 MPa.

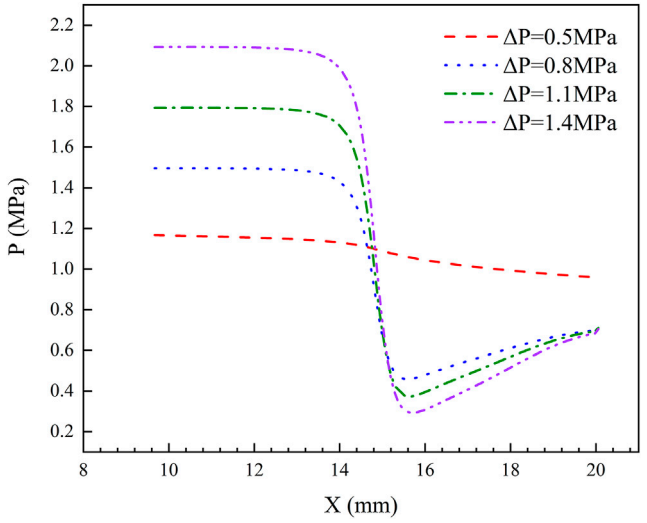

FIGURE 9 | The local pressure distribution along the outline of the valve core tip under various differential pressure conditions.

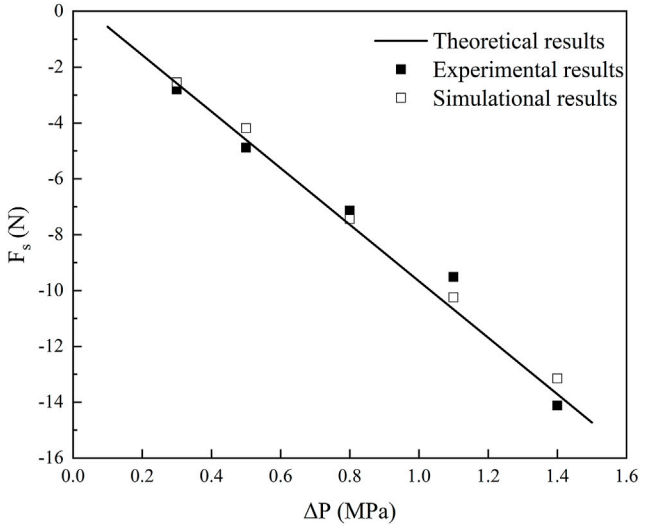

FIGURE 10 | The relationship between the differential pressure and steady-state flow force under various differential pressure conditions.

through the orifice is small, which will result in smaller change of fluid momentum, so the steady-state flow force is small. With the gradual increase of the pressure differential, the flow rate and change of fluid momentum through the orifice increase, which also increases the steady-state flow force. The experimental data, calculation, and simulation results agree well with each other, which reveal the reliability and feasibility of the proposed theoretical model. Furthermore, there are also some small deviations among them because of the simplification of the two-dimensional model and assumptions in the calculation. Machining tolerance of the test valve, ignoring the frictional resistance between valve core and valve body, ignoring oil compressibility in the simulation, etc. are all the reasons for this deviation.

Effects of Opening on Steady-State Flow Force Characteristics of the Valve

Figure 11 shows the pressure and velocity nephogram near the orifice at the same pressure differential and increasing opening of the valve. Although the opening is different, the distribution of pressure is almost the same. The highest pressure is located at the inlet port, and the pressure changes more violently at the orifice. It also could be seen from **Figure 11** that there are two low-pressure areas, which locate near the tip of the valve core and the orifice, respectively. With the increase of the valve opening, the pressure decreases first and then increases. The pressure acting on the surface of the valve core will vary with the oil velocity, which satisfies the Bernoulli equation. Furthermore, the change of velocity nephogram shows that the variation of velocity at larger opening is more significant than that at smaller openings. The maximum velocity increases rapidly with increasing valve opening, and the high-velocity area also increases rapidly with increasing valve opening. Also, the average velocity at the orifice rises with increasing opening. Higher flow velocities occurring at the orifice will result in larger value of the flow force.

Figure 12 shows the numerical calculation results of pressure distribution along the outline of the valve core tip at different valve openings. To better demonstrate the change of pressure distribution, this line starts at the bottom of the cone angle. When the opening gradually increases, the pressure along the outline of the valve core tip downstream decreases first and then increases, and the position of the minimum pressure move toward downstream gradually. The position where the dividing point of the pressure near the orifice gradually moves to the cone tip is the same as that shown in the pressure nephogram in **Figure 11**.

Figure 13 shows the variation of the axial steady-state flow force acting on the valve core with changing opening. It could be seen that the value of flow force increases first and then decreases with the increase of opening. When the opening is very small (0–0.5 mm), the flow rate in the valve is relatively small and the momentum change is also small, which will result in small flow force. While the opening of the valve gradually increases (0.5~2 mm), the flow rate increases significantly, and so does the corresponding change of momentum, which induces a significant increase in the flow force. At the opening of 2 mm, the steady-state fluid force reaches its maximum value. If the opening of the valve is larger than 2 mm, the throttling effect of the conical valve will be seriously affected. Although the flow rate continues to increase, its variation amplitude of momentum begins to decrease, which also decreases the flow force. At the opening of 4–5 mm, the throttling effect of the valve is not obvious; the steady fluid force is tiny but not equal to zero. Furthermore, the change trend of the axial steady-state flow

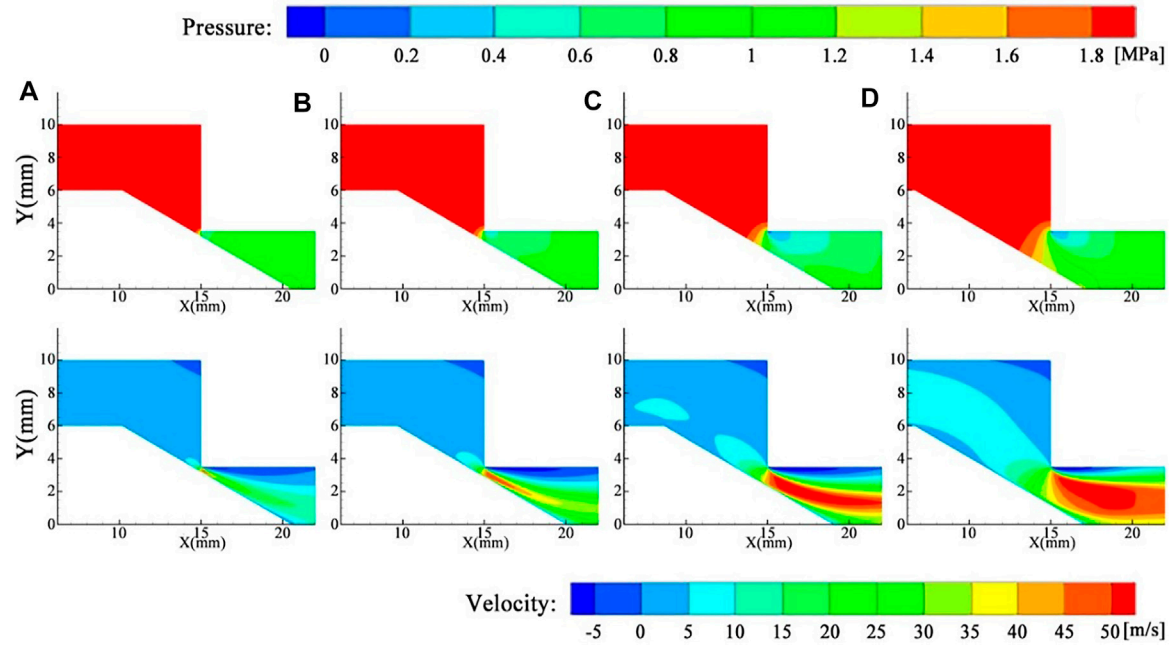

FIGURE 11 | Pressure and velocity nephogram at different openings: **(A)** 0.5 mm; **(B)** 1 mm; **(C)** 2 mm; **(D)** 4 mm.

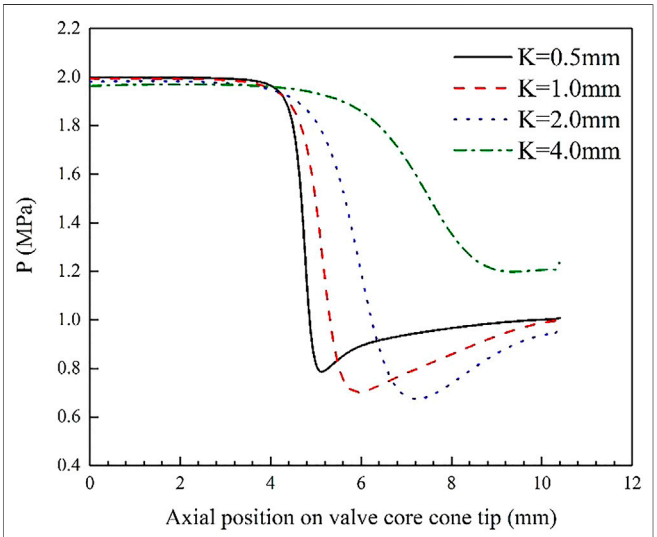

FIGURE 12 | Pressure distribution along the outline of the valve core tip at different openings.

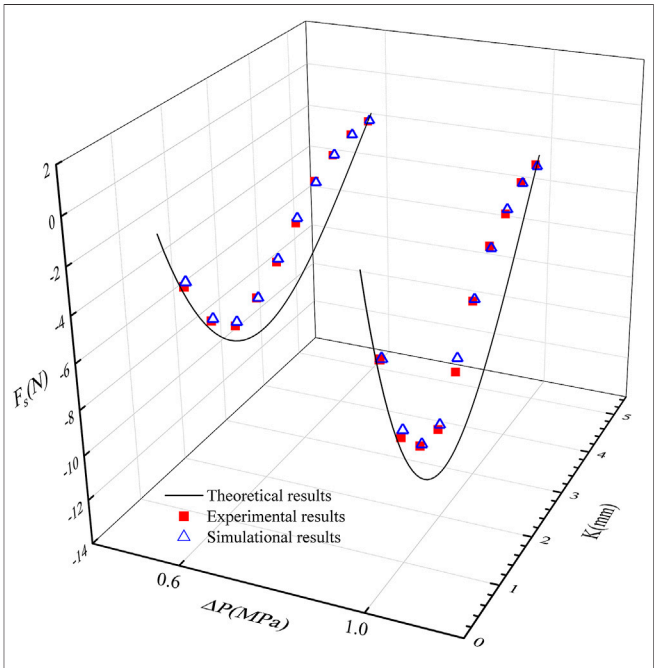

FIGURE 13 | The curve of the axial steady-state flow force acting on the valve core with different openings.

force under different pressure differentials also has similar characteristics.

The flow force is one of the important factors affecting the performance and control accuracy of the valve, which will lead to poor control performance of the system. Reasonable geometric parameters and operating conditions are beneficial for normal operation of valve, avoiding suffering from the negative impact derived from the flow force, reducing power consumption, and improving efficiency. This paper concerns the rules of how flow force works on the valve core, providing a foundation for the improvement of the valve's stability.

CONCLUSION

In this paper, the characteristics of the axial steady-state flow force acting on the internal flow valve core are investigated by theoretical, numerical calculation and experiment investigation. A mathematical model of calculating the steady-state flow force is proposed. Also, the orthogonal test is designed with the help of the four-factor, four-level orthogonal table, which is used to investigate combing geometric parameters and operating conditions affecting the axial steady-state flow force. By extremum difference analysis, the pressure differential and the opening are the main factors affecting the axial steady-state flow force on the internal flow inside the valve. The pressure acting on the surface of the valve core will vary with the changing oil velocity. High flow velocity occurring at the orifice will result in a significant increase in flow force. The larger the pressure differential is, the larger the flow rate and the axial steady-state flow force on the internal flow field of the valve core are. Furthermore, the flow force is small when the opening is very small. With the increase of the valve opening, the flow force increases first and then decreases when the pressure differential remains the same. The results help to improve the reliability, control performance, and service life of the hydraulic systems.

DATA AVAILABILITY STATEMENT

The original contributions presented in the study are included in the article/Supplementary Material, further inquiries can be directed to the corresponding author.

AUTHOR CONTRIBUTIONS

XL and JH contributed to the conception and design of the study. JM, YZ, SX, and QL contributed to comprehensive tests. BL and FX contributed to discussion. All authors contributed to article revision and read and approved the submitted version.

FUNDING

This work was supported by the National Natural Science Foundation of China (Grant Number 51875559), the Fundamental Research Funds for the Central Universities (Grant Number 2015XKMS026), and the Priority Academic Program Development of Jiangsu Higher Education Institutions (PAPD).

REFERENCES

Filo, G., Lisowski, E., and Rajda, J. (2019). Flow Analysis of a Switching Valve with Innovative Poppet Head Geometry by Means of CFD Method. *Flow Meas. Instrumentation* 70, 101643. doi:10.1016/j.flowmeasinst.2019.101643

Gao, L., Wu, C., Zhang, D., Fu, X., and Li, B. (2019). Research on a High-Accuracy and High-Pressure Pneumatic Servo Valve with Aerostatic Bearing for Precision Control Systems. *Precision Eng.* 60, 355–367. doi:10.1016/j.precisioneng.2019.09.005

Han, M., Liu, Y., Wu, D., Zhao, X., and Tan, H. (2017). A Numerical Investigation in Characteristics of Flow Force under Cavitation State inside the Water Hydraulic Poppet Valves. *Int. J. Heat Mass Transfer* 111, 1–16. doi:10.1016/j.ijheatmasstransfer.2017.03.100

Jia, W., Yin, C., Hao, F., Li, G., and Fan, X. (2019). Dynamic Characteristics and Stability Analysis of Conical Relief Valve. *mech* 25 (1), 25–31. doi:10.5755/j01.mech.25.1.22881

Kang, J., Yuan, Z., and Tariq Sadiq, M. (2020). Numerical Simulation and Experimental Research on Flow Force and Pressure Stability in a Nozzle-Flapper Servo Valve. *Processes* 8 (11), 1404. doi:10.3390/pr8111404

Lain, S., Broder, D., Sommerfeld, M., and Goz, M. F. (2002). Modelling Hydrodynamics and Turbulence in a Bubble Column Using the Euler-Lagrange Procedure. *Int. J. Multiphase Flow* 28 (8), 1381–1407. doi:10.1016/s0301-9322(02)00028-9

Lei, J., Tao, J., Liu, C., and Wu, Y. (2018). Flow Model and Dynamic Characteristics of a Direct spring Loaded Poppet Relief Valve. *Proc. Inst. Mech. Eng. C: J. Mech. Eng. Sci.* 232 (9), 1657–1664. doi:10.1177/0954406217707546

Li, L., Yan, H., Zhang, H., and Li, J. (2018). Numerical Simulation and Experimental Research of the Flow Force and Forced Vibration in the Nozzle-Flapper Valve. *Mech. Syst. Signal Process.* 99, 550–566. doi:10.1016/j.ymssp.2017.06.024

Liang, J., Luo, X., Liu, Y., Li, X., and Shi, T. (2016). A Numerical Investigation in Effects of Inlet Pressure Fluctuations on the Flow and Cavitation Characteristics inside Water Hydraulic Poppet Valves. *Int. J. Heat Mass Transfer* 103, 684–700. doi:10.1016/j.ijheatmasstransfer.2016.07.112

Lin, T., Chen, Q., Ren, H., Lv, R., Miao, C., and Chen, Q. (2018). Computational Fluid Dynamics and Experimental Analysis of the Influence of the Energy Recovery Unit on the Proportional Relief Valve. *Proc. Inst. Mech. Eng. Part C: J. Mech. Eng. Sci.* 232 (4), 697–705. doi:10.1177/0954406216687790

Park, S., and Rhee, S. H. (2012). Computational Analysis of Turbulent Super-cavitating Flow Around a Two-Dimensional Wedge-Shaped Cavitator Geometry. *Comput. Fluids* 70, 73–85. doi:10.1016/j.compfluid.2012.09.012

Scuro, N. L., Angelo, E., Angelo, G., and Andrade, D. A. (2018). A CFD Analysis of the Flow Dynamics of a Directly-Operated Safety Relief Valve. *Nucl. Eng. Des.* 328, 321–332. doi:10.1016/j.nucengdes.2018.01.024

Tan, L., Xie, H., Chen, H., and Yang, H. (2019). Structure Optimization of Conical Spool and Flow Force Compensation in a Diverged Flow Cartridge Proportional Valve. *Flow Meas. Instrumentation* 66, 170–181. doi:10.1016/j.flowmeasinst.2019.03.006

Xie, H., Tan, L., Liu, J., Chen, H., and Yang, H. (2018). Numerical and Experimental Investigation on Opening Direction Steady Axial Flow Force Compensation of Converged Flow Cartridge Proportional Valve. *Flow Meas. Instrumentation* 62, 123–134. doi:10.1016/j.flowmeasinst.2018.05.013

Yang, H., Wang, W., and Lu, K. (2019). Cavitation and Flow Forces in the Flapper-Nozzle Stage of a Hydraulic Servo-Valve Manipulated by Continuous Minijets. *Adv. Mech. Eng.* 11 (5), 168781401985143. doi:10.1177/1687814019851436

Yang, H., Wang, W., and Lu, K. (2019). Numerical Simulations on Flow Characteristics of a Nozzle-Flapper Servo Valve with Diamond Nozzles. *Ieee Access* 7, 28001–28010. doi:10.1109/access.2019.2896702

Ye, Y., Yin, C.-B., Li, X.-D., Zhou, W.-j., and Yuan, F.-f. (2014). Effects of Groove Shape of Notch on the Flow Characteristics of Spool Valve. *Energ. Convers. Manag.* 86, 1091–1101. doi:10.1016/j.enconman.2014.06.081

Yuan, C., Song, J., Zhu, L., and Liu, M. (2019). Numerical Investigation on Cavitating Jet inside a Poppet Valve with Special Emphasis on

Cavitation-Vortex Interaction. *Int. J. Heat Mass Transfer* 141, 1009–1024. doi:10.1016/j.ijheatmasstransfer.2019.06.105

Zhang, Z., Jia, L., and Yang, L. (2019). Numerical Simulation Study on the Opening Process of the Atmospheric Relief Valve. *Nucl. Eng. Des.* 351, 106–115. doi:10.1016/j.nucengdes.2019.05.034

Zong, C., Zheng, F., Chen, D., Dempster, W., and Song, X. (2020). Computational Fluid Dynamics Analysis of the Flow Force Exerted on the Disk of a Direct-Operated Pressure Safety Valve in Energy System. *J. Press. Vessel Technol-trans ASME* 142 (1), 14. doi:10.1115/1.4045131

Conflict of Interest: The authors declare that the research was conducted in the absence of any commercial or financial relationships that could be construed as a potential conflict of interest.

Publisher's Note: All claims expressed in this article are solely those of the authors and do not necessarily represent those of their affiliated organizations, or those of the publisher, the editors, and the reviewers. Any product that may be evaluated in this article, or claim that may be made by its manufacturer, is not guaranteed or endorsed by the publisher.

frontiers in Energy Research

ORIGINAL RESEARCH
published: 28 March 2022
doi: 10.3389/fenrg.2022.836456

Hydraulic Characteristics of Axial Flow Pump Device With Different Guide Vane Inlet Angles

Lei Xu[1], Hucheng Zhang[1], Chuan Wang[2,3], Dongtao Ji[1], Wei Shi[4], Weigang Lu[1] and Linguang Lu[1]*

[1]College of Hydraulic Science and Engineering, Yangzhou University, Yangzhou, China, [2]International Shipping Research Institute, GongQing Institute of Science and Technology, Jiujiang, China, [3]High-tech Key Laboratory of Agricultural Equipment and Intelligentization of Jiangsu Province, Jiangsu University, Zhenjiang, China, [4]Jiangsu Water Supply Co., Ltd. In Eastern Route of S-to-N Water Diversion Project, Nanjing, China

To improve the efficiency of low-head pump device in the large-discharge and low-head domain, the hydraulic characteristics of vertical axial flow pump devices with different guide vane inlet angles were studied using computational fluid dynamics (CFD) and model test methods. The $Q \sim H_{zz}$ and $Q \sim \eta_{zz}$ curves of the pump device were obtained for different impeller blade angles when the inlet angle adjustments of the guide vane were 0° and −12°. The resulting hydraulic performance was compared and analyzed. The results showed that the pump device efficiency under low-head and large-discharge conditions was improved when the guide vane inlet angle was rotated in the clockwise direction. The reason for the increased pump device efficiency was analyzed using CFD. When the guide vane inlet angle adjustments were 0° and −12° under low-head working conditions, the vortex in the guide vane was eliminated, the hydraulic loss of the guide vane decreased, and the energy performance of the pump improved. When the operational conditions of the pump device deviate from its high-efficiency zone due to limitations in the pump model or the motor itself, the application of these results could improve its hydraulic performance, which is of great significance to the design and application of low-head pump devices.

Keywords: axial-flow pump device, guide vane, inlet angle, hydraulic characteristics, numerical simulation, model test

OPEN ACCESS

Edited by:
Xiaojun Li,
Zhejiang Sci-Tech University, China

Reviewed by:
Kan Kan,
College of Energy and Electrical Engineering, China
Peijian Zhou,
China Jiliang University, China
Yu Chen,
Nanjing Institute of Technology (NJIT), China

****Correspondence:***
Lei Xu
leixu@yzu.edu.cn

Specialty section:
This article was submitted to Process and Energy Systems Engineering, a section of the journal Frontiers in Energy Research

Received: *15 December 2021*
Accepted: *24 January 2022*
Published: *28 March 2022*

Citation:
Xu L, Zhang H, Wang C, Ji D, Shi W, Lu W and Lu L (2022) Hydraulic Characteristics of Axial Flow Pump Device With Different Guide Vane Inlet Angles. Front. Energy Res. 10:836456. doi: 10.3389/fenrg.2022.836456

INTRODUCTION

Low-head pumping stations are widely used in fields such as water resource allocation, agriculture irrigation and drainage, urban drainage, and water environment improvement plans. The design heads of many of these pumping stations can be very low—that is, approximately 1.0 m (Qi et al., 2017; Yu et al., 2018). Affected by the pump model and motor, the pump devices used in these pumping stations often operate in low-head and large-discharge areas, which deviate from high-efficiency areas, resulting in the operational efficiency of the pumping stations being low (Wu et al., 2016).

The vertical axial flow pump device is arranged in the vertical direction, having the advantages of a simple structure, excellent heat dissipation, convenient installation and maintenance, and mature design and manufacture (Liu et al., 2008; Zhang et al., 2011); it is also widely applied in low-head pumping stations. It consists of an inlet conduit, impeller, guide vane, and outlet conduit, the hydraulic characteristics of the pump device being determined by these four components and their

mutual matching. For example, the guide vane is used to recycle the kinetic energy of the water flow, its hydraulic design impacting the hydraulic performance of the pump and pump device. With a guide vane installed in the pump, water flow from the impeller outlet with tangential velocity is partly eliminated, and the water flow energy is converted into pressure energy, the recyclable rotation kinetic energy of the flow using the guide vane accounting for 10–15.7% of the total energy of the impeller outlet (Tang and Wang, 2006; Li et al., 2009). Compared to an axial flow pump with no guide vane, the efficiency can be improved by 5% when a guide vane is installed in the pump (Hu et al., 2008). The design of the guide vane clearly influences the position of the high-efficiency area for the pump (Zhou and Xu, 2007). Previous studies have shown that the pump device efficiency and discharge with the guide vane were higher than those for a pump device with no guide vane under design working conditions (Feng et al., 2012). To improve the efficiency of the axial flow pump, the influence of the guide vane angle adjustments on the hydraulic performance of the axial flow pump has been studied; the results have shown that the water head and efficiency of the axial flow pump increase when the guide vane is adjusted from the off-design condition, the pump efficiency improving by a maximum of 2.16%, and the stable operating range broadening (Qian et al., 2010; Qian et al., 2013).

The vertical axial flow pump device used in extra-low-head pumping stations usually works in a large-discharge area deviating from the high-efficiency area of the pump device, with the inlet angle of the guide vane not matching the direction of water flow at the impeller outlet. Consequently, the pump device efficiency can be improved by adjusting the inlet angle of the guide vane. Another function of the guide vane is that it can be used to fix the guide bearing in its wheel hub so that only the inlet angle of the guide vane can be adjusted.

Computational fluid dynamics (CFD) has been widely used in studies of the axial flow pump (Kan et al., 2021a; Al-Obaidi, 2021), submersible pump (Patil et al., 2019; Wang et al., 2021), centrifugal pump (Gonzalez and Santolaria, 2006; Wang et al., 2020a), the intake of pumping stations (Zhou et al., 2021) and the pump device (Kan et al., 2017), and other aspects (Wang et al., 2020b; Tang et al., 2021; Zawistowski and Kleiber, 2021; Zhang et al., 2021; Zhu et al., 2021), providing a convenient and effective method for their design and performance optimization. This study focuses on the vertical axial flow pump device and examines the influence of adjusting the guide vane inlet angle on energy performance of the pump device using three-dimensional turbulence flow numerical simulations. The results of the study are verified using a pump device model test.

PUMP DEVICE AND METHODS

Parameters of Axial Flow Pump Device

Based on the parameters of a low-head pumping station, the influence of the guide vane inlet angle adjustment on energy performance of a vertical axial flow pump device was investigated. The parameters of the pumping station were as follows: the design head, maximum head, and minimum head were 1.08, 1.5, and 0.11 m respectively; the design discharge of one pump was 6.67 m^3/s; the TJ04-ZL-07 pump model, used in the pump test in the same test-bed as for the South-to-North Water Diversion Project, was chosen (Liu et al., 2006); the prototype pump impeller diameter (D_P) and prototype pump rotation speed (n_P) were 1,460 mm and 247 r/min, respectively, based on the principle that the prototype (nD) and the model (nD) were equal, the model pump impeller diameter (D_m) and model pump rotation speed (n_m) being 300 mm and 1,200 r/min, respectively. The performance curve of the pump selection for this pumping station is shown in **Figure 1**. It can be seen that the design operating point is in the large-discharge and low-head area and that the pump efficiency is low.

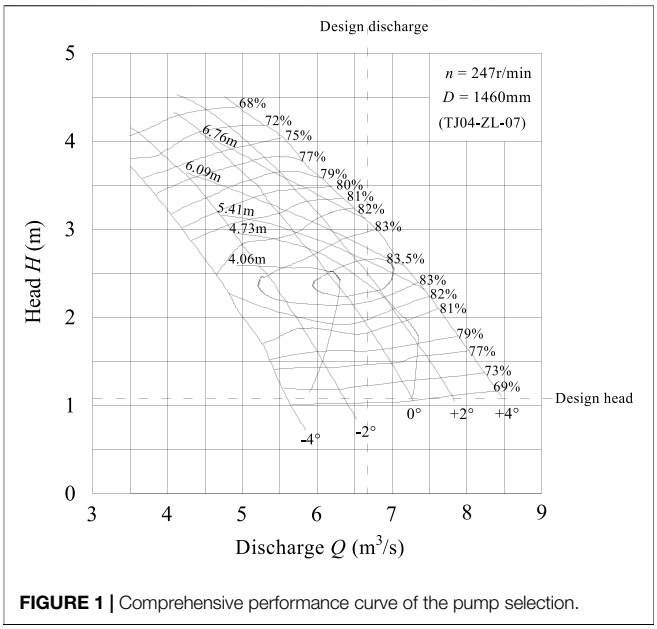

FIGURE 1 | Comprehensive performance curve of the pump selection.

The elbow inlet and siphon outlet conduits were adopted in the pumping station, a drawing of the vertical axial flow pump device model being shown in **Figure 2**.

Adjustment Scheme of Guide Vane Inlet Angle

In the vertical axial flow pump device, the guide vane inlet continues the water flow from the impeller; thus, the inlet shape line design needs to meet the requirement that the stream flows into the guide vane smoothly. The stream then flows into the outlet conduit from the guide vane. Therefore, the outlet shape line design needs to meet the requirement that it efficiently adjusts the flow direction. From a structural design point of view, a guide bearing is installed in the guide vane wheel hub. Thus, the guide vane needs to meet the requirement of securing the guide bearing block.

Based on the guide vane hydraulic design and structure requirements, the guide vane can be divided into three sections—that is, the inlet, middle, and outlet sections, as shown in **Figure 3**, where H is the total height of the guide vane and h is the inlet height of the guide vane. In this study, the

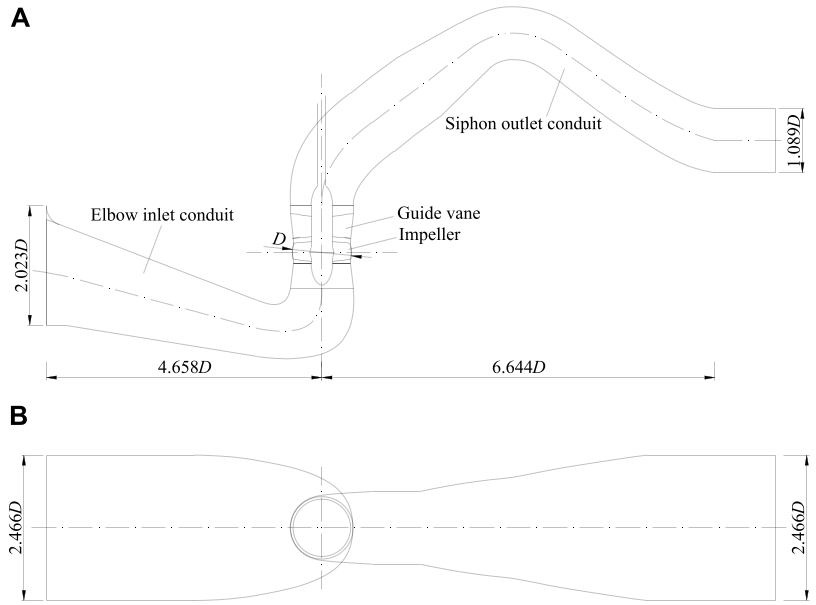

FIGURE 2 | Drawing of the vertical axial-flow pump device. **(A)** Elevation, **(B)** Plan.

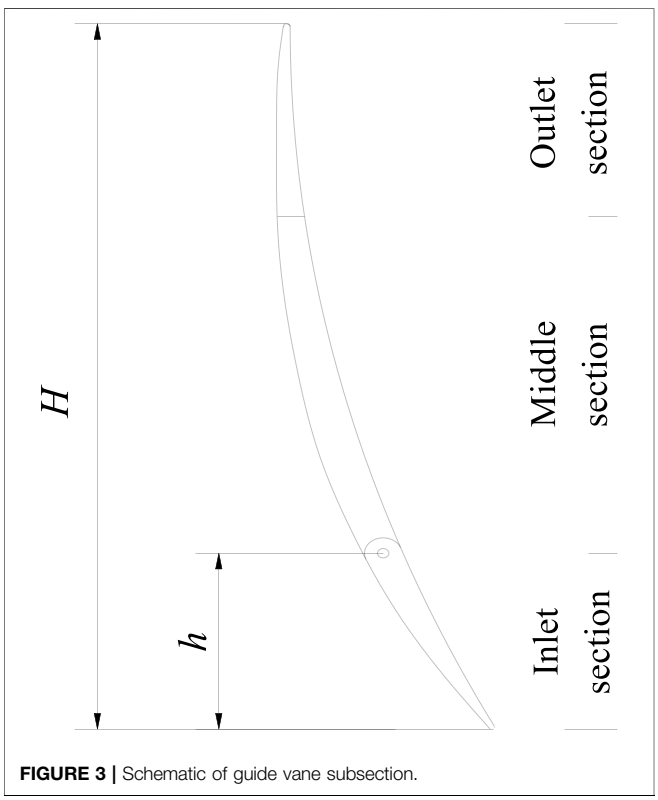

FIGURE 3 | Schematic of guide vane subsection.

middle and outlet sections were fixed, and only the angle of the inlet section could be adjusted. When the total height of guide vane (H) is a constant value, when the inlet height of the guide vane (h) is higher, the fixed length of the guide vane is reduced, adversely impacting the function of the fixed guide bearing block. Moreover, when h is lower, the influence of the guide vane adjustment on the hydraulic performance of the pump is adversely impacted. Consequently, h was taken to be $0.25{\cdot}H$.

For an axial flow pump, the guide vane inlet angle (β_0) can be determined based on the design condition, the guide vane inlet angle being consistent with the direction of the flow absolute velocity at the impeller outlet based on the design discharge condition (**Figure 4A**), the stream flowing into the guide vane smoothly. When the pump operates in an off-design condition, the inlet angle does not match the flow direction (**Figures 4B,C**), flow impact and separation being generated in the guide vane, increasing the hydraulic loss and reducing efficiency. In **Figure 4**, v_0, v_s, v_L are the absolute velocity of the flow at impeller outlet under the design condition, smaller discharge condition, and larger discharge condition, respectively; w_0, w_s, w_L are the relative velocity of the flow at impeller outlet under the design condition, smaller discharge condition, and larger discharge condition, respectively; u is the transport velocity; α_0, α_s, α_L are the angle between absolute velocity and transport velocity under the design condition, smaller discharge condition, and larger discharge condition, respectively.

The guide vane inlet angle (β_0) can be determined based on the design working conditions. For ease of expression, the inlet angle adjustment ($\Delta\beta$) can be taken to be 0° when the guide vane inlet angle is β_0, as shown in **Figure 5A**. To improve the efficiency under the larger discharge condition, based on the flow direction at the impeller outlet, the guide vane inlet angle should be rotated clockwise based on β_0, as shown in **Figure 5B** so that the stream can flow smoothly into the guide vane. For the vertical axial flow pump of the pumping station, the inlet angle adjustment (u) can be taken to be −12°.

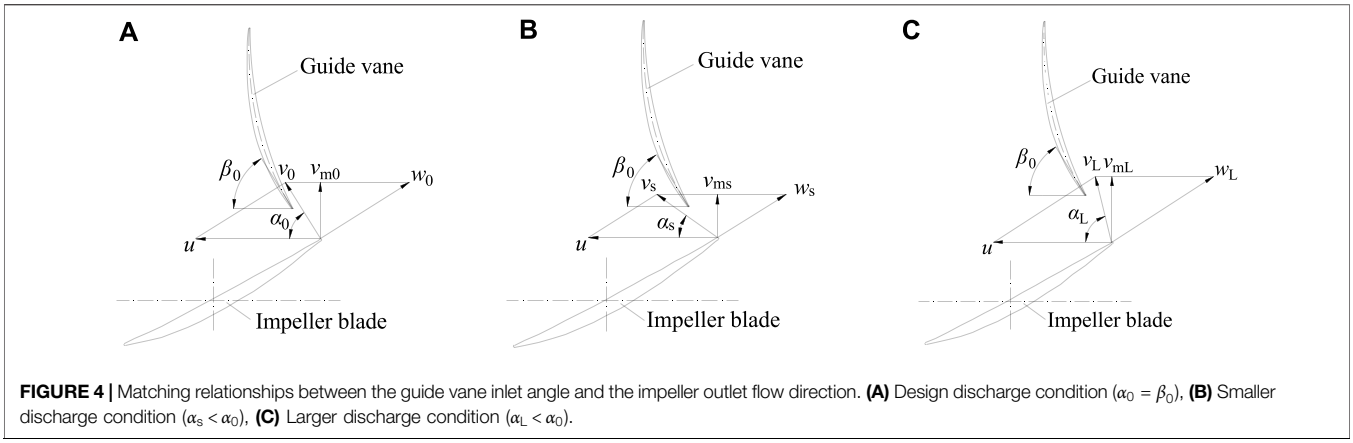

FIGURE 4 | Matching relationships between the guide vane inlet angle and the impeller outlet flow direction. **(A)** Design discharge condition ($\alpha_0 = \beta_0$), **(B)** Smaller discharge condition ($\alpha_s < \alpha_0$), **(C)** Larger discharge condition ($\alpha_L < \alpha_0$).

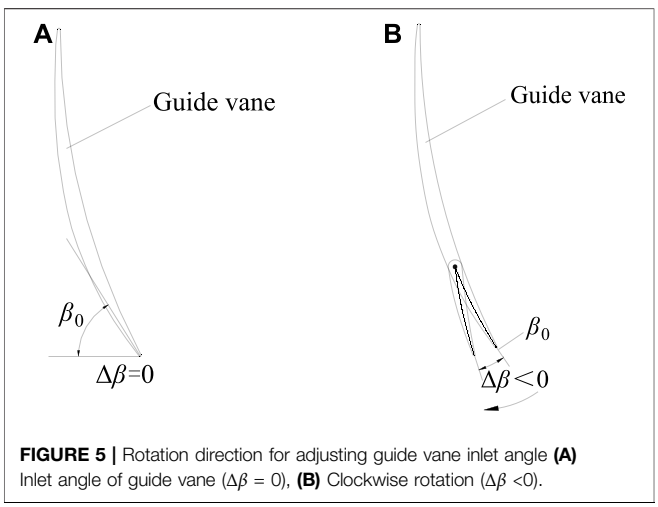

FIGURE 5 | Rotation direction for adjusting guide vane inlet angle **(A)** Inlet angle of guide vane ($\Delta\beta$ = 0), **(B)** Clockwise rotation ($\Delta\beta$ <0).

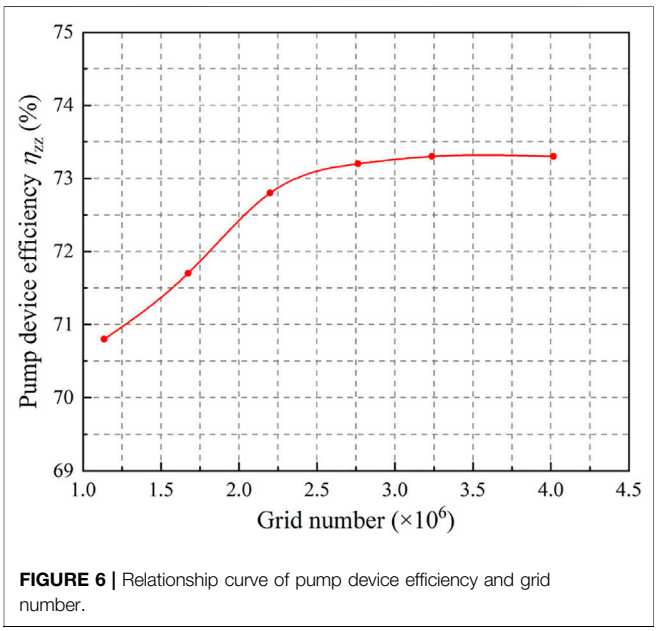

FIGURE 6 | Relationship curve of pump device efficiency and grid number.

Numerical Simulation Method

Governing Equations and Turbulence Model

The Reynolds-averaged Navier-Stokes equations can be applied to solve the flow field in a vertical axial flow pump device, as follows:

$$\frac{\partial \rho}{\partial t} + \rho \frac{\partial \overline{u_i}}{\partial x_i} = 0 \tag{1}$$

$$\rho \frac{\partial \overline{u_i}}{\partial t} + \rho \frac{\partial \overline{u_i}\,\overline{u_j}}{\partial x_j} = -\frac{\partial \bar{p}}{\partial x_i} + \frac{\partial}{\partial x_j}\left[\mu\left(\frac{\partial \overline{u_i}}{\partial x_j} + \frac{\partial \overline{u_j}}{\partial x_i}\right) - \rho \overline{u_i' u_j'}\right] + F_i \tag{2}$$

where ρ is the density, t is time, $\overline{u_i}$ and $\overline{u_j}$ are the mean velocity components, $\bar{p}$ is the mean pressure, x_i and x_j are coordinate directions, μ is the dynamic viscosity, F_i is the body force component, $\rho \overline{u_i' u_j'}$ is the Reynolds stress, and u_i' and u_j' are fluctuating velocity components, respectively.

There are many turbulence models for fluid flow simulations (Li et al., 2020; Kan et al., 2021b; Han et al., 2021). The Renormalization Group (RNG) $k-\varepsilon$ turbulence model was chosen to solve the flow in the pump device, because this model is suitable for solving rotating, separated, and vortex flows (Jafarzadeh et al., 2011; Qiao et al., 2018; Jiao et al., 2019; Caruso amd Meskell, 2021). The k and ε equations of the RNG $k-\varepsilon$ turbulence model can be expressed as follows:

$$\rho \frac{\partial k}{\partial t} + \rho \frac{\partial k \overline{u_i}}{\partial x_i} = \frac{\partial}{\partial x_j}\left[\left(\mu + \frac{\mu_t}{\sigma_k}\right)\frac{\partial k}{\partial x_j}\right] + G_k - \rho\varepsilon \tag{3}$$

$$\rho \frac{\partial \varepsilon}{\partial t} + \rho \frac{\partial \varepsilon \overline{u_i}}{\partial x_i} = \frac{\partial}{\partial x_j}\left[\left(\mu + \frac{\mu_t}{\sigma_\varepsilon}\right)\frac{\partial \varepsilon}{\partial x_j}\right] + \frac{C_{1\varepsilon}}{k} G_k - C_{2\varepsilon}\rho\frac{\varepsilon^2}{k} \tag{4}$$

where G_k is the turbulence kinetic energy production term, $C_{1\varepsilon}$ is an empirical constant, $C_{2\varepsilon}$ is an empirical constant, σ_k is the corresponding Prandtl number for the turbulence kinetic energy k, and σ_ε is the corresponding Prandtl number for the turbulence kinetic energy dissipation rate ε.

Computational Domain and Mesh Generation

The computational domain of the three-dimensional turbulence flow simulations for the pump device comprises the forebay, inlet conduit, impeller, guide vane, outlet conduit, and outlet sump. The bodies of the inlet conduit, impeller, guide vane, and

TABLE 1 | Grid number of each component of the computational domain of the pump device.

Component of computational domain	Forebay	Inlet conduit	Impeller	Guide vane	Outlet conduit	Outlet sump
Grid number ($\times 10^4$)	33.2	53.2	57.9	91.5	55.9	32.3

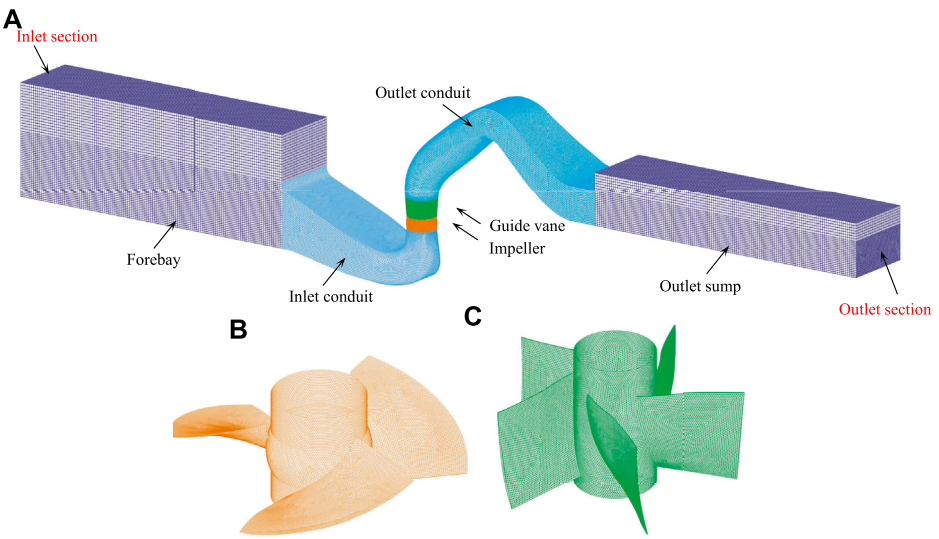

FIGURE 7 | Computational domains and mesh generations of vertical axial flow pump device. **(A)** Pump device, **(B)** Impeller, **(C)** Guide vane.

outlet conduit and the fluid flow within them are complex; thus, an unstructured mesh was adopted. The bodies and fluid flow of the forebay and outlet sump are, however, simple; therefore, a structured mesh was adopted. To obtain the most economical grid number, the grid independence was checked. **Figure 6** shows the relationship between the pump device efficiency and grid number under the conditions of a blade angle of 0°, guide vane inlet angle adjustment of 0°, and discharge of 245 L/s. When the gird number exceeds approximately 3,240,000, the pump efficiency changes slightly. Consequently, the number of mesh cells for the vertical axial flow pump device was chosen to be 3,240,000, the grid numbers of each component being listed in **Table 1**. The value of $y+$ affects the calculation accuracy: in this calculation the $y+$ value of the impeller wall was 14.8. The computational domains and mesh generations for them are shown in **Figure 7**.

Boundary Conditions and Numerical Settings

The inlet boundary was set in the forebay, the velocity being uniformly distributed on the inlet boundary, and the flow direction being perpendicular to it. Because the discharge was known, the velocity inlet boundary condition was adopted. The outlet boundary was set at the outlet sump, far from the outlet section of the outlet conduit. The flow direction was perpendicular to the outlet boundary, the flow being fully developed there so that the outflow boundary condition could be adopted there. The bottom of the forebay and outlet sump, the side walls of the conduit, the surface of the guide vane, and the surface of the impeller blade were solid walls, the impeller blade surfaces being set as a rotation wall. The surfaces of the forebay and outlet sump were free water surfaces, the symmetry boundary being specified on the water surface.

In the numerical simulations, the SIMPLEC algorithm was used to solve the pressure-velocity coupling equations, the first-order upwind differencing scheme was used to solve the governing equations, k and ε , and the convergence precision was set to 1×10^{-7}.

The numerical simulation conditions were as follows: the model pump impeller diameter (D_m) and rotation speed (n_m) were 300 mm and 1,200 r/min, respectively; the impeller blade angles (α) were −4°, −2°, and 0°; and the guide vane inlet angle adjustments ($\Delta\beta$) were 0° and −12°. **Figure 8** shows a perspective view of the vertical axial flow pump with two guide vane inlet angle adjustments.

Model Test Method

The model vertical axial flow pump device included all flow conduits, the model inlet and outlet conduits being made of steel plates. An image of the model vertical axial flow pump device installed on the pumping station test bench at Yangzhou University is shown in **Figure 9**. The uncertainty of the pump device efficiency test in this experimental study was ±0.36%, the main test instruments of the test bench being listed in **Table 2**. Consistent with the numerical calculations, the energy

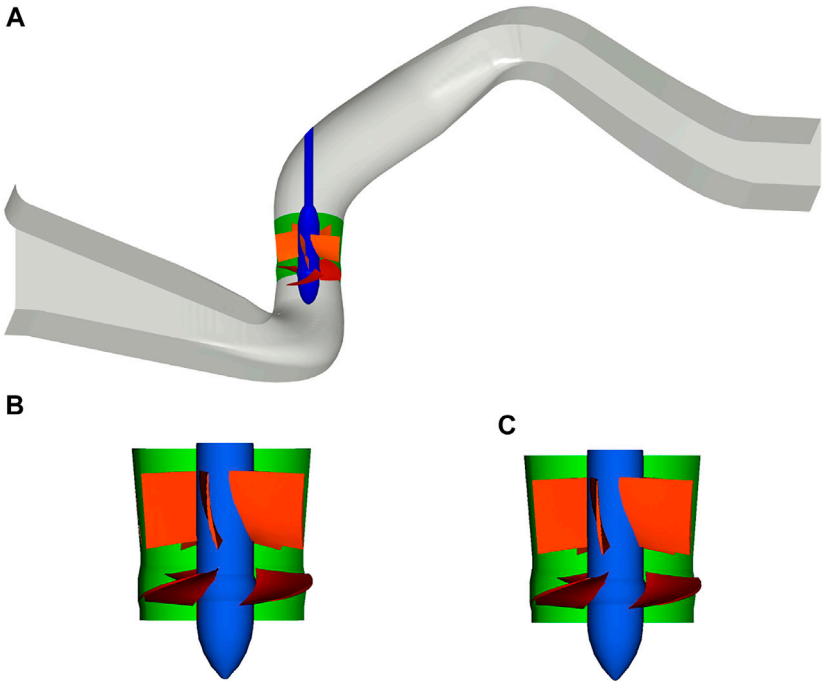

FIGURE 8 | Perspective view of the model vertical axial flow pump device. **(A)** Pump Device, **(B)** Pump Segment ($\Delta\beta = 0^{\circ}$), **(C)** Pump Segment ($\Delta\beta = -12^{\circ}$)

FIGURE 9 | Image of vertical axial flow pump device model.

TABLE 2 | Main test instruments of test bench.

Measuring items	Instrument	Instrument model	Accuracy
Head	Differential pressure transmitter	EJA110A	±0.1%
Flow rate	Electromagnetic flowmeter	E-mag	±0.2%
Torque and rotation speed	Torque and speed sensor	JC1A-500	±0.1%

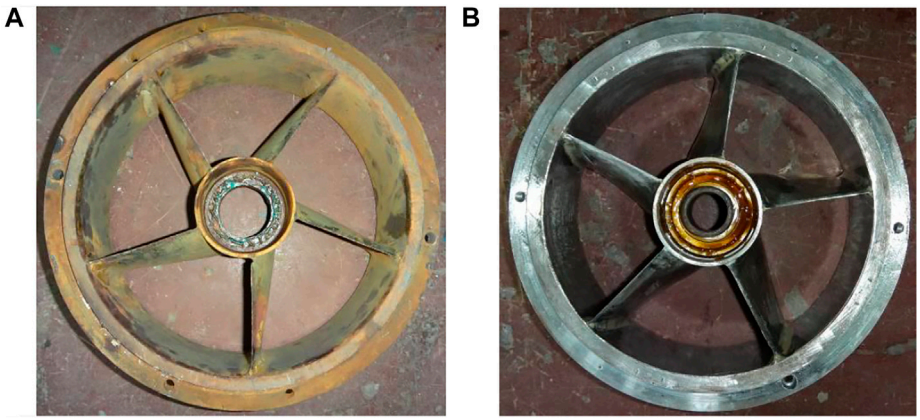

FIGURE 10 | Images of model guide vanes with inlet angle adjustments $\Delta\beta$ of 0° and −12°, respectively. **(A)** $\Delta\beta$ = 0°, **(B)** $\Delta\beta$ = −12°.

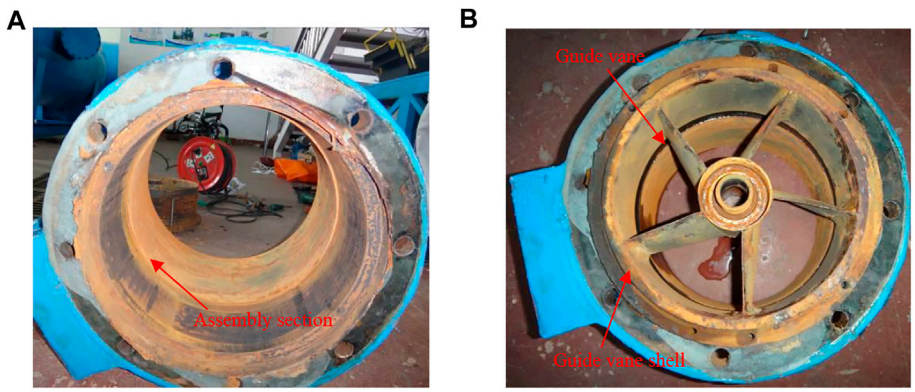

FIGURE 11 | Images of the model guide vane assembly. **(A)** Guide vane shell, **(B)** Assembled guide vane.

performance test of the pump devices with inlet angle adjustments ($\Delta\beta$) of 0° and −12° was conducted under 3 impeller blade angles (α) of −4°, −2°, and 0°, respectively. The head, torque, and rotation speed of the pump device are measured at different flow discharges under each impeller blade angle and inlet angle adjustment of guide vane, and the pump device efficiency is calculated according to the test results. The flow discharge change is regulated by valve.

The impeller blade angle was changed by adjusting the blade angle, while the guide vane inlet angle was changed by using two model guide vanes. The guide vane with an inlet angle adjustment ($\Delta\beta$) of 0° was the original guide vane of the TJ04-ZL-07 pump model, as shown in **Figure 10A**. The guide vane with an inlet angle adjustment ($\Delta\beta$) of −12° was constructed, as shown in **Figure 10B**. The model guide vane was divided into two parts—that is, the guide vane shell and the guide vane itself, the guide vane shell being shown in **Figure 11A**. The two model guide vanes had the same shell; thus, the energy performance of the pump device with two guide vane inlet angles could be tested and compared simply by replacing the guide vane. The assembly of the guide vane and guide vane shell is shown in **Figure 11B**.

RESULTS AND ANALYSIS

Numerical Simulation Results and Analysis

Under the conditions of the impeller blade angles (α) of −4°, −2°, and 0°, respectively, three-dimensional turbulence flow in the vertical axial flow pump device was calculated when the inlet angle adjustments of the guide vane ($\Delta\beta$) were 0° and −12°, respectively. Based on the calculation results, the $Q \sim H_{zz}$ and $Q \sim \eta_{zz}$ relationship curves of the vertical axial flow pump device are shown in **Figure 12**.

From **Figure 10**, it can be seen that there is an intersection point (O) between the two $Q \sim \eta_{zz}$ curves with inlet angle adjustments ($\Delta\beta$) of 0° and −12°, respectively. On the left side of point O, the pump device efficiency (η_{zz}) at an inlet angle adjustment ($\Delta\beta$) of 0° is higher than that at an inlet angle adjustment ($\Delta\beta$) of −12°; on the right side of point O, the pump device efficiency (η_{zz}) at an inlet angle adjustment ($\Delta\beta$)

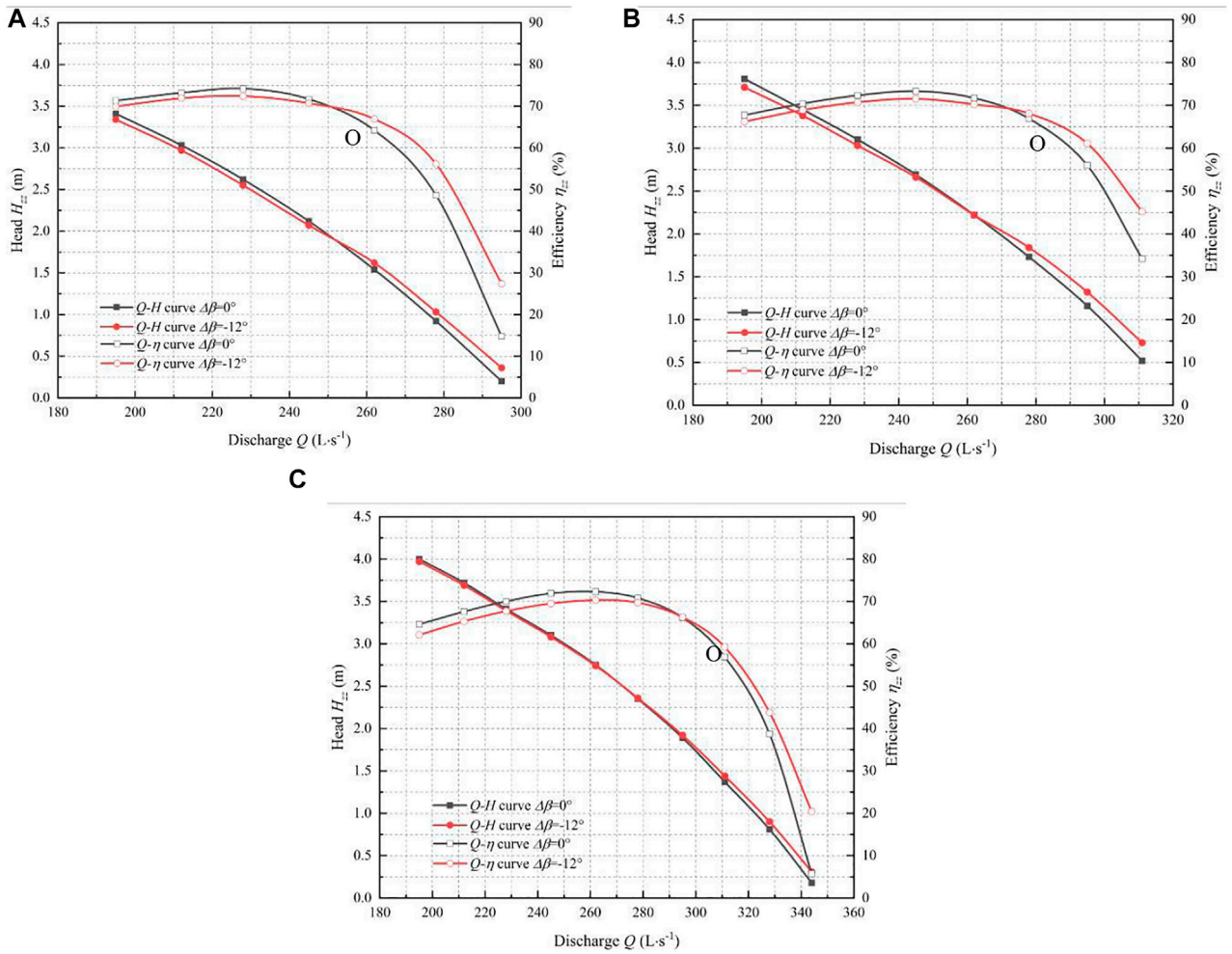

FIGURE 12 | Numerical calculation results of $Q \sim H_{zz}$ and $Q \sim \eta_{zz}$ relationship curves of the axial flow pump device with $\Delta\beta$ of 0° and −12°, respectively. **(A)** $\alpha = -4°$, **(B)** $\alpha = -2°$, **(C)** $\alpha = 0°$.

of 0° is lower than that at an inlet angle adjustment ($\Delta\beta$) of −12°. That is, the farther away from point O one gets, the larger the difference between the efficiency of the two pump devices. Compared with the pump device with an inlet angle adjustment ($\Delta\beta$) of 0°, the optimal efficiency of the pump device with an inlet angle adjustment ($\Delta\beta$) of −12° is reduced by approximately 2%.

To analyze the influence of the guide vane inlet angle adjustment, based on the composition of the pump, the relationship between the pump device efficiency (η_{zz}), impeller efficiency (H_{yl}), vane efficiency (η_{dy}), and conduit efficiency (η_{ld}) can be expressed as follows:

$$\eta_{zz} = \frac{\rho g Q H_{zz}}{P_{bz}} = \frac{\rho g Q H_{bd}}{P_{bz}} \times \frac{H_{zz}}{H_{bd}} = \eta_{bd} \times \eta_{ld} = \eta_{yl} \times \eta_{dy} \times \eta_{ld} \tag{5}$$

where η_{zz} is the pump device efficiency, g is the acceleration of gravity, Q is the discharge, H_{zz} is the pump head, P_{bz} is the pump shaft power, η_{bd} is the pump segment efficiency, η_{yl} is the impeller efficiency, and H_{yl} is the impeller head.

The pump segment efficiency (η_{bd}), impeller efficiency (η_{yl}), guide vane efficiency (η_{dy}), and conduit efficiency (η_{ld}) can be expressed as follows:

$$\eta_{bd} = \frac{\rho g Q H_{bd}}{P_{bz}} \times 100\% \tag{6}$$

$$\eta_{yl} = \frac{\rho g Q H_{yl}}{P_{bz}} \times 100\% \tag{7}$$

$$\eta_{dy} = \frac{\rho g Q H_{bd}}{\rho g Q H_{yl}} = \frac{H_{bd}}{H_{yl}} = \frac{H_{yl} - \Delta h_{dy}}{H_{yl}} \times 100\% \tag{8}$$

$$\eta_{ld} = \frac{\rho g Q H_{zz}}{\rho g Q H_{bd}} = \frac{H_{zz}}{H_{bd}} = \frac{H_{zz}}{H_{zz} + \Delta h_{ld}} \times 100\% \tag{9}$$

where H_{bd} is the pump segment head, H_{yl} is the impeller head, Δh_{dy} is the guide vane hydraulic loss, and Δh_{ld} is the conduit hydraulic loss.

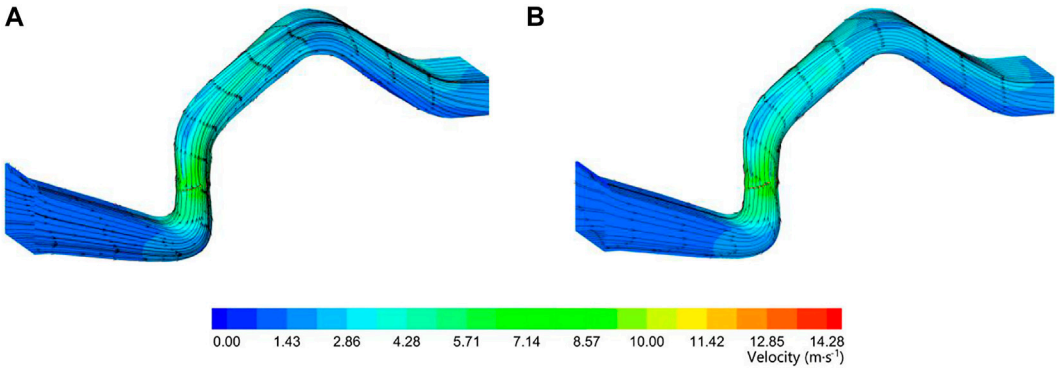

FIGURE 13 | Pump device flow fields with $\Delta\beta$ of 0° and −12°, respectively. **(A)** $\Delta\beta$ = 0°, **(B)** $\Delta\beta$ = −12°.

TABLE 3 | Comparison of energy performance parameters of pump devices with $\Delta\beta$ of 0° and −12°.

$\Delta\beta$ (°)	H_{yl} (m)	η_{yl} (%)	H_{bd} (m)	Δh_{dy} (m)	η_{dy} (%)	η_{bd} (%)	Δh_{ld} (m)	H_{zz} (m)	η_{ld} (%)	η_{zz} (%)
0	1.625	77.1	1.414	0.211	87.0	67.1	0.603	0.811	57.4	38.5
−12	1.634	77.3	1.496	0.138	91.6	70.8	0.596	0.900	60.2	42.6

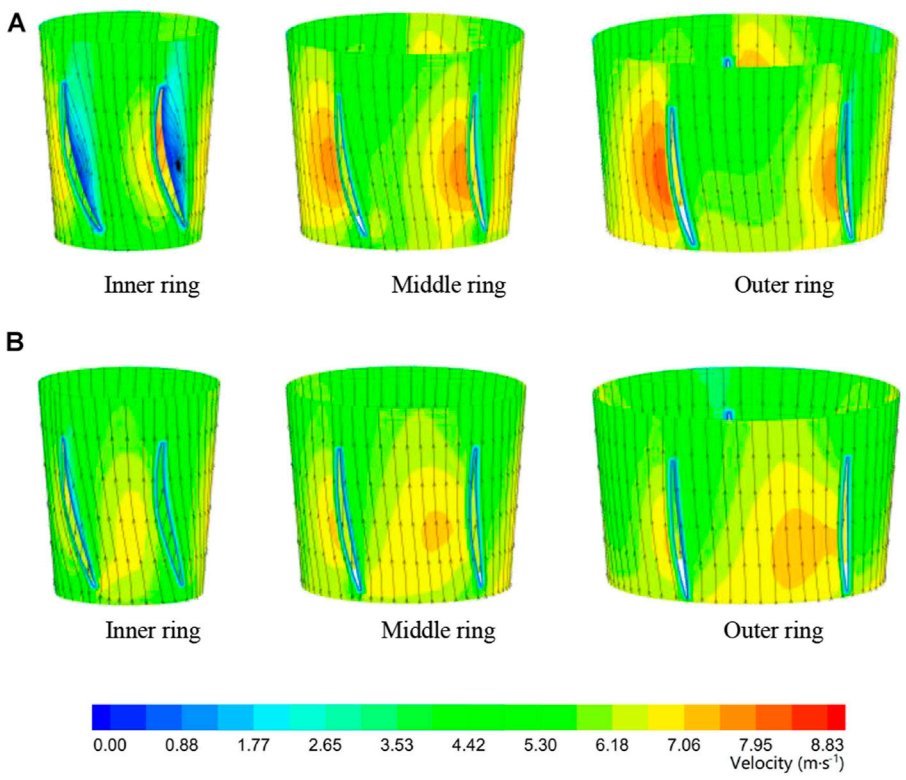

FIGURE 14 | Guide vane flow fields with $\Delta\beta$ of 0° and −12°, respectively. **(A)** $\Delta\beta$ = 0°, **(B)** $\Delta\beta$ = −12°.

The three-dimensional turbulence flow in the pump device with a guide vane inlet angle adjustment ($\Delta\beta$) of 0° and −12° were simulated when the impeller blade angle (α) was 0° and the discharge (Q) was 0.33 m^3/s, the flow fields of the two pumps being shown in **Figure 13**. It can be seen that the flow fields in the conduits of the pump device are the same when the inlet angles of

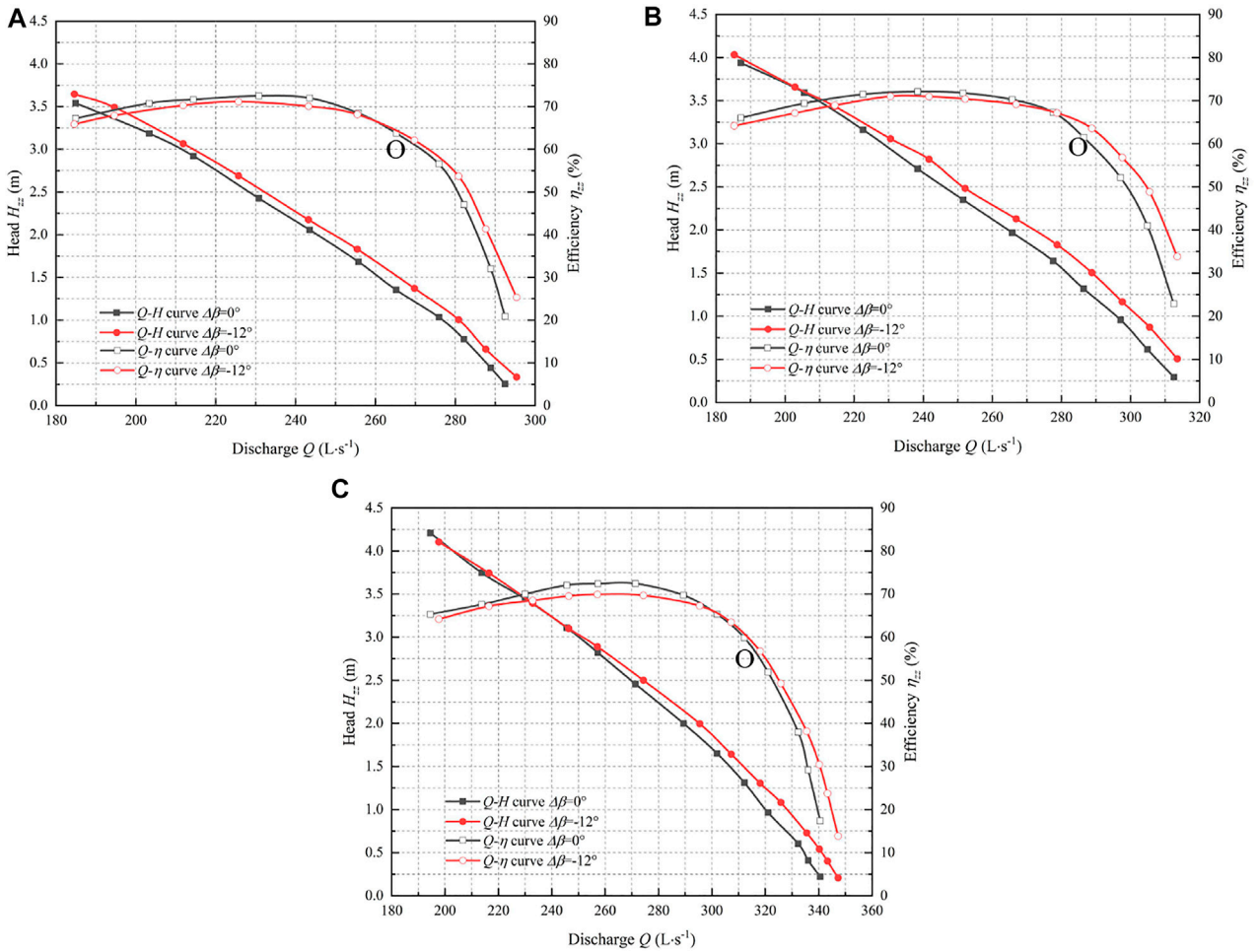

FIGURE 15 | Model test results of $Q \sim H_{zz}$ and $Q \sim \eta_{zz}$ relationship curves of the axial flow pump device with $\Delta\beta$ of 0° and −12°, respectively. **(A)** $\alpha = -4°$, **(B)** $\alpha = -2°$, **(C)** $\alpha = 0°$.

the guide vane differ, the flow velocity of the water in the inlet conduit gradually increases, the flow decreases smoothly and evenly, and the water flow in the outlet conduit diffuses smoothly without poor flow patterns. Based on the calculated hydraulic loss of each part, the relationships between Δh_{dy} and η_{dy}, η_{bd}, and η_{zz} were analyzed, and the influence of $\Delta\beta$ on the vertical axial flow pump device efficiency was examined. The main energy performance parameters of the pump device with inlet angle adjustments ($\Delta\beta$) of 0° and −12° under the chosen working conditions are listed in **Table 3**.

It can be seen that when $\Delta\beta$ is adjusted from 0° to −12° for the vertical axial flow pump device, the impeller heads (H_{yl}) and impeller efficiencies (η_{yl}) are the same, the conduit hydraulic losses (Δh_{ld}) change a little, and the conduit flow fields remain the same. However, the guide vane hydraulic loss (Δh_{dy}) decreases from 0.211 to 0.138 m; thus, the guide vane efficiency (η_{dy}) increases from 87.0 to 91.6%, the pump segment efficiency (η_{bd}) increases from 67.1 to 70.8%, and the pump device efficiency increases from 38.5 to 42.6%.

Under the conditions of an impeller angle of 0° and a discharge of 0.33 m^3/s, the flow fields of the outer, middle, and inner rings of the guide vane when $\Delta\beta$ is 0° are shown in **Figure 14A**, the flow fields when $\Delta\beta$ is −12° being shown in **Figure 14B**. It can be seen that when $\Delta\beta$ is 0°, the direction of water flow entering the guide vane does not match the guide vane inlet angle; therefore, the separation flow and vortex are at the front of the guide vane, as shown in **Figure 14A**. Conversely, when $\Delta\beta$ is −12°, the direction of water flow entering the guide vane matches the guide vane inlet angle. Thus, there is no vortex in the guide vane, as shown in **Figure 14B**, and the guide vane hydraulic loss decreases.

Model Test Results and Analysis

A model test for the vertical axial flow pump device was conducted to verify the numerical computational results. Based on the test results, the $Q \sim H_{zz}$ and $Q \sim \eta_{zz}$ curves of the model pump device with inlet angle adjustments ($\Delta\beta$) of 0° and −12°, respectively, under different impeller blade angles are shown in **Figure 15**. The energy performance parameters of the main working conditions for the model vertical axial flow pump device with $\Delta\beta$ of 0° and −12° are listed in **Table 4**.

From the pump device model test results, it can be concluded that

TABLE 4 | Comparison of performance parameters at main operating points of the pump devices.

α (°)	$\Delta\beta$ (°)	Optimal operating point of the pump			Intersection point O of Q ~ H_{zz} curve	
		Q (L/s)	H_{zz} (m)	η_{zz} (%)	Q (L/s)	η_{zz} (%)
−4	0	230.8	2.43	72.5	258.6	67.5
	−12	225.7	2.69	71.1		
−2	0	238.4	2.71	72.1	278.7	67.1
	−12	230.5	3.06	71.0		
0	0	271.4	2.46	72.4	301.9	65.3
	−12	257.1	2.89	69.9		

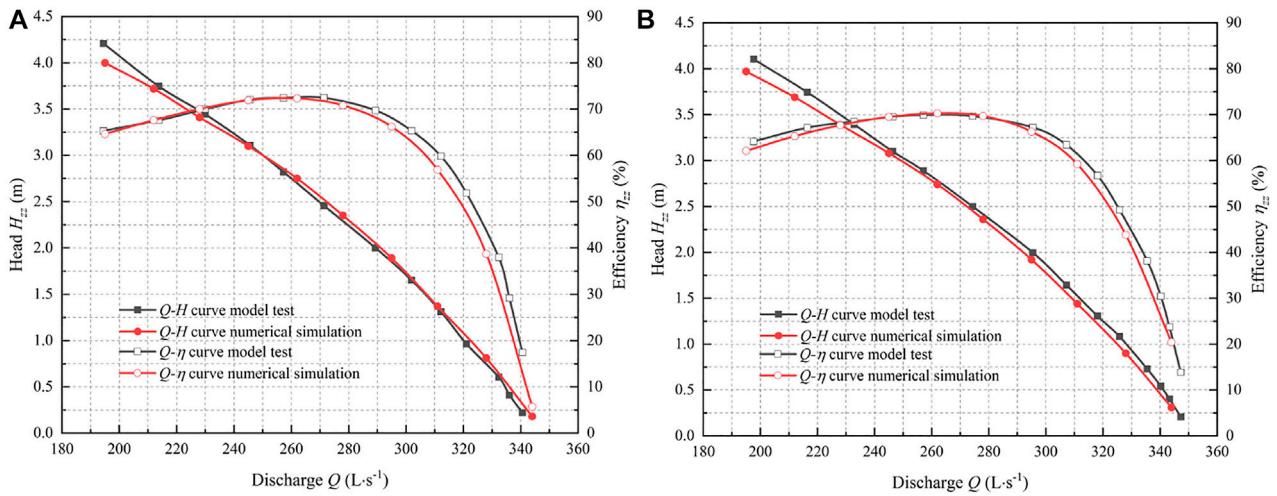

FIGURE 16 | Comparison of model test and numerical calculation results of energy performance of the pump device with α of 0°. **(A)** $\Delta\beta$ = 0°, **(B)** $\Delta\beta$ = −12°.

1) There is an intersection point O between the two $Q \sim \eta_{zz}$ curves of the pump device with two inlet angle adjustments of 0° and −12°. The discharge and pump device efficiency are 258.6 L/s and 67.5%, respectively, when the impeller blade angle is −4°, the discharge and pump device efficiency are 278.7 L/s and 67.1%, respectively, when the impeller blade angle is −2°, and the flow discharge and pump device efficiency are 301.9 L/s and 65.3%, respectively, when the impeller blade angle (α) is 0°.
2) When $\Delta\beta$ is adjusted from 0° to −12°, the pump device efficiency is reduced. For the pump impeller blade angles of −4°, −2°, and 0°, the pump device efficiency decreases by 1.4, 1.1, and 2.5%, respectively.
3) When $\Delta\beta$ is adjusted from 0° to −12°, in the large-discharge area—which is on the right-hand side of point O—the pump device efficiency with a $\Delta\beta$ of −12° is higher than with a $\Delta\beta$ of 0°. Consequently, the lower the head and the greater the discharge, the greater the difference in pump efficiency.

A comparison between the numerical simulation and model test results of the pump device energy performance with an impeller blade angle (α) of 0° is shown in **Figure 16**. The maximum difference in the pump device efficiency (between numerical simulation and model test results) is approximately 3%, the maximum difference of the pump device head being approximately 0.2 m. In short, the numerical calculations are consistent with the model test results.

CONCLUSION

1) The guide vane inlet angle had a significant impact on the energy performance of vertical axial flow pump device. When the guide vane inlet angle was adjusted in a clockwise direction, the pump device efficiency was reduced at the pump device optimal operating point, but its efficiency improved in low-head and large-discharge areas.
2) When the guide vane inlet angle did not match the direction of flow from the impeller outlet in the axial flow pump device, flow separation and a vortex were generated in the guide vane. By adjusting the guide vane inlet angle, the flow field could be significantly improved, the hydraulic loss of guide vane decreasing, and the energy performance of the axial flow pump device improving.
3) When the operating conditions of the low-head pump device are frequently in the large-discharge and low-head areas that deviate from the high-efficiency area due to limitations of the pump model or motor itself, these research results could be used to improve the energy performance of pump device in the low-head area.

DATA AVAILABILITY STATEMENT

The raw data supporting the conclusions of this article will be made available by the authors, without undue reservation.

AUTHOR CONTRIBUTIONS

LX, analysis, writing and revision; HZ, methodology and revision; CW, analysis and revision; DJ and WS, validation and revision; and WL and LL, data analysis and revision.

FUNDING

This work was supported by the National Natural Science Foundation of China (Grant No. 51309200, Grant No. 51779215), the High-tech Key Laboratory of Agricultural Equipment and Intelligentization of Jiangsu Province, Key Laboratory of Modern Agricultural Equipment and Technology (Jiangsu University), the Ministry of Education (NZ201604), and the Jiangsu South-to-North Water Diversion Technology R and D Project (JSNSBD202105).

REFERENCES

Al-Obaidi, A. R. (2021). Analysis of the Effect of Various Impeller Blade Angles on Characteristic of the Axial Pump with Pressure Fluctuations Based on Time- and Frequency-Domain Investigations. *Iran J. Sci. Technol. Trans. Mech. Eng.* 45, 441–459. doi:10.1007/s40997-020-00392-3

Caruso, F., and Meskell, C. (2021). Effect of the Axial gap on the Energy Consumption of a Single-Blade Wastewater Pump. *Proc. Inst. Mech. Eng. A: J. Power Energ.* 235, 432–439. doi:10.1177/0957650920927366

Feng, J., Zheng, Y., and Luo, X. (2012). Effects of Exit Guide Vane on Performance of Axial-Flow Pump Device. *Water Resour. Power* 30, 126–128. doi:10.3969/j.issn.1000-7709.2012.08.037

González, J., and Santolaria, C. (2006). Unsteady Flow Structure and Global Variables in a Centrifugal Pump. *J. Fluids Eng. Trans. ASME.* 128, 937–946. doi:10.1115/1.2234782

Han, Y., Zhou, L., Bai, L., Shi, W., and Agarwal, R. (2021). Comparison and Validation of Various Turbulence Models for U-bend Flow with a Magnetic Resonance Velocimetry experiment. *Phys. Fluids* 33. doi:10.1063/5.0073910

Hu, J., Huang, S., and Wang, P. (2008). Research on Hydrodynamic Characteristics of Axial Waterjet Pump with Guide Vane. *J. Hydroelectr. Eng.* 27, 32–36. doi:10.3969/j.issn.1003-1243.2008.01.007

Jafarzadeh, B., Hajari, A., Alishahi, M. M., and Akbari, M. H. (2011). The Flow Simulation of a Low-Specific-Speed High-Speed Centrifugal Pump. *Appl. Math. Model.* 35, 242–249. doi:10.1016/j.apm.2010.05.021

Jiao, W., Cheng, L., Xu, J., and Wang, C. (2019). Numerical Analysis of Two-phase Flow in the Cavitation Process of a Waterjet Propulsion Pump System. *Processes* 7, 690. doi:10.3390/pr7100690

Kan, K., Chen, H., Zheng, Y., Zhou, D., Binama, M., and Dai, J. (2021a). Transient Characteristics during Power-Off Process in a Shaft Extension Tubular Pump by Using a Suitable Numerical Model. *Renew. Energ.* 164, 109–121. doi:10.1016/j.renene.2020.09.001

Kan, K., Yang, Z., Lyu, P., Zheng, Y., and Shen, L. (2021b). Numerical Study of Turbulent Flow Past a Rotating Axial-Flow Pump Based on a Level-Set Immersed Boundary Method. *Renew. Energ.* 168, 960–971. doi:10.1016/j.renene.2020.12.103

Kan, K., Zheng, Y., Fu, S., Liu, H., Yang, C., and Zhang, X. (2017). Dynamic Stress of Impeller Blade of Shaft Extension Tubular Pump Device Based on Bidirectional Fluid-Structure Interaction. *J. Mech. Sci. Technol.* 31, 1561–1568. doi:10.1007/s12206-017-0303-1

Li, X., Shen, T., Li, P., Guo, X., and Zhu, Z. (2020). Extended Compressible thermal Cavitation Model for the Numerical Simulation of Cryogenic Cavitating Flow. *Int. J. Hydrogen Energ.* 45, 10104–10118. doi:10.1016/j.ijhydene.2020.01.192

Li, Z., Yang, M., and Wang, X. (2009). Experimental Study of Guide Vane Influence on Performance of Axial-Flow Pump. *Drain. Irrig. Mach.* 27, 15–18.

Liu, J., Gong, Y., and Wang, Y. (2008). Influence of Pump Diameter on Hydraulic Loss of Vertical Pump Device. S. North Water Transfers Water Sci. *Technol.* 6, 67–69. doi:10.13476/j.cnki.nsbdqk.2008.05.026

Liu, N., Wang, Y. S., and Zhang, G. (2006). *Model Pump Test on the Same Test-Bed for the South-To-North Water Diversion*. Beijing, China: China Water Power Press.

Patil, A., Sundar, S., Delgado, A., and Gamboa, J. (2019). CFD Based Evaluation of Conventional Electrical Submersible Pump for High-Speed Application. *J. Petrol. Sci. Eng.* 182. doi:10.1016/j.petrol.2019.106287

Qi, L., Zhang, Y., and Zhang, G. (2017). Model Test and Analysis of Pump Device of Miyun Reservoir Regulation and Storage Project of Incoming Water from South-To-North Transfer Project. *Yellow River* 6, 133–137. doi:10.3969/j.issn.1000-1379.2017.06.031

Qian, J., Gao, Z., Liu, B., and Jin, Z. (2018). Parametric Study on Fluid Dynamics of Pilot-Control Angle globe Valve. *J. Fluids Eng.* 140. doi:10.1115/1.4040037

Qian, Z., Wang, F., Wang, Z., and Zhou, W. (2013). Experimental Study on Hydraulic Performance of Saddle Zone in Axial-Flow Pump with Adjustable Guide Vane. *J. Drain. Irrig. Mach. Eng.* 31, 461–465. doi:10.3969/j.issn.1674.8530.2013.06.001

Qian, Z., Wang, Y., Huai, W., and Lee, Y. (2010). Numerical Simulation of Water Flow in an Axial Flow Pump with Adjustable Guide Vanes. *J. Mech. Sci. Technol.* 24, 971–976. doi:10.1007/s12206-010-0212-z

Tang, F., and Wang, G. (2006). Influence of Outlet Guide Vanes upon Performances of Waterjet Axial-Flow Pump. *J. Ship Mech.* 6, 19–26. doi:10.3969/j.issn.2006.06.003

Tang, S., Zhu, Y., and Yuan, S. (2021). An Improved Convolutional Neural Network with an Adaptable Learning Rate towards Multi-Signal Fault Diagnosis of Hydraulic Piston Pump. *Adv. Eng. Inform.* 50. doi:10.1016/j.aei.2021.101406

Wang, H. L., Hu, Q. X., Yang, Y., and Wang, C. (2021). Performance Differences of Electrical Submersible Pump under Variable Speed Schemes. *Int. J. Simul. Model.* 20, 76–86. doi:10.2507/ijsimm20-1-544

Wang, H., Long, B., Wang, C., Han, C., and Li, L. (2020a). Effects of the Impeller Blade with a Slot Structure on the Centrifugal Pump Performance. *Energies* 13, 1628. doi:10.3390/en13071628

Wang, H., Qian, Z., Zhang, D., Wang, T., and Wang, C. (2020b). Numerical Study of the Normal Impinging Water Jet at Different Impinging Height, Based on Wray-Agarwal Turbulence Model. *Energies* 13, 1744. doi:10.3390/en13071744

Wu, H., Tian, Y., Liao, W., Liu, B., and Song, W. (2016). Pumping Device Performance Analysis Based on the Miyun Storage Project of Cascade Pumping Stations. *China Rural Water Hydropower.* 11, 178–182.

Yu, J., Chen, Y., Zhu, Y., Lv, B., and Sun, P. (2018). Study on Pump Type Selection for Extra-low Head Pumping Station with Large Difference between Average and Highest Heads. *Water Resour. Hydropower Eng.* 49, 68–76. doi:10.13928/j.cnki.wrahe.2018.05.011

Zawistowski, T., and Kleiber, M. (2017). Gap Flow Simulation Methods in High Pressure Variable Displacement Axial Piston Pumps. *Arch. Computat Methods Eng.* 24, 519–542. doi:10.1007/s11831-016-9180-5

Zhang, L., Li, Y., Zong, L., Duan, Z., and Hua, X. (2011). Type Selection and Hydraulic Optimization of Vertical Axial-Flow Pump Assembly in Changgou Pumping Station of the East Route of South-To-North Water Transfer Project. S. North Water Transfers Water Sci. *Technol* 9, 15–18. doi:10.3724/SP.J.1201.2011.05015

Zhang, L., Wang, C., Zhang, Y., Xiang, W., He, Z., and Shi, W. (2021). Numerical Study of Coupled Flow in Blocking Pulsed Jet Impinging on a Rotating wall. *J. Braz. Soc. Mech. Sci. Eng.* 43, 508. doi:10.1007/s40430-021-03212-0

Zhou, J., Zhao, M., Wang, C., and Gao, Z. (2021). Optimal Design of Diversion Piers of Lateral Intake Pumping Station Based on Orthogonal Test. *Shock and Vibration* 2021, 1–9. doi:10.1155/2021/6616456

Zhou, Y., and Xu, H. (2007). The Influence of Diffuser on the Function of the Axial-Flow Pump. *Water Conserv. Electr. Power Mach.* 29, 28–29. doi:10.3969/j.issn.1674-1951.2007.09.010

Zhu, Y., Li, G., Wang, R., Tang, S., Su, H., and Cao, K. (2021). Intelligent Fault Diagnosis of Hydraulic Piston Pump Combining Improved Lenet-5 and Pso Hyperparameter Optimization. *Appl. Acoust.* 183. doi:10.1016/j.apacoust.2021.108336

Conflict of Interest: Author WS is employed by Jiangsu Water Supply Co., Ltd. In the Eastern Route of the S-to-N Water Diversion Project.

The remaining authors declare that the research was conducted in the absence of any commercial or financial relationships that could be construed as a potential conflict of interest.

Publisher's Note: All claims expressed in this article are solely those of the authors and do not necessarily represent those of their affiliated organizations, or those of the publisher, the editors and the reviewers. Any product that may be evaluated in this article, or claim that may be made by its manufacturer, is not guaranteed or endorsed by the publisher.

frontiers in Energy Research

ORIGINAL RESEARCH
published: 29 March 2022
doi: 10.3389/fenrg.2022.819230

Research of the Flow Attenuation Mechanism of a Double-Suction Pump

Dongrong Meng[1], *Ting Jiang*[2], *Zhengguang Liu*[3], *Meng Zhao*[3], *Wei Jiang*[3] *and Gaoyang Hou*[3]*

[1]School of Mechanical Engineering, Xijing University, Xi'an, China, [2]Innovation Institute of Shaanxi Aerospace Power High Tech Co., Ltd., Xi'an, China, [3]Department of Power and Electrical Engineering, Northwest A&F University, Shaanxi, China

As an important machine for energy conversion and fluid transmission, centrifugal pump has the advantages of high efficiency, reliable performance, and easy adjustment. In order to improve the stability of the pump, this article adopts the method of experimental and numerical simulation in the pump and studies the variation of the vibration characteristics in the operation process. Based on the numerical simulation results, the intake condition and the cavitation inside the centrifugal pump are analyzed and summarized, which reveals the flow attenuation mechanism of a pumping station. The main results of the work reported in this article are as follows: 1) Various experimental schemes to monitor the vibration of centrifugal pumps in real time have been designed. The vibration characteristics of the pumps have been significantly improved by adding special trash barriers. 2) The gas entering the pump was not enough to affect the normal operation of the pump, but cavitation did occur in the actual operation process. 3) The critical net positive suction head under the three conditions is calculated to be 8.9, 10.9, and 12.9 m, respectively.

Keywords: centrifugal pump, vibration, external characteristics, cavitation, numerical simulation

OPEN ACCESS

Edited by:
Ling Zhou,
Jiangsu University, China

Reviewed by:
Jiang Lai,
Nuclear Power Institute of China (NPIC), China
Scappaticci Lorenzo,
Università degli Studi Guglielmo Marconi, Italy

***Correspondence:**
Gaoyang Hou
gyhou415@nwafu.edu.cn

Specialty section:
This article was submitted to Process and Energy Systems Engineering, a section of the journal Frontiers in Energy Research

Received: *21 November 2021*
Accepted: *03 March 2022*
Published: *29 March 2022*

Citation:
Meng D, Jiang T, Liu Z, Zhao M, Jiang W and Hou G (2022) Research of the Flow Attenuation Mechanism of a Double-Suction Pump. Front. Energy Res. 10:819230. doi: 10.3389/fenrg.2022.819230

INTRODUCTION

Centrifugal pumps are widely used in chemical, petroleum, aerospace, and other fields (Zhou et al., 2013) (Botros et al., 2016), and the requirements of its hydraulic performance and operational stability are becoming higher (Dong and Chu, 2018). With high efficiency, reliable performance, easy adjustment, and other advantages (Guo et al., 2018), centrifugal pump has become an indispensable part of the economic development (Nishida et al., 2016) (Adamkowski et al., 2016). Therefore, it is important to research the internal situation of centrifugal pumps for technological development.

Kreuz-Ihli et al. (1999) demonstrated the excitation effect of the tongue region in a vaneless radial inflow turbine, and their results showed that the phenomenon of partial load cyclone has a great influence on the generation of cavitation (Muggli et al., 1997), but no analysis has been made on the net positive suction head (NPSH). Kaupert and Staubli (1999) studied the full-load disturbance phenomenon in centrifugal pumps with guide vanes at different specific speeds, and the results showed that the frequency of full-load disturbance phenomenon increases with the increase in specific speed (Yang et al., 2015) (Zhang et al., 2019). However, no detailed analysis of the operating conditions in sandy rivers has been made. Guelich and Egger (1992) used experimental and numerical simulation methods to study the unstable flow field inside the centrifugal pump with a guide vane, and the results showed that the frequency gradually increased to the level of full-load disturbance in the impeller (Posa and Lippolis, 2019) (Yousefi et al., 2019). The main cause of this phenomenon is a rotational stall (de O. Turci et al., 2020). Centrifugal pump optimization methods based on computational fluid dynamics (ELM/CFD) and actual experiments have been widely applied (Wang et al., 2017) (Li et al., 2018), but there is insufficient

research on pump cavitation (Schäfer et al., 2017). The combination of experimental and numerical simulation methods can effectively predict the centrifugal pump axial force (Mortazavi et al., 2017) (Liu et al., 2014), so this combined method has been used in this research.

This research took the selected pumping station with double-suction pumps and four water pumps as the experimental object. The drainage area of this station is the Yellow River, with a maximum sand content of 69 kg/m^3 (Wang et al., 2016). The sand in the water flow caused serious abrasion to the pump and restricted the effective use. At present, the pumping station has experienced a significant flow decline from 5.1 m^3/s to 3.7 m^3/s. This research adopted numerical simulation (Lomakin et al., 2016) and experimental methods (Fu et al., 2020) to study the internal flow performance of the pumping channels and analyzed the reason of flow decay in the pumping station. This further revealed the mechanism of flow decay in the pump station and provided the theoretical basis for the stable operation of the pump station.

METHODS AND EXPERIMENTS

Numerical Simulation Settings

The proper setting of the boundary conditions greatly affects the accuracy of the numerical simulation. In thisarticle, the specific boundary conditions are set as follows: the fluid is incompressible, and the turbulent flow model uses the SST *k-ω* model. The inlet boundary in the stationary, under non-cavitation, conditions uses the inlet pressure of 101325Pa. With a constant discharge (or head), the inlet pressure has to be decreased to allow the static pressure at some areas inside the pump (at the impeller blade inlet edge or suction side) to fall sufficiently below that of the saturated liquid vapor. According to the actual conditions, the boundary condition of the outlet is mass flow. The solid-wall surface uses the no-slip boundary condition, which means that the wall surface velocity is the same as the fluid velocity. The standard wall is applied to the surface near the wall. The saturation pressure is 3169Pa, and the default value of 2×10^{-6} m is selected for the mean diameter. The frozen rotor is used for steady-state simulations, and the stator–rotor interface is used for unsteady simulations. The convergence accuracy (*RMS*) is set to 10^{-5}.

Computational Area and Grid

Calculation Area

According to the actual situation of the pumping units in the double-suction pumping station, Pro/E 2018 software is used to establish the 3D model of the full flow path of the centrifugal pump. The cross-sectional length of the inlet and the outlet of the centrifugal pump will reduce the influence of boundary conditions on the internal flow field during the modeling process.

Grid

Grid is the calculation carrier of numerical simulation, which imposes strict requirements on the resolution of the grid. The inlet flow channel is divided into three parts: inlet section, channel, and outlet section. The 3D model of the centrifugal pump is divided into five parts: inlet section, suction chamber, impeller, spiral casing, and outlet section, which are further divided into different numbers of grids. In this article, we choose the unstructured tetrahedral mesh. The grid of some parts is shown in **Figure 1**.

Grid Independence Study

Table1 Grid recorded the results with different node numbers used in the simulation. It can be seen from the table that when the number of grids reaches 14 million, the efficiency and head remain unchanged with an increased number of grids. Considering the time and computer performance, the final number of cells is 14 million. There are 1.4 million grid cells in the inlet section, 5.9 million grid cells in the suction chamber, 2.6 million grid cells in the impeller, 3.14 million grid cells in the volute, and 0.9 million grid cells in the outlet section.

Centrifugal Pump Experiment

In thisarticle, the centrifugal pump experimental system includes double-suction centrifugal pumps, accelerometers, a wireless gateway data acquisition system, and a software data analysis system. The acceleration sensor (frequency range 2–10 KHz; noise <20 mV) can measure the velocity and acceleration in all directions at the same time. In this experiment, the main collection is the vibration velocity of the pump casing under each monitoring point. The acceleration sensor specification model is *GY7600WS,* which is produced by Zhongke Genyun in China. The data acquisition system is mainly a wireless gateway by *ZigBee* whose specification model is *GY7800WS*. The design flow rate *QD* of the double-suction centrifugal pump is 4.57 m^3/s, the design head is 108.08 m, and the design speed is 750 r/min. Specific parameters are shown in **Table 2**.

The real-time monitoring system used the velocity sensor, acceleration sensor, and temperature sensor to monitor the state of the pump at five different locations and the data is recorded during 72 h without drastic changes in the flow. The monitoring points are shown in **Figure 2**. Choose the flow channel after the front pond to put the trash rack and monitor the data after 4–5 h. Close the valve of the pump and remove the gas in the pump. After reaching the maximum flow, record the inlet and outlet pressure and flow data until the flow becomes stable again.

Verification of Numerical Simulation Results and Experimental Results

Figure 3 shows the comparison between the simulation results and the experimental results in the clear water state to verify the accuracy of the numerical simulation. The numerical simulation results are in good agreement with the experimental results. Some load and overload conditions show large errors, which may have come from unstable factors such as reflux and flow separation. However, the error is still within the acceptable range, and the efficiency error and head error are less than 5.0%. Near the effective area (0.7–1.1Q_D), the errors of head and efficiency are less than 3.0 and 3.5%, respectively. Therefore, the numerical model in this article can meet the requirements of the calculation accuracy.

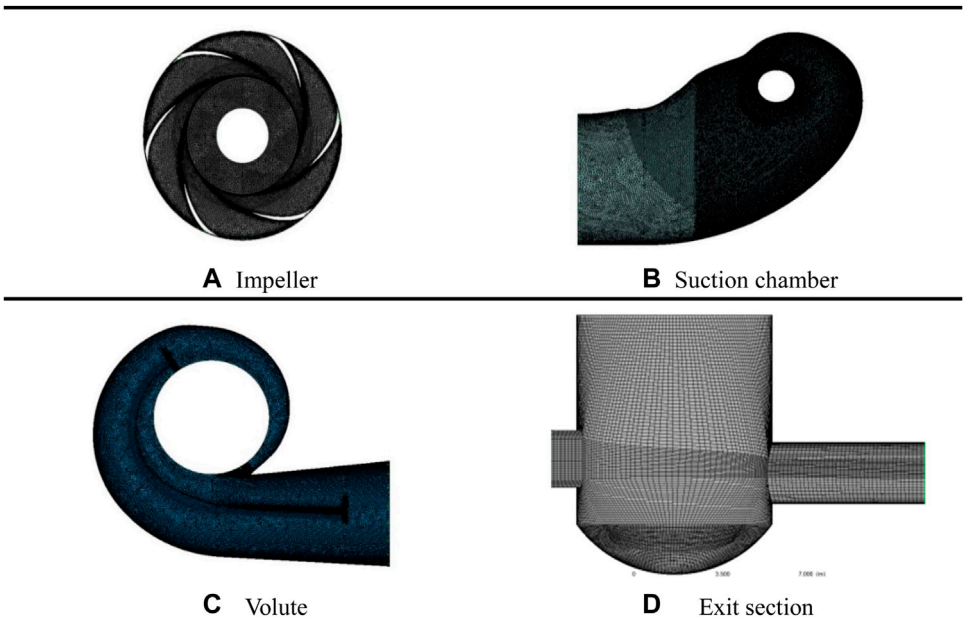

FIGURE 1 | The grid of flow system components. **(A)** Impeller; **(B)** Suction chamber; **(C)** Volute; **(D)** Exit section.

TABLE 1 | Grid independence analysis.

Parameter	Number of grids			
	Grid 1	Grid 2	Grid 3	Grid 4
Number of cells/10,000	500	900	1,400	1,600
Efficiency/%	81.86	83.39	89.97	90.03
Head/m	98.77	103.81	106.83	106.95

TABLE 2 | Centrifugal pump parameters.

Parameters	Valuer	Parameters	Value
Rotation speed	750 rpm	Flow rate	4.57 m^3/s
Head	108.08 m	Mechanical input	8,000 kW
Efficiency	88%	Number of blades	6
NPSH	10.5 m	Impeller inlet diameter	730 mm
Suction chamber Inlet diameter	1,325 mm	Impeller outlet diameter	125 mm
Outlet diameter of volute	1,200 mm	Impeller outlet width	800 mm

NUMERICAL SIMULATION RESULTS AND DISCUSSION

Gas–Liquid Flow Characteristics of the Inlet

The gas (air)–liquid (water) distribution diagram of each part of the inlet flow channel of the pump under different flow conditions is shown in **Figure 4**. The volume of the gas increases with the increasing flow rate, but it can be found that the volume of the gas entering the pump from the outlet section is very small. Therefore, it can be considered that the gas entering the pump is not enough to affect the normal operation of the pump.

Pressure Distribution of Overflow Components

Cross-Sectional Pressure Distribution in the Suction Chamber

Taking XY as the plane, we draw the pressure distribution diagram of the oil suction cavity section under different flow conditions in the *Z*-direction. Blue represents the lowest pressure and red represents the highest pressure. It can be seen from **Figure 5** that with a rising Z value, the blue area at the interface between the suction chamber and the impeller is decreasing, which means that the pressure is increasing. While the whole area at the housing and other areas of the suction chamber is becoming lighter and the pressure is decreasing. Comparing the position of the blue area, the pressure in the suction chamber near the contact surface of the impeller decreases with the increase in the distance in the *Z*-direction. **Figure 5** shows the pressure distribution of the suction chamber cross section at low flow rate (Q = 4.0 m^3/s). Comparing the different flow conditions, in the small flow condition, the pressure on the section of the entire suction chamber is greater than the pressure on the section under the design flow condition, particularly at the curved part of the suction chamber inlet. Because the direction of the fluid changes at these positions, the pressure value is greater than other positions.

Impeller Cross-Sectional Pressure Distribution

Taking XY as the plane, we analyze the pressure distribution of the impeller cross section in the *Z*-direction under the design condition. The maximum cross-sectional pressure at $Z = 0.1$ m is 881.7 kPa, at $Z = 0.15$ m is 632.5 kPa, and at $Z = 0.2$ m is 8,437.9 kPa. The overall

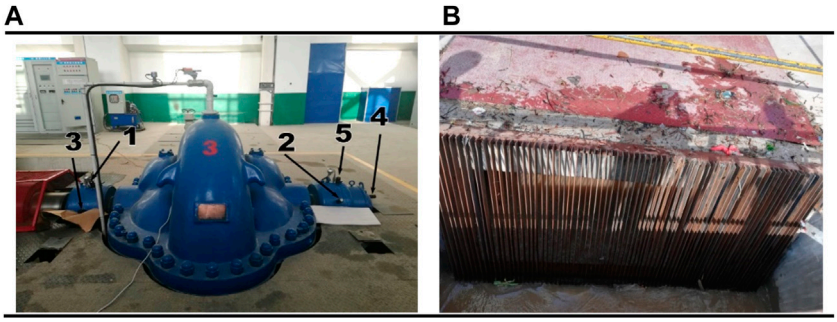

FIGURE 2 | Experimental scheme: **(A)** monitoring points; **(B)** trash rack.

pressure decreases with the increase in the cross-sectional distance in the *Z*-direction. The pressure at the inlet of the blade is the lowest, and gradually increases in the direction of the outlet of the blade. **Figure 6** shows the pressure distribution of each impeller section at $Q = 4.0\ m^3/s$. The maximum cross-sectional pressure at $Z = 0.1$ m is 897.5 kPa, at Z = 0.15 m is 647.0 kPa, and at $Z = 0.2$ m is 462.6 kPa. The relationship between the pressure and the distance in the *Z*-direction is the same as the design flow condition. Furthermore, the pressure at the inlet of the impeller is smaller than the pressure at the outlet of the impeller, and the pressure on each blade increases gradually in the clockwise direction.

Pressure Distribution of the Spiral Shell Cross Section

Plot the pressure distribution of the spiral shell cross section in the *Z*-direction in the design flow condition and low flow condition ($Q = 4.0\ m^3/s$), the results are showed in **Figure 7**. The position of $Z = 0$ m is also the position of the central section of the shell. According to its pressure distribution, the annular channel of the inlet of the shell owns the smallest pressure of the whole shell components. With the direction of water flow till the outlet part of the shell, the pressure from the inner wall surface to the outer wall surface is increasing. In the diagram with $Z = 0$ m for design flow and low flow, a circular orange area at the exit of the shell can be seen, surrounded by a red area at higher pressures, indicating the possible presence. In the cross section away from the central section, the pressure in the shell decreases slightly. But in the cross section away from the profile, there are more red areas, filling almost the entire exit section of the shell. But the cross section between $Z = 0.05$ m and $Z = 0.1$ m does not show any orange areas in the central section. It can be observed that as the flow rate increases, the pressure in the various sections of the shell decreases (Lomakin et al., 2016).

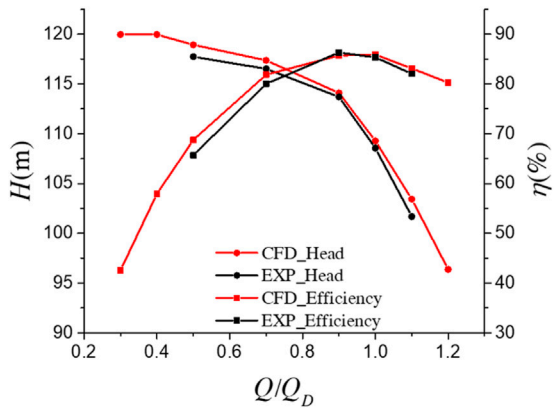

FIGURE 3 | Comparison between the simulation results and the experimental results.

Pump Cavitation Characteristic

Based on the experimental results and external characteristics analysis, the cavitation may occur in the pump. Three flow conditions are designed in the numerical simulation of cavitation, the pump inlet pressure is reduced from 2 atm (101,325 Pa) to 1 atm, forcing the centrifugal pump cavitation.

Design Flow Conditions

It can be seen from **Figure 8** that when the inlet pressure is reduced from 2 to 1 atm, the volume of the bubbles on the back of the blade changes during the whole process. From the beginning of the bubble, the volume of the bubble on the blade suction side will increase with every 0.1 atm decreasing until the inlet pressure drops to 1 atm. It can be found that the bubble volume at the inlet of the blade gradually increases until it reaches the maximum at 1 atm. On the contrast, the bubble volume in the direction of the outlet gradually decreases and reaches the lowest. And there is no cavitation on the outside of the blade because of the inlet pressure on the back of the blade reaching the lowest. As showed in **Figure 8**, the bubbles first appeared at the back of the blade. As the pressure increased, the bubbles moved toward the blade outlet and gradually spread to the inside through the flow channel. The pressure of the blade inlet penetrated again and gradually started to compress the bubble, made the volume of the bubble rapidly decrease until it busted. The surrounding high-pressure liquid quickly fills the volume left by the burst of the bubble. When the inlet pressure drops to 1atm, the volume of the bubbles on the back of the blade has almost reached 1/2 of the entire blade.

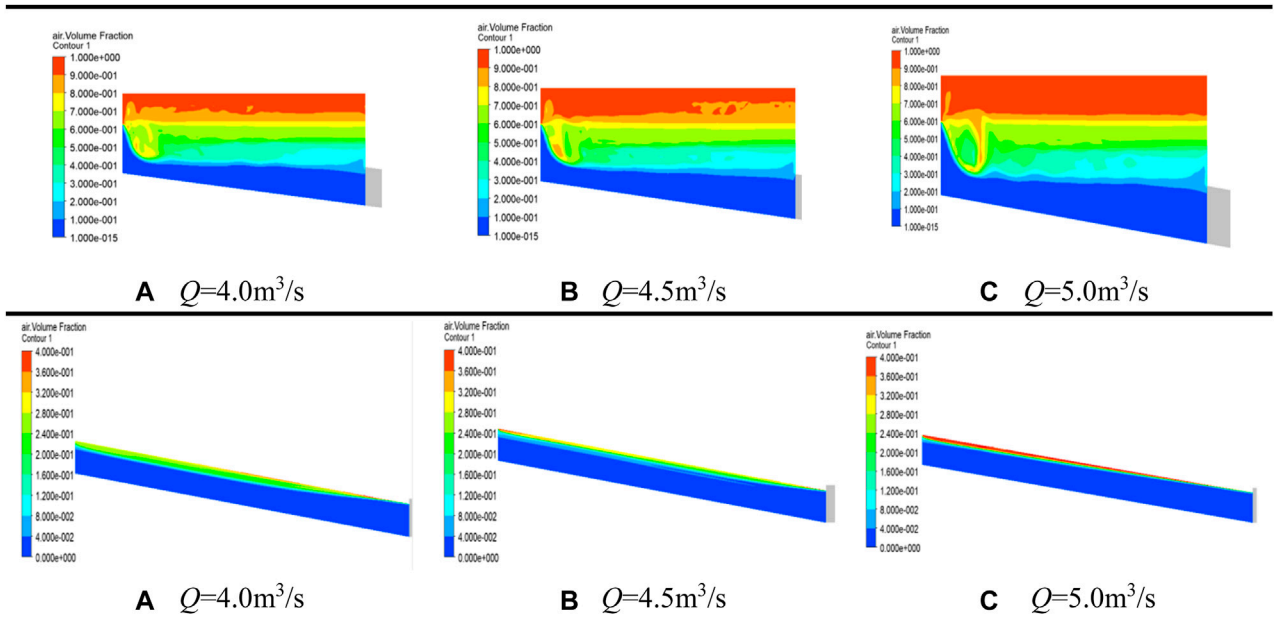

FIGURE 4 | The gas–liquid distribution of the inlet flow channel under different water levels. Q in represents different flow rates.

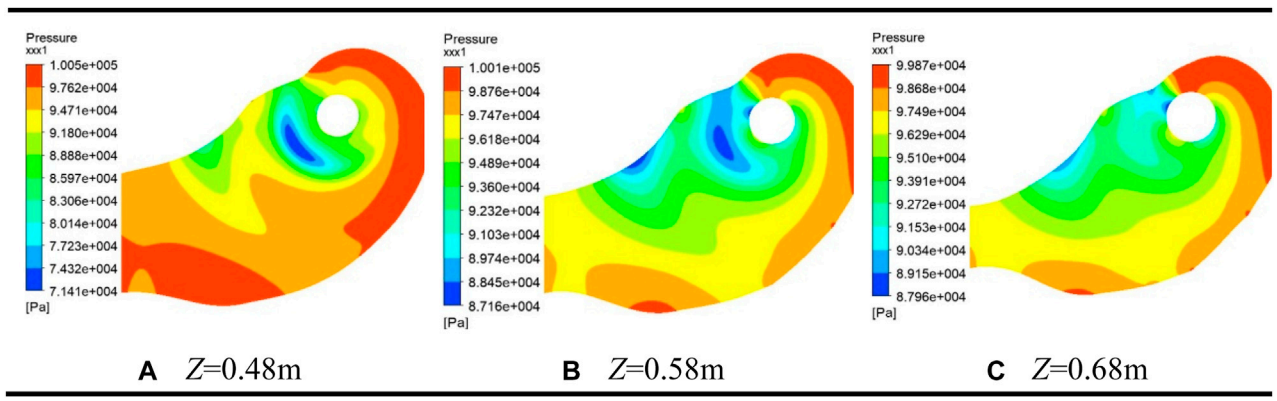

FIGURE 5 | Cross-sectional pressure diagram of the suction chamber at Q = 4.0 m^3/s. Z in represents different cross-sectional heights.

With the reduced inlet pressure, the vapor phase volume fraction in the impeller runner changes a lot - the results are shown in **Figure 9**. The inlet pressure from 2.0 atm down to 1.5 atm, the impeller runner volume of the bubbles did not change much. When the pressure falls, the impeller runner volume fraction of the bubbles begins to grow substantially. The inlet pressure at 1.3 atm of the bubble volume fraction has increased significantly. The vapor phase volume fraction increases significantly with every 0.1 atm decreasing of the inlet pressure.

Off-Design Conditions

The head and NPSH at the corresponding inlet pressure can be solved by the relevant formula. The cavitation characteristic curve of the centrifugal pump under different flow conditions have been plotted in **Figures 10A–C**. As the NPSH decreases, the pump head also decreases in all the figures. At $Q = 4.0$ m^3/s, when the NPSH drops to 15 m, the head starts to drop. After that, when the pressure is reduced by 1atm, the head will be greatly reduced. It is generally believed that when the head of the pump drops by 3%, it is considered that the cavitation has occurred inside the pump. The cavitation margin at this time is the critical cavitation margin, which can be calculated. The critical cavitation allowance under small flow conditions is 8.9 m. The critical cavitation can be calculated as 10.9 m, and the centrifugal pump in the design flow conditions is 10.5 m, which also confirms the accuracy of the numerical simulation.

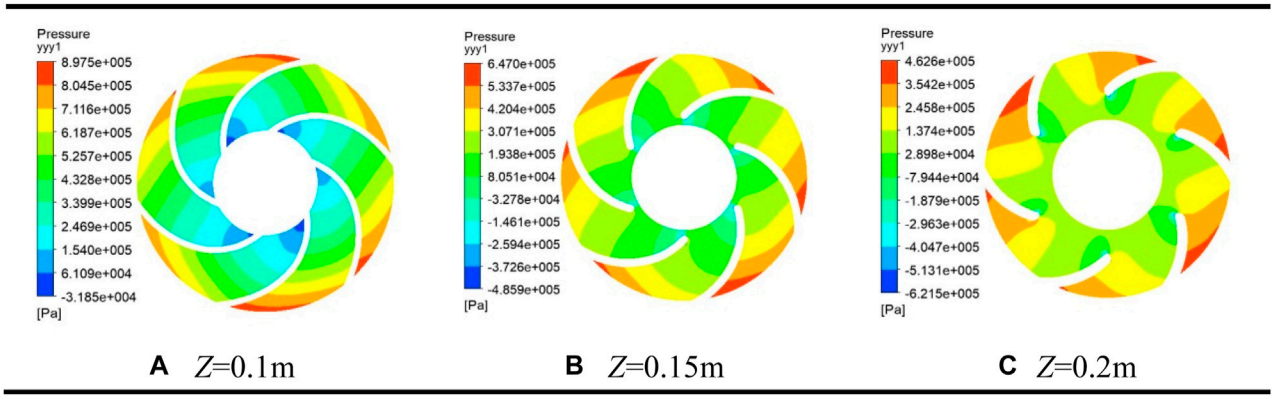

FIGURE 6 | Impeller cross-sectional pressure diagram at Q = 4.0 m^3/s. Z in represents different cross-sectional heights.

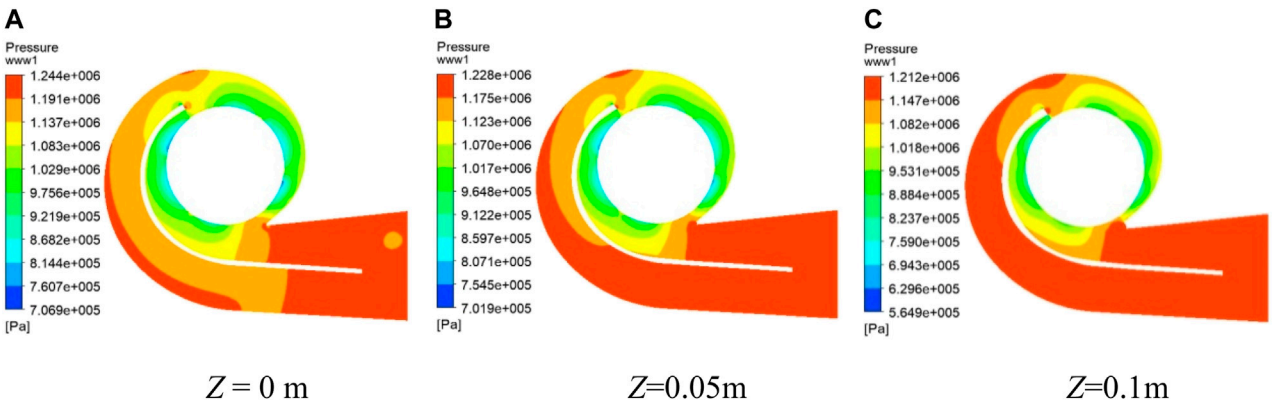

FIGURE 7 | Q = 4.0 m^3/s spiral shell cross-sectional pressure diagram. Z in represents different cross-sectional heights.

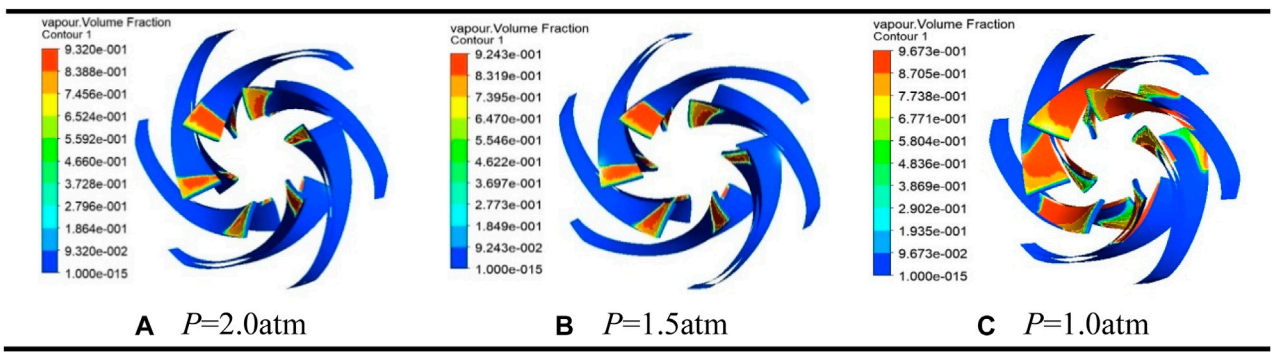

FIGURE 8 | Volume distribution of cavitation on the blade suction side. P in represents different atmospheric pressures.

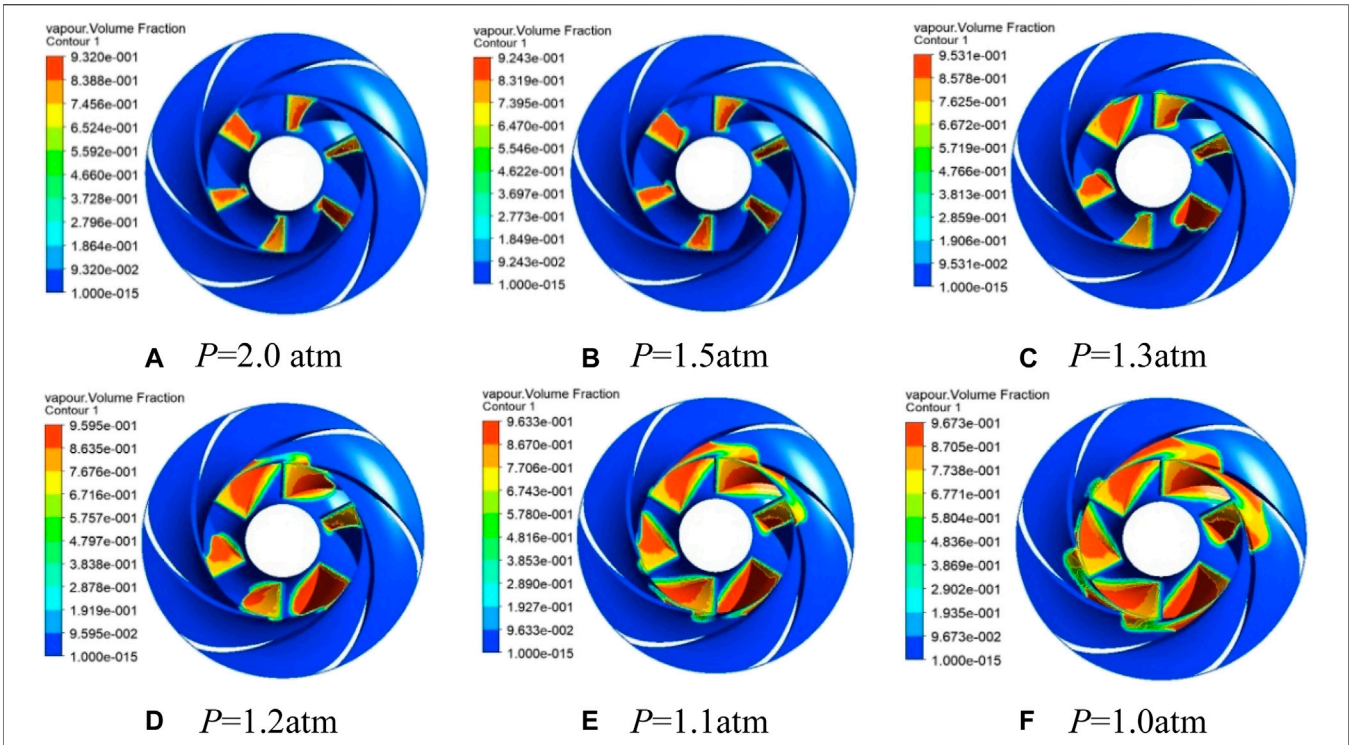

FIGURE 9 | Volume distribution of cavitation with the trash rack. P in represents different atmospheric pressures.

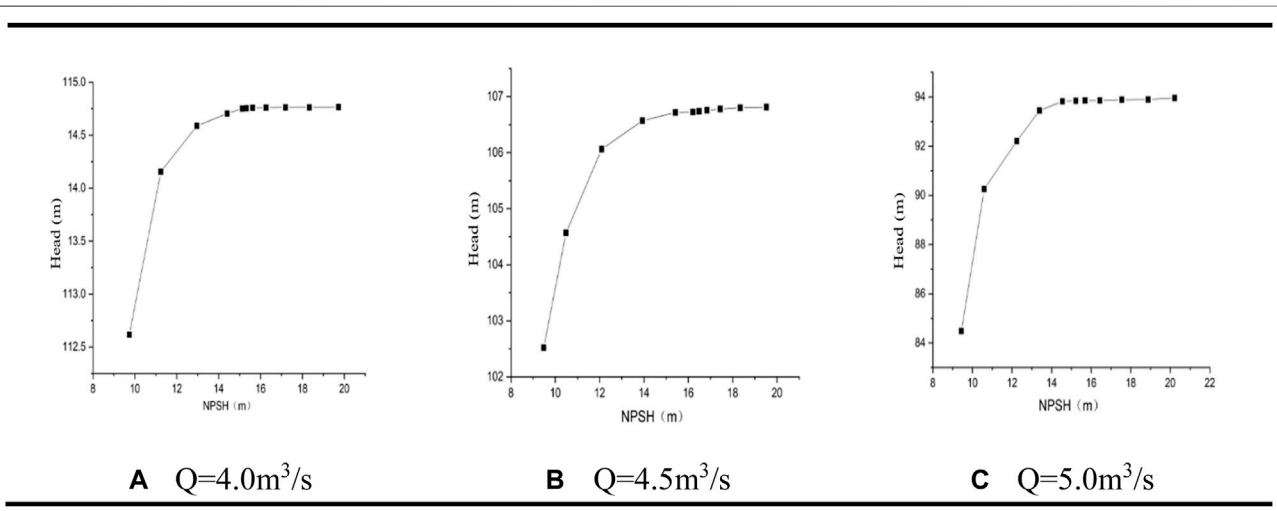

FIGURE 10 | Cavitation curves for different operating conditions. Q in represents different flow rates.

VIBRATION CHARACTERISTICS OF THE CENTRIFUGAL PUMP WITH TRASH RACK

Vibration of Bearing Housing at the P1 Monitoring Site

The design flow rate is 4.57 m^3/s, the speed is 750 r/min, and the theoretical shaft frequency is 75 Hz. **Figure 11A** is the bearing vibration velocity of the unit under different flow conditions without the trash rack. It can be seen from **Figure 11A** the diagram of the vibration velocity amplitude of the pump casing in the low-frequency section. The vibration amplitude at the maximum flow rate can reach 4.65 mm/s, and the minimum vibration amplitude at the minimum flow rate is about 4.3 mm/s. The maximum velocity amplitude at the low-frequency band in **Figure 11A** will decrease as the flow rate decreases.

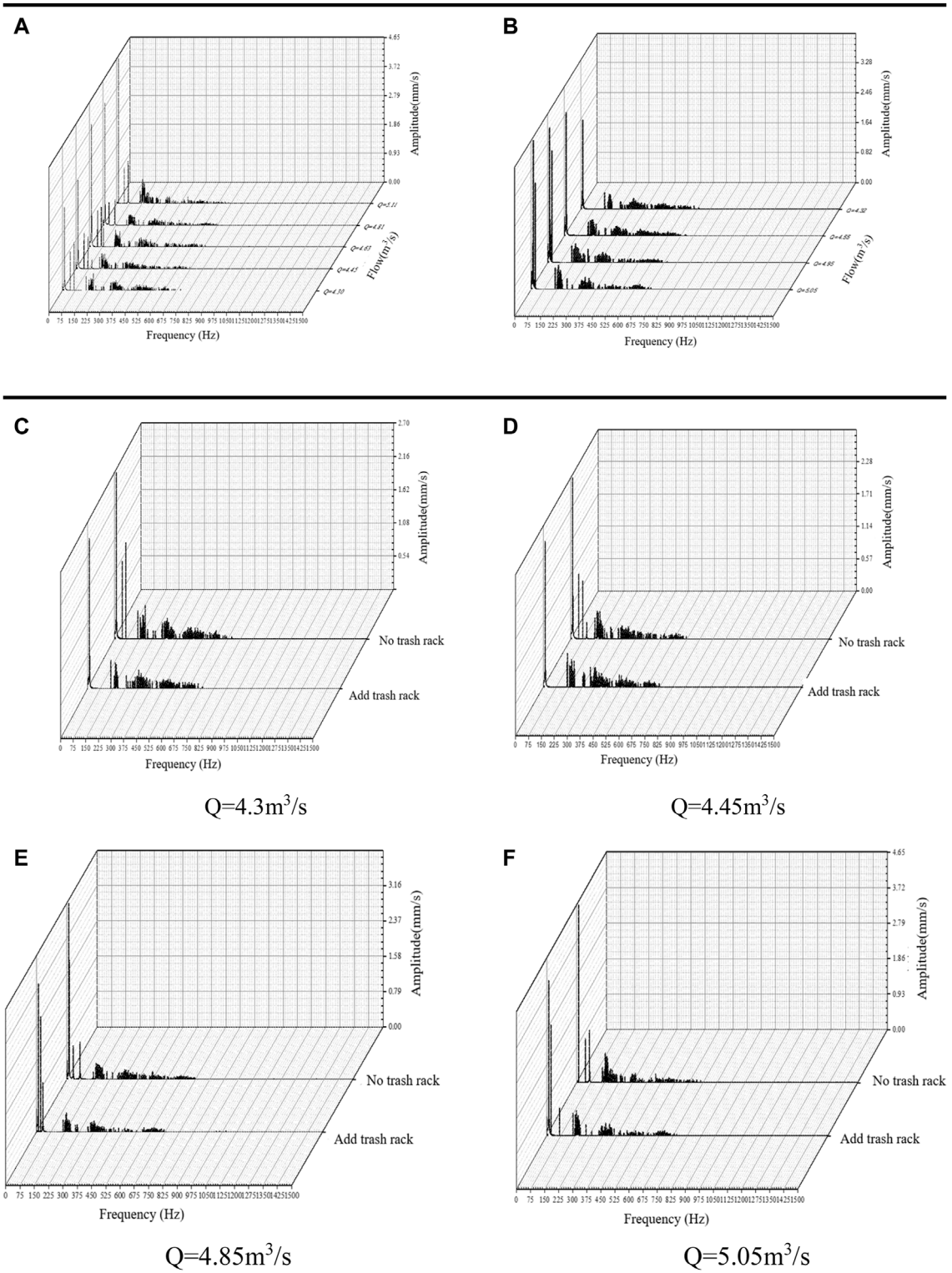

FIGURE 11 | Vibration velocity distribution of P1 monitoring point. (**(A)** Vibration velocity distribution of P1 without the trash rack. **(B)** Velocity frequency domain distribution of P1 with the trash rack. **(C)–(F)** Distribution of velocity frequency domain for different flow conditions at P1 **(C)** Q = 4.3 m^3/s, **(D)** Q = 4.45 m^3/s, **(E)** Q = 4.85 m^3/s, and **(F)** Q = 5.05 m^3/s).

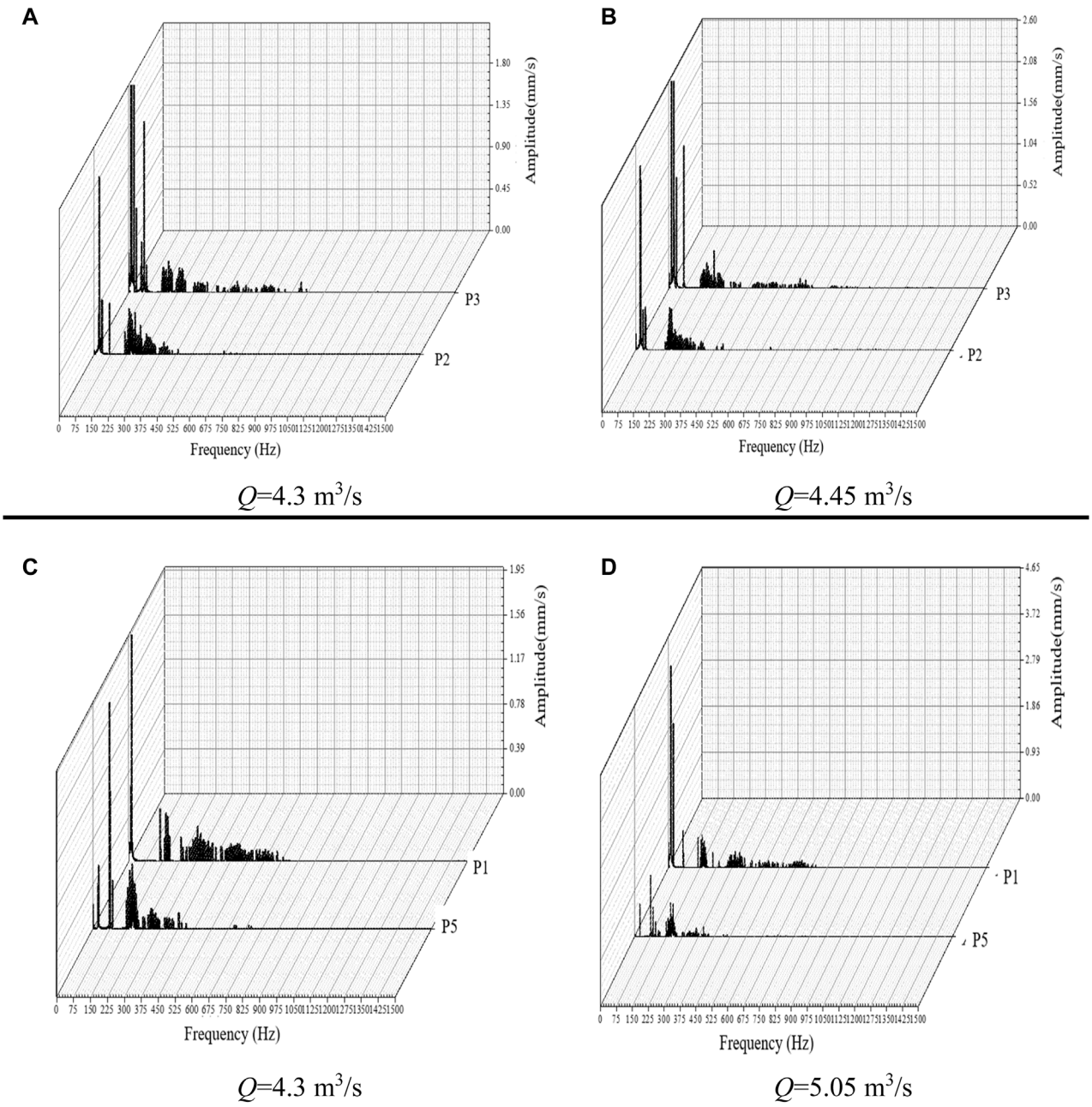

FIGURE 12 | Velocity frequency spectra at P3 for each flow condition. Q in represents different flow rates.

Figure 11B shows the vibration velocity amplitude distribution in the frequency spectrum with different flow conditions after adding the trash rack. The vibration velocity amplitude can reach 4.0 mm/s at the maximum flow and 2.45 mm/s at the minimum flow. Comparing **Figure 11A** with **Figure 11B**, the velocity amplitude in the low-frequency band is much larger after adding the trash rack. The amplitude of the velocity frequencies decreases as the flow rate decreases.

Figures 11C–F represent the frequency spectra of the bearing housing vibration velocity at each flow condition. No matter in which flow condition without the trash rack, there will always be many irregular vibration velocity spectral components in the low-frequency band. The figure shows that the large vibration velocity amplitude occurs again 2 times at the shaft frequency in both the high flow conditions, which is probably due to the higher flow and poor stability of the pump shortly after discharge.

Vibration of Bearing Housing at the P2 Monitoring Site

The vibration pattern at the P2 monitoring point of the pump in the low-frequency band is more complicated without the trash rack. In each flow condition, the largest value can reach upto 2.5 mm/s. Near the designed condition, the smallest amplitude is 1.8 mm/s which is smaller than the range of the velocity amplitude at P1. The vibration amplitude variation pattern at P2 is more complex due to the turbulence. The vibration pattern of the pump casing at P2 is more simplified after adding the trash rack, and the vibration amplitude in the low-frequency band is also much smaller. The maximum vibration amplitude can reach upto 4.7 mm/s and the minimum vibration amplitude is 1.8 mm/s, which is better optimized compared with the vibration amplitude without the trash rack.

By comparing the velocity frequency domain diagrams at the same flow condition, it can be found that under small flow condition, the largest values of velocity appear at the shaft frequency, but the largest values of velocity appear at the blade frequency in the large flow condition. Moreover, after excluding the influence of weeds and other debris, the pump vibration condition under the P2 monitoring point is well improved. The vibration amplitude in the wide frequency area will become relatively simple with the decrease of weeds and other debris with the trash rack.

Vibration of Bearing Housing at Different Flow Conditions

The change of P3 (different from the position monitored by P1) is very similar to the change of the P1 monitoring point. Without the trash rack, the vibration velocity amplitude is slightly higher, the velocity amplitude is larger, and the vibration velocity spectral components are also higher. The vibration velocity spectral components of P2, P3, P1, and P5 under low and high flow conditions are compared, as shown in **Figures 12A–D**. It can be found that the largest vibration velocity amplitude of P2 is greater than the largest vibration velocity amplitude of P3 in all the conditions. At the low frequency, the vibration times of P3 becomes longer than P2, and in the high frequency, the broadband region of P2 becomes wider than P3. For P1 and P5, it can be found that the vibration of P1 in the low-frequency band is slightly better than that of the P5 monitoring points. The vibration amplitude of P1 in low-frequency band is higher than P5. The vibration amplitude of P1 in the high-frequency area is smaller than the P5. But at the higher frequency, the P5 monitoring point does not have a significant vibration amplitude.

The changes in the vibration frequency spectra taken at the monitoring sites show some similarity in the pump casing vibration when measured in the same direction. As the pump is a double-suction centrifugal pump, flow inlets, the influence of water flow velocity, inlet size, and other factors will lead to a certain difference in the flow field. According to the vibration velocity spectral components of all the monitoring points, it is obvious that: 1) after adding the trash rack, the vibration frequency domain of each monitoring point is better than the speed frequency domain. 2) Irregular vibration amplitude is found in the low-frequency region of each monitoring point, but is further reduced in the frequency domain after adding the trash rack. 3) The irregular vibration amplitude may be caused by the cavitation in the centrifugal pump.

CONCLUSION

In thisarticle, the change law of the vibration of the centrifugal pump during operation was studied by using experimental and numerical simulations. The results presented the flow decay mechanism of a double-suction pump station. The main works and findings can be summarized as follows:

1) We monitored the vibration of the pump bearings in real time. The results showed that the pump vibration curves were significantly improved after adding the trash rack.
2) We compared and analyzed the gas (air)–liquid (water) characteristics of each component under different conditions by the numerical simulations. The gas in the inlet flow channel could not affect the normal operation of the pump.
3) The head gradually decreases as the flow rate rises, and the efficiency reached the maximum when the flow rate was 4.5 m^3/s.
4) Based on the numerical simulation of cavitation, the change law between the bubble volume on the blade suction side and the inlet pressure under the three flow conditions was analyzed. The critical NPSH was calculated to be 8.9, 10.9, and 12.9 m, respectively.
5) Serious cavitation has happened inside the pump. This is the main reason that causes the centrifugal pump performance and pump flow to drop. It is hoped that the cavitation of the pump can be more effectively solved with the joint cooperation of more scholars in the future.

DATA AVAILABILITY STATEMENT

The raw data supporting the conclusion of this article will be made available by the authors, without undue reservation.

AUTHOR CONTRIBUTIONS

DM contributed to the conception of the study; ZL performed the data analyses and wrote the manuscript; TJ performed the experiment; MZ contributed significantly to analysis and manuscript preparation; WJ helped perform the analysis with constructive discussions; and GH performed the analysis with constructive discussions.

FUNDING

The present study was financially supported by the Xijing University Research Foundation (Grant No. XJ170201).

REFERENCES

Adamkowski, A., Henke, A., and Lewandowski, M. (2016). Resonance of Torsional Vibrations of Centrifugal Pump Shafts Due to Cavitation Erosion of Pump Impellers. *Eng. Fail. Anal.* 70, 56–72. doi:10.1016/j.engfailanal.2016.07.011

Botros, K. K., Clavelle, E. J., and Vogt, G. M. (2016). Interfacial Contamination between Batches of Crude Oil Due to Dead-Legs in Pump Station Piping. *J. Energ. Resour. Techn.* 138 (5). doi:10.1115/1.4033401

de O Turci, L., Wang, J., and Brahmia, I. (2020). Adaptive and Improved Multi-Population Based Nature-Inspired Optimization Algorithms for Water Pump Station Scheduling. *Water Resour. Manage.* 34 (9), 2869–2885. doi:10.1007/s11269-020-02588-3

Dong, W., and Chu, W.-L. (2018). Numerical Investigation of the Fluid Flow Characteristics in the Hub Plate Crown of a Centrifugal Pump. *Chin. J. Mech. Eng.* 31 (1), 64. doi:10.1186/s10033-018-0264-z

Fu, S., Zheng, Y., Kan, K., Chen, H., Han, X., Liang, X., et al. (2020). Numerical Simulation and Experimental Study of Transient Characteristics in an Axial Flow Pump during Start-Up. *Renew. Energ.* 146, 1879–1887. doi:10.1016/j.renene.2019.07.123

Guelich, J. F., and Egger, R. (1992). *Part-load Flow and Hydraulic Stability of Centrifugal Pumps*. United States. Final Report. Available at: https://www.osti.gov/biblio/10131487.

Guo, S., Qian, Y., Zhu, D. Z., Zhang, W., and Edwini-Bonsu, S. (2018). Effects of Drop Structures and Pump Station on Sewer Air Pressure and Hydrogen Sulfide: Field Investigation. *J. Environ. Eng.* 144 (3), 04018011. doi:10.1061/(asce)ee.1943-7870.0001336

Kaupert, K. A., and Staubli, T. (1999). The Unsteady Pressure Field in a High Specific Speed Centrifugal Pump Impeller-Part I: Influence of the Volute. *J. Fluids Eng.* 121 (3), 621–626. doi:10.1115/1.2823514

Kreuz-Ihli, T., Filsinger, D., Schulz, A., and Wittig, S. (1999). Numerical and Experimental Study of Unsteady Flow Field and Vibration in Radial Inflow Turbines. *J. Turbomach.* 122 (2), 247–254. doi:10.1115/1.555441

Li, X., Gao, P., Zhu, Z., and Li, Y. (2018). Effect of the Blade Loading Distribution on Hydrodynamic Performance of a Centrifugal Pump with Cylindrical Blades. *J. Mech. Sci. Technol.* 32 (3), 1161–1170. doi:10.1007/s12206-018-0219-4

Liu, H., Ding, J., Dai, H., and Tan, M. (2014). Investigation into Transient Flow in a Centrifugal Pump with Wear Ring Clearance Variation. *Adv. Mech. Eng.* 6, 693097. doi:10.1155/2014/693097

Lomakin, V. O., Kuleshovav, M. S., and Bozh'eva, S. M. (2016). Numerical Modeling of Liquid Flow in a Pump Station. *Power Technol. Eng.* 49 (5), 324–327. doi:10.1007/s10749-016-0623-9

Mortazavi, F., Riasi, A., and Nourbakhsh, A. (2017). Numerical Investigation of Back Vane Design and its Impact on Pump Performance. *J. Fluids Eng.* 139 (12). doi:10.1115/1.4037281

Muggli, F. A., Eisele, K., Casey, M. V., Gu¨lich, J., and Schachenmann, A. (1997). Flow Analysis in a Pump Diffuser-Part 2: Validation and Limitations of CFD for Diffuser Flows. *J. Fluids Eng.* 119 (4), 978–984. doi:10.1115/1.2819526

Nishida, M., Nakayama, K., Sakota, D., Kosaka, R., Maruyama, O., Kawaguchi, Y., et al. (2016). Effect of Impeller Geometry on Lift-Off Characteristics and Rotational Attitude in a Monopivot Centrifugal Blood Pump. *Artif. Organs* 40 (6), E89–E101. doi:10.1111/aor.12697

Posa, A., and Lippolis, A. (2019). Effect of Working Conditions and Diffuser Setting Angle on Pressure Fluctuations within a Centrifugal Pump. *Int. J. Heat Fluid Flow* 75, 44–60. doi:10.1016/j.ijheatfluidflow.2018.11.011

Schäfer, T., Neumann, M., Bieberle, A., and Hampel, U. (2017). Experimental Investigations on a Common Centrifugal Pump Operating under Gas Entrainment Conditions. *Nucl. Eng. Des.* 316, 1–8. doi:10.1016/j.nucengdes.2017.02.035

Wang, C., Shi, W., Wang, X., Jiang, X., Yang, Y., Li, W., et al. (2017). Optimal Design of Multistage Centrifugal Pump Based on the Combined Energy Loss Model and Computational Fluid Dynamics. *Appl. Energ.* 187, 10–26. doi:10.1016/j.apenergy.2016.11.046

Wang, S., Fu, B., Piao, S., Lü, Y., Ciais, P., Feng, X., et al. (2016). Reduced Sediment Transport in the Yellow River Due to Anthropogenic Changes. *Nat. Geosci* 9 (1), 38–41. doi:10.1038/ngeo2602

Yang, J., Pavesi, G., Yuan, S., Cavazzini, G., and Ardizzon, G. (2015). Experimental Characterization of a Pump–Turbine in Pump Mode at Hump Instability Region. *J. Fluids Eng.* 137 (5). doi:10.1115/1.4029572

Yousefi, H., Noorollahi, Y., Tahani, M., Fahimi, R., and Saremian, S. (2019). Numerical Simulation for Obtaining Optimal Impeller's Blade Parameters of a Centrifugal Pump for High-Viscosity Fluid Pumping. *Sustainable Energ. Tech. Assessments* 34, 16–26. doi:10.1016/j.seta.2019.04.011

Zhang, N., Liu, X., Gao, B., and Xia, B. (2019). DDES Analysis of the Unsteady Wake Flow and its Evolution of a Centrifugal Pump. *Renew. Energ.* 141, 570–582. doi:10.1016/j.renene.2019.04.023

Zhou, L., Shi, W., Li, W., and Agarwal, R. (2013). Numerical and Experimental Study of Axial Force and Hydraulic Performance in a Deep-Well Centrifugal Pump with Different Impeller Rear Shroud Radius. *J. Fluids Eng.* 135 (10). doi:10.1115/1.4024894

Conflict of Interest: Author TJ was employed by the company Innovation Institute of Shaanxi Aerospace Power High Tech Co., Ltd.

The remaining authors declare that the research was conducted in the absence of any commercial or financial relationships that could be construed as a potential conflict of interest.

frontiers in Energy Research

ORIGINAL RESEARCH
published: 29 March 2022
doi: 10.3389/fenrg.2022.861134

Effect of Incident Angle of Wear-Ring Clearance on Pressure Pulsation and Vibration Performance of Centrifugal Pump

*XiaoQi Jia[1], Jilin Yu[1], Bo Li[2], Li Zhang[3] and ZuChao Zhu[1]**

[1]Key Laboratory of Fluid Transmission Technology of Zhejiang Province, Zhejiang Sci-Tech University, Hangzhou, China, [2]Hangzhou Weiguang Electronic Co., Ltd., Hangzhou, China, [3]Department of Application and Engineering, Zhejiang Economic and Trade Polytechnical, Hangzhou, China

A wear-ring is an important part of the centrifugal pump. The leakage flow in the wear-ring clearance and main flow at the impeller inlet form crossed mixed flows perpendicular to each other. Large eddies and shocks are produced at the intersection of the two flows due to great velocity difference and different directions, resulting in flow losses, unsteady flow, and even flow-induced vibration. Consequently, the pump performance, pressure pulsation and vibration, and other characteristics will be greatly affected. In this paper, 5 incident angles between the incident section of the wear-ring clearance and the circumferential direction of impeller inlet, i.e., the original angle (90°), 75°, 60°, 45°, and 30°, were formed with a low-specific-speed centrifugal pump as the study object. Unsteady flow calculation and fluid–structure interaction calculation were performed on centrifugal pumps with different wear-ring clearances; the effect of the incident angle of the wear-ring clearance on the distribution of pressure pulsation and vibration performance of centrifugal pump was analyzed. The results showed that the improved efflux angle of the wear-ring clearance could effectively weaken the impact disturbance of the leakage flow in the wear-ring clearance to the main flow at the inlet. Accordingly, the flow status at the inlet of the centrifugal pump was improved, flow losses were reduced, the efficiency of the centrifugal pump was improved, and the vibration amplitude and vibration energy of the pump were also reduced.

Keywords: incident angle, wear-ring clearance, pressure pulsation, vibration performance, vibration energy, centrifugal pump

OPEN ACCESS

Edited by:
Lei Tan,
Tsinghua University, China

Reviewed by:
Alin Bosioc,
Politehnica University of Timişoara, Romania
Aly Abdelbaky Elbatran,
Arab Academy for Science, Technology and Maritime Transport (AASTMT), Egypt

****Correspondence:***
ZuChao Zhu
zhuzuchao01@163.com

Specialty section:
This article was submitted to Process and Energy Systems Engineering, a section of the journal Frontiers in Energy Research

Received: *24 January 2022*
Accepted: *21 February 2022*
Published: *29 March 2022*

Citation:
Jia X, Yu J, Li B, Zhang L and Zhu Z (2022) Effect of Incident Angle of Wear-Ring Clearance on Pressure Pulsation and Vibration Performance of Centrifugal Pump. Front. Energy Res. 10:861134. doi: 10.3389/fenrg.2022.861134

INTRODUCTION

The leakage flow in the wear-ring clearance and main flow at the impeller inlet form crossed mixed flows perpendicular to each other. Large eddies and shocks are produced at the intersection of the two flows due to great velocity difference and different directions, resulting in flow losses, unsteady flow, and even flow-induced vibration. Consequently, the pump performance, pressure pulsation and vibration, and other characteristics will be greatly affected. Wu et al. (Xianfang et al., 2021) studied the effect of the front and rear wear-ring clearance on the pump performance and investigated the changes in the pump performance by a test and numerical simulation. Yan et al. (Yan et al., 2019) found that the wear-ring clearance leakage seriously affects the pump performance. Adistiya et al.

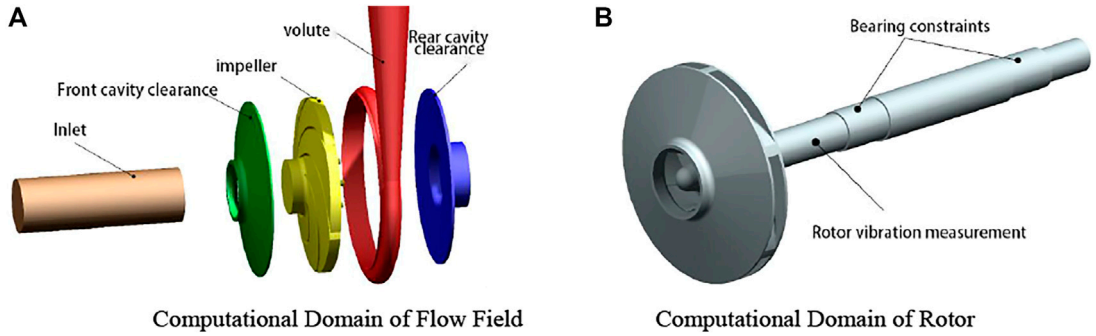

FIGURE 1 | Diagram of computational domain of flow field and rotor. **(A)** Computational domain of flow field. **(B)** Computational domain of rotor.

TABLE 1 | Main geometrical parameters of centrifugal pumps.

Main geometric parameters	Parameter values
Centrifugal pump inlet diameter D_s (mm)	50
Centrifugal pump outlet diameter D_o (mm)	40
Impeller inlet diameter D_1 (mm)	50
Impeller outlet diameter D_2 (mm)	160
Impeller outlet width b_2 (mm)	10
Number of impeller blades Z	6
Blade inlet angle β_1 (°)	23
Blade outlet angle β_2 (°)	23
Blade thickness δ (mm)	2.7
Base circle diameter of spiral case D_b (mm)	165
Width of volute inlet b_2 (mm)	15

(Adistiya and Wijayanta, 2019) studied the effect of the wear-ring clearance by changing the clearance, so as to get higher efficiency. The study of Zheng et al. (Zheng et al., 2020) found that the changes in the wear-ring clearance cause a decrease in the lift, efficiency, and pressure pulsation of a centrifugal pump, and that the clearance efflux angle has a great influence on the pressure distribution at the impeller inlet. Liu et al. (Liu, 2014) found that the pressure distribution in the anterior clearance is greatly affected by the size and radial position of the wear-ring clearance. The study of Li et al. (Li, 2012) found that clearance expansion reduces the efficiency of the centrifugal pump, but the amplitude decreases as the viscosity increases. According to the study of DaqiqShirazi et al. (DaqiqShirazi et al., 2018), when the wear-ring clearance is small, disc friction efficiency has the greatest effect on the efficiency; with the increase of the wear-ring clearance, the volumetric efficiency decreases, but the friction efficiency increases, and the overall efficiency does not decrease significantly. Chen et al. (Chen et al., 2012) indicated that the reason for the decrease in the lift and efficiency of the centrifugal pump is as follows: a small wear-ring clearance reduces the internal turbulence and hydraulic loss, and the increase of clearance decreases the eccentric vortex. Gupta et al. (Gupta and Childs, 2006) established a compressible fluid model for leakage flow of the front and rear wear-ring clearance and obtained the dynamic performance of leakage flow. Zhang (Zhang et al., 2017) found that, within a certain clearance range, the clearance leakage has little effect on pressure fluctuation at the impeller inlet and in the center area; beyond this range, the fluctuation of the whole flow passage increases obviously, but clearance change has little effect on the fluctuation of a guide vane. Yu et al. (Yu, 2019) studied the effect of tip clearance on the performance of low-specific-speed mixed-flow pumps and found that the changes in the size of the tip clearance have a greater effect on the external performance under high flow. Anish et al. (Anish and Sitaram, 2017) found that pressure fluctuation is still controlled by the blade passing frequency in the clearance. Hao (Hao and Tan, 2018) studied the effect of different radial clearances on vibration noise by the fluid–structure interaction (FSI) method and found that increasing the radial clearance will not only reduce the efficiency but also reduce the vibration and noise. In addition to the effect of the wear-ring clearance on the efficiency, lift, and other performance of the pump, the leakage flow in the wear-ring clearance and main flow at impeller inlet form crossed mixed flows perpendicular to each other. Large eddies and shocks are produced at the intersection of the two flows due to great velocity difference and different directions, resulting in flow losses, unsteady flow, and even flow-induced vibration (Sergio and Francesco, 2016; Norrbin et al., 2017; Shi et al., 2017-7). At present, the studies on the wear-ring clearance of centrifugal pumps mainly focus on the effect of clearance flow on the pump performance, and the effect on pressure pulsation and vibration performance is seldom involved. In this paper, the pressure pulsation and vibration performance of the pump under different incident angles were studied by changing the incident angle of the wear-ring clearance of the centrifugal pump. This study showed that the improved efflux angle of the wear-ring clearance could effectively weaken the impact disturbance of the leakage flow in the wear-ring clearance to the main flow at the inlet. Accordingly, the flow status at the inlet of the centrifugal pump was improved, flow losses were reduced, the efficiency of the centrifugal pump was improved, and the vibration amplitude and vibration energy of the pump were also reduced.

CENTRIFUGAL PUMP MODEL

In this paper, the speed of the model pump n = 2,950 r/min, the design flow Q_d = 11 m^3/h, and the rated lift H_d = 40 m. The pump inlet diameter D_s = 50 mm, the outlet diameter D_o = 40 mm, the

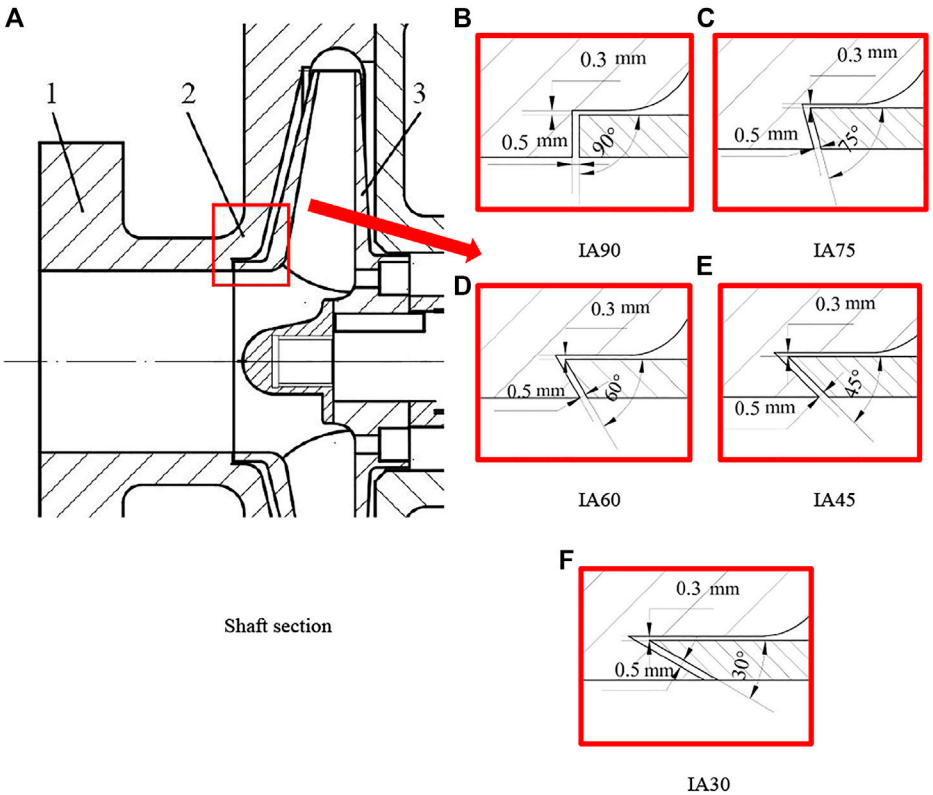

FIGURE 2 | Diagram of incident angle of different wear-ring clearances.

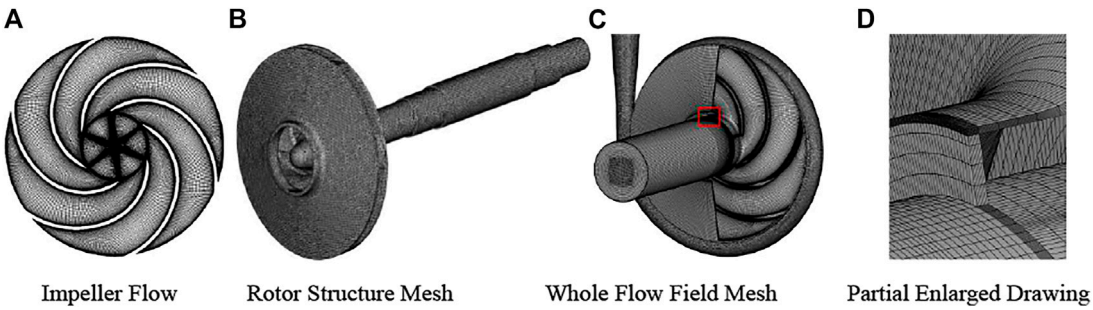

FIGURE 3 | Diagram of flow field domain and rotor mesh. **(A)** Impeller flow. **(B)** Rotor structure mesh. **(C)** Whole flow field mesh. **(D)** Partial enlarged drawing.

impeller inlet diameter D_1 = 50 mm, the impeller outlet diameter D_2 = 160 mm, the impeller outlet width b_2 = 10 mm, the number of impeller blades Z = 6, the blade inlet angle β_1 = 23°, the blade outlet angle β_2 = 23°, the blade thickness δ = 2.7 mm, the volute base circle diameter D_b = 165 mm, and the volute inlet width b_2 = 15 mm. The model pump is shown in **Figure 1**. The main geometric parameters of the prototype pump are shown in **Table 1**.

In this paper, the incident angle of the wear-ring clearance was changed to 90° (IA90), 75° (IA 75), 60° (IA 60), 45° (IA 45), and 30°(IA 30) by changing the outer contour of 1-pump and 2-impeller wear-rings; the same wear-ring clearance (0.3 mm) and same incident position were maintained; the diagram of the incident angle of different wear-ring clearances is shown in **Figure 2**.

NUMERICAL CALCULATION METHOD AND TEST APPARATUS

Numerical Calculation Method

The model in this paper was the SST k–ω model. When the compressibility of the fluid is not considered, this model can be expressed as (Menter, 1992; Versteeg and Malalasekera, 1995)

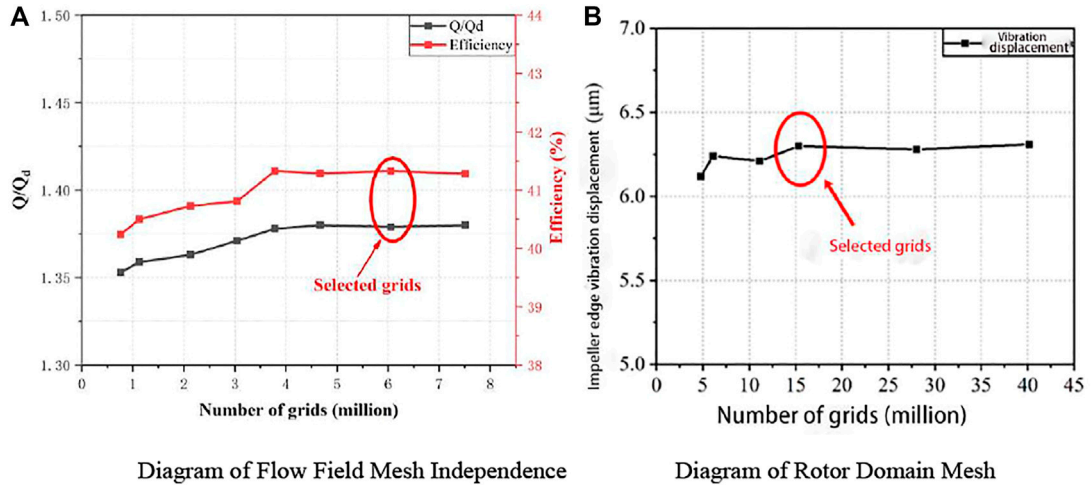

FIGURE 4 | Diagrams of mesh independence verification. **(A)** Diagram of flow field mesh independence. **(B)** Diagram of rotor domain mesh.

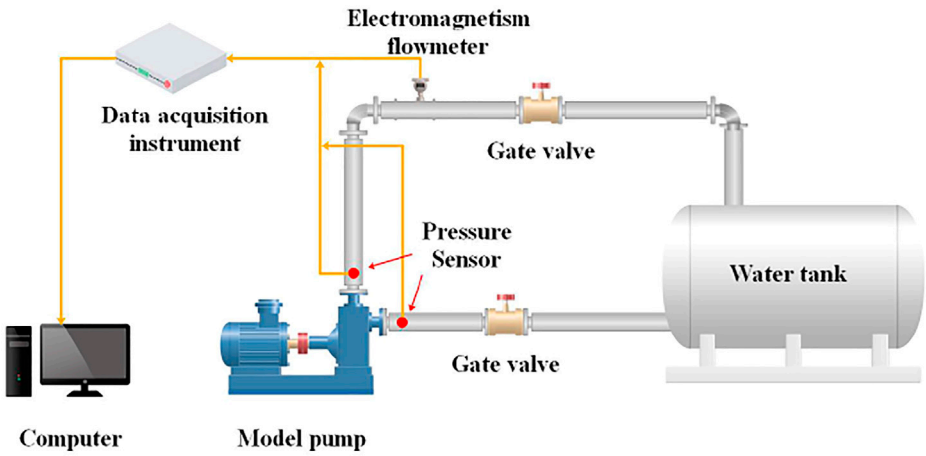

FIGURE 5 | The test apparatus and piping system.

$$\frac{\partial(\rho k)}{\partial t}+\frac{\partial(\rho k u_i)}{\partial x_i}=\frac{\partial}{\partial x_j}\left[\left(\mu+\frac{\mu_t}{\sigma_k}\right)\frac{\partial k}{\partial x_j}\right]+G_k+\rho k\omega\beta* \quad (1)$$

$$\frac{\partial(\rho\omega)}{\partial t}+\frac{\partial(\rho\omega\bar{u}_i)}{\partial x_i}=\frac{\partial}{\partial x_j}\left[\left(\mu+\frac{\mu_t}{\sigma_\omega}\right)\frac{\partial\omega}{\partial x_j}\right]+\frac{\partial_\omega}{k}G_k-\rho\omega^2\beta + 2(1-F_1)\rho\frac{1}{\omega\sigma_\omega}\frac{\partial k}{\partial x_j}\frac{\partial\omega}{\partial x_j} \quad (2)$$

$$\mu_t=\frac{\rho k}{\omega} \quad (3)$$

where $\sigma_k = 0.5$, $\sigma_w = 0.5$, $\beta = 0.075$, $\beta^* = 0.09$, $\alpha = 5/9$.

In this paper, the velocity inlet and free outflow were used in the numerical calculation of the whole flow field of the centrifugal pump. The walls of the impeller flow domain and those in contact with the solid region of the impeller were set to rotate walls, the walls of other flow domains were set to stationary walls, and all walls were set to smooth walls. The coupling between speed and pressure was realized by the SIMPLEC algorithm. The second-order upwind and central difference scheme were adopted for the spatial dispersion of the convective term and diffusive term, respectively. In the unsteady calculation of the whole flow field, the time step of every 1° rotation of the impeller was taken as a time step, and a rotation cycle contained 360 time steps in total. The speed of the model pump was 2,950 r/min, the time step was 5.64972×10^{-5} s, and the convergence residual accuracy of each physical quantity was set to 10^{-5}.

In the FSI calculation, the calculation of the three parts, the flow field, solid structure field, and data transfer of the FSI surface, converged. The convergence criterion in the data transfer of the FSI surface was

$$\phi^*=\frac{\sqrt{\sum\left(a^*_{new}-a^*_{old}\right)^2}}{\sqrt{\sum\left(a^{*\,2}_{new}\right)}} \quad (4)$$

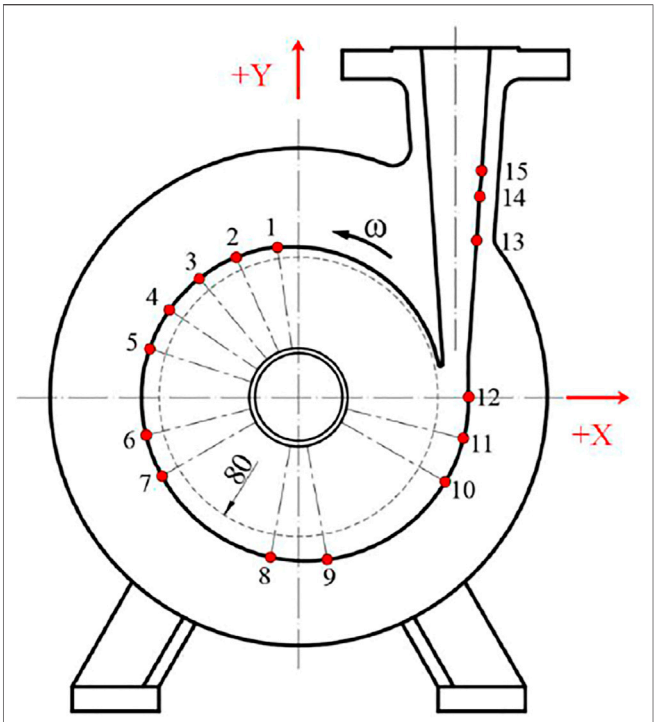

FIGURE 6 | Installation position of pressure sensor.

TABLE 2 | Installation position of the pressure sensor.

No.	Location	No.	Location
1	θ = 8°	9	θ = 190°
2	θ = 24°	10	θ = 240°
3	θ = 40°	11	θ = 255°
4	θ = 56°	12	θ = 270°
5	θ = 72°	13	h = 90 mm
6	θ = 104°	14	h = 115 mm
7	θ = 120°	15	h = 130 mm
8	θ = 170°	—	—

where, a^*_{old} is the load component of the previous iteration and a^*_{new} is the load component of the current iteration. A convergence precision $\phi^*_{\min}$ is pre-given, only when ϕ^* is smaller than $\phi^*_{\min}$. Data transfer can be considered to have been converged. The convergence criterion in the data transfer of FSI surface was

$$e^* = \frac{\log(\phi^*/\phi^*_{\min})}{\log(10/\phi^*_{\min})}, 0 < \phi^*_{\min} < 1 \quad (5)$$

The criterion for determining the convergence of the FSI load data transfer is: $e^* < 0$.

Figure 3 shows a diagram of the flow field domain and rotor mesh. **Figures 4A,B** are mesh independence verification diagrams of the flow field domain and impeller rotor domain, respectively. According to the mesh independence verification, the number of mesh cells finally selected herein for the flow field and rotor domain was 6.06×10^6 and 15.31×10^4, respectively.

Test Apparatus

The test apparatus and piping system are shown in **Figure 5**. The pressure pulsation sensor used herein is a high-frequency dynamic pressure sensor. Its model is GYS-I, its measuring range is -0.01–1 MPa, its accuracy is 0.2, and its frequency response is 10 kHz. The installation position of the sensor is shown in **Figure 6** and **Table 2**. In this paper, a non-contact electric vorticity sensor with a sensitivity of 4 mV/μm and a range of 0–2 mm was used to measure the vibration displacement of the centrifugal pump. The installation position of the vibration sensor is shown in **Figure 7**.

RESULTS AND DISCUSSION

Effect of Wear-Ring Incident Angle on Pump Pressure Pulsation

Figure 8 shows the comparison of the experimental value and calculation results of the pressure pulsation of the prototype

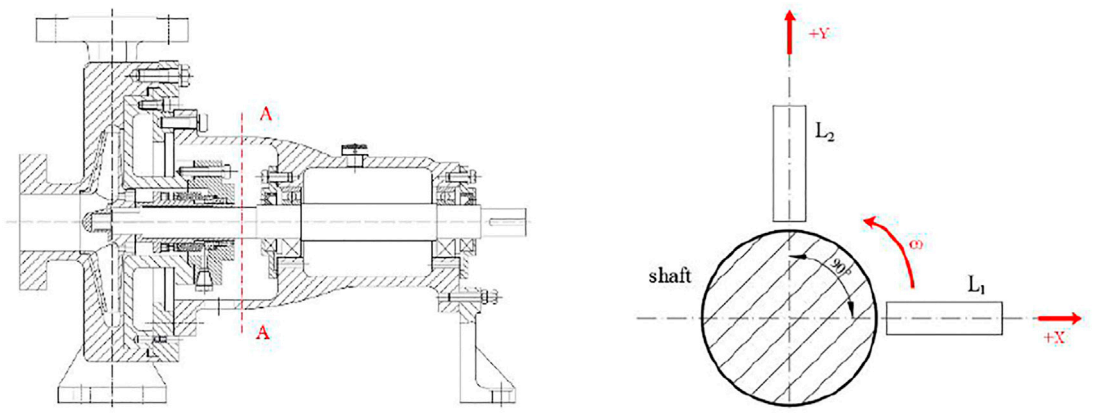

FIGURE 7 | Schematic diagram for installation of vibration displacement sensor.

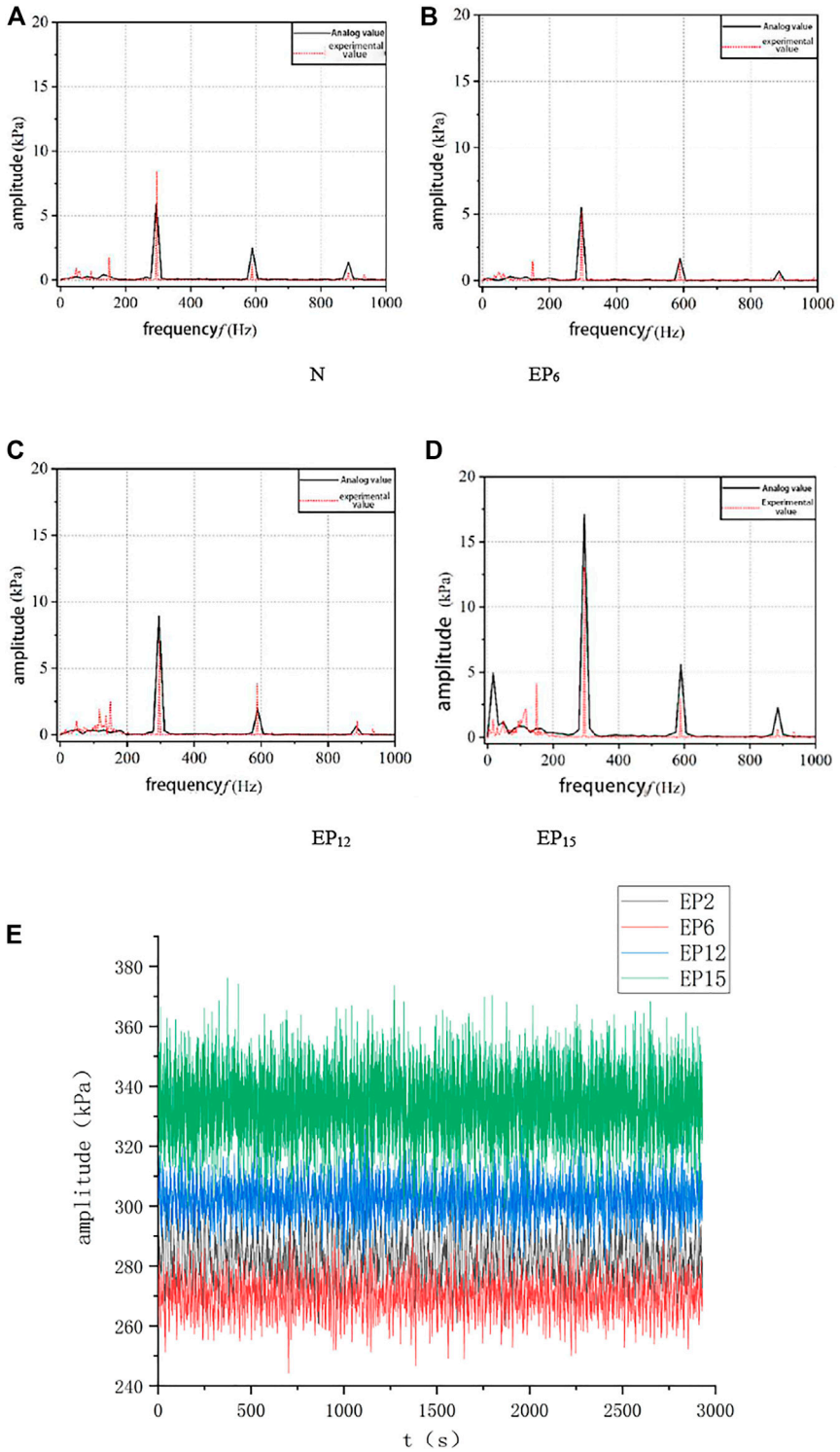

FIGURE 8 | Comparison of experimental value and calculation results of pressure pulsation of the prototype pump (IA90) at different observation points under design conditions and the original pressure signal.

pump (IA90) at different observation points under design conditions. According to the figure, under the design flow (11 m^3/h), the main frequency of pressure pulsation at different observation points was near the blade frequency, and the maximum amplitude of the experimental value and calculation results was at observation point EP_{15}. In general,

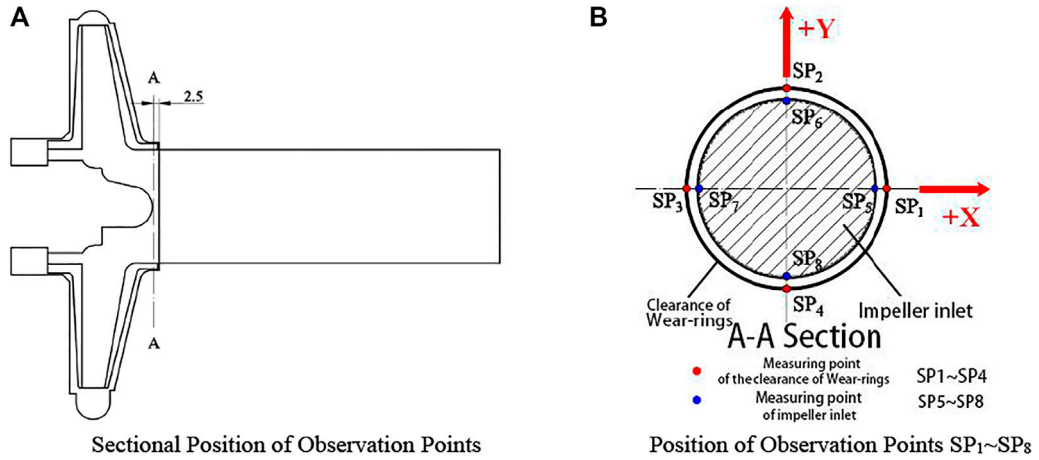

FIGURE 9 | Diagram of position of observation points for wear-ring pressure pulsation. **(A)** Sectional position of observation points. **(B)** Position of observation points SP_1~SP_8.

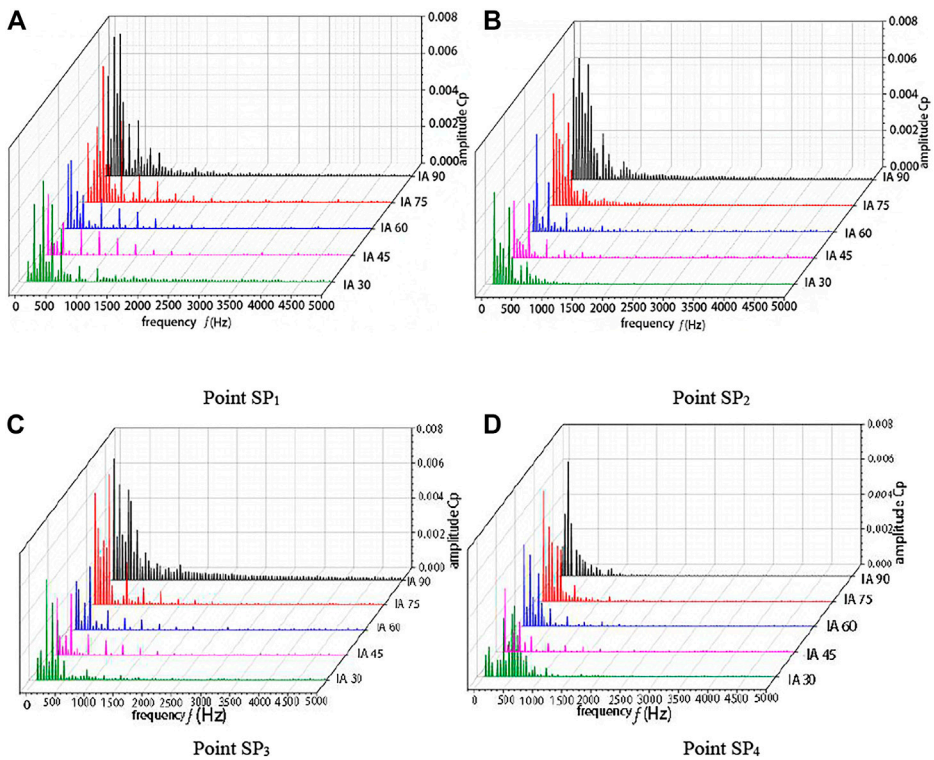

FIGURE 10 | Comparison of shaft frequency and blade frequency of pressure pulsation in wear-ring clearance under design conditions and different incident angles of wear-ring clearance. **(A)** Point SP_1. **(B)** Point SP_2. **(C)** Point SP_3. **(D)** Point SP_4.

under design conditions, the experimental value and calculation results of pressure pulsation have a consistent distribution trend, with the main frequency at the blade frequency (with an error of only 0.2%). This verified that the numerical calculation method used herein is accurate and reliable.

In order to further analyze the flow status in the wear-ring clearance and at the impeller inlet, 4 observation points were arranged in the wear-ring clearance and on the near wall of the impeller inlet, respectively. The position of observation points is shown in **Figure 9**. SP_1~SP_4 are observation points

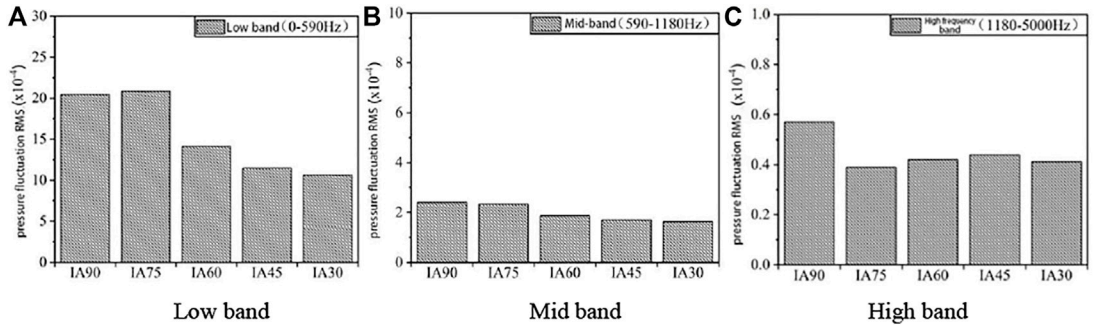

FIGURE 11 | Comparison of RMS values of pressure pulsation in wear-ring clearance under different incident angles of wear-ring clearance. **(A)** Low band. **(B)** Mid band. **(C)** High band.

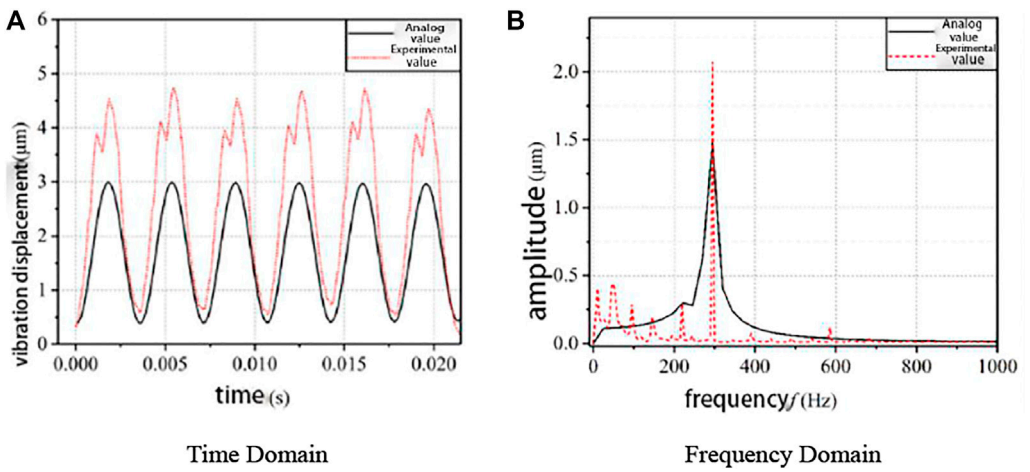

FIGURE 12 | Time domain and frequency domain of simulated vibration and experimental vibration. **(A)** Time domain **(B)** Frequency domain.

in the wear-ring clearance; SP_5~SP_8 are observation points on the near wall of the impeller inlet.

Figure 10 shows the frequency domain distribution at observation points in the wear-ring clearance under the design flow and different incident angles of the wear-ring clearance. This figure shows that the pressure pulsation frequency domain of centrifugal pumps with the different incident angles of the wear-ring clearance also shows strong asymmetry. The frequency domain of pressure pulsation is mainly in the low-frequency band. The intermediate frequency is mainly the frequency multiplier (295 Hz) of the blade passing frequency. The reason for this is that after a long anterior flow domain, the flow gradually becomes orderly and the high-frequency pulsation is gradually weakened. The main frequency of each observation point is different and is mainly concentrated in the multiplier and shaft frequency multiplier and shaft frequency. The pulsation amplitudes in each frequency domain decrease with the decrease of the incident angle of the wear-ring clearance. The reason is that the decrease of the incident angle of the wear-ring clearance makes the flow in the wear-ring clearance more orderly. Compared with the maximum amplitude of pressure pulsation of IA90, the maximum amplitude of pressure pulsation of IA75, IA60, IA45, and IA30 decreased by 5.9%, 44.3%, 49.6%, and 42.7%, respectively.

Figure 11 shows the comparison of the RMS values of pressure pulsation in the wear-ring clearance under the design conditions and different incident angles of the wear-ring clearance. It can be seen from **Figure 11** that compared with IA90, the RMS values in each band of IA75 did not change greatly. This indicates that IA75 has no obvious effect on pressure pulsation in the wear-ring clearance. However, compared with the IA90 model, the amplitude of pressure pulsation in the low-frequency band of IA60, IA45, and IA30 models was greatly improved, while the amplitude of the low-frequency RMS value decreased by 30.8%, 44.0%, and 37.4%, respectively. The amplitude of the RMS value of pressure pulsation in the middle frequency band of IA60, IA45, and IA30 models also decreased significantly and was 22.4%, 29.3%, and 32.2% lower than that of the IA90 model, respectively. The amplitude of the RMS value of pressure pulsation in the high-frequency band of the three models was also greatly improved

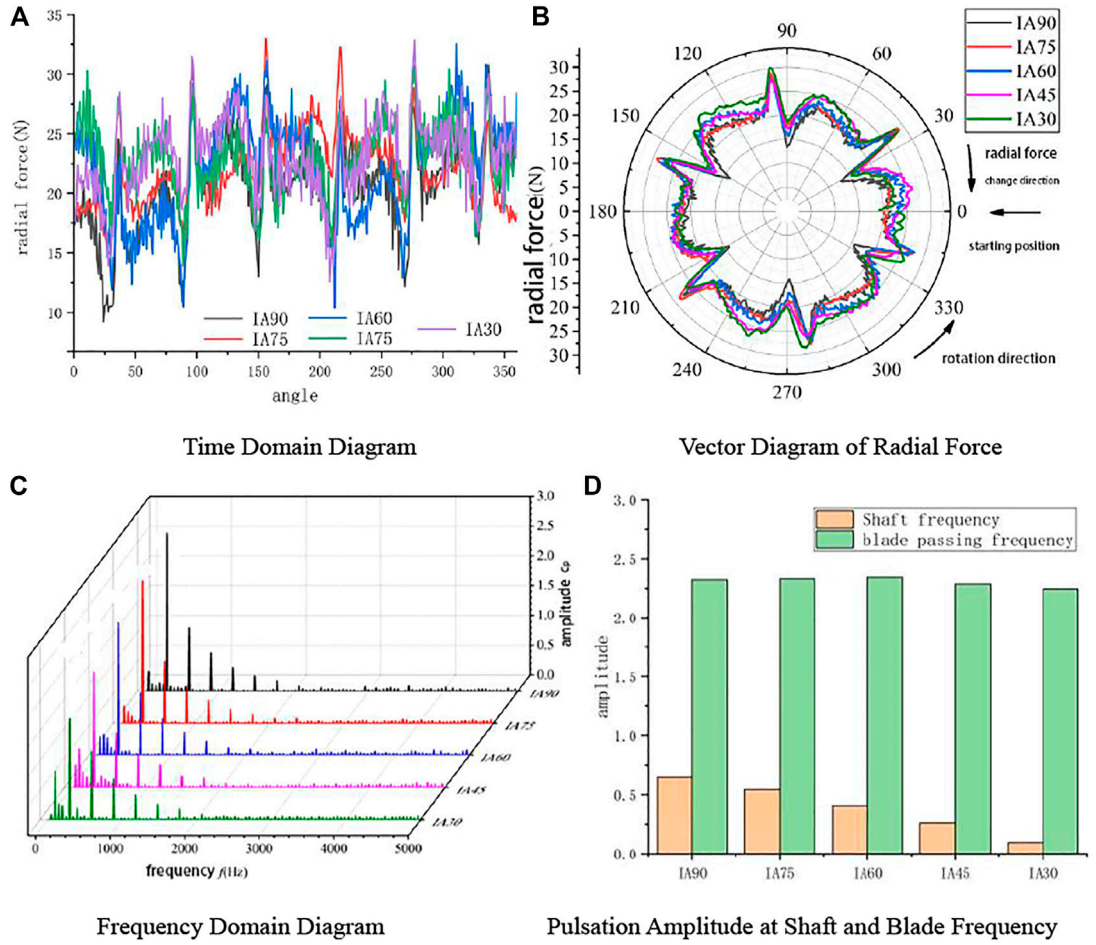

FIGURE 13 | Time domain diagram and frequency domain diagram of radial force of centrifugal pump under different wear-ring incident angles and the design flow. **(A)** Time domain diagram. **(B)** Vector diagram of radial force. **(C)** Frequency domain diagram. **(D)** Pulsation amplitude at shaft and blade frequency.

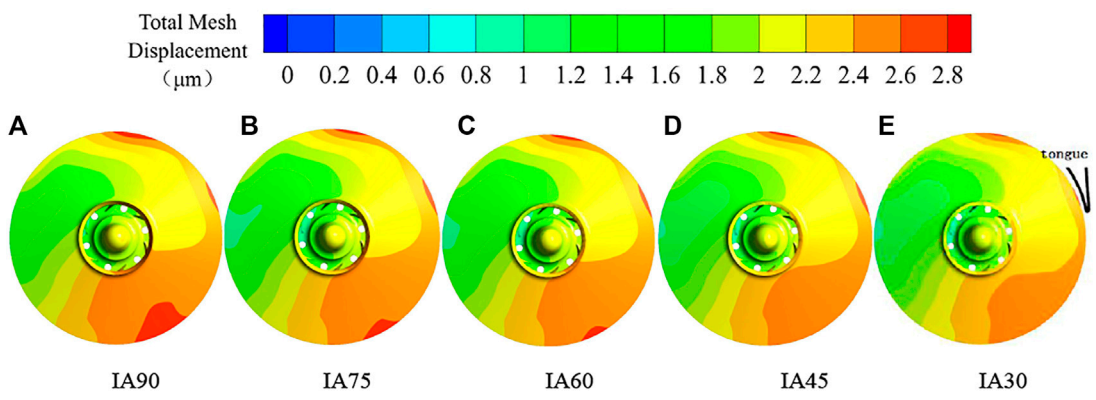

FIGURE 14 | Cloud map of vibration displacement of impeller under the design flow.

and was 12.4%, 9.3%, and 24.2% lower than that of the IA90 model. Thus, it can be seen that the decrease of the incident angle of the wear-ring clearance can effectively reduce the amplitude of pressure pulsation in the low-frequency band and has little effect on the amplitude of pressure pulsation in the high-frequency band.

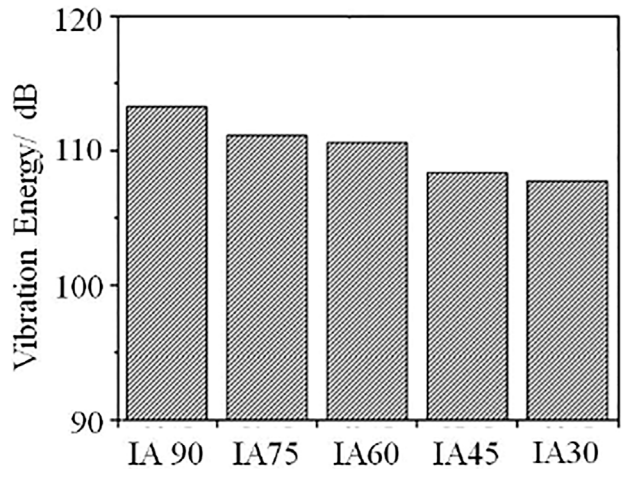

FIGURE 15 | Vibration energy distribution of impeller under different incident angles.

Effect of Wear-Ring Incident Angle on Pump Vibration Performance

Figure 12 shows the comparison of time domain and frequency domain of the results of the vibration displacement experiment and numerical simulation of the IA90 centrifugal pump. According to **Figure 12**, the time–domain diagram of vibration displacement shows obvious periodicity and has six peaks and troughs; experimental values are slightly greater than calculated ones; the amplitude is mainly concentrated in the shaft frequency and blade frequency. The experimental values at the design flow and the FSI calculation results have a consistent trend, which indicates that the results of the FSI calculation adopted in this paper are relatively accurate.

Figure 13 shows the distribution diagram of the time domain and frequency domain of radial force on the pump impeller under the design flow and different incident angles. As shown in **Figure 13C**, the radial force on the impeller shows obvious periodicity; the decrease of the incident angle of the wear-ring clearance will gradually decrease the radial force on the impeller, and the pulsation amplitude of the radial force will also gradually decrease; however, from the frequency domain distribution of the radial force, the changes in the incident angle of the wear-ring clearance have a greater influence on the pulsation amplitude of the radial force at the shaft frequency and have a minor influence on the pulsation amplitude of the radial force at the blade frequency.

Figure 14 shows the overall vibration displacement diagram of the impeller rotor system of a centrifugal pump under different incident angles of the wear-ring clearance at $t = 0.02$ s. It can be seen from the figure that the maximum vibration displacements of centrifugal pumps with different incident angles of the wear-ring clearance appeared at the outer edge of the impeller, mainly at the highest and lowest point along the gravity direction and at the cutwater, and the minimum displacements appeared at the furthest distance from the cutwater. The maximum vibration displacement of IA90 under the original incident angle of the wear-ring clearance was 2.78 μm, while the vibration displacement of IA75 was slightly greater and was 2.72 μm. The maximum vibration displacement of IA60, IA45, and IA30 gradually decreased with the decrease of the incident angle of the wear-ring clearance. Moreover, the average of the deformed area decreased significantly; the maximum vibration displacement was 2.63, 2.59 and 2.55 μm, respectively. This shows that the decrease of the incident angle of the wear-ring clearance can effectively inhibit the vibration of the centrifugal pump impeller.

In order to further study the vibration performance of the centrifugal pump, the root mean square of the vibration power spectrum signal was calculated and was defined as the vibration energy RMS [1,66]. **Figure 15** shows the vibration energy distribution of the impeller under different incident angles. As shown in this figure, the changes in the incident angle of the wear-ring clearance have a certain effect on the vibration energy of the pump. The vibration energy of the pump impeller gradually decreases and is inhibited to some extent with the gradual decrease of the wear-ring incident angle.

CONCLUSION

In this paper, IA30 is the best case of clearance shape from the analyzed ones; the pressure pulsation and vibration performance of the centrifugal pump under 5 different incident angles of the wear-ring clearance were analyzed by calculating the unsteady flow and FSI in the whole flow field of the centrifugal pump. The main conclusions are as follows:

1) Small incident angles of the wear-ring clearance will weaken the impact and disturbance of the wear-ring jet flow on the main flow, thus reducing the pressure pulsation of the pump, and the smaller the incident angle, the smaller the pressure pulsation amplitude.
2) The decrease of the incident angle of the wear-ring clearance can effectively reduce the amplitude of pressure pulsation in the low-frequency band and has little effect on the amplitude of pressure pulsation in the high-frequency band.
3) The analysis of the radial force on the impeller and vibration displacement and vibration energy of the impeller showed that the decrease of the incident angle of the wear-ring clearance will decrease the radial force on the impeller and also inhibit the vibration amplitude and vibration energy of the impeller.
4) The smaller the incident angle of the orifice ring gap, the higher the head and efficiency. This is because with the decrease of the incident angle of the orifice ring gap, the leakage of the front orifice ring gap decreases gradually, which improves the volumetric efficiency and thus the head and efficiency.

DATA AVAILABILITY STATEMENT

The raw data supporting the conclusion of this article will be made available by the authors, without undue reservation.

AUTHOR CONTRIBUTIONS

XJ and JY conceived of the presented idea. XJ developed the theory and performed the computations. JY encouraged XJ to investigate and supervised the findings of this work. BL, LZ, and ZZ were involved in planning and supervised the work, All authors discussed the results and contributed to the final manuscript.

FUNDING

This work was supported by the National Natural Science Foundation of China (Grant No. 51906221) and the Joint Fund of Zhejiang Natural Science Foundation (Grant No. LZY21E060002).

REFERENCES

Adistiya, Suryana., and Wijayanta, A. T. (2019). Effect of Clearance gap on Hydraulic Efficiency of Centrifugal Pump. *THE 4TH INTERNATIONAL CONFERENCE INDUSTRIAL, MECHANICAL, ELECTRICAL, CHEMICAL ENGINEERING* 5. doi:10.1063/1.5098228

Anish, S., and Sitaram, N. (2017). Computational Study of Radial gap Effect between Impeller and Diffuser on the Unsteadiness of Vaned Diffuser in a Centrifugal Compressor. *J. Mech. Sci. Technol.* 31 (11), 5291–5298. doi:10.1007/s12206-017-1023-2

Chen, B., Li, X., and Zhu, Z. (2022a). Time-Resolved Particle Image Velocimetry Measurements and Proper Orthogonal Decomposition Analysis of Unsteady Flow in a Centrifugal Impeller Passage. *Front. Energ. Res.* 9. doi:10.3389/fenrg.2021.818232

Chen, B., Li, X., Zhu, Z., and Zhu, Zu. Chao. (2022b). Investigations of Energy Distribution and Loss Characterization in a Centrifugal Impeller through PIV experiment. *Ocean Eng.* 247 (2022), 110773. doi:10.1016/j.oceaneng.2022.110773

Chen, S. X., Pan, Z. Y., Wu, Y. L., and Zhang, D. Q. (2012). Simulation and experiment of the Effect of Clearance of Impeller Wear-Rings on the Performance of Centrifugal Pump. *IOP Conf. Ser. Earth Environ. Sci.* 15, 072017. doi:10.1088/1755-1315/15/7/072017

DaqiqShirazi, M., Torabi, R., Riasi, A., and Nourbakhsh, S. A. (2018). The Effect of Wear Ring Clearance on Flow Field in the Impeller Sidewall gap and Efficiency of a Low Specific Speed Centrifugal Pump. *ARCHIVE Proc. Inst. Mech. Eng. C J. Mech. Eng. Sci. 1989-1996 (vols 203-210)* 232 (17), 3062–3073. doi:10.1177/0954406217729420

Gupta, M. K., and Childs, D. W. (2006). Rotordynamic Stability Predictions for Centrifugal Compressors Using a Bulk-Flow Model to Predict Impeller Shroud Force and Moment Coefficients[J]. *J. Eng. Gas Turbines Power* 132 (9), 1211–1223. doi:10.1115/1.2720519

Hao, Y., and Tan, L. (2018). Symmetrical and Unsymmetrical Tip Clearances on Cavitation Performance and Radial Force of a Mixed Flow Pump as Turbine at Pump Mode. *Renew. Energ.* 127 (NOV), 368–376. doi:10.1016/j.renene.2018.04.072

Li, W. G. (2012). An Experimental Study on the Effect of Oil Viscosity and Wear-Ring Clearance on the Performance of an Industrial Centrifugal Pump[J]. *J. Fluids Eng.* 134 (1), 014501. doi:10.1115/1.4005671

Liu, Houlin. (2014). Investigation into Transient Flow in a Centrifugal Pump with Wear Ring Clearance Variation [J]. *Adv. Mech. Eng.* 6, 354–359. doi:10.1155/2014/693097

Menter, F. R. (1992). Influence of Freestream Values on K-ω Turbulence Model Predictions. *AIAA J.* (6), 1651–1659. doi:10.2514/3.11115

Norrbin, C. S., Childs, W. D., and Phillips, S. (2017). Including Housing-Casing Fluid in a Lateral Rotordynamics Analysis on Electric Submersible Pumps. *J. Eng. Gas Turbines Power Trans. Asme*. doi:10.1115/gt2016-58087

Sergio, Baragetti., and Francesco, V. (2016). Effects of Geometrical Clearances, Supports Friction, and Wear Rings on Hydraulic Actuators Bending Behavior. *Math. Probl. Eng.* 2016, 1–17.

Shi, W., Gao, X., Zhang, Q., Zhang, D., and Ye, D. (2017-7-01201). Numerical Investigations on Effect of Wear-Ring Clearance on Performance of a Submersible Well Pump. *Adv. Mech. Eng.* 97 (7), 168781401770415. doi:10.1177/1687814017704155

Versteeg, H. K., and Malalasekera, W. (1995). *An Introduction to Computational Fluid dynamics[M]*. British: Longman Group Ltd.

Xianfang, W., Xinlai, D., Minggao, T., and Houlin, L. (2021). Experiment and Simulation about the Effect of Wear-Ring Abrasion on the Performance of a marine Centrifugal Pump. *Adv. Mech. Eng.* 13, 168781402199811. doi:10.1177/1687814021998115

Yan, J., Zuo, Z., Guo, W., Hou, H., Zhou, X., and Chen, H. (2019). Influences of Wear-Ring Clearance Leakage on Performance of a Small-Scale Pump-Turbine. *Proc. Inst. Mech. Eng. A: J. Power Energ.* 234, 454–469. doi:10.1177/0957650919865052

Yu, Zhiyi. (2019). Numerical Analysis for the Effect of Tip Clearance in a Low Specific Speed Mixed-Flow Pump. *Adv. Mech. Eng.* 11, 3. doi:10.1177/1687814019832222

Zhang, W., Yu, Z., and Zhu, B. (2017). Influence of Tip Clearance on Pressure Fluctuation in Low Specific Speed Mixed-Flow Pump Passage. *Energies* 10 (2), 148. doi:10.3390/en10020148

Zheng, L., Chen, X., Dou, H.-S., Zhang, W., Zhu, Z., and Cheng, X. (2020). Effects of Clearance Flow on the Characteristics of Centrifugal Pump under Low Flow Rate. *J. Mech. Sci. Technol.* 34, 189–200. doi:10.1007/s12206-019-1220-2

Conflict of Interest: BL was employed by the company Hangzhou Weiguang Electronic Co. Ltd.

The remaining authors declare that the research was conducted in the absence of any commercial or financial relationships that could be construed as a potential conflict of interest.

Publisher's Note: All claims expressed in this article are solely those of the authors and do not necessarily represent those of their affiliated organizations, or those of the publisher, the editors and the reviewers. Any product that may be evaluated in this article, or claim that may be made by its manufacturer, is not guaranteed or endorsed by the publisher.

frontiers in Energy Research

METHODS
published: 30 March 2022
doi: 10.3389/fenrg.2022.865252

Reliability Synthesis and Prediction for Complex Electromechanical System: A Case Study

Chunyu Yu[1,2]*, *Yuanlin Guan*[1,2]* and *Xixin Yang*[3]

[1]Key Lab of Industrial Fluid Energy Conservation and Pollution Control (Qingdao University of Technology), Ministry of Education, Qingdao, China, [2]School of Mechanical and Automotive Engineering, Qingdao University of Technology, Qingdao, China, [3]College of Computer Science and Technology, Qingdao University, Qingdao, China

The life test of a complex electromechanical system (CEMS) is restricted by many factors, such as test time, test cost, test environment, test site, and test conditions. It is difficult to realize system reliability synthesis and prediction of a CEMS which consists of units with different life distributions. Aiming at the problems, a numerical analysis method based on the computer simulation and the Monte Carlo (MC) method is proposed. First, the unit's life simulation values are simulated using the MC method with the given each unit's life distribution and its distribution parameter point estimation. Next, using the unit's life simulation values, the CEMS life simulation value can be obtained based on the CEMS reliability model. A simulation test is realized instead of the life test of the CEMS when there are enough simulation values of the CEMS life. Then, simulation data are analyzed, and the distribution of the CEMS life is deduced. The goodness-of-fit test, point estimation and confidence interval of the parameters, and reliability measure are estimated. Finally, as a test example of the wind turbine, the practicability and effectiveness of the method proposed in this paper are verified.

Keywords: Monte Carlo simulation, computer simulation, system reliability prediction, system reliability synthesis, complex electromechanical system

OPEN ACCESS

Edited by:
Ling Zhou,
Jiangsu University, China

Reviewed by:
Shiyuan Han,
University of Jinan, China
Tong Ruipeng,
China University of Mining and Technology, China

***Correspondence:**
Chunyu Yu
honeychunyu@126.com
Yuanlin Guan
guanyuanlin@qut.edu.cn

Specialty section:
This article was submitted to Process and Energy Systems Engineering, a section of the journal Frontiers in Energy Research

Received: *29 January 2022*
Accepted: *03 March 2022*
Published: *30 March 2022*

Citation:
Yu C, Guan Y and Yang X (2022) Reliability Synthesis and Prediction for Complex Electromechanical System: A Case Study. Front. Energy Res. 10:865252. doi: 10.3389/fenrg.2022.865252

INTRODUCTION

Complex electromechanical systems (CEMSs) have been used in industry, civil machinery, aerospace, and so on (Mi et al., 2016; Wang et al., 2022). Reliability synthesis and prediction of CEMSs have long been critical issues within the field of reliability engineering. CEMSs are usually composed of optics, machinery, and electricity (Tang et al., 2021). Some CEMSs have very complex structures, some have huge volumes, some have long service life, and some are expensive (Han et al., 2021). Thus, reliability synthesis and prediction of CEMSs only relying on life testing are limited by multiple factors such as test scheme, test site, test time, test cost, and test conditions. However, at the stage of the project demonstration and initial design of CEMSs, reliability synthesis and prediction of CEMSs are necessary (Fuqiu et al., 2020). Therefore, it challenges the realization of reliability synthesis and prediction of CEMSs.

Since Buehler proposed a reliability synthesis method for a series system with two binomial components (Buehler, 1957), scholars from classical, Bayes, and fiducial schools have conducted a lot of research on reliability synthesis and prediction of systems. The classical school put forward the maximum likelihood estimation (MLE) method, modified maximum likelihood estimation (MML) method, sequential reduction (SR) method, combined MML and SR method (CMSR), and so on (Yu

et al., 2013). The MLE method is only applicable to large sample tests, and the failure distribution is an unbounded symmetric normal distribution. The MML method is only applicable to binomial (pass–fail) component systems (Fo and Xiong, 2009). The disadvantage of the SR method is that successive compression of test data leads to information loss, resulting in large estimation variance and a more conservative confidence limit of system reliability (Zhu and J Sh, 1990). The algorithm of the CMSR method is complex, and it is not suitable for the system with zero failure number of unit test data. The Bayes method only solves the reliability interval estimation of binomial or exponential approximation for complex systems (Guo and Wilson, 2013). The fiducial method has been proved unsuitable for system reliability evaluation (Zhou and Weng, 1990). Therefore, it is difficult to use the abovementioned methods to synthesize and predict the CEMSs' reliability, and reliability synthesis and prediction of CEMSs are still problems in reliability engineering (Peng et al., 2013). Although the Monte Carlo method can easily deal with the reliability synthesis problem of systems with different unit distributions (Yeh et al., 2010), the simple Monte Carlo method, bootstrap method, double Monte Carlo method, and asymptotic method introduced in many studies can only solve the lower confidence limit of system reliability, and the interval estimation problem of system life distribution types and parameters are unsolved (Meng and Wen-Tao, 2021). Despite decades of research, there is still no general method to realize the reliability synthesis and prediction of CEMSs (Kovacs et al., 2019).

It is well known that a CEMS is composed of several units (subsystems), and the system reliability depends on the reliability of its constituent units (subsystems) (Negi and Singh, 2015), (Liu et al., 2015). When the constituent units' life of CEMS follows different distributions, it is difficult to synthesize and predict the CEMS reliability from units' reliability data information (Weiyan et al., 2009). Hence, some scholars have conducted a lot of correlational research. For example, Guo et al. (2014) analyzed some theories and methods for system reliability synthesis, and the new idea was proposed for the problem aiming at specific engineering backgrounds. Considering that some CEMSs contain outsourced components, Sun et al. (2018) computed system reliability and component importance measures. According to the equal-principle first and second moment of reliability, Yu et al. (2013) investigated Bayes reliability confidence limit for a series-parallel system consisting of different distribution units. Graves and Hamada (2016) evaluated the likelihood for simultaneous failure time data when monitoring was stopped. In view of the lack of reliability data information of CEMSs, Wilson et al. (2006) and Yuan et al. (2019) discussed how to make full use of limited reliability data information of CMESs to synthesize and predict system reliability. Although scholars have discussed the reliability synthesis and prediction of CEMS from many aspects, there are still challenges by many factors such as difficulty in establishing a reliability model for CMES, lack of reliability data information, high test cost, and so on. It is necessary to be studied further.

In order to solve the above problems and realize the reliability synthesis and prediction of CEMS, a numerical analysis method based on the computer simulation and the Monte Carlo (MC) method is proposed in this article. The remainder of this article is organized as follows: In **Section 2**, we propose a method to obtain the life simulation values for the constituent units of CEMS when the life distribution types and distribution parameters of constituent units are known. In **Section 3**, we take a method to obtain the system life simulation value from the units' life simulation values. One system life simulation value represents a reliability test of CEMS. Computer simulation can be realized instead of life test when there are enough system life simulation values. In **Section 4**, we carry out the initial selection of CMES life distribution types and goodness-of-fit test. In **Section 5**, a case study of a CMES is presented to demonstrate the effectiveness of our proposed method. Finally, conclusions are made in **Section 6**.

LIFE SIMULATION VALUES FOR THE CONSTITUENT UNITS OF COMPLEX ELECTROMECHANICAL SYSTEMS

It is assumed that a CEMS is composed of n different life distribution units, and the life distribution and the appropriate parameters of each constituent unit are known. The life simulation values for n units are generated using the random variable simulation conversion equation and through Monte Carlo simulation (Yoshida and Akiyama, 2011; Wang et al., 2012; Zhang et al., 2014). According to the common distributions in engineering, such as the exponential distribution, Weibull distribution, normal distribution, logarithmic normal distribution, extreme value distribution, Gamma distribution etc., the respective random variable simulation conversion equations $g(\vartheta_i)$ are deduced and listed in **Table 1**. If a unit is subject to any other distribution, its random variable simulation conversion equation can be solved similarly using the inverse function method.

In order to ensure that all units are independent of each other, the pseudo-random number is computer-generated for each unit and subject to 0-1uniform distribution.

$$\vartheta_i = \mathrm{RND}(1) \quad i = 1, 2, \cdots, n.$$

According to the life distribution and parameters of each constituent unit, the life simulation value t_i for the corresponding unit can be obtained through logical operation.

$$t_i = g(\vartheta_i) \quad i = 1, 2, \cdots, n.$$

In this way, a set of life simulation values of n units can be obtained, and the first simulation values are completed. The m groups of life simulation values are obtained after m cycles.

LIFE SIMULATION VALUES FOR THE COMPLEX ELECTROMECHANICAL SYSTEMS

For the CEMS composed of n units, the life simulation value for each unit can be obtained through each simulation, and they are

TABLE 1 | Conversion formulas of different distributions.

Probability density function	Distribution function	Conversion formula $g(\vartheta_i)$
$f_e(t) = \lambda e^{-\lambda(t-t_0)}$	λ t_0	$t = -\frac{\ln(\vartheta)}{\lambda} + t_0$
$f_w(t) = \frac{m(t-t_0)^{m-1}}{\eta^m} e^{-(\frac{t-\gamma}{\eta})^m}$	m η t_0	$t = \eta(-\ln\vartheta)^{1/m} + t_0$
$f_N(t) = \frac{1}{\sigma\sqrt{2\pi}} e^{-\frac{(t-\mu)^2}{2\sigma^2}}$	μ σ	$t_1 = \sqrt{-\ln\vartheta_1}\sin 2\pi\vartheta_2$ $t_2 = \sqrt{-\ln\vartheta_1}\cos 2\pi\vartheta_2$
$f_L(t) = \frac{1}{\sqrt{2\pi}\sigma_L t} e^{-\frac{(\ln t-\mu_L)^2}{2\sigma_L^2}}$	μ_L σ_L	$t_1 = e^{\sqrt{-\ln\vartheta_1}\sin 2\pi\vartheta_2}$ $t_2 = e^{\sqrt{-\ln\vartheta_1}\cos 2\pi\vartheta_2}$
$f_m(t) = \frac{1}{\sigma_m} e^{\frac{t-\mu_m}{\sigma_m}} e^{-e^{\frac{t-\mu_m}{\sigma_m}}}$	μ_m σ_m	$t = \mu_m + \sigma_m \ln(-\ln\vartheta)$
$f_M(t) = \frac{1}{\sigma_M} e^{-\frac{t-\mu_M}{\sigma_M}} e^{-e^{\frac{t-\mu_M}{\sigma_M}}}$	μ_M σ_M	$t = \mu_M - \sigma_M \ln(-\ln\vartheta)$
$f_\Gamma(t) = \frac{\lambda_\Gamma^\alpha t^{\alpha-1}}{\Gamma(\alpha)} e^{\lambda_\Gamma t}$	λ_Γ α	$t = -\frac{\ln(\vartheta_1,\ldots,\vartheta_\alpha)}{\lambda_\Gamma\Gamma(\alpha)}$

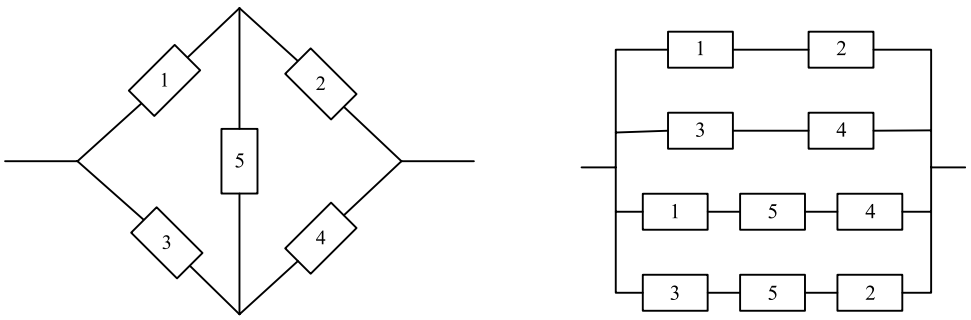

FIGURE 1 | Minimal path sets of typical system.

denoted by $t_{j1}, t_{j2}, \cdots, t_{jn}$. According to the reliability logical relationship between the CEMS and each component unit, the life simulation values for the CMES are obtained on the minimal path set method (Cancela et al., 2013; Schallert, 2014).

$$\boldsymbol{S} = \bigcup_{h=1}^{q} \boldsymbol{S}_h = \bigcup_{h=1}^{q} \left[\bigcap_{x_i, x_j, \cdots \in S_h} \left(x_i, x_j, \cdots \right) \right], \tag{1}$$

where S denotes the CEMS, q denotes the number of the minimum path sets in the CEMS, $h = 1, 2, \cdots, q$, and $S_h = (x_i, x_j, \cdots)$, $x_i, x_j \ldots$ is all the units in a minimum path set.

Therefore, the life simulation value t_S for a CEMS can be obtained through logical operation after each simulation.

$$t_S = \max_{1<h<q} \left(t_{S_h} \right) = \max_{1<h<q} \left[\min_{t_i, t_j \ldots \in S_h} \left(t_i, t_j, \ldots \right) \right], \tag{2}$$

where t_S is the life simulation value for the CEMS, $t_i, t_j \ldots$ is the life simulation value for each unit in the minimum path set, and t_{S_h} is the life simulation value for the hth minimum path set.

The minimal path sets of the typical system are shown in **Figure 1**, and the system has four minimum path sets: (x_1, x_5, x_4), (x_2, x_5, x_3). The life simulation values for the system are obtained by the following equation (Hong-Bo and Guo, 2009):

$$t_S = \max[\min(t_1, t_2), \min(t_3, t_4), \min(t_1, t_5, t_4), \min(t_3, t_5, t_2)]. \tag{3}$$

In general, the CEMS is usually considered to be composed of several simple serial or parallel subsystems, and the following equations are established:

$$t_{Sk} = \min_{t_i, t_j \ldots \in S_k} \left(t_i, t_j, \ldots \right), \tag{4}$$

$$t_{Sl} = \max_{t_i, t_j \ldots \in S_l} \left(t_i, t_j, \ldots \right), \tag{5}$$

where t_{Sk} is the life simulation value for the serial subsystem and t_{Sl} is the life simulation value for the parallel subsystem.

For any CEMS, the simulation value array $T(r \times n)$ for the units can be obtained by carrying out r simulations over n component units.

$$T(r \times n) = \begin{vmatrix} t_{11}, t_{21}, \cdots, t_{n1} \\ t_{12}, t_{22}, \cdots, t_{n2} \\ \vdots \\ t_{1r}, t_{2r}, \cdots, t_{nr} \end{vmatrix}. \tag{6}$$

Each simulation can yield a set of life simulation values for the units, and one life simulation value for the system can be obtained by **Eq. 2**. If r simulations are performed, r life simulation values

can be obtained, namely, $t_{S1}, t_{S2}, ..., t_{Sr}$, and t_{Sr} is equivalent to the full life test over r CEMSs. If r is large enough, the life distribution types for CEMSs can be counted and deduced from $t_{S1}, t_{S2}, ..., t_{Sr}$. Therefore, the probability estimation for the reliability measures of the CEMS is taken.

INITIAL SELECTION OF LIFE DISTRIBUTION TYPES FOR THE COMPLEX ELECTROMECHANICAL SYSTEMS AND GOODNESS-OF-FIT TEST

In order to determine the life distribution types for the system, this thesis makes use of the probability graph estimation method and goodness-of-fit test method. First, the probability graph for common distributions is designed and constructed on the computer, and $t_{S1}, t_{S2}, ..., t_{Sr}$ is drawn and fit on the probability graph. Then, the residual sum of squares under each distribution is calculated, and the distribution whose residual sum of squares is minimal is selected as the initial distribution. Finally, the Pearson χ^2 goodness-of-fit test is performed (Praks and Gono, 2011; Aguwa and Sadiku, 2012), and the life distribution type for the system is determined after the hypothesis test is accepted.

Data Processing and Initial Selection of Distribution Types

The basic principle for the probability idea design is to linearize the distribution function, and **Table 2** shows the linearized conversion equations for seven common distributions. The system life data are drawn in the new coordinate system, respectively. According to the discretization of the fitting line, the life distribution types for the system are initially decided.

TABLE 2 | Design of different probability plots.

Distribution functions	X–Y coordinate transformation
$F_e(t) = 1 - \exp[-\lambda(t - t_0)]$	$Y = \ln\frac{1}{1 - F_e(t)}$ $X = t - t_0$
$F_w(t) = 1 - \exp[-(\frac{t-t_0}{\eta})^m]$	$Y = \ln\ln\frac{1}{1 - F_w(t)}$ $X = \ln(t - t_0)$
$F_N(t) = \frac{\int_0^t e^{-\frac{(x-\mu)^2}{2\sigma^2}} dx}{\sigma\sqrt{2\pi}} = \Phi(u)$	$Y = u_\alpha \rightarrow \Phi(u_\alpha)$ $X = t$
$F_L(t) = \frac{\int_0^t e^{-\frac{(\ln x - \mu_L)^2}{2\sigma_L^2}} dx}{\sigma_L\sqrt{2\pi}} = \Phi(u_L)$	$Y = u_{L\alpha} \rightarrow \Phi(u_{L\alpha})$ $X = \ln t$
$F_m(t) = 1 - \exp[-e^{(\frac{t-\mu_m}{\sigma_m})}]$	$Y = \ln\ln\frac{1}{1 - F_m(t)}$ $X = t$
$F_M(t) = \exp[-e^{-(\frac{t-\mu_M}{\sigma_M})}]$	$Y = \ln\frac{1}{\ln[1/F_M(t)]}$ $X = t$
$F_\Gamma(t) = \frac{1}{\Gamma(\alpha)}\int_0^{\lambda_\Gamma t} x^{\alpha-1}e^{-x}dx$	$Y = F_\Gamma(t)$ $X = \lambda_\Gamma t$

To improve the accuracy of statistical inference, the value of r is relatively larger. To reduce the amount of calculation, the life simulation values for the system t_{Sj}, $(j = 1, 2, ..., r)$ are arranged in ascending order of time.

$$t_{s(1)} \le t_{s(2)} \le \ldots \le t_{s(j)} \le \ldots \le t_{s(r)}.$$

Then $[t_{s(1)}, t_{s(r)}]$ is evenly divided into p intervals, and p can be determined according to the number of simulations, r, generally $p = 20 \sim 100$. The time interval is calculated as follows:

$$\Delta t_{S,k} = t_{S,k+1} - t_{S,k} \quad k = 1, 2\cdots, p, \tag{7}$$

where $t_{S,k+1}, t_{S,k}$ is the boundary of the kth interval and $\Delta t_{S,k}$ is the kth interval space.

The median $\bar{t}_{S,k}$ of all intervals is denoted as follows:

$$\bar{t}_{S,k} = t_{S,k} + \frac{\Delta t_{S,k}}{2}. \tag{8}$$

The frequency number of the life simulation value for the system in the kth interval $[t_{S,k+1}, t_{S,k}]$ is denoted as r_k. $\bar{t}_{S,k}$, and the corresponding cumulative failure probability constitutes p scattered data pairs $[F(\bar{t}_{S,k}), \bar{t}_{S,k}]$.

$$\left[F(\bar{t}_{S,k}) = \frac{1}{r}\left(\sum_{i=1}^{k} r_i - \frac{r_k}{2}\right), \bar{t}_{S,k} = t_{S,k} + \frac{\Delta t_{S,k}}{2}\right]. \tag{9}$$

Each scattered data pair $[F(\bar{t}_{S,k}), \bar{t}_{S,k}]$ corresponds to 1 point on the probability graph, and the least square method is used to fit the straight line.

$$Y_j = a_j + b_j X_j \quad j = 1, 2, \cdots, q,$$

where a_j and b_j are the linear parameters of the fitting line, and q is the number of the selected probability graphs.a_j and b_j and the residual sum of squares Q_j are calculated on the probability graph, respectively.

$$\begin{cases} b_j = \dfrac{p\sum_{k=1}^{p} X_{jk}Y_{jk} - \sum_{k=1}^{p} X_{jk}\sum_{k=1}^{p} Y_{jk}}{p\sum_{k=1}^{p} X_{jk}^2 - \left(\sum_{k=1}^{p} X_{jk}\right)^2} \\ a_j = \dfrac{1}{p}\left[\sum_{k=1}^{p} Y_{jk} - b_j\sum_{k=1}^{p} X_{jk}\right] \end{cases}, \tag{10}$$

$$Q_j = \sum_{k=1}^{p}\left(Y_{jk} - a_j - b_j X_{jk}\right)^2, \tag{11}$$

where X_{jk} and Y_{jk} are the horizontal and vertical coordinate of the kth data point.

The values of Q_j on different distribution probability graphs are compared, and the distribution corresponding to the minimum value of Q_j is selected as the initial life distribution for the CEMS.

Pearson χ^2 Goodness-of-Fit Test

The goodness-of-fit test should be performed after the initial distribution is determined.

The initial distribution function as $F_x(t)$ is set, and the sample observation is the median value of p intervals, $\bar{t}_{S,1}, \bar{t}_{S,2}, ..., \bar{t}_{S,p}$. The Pearson χ^2 goodness-of-fit test is performed as follows:

1) The hypotheses are established.

The original hypothesis H_0: the sample is from $F_x(t)$, and the alternative hypothesis: the sample is not from $F_x(t)$.

2) The point estimate value $\widehat{\theta_x}$ (or $\hat{\theta}_{x1}, \hat{\theta}_{x2}, \ldots, \hat{\theta}_{xl}$) of $F_x(t)$ is estimated using the probability graph method.

The probability for p intervals is calculated as follows:

$$P_k = F_x\left(\bar{t}_{S,k+1}, \hat{\theta}_x\right) - F_x\left(\bar{t}_{S,k}, \hat{\theta}_x\right) \quad k = 1, 2\cdots, p. \tag{12}$$

3) The Pearson χ^2 test statistics is calculated by

$$\chi^2 = \sum_{k=1}^{p} \frac{(r_k - rp_k)^2}{rp_k}. \tag{13}$$

4) When the confidence probability γ is given, the following formula holds:

$$P\left[\chi^2 \le \chi_\gamma^2(v)\right] = \gamma, \tag{14}$$

where v is the degree of freedom, $v = p - 1 - l$, and l is the number of parameters of initial distribution.

If $\chi^2 \le \chi_\gamma^2(v)$, the original hypothesis is accepted at a high probability, and then, the sample can be identified from $F_x(t)$. Otherwise, the original hypothesis shall be rejected.

To facilitate the computer analysis, the Fisher approximation of $\chi_\gamma^2(v)$ is given

$$\chi_\gamma^2(v) \approx \frac{1}{2}\left[\sqrt{2v-1} + u_\gamma\right]^2, \tag{15}$$

where u_γ is the γ quantile of the standard normal distribution, which can be approximated as follows:

$$u_\gamma \approx \frac{a_0 + a_1 z}{1 + b_1 + b_2 z^2}, \tag{16}$$

where $a_0 = 2.3075$; $a_1 = 0.2706$; $b_1 = 0.9922$; $b_2 = 0.0448$; and $z = \sqrt{\ln(1-\gamma)^{-2}}$.

ENGINEERING APPLICATION–SYSTEM RELIABILITY PREDICTION ON WIND TURBINE

An MW wind turbine unit is mainly composed of impeller, gearbox, generator, yaw system, pitch system, brake system, lubrication system, electrical system, and frequency converter in serial connection, and its reliability block diagram (RBD) is shown in **Figure 2**.

The given life distributions and parameters for all components in the wind power generator unit are listed in **Table 3** (Tavner et al., 2007; Spinato et al., 2009; Guo et al., 2012).

According to the relevant parameters of each unit listed in **Table 3**, the life simulation value for each unit is generated using the simulation conversion equation in **Table 1**. We set $r = 500$, and the 500 life simulation values for units are obtained as listed in **Table 4** (excerpt). 500 life simulation values for the system are obtained through logical operation.

1) Initial selection of the life distribution types for the wind turbine.

The characteristic data in **Table 5** are processed using probability graph estimation to get the residual sum of squares under different distributions, Q_j, as listed in **Table 6**.

It is shown in **Table 6** that the residual sum of squares for the two-parameter Weibull distribution was the least, and it can be used as the initial distribution.

2) Goodness-of-fit test for the initial distribution.

According to the probability graph estimation, $m = 1.1925$, $\eta = 13207h$, the Pearson χ^2 test statistics is obtained from **Eqs 12** and **13**:

$$\chi^2 = 58.7058.$$

Given the confidence probability $\gamma = 0.9$, $\chi_{0.9}^2(47)$ is obtained from **Eq. 15**.

$$\chi_{0.9}^2(47) = 60.0312.$$

We can obtain χ^2 less than $\chi_{0.9}^2(47)$.

$$\chi^2 < \chi_{0.9}^2(47).$$

The hypothesis test is passed at a high probability, and then the life data of this wind turbine follows the two-parameter Weibull distribution, the distribution parameters, the point estimation and the interval estimation of reliability measures can be further solved.

We set $\bar{t}_{S,1}, \bar{t}_{S,2}, ..., \bar{t}_{S,p}$ as a complete sample, the likelihood function for the two-factor Weibull distribution can be expressed as

$$L(m, \eta) = \prod_{k=1}^{p} \frac{m}{\eta}\left(\frac{\bar{t}_{S,k}}{\eta}\right)^{m-1} \exp\left[-\left(\frac{\bar{t}_{S,k}}{\eta}\right)^m\right]. \tag{17}$$

The logarithm is taken from

$$\ln L(m, \eta) = p \ln \frac{m}{\eta} + (m-1)\sum_{k=1}^{p} \ln \frac{\bar{t}_{S,k}}{\eta} - \sum_{k=1}^{p}\left(\frac{\bar{t}_{S,k}}{\eta}\right)^m. \tag{18}$$

The constraint conditions are set as

$$\frac{\partial \ln L}{\partial m} = 0, \quad \frac{\partial \ln L}{\partial \eta} = 0.$$

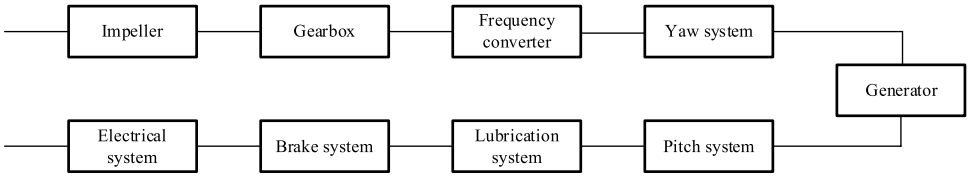

FIGURE 2 | Reliability block diagram of the wind turbine.

TABLE 3 | Distribution parameters of the units.

Component	Distribution	Mean value μ	Standard deviation σ	Scale parameter η	Shape parameter m
Blade	Normal distribution	42000	663	—	—
Gearbox	Logarithmic normal distribution	11	1.2	—	—
Generator	Weibull distribution	—	—	76000	1.2
Yaw system	Extreme maximum value distribution	65000①	370②	—	—
Pitch control system	Normal distribution	84534	506	—	—
Brake system	Exponential distribution	120000	—	—	—
Lubrication system	Weibull distribution	—	—	66000	1.3
Electrical system	Weibull distribution	—	—	35000	1.5
Frequency converter	Exponential distribution	45000	—	—	—

① denotes the location parameter of the maximum value distribution, and ② denotes the scale parameter of the maximum value distribution.

TABLE 4 | Units' life simulation data (*h*).

Times	Impeller	Gearbox	Generator	Pitch control system	Yaw system	Brake system	Lubrication system	Electrical system	Frequency converter
1	43311	40009	74395	65193	84351	20324	50765	48938	55911
2	42201	16828	185946	65318	84236	4826	39547	19360	23634
3	41248	48744	86633	64261	84653	123818	63409	6771	14843
4	41940	58750	1673	65331	84583	45553	116354	24337	59810
5	42013	14828	35490	65000	85129	99210	106863	57828	5754
6	42133	125633	75981	64158	85021	101249	9013	36303	13516
7	43656	175291	41034	64586	84203	37468	14264	6903	9821
8	42372	28295	175973	64914	84273	21075	91015	11582	162175
9	41716	363928	38274	65426	85453	125173	44053	59533	47344
10	42558	47368	6393	65447	83788	20456	81417	57654	94197
11	42667	70521	22551	64348	85127	57006	41832	68821	9781
12	41678	24014	37799	65466	84852	8933	65919	49767	286468
13	41753	19934	28705	65425	84414	297109	49832	27628	33671
14	43029	21064	40274	64849	84405	51099	65566	24296	10853
15	42602	57290	33770	65176	85297	172179	89127	21851	18474
16	41605	56145	139157	64305	84050	38637	98599	31637	16932
17	42969	17676	56570	64777	84433	57656	51311	3445	66923
18	41590	372267	207061	65335	84546	34188	11249	16269	104821
19	41921	30931	21816	65167	85164	65177	3692	50081	26140
20	42121	137379	28842	65431	86255	85724	30947	19872	7451
21	43323	34659	104992	65024	85339	50258	104110	5776	29574
22	41598	1375050	40966	63774	84082	4140	16036	2046	29741
23	42661	36847	14916	65236	83399	20625	37707	9471	8159
24	41058	179747	8944	65370	84464	61753	104395	19642	70728
25	41747	18501	76860	65047	84158	120728	7691	37303	1066
⋮	⋮	⋮	⋮	⋮	⋮	⋮	⋮	⋮	⋮
⋮	⋮	⋮	⋮	⋮	⋮	⋮	⋮	⋮	⋮
500	42109	283068	46822	64981	84803	93965	1632	39312	7857

Setting p = *50, we can get 50 characteristic data as listed in* ***Table 5****.*

TABLE 5 | The system simulation life data.

Sequence number	Data		Sequence number	Data		Sequence number	Data	
	r_k	$\bar{t}_{S,k}$		r_k	$\bar{t}_{S,k}$		r_k	$\bar{t}_{S,k}$
1	11	250	18	10	8750	35	9	20000
2	13	750	19	10	9250	36	8	21000
3	16	1250	20	16	9750	37	10	22000
4	5	1750	21	9	10250	38	5	23000
5	14	2250	22	8	10750	39	12	24000
6	15	2750	23	13	11250	40	5	25000
7	13	3250	24	18	11750	41	6	26250
8	14	3750	25	14	12250	42	7	27750
9	13	4250	26	4	12750	43	6	29250
10	9	4750	27	7	13250	44	4	30750
11	15	5250	28	8	13750	45	2	32000
12	18	5750	29	7	14250	46	3	34000
13	12	6250	30	6	15000	47	5	36000
14	18	6750	31	13	16000	48	4	38000
15	10	7250	32	15	17000	49	5	40000
16	15	7750	33	16	18000	50	9	42000
17	7	8250	34	8	19000			

TABLE 6 | The life distribution deduction result.

Distribution	Normal distribution	Exponential distribution	Weibull distribution	Logarithmic normal distribution	Extreme minimum value distribution	Extreme maximum value distribution
Q_j	14.3679	0.9514	0.1737	19.2132	9.6881	1.3746

The likelihood equations are established and arranged as

$$\begin{cases} \dfrac{\sum_{k=1}^{p}(\bar{t}_{S,k})^m \ln \bar{t}_{S,k}}{\sum_{k=1}^{p}(\bar{t}_{S,k})^m} - \dfrac{1}{m} = \dfrac{1}{p}\sum_{k=1}^{p}\ln \bar{t}_{S,k} \\ \eta^m = \dfrac{1}{p}\sum_{k=1}^{p}(\bar{t}_{S,k})^m \end{cases}, \tag{19}$$

$\bar{t}_{S,1}, \bar{t}_{S,2}, \cdots, \bar{t}_{S,50}$ are substituted into **Eq. 19** to solve the maximum likelihood estimation for the parameter m, η.

$$\begin{cases} \hat{m} = 1.2427 \\ \hat{\eta} = 13114 \end{cases}.$$

Therefore,

$$\bar{T}_S = \hat{\eta}\Gamma\left(1 + \frac{1}{\hat{m}}\right), \tag{20}$$

where $\bar{T}_S$ is the maximum likelihood estimation for the average life of the wind turbine.

As $\hat{m} > 1$, gamma function can be approximated as

$$\Gamma\left(1 + \frac{1}{\hat{m}}\right) \approx 1 - 0.5748646\frac{1}{\hat{m}} + 0.9512363\left(\frac{1}{\hat{m}}\right)^2 - 0.6998588\left(\frac{1}{\hat{m}}\right)^3 - 0.6998588\left(\frac{1}{\hat{m}}\right)^3 + 0.4245549\left(\frac{1}{\hat{m}}\right)^4 - 0.1010678\left(\frac{1}{\hat{m}}\right)^5. \tag{21}$$

If $\hat{m} \le 1$, the calculation can be simplified using the recursive equation and $\bar{T}_S$ can be calculated as follows:

$$\bar{T}_S = 12287.02h.$$

With the given t value, the maximum likelihood estimation for the reliability function $R(t)$ is

$$\hat{R}_S(t) = \exp\left[-\left(\frac{t}{\hat{\eta}}\right)^{\hat{m}}\right]. \tag{22}$$

Therefore, the maximum likelihood estimation for the failure rate function $\lambda(t)$ is

$$\hat{\lambda}_S(t) = \frac{\hat{m}}{\hat{\eta}}\left(\frac{t}{\hat{\eta}}\right)^{\hat{m}-1}. \tag{23}$$

If the confidence probability is set as $1 - \alpha$, the confidence interval for the distribution parameter m, η is

$$\begin{cases} m_L = \hat{m}\exp\left(-u_{1-\frac{\alpha}{2}}\dfrac{1.0490}{\sqrt{p-1}}\right) \\ m_U = \hat{m}\exp\left(u_{1-\frac{\alpha}{2}}\dfrac{1.0490}{\sqrt{p-1}}\right) \end{cases}, \tag{24}$$

$$\begin{cases} \eta_L = \hat{\eta}\exp\left(-u_{1-\frac{\alpha}{2}}\dfrac{1.0810}{\hat{m}\sqrt{p-1}}\right) \\ \eta_U = \hat{\eta}\exp\left(u_{1-\frac{\alpha}{2}}\dfrac{1.0810}{\hat{m}\sqrt{p-1}}\right) \end{cases}, \tag{25}$$

TABLE 7 | The confidence interval for the distribution parameter and lower confidence limit for the average life of the wind turbine under different confidence probabilities.

$1-\alpha$	m_L	m_U	η_L	η_U	$(\bar{T}_S)_L$
0.9	0.9712	1.4374	10689.6575	16088.1672	10015.5596
0.8	1.0256	1.4491	11183.3236	15377.9862	10478.0948
0.7	1.0639	1.4575	11529.2156	14916.6259	10802.1745

Given the t *value, the lower confidence limit* $(1-\alpha)$ *for the reliability of the wind turbine is approximated.*

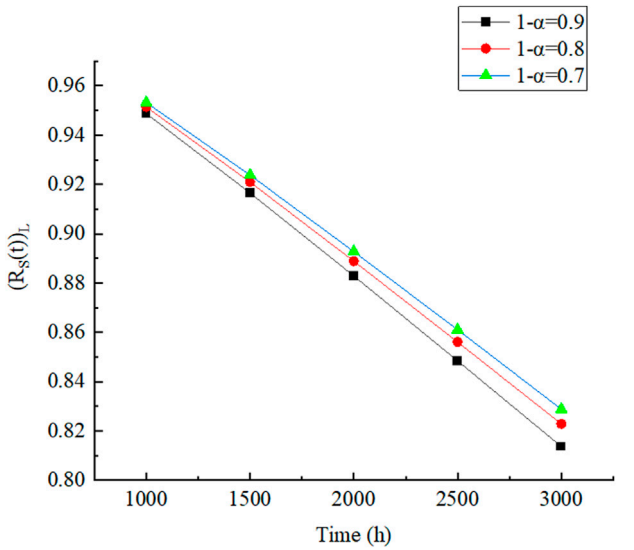

FIGURE 3 | Reliability lower confidence limit $(1-\alpha)$ of the wind turbine under different confidence probabilities and life.

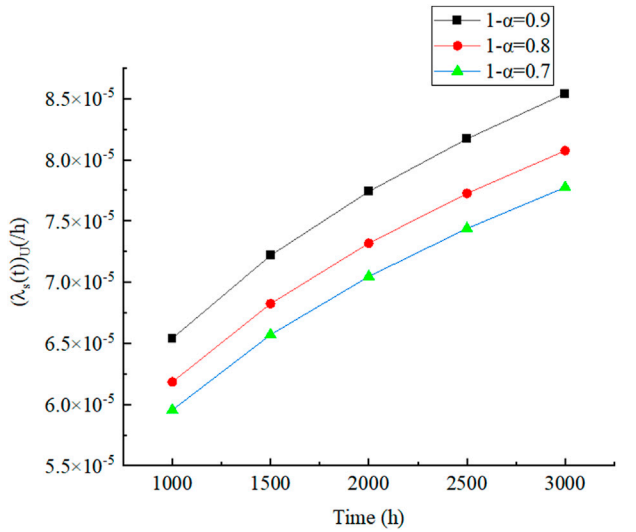

FIGURE 4 | Failure rate upper confidence limit $(1-\alpha)$ of the wind turbine under different confidence probabilities and life.

where $u_{1-\frac{\alpha}{2}}$ is the quantile of standard normal distribution, and it can be calculated by **Eq. 16**.

To simplify the calculation, the shape parameter m can be taken as its maximum likelihood estimation, and it is taken as $\hat{m} = 1.2427$.

When the given confidence probabilities $1-\alpha$ are 0.9, 0.8, and 0.7, respectively, the confidence interval for the distribution parameter m, η, and lower confidence limit for the average life of the wind turbine are shown in **Table 7**.

$$(R_S(t))_L = \exp\left[-\left(\frac{t}{\eta_L}\right)^{\hat{m}}\right]. \tag{26}$$

The upper confidence limit $(1-\alpha)$ for its failure rate is approximated as

$$(\lambda_S(t))_U = \frac{\hat{m}}{\eta_L}\left(\frac{t}{\eta_L}\right)^{\hat{m}-1} \Big/ \mathrm{h}, \tag{27}$$

when t is 1000, 1500, 2000, 2500, and 3000h, and the confidence probabilities $1-\alpha$ are 0.9, 0.8, and 0.7, respectively, the reliability lower confidence limit $(1-\alpha)$ and failure rate upper confidence limit $(1-\alpha)$ of wind turbine are shown in **Figure 3** and **Figure 4**, respectively.

It can be seen from **Figure 3** and **Figure 4** that all lower limits of reliability $(R_S(t))_L$ show a downward trend, while all failure rates show an upward trend under different confidence probabilities.

CONCLUSION

For the CEMS with many limiting factors, this article presented a method of replacing life test with computer analog simulation for CEMS. The life simulation values of system constituent units of CEMS could be obtained by their life distribution types and relevant distribution parameters. The life simulation values of CEMS were obtained according to the reliability logic relationship and reliability logic block diagram of the CEMS, and the simulation was instead of the life test of CEMS when the simulation times were enough. The method proposed in this thesis was of great significance to save test time and test cost, especially for the CEMSs that could not carry out reliability life test.

The method proposed in this thesis could solve the problems of system reliability synthesis and prediction of CEMS with different distributions of units. When the "pyramid model" was used for system reliability level by level synthesis and prediction. Compared with the traditional life test method of CMES, it could save a lot of test cost, test time, test site, and so on. This approach could be applied to the early program design, prototype development, trial production, and other stages of production. In engineering applications, the CMES reliability logic block diagram could be drawn by computer, and all the smallest path sets could be obtained by the node traversal

optimization algorithm. Therefore, it has obvious application value in engineering.

Finally, the proposed method was applied to the wind turbine, and the reliability lower confidence limit $(1 - \alpha)$ and failure rate upper confidence limit $(1 - \alpha)$ of wind turbine were calculated with given the life time t. The method is also applicable to other CEMSs and can be utilized to provide guidance for system design, maintenance planning, and so on. This paper provides an effective and flexible method for reliability synthesis and prediction of CEMS, which can be easily implemented in engineering practices.

DATA AVAILABILITY STATEMENT

The raw data supporting the conclusions of this article will be made available by the authors, without undue reservation.

AUTHOR CONTRIBUTIONS

CY: writing, reviewing, and editing, YG: reviewing and drawing, and XY: funding acquisition.

FUNDING

This work was supported by the project of the Natural Science Foundation of Shandong Province, China (No. ZR2019PEE018) and Shandong Province Science and Technology SMES Innovation Ability Enhancement Project (No. 2021TSGC1063).

ACKNOWLEDGMENTS

The authors thank all the editors and referees for their helpful suggestions.

REFERENCES

Aguwa, J. I., and Sadiku, S. (2012). Reliability Studies on Timber Data from Nigerian Grown Iroko Tree (Chlorophora Excelsa) as Bridge Beam Material. *Jera* 8 (12), 17–35. doi:10.4028/www.scientific.net/jera.8.17

Buehler, R. J. (1957). Confidence Intervals for the Product of Two Binomial Parameters. *J. Am. Stat. Assoc.* 52 (280), 482–493. doi:10.1080/01621459.1957.10501404

Cancela, B., Ortega, M., Penedo, M. G., Novo, J., and Barreira, N. (2013). On the Use of a Minimal Path Approach for Target Trajectory Analysis. *Pattern Recognition* 46 (7), 2015–2027. doi:10.1016/j.patcog.2013.01.013

Fo, X. C., and Xiong, H. L. (2009). MML Method and its Application in the Reliability Analysis of Navigating System. *Electron. Product. Reliability Environ. Test.* 27 (1), 16–19. doi:10.3969/j.issn.1672-5468.2009.01.005

Fuqiu, L., Wang, Z., Xiaopeng, L., and Zhang, W. (2020). A Reliability Synthesis Method for Complicated Phased Mission Systems[J]. *IEEE Access* 8, 193681–193685. doi:10.1109/ACCESS.2020.3028303

Graves, T. L., and Hamada, M. S. (2016). A Note on Incorporating Simultaneous Multi-Level Failure Time Data in System Reliability Assessments. *Qual. Reliab. Engng. Int.* 32, 1127–1135. doi:10.1002/qre.1820

Guo, J., Sun, Y., and Wang, M. (2012). System Reliability Synthesis of Wind Turbine Based on Computer Simulation[J]. *J. Mech. Eng.* 48 (2), 1–7. doi:10.3901/JME.2021.02.002

Guo, J., Sun, Y., Yu, C., Yuan, H., and Su, Z. (2014). Some Theory and Method for Complex Electromechanical System Reliability Prediction[J]. *J. Mech. Eng.* 50 (4), 1–13. doi:10.3901/jme.2014.14.001

Guo, J., and Wilson, A. G. (2013). Bayesian Methods for Estimating System Reliability Using Heterogeneous Multilevel Information. *Technometrics* 55 (4), 461–472. doi:10.1080/00401706.2013.804441

Han, S.-Y., Zhou, J., Chen, Y.-H., Zhang, Y.-F., Tang, G.-Y., and Wang, L. (2021). Active Fault-Tolerant Control for Discrete Vehicle Active Suspension via Reduced-Order Observer. *IEEE Trans. Syst. Man. Cybern, Syst.* 51 (11), 6701–6711. doi:10.1109/tsmc.2020.2964607

Hong-Bo, Z., and Guo, J. (2009). Method of System Reliability Synthesis Based on Minimal Path Sets[J]. *Transducer Microsystem Tech.* 28 (8), 20–23. doi:10.13873/j.100-97872009.08.14

Kovacs, Z., Orosz, A., and Friedler, F. (2019). Synthesis Algorithms for the Reliability Analysis of Processing Systems. *Cent. Eur. J. Oper. Res.* 27, 573–595. doi:10.1007/s10100-018-0577-0

Liu, Y., Zuo, M. J., Li, Y.-F., and Huang, H.-Z. (2015). Dynamic Reliability Assessment for Multi-State Systems Utilizing System-Level Inspection Data. *IEEE Trans. Rel.* 64 (4), 1287–1299. doi:10.1109/tr.2015.2418294

Meng, J., and Wen-Tao, Z. (2021). Research on the Reliability of Differential Protection Based on Monte Carlo[J]. *Computer Simulation* 38 (11), 112–116. doi:10.3969/j.issn.1006-9348.2021.11.023

Mi, J., Li, Y. F., Yang, Y. J., Peng, W., and Huang, H. Z. (2016). Reliability Assessment of Complex Electromechanical Systems under Epistemic Uncertainty. *Reliability Eng. Syst. Saf.* 152 (8), 1–15. doi:10.1016/j.ress.2016.02.003

Negi, S., and Singh, S. B. (2015). Reliability Analysis of Non-repairable Complex System with Weighted Subsystems Connected in Series. *Appl. Math. Comput.* 262 (262), 79–89. doi:10.1016/j.amc.2015.03.119

Peng, W., Huang, H., Xie, M., Yang, Y., and Liu, Y. (2013). A Bayesian Approach for System Reliability Analysis with Multilevel Pass-Fail, Lifetime and Degradation Data Sets. *IEEE Trans. Rel.* 62 (3), 689–699. doi:10.1109/tr.2013.2270424

Praks, P., and Gono, R. (2011). "Uncertainty Analysis of Failure Rate of Selected Transformers in a Power Distribution Network[C]," in Proceedings of the 12th International Scientific Conference Electric Power Engineering 2011, EPE 2011, 645–648.

Schallert, C. (2014). A Safety Analysis via Minimal Path Sets Detection for Object-Oriented Models. *ESREL*, 2019–2027. doi:10.1201/b17399-277

Spinato, F., Tavner, P. J., Bussel Van, G. J. W., and Koutoulakos, E. (2009). Reliability of Wind Turbines Subassemblies [J]. *IET Renew. Power Generator* 3 (4), 1–15. doi:10.1049/iet-rpg.2008.0060

Sun, Y., Sun, T., Pecht, M. G., and Yu, C. (2018). Computing Lifetime Distributions and Reliability for Systems with Outsourced Components: A Case Study. *IEEE Access* 6, 31359–31366. doi:10.1109/access.2018.2843375

Tang, S., Zhu, Y., and Yuan, S. (2021). An Improved Convolutional Neural Network with an Adaptable Learning Rate towards Multi-Signal Fault Diagnosis of Hydraulic Piston Pump. *Adv. Eng. Inform.* 50, 101406. doi:10.1016/j.aei.2021.101406

Tavner, P. J., Xiang, J., and Spinato, F. (2007). Reliability Analysis for Wind Turbines. *Wind Energy* 10, 1–18. doi:10.1002/we.204

Wang, H., Gong, Z., Huang, H. Z., Xiaoling, Z., and Zhiqiang, Lv. (2012). "System Reliability Based Design Optimization with Monte Carlo Simulation[C]," in 2012 International Conference on Quality, Reliability, Risk, Maintenance, and Safety Engineering, Chengdu, China, 15-18 June 2012, 1143–1147.

Wang, Y., Zhou, J., Wang, R., Chen, L., Zhang, T., Han, S., et al. (2022). Transfer Collaborative Fuzzy Clustering in Distributed Peer-To-Peer Networks[J]. *IEEE Trans. Fuzzy Syst.* 30 (2), 500–514. doi:10.1109/TFUZZ.2020.3041191

Weiyan, M., Xingzhong, X., and Shifeng, X. (2009). Inference on System Reliability for Independent Series Components[J]. *Commun. Statistics-Theory Methods* 38 (3), 409–418. doi:10.1080/03610920802220793

Wilson, A. G., Graves, T. L., Hamada, M. S., and Reese, C. S. (2006). Advances in Data Combination, Analysis and Collection for System Reliability Assessment [J]. *Stat. Sci.* 21 (4), 514–531. doi:10.1214/088342306000000439

Yeh, W., Lin, Y., Chung, Y., and Mingchang, C. (2010). A Particle Swarm Optimization Approach Based on Monte Carlo Simulation for Solving the Complex Network Reliability Problem. *IEEE Trans. Rel.* 59 (1), 212–221. doi:10.1109/tr.2009.2035796

Yoshida, I., and Akiyama, M. (2011). "Reliability Estimation of Deteriorated RC-Structures Considering Various Observation Data[C]," in 11th International Conference on Applications of Statistics and Probability in Civil Engineering, 1231–1239. doi:10.1201/b11332-187

Yu, C., Guo, J., Sun, Y., Su, Z., and Yuan, H. (2013). Bayes Confidence Limit of Reliability for Series-Parallel System Consisting of Different Distribution Units[J]. *Chin. J. Scientific Instrument* 34 (2), 428–433. doi:10.19650/j.cnki.cjsi.2013.02.028

Yuan, R., Tang, M., Wang, H., and Li, H. (2019). A Reliability Analysis Method of Accelerated Performance Degradation Based on Bayesian Strategy. *IEEE Access* 7, 169047–169054. doi:10.1109/ACCESS.2019.2952337

Zhang, M., Hu, Q., Xie, M., and Yu, D. (2014). Lower Confidence Limit for Reliability Based on Grouped Data Using a Quantile-Filling Algorithm. *Comput. Stat. Data Anal.* 75 (75), 96–111. doi:10.1016/j.csda.2014.01.010

Zhou, Y. Q., and Weng, Z. X. (1990). *Reliability evaluation[M]*. Beijing: Science Press.

Zhu, X. B., and J Sh, L. (1990). Combined MML & SR Method (CMSR) for System Reliability Assessment. *J. Astronautics* (2), 29–34.

Conflict of Interest: The authors declare that the research was conducted in the absence of any commercial or financial relationships that could be construed as a potential conflict of interest.

frontiers in Energy Research

ORIGINAL RESEARCH
published: 31 March 2022
doi: 10.3389/fenrg.2022.866044

Numerical and Experimental Study on the Opening Angle of the Double-Stage Flap Valves in Pumping Stations

Wang Xi[1], *Weigang Lu*[1]*, *Chuan Wang*[2,3] *and Guocong Fu*[1]

[1]College of Hydraulic Science and Engineering, Yangzhou University, Yangzhou, China, [2]International Shipping Research Institute, GongQing Institute of Science and Technology, Jiujiang, China, [3]High-tech Key Laboratory of Agricultural Equipment and Intelligentization of Jiangsu Province, Jiangsu University, Zhenjiang, China

Double-stage flap valves are widely used in new pumping stations. The different opening angles of the double-stage flap valves have a great influence on the outflow. To gain insight into this phenomenon, four commonly used operating conditions with opening angles were selected to perform three-dimensional simulation calculations and physical model studies on the flow pattern of the water behind the valves at different flow rates. The flow pattern of the water flow is analyzed by three indicators: the streamline of the water flow, the uniformity of the flow velocity, and the head loss in the culvert. The result shows that the coefficient of resistance loss along the way of the outlet culvert has a negative correlation with the opening angle. The larger the opening angle of the flap valve, the less the head loss of the water flow in the outlet culvert, and the flow pattern of the water flow in the culvert gradually becomes better.

Keywords: double-stage flap valves, flow analysis, numerical simulation, physical model experiment, flow velocity uniformity

OPEN ACCESS

Edited by:
Xiaojun Li,
Zhejiang Sci-Tech University, China

Reviewed by:
Renqing Zhu,
Jiangsu University of Science and Technology, China
Lingling Wang,
Hohai University, China

***Correspondence:**
Weigang Lu
wglu@yzu.edu.cn

Specialty section:
This article was submitted to Process and Energy Systems Engineering, a section of the journal Frontiers in Energy Research

Received: *30 January 2022*
Accepted: *04 March 2022*
Published: *31 March 2022*

Citation:
Xi W, Lu W, Wang C and Fu G (2022) Numerical and Experimental Study on the Opening Angle of the Double-Stage Flap Valves in Pumping Stations. Front. Energy Res. 10:866044. doi: 10.3389/fenrg.2022.866044

1 INTRODUCTION

Pump stations play an important role in water resource deployment, urban flood control, stable and high agricultural production, drought and flood protection, etc. The flap valve is an important part of the pumping station operation process, and its role is to use its gravity and the pressure of the water flow to fall on its own after the pumping station has finished running to block the water flow. The more common flap valve types are integral flap valves, double-stage flap valves, multi-stage flap valves, suspension flap valves, side single-opening flap valves, side double-opening flap valves, etc. The flap valve design is related to the stable operation of the pump station.

Compared with other cut-off methods, flap valves have certain apparent advantages: the first is its simple structure design. In addition to the valve seat and the valve body, the structure of the flap valve only needs a one-to-one chain to connect the two. As a result, the impact of the water flow will open the flap valves, and it will work typically. When the current is cut off and locked, the flap valve will close automatically by its weight and water pressure. The second is its low production price and easy-to-obtain raw materials; the third is its high reliability in the operation process and low failure rate. The length of the valve body of the flap valve is many times the length of the valve shaft. Therefore, the valve body can be opened when impacted, with the impact force of the valve shaft, and with other influences, so there are very few valves that are affected. Finally, it is easy to maintain and install without complicated procedures. The water flow and itself do the closing and

opening of the flap valve, no precise positioning is required, and it is easier to use automatic control equipment.

With the development of the society and the need to deploy water resources, more and more pumping stations have been built. As the main intercepting device, flap valves have a significant impact on the safe operation of the pumping station, so it is essential to study the flow pattern of the water behind the flap valve and choose the suitable buffer device. With the advent of fluid simulation software, in the research of numerical simulation theory (Sudo et al., 1998; Ahmed, 2000; Luo et al., 2018; Zhang et al., 2021; Wang et al., 2021; Zhou et al., 2021; Hu et al., 2022; Zhang et al., 2022), analysis of the turbulence model, and formulation of the turbulent kinetic energy equation (Zeng and Li, 2010; Shin, 2018), more and more high-precision numerical simulation technologies have been used to simulate the complex flow in the pump station. The standard K-ε model, the realizable K-ε model, the renormalized group (RNG) K-ε model, and the shear stress transfer (SST) K-ε fluid volume (VOF) multiphase model (Qian et al., 2016) are used to simulate the three-dimensional (3D) unsteady turbulence in the pump basin. The LES (large eddy simulation) technology (Yamade et al., 2020) is used to analyze the causes and influencing factors of the inspiratory vortex in the intake tank of the pumping station.

Based on this, researchers only conducted optimization research on the simulation of the operation of the flap valve through numerical simulation or physical experiments and few studies on the flow state behind the flap valve. In this study, the numerical simulation method and physical model experiments were used to analyze the flow pattern from three aspects: velocity uniformity, streamline, and head loss of the outlet culvert after tapping the flap valve. It provides academic help for optimizing the flow state of the culvert in the pumping stations.

At present, some scholars have carried out relevant research, mainly in the following aspects: in the study of pump station optimization (Alawadhi et al., 2021; Shen et al., 2021; Shi et al., 2020), based on the multidisciplinary optimization design method of the approximate model, established the objective function based on the blade quality and efficiency of design conditions and optimized the impeller of the axial-flow pump, but only the impeller of the axial flow pump is analyzed, and the outflow conditions of the axial flow pump are not studied. Wang et al. (2020) studied and tested the geometric parameters of the blade groove structure of various impellers and analyzed the influencing factors by numerical simulation and physical model studies. In the study of pump station faults, Zhu et al. (2022) analyzed multi-signal defects of hydraulic piston pumps by using a profoundly improved convolutional neural network. Zhu et al. (2021) used ENET-5 and particle swarm optimization hyperparameter optimization to study the faults of hydraulic piston pumps and analyzed the advantages of this method. Moreover, in the research of the pump station flap valve, Yang (2011) used computational fluid dynamics (CFD) software to carry out the numerical calculation of the outflow flow state when the opening angle of the valve was 25° in the design condition of the pump device and when there was no tap valve and analyzed the outflow flow state with and without the valve. Gao et al. (2021) investigated the velocity distribution and streamlining of the distribution of pipelines at different sections, the distribution uniformity of outlet sections, and the hydraulic loss of pipelines at different flows through the standard K-ε model. Yu and Zhu (2014) used the standard k-ε turbulence model and the SIMPLEC algorithm to conduct CFD numerical tests on the flow field in the rear pressure water tank of the pumping station. Hong and Li (2015) analyzed the flow state of the upside-down and side-down flap valves using the velocity vector diagram through numerical simulation analysis of hydraulic characteristics. Yan et al. (2020) used CFD technology to conduct numerical simulation calculations on the straight pipe outlet passage of the horizontal pump station and analyzed the flow characteristics inside the outlet passage and the influence of hydraulic loss by changing the outlet passage profile.

The above research results are mainly about the flow in the culvert and wall turbulence. There are also some research papers about machine learning optimization flow (Zhu et al., 2021; Tang et al., 2022). However, there are few research studies on the near-wall vortex in pump station engineering, especially on the formation mechanism of the asymmetric wall-attached vortex in pump station engineering. In this study, the standard K-ε model is selected to conduct numerical simulation research on the flap valves of a pumping station in a practical project. The semi-implicit SIMPLE (Semi-Implicit Method for Pressure-Linked Equations) algorithm is used to solve the velocity and pressure coupling equations. The VOF (Volume of Fluid) method is used to simulate the free surface. The uniformity of the flow velocity of the culvert behind the double-stage flap valves is studied, and its proper opening angle is analyzed. By using the physical model experiment, the reasonable opening angle of the double-stage flap valves is analyzed by studying the head loss before and after the valves. Finally, combined with the results of numerical calculations and physical models, a comprehensive analysis of the proper opening angle of the double-stage flap valves is made. It provides theoretical help for solving this problem in pumping station engineering.

The rest of the article is organized as follows: the first section describes the parameter settings of pumping station outlet modeling, numerical simulation, and physical model experiments. The second section summarizes the flow pattern behind the side flap valve of the pump station with the change of opening angle through numerical simulation results. Next, the flow pattern is translated behind the side flap valve of the pump station with the evolution of opening angle through numerical simulation results. By using the physical model experiment, the reasonable opening angle of the double-stage flap valves is analyzed by studying the head loss before and after the valves. The flow pattern is analyzed from three aspects: velocity uniformity, streamline, and head loss of the outlet culvert pipe behind the flap valve. The last section summarizes the thesis and gives relevant conclusions.

2 METHODS

2.1 Model Design

The total height of the pumping station is 3.30 m, and the total width is 3.24 m. The upper and lower flap valves have a 0.4 m

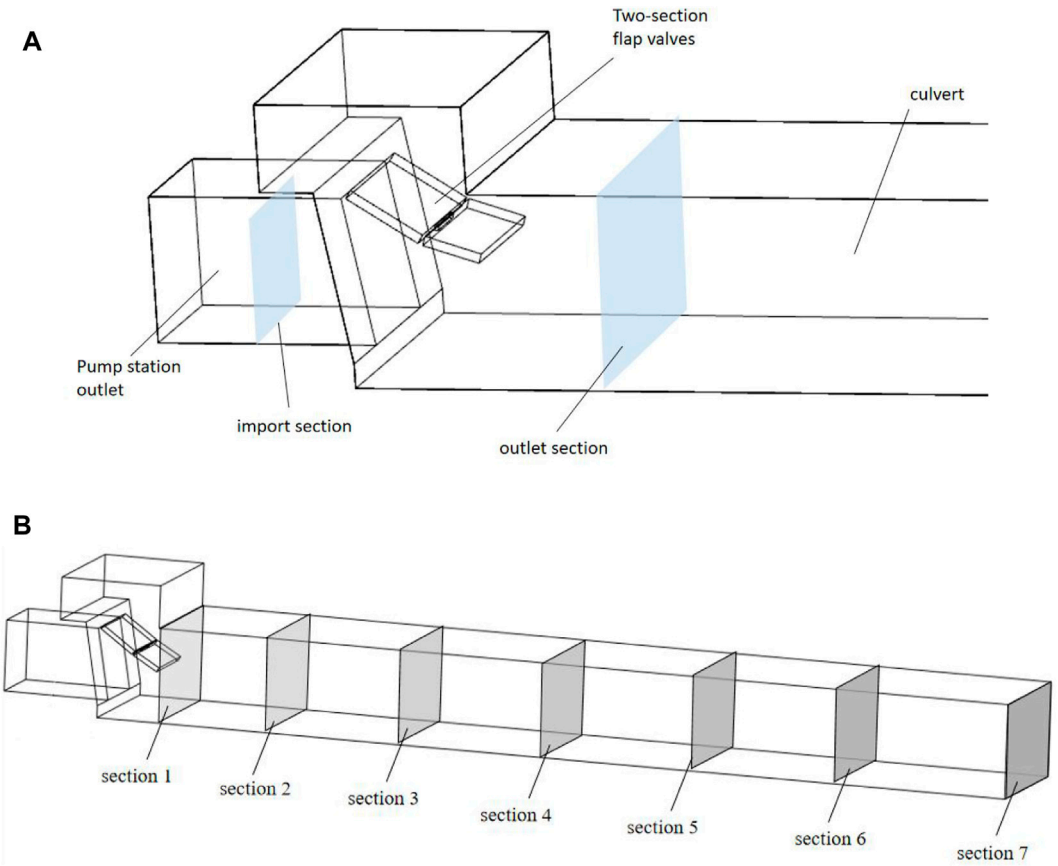

FIGURE 1 | Diagram of the model and cross-section: **(A)** diagram of the flap valves section and **(B)** diagram of the culvert section.

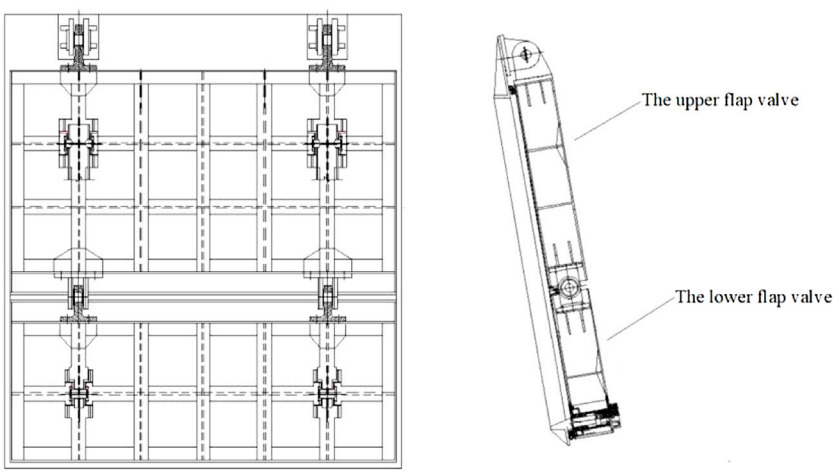

FIGURE 2 | Structure diagram of the double-stage flap valve.

pump station design lower hinge section. The height of the upper flap valves is 1.7 m, and that of the lower flap valves is 1.2 m.

The pump station engineering design drawings and relevant data build a computational area model for its exit buildings. First, the flow state under different flow rates was analyzed by numerical simulation. Then, the influence of different opening angles of the flap valves on the water flow behind the flap valves is obtained. It is found that the flow state behind the flap valves is

more complicated when the flow rate is 16 m^3/s. Therefore, the working condition under this flow rate is selected for further studies. Based on the 3D modeling software UG, Build the 3D model including a water pump outlet pipe, double-stage flap valves, a pressure box culvert, and a road culvert (four parts). The elevation of the pump station body and the culvert through the road is shown in **Figure 1**, and the structure diagram of the double-stage flap valve is shown in **Figure 2**.

2.2 Numerical Simulation

The governing equations used in the numerical simulation in this paper are the continuity equation of the incompressible fluid and the Reynolds time-mean N-S equation. Common turbulence models for numerical value simulation include the standard k-ε model, RNG k-ε model, realizable k-ε model, standard k-ε model, etc. This paper adopts the realizable k-ε model (Jafarzadeh et al., 2011; Lu et al., 2021). The numerical calculation methods of the flow field mainly include the coupling calculation method and separated calculation method. The numerical solution of the equation in this paper adopts the separated semi-implicit pressure coupling algorithm (SIMPLEC method) (Axell and Liungman, 2001; Xi et al., 2021; Xi and Lu, 2021).

The 3D turbulent N-S equation was filtered using a spatial filter function. The governing equation of the large eddy model is

$$\frac{\partial \rho}{\partial t} + \frac{\partial \rho u_i}{\partial x_i} = 0 \tag{1}$$

The equation for k in the transport equation of the standard model is

$$\frac{\partial (\rho k)}{\partial t} + \frac{\partial (\rho k u_i)}{\partial x_i} = \frac{\partial}{\partial x_j}\left[\left(\mu + \frac{\mu_t}{\sigma_k}\right)\frac{\partial k}{\partial x_j}\right] + G_k + G_p - \rho\varepsilon - Y_M + S_k \tag{2}$$

The equation for ε is

$$\frac{\partial (\rho \varepsilon)}{\partial t} + \frac{\partial (\rho \varepsilon u_i)}{\partial x_i} = \frac{\partial}{\partial x_j}\left[\left(\mu + \frac{\mu_t}{\sigma_\varepsilon}\right)\frac{\partial \varepsilon}{\partial x_j}\right] + C_{1\varepsilon}\frac{\varepsilon}{k}(G_k + C_{3\varepsilon}G_b) - C_{2\varepsilon}\rho\frac{\varepsilon^2}{k} + S_\varepsilon \tag{3}$$

k is the methodical kinetic energy; ε is the turbulent dissipation rate; u_i is the velocity component; x_i is the coordinate component; ρ is the density of water; μ_t is the turbulent viscosity coefficient; G_k is the turbulent dynamic energy generated by the laminar gradient; Y_M indicates that the transition–diffusion fluctuations in compressible turbulence are constant; $C_{1\varepsilon}$, $C_{2\varepsilon}$, $C_{3\varepsilon}$ are constant; and S_k and S_ε are custom.

The basic idea of the VOF method is as follows: define volume rate function F = F (x, y, z, t), which indicates the relative ratio of the volume of the fluid in the calculation area to the volume of the calculation area. For a certain computing unit, when F (x, y, z, t) = 1, it means that the unit is full; when F (x, y, z, t) = 0, it means that the unit is empty; when 0 < F (x, y, z, t) < 1, it means that part of the unit is filled with the liquid. The free surface exists in the third unit. The gradient of F can determine the average direction of the free boundary. After calculating the value and angle of each element, the approximate position of the free surface in each element can be determined. The sum of the volume fractions of water and gas in each unit is 1. There will be one more (water or gas) volume fraction variable compared with the real single-phase flow. Let a_w denote the volume fraction of water; then, the volume fraction of gas a_a can be expressed as $a_a = 1 - a_w$.

As long as the volume fractions of water and gas are known everywhere in the flow field, the unknown quantities and characteristic parameters shared by all other water and gas can be represented by the weighted average of the volume integral. Therefore, in any given unit, these variables and characteristic parameters represent either pure water or gas or a mixture of the two. Therefore, the determination of the water–air interface requires solving the following equation:

$$\frac{\partial a_w}{\partial t} + \bar{u}_i\frac{\partial a_w}{\partial x_i} = 0 \tag{4}$$

t is the time. After the introduction of VOF, ρ and v are functions of the volume fraction, not constants, and through the iterative solution to the volume fraction of water a_w, ρ and v can be obtained by the following formula:

$$\rho = a_w\rho_w + (1 - a_w)\rho_a \tag{5}$$

$$\nu = a_w\rho_w + (1 + a_w)\nu_a \tag{6}$$

In the formula, ρ_a and ρ_w indicate the density of air and water, respectively, and v_a and v_w indicate the molecular viscosity coefficients of air and water, respectively.

Boundary conditions such as the inlet section, outlet section, and outlet flow mode should be set for the numerical simulation calculation. In this numerical calculation, the inlet section was controlled using the velocity inlet (Shi et al., 2010); the water body velocity is 1.778 m/s. The outflow section selected outflow of the culvert, set as free outflow. The relative pressure was 1 standard atmospheric pressure. Other surfaces are set as the solid wall. The flap valve is also treated as a solid wall surface but set as a separate structural surface. The model grid is meshed by ANSYS's meshing software ICEM CFD. After study and trial calculations, the maximum size of the overall structure grid is 0.2, and the maximum size of the flap valve panel is 0.05. The mesh density has a significant influence on the results of numerical calculations. The finite volume method solves the nodes composed of each grid discrete in the whole computational domain; the internal flow structure cannot be captured when the grid nodes are insufficient (Xu et al., 2014). For the progressively increasing irrelevance analysis of 1.2 times the total number of grids, the hydraulic loss of double-stage flap valves under different grids is taken out. When the number of grids exceeds 899721, the hydraulic loss tends to be stable, and the grid size is selected as the dividing basis. The maximum size of the overall structure grid is 0.2, and the maximum size of the flap valve panel is 0.05. The grid diagram and the diagrams of hydraulic loss under different grids are shown below.

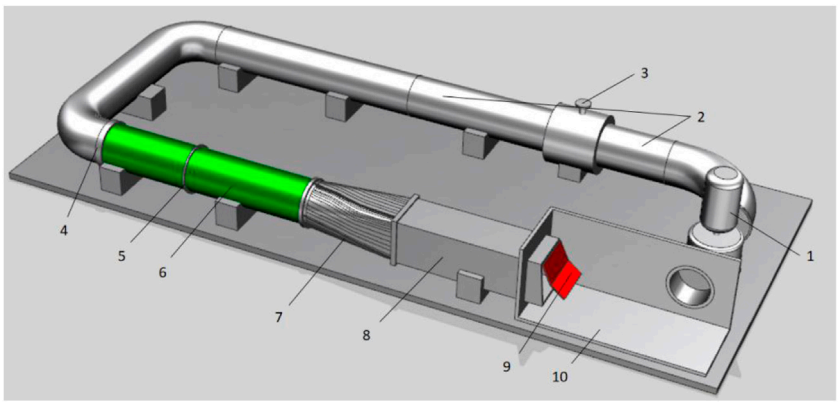

FIGURE 3 | Diagram of the model test device: (1) pump, (2) connecting pipe, (3) control gate valve, (4) steady flow plate, (5) pressure-measuring node, (6) plexiglass tube, (7) gradient tube, (8) transparent square box, (9) flap valve body, and (10) transparent outlet pipe.

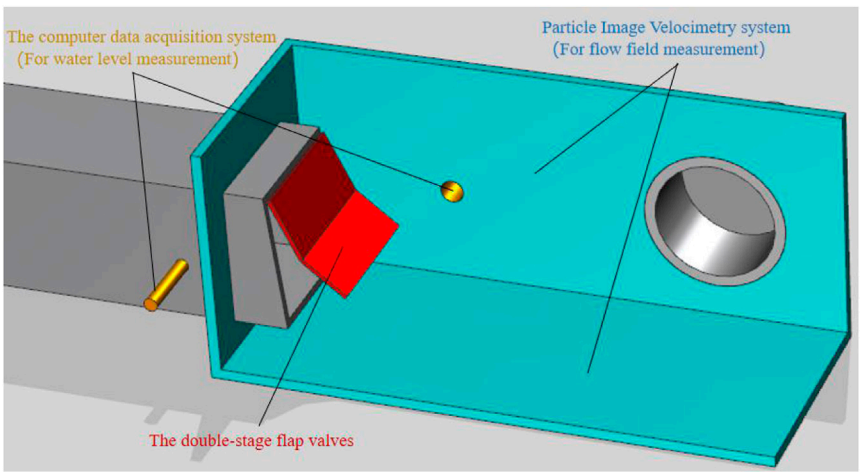

FIGURE 4 | Diagram of the model test measurement.

2.3 Physical Model

The hydraulic loss model test device of the double-section door flap consists of water supply and return equipment and systems, flow stabilization facilities, regulation and control facilities, measuring equipment and facilities, and the door body model. In a typical operation, the circulation system is composed of a pump, connecting pipe, control gate valve, steady flow plate, pressure-measuring node, plexiglass tube, gradient tube, transparent square box, flap valve body, and transparent outlet pipe, and the water level is controlled by regulating the gate. The door model is made of plexiglass, and the weight and buoyancy of the door and its corresponding moment are simulated by the counterweight method. At the same time, the geometric similarity of the prototype and model door body is ensured. **Figures 3**, **4** for the model test.

The scale of the original model is 5:1, and the water level inside and outside the gate is displayed by the computer data acquisition system. The water level measurement point outside the pat door is located under the pat door, and the water level measurement point inside the pat door is located at the bottom of the pipe 50 cm inside the door. The flow measurement is taken through a throttling differential pressure flow meter. The standard orifice plate is stainless steel, and the pressure method is flange pressure. During the model test, speed measurement points 0.7 m inside and 1.5 m outside the exit of the model are set. PIV (Particle Image Velocimetry) is used to measure the culvert flow field in the transparent plastic pipe.

The PIV system (Chen et al., 2022a; Chen et al., 2022b) was used to simultaneously measure the flow field in the transparent plastic tube behind the flap valves. The working frequency of the PIV test laser is 50 HZ, the acquisition speed is 260 frames per second, and the interval is 100 microseconds. The CCD camera takes 600 PIV particle pictures each time. It analyzes them through Microver software. Then, the data are further processed by Tecplot software to obtain the steady-state flow field diagram and velocity field diagram after the flap valves. To

analyze the flow field characteristics after the flap valves are shut based on the cloud image, the flow field characteristics after the flap valves at different opening angles are processed through the Tecplot software.

A certain depth of pure colorless water is injected into the entire circulation device; lasers, synchronizers, etc., are installed and connected; and the light source generated by the laser is aligned at the test section. The position of the CCD camera is adjusted, and the corresponding test parameters of the PIV system are set so that the particle image of the test section is displayed on the computer screen. During the test, the camera and laser light source should not be shaken or displaced. During the experiment, the pump is turned on to form a stable water injection form. The water injection volume can be controlled through the regulating gate valve on the water injection pipe, and the water level in the test section can be adjusted and stabilized. The water flows into the transparent plastic pipe, and the water injection process is formed continuously. When the water flow circulates in the flow channel, until the water flow movement in the test section becomes stable, the computer pre-installed program is used to collect the flow field behind the flap valves and the water level and flow before and after the flap valves.

2.4 Velocity Uniformity of a Cross Section

The outlet of the culvert has better flow conditions, and the opening angle of the flap valve directly affects the flow pattern behind the flap valve. Therefore, when designing the flap valve, it is necessary to consider the complete development of water flow in the culvert, and the flow state should be relatively stable. Furthermore, the velocity distribution should be relatively uniform when it reaches the outlet of the culvert (Xu and Zheng, 2013). In this paper, several calculated sections of the culvert section are selected for comparative analysis to consider the flow pattern of water entering the culvert through the flap valve.

Velocity uniformity of a section is the distribution uniformity of axial velocity on the section. It can be used as a quantitative index for flow field analysis, reflecting the flow field environment of the outlet section (Nejadrajabali et al., 2016). The higher the velocity uniformity of the section is, the more uniform the velocity distribution on the section is and the better the flow condition is. The formula for calculating the uniformity of axial velocity distribution is as follows:

$$\eta = \left[1 - \bar{v}_a^{-1}\sqrt{\sum_{i=1}^{n}(v_{ai} - \bar{v}_a)^2 \Big/ n}\right] \times 100\% \tag{7}$$

Type: $\bar{v}_a$ is the average axial velocity of the calculated section, v_{ai} is the axial velocity of each calculation unit of the calculation section, and n is the number of units for calculating the section.

2.5 Head Loss in the Outlet Culvert Section

After the culvert follows the flap valve, the additional flap valve will affect the flow in the culvert. This is because different opening angles of the flap valve affect the flow head loss in the culvert section. To get a complete understanding of the effect of the opening angle of the valve on the flow of water behind the valve, the change of culvert head loss with different opening angles of the flap valve is analyzed and the relationship between hydraulic λ, the resistance coefficient along the path, the opening angle of the valve, and the flow rate are explored. In the case of determining the opening angle of the flap valves, the following formula can be used to estimate the head loss of the flap valves:

$$\xi_p = 0.012e^{0.076(90-\alpha+\alpha_0)} \tag{8}$$

α_0 is the upward warping angle of the front flow direction based on the horizontal plane (°) , and $\alpha_0 = 0°$ is the opening angle of the flap valves (°) . In the calculation process of head loss of double-section flap valves, the opening angle of the flap valves can be calculated as the average opening angle of the upper and lower flap valves ($\alpha = \frac{(\alpha_1+\alpha_2)}{2}$). Using the proportion of weight to estimate the angle, the head loss of the flap valves Δh_p can be determined more objectively and accurately. It can be calculated by the following formula:

$$\Delta h_p = \xi V^2 p/2g \tag{9}$$

In this formula, v is the flow rate at the pump outlet (m/s) , g is the acceleration of gravity (m/s^2) , and ξ_p is the head loss coefficient.

2.6 Case Selection

To study the influence of the opening angle of the double-section flap valves on the flow pattern of the outlet pipe behind the culvert, this example mainly calculates the flow state of the outlet culvert at different opening angles of flap valves under multiple flow rates of the pump station. As the flow rate continues to increase, the opening angle of the flap valves will gradually increase. Under different opening angles, the hydraulic loss and flow pattern will be different. It will also have a particular impact on the flow pattern of the water flow behind the flap valves. The opening angle is formed by water flow and the flap valves. The flap valves have a specific working state when they are working. The four options selected here are commonly used in the operating state corresponding to the flow in the actual project. The angle of the upper flap valve is set as α1. The angle of the lower flap valve is set as α2. **Table 1** for the opening angle scheme of double-section flap valves. **Figure 5** is the diagram of flap valve angles.

3 ANALYSIS OF THE RESULTS

3.1 Analysis of Numerical Simulation Results

3.1.1 Flow Field Analysis

Taking a design flow rate of the pumping station of 16 m^3/s as an example, the water flow in the culvert behind the gate of the four schemes is simulated by the numerical simulation method. The flow field distribution diagram is obtained (**Figure 6** below). The flow line variation of the outlet pressure water tank and culvert section was studied. Analyzing the flow of the entire outlet culvert, at the same time, the culvert outlet section was selected to observe the velocity vector diagram at the section.

TABLE 1 | Opening angles for each case.

Case	Angle of the upper flap valve α1 (°)	Angle of the lower flap valve α2 (°)
1	15	32
2	33	55
3	46	64
4	53	70

According to **Figure 8**, when the flap valve opens at a tiny angle, the water flow in the culvert is spiral, streamline disorderly, and there will be water retention in the pressure box culvert, accompanied by whirlpools. As the opening angle increases, the flow of water gradually straightens, the streamlines are no longer out of order, and there is no water retention in the pressure box culvert. In order to conduct an in-depth study on flow field changes in pressure box culverts, the cross-section flow velocity vector diagrams 40 m away from the entrance of the four schemes were intercepted for comparison (**Figure 7**).

According to **Figure 9**, in case 1, there are two reverse vortices in the section with axial symmetry. The high velocity is distributed in the upper part of the vortex on both sides. The vortexes on both sides are asymmetric and collide in the middle of the upper side of the culvert so that the velocity vector is concentrated here; in case 2, the vortex positions on both sides gradually move downward, and the collision area of the vortex becomes larger, extending to the T-shaped area on the upper side, and the vortex is gradually symmetrical. The flow pattern is still poor; as the valve continues to open, the vortex gets smaller and the flow pattern gets better. In case 3, the vortex is further reduced. The collision area of the vortex is further enlarged. The high-velocity region spreads to the upper M-shaped part, and the low-velocity area is compressed below the culvert. The high-speed area is inclined to the lower side. In case 4, the overall flow velocity of the section decreases, the range of vortex becomes smaller, and there is no apparent high-velocity zone. This is due to the friction of the sidewall and the gradient of the flow velocity. The flow velocity in the center of the water flow in front of the shutter is more significant, and the flow velocity near the sidewall is lower, a new flow rate gradient. After passing through the valves, the water flow is fully developed, thus forming two large-scale axis-symmetric vortexes. After the valves are slapped, the inflection affects the water flow, and the high-velocity area is concentrated on the upper part. As the flap valves' opening increases, the flap valves' effect gradually decreases, the water flow can pass the flap valves smoothly, and the vortex gradually decreases and disappears.

3.1.2 Flow Field Analysis of the Axial Section

Taking the flow rate of 16 m^3/s as an example for analysis, the influence of opening angle change on velocity uniformity was analyzed. In order to study the development and change of water flow, a section every 6 m in the culvert is set to analyze its change rule in order to study the influence of the opening of double-stage flap valves on the water flow behind the valve. The schematic diagram of selected research sections is shown in **Figure 8**.

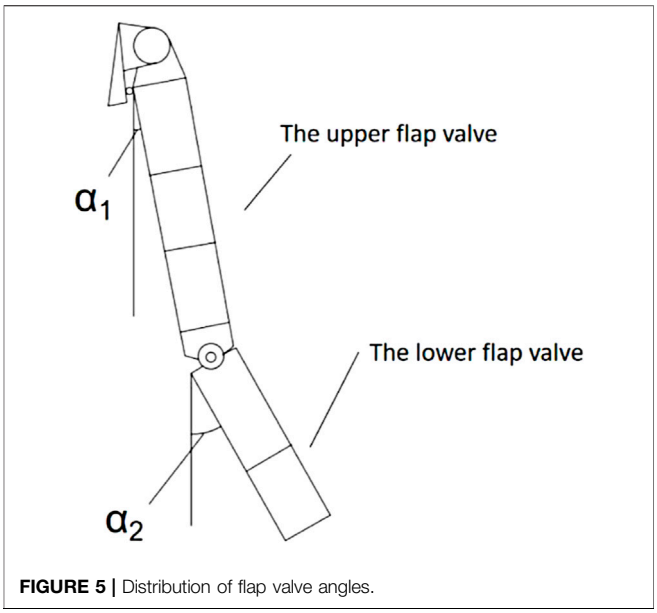

FIGURE 5 | Distribution of flap valve angles.

As shown from the figure above, in case 1, when the water flows through the flap valves, the flow pattern is chaotic, and the velocity distribution is irregular. After leaving the flap valves, the water flow shows a trend of rolling up and down. The high-flow velocity area gradually moves upward and forms a reverse vortex on both sides of the cross-section at the backside of the culvert. The distribution of the reverse vortex on both sides of the exit also moves to the upper side, and it is asymmetrically distributed. In case 2, the high-velocity inlet area is mainly compressed on the lower side. In moving to the outlet, the high-velocity area gradually spreads upward from the lower side of the culvert along both sides. Low-speed vortexes are formed on both sides of the middle part of the culvert. The low-velocity area at the exit gathers on both sides of the section, and the vortex range is more extensive than that on both sides of case 1. In case 3, the range of high-velocity area under the inlet gradually increases. The high-velocity area slowly spreads upward along both sides and forms a reverse low-speed vortex on both sides in the middle and front of the culvert. At the outlet, the range of low velocity zone further increases and the velocity gradient decreases. In case 4, the range of high-velocity inlet area is further expanded, and the upward position of the high-velocity zone further advances. The flow tends to be stable, and the outlet velocity distribution is uniform. The overall velocity is low, and there is no obvious velocity gradient.

3.2 Analysis of Physics Experiment Results

3.2.1 Flow Field Analysis of the Axial Section

Physical model tests were used to analyze the flow field at different sections in the culvert using a flow rate of 16 m^3/s as an example to analyze the effect of the change in angle of opening of the double-jointed flapper gate on the uniformity of the flow rate. To study the development and variation of the flow, PIV was

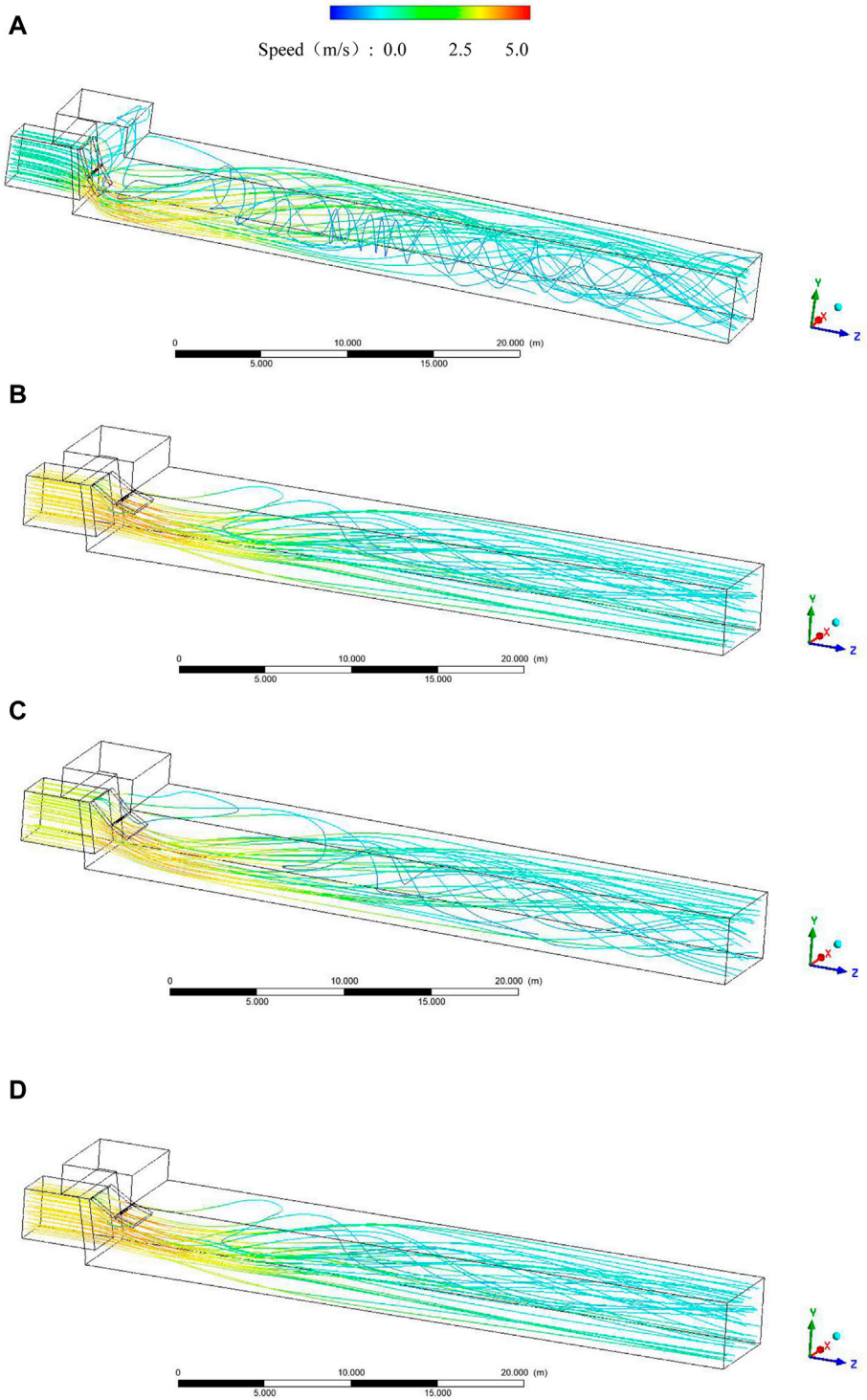

FIGURE 6 | Distribution of streamlines: **(A)** case 1, **(B)** case 2, **(C)** case 3, and **(D)** case 4.

used to analyze the variation pattern at 6 m intervals in the culvert and to study the effect of the double-jointed flapper gate opening on the flow behind the gate. **Figures 1**, **2**, **9**, **10** correspond to the cross-sectional flow field from the inlet to the outlet. The 3D distribution of the specific section flow patterns is shown in **Figure 11**.

In case 1, the flow pattern at the flap valves is relatively turbulent, and the high-velocity area is concentrated on the

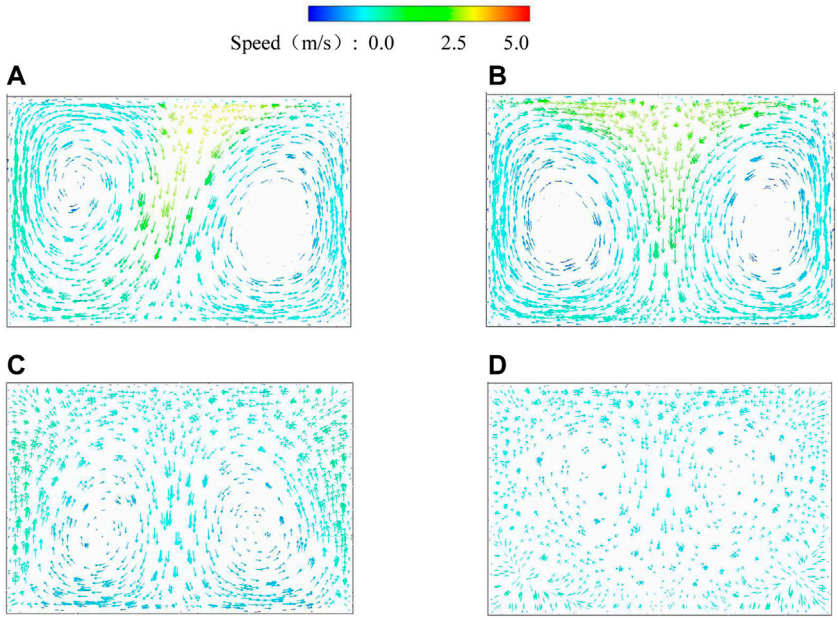

FIGURE 7 | Vector diagram of cross-section velocity: **(A)** case 1, **(B)** case 2, **(C)** case 3, and **(D)** case 4.

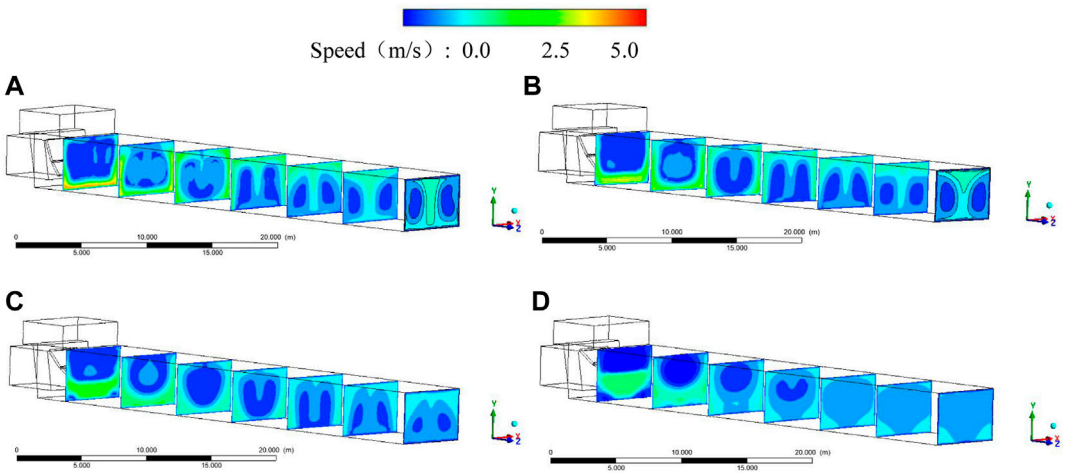

FIGURE 8 | Flow field distribution of axial sections: **(A)** case 1, **(B)** case 2, **(C)** case 3, and **(D)** case 4.

lower side. This is because the opening angle of the flap valves is slight, and the water flow is affected by the flap valves. Behind the valves, the water flow develops in the culvert. The high-velocity area spreads upward from both sides along the edge until it gradually fills the entire culvert and forms two asymmetric reverse vortices in the axial section. In case 2, the opening angle of the flap valves is slightly more prominent, and the high-velocity area is still compressed on the lower side, but the water flow development on the rear side is more lagging than that in case 1, the axial tumbling cycle of the water flow becomes smaller, and the flow state becomes better. In case 3, the opening angle of the flap valves is further increased, the axial tumbling cycle of the flow is reduced, and the flow velocity gradient in the culvert is significantly reduced compared to the first two options. In case 4, the flow tends to stabilize in the middle of the culvert, with no significant velocity gradients and no significant tumbling of the water in the culvert, resulting in perfect flow patterns.

Through observation, it can be found that the results of the physical model test and the numerical simulation show the same trend, indicating that the numerical simulation results are credible.

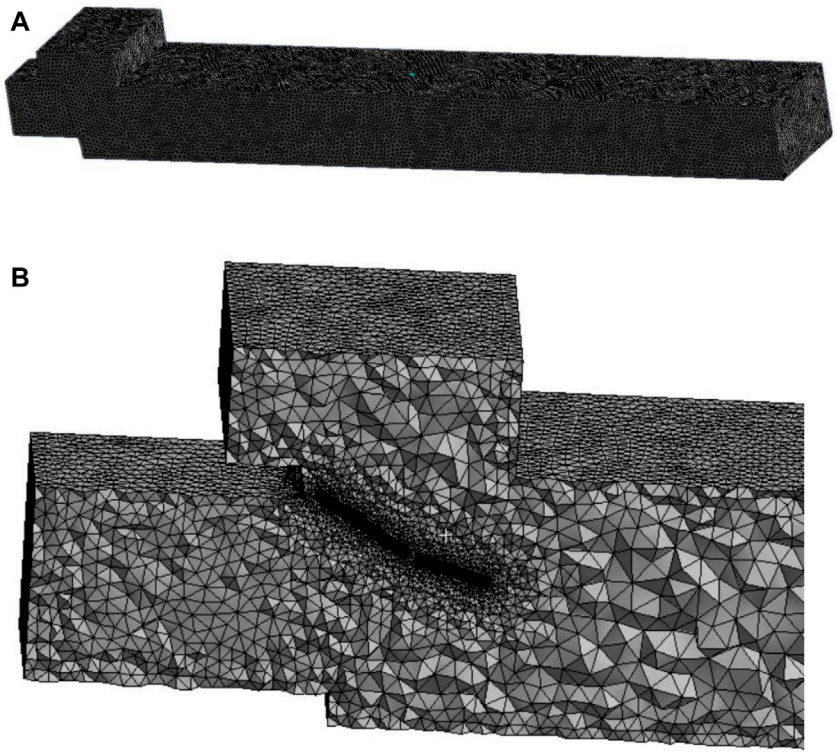

FIGURE 9 | Diagram of the grid division: **(A)** overall grid diagram and **(B)** local grid diagram.

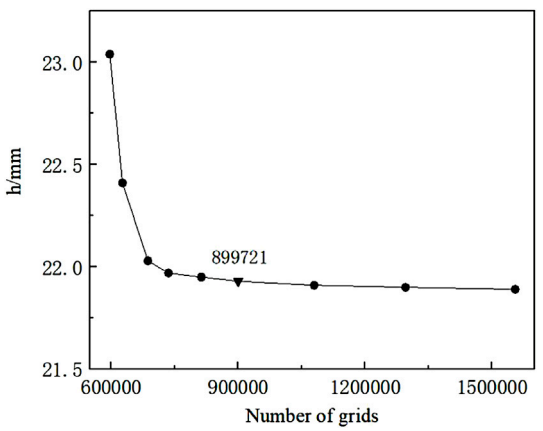

FIGURE 10 | Diagrams of hydraulic loss under different grids.

3.2.2 Vector Analysis of the Outlet Section

\nolimitsTaking the flow rate of 16 m^3/s as an example, the physical model is studied. To conduct an in-depth study on the flow field changes in the culvert, the outlet section water flow velocity vector diagrams in the four schemes are intercepted for comparison (**Figure 12**).

According to the above figure, in case 1, two reverse vortexes are asymmetric along the axial direction in the section. As a result, the vortex area on the right side is significantly larger than that on the left side, and the vortexes on both sides are squeezed, resulting in a strip-shaped high-velocity area in the center of the section. In the second scheme, the vortexes on both sides gradually become symmetrical, the squeezed area of the vortex becomes larger and extends to the X-shaped area in the middle, the range of the low-velocity area at the center of the vortex becomes smaller, and the flow state gradually gets better. In case 3, the vortex position moves to the lower side of the culvert, the high-velocity area spreads to the upper M-shaped area, and the velocity gradient in the culvert decreases. In case 4, the overall flow rate is reduced, there is no apparent vortex and no evident flow rate gradient, the flow pattern is good, and the water flow is stable. The experimental results of the physical model verify the numerical simulation results, so the results of the numerical simulation are credible.

3.3 Analysis of Flow Velocity Uniformity

By using the formula of axial velocity uniformity to calculate the velocity uniformity of each section, the results of velocity uniformity of each calculated section under each scheme were compared with those without the flap valve. The results are shown in **Figure 13**.

According to the curve changes in **Figure 12**, as the distance increases, the uniformity index of flow velocity improves. According to case 1, when the flap valve opening is small, the overall flow velocity uniformity is low. Still, as the water moves away from the flap valve, the uniformity of flow velocity

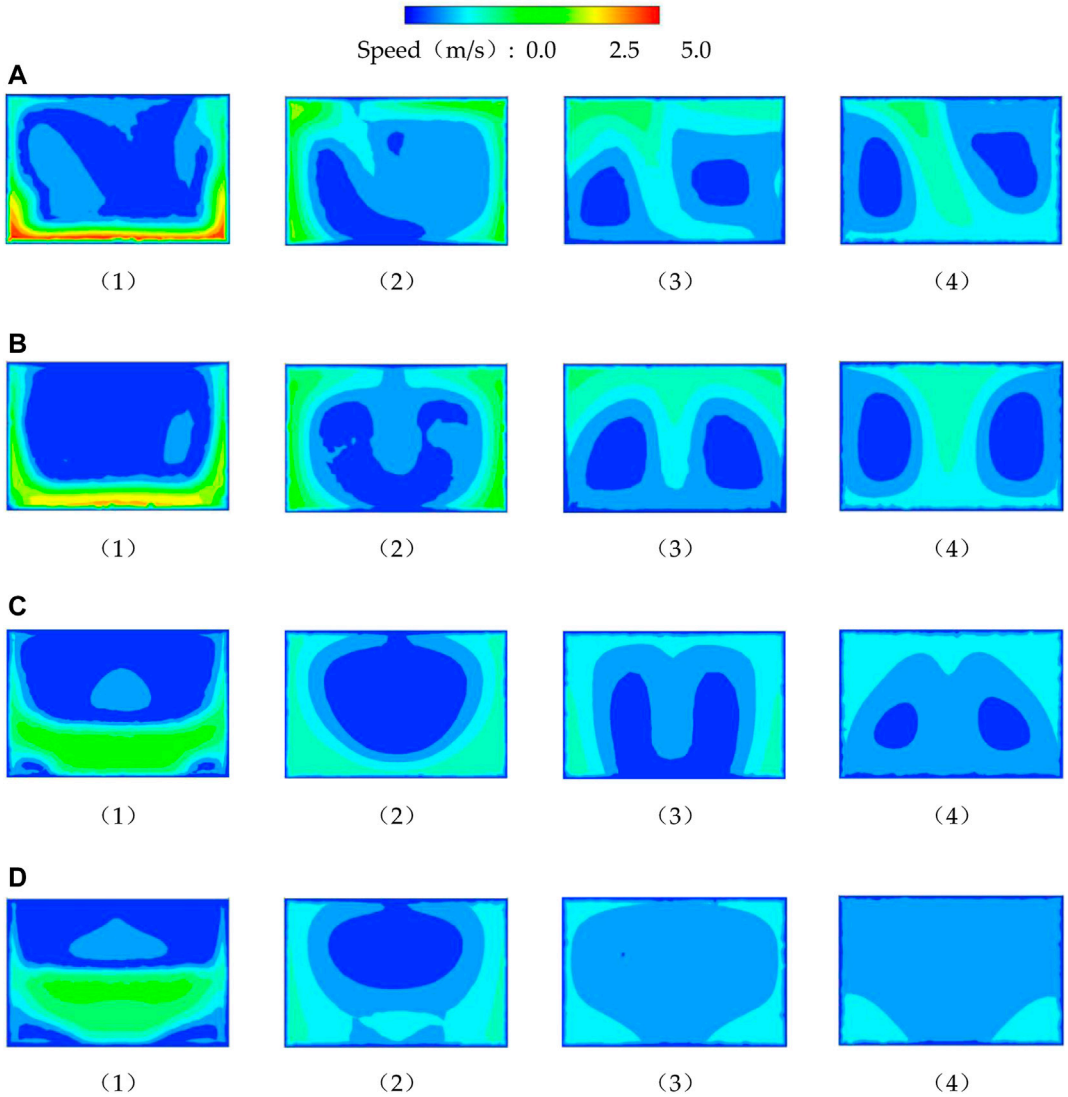

FIGURE 11 | Flow field distribution of axial sections: **(A)** case 1, **(B)** case 2, **(C)** case 3, and **(D)** case 4.

increases slowly. In the second scheme, where the opening angle of the flap valve is slightly increased, the overall flow velocity uniformity is slightly improved, but like case 1, the uniformity of flow rate increases gradually when it is at a lower level and far from the racket flap valve. In case 3, at 14 m away from the flap valve, the uniformity of flow velocity increases significantly. The uniformity of flow velocity at 33 m exceeds that of the no-flap valve scheme, which shows that the flow pattern in the culvert is improved. In case 4, the uniformity of flow velocity increases rapidly between 14 and 19.5 m and maintains a steady increase in the level higher than the open-valve scheme. At this time, the flow pattern in the culvert has been significantly improved.

According to the analysis of the flow pattern behind the flap valve and the uniformity of the axial flow velocity at the outlet, when the opening angle reaches case 3 and case 4, the flow pattern at the outlet of the culvert pipe can achieve a better state.

4 COMPREHENSIVE ANALYSIS

After the pump unit is started, the residual air in the pipeline will be quickly compressed. When the gas is compressed to a certain level, its pressure may exceed the water pressure outside the flap valves and push the flap valves open. When the flap valves are made available by the air pressure, a large amount of air quickly leaks out, causing the air pressure of the pipe to drop sharply. If there is more residual air in the tube, the above process will be repeated. Finally, after several repeated openings and closings, the lower flap valve will first be pushed open by the water. As the flow increases, the upper flap valve is also made open. At the same time, because of the flap valves, the water flow direction at the pipe outlet will change sharply. At this time, there must be a specific head loss. As the flow rate continues to increase, the opening angle of the flap valves will gradually increase. Under different opening angles, the hydraulic loss and flow pattern will

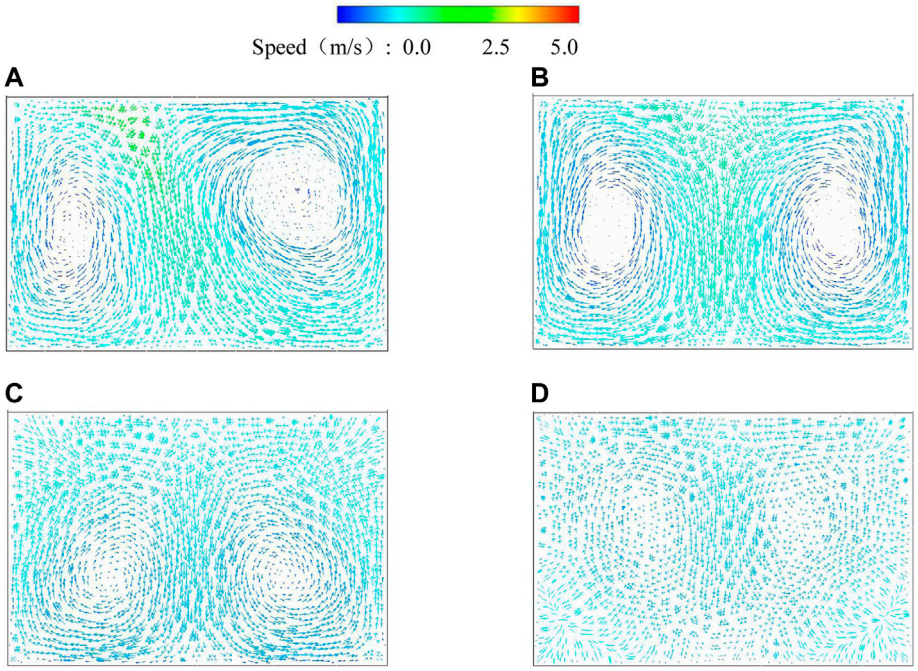

FIGURE 12 | Vector diagram of cross-section velocity: **(A)** case 1, **(B)** case 2, **(C)** case 3, and **(D)** case 4.

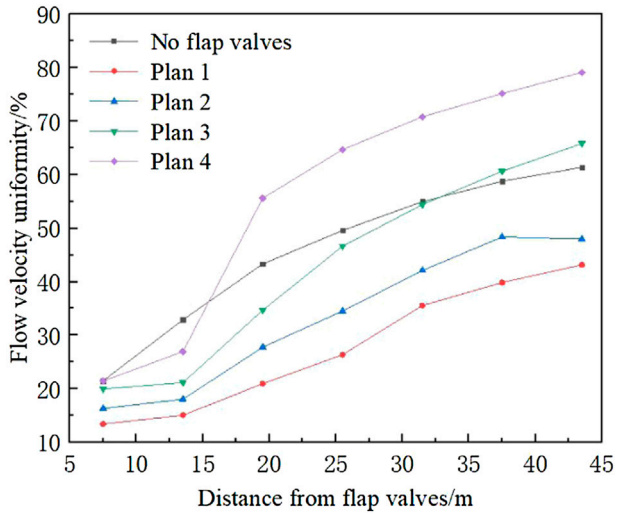

FIGURE 13 | Velocity uniformity at different distances.

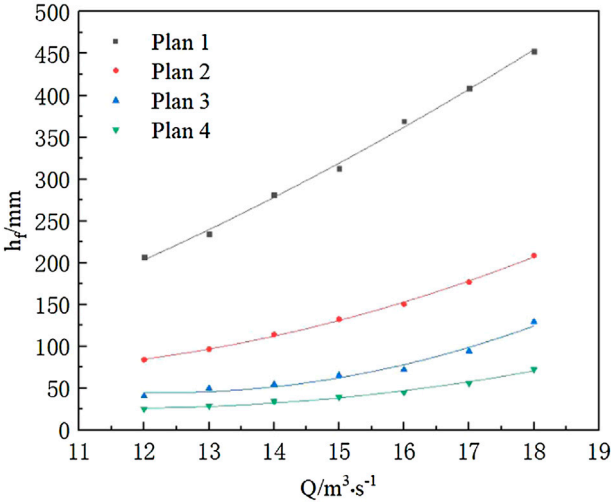

FIGURE 14 | Hydraulic loss under different flow rates.

be different. It will also have a particular impact on the flow pattern of the water flow behind the flap valves.

The physical model experiment is used to measure the head loss before and after the double-stage flap valves. The hydraulic loss of the outlet culvert pipe is calculated under eight different flow rates and four schemes of flap valve opening, and its patterns are analyzed. Hydraulic loss results of the culvert pipe under each case are shown in **Figure 8**. At the same time, the resistance coefficient λ of the pipeline under each scheme is calculated and the relationship between λ and the opening angle of the flap valve under each flow is analyzed, and the calculation results are shown in **Figure 14**.

According to the curve changes in **Figure 13**, the hydraulic loss at each flow rate of the four schemes decreases with the opening of the flap valve. Under the same flow rate, the hydraulic loss of the culvert pipe decreases when the opening angle of the flap valve increases. With the increase of opening angle, the rise of head loss caused by flow growth becomes smaller and smaller.

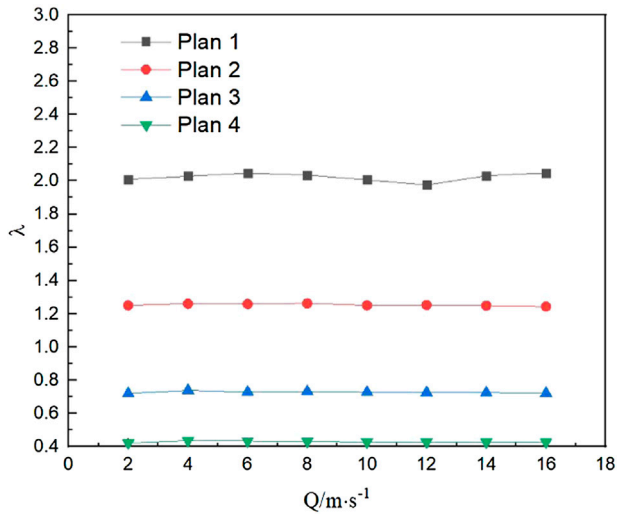

FIGURE 15 | Change of resistance coefficient along the way.

Taking the design flow rate of 16 m^3/s as an example, the hydraulic loss value of Scheme 1 is 0.353 m, while the hydraulic loss of case 4 is 0.035 m; the hydraulic losses decreased by 79.1%.

According to the result analysis in **Figure 15**, at the same opening angle, the resistance coefficient λ along the inner section of the culvert pipe has nothing to do with the change of flow rate. It is always stable around a value. However, as the opening angle increases, the drag coefficient decreases along the way, which means that the more the opening angle of the flap valve is, the smaller the resistance coefficient is and the less the hydraulic loss is.

According to the results, as the opening angle increases, the hydraulic loss in the culvert is significantly reduced. This also shows the better flow pattern of the water in the culvert. Therefore, the larger the opening angle of the flap valve is, the more favorable the flow pattern of the culvert pipe is.

5 CONCLUSION

Numerical simulation is used to analyze the flow pattern behind the double-stage flap valves from three aspects of streamline and velocity uniformity. The physical model test analyzes it from the hydraulic loss. It is found that the greater the opening of the double-stage flap valves, the more uniform the flow of water behind the flap valve and the better the flow pattern. Under the opening angle of double-stage flap valves corresponding to case 3 and case 4, compared with case 1 and case 2, the vortex area is significantly reduced, the flow pattern has been dramatically improved, water flows can be fully developed in culverts, and the uniformity index of flow velocity in the culvert is higher than that of the open-valve scheme. As a result, in order to ensure the flawless operation of the pump station, the impact on the water flow behind the flap valve is reduced, and it is recommended to make the maximum opening angle reached when the flap valve runs as large as possible.

This study focuses on the influence of the opening angle of double-stage flap valves on the water flow behind the flap valve. The relationship between the flow pattern after the valve and the opening angle of the flap valves is analyzed by numerical simulation analysis and the physical model test from the three aspects of streamline, uniformity of flow velocity, and hydraulic loss, and the following conclusions are obtained:

1) After the double-stage flap valves are opened, two axisymmetric reverse vortexes appear in the culvert section behind the flap valve. As the opening angle increases, the flow line in the culvert pipe after the gate gradually moves down and disappears in the high-velocity zone. The eddy dissipates at the outlet.
2) As the distance between water flow and the racket flap valve increases, the uniformity of flow velocity rises gradually. The water flow can be fully developed in the culvert. The uniformity index starts to be higher than the uniformity index without the door at a distance of about 35 m from the entrance.
3) The hydraulic loss coefficient of the culvert section has nothing to do with the volume of flow and is negatively correlated with the opening angle of the flap valve; the bigger the opening angle, the smaller the hydraulic loss coefficient of the culvert section and the smaller the head loss.

DATA AVAILABILITY STATEMENT

The raw data supporting the conclusion of this article will be made available by the authors, without undue reservation.

AUTHOR CONTRIBUTIONS

Conceptualization, WL and WX. Methodology, GF. Software, WX. Validation, WL, WX, and GF. Formal Analysis, WX. Investigation, WX. Resources, WX. Data Curation, WX. Writing—Original Draft Preparation, WX. Writing—Review and Editing, WX. Visualization, WX. Supervision, WX. Project Administration, WX. Funding Acquisition, WL. All authors have read and agreed to the published version of the manuscript.

FUNDING

This research was funded by the National Natural Science Foundation of China (51779215), the National Natural Science Foundation of China (52079120), the Jiangsu Graduate Research and Innovation Program (KYCX20_2980), and the Priority Academic Program Development of Jiangsu Higher Education Institutions (PAPD).

REFERENCES

Ahmed, F. (2000). Three-dimensional Mean Velocity Analysis of a 30 Degree bend Flow. *J. Eng. Mech.* 126126 (12), 126212–131272. doi:10.1061/(ASCE)0733-939910.1061/(asce)0733-9399(2000)126:12(1262)

Alawadhi, K., Alzuwayer, B., Mohammad, T. A., and Buhemdi, M. H. (2021). Design and Optimization of a Centrifugal Pump for Slurry Transport Using the Response Surface Method. *Machines* 9 (3), 60. doi:10.3390/machines9030060

Axell, L. B., and Liungman, O. (2001). A One-Equation Turbulence Model for Geophysical Applications: Comparison with Data and the K– ε Model. *Environ. Fluid Mech.* 1 (1), 71–106. doi:10.1023/A:1011560202388

Chen, B., Li, X., and Zhu, Z. (2022b). Investigations of Energy Distribution and Loss Characterization in a Centrifugal Impeller through PIV experiment. *Ocean Engineering* 247, 110773. doi:10.1016/j.oceaneng.2022.110773

Chen, B., Li, X., and Zhu, Z. (2022a). Time-Resolved Particle Image Velocimetry Measurements and Proper Orthogonal Decomposition Analysis of Unsteady Flow in a Centrifugal Impeller Passage. *Front. Energ. Res.* 9. doi:10.3389/fenrg.2021.818232

Gao, C., Gao, Y., and Sun, L. (2021). Research on Hydraulic Characteristics of Inlet Pipeline of Pumping Station Based on Standard K-ε Turbulence Model. *J. Irrigation Drainage* 40 (05), 44. doi:10.3390/w11010044

Hong, S., and Li, Z. (2015). Comparative Study on Hydraulic Characteristics of Flip-Up and Side Flip-Doors. *South-to-North Water Diversion Water Conservancy Sci. Tech.* 13 (02), 955. doi:10.13476/j.cnki.nsbdqk.2015.02.025

Hu, B., Wang, H., Liu, J., Zhu, Y., Wang, C., Ge, J., et al. (2022). A Numerical Study of a Submerged Water Jet Impinging on a Stationary Wall. *J. Mar. Sci. Eng.* 10 (2), 228. doi:10.3390/jmse10020228

Jafarzadeh, B., Hajari, A., Alishahi, M. M., and Akbari, M. H. (2011). The Flow Simulation of a Low-Specific-Speed High-Speed Centrifugal Pump. *Appl. Math. Model.* 35 (1), 242–249. doi:10.1016/j.apm.2010.05.021

Lu, Z., Tao, R., Jin, F., Li, P., Xiao, R., and Liu, W. (2021). The Temporal-Spatial Features of Pressure Pulsation in the Diffusers of a Large-Scale Vaned-Voluted Centrifugal Pump. *Machines* 9 (11), 266. doi:10.3390/machines9110266

Luo, H., Fytanidis, D. K., Schmidt, A. R., and García, M. H. (2018). Comparative 1D and 3D Numerical Investigation of Open-Channel junction Flows and Energy Losses. *Adv. Water Resour.* 117, 120–139. doi:10.1016/j.advwatres.2018.05.012

Nejadrajabali, J., Riasi, A., and Nourbakhsh, S. A. (2016). Flow Pattern Analysis and Performance Improvement of Regenerative Flow Pump Using Blade Geometry Modification. *Int. J. Rotating Machinery* 2016, 1–16. doi:10.1155/2016/8628467

Qian, Z., Wu, P., Guo, Z., and Huai, W. (2016). Numerical Simulation of Air Entrainment and Suppression in Pump Sump. *Sci. China Technol. Sci.* 59 (12), 1847–1855. doi:10.1007/s11431-016-0237-8

Shen, P., Wang, Y., Chen, Y., Fu, P., Zhou, L., and Liu, L. (2021). Hydrodynamic Bearing Structural Design of Blood Pump Based on Axial Passive Suspension Stability Analysis of Magnetic-Hydrodynamic Hybrid Suspension System. *Machines* 9 (11), 255. doi:10.3390/machines9110255

Shi, L., Zhu, J., Tang, F., and Wang, C. (2020). Multi-disciplinary Optimization Design of Axial-Flow Pump Impellers Based on the Approximation Model. *Energies* 13 (4), 779. doi:10.3390/en13040779

Shi, W., Desheng, Z., Xingfan, G., and Hongfei, L. (2010). Numerical and Experimental Investigation of High-Efficiency Axial-Flow Pump. *Chin. J. Mech. Eng.* 23 (1), 38–44. doi:10.3901/cjme.2010.01.038

Shin, B. (2018). Effect of Submergence and Flow Rate on Free Surface Vortices in a Pump Sump. *Inter. J. Fluid Mech. Res.* 45 (3), 225–236. doi:10.1615/interjfluidmechres.2018020379

Sudo, K., Sumida, M., and Hibara, H. (1998). Experimental Investigation on Turbulent Flow in a Circular-Sectioned 90-degree bend. *Experiments in Fluids* 25 (1), 42–49. doi:10.1007/s003480050206

Tang, S., Zhu, Y., and Yuan, S. (2022). Intelligent Fault Diagnosis of Hydraulic Piston Pump Based on Deep Learning and Bayesian Optimization [J]. *ISA Trans.* doi:10.1016/j.isatra.2022.01.013

Wang, H. L., Hu, Q. X., Yang, Y., and Wang, C. (2021). Performance Differences of Electrical Submersible Pump under Variable Speed Schemes. *Int. J. Simul. Model.* 20 (1), 76–86. doi:10.2507/IJSIMM20-1-544

Wang, H., Long, B., Wang, C., Han, C., and Li, L. (2020). Effects of the Impeller Blade with a Slot Structure on the Centrifugal Pump Performance. *Energies* 13 (7), 1628. doi:10.3390/en13071628

Xi, W., and Lu, W. G. (2021). Formation Mechanism of an Adherent VorteX in the Side Pump Sump of a Pumping Station. *Int. J. Simul. Model.* 20 (2), 327–338. doi:10.2507/IJSIMM20-2-562

Xi, W., Lu, W., Wang, C., and Xu, B. (2021). Optimization of the Hollow Rectification Sill in the Forebay of the Pump Station Based on the PSO-GP Collaborative Algorithm. *Shock and Vibration* 2021, 1–11. doi:10.1155/2021/6618280

Xu, D., and Zheng, H. (2013). Mesh independence Test of Numerical Manifold Method in Treating strong Singularity. *Rock Soil Mech.* 35 (8), 91–96. doi:10.1201/b15791-11

Xu, L., Lu, W.-g., Lu, L.-g., Dong, L., and Wang, Z.-f. (2014). Flow Patterns and Boundary Conditions for Inlet and Outlet Conduits of Large Pump System with Low Head. *Appl. Math. Mech.-Engl. Ed.* 35 (6), 675–688. doi:10.1007/s10483-014-1821-6

Yamade, Y., Kato, C., Nagahara, T., and Matsui, J. (2020). Suction Vortices in a Pump Sump-Their Origin, Formation, and Dynamics. *J. Fluids Eng.* 142 (3), 031110. doi:10.1115/1.4045953

Yan, H., Tan, F., Liu, C., Shi, L., Liu, H., Sun, Z., et al. (2020). Numerical Simulation of Hydraulic Performance of Horizontal Pumping Station with Straight-Pipe Outlet Flow Channel Profile Change. *China Rural Water Resour. Hydropower* 2020 (1), 188–191. doi:10.3969/j.issn.1007-2284.2020.01.038

Yang, F. Z. (2011). Numerical Simulation and experiment on Resistance Loss of Flap Gate. *Trans. Chin. Soc. Agric. Machinery* 42 (9), 108–112+44. doi:10.1002/clc.20818

Yu, Y., and Zhu, J. (2014). Improving the Shut-Off Performance of the Pumping Station's Pressure Water Tank Based on Numerical Experiments. *China Rural Water and Hydropower* 2014 (6), 125–128. doi:10.3969/j.issn.1007-2284.2014.06.029

Zeng, C., and Li, C. W. (2010). A Hybrid RANS-LES Model for Combining Flows in Open-Channel T-Junctions. *J. Hydrodynamics* 22 (1), 154–159. doi:10.1016/s1001-6058(09)60186-4

Zhang, D., Jiao, W., Cheng, L., Xia, C., Zhang, B., Luo, C., et al. (2021). Experimental Study on the Evolution Process of the Roof-Attached Vortex of the Closed Sump. *Renew. Energ.* 164, 1029–1038. doi:10.1016/j.renene.2020.10.045

Zhang, D., Wang, H., Liu, J., Wang, C., Ge, J., Zhu, Y., et al. (2022). Flow Characteristics of Oblique Submerged Impinging Jet at Various Impinging Heights [J]. *J. Mar. Sci. Eng.* 10 (3), 399. doi:10.3390/jmse10030399

Zhou, J., Zhao, M., Wang, C., and Gao, Z. (2021). Optimal Design of Diversion Piers of Lateral Intake Pumping Station Based on Orthogonal Test. *Shock and Vibration* 2021, 1–9. doi:10.1155/2021/6616456

Zhu, Y., Li, G., Tang, S., Wang, R., Su, H., and Wang, C. (2022). Acoustic Signal-Based Fault Detection of Hydraulic Piston Pump Using a Particle Swarm Optimization Enhancement CNN. *Applied Acoustics* 192, 108718. doi:10.1016/j.apacoust.2022.108718

Zhu, Y., Li, G., Wang, R., Tang, S., Su, H., and Cao, K. (2021). Intelligent Fault Diagnosis of Hydraulic Piston Pump Combining Improved LeNet-5 and PSO Hyperparameter Optimization. *Appl. Acoust.* 183, 108336. doi:10.1016/j.apacoust.2021.108336

Conflict of Interest: The authors declare that the research was conducted in the absence of any commercial or financial relationships that could be construed as a potential conflict of interest.

frontiers | Frontiers in Energy Research

ORIGINAL RESEARCH
published: 06 April 2022
doi: 10.3389/fenrg.2022.882747

Research on the Effect of Needle Eccentricity on the Jet Flow Characteristics

Huang Jinwei[1,2], *Ge Xinfeng*[1]*, *Chu Dongdong*[3], *Zhang Jing*[1], *Xu Bing*[4], *Gao Fei*[1,4] and *Zheng yuan*[1]

[1]Hohai University, Nanjing, China, [2]China Eastern Route Corporation of South-to-North Water Diversion, Beijing, China, [3]Jiangsu Water Conservancy Research Institute, Yang Zhou, China, [4]Harbin Electric Machinery Factory Co., Ltd., Harbin, China

The position of the nozzle in the jet mechanism of the impulse turbine may cause an eccentric jet due to size processing and installation deviations. To study the effect of jet needle eccentricity on the jet, this article first analyzes the jet characteristics of the jet mechanism with different openings (20, 40, 60, 80, 100%) under 4.8% eccentricity, verify the reliability of the research method in this paper. Then the focus is on the jet characteristics of the jet mechanism at different eccentricities (0, 1, 2.1, 4.8, 8, and 14%) at 40% opening. The results show that as the eccentricity of the nozzle increases, the jet appears to be asymmetrical, and the shape of the jet at the inlet section of the runner gradually changes and becomes an irregular shape. The eccentricity of the water jet increases with the increase of the eccentricity of the needle; the efficiency of the injection mechanism gradually decreases, and the energy loss gradually increases. Before the eccentricity of 4.8%, the efficiency decreases more slowly, and after the eccentricity of 4.8%, the rate of efficiency decrease is accelerated.

Keywords: pelton turbine, needle, eccentric jet, eccentricity, JET shape

OPEN ACCESS

Edited by:
Ling Zhou,
Jiangsu University, China

Reviewed by:
Deyou Li,
Harbin Institute of Technology, China
Parvathy Rajendran,
Universiti Sains Malaysia Engineering Campus, Malaysia
Kh S. Mekheimer,
Al-Azhar University, Egypt

***Correspondence:**
Ge Xinfeng
gexinfeng@hhu.edu.cn

Specialty section:
This article was submitted to Process and Energy Systems Engineering, a section of the journal Frontiers in Energy Research

Received: *24 February 2022*
Accepted: *21 March 2022*
Published: *06 April 2022*

Citation:
Jinwei H, Xinfeng G, Dongdong C, Jing Z, Bing X, Fei G and yuan Z (2022) Research on the Effect of Needle Eccentricity on the Jet Flow Characteristics. Front. Energy Res. 10:882747. doi: 10.3389/fenrg.2022.882747

1 INTRODUCTION

Hydropower is the most abundant renewable energy source in the world, accounting for about 20% of the total global electricity production (Mulu, et al., 2012). Among them, the high-head hydraulic resources are very rich in the western region of my country, and the exploitable water head is between 200 and 2000 m (Yang, 2009; Guo et al., 2020). The pelton turbine applied to the high water head has become the first choice, and the jet mechanism is an important part of the pelton turbine, which has an important impact on the overall efficiency of the turbine. The jet of the impingement turbine nozzle is a complex unsteady multiphase flow (Han et al., 2005). If there is a deviation in the size of the injection mechanism, wear of the support device, or unstable system pressure, the central axis of the injection needle will deviate from the central axis of the nozzle, resulting in an eccentric jet (Park et al., 2021; Wang et al., 2021). Deviating from the original jet trajectory, reducing the flow rate of water injected into the bucket, resulting in water flow loss, thereby affecting the jet efficiency of the jet

Abbreviations: d, water inlet diameter; d_0, Nozzle outlet diameter; d_1, Jet outlet air domain; s, Water inlet area; ρ, Density; α, the volume fraction; $\vec{v}$, average velocity; e, eccentricity; l, eccentric distance; v, jet outlet velocity; v_c, theoretical speed of runner inlet; η, Efficiency of the jet mechanism; ξ, The energy loss rate of the injection mechanism; E, the water flow specific energy at the jet outlet; E_c, the water flow specific energy at the nozzle inlet.

TABLE 1 | Model parameters.

Water Inlet Diameter *d*	**125 mm**
Nozzle outlet diameter d_0	43 mm
Jet outlet air domain d_1	130 mm
Water inlet area *s*	0.0116m^3

mechanism. Therefore, it is of great significance to study the eccentric jet of jet mechanism of the impingement turbine to improve the efficiency of the impingement turbine.

Research on gas-liquid two-phase free jets (Sun et al., 2021; Zhang et al., 2021; Ouyang et al., 2021; Zhang et al., 2021) is widely used in fluid mechanics calculations. However, most of them focus on the research fields of jet cutting technology and jet atomization (Li et al., 2019; Deng et al., 2016), and the research on jets ejected from nozzles in impingement turbines is still very limited. Li et al. (2003) studied the influence of nozzles of different shapes on the jet performance, Wei et al. (2001) analyzed the influence of jet interference on the efficiency of the runner, providing a basis for the selection and design of impingement turbines. The research on jet eccentricity is mostly the research on the eccentric jet of the pump (Yan and Long, 2010; Du, 2019)and the eccentricity of the needle valve in the injector (Guo et al., 2015). For the research on the eccentricity of the injection needle in the impingement turbine, foreign scholars In Jung, et al. (2019) studied the eccentricity of the injection needle of the impingement turbine, which caused the jet to spread and increased the loss of the nozzle. The quality has a significant effect, but there is no relevant research on the effect of eccentricity and efficiency characteristics.

In this paper, the jet mechanism of the impingement turbine is modeled by UG, and the jet flow under different eccentricities of the nozzle is calculated and analyzed based on FLUENT, To provide a reference for improving the efficiency of the impingement turbine. To study the influence of the eccentricity of the nozzle of the injection mechanism on the jet flow, according to the literature (Jung et al., 2019), it can be seen that the smaller flow rate has a greater impact on the eccentricity of the nozzle, and 20% opening, 40% opening, 60 opening, and 80% opening are selected., The model of injection mechanism with the eccentricity of 4.8% at 100% opening is verified and analyzed. Select 0, 0.22, 0.45, 1, 1.72, 3 mm eccentricity at 40% opening, that is, 0, 1, 2.1, 4.8, 8, 14% eccentricity. Calculate and discuss the influence of different eccentricities of the nozzle on the jet characteristics.

2 MODEL SETUP AND MESHING

2.1 Model Parameters

In this paper, the injection mechanism of the impingement turbine with the model CJC601-L-45/2 × 3.5 is used for research. The structural parameters of the model and the experimental data are shown in **Table 1**.

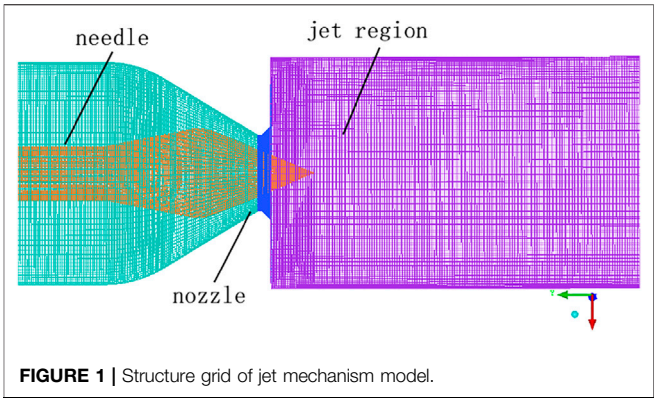

FIGURE 1 | Structure grid of jet mechanism model.

2.2 Meshing and Mesh Independence Verification

The purpose of fluid meshing is to realize the discretization of the fluid computational domain. The quantity and quality of the meshes will greatly affect the convergence and accuracy of the numerical calculation. The model in this paper is relatively simple, so the structured grid division method is adopted, which has the characteristics of good grid quality, short calculation time, and high calculation accuracy. The injection mechanism model was meshed by ICEM CFD, as shown in **Figure 1**.

To ensure the accuracy and efficiency of the calculation, it is necessary to verify the grid independence of the grid. The six grid division schemes of the injection model under normal conditions are shown in **Table 2**. Based on the FLUENT platform, the digital-analog calculation of the six grid division schemes is carried out, and the results are shown in **Figure 2**. It can be seen that with the increase of the number of grids, the maximum velocity of the jet mechanism is increasing, but after 2.631 million and the number of grids is increased, the increase of the speed does not exceed 0.78%, while the amount of calculation is greatly increased. Therefore, to save the calculation amount while ensuring the calculation accuracy, the fourth grid division scheme is selected, and the number of grids is 2.631 million.

3 COMPUTATIONAL FIELD SETTINGS

3.1 Model Settings

3.1.1 Fluid Basic Governing Equations

For incompressible fluids, the density is constant and the equation is as follows.

Continuity Equation

$$\frac{\partial(\rho v_i)}{\partial x_i} = 0 \tag{1}$$

Momentum equation

$$\rho\frac{Dv_i}{Dt} - \rho F_i - \frac{\partial p_{ij}}{\partial x_j} = 0 \tag{2}$$

TABLE 2 | Meshing scheme.

case	Case1	Case2	Case3	Case4	Case5	Case6
Number of grids ($\times 10^4$)	14.85	85.6	169.5	263.1	356.6	459.4

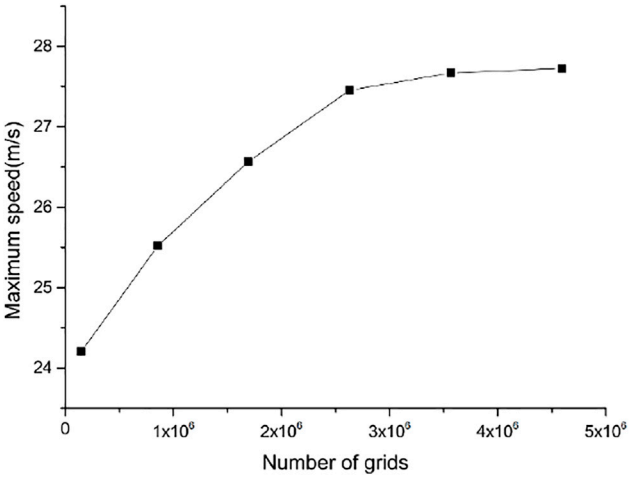

FIGURE 2 | Grid independence verification.

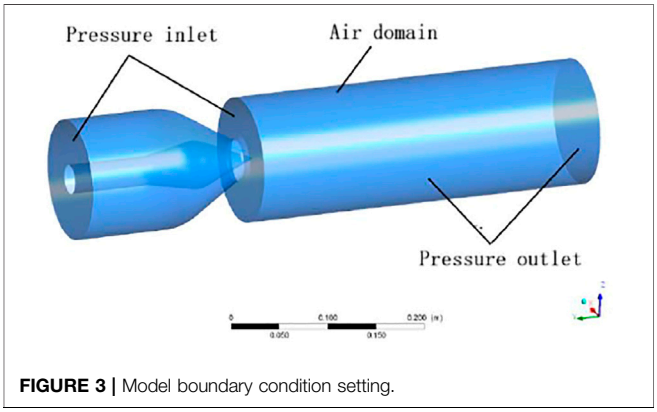

FIGURE 3 | Model boundary condition setting.

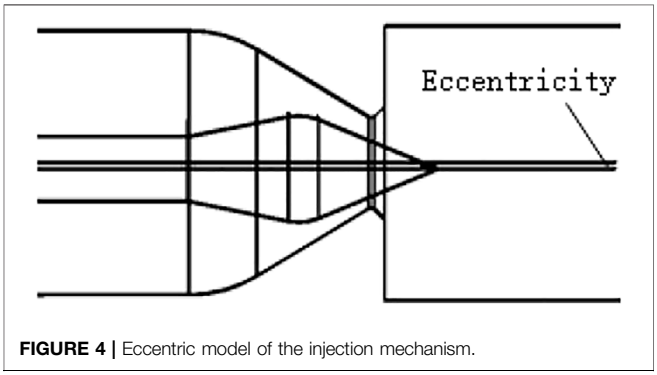

FIGURE 4 | Eccentric model of the injection mechanism.

Where ρ is the fluid density; $v_i\,(1 = 1, 2, 3)$ is the velocity component; $x_i, x_j\,(i, j = 1, 2, 3)$ represents each coordinate component; ρF_i is the mass force per unit volume; $divp = \frac{\partial p_{ij}}{\partial x_j}$ is the divergence of the stress tensor per unit volume.

3.1.2 VOF Multiphase Flow Model

At present, there are two numerical calculation methods for dealing with the multiphase flow, namely the Euler-Lagrange equation and the Euler-Eulerian equation. The calculation in this paper is that the water jet is injected into the air domain, and the motion of the particles is not involved, so the Euler-Eulerian multiphase flow model in which different phases are processed into an interpenetrating continuum is adopted. In FLUENT, the Euler-Eulerian multiphase flow model is divided into three types, namely the volume of the fluid model (VOF), the Euler model, and the mixture model. The free jet at the nozzle outlet is a two-phase flow of water and air (Ge et al., 2021a). In this paper, water and air are regarded as continuous phases, so the VOF multiphase flow model that can track the free liquid surface of the jet is adopted (Ge et al., 2021b). The model has the advantages of easy implementation, low computational complexity, and high precision. Its governing equation (Ge et al., 2021c) is as follows:

$$\rho = \alpha_1\rho_1 + \alpha_2\rho_2 \tag{3}$$

$$\mu = \alpha_1\mu_1 + \alpha_2\mu_2 \tag{4}$$

$$\alpha_1 + \alpha_2 = 1 \tag{5}$$

$$\frac{\partial}{\partial t}\left(\alpha_1\rho_1\right) + \nabla\cdot\left(\alpha_1\rho_1\overrightarrow{v_1}\right) = 0 \tag{6}$$

$$\frac{\partial}{\partial t}\left(\alpha_2\rho_2\right) + \nabla\cdot\left(\alpha_2\rho_2\overrightarrow{v_2}\right) = 0 \tag{7}$$

Where, subscripts 1 and 2 represent the gas phase and the water phase, respectively; ρ represents the physical density; α represents the volume fraction; $\vec{v}$ represents the average velocity.

3.1.3 *RNG* $k-\varepsilon$ Model

The turbulence model is the most widely used in engineering (Han et al., 2021). It includes three types: the standard model, the RNG model, and the achievable model. Compared with the standard model, the RNG model adds a condition to the equation and takes into account the turbulent vortex, which improves the accuracy, so this paper adopts higher confidence and accuracy in a wider range of flows. Accurate RNG model.

The turbulent kinetic energy and dissipation rate equations for the RNG $k-\varepsilon$ model are as follows:

$$\frac{\partial}{\partial t}\left(\rho k\right) + \frac{\partial}{\partial x_i}\left(\rho k u_i\right) = \frac{\partial}{\partial x_j}\left(\alpha_k u_{eff}\frac{\partial k}{\partial x_j}\right) + G_k + G_b - \rho\varepsilon - Y_M + S_k \tag{8}$$

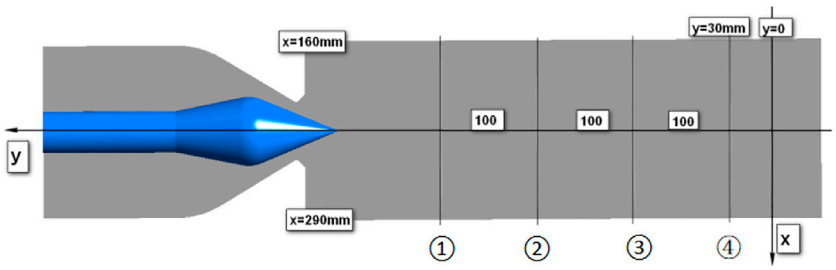

FIGURE 5 | Coordinate system and monitoring surface layout.

$$\frac{\partial}{\partial t}(\rho\varepsilon)+\frac{\partial}{\partial x_i}(\rho\varepsilon u_i)=\frac{\partial}{\partial x_j}\left(\alpha_\varepsilon u_{eff}\frac{\partial\varepsilon}{\partial x_j}\right)+C_{1\varepsilon}\frac{\varepsilon}{k}(G_k+G_{3\varepsilon}G_b) -C_{2\varepsilon}\rho\frac{\varepsilon^2}{k}-R_\varepsilon+S_\varepsilon \tag{9}$$

3.2 Boundary Conditions

The model boundary conditions are shown in **Figure 3**.

Inlet boundary conditions: the water inlet is set as the pressure inlet: the pressure is 0.49MPa, the jet inlet is the air domain, and the relative pressure is 0Pa.

Outlet boundary conditions: the outlet is also an air domain, set as a pressure outlet, and the relative pressure is 0Pa.

Wall: The no-slip boundary condition is used for the wall, and the standard wall function is used for the flow in the near-wall region.

3.3 Parameter Definition

(1) Define the eccentricity as the distance between the central axis of the needle and the central axis of the nozzle, as shown in **Figure 4** (the eccentricity in this paper is the radial direction of the needle). The coordinate system and monitoring surface layout are shown in **Figure 5**.

(2) The eccentricity is defined as the ratio of the eccentric distance to the nozzle radius, as in **Formula 10**, where l is the eccentric distance and d0 is the nozzle outlet diameter.

$$e=\frac{2l}{d_0} \tag{10}$$

(3) To reduce the computational resources, it can be seen from the literature (Li et al., 2003; Liu, 2005) that the jet area is generally set to be about 7 times the diameter of the nozzle outlet. According to the size of the test model used in this paper, 7.4 *d0* (y = 30 mm) is defined as the runner inlet.

(4) The pelton turbine is a turbine that uses the kinetic energy of water to do work. The water flow is accelerated through the nozzle and then injected into the atmosphere. Since the jet has no potential energy, all the energy of the water flow is converted into the kinetic energy of the water. Therefore, the theoretical velocity of the jet can be calculated from the head as:

$$v_c=\sqrt{2gH} \tag{11}$$

The specific energy loss of the injection mechanism is:

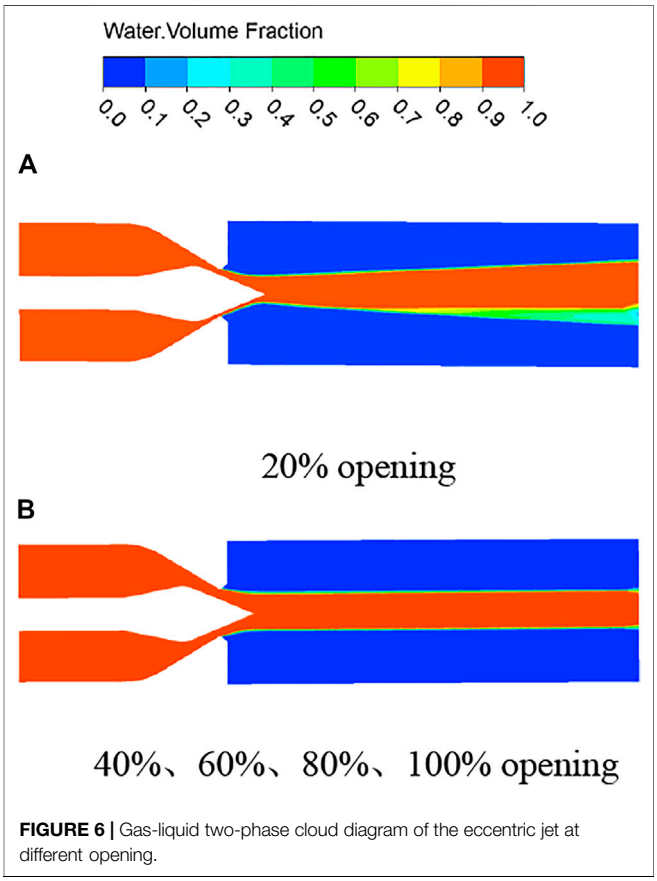

FIGURE 6 | Gas-liquid two-phase cloud diagram of the eccentric jet at different opening.

$$\Delta E=E_c-E \tag{12}$$

In the formula: E is the water flow specific energy at the jet outlet (runner inlet), and E_c is the water flow specific energy at the nozzle inlet.

The jet efficiency of this jet mechanism (Liu, 2005) can be defined as

$$\eta=\frac{E}{E_c}=\frac{v^2}{v_c^2} \tag{13}$$

In the formula: v is the jet outlet (runner inlet) velocity, and v_c is the theoretical runner inlet velocity value.

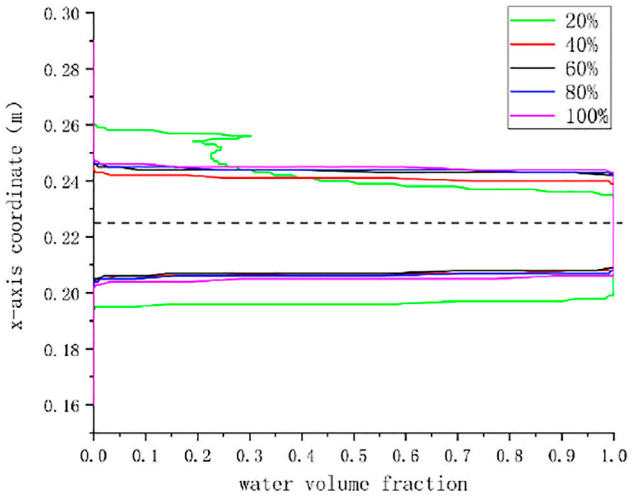

FIGURE 7 | The eccentric jet state on the z = 0 mm straight line on the y = 30 mm section under different openings.

The energy loss rate of the injection mechanism is:

$$\xi = 1 - \eta \tag{14}$$

(5) The jet eccentricity is defined as the ratio of the distance from the center of the outgoing water flow from the center axis of the model to the radius of the jet area obtained from the water volume fraction program.

3.4 Solve Settings

This paper is for the unsteady calculation of water-gas two-phase flow, and the time step is set to 0.001s. The solution method adopts the SIMPLE algorithm, which is a semi-implicit method for solving the pressure coupling equation and is also an algorithm generally adopted by various commercial CFD software. The discrete format adopts the first-order upwind discrete format. When setting the relaxation factor, set pressure to 0.3 and momentum to 0.2 to ensure convergence. Since both Fr and We of unsteady flow are relatively large, the influence of gravity and surface tension on the mainstream characteristics is small, so the influence of these forces is ignored in the calculation process in this paper (Ge et al., 2020).

4 ANALYSIS OF NUMERICAL SIMULATION RESULTS

4.1 Calculation Method Validation

It can be seen from the results of previous studies that the eccentricity of the spray needle has a significant effect on the flow at a small flow rate. In this paper, the flow rate is controlled by the opening of the nozzle, and the eccentricity of the nozzle at different openings is calculated to verify the accuracy of the model and calculation method in this paper. The injection models of 20, 40, 60, 80, and 100% opening under 4.8% eccentricity are selected for numerical calculation.

Figure 6 is the gas-liquid two-phase cloud diagram of the eccentric jet of the jet mechanism under different opening degrees, and the figure shows the flow state of water when the jet is stable. The gas-liquid two-phase diagrams are consistent at 40, 60, 80, and 100% opening, and the water flow is stable and symmetrical; but at 20% opening, the jet appears to diffuse significantly, and a piece of air doped with a large amount of air appears. area, which is consistent with the literature results. **Figure 7** shows the jet state of the runner inlet at different openings. The water volume fraction on the upper side is smaller at 20% opening, which corresponds to the lower side in the cloud diagram. Due to the serious water flow diffusion, some air is mixed in the middle, causing the water body a reduction in the number of points. It can be seen from the graph that the eccentricity of the nozzle has a greater influence on the small flow rate. With the increase of the jet opening, the curve gradually moves to the center, the two sides are gradually symmetrical, and the influence of the eccentricity on the jet gradually decreases.

Figure 8 is the velocity cloud diagram of the jet with a z = 0 mm section under three different openings of the selected jet mechanism. It can be seen from the figure that when the opening is 20%, the upper and lower boundaries of the jet velocity of the cross-section appear in the middle of a low-velocity area. This is because the development of the needle boundary layer affects the jet velocity, resulting in a low-velocity area in the middle. However, as the opening increases, the needle The influence of the boundary layer on the jet is gradually reduced, and the middle low-velocity area is gradually reduced; the upper and lower high-speed jet areas are different due to eccentricity, but due to different openings, the influence of eccentricity on the jet is different, and it is more obvious at small openings, while the smaller eccentricity has almost no effect on the jet at large openings; the tail diffusion is more serious at small openings, and the diffusion decreases gradually as the opening increases.

The shape of the jet can be seen from the program of the circular section, which reflects the influence of eccentricity on the shape of the jet. Due to the existence of the spray needle, the water flow shape of the jet outlet section should be annular, and there is a certain distance between the nozzle outlet and the runner inlet, and the annular water flow intersects to form a circular jet area. However, due to the influence of the eccentricity of the nozzle, the shape of the jet at several openings is different. At 100% opening, the shape of the jet is circular, and the influence of the eccentricity can be ignored. At 60% opening, the shape of the jet is close to a circle, but the shape deviation is large at 20% opening. With the continuous development of the jet, the diffusion is serious. Due to the influence of eccentricity, an irregular shape as shown in the figure is formed. It can be seen that the eccentricity has a great influence on the jet flow under the condition of small flow, but has almost no effect under the condition of large flow, which is in line with the previous research and verifies the accuracy of the research method in this paper.

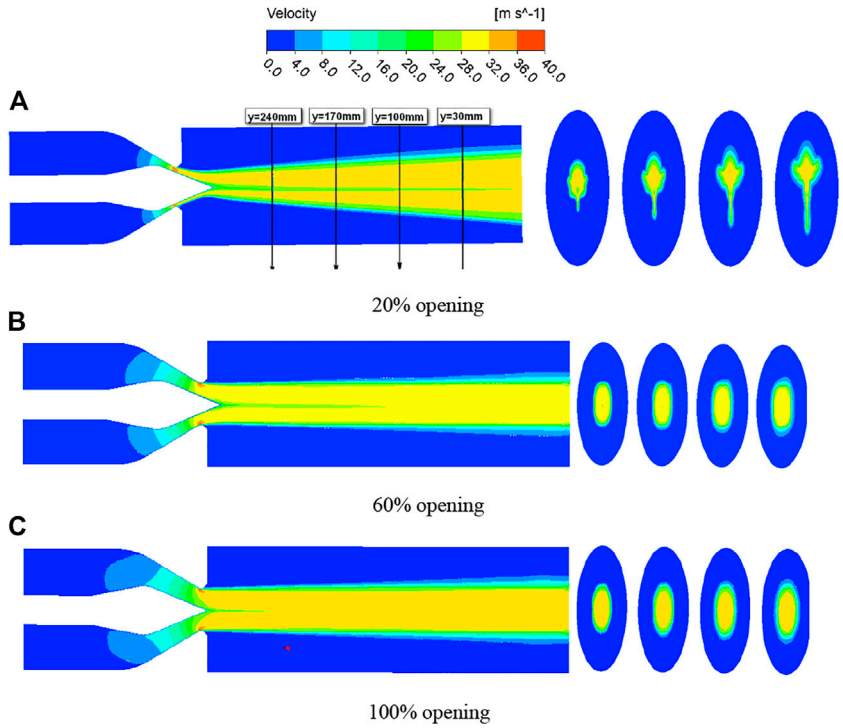

FIGURE 8 | Jet velocity cloud diagram at different opening degrees.

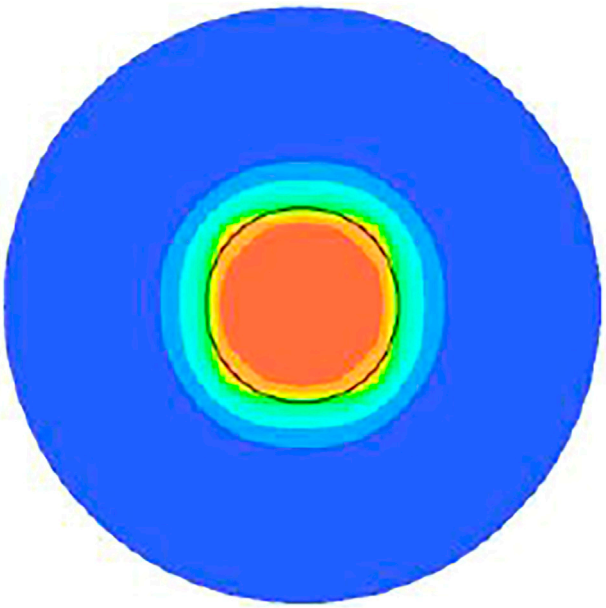

FIGURE 9 | Effective jet area.

4.2 Flow Characteristics at Different Eccentricities

The quality of the jet directly affects the rotation of the bucket, and the eccentricity of the jet will prevent all the water from hitting the bucket, thereby reducing the efficiency of the turbine and even causing the bucket to be damaged. To study the jet characteristics of the jet mechanism under different eccentricities, this paper selects the jet models with eccentricities of 0, 1, 2.1, 4.8, 8, and 14% at 40% opening for numerical calculation.

4.2.1 Efficiency and Energy Loss of Injection Mechanism

The loss of flow in the pipe caused by the sudden reduction of the nozzle outlet section, the friction loss of the nozzle, and the eccentricity of the spray needle will lead to the eccentricity of the jet so that the loss of water flow that cannot be completely shot on the bucket will lead to a decrease in the efficiency of the spray mechanism. To accurately reflect the efficiency of the eccentric injection mechanism, the average velocity of the central circular section should be selected as the runner inlet velocity. According to **Figure 9** it can be seen from the numerical results that the area enclosed by the black circle with the center as the dot and the radius of 22 mm is defined as the effective jet area, which can include the main velocity of the jet. Therefore, the average speed of the area is taken as the speed of the runner inlet.

The calculation conditions are that the nozzle opening is 40%, the water head is 49m, and the theoretical velocity is 31 m/s. The numerical calculation results are shown in **Table 3**.

Figure 10 shows the efficiency and energy loss rate of the jetting mechanism under different eccentricities. It can be seen from this that with the increase of the eccentricity of the needle, the jetting efficiency of the jetting mechanism is continuously decreasing. It decreases slowly before the eccentricity is 4.8%, and then decreases more quickly. It can

TABLE 3 | The efficiency and energy loss of the injection mechanism under different working conditions.

Eccentricity (%)	Surface Average Speed (m/s)	Efficiency of Injection mechanism (%)	Energy Loss rate (%)
0	29.90	93.03	6.97
1	29.82	92.53	7.47
2.1	29.78	92.28	7.72
4.8	29.64	91.42	8.58
8	29.24	88.97	11.03
14	27.38	78.01	21.99

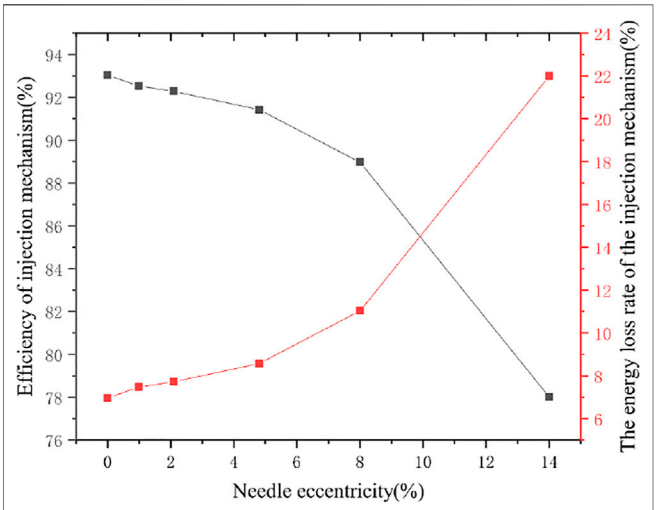

FIGURE 10 | The efficiency and energy loss rate of the injection mechanism under different eccentricities.

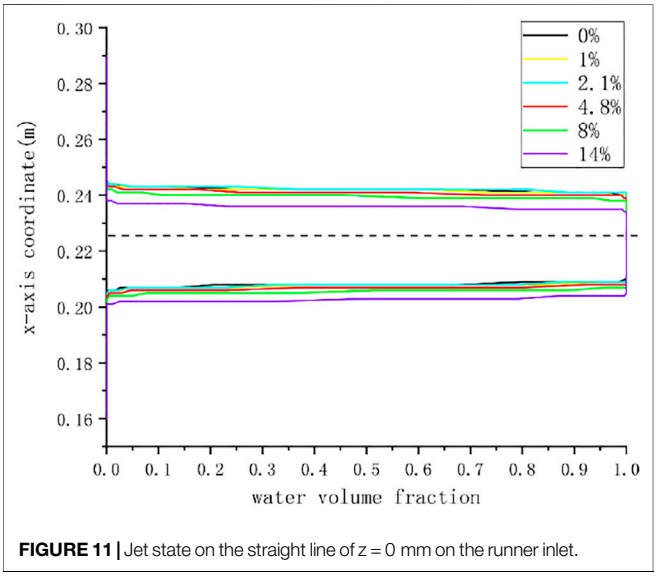

FIGURE 11 | Jet state on the straight line of z = 0 mm on the runner inlet.

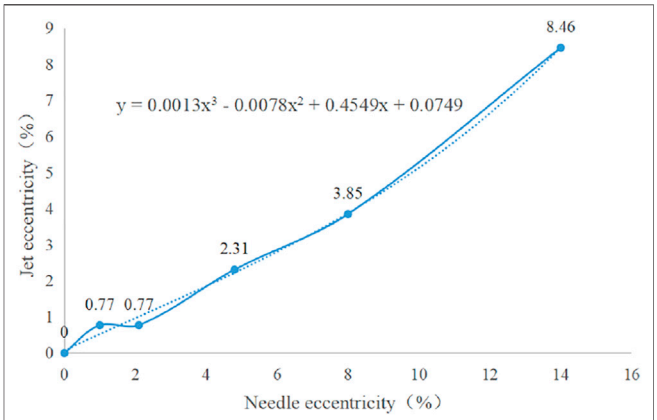

FIGURE 12 | Change of jet eccentricity.

be seen that the smaller eccentricity has little effect on the jet. It can be seen from the above that the shape of the jet has only a small change under the smaller eccentricity, but when the eccentricity is large, the shape of the jet changes greatly, resulting in The jet cannot be injected into the water bucket according to the predetermined trajectory, resulting in the loss of water flow energy. Therefore, with the increase of the eccentricity of the spray needle, the efficiency of the spray mechanism will decrease, and the energy loss will increase.

4.2.2 Jet Flow State Under Different Eccentricity

As shown in **Figure 11**, when the water flow reaches the bucket position under 0, 1, 2.1, 4.7, 8, and 14% eccentricity, the center eccentricity of the water column is 0, 0.5, 0.5, 1.5, 2.5, and 5.5 mm, respectively., the jet area is a cylindrical area with a diameter of 130mm, that is, the jet eccentricity is 0, 0.77, 0.77, 2.31, 3.85, and 8.46%, respectively. Compared with normal without eccentricity, with the increase of needle eccentricity, the jet eccentricity gradually increases, as shown in **Figure 12**. The increase of jet eccentricity will cause the water flow to fail to shoot on the water bucket completely, resulting in a decrease in the efficiency of the turbine. By fitting the trend line, the water flow eccentricity **formula (15)** that changes with the change of the eccentricity of the nozzle can be obtained. Because the eccentricity of the nozzle will not increase indefinitely, assuming that the nozzle is ideally attached to the other side of the nozzle outlet, the maximum eccentricity of the nozzle is 42%, and this situation is impossible, and a large eccentricity is easily affected. Found to be overhauled, so only needles with smaller eccentricities will have eccentric jets. Therefore, the eccentricity of 14% is relatively large. The curves fitted by several eccentricities in this paper can

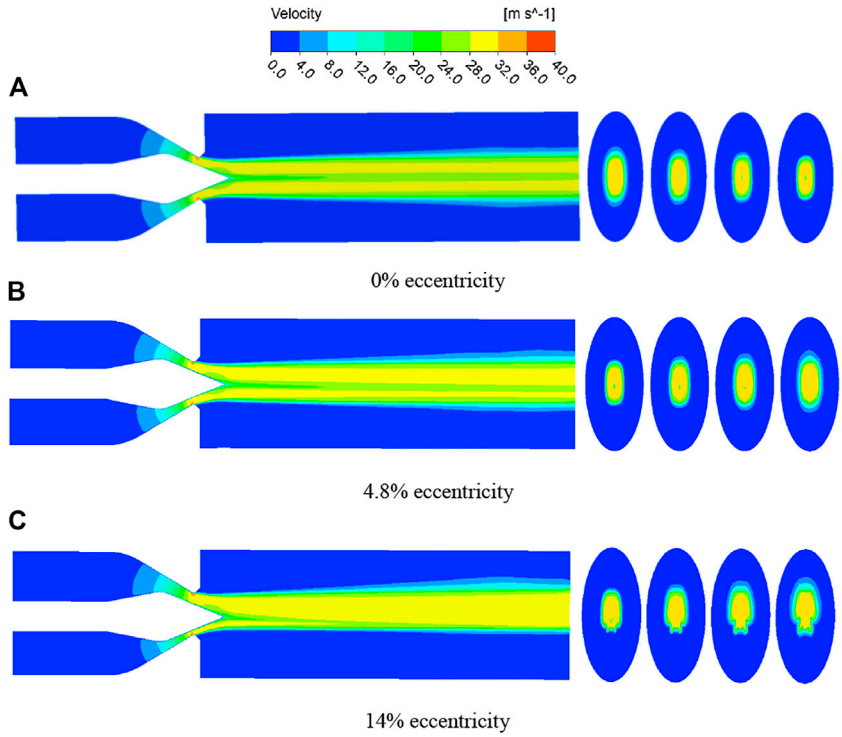

FIGURE 13 | Cloud diagram of jet velocity under different eccentricity.

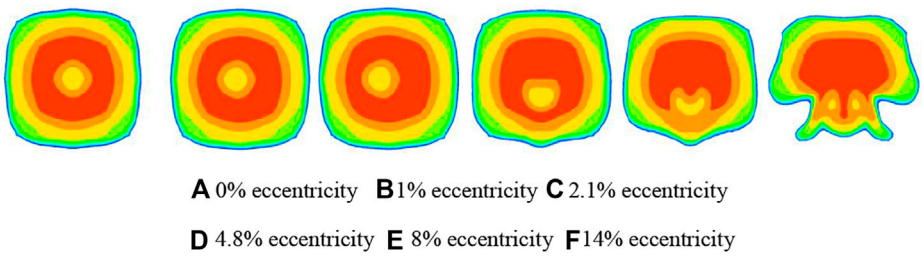

FIGURE 14 | Velocity cloud diagram of jet velocity greater than 20 m/s in y = 30 mm section under different eccentricity.

completely predict the eccentricity of jets with different eccentricities at 40% opening, which provides a basis for the design of the nozzle and bucket positions.

$$y = 0.0013x^3 - 0.0078x^2 + 0.4549x + 0.0749 \quad (15)$$

4.2.3 Speed Characteristics at Different Eccentricities

Figure 13 is the velocity cloud diagram of the jet under three different eccentricities of the selected jet mechanism. It can be seen from the cloud diagram that the jet is divided into two high-speed jets. Under normal conditions, the two jets are symmetrical, but in the case of eccentricity, the two jets are no longer symmetrical. The high-speed jet area on one side keeps getting narrower, while the other side keeps getting thicker, and the greater the eccentricity, the more serious the divergence of the tail, 14% of the eccentricity causes the water flow to concentrate almost entirely on one side. The low-velocity zone near the tip of the needle is due to the continuously developing boundary layer on the surface of the needle, which affects the velocity of the jet, resulting in a lower velocity at the center of the jet, but along the direction of the jet, the effect is decreasing (Zeng, 2018).

Figure 14 shows the program of jet velocity in the y = 30 mm section under different eccentricities. The high-speed jet area in the middle is all water phase, and the flow rate is high. The surrounding high-speed area is doped with a lot of air, and the flow rate is low. Therefore, the cloud image with a speed greater than 20 m/s is selected for analysis, and the shape of the jet can also be observed. Due to the influence of the acceleration of the nozzle outlet, the development of the boundary layer of the water flow on the sidewall of the nozzle and the nozzle will be inhibited, forming a

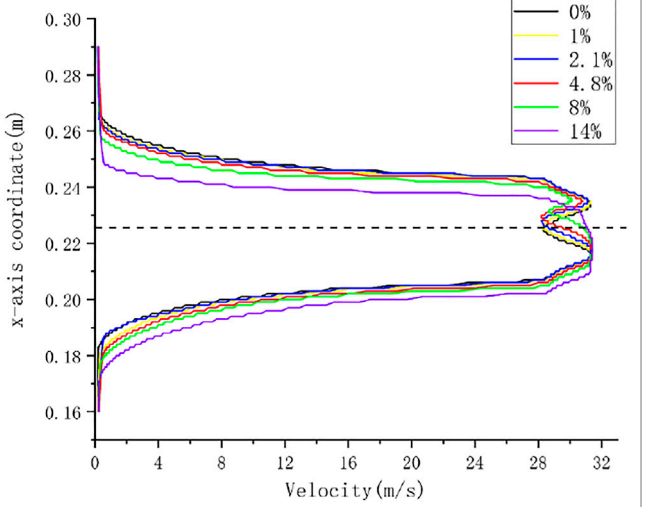

FIGURE 15 | Jet velocity on the straight line of z = 0 mm on the y = 30 mm section.

flow in the center of the ring, so there will be an area with a small speed in the middle of the cloud image.

However, due to the influence of the eccentricity of the spray needle, with the increase of the eccentricity, the shape of the water flow gradually changes and deviates from the center, and the area with a small intermediate speed will also move in the direction of the deviation of the spray needle, forming **Figures 14C–E** The effect of moving downwards, the high-speed area above will also move downwards closely. When the eccentricity is serious, the speed of the side with the larger water flow will also be greater, and the high-speed area will follow the middle low-speed area downwards. When moving, it will pass through the low-velocity region, forming the deformed shape of **Figure 14F**. When it hits the bucket, the water flow in the high-speed area will be offset, resulting in waste of water flow energy, thereby reducing the efficiency of the turbine.

Figure 15 shows the velocity distribution of the jet to the cross-section of the water column on the surface of the bucket, from which we can see the effect of different eccentricities on the velocity that can be jetted to the bucket section. When the eccentricity is small, the velocity distribution is almost the same up and down. With the increase of the eccentricity, the high-speed area of the water flow gradually deviates from the center and moves in the negative direction of the x-axis, and the low-speed area in the middle gradually disappears. The upper and lower velocity distributions are no longer consistent. The results of cloud map 14 are consistent.

5 CONCLUSION

For the Pelton turbine, the quality of the jet mechanism is the key factor that determines the operation performance of the turbine. Based on the fluent software, this paper uses the VOF multiphase flow model and the RNG turbulence model to study and analyze the eccentric jet characteristics of the jet mechanism under different eccentricities of the needle and different openings. The conclusions are as follows:

(1) The eccentricity has a great influence on the jet flow under the condition of small flow but has almost no effect under the condition of large flow, which is in line with the previous research conclusions and verifies the accuracy of the research method.
(2) With the increase of the eccentricity of the needle, the jet is asymmetrical. When the eccentricity of the jet is small, the jet is concentrated and symmetrical, and when the eccentricity is large, the jet is dispersed; At 40% opening, when the water flow reaches the water bucket position with 0, 1, 2.1, 4.7, 8, and 14% needle eccentricity, the jet eccentricity in the center of the water column is 0, 0.77, 0.77, 2.31, 3.85, and 8.46% respectively. Through curve fitting, the water flow eccentricity formula that changes with the change of the needle eccentricity is obtained: $y = 0.0013x^3 - 0.0078x^2 + 0.4549x + 0.0749$.
(3) With the increase of the eccentricity of the needle, the jet shape of the inlet section of the runner changes and gradually becomes an irregular shape, the efficiency of the injection mechanism gradually decreases, and the energy loss gradually increases; before the eccentricity of 4.8%, the efficiency decreases relatively slowly. After 4.8% eccentricity, the jet shape changes greatly, and the rate of efficiency decrease is accelerated.

DATA AVAILABILITY STATEMENT

The original contributions presented in the study are included in the article/Supplementary Material, further inquiries can be directed to the corresponding author.

AUTHOR CONTRIBUTIONS

HJ: Writing—original draft. ZJ: Formal analysis and editing. CD: Data curation. GX: review. GF: Formal analysis. XB: Investigation. YZ: Supervision.

FUNDING

Project supported by the following funding: the Central Universities fundamental research funds (2015B02814); the National Natural Science Foundation of China (51339005).

REFERENCES

Deng, H., Feng, F., Wu, X., Yu, X., and Zuo, Y. (2016). Experimental Research on the Impinging Atomization of Gel Propellant[J]. *Acta Armamentarii* 37 (04), 612–620.

Du, Q. (2019). Application Analysis of Eccentric Jet Pump in Field Production Logging[J]. *China Pet. Chem. Stand. Qual.* 39 (08), 20–21.

Ge, X., Sun, J., Cai, J., Zhang, L., Zhang, H., Wang, J., et al. (2021a). Study of the Erosion Influence on Bucket Profile and Performance of Pelton Turbine[J/OL]. *Proc. CSEE* 41 (21), 7391–7403. doi:10.13334/j.0258-8013.pcsee.202212

Ge, X., Sun, J., Li, Y., Wu, D., Zhang, L., and Hua, H. (2020). Numerical Simulation of silt Erosion Characteristics of an Injector of Pelton Turbine[J]. *Shuili Xuebao* 51 (12), 1486–1494.

Ge, X., Sun, J., Li, Y., Zhang, L., Deng, C., and Wang, J. (2021b). Erosion Characteristics of Sediment Diameter and Concentration on the Runner of Pelton Turbines[J]. *Proc. CSEE* 41 (14), 5025–5033. doi:10.13334/j.0258-8013.pcsee.201843

Ge, X., Sun, J., Zhou, Y., Cai, J., Zhang, H., Zhang, L., et al. (2021c). Experimental and Numerical Studies on Opening and Velocity Influence on Sediment Erosion of Pelton Turbine Buckets. *Renew. Energ.* 173, 1040–1056. 1040-1056, ISSN 0960-1481. doi:10.1016/j.renene.2021.04.072

Guo, B., Xiao, Y., Rai, A., Zhang, J., and Liang, Q. (2020). *Sediment-laden Flow and Erosion Modeling in a Pelton Turbine injector[J]*. Renewable Energy, 162.

Guo, L., Yang, L., Zhou, Z., Song, Y., and Fu, L. (2015). Simulation Analysis on Flow Characteristics inside Nozzle Effected by Eccentric Displacement of Needle[J]. *Mod. Vehicle Power* (03), 20–26+55.

Han, F., Lin, Z., Xiao, Y., and Kubota, T. (2005). Study on Geometry Prediction of Unsteady Nozzle Jet Flow[J]. *Water Resour. Power* (03), 14–16+90.

Han, Y., Zhou, L., Bai, L., Shi, W., and Agarwal, R. (2021). Comparison and Validation of Various Turbulence Models for U-bend Flow With a Magnetic Resonance Velocimetry Experiment. *Phys. Fluids* 33, 125117.

Jung, H., Soo Kim, Y., Ho Shin, D., Taek Chung, J., and Shin, Y. (2019). *Influence of Spear Needle Eccentricity on Jet Quality in Micro Pelton Turbine for Power generation[J]*. Energy, 175.

Li, G., Wei, C., Liu, J., and Xu, P. (2003). CFD Technique of Nozzle Jet Flow in Pelton Turbine[J]. *Water Resour. Power* (01), 71–72+79.

Li, J., Lei, F., Zhou, L., and Yang, A. (2019). Effects of Misaligned Impingement on Atomization Characteristics of Impinging Jet Injector[J]. *J. Aerospace Power* 34 (10), 2280–2293.

Liu, J. (2005). *Study on Internal Flow Simulation and Performance of Pelton Turbine[D]*. Huazhong University of Science and Technology.

Mulu, B. G., Jonsson, P. P., and Cervantes, M. J. (2012). Experimental Investigation of a Kaplan Draft Tube – Part I: Best Efficiency Point[J]. *Appl. Energ.* 93. doi:10.1016/j.apenergy.2012.01.004

Ouyang, T., Su, Z., Yang, R., Wang, Z., Mo, X., and Huang, H. (2021). Advanced Waste Heat Harvesting Strategy for marine Dual-Fuel Engine Considering Gas-Liquid Two-phase Flow of Turbine[J]. *Energy*, 224.

Park, Y., Park, H., Ma, Z., You, J., and Shi, W. (2021). Multibody Dynamic Analysis of a Wind Turbine Drivetrain in Consideration of the Shaft Bending Effect and a Variable Gear Mesh Including Eccentricity and Nacelle Movement[J]. *Front. Energ. Res.* 8. doi:10.3389/fenrg.2020.604414

Sun, J., Ge, X., Cai, J., Li, L., Zhao, L., Zhang, L., et al. (2021). Analysis of Pressure Pulsation Characteristics of Solid-Liquid Two-phase Flow in Bulb Turbine[J]. *Proc. CSEE* 41 (22), 7692–7702. doi:10.13334/j.0258-8013.pcsee.202362

Wang, G., Liu, Y., and Liu, Z. (2021). Research and Application of Cold Productivity Formula of Horizontal Well in the Power-Law Fluid Heavy Oil Reservoir. *Front. Energ. Res.* 9, 792427. doi:10.3389/fenrg.2021.792427

Wei, C., Han, F., Xu, P., and Zhang, Z. (2001). The Study of Jet Interference in Pelton Turbine[J]. *J. Huazhong Univ. Sci. Tech.* (04), 82–84.

Yan, H., and Long, X. (2010). Numerical Simulation of the Influence of Eccentricity of Nozzle on Jet Pump Performance[J]. *Eng. J. Wuhan Univ.* 43 (01), 34–37.

Yang, R. (2009). Development Trend of Selection and Application of Turbines for High-Head Power Stations[J]. *China Water Power & Electrification* (07), 32–34.

Zeng, C. (2018). *Research on the Internal Flow Characteristic and Flow Interference in the Pelton Turbine[C]*. Tsinghua University.

Zhang, H., Li, W., He, X., Liu, N., and Jin, J. (2021). Numerical Simulation of Gas-Liquid Two-phase Flow in Horizontal Pipeline with Different Diameters[J]. *J. Drainage Irrigation Machinery Eng.* 39 (05), 488–494.

Zhang, H., Yuan, S., Deng, F., Liao, M., Chen, M., and Si, Q. (2021). Characteristics of Gas-Liquid Two-phase Flow in Centrifugal Pump Based on the Dimensionless Method[J]. *J. Drainage Irrigation Machinery Eng.* 39 (05), 451–456+463.

Conflict of Interest: HJ is employed by China Eastern Route Corporation of South-to-North Water Diversion; XB and GF were employed by Harbin Electric Machinery Factory Co., Ltd.

The remaining authors declare that the research was conducted in the absence of any commercial or financial relationships that could be construed as a potential conflict of interest.

frontiers | Frontiers in Energy Research

ORIGINAL RESEARCH
published: 08 April 2022
doi: 10.3389/fenrg.2022.865885

Influence of Geometric Parameters of Tiny Blades on the Shroud of a Centrifugal Pump on the Cavitation Suppression Effect

Weiguo Zhao[1,2]* *and Zhongliang Zhou*[1]

[1]College of Energy and Power Engineering, Lanzhou University of Technology, Lanzhou, China, [2]Key Laboratory of Fluid Machinery and Systems of Gansu Province, Lanzhou University of Technology, Lanzhou, China

In this paper, the effect of adding non-connected forms of tiny blades with different parameters of radial position, width, and length to the shroud of the impeller on the cavitation performance of a centrifugal pump is researched. A modified SST k-ω turbulence model combined with the Zwart–Gerber–Belamri cavitation model is used for numerical simulation of the model pump. The results show that the numerical prediction of the original pump agrees well with the experimental results. Adding tiny blades with different radial positions, widths, and lengths has a small effect on the pump head and efficiency under each working condition. Adding tiny blades near the impeller inlet has better suppression of cavitation in the initial stage, and adding tiny blades in the middle and backward positions has a better suppression effect on all stages of cavitation. There is an optimal tiny blade width to make the cavitation suppression effect optimal, and the optimal width of the model in this study is 3/4 of that of the main blade. The effect of a tiny blade length on cavitation performance is small. The existence of tiny blades slightly increases the turbulent kinetic energy in the low-turbulent kinetic energy region near the impeller inlet, significantly reduces the turbulent kinetic energy in the high-turbulent kinetic energy region near the outlet, and reduces the overall pressure pulsation main frequency amplitude during pump operation, making its operation more stable.

Keywords: centrifugal pump, low specific speed, cavitation suppression, tiny blades, geometric parameters, the shroud of the impeller, numerical simulation

OPEN ACCESS

Edited by:
Ling Zhou,
Jiangsu University, China

Reviewed by:
Florent Ravelet,
Arts et Metiers Institute of Technology, France
Alin Bosioc,
Politehnica University of Timişoara, Romania

***Correspondence:**
Weiguo Zhao
zhaowg@zju.edu.cn

Specialty section:
This article was submitted to Process and Energy Systems Engineering, a section of the journal Frontiers in Energy Research

Received: *30 January 2022*
Accepted: *28 February 2022*
Published: *08 April 2022*

Citation:
Zhao W and Zhou Z (2022) Influence of Geometric Parameters of Tiny Blades on the Shroud of a Centrifugal Pump on the Cavitation Suppression Effect. Front. Energy Res. 10:865885. doi: 10.3389/fenrg.2022.865885

1 INTRODUCTION

As fluid-transfer power equipment, centrifugal pumps are widely used in the national life and economic production and play an important role. Cavitation is a flow phenomenon that is difficult to avoid during the operation of centrifugal pumps. Its generation is due to the process of cavitation generation, development, and collapse when the local pressure in the liquid medium decreases to the critical pressure. Cavitation can interfere with the normal flow of the flow field. In serious cases, it will reduce the normal energy conversion inside the impeller (Brennen, 1994), accompanied by noise and vibration (Chudina, 2003; Li et al., 2018), which will reduce the hydraulic performance of the pump. Moreover, the bubble collapse process will produce an extremely high local pressure and temperature and high-speed microjets, which can cause erosion of the overflow components (Brujan and

Matsumoto, 2012; Wijngaarden, 2016; Dular et al., 2019) and greatly reduce the service life of the pump. Therefore, the research of cavitation suppression in centrifugal pumps is a popular field.

Many scholars have done a lot of research work on centrifugal pump cavitation suppression. Luo et al. and Pei et al. (Luo et al., 2008; Pei et al., 2017) improved the hydraulic and cavitation performance of the pump by optimizing the geometric parameters of the impeller. Adding inducers to the impeller inlet (Acosta, 1958), inducing partial high-pressure fluid injection into the inlet from the pump outlet (Wong et al., 1965; Cui et al., 2019), etc., are methods to suppress cavitation by increasing the impeller inlet pressure. Zhao and Zhao, (2017) placed obstacles at suitable locations on the pressure surface of the blade to inhibit cavitation development. Wei et al. (Wei et al., 2021) improved the fluid dynamics at the inlet of centrifugal pumps by adding a deflector plate, which contributed to the suppression of cavitation instability in high-speed centrifugal pumps. Kurokawa, (2011) designed J-slots in the inlet section wall of centrifugal pumps with inducers to suppress various anomalous flow phenomena such as cavitation by controlling the angular momentum of the main flow. Zhao et al., (2020) studied the method of opening slits on the blade of a centrifugal pump, leading the fluid from the high-pressure region to the low-pressure region and effectively restraining the development of cavitation. (Zhu and Chen, 2012) added a small vice blade to the leading edge of the blade and improved the cavitation performance and hydraulic efficiency by taking advantage of the inflow characteristics and the automatic pressure balancing effect of the clearance channel. Slotting on the pressure side of the leading edge of the blades induces a relatively high pressure, which suppresses the growth of the bubble volume within the impeller (Zhao et al., 2018). A proper inlet diameter of the splitter blade can effectively avoid flow obstruction at the impeller inlet and vortex cavitation in the blade channel (Zhang et al., 2014).

Cavitation occurs at the location of the lowest pressure, usually slightly behind the suction surface of the blade inlet and close to the hub of the impeller (Guan, 2011). Therefore, in this paper, different schemes were designed successively and the effect of adding non-connected forms of tiny blades on the shroud of the impeller with different radial positions, widths, and length parameters on the cavitation performance of a centrifugal pump was investigated. Moreover, by the numerical simulation method, the changes of the bubble volume, flow field structure, turbulent kinetic energy distribution, pressure distribution, and the pressure pulsation amplitude of the main frequency in the impeller under different cavitation margins were compared and analyzed.

2 NUMERICAL METHODS

2.1 Governing Equations

The governing equations for fluid motion are the Reynolds averaged Navier–Stokes equations.

Continuity equation:

$$\frac{\partial \rho_m}{\partial t} + \frac{\partial (\rho_m u_i)}{\partial x_i} = 0 \tag{1}$$

Momentum equation:

$$\frac{\partial (\rho_m u_i)}{\partial t} + \frac{\partial (\rho_m u_i u_j)}{\partial x_j} = -\frac{\partial p}{\partial x_i} + \frac{\partial}{\partial x_j}\left[(\mu + \mu_t)\left(\frac{\partial u_i}{\partial x_j} + \frac{\partial u_j}{\partial u_i} - \frac{2}{3}\frac{\partial u_k}{\partial x_k}\delta_{ij}\right)\right] \tag{2}$$

where ρ_m is the mixture density; t is the time; u_i, u_j, and u_k are the velocity components; p is the local pressure; μ is the viscosity; μ_t is the turbulence viscosity; and δ_{ij} is the Kronecker symbol.

Here, the mixture density ρ_m is defined as

$$\rho_m = \alpha_v \rho_v + \rho_l (1 - \alpha_v) \tag{3}$$

where α is the volume fraction of one component. The subscripts v and l refer to the vapor and liquid components, respectively.

2.2 Turbulence Model

The SST k-ω turbulence model (Menter, 1994) was used to close the Reynolds-averaged Navier–Stokes equations. The SST k-ω turbulence model takes the k-ω model in the boundary layer region of the wall and the k-ε model in the region away from the boundary layer, which combines the advantages of both models and can predict flow separation on smooth surfaces more accurately

$$\frac{\partial (\rho_m k)}{\partial t} + \frac{\partial (\rho_m k u_i)}{\partial x_i} = \frac{\partial}{\partial x_j}\left(\Gamma_k \frac{\partial k}{\partial x_j}\right) + G_k - Y_k + S_k \tag{4}$$

$$\frac{\partial (\rho_m \omega)}{\partial t} + \frac{\partial (\rho_m \omega u_i)}{\partial x_i} = \frac{\partial}{\partial x_j}\left(\Gamma_\omega \frac{\partial \omega}{\partial x_j}\right) + G_\omega - Y_\omega + D_\omega + S_\omega \tag{5}$$

$$\mu_t = \rho_m \frac{k}{\omega} \tag{6}$$

where G_k and G_ω are the generating terms of turbulent kinetic energy k and dissipation rate ω, respectively; Γ_k and Γ_ω are the effective diffusion coefficients of k and ω, respectively; Y_k and Y_ω are the dissipations of k and ω, respectively; S_k and S_ω are user-defined source phases; and D_ω is the cross-diffusion term.

However, the uncorrected SST k-ω turbulence model will overpredict the viscosity of the two-phase mixture of vapor and liquid phases during cavitation, resulting in inaccurate prediction of bullbe shedding (Reboud and Dellanoy, 1994; Zheng et al., 2018). In this paper, a modified SST k-ω turbulence model is adopted to reduce the turbulent viscosity in order to capture the flow state of the cavitation flow more accurately. The turbulent viscosity in the region where cavitation occurs is reduced by modifying the density function $f(\rho_m)$ as follows:

$$\mu_t = f(\rho_m)\frac{k}{\omega} \tag{7}$$

$$f(\rho_m) = \rho_v + \frac{(\rho_m - \rho_v)^n}{(\rho_l - \rho_v)^{n-1}};\ n \geq 1 \tag{8}$$

where n is taken as 10 (Coutier-Delgosha et al., 2003; Ji et al., 2014).

The variation curve of the $f(\rho_m)$ function is shown in **Figure 1**. It can be seen from the figure that the corrected density is

significantly reduced in the mixing region of the two-phase flow, thereby reducing the turbulent viscosity.

2.3 Cavitation Model

The Zwart–Gerber–Belamri cavitation model (Zwart et al., 2004) based on the Rayleigh–Plesset equation was used, neglecting the surface tension term and the second-order time derivative term, assuming a constant gas nucleus density in the fluid domain, and focusing on the effect of the change in the radius of the bubble during the initial generation and development of cavitation. It is suitable for calculating the transient characteristics of cloud cavitation within a centrifugal pump, and the equation is

$$\frac{\partial(\rho_m f_v)}{\partial t} + \frac{\partial(\rho_m u_i f_v)}{\partial x_i} = m^+ - m^- \tag{9}$$

$$m^+ = F_{vap}\frac{3\alpha_{nuc}(1-\alpha_v)\rho_v}{R_b}\sqrt{\frac{2}{3}\frac{p_v - p}{\rho_l}};\ p \le p_v \tag{10}$$

$$m^- = F_{cond}\frac{3\alpha_v\rho_v}{R_b}\sqrt{\frac{2}{3}\frac{p - p_v}{\rho_l}};\ p > p_v \tag{11}$$

where f_v is the vapor-phase mass fraction, m^+ is the evaporating phase, m^- is the condensing phase, F_{vap} is the evaporation coefficient, F_{cond} is the condensation coefficient, R_b is the vacuole radius, α_{nuc} is the volume fraction of cavitation nuclei, p is the flow field pressure, and p_v is the saturated vapor pressure. Based on the experience of previous research (Zwart et al., 2004; Ji et al., 2013), $F_{vap} = 50$, $F_{cond} = 0.01$, $R_b = 1 \times 10^{-6}$ m, $\alpha_{nuc} = 5 \times 10^{-4}$, and saturated vapor pressure $p_v = 3169$ Pa at 25°C.

3 RESEARCH MODEL AND PRELIMINARY LOCATION SCHEME DESIGN

3.1 Research Model

In this paper, a low-specific speed centrifugal pump with a specific speed of ns = 32 was adopted as the research object, which mainly consists of five parts, such as the inlet section, impeller, volute, shroud, and hub. The rated head $H_0 = 4.2$ m, the rated flow rate $Q_0 = 8.6$ m3/h, and the rated speed $n = 500$ rpm. The main geometric parameters of the model pump are as follows: the inlet section diameter $D_j = 107$ mm, the impeller inlet diameter $D_i = 90$ mm, the impeller outlet diameter $D_2 = 310$ mm, the impeller outlet width $b_2 = 12$ mm, the blade inlet diameter $D_b = 80$ mm, the blade inlet angle $\beta_1 = 37°$, the blade outlet angle $\beta_2 = 37°$, blades are cylindrical blades, the blade number $Z = 6$, and the blade thickness $\delta = 4$ mm, as shown in **Figure 2A**, where D_X, L, W, and δ_1 are the inlet diameter, length, width, and thickness of the tiny blades, respectively.

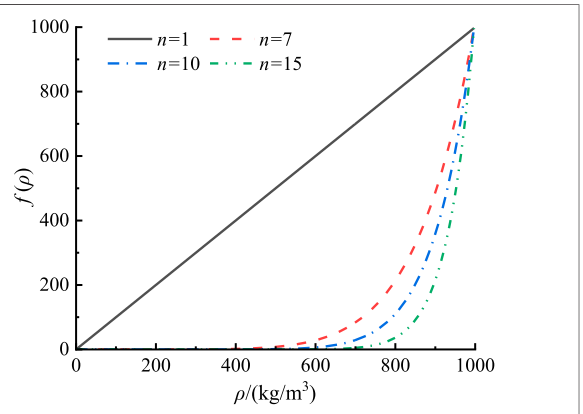

FIGURE 1 | Modified function of turbulent viscosity.

3.2 Preliminary Location Scheme Design

According to previous studies (Zhang et al., 2015), the design of splitting blades in the impeller of a centrifugal pump will have a certain suppression and optimization effect on cavitation but will have a greater impact on the hydraulic performance of the centrifugal pump. In order to minimize the influence on the external characteristics of the centrifugal pump and to reduce the disturbance of the flow in the impeller, the effect of arranging tiny blades of a non-connected form with different radial positions, widths, and length parameters on the inner surface of the shroud of the impeller on the cavitation performance is investigated. When the splitting blades are located in the middle of the flow channel, the pressure distribution of the flow channel of the impeller conforms to the general principle of the pressure distribution of the centrifugal pump, and the inlet diameter of the splitter blade has the greatest impact on the performance. Therefore, the middle position of the tiny blade should be determined first (He et al., 2006; Yuan et al., 2008). The shape of the tiny blade is the same as that of the corresponding position of the main blade. The length L of the tiny blade is 1/8 of the length of the main blade, and the width W and thickness δ_1 of the tiny blade are 1/2 of the main blade. The number of the tiny blades is the same as the quantity of the main blade, and the inlet diameter of the tiny blade is D_x. First, five location schemes are designed, as shown in **Table 1**.

4 GRID GENERATION

ICEM CFD software was used to discretize the hexahedral structured mesh of the inlet section, impeller, front and rear cavities, and volute of the centrifugal pump model, as shown in **Figure 3A, B**. In order to improve the calculation accuracy, the grid was locally densified on the walls of each part of the model. The calculation domain of the Scheme A1 model was divided into four groups of grids with different numbers to verify the grid independence, which was used to exclude the influence of the number of grids on the error of the calculation results, as shown in **Table 2**. From the calculated results, it can be seen that the relative error of the head is within 1% as the number of meshes increases, and finally, the number of meshes of all calculated models is discrete into a number of meshes comparable to Mesh4 for simulation.

Since different turbulence models have different requirements on the grid density near the wall, in order to

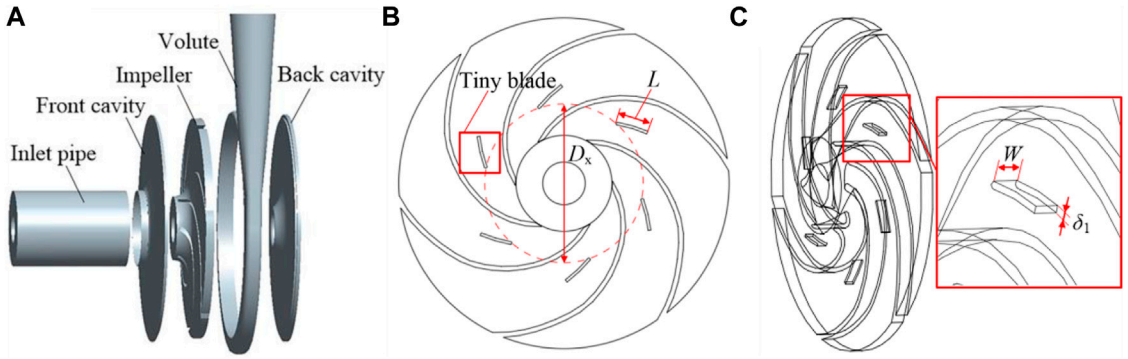

FIGURE 2 | (A) Geometric model of the centrifugal pump. **(B,C)** Schematic diagram of geometric parameters such as length, inlet diameter, width, and thickness of tiny blades.

TABLE 1 | Radial position scheme of tiny blades.

Location schemes	A0	A1	A2	A3	A4
D_x/(mm)	—	80	114.7	151.6	189.1

ensure that the grid density near the wall can accurately capture the flow in the boundary layer, it is necessary to analyze the Y^+ value of the near wall. Y^+ is defined as

$$Y^+ = \frac{\Delta n\sqrt{\tau_\omega/\rho}}{\nu} \tag{12}$$

where Δn is the distance between the two mesh nodes closest to the wall and τ_ω is the wall shear stress.

In this study, the modified SST k-ω turbulence model is selected. The requirements of the k-ω model for the mesh quality of the near-wall region can be satisfied when Y^+ is less than 100 (Li et al., 2012). The maximum Y^+ value of the impeller models with small blades arranged is 15, as shown in **Figure 3C**.

5 BOUNDARY CONDITION SETTING

ANSYS CFX software was used for numerical simulation. The main boundary conditions are set as follows: pressure inlet and

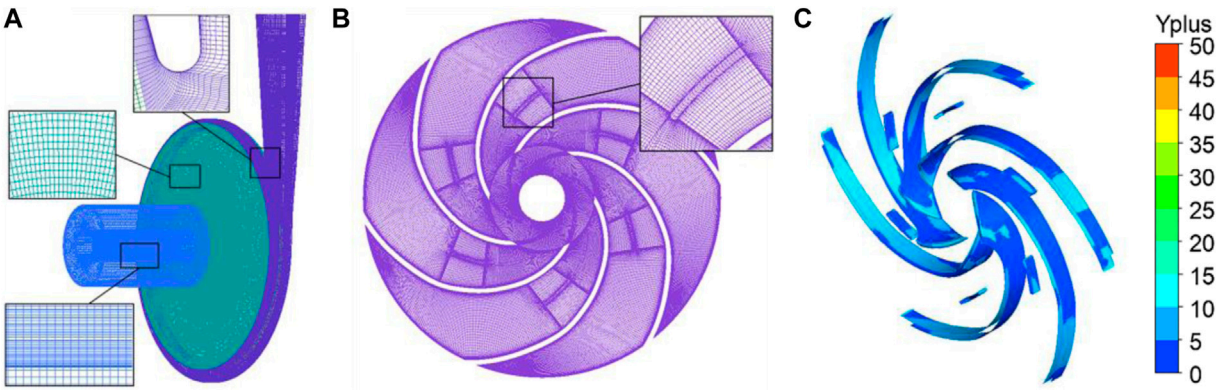

FIGURE 3 | (A,B) Grid of calculation domains. **(C)** Y^+ distribution of blades.

TABLE 2 | Mesh independence analysis.

Mesh	Inlet /10^4	Volute /10^4	Impeller /10^4	Front cavities /10^4	Back cavities /10^4	Total mesh /10^4	Head /m
Mesh1	18.7	24.0	82.2	18.2	15.2	163.4	4.552
Mesh2	18.7	24.0	135.3	18.2	15.2	211.5	4.476
Mesh3	22.7	35.5	135.3	29.9	23.3	246.8	4.531
Mesh4	22.7	35.5	233.6	29.9	23.3	345.1	4.528

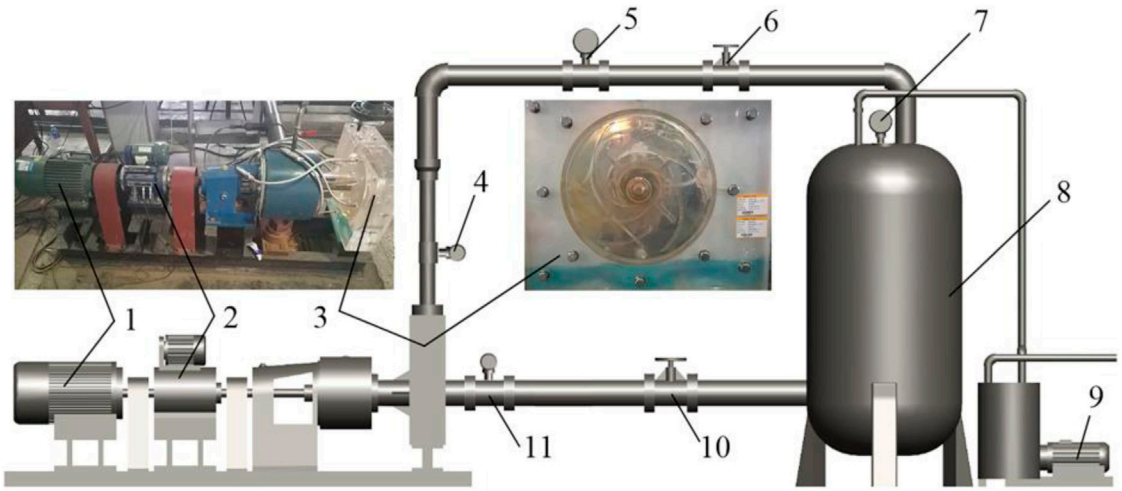

FIGURE 4 | Sketch map of the centrifugal pump closed test bench (1, electric motor; 2, torque meter; 3, visual centrifugal pump; 4, outlet pressure sensor; 5, electromagnetic flow meter; 6, outlet valve; 7, vacuum gauge; 8, cavitation tank; 9, liquid ring vacuum pump; 10, inlet valve; 11, inlet pressure sensor).

mass flow outlet. The impeller domain was set as the rotating domain, and the others were the static domains. The two outer surfaces of the hub and shroud were set as rotating wall surfaces, and the rest were isothermal and non-slip wall surfaces. In the steady calculation, the dynamic static interface was set to the frozen rotor. In the unsteady calculation, the dynamic static interface was set as the transient rotor stator. In the process of solving, the advection scheme adopted the high-resolution format, and the transient scheme adopted the second-order backward Euler difference format. The two-phase medium calculated by the simulation was water and water vapor at 25°C. The volume fractions of the liquid and vapor phases at the inlet were set to 1 and 0, respectively. The reference pressure of the calculation domain was 0 Pa, the saturated vapor pressure was 3,169 Pa, and the convergence accuracy was set to 1×10^{-5}. In the simulation, cavitation occurs in the centrifugal pump by continuously reducing the inlet pressure. First, the steady calculation is carried out, and then, the steady calculation result is taken as the initial value for unsteady calculations. For unsteady calculations, the time step was taken as $\Delta t = 0.001$ s; that is, every 3° rotation of the impeller is a time step. Then, each time step was iteratively calculated 20 times, and finally, a convergence result was saved every 15° rotation. The total number of calculation steps was 600 steps, and the last calculation stable rotation period was selected for unsteady characteristic analysis.

TABLE 3 | Simulation results.

	P_i	101,325	6,000	4,000	3,700
A0	***H***	4.51	4.51	4.51	3.36
	Va	0.0049	6.21	20,145	3,42,080
A1	***H***	4.49	4.49	4.54	2.39
	Va	0.0040	2.74	23,510	5,63,000
	Vr	—	–55.80%	16.70%	64.58%
A2	***H***	4.49	4.50	4.51	3.47
	Va	0.0040	0.62	21,536	3,00,470
	Vr	—	–90.06%	6.90%	–12.16%
A3	***H***	4.49	4.49	4.51	3.71
	Va	0.0041	1.65	18,970	2,53,140
	Vr	—	–73.37%	–5.83%	–26.00%
A4	***H***	4.49	4.49	4.50	3.67
	Va	0.0041	1.27	19,026	2,62,200
	Vr	—	–79.60%	–5.55%	–23.35%

6 SIMULATION ALGORITHM VERIFICATION AND PRELIMINARY RESULT ANALYSIS

6.1 Simulation Algorithm Verification

The external characteristics and cavitation performance tests of the original model centrifugal pump were completed on the visualized closed centrifugal pump test platform in the Key Laboratory of Fluid Machinery and Systems of Gansu Province, and the test system is shown in **Figure 4**. The medium of test is clear water at room temperature (25°C). The test is conducted in accordance with the national standard GB/T 3216-2016 "Hydraulic Performance Acceptance Test for Rotary Power Pumps Level 1, Level 2, and Level 3". The tested curves of external characteristics and cavitation characteristics of the centrifugal pump are shown in **Figure 5A,B**, respectively. From **Figure 5A**, it can be seen that the simulated values of head and efficiency of the original pump under each flow rate condition are basically consistent with the trend of the experimental values. The maximum error between the simulated value of the original pump head and the experimental value occurs when Q/Q_0 is 1.3, and the error is 3.25%. Also, the original pump efficiency simulation value is higher than the experimental value, and the maximum efficiency error is 5.68%. These errors are caused by measurement errors, manufacturing errors of the test pump, and insufficient consideration of wear-ring clearance

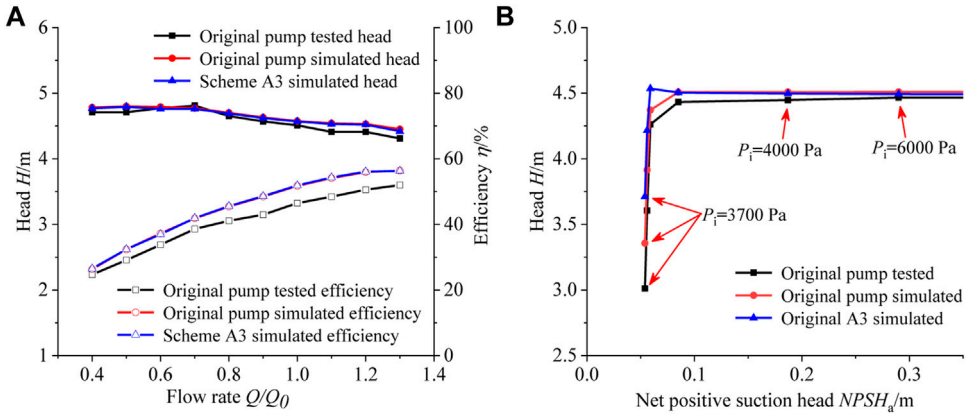

FIGURE 5 | (A) Hydraulic performance and **(B)** cavitation performance curves of the centrifugal pump.

and surface roughness in the simulation calculation model. It can be seen from **Figure 5B** that the simulated value of the original pump is slightly larger than the experimental value under different cavitation margins, and the simulated value is in close agreement with the experimental value. Therefore, the reasonableness and accuracy of the simulation algorithm for the hydraulic performance and cavitation performance of the centrifugal pump were verified.

6.2 Preliminary Location Scheme Results and Analysis

Numerical simulations of external characteristics and cavitation performance were carried out for the original pump model and four radial position scheme models at the design flow rate Q_0, respectively, and the calculation results are shown in **Table 3**, where P_i is the centrifugal pump inlet pressure, Pa; H is the head, m; V_a is the volume of cavitation in the impeller, mm^3; and V_r is the percentage change in cavitation volume compared with the original impeller at the same inlet pressure. When the centrifugal pump inlet pressure P_i = 6,000 Pa ($NPSH_a$ = 0.290 m), it is the initial stage of cavitation; when P_i = 4,000 Pa ($NPSH_a$ = 0.085 m), it is the development stage of cavitation; and when P_i = 3,700 Pa ($NPSH_a$ = 0.054 m), it is the serious stage of cavitation.

From the data in **Table 3**, it can be seen that when the pump inlet pressure P_i = 101,325 Pa, the head H of schemes A1–A4 is slightly reduced compared with that of the original pump A0; when P_i = 6,000 Pa, the head H of schemes A1–A4 is slightly reduced compared with that of the original pump A0, but the bubble volume V_a of schemes A1–A4 becomes smaller compared with that of A0, indicating that schemes A1–A4 all have the effect of cavitation suppression, the suppression effect is obvious, and the maximum reduction of cavitation volume of the A2 scheme was 90.06%; when P_i = 4,000 Pa, the H of schemes A1–A4 do not change much, but V_a of schemes A1 and A2 increase slightly compared with that of A0, indicating that the cavitation development is promoted. V_a of schemes A3 and A4 decreased compared with that of A0, indicating that the cavitation development is suppressed; when P_i = 3,700 Pa, H of scheme A1 decreased more compared with that of A0, and H the other three schemes were higher than that of A0. The bubble volume of scheme A1 was larger than that of scheme A0, and those of the other three schemes were all lower than that of scheme A0, indicating that A1 promotes cavitation at this time, while A2, A3, and A4 all inhibited the development of cavitation.

After comprehensive analysis, the cavitation volume in the impeller of scheme A3 was reduced at each selected inlet pressure point (cavitation incipient to cavitation severe stage), with a maximum reduction of 73.37%, and the head was the highest at the lowest inlet pressure point P_i = 3,700 Pa, which was 10.4% higher than that of the original pump. Compared with the simulated value of the external characteristics of the original pump, the hydraulic performance of scheme A3 at

TABLE 4 | Scheme of tiny blade width.

Width schemes	A0	B1	A3	B2	B3	B4	B5
W	—	1/4 *b*	1/2 *b*	5/8 *b*	3/4 *b*	7/8 *b*	1*b*

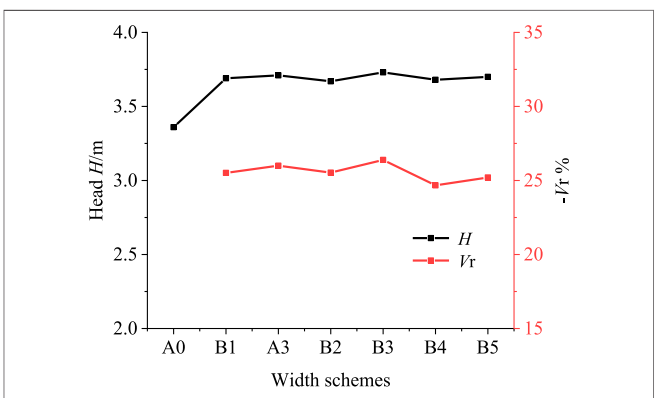

FIGURE 6 | Head and percentage reduction of bubble volume, $NPSH_a$ = 0.054 m.

different operating points changes less, as shown in **Figure 5A**, and reduces the critical cavitation allowance point, as shown in **Figure 5B**. After comprehensive comparison, it can be concluded that A3 has the best comprehensive effect on cavitation suppression.

7 FURTHER WIDTH SCHEME DESIGN AND RESULT ANALYSIS

7.1 Width Scheme Design

The preliminary scheme studied the influence of the radial position parameters of the tiny blades on the cavitation performance and hydraulic performance, and numerical simulations were carried out at the design flow rate of Q_0. The results showed that the radial position of the tiny blades of scheme A3 has the best comprehensive suppression effect on the cavitation of the centrifugal pump, and the influence on the hydraulic performance of the centrifugal pump is small. Next, based on the location of this scheme, the effect of the width parameter of the tiny blade on the cavitation performance and hydraulic performance of the centrifugal pump was studied. Five additional schemes with tiny blade widths are designed, in which the tiny blade thickness remains unchanged. W represents the tiny blade width, and b is the main blade width at the scheme A3 radial position. The design scheme is shown in **Table 4**.

7.2 Effect of Width Parameters on Performance

Figure 6 depicts the percentage reduction in head and bubble volume for different tiny blade width schemes at $NPSH_a$ = 0.054 m. It can be seen that compared with the original pump, the addition of different widths of tiny blades increased the head after breakage and reduced the volume of bubbles, and all schemes improved the cavitation performance of the centrifugal pump. With the gradual increase in the width of the tiny blade, the change trend of the percentage reduction in the volume of the bubble is consistent with the change trend of the head, showing a trend of first increase and then decrease. It can be seen that there is an optimal width parameter for the cavitation suppression effect. As far as scheme B3 (the tiny blade width is 3/4 of the width of the same radial position of the main blade) is concerned, its head is the highest, 3.73 m, 11% higher than that of the original pump, and the smallest volume of the bubble is 26.39% less than that of the original pump. Next, the optimal width of scheme B3 will be selected for analysis of the internal flow field.

7.3 Analysis of The Internal Flow Field of The Width Scheme

7.3.1 Vapor Volume Fraction Contour

Figure 7 shows the contour of the isosurface of the steam volume fraction (α_v = 10%) in the impeller at different cavitation margins. Analysis of the figure shows that the bubbles first appear near the inlet of the impeller blades, and as the cavitation margin decreases, the volume of the bubbles gradually increases and spreads toward the outlet of the flow channel. The existence of bubbles seriously obstructs the normal flow in the flow channel. Compared with the original impeller, after adding tiny blades, when $NPSH_a$ = 0.290 m, the bubble volume in the impeller of scheme B3 decreased by 84.42%. When $NPSH_a$ = 0.085 m, the bubble volume in the B3 impeller decreased by 5.73%. When $NPSH_a$ = 0.054 m, the bubble volume in the B3 impeller was reduced by 26.39%. After adding the tiny blade, the bubble volume in the impeller under different

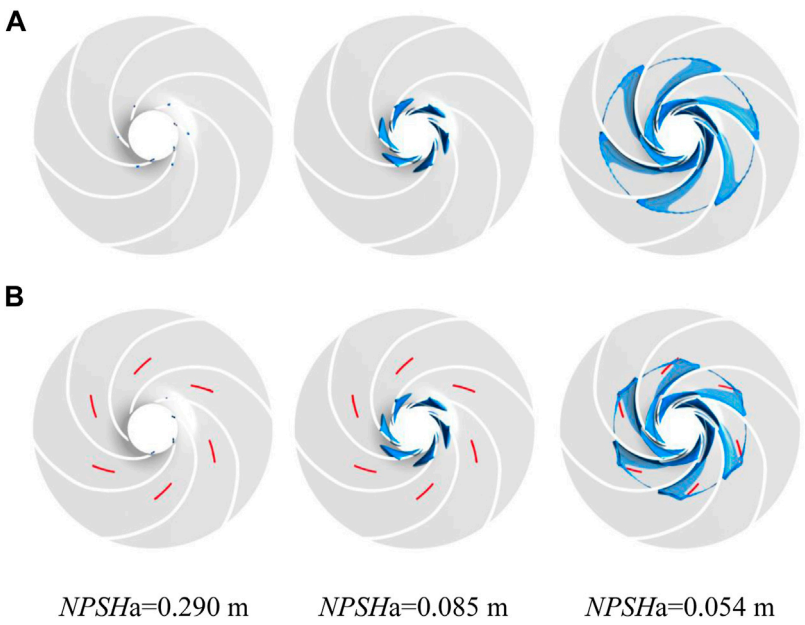

FIGURE 7 | Vapor volume fraction distribution of the impeller: **(A)** original impeller and **(B)** B3 impeller.

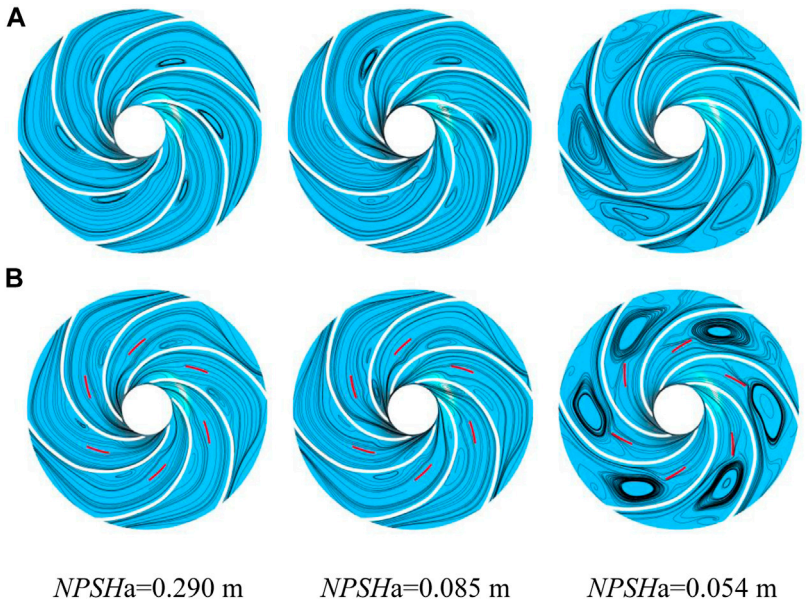

FIGURE 8 | Distribution of Streamlines: **(A)** original impeller and **(B)** B3 impeller.

cavitation margins is significantly reduced, which effectively suppresses the occurrence and development of cavitation and improves the cavitation performance of the centrifugal pump.

7.3.2 Flow Field Structure

Figure 8 shows the flow distribution in the middle section of the impeller at different cavitation margins. Analysis of the figure shows that at each stage of cavitation, vortices are generated in each flow channel of the impeller, and the existence of vortices hinders the normal flow of the fluid, and as the cavitation margin decreases, the vortices move toward the outlet direction, the intensity and the scale of vortices increase, and the flow becomes more turbulent. After the shroud of the impeller increases the tiny blades, in the initial and development stages of cavitation, the vortex intensity is significantly reduced, the flow loss is reduced, and the existence of tiny blades plays a role in combing the flow field structure. However, in the cavitation severe stage, the tiny blades make the vortex intensity enhanced. This is because in the serious cavitation stage, there are many bubbles in the impeller, the two-phase flow is extremely complex, and the vortex is behind the tiny blade. The tiny blade does work on the fluid flowing through it, the fluid kinetic energy increases, the fluid with increased kinetic energy accelerates the rotation speed of the vortex when flowing through the edge of the vortex, and there is sudden diffusion of the channel after flowing through the small blade.

8 FINAL LENGTH PARAMETER SCHEME DESIGN AND RESULT ANALYSIS

8.1 Length Parameter Scheme Design

The previous group of schemes studied the effect of the tiny blade width parameter on the cavitation performance and hydraulic performance of the centrifugal pump, and it was found that the tiny blades width of scheme B3 has the best effect on cavitation suppression and less effect on the hydraulic performance of the centrifugal pump. Next, with the tiny blade width (W = 3/4 b) of scheme B3 as the basis, we continued to control the tiny blade inlet diameter constant for a deeper study and to study the influence of tiny blade length parameters on the performance of centrifugal pumps and design as shown in **Table 5**, with three groups of length schemes for research, where L represents the length of the tiny blades and l represents the length of the main blade.

8.2 Effect of Length Parameters on Performance

Figure 9 depicts the head and cavitation volume reduction percentages for different tiny blade length schemes at $NPSH_a$ = 0.054 m. From the figure, it can be seen that under different cavitation margins, compared with the original pump A0 scheme, with the length change of the tiny blades, their hydraulic performance changes less and the cavitation suppression effect is similar to that of scheme B3, indicating that the length parameter of the tiny blades has less influence on the cavitation performance. Since scheme C1 has the shortest length of 5 mm but the hydraulic performance and cavitation performance are also better in all stages of

TABLE 5 | Tiny blade length schemes.

Length schemes	A0	A3	C1	C2	B3	C3
W	—	1/2 b	3/4 b	3/4 b	3/4 b	3/4 b
L/(mm)	—	1/8 l	5	1/16 l	1/8 l	1/4 l

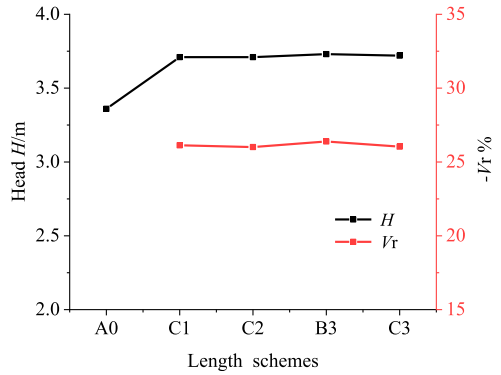

FIGURE 9 | Head and percentage reduction of vacuole volume, $NPSH_a$ = 0.054 m.

cavitation, scheme C1 is chosen next for impeller internal flow field analysis.

8.3 Analysis of the Internal Flow Field of the Width Scheme

8.3.1 Bubble Volume Analysis

The bubble volume, V_{cav}, is defined as

$$V_{cav} = \sum_{i=1}^{N} \alpha_{v,i} V_i \tag{13}$$

where N is the total number of control units in the impeller; $\alpha_{v,i}$ is the volume fraction of the vapor phase in control unit i; and V_i is the volume of control unit i.

Figure 10 shows the variation of the bubble volume inside the impeller at the last rotation cycle at different cavitation margins. The results show that at the initial stage of cavitation, the bubble volume curve fluctuates up and down with time, showing a clear unsteady characteristic. However, as the cavitation margin decreases, the bubble volume in the impeller increases, and the bubble volume continues to fluctuate with the rotation of the impeller, but the fluctuation is relatively small. Scheme C1 shows a significant decrease in the volume of the bubble in the impeller compared with the original impeller at the same cavitation margins. At the initial stage of cavitation with a cavitation margin of $NPSH_a$ = 0.290 m, the average volume of bubbles in the original impeller and scheme C1 impeller during the rotation cycle was 6.21 and 0.98 mm^3, respectively, and the volume of bubbles in the C1 impeller was reduced by 84.15%; at the stage of cavitation development with a cavitation margin of $NPSH_a$ = 0.085 m, the volume of bubbles in the original impeller and C1 impeller during the rotation cycle was 20,145 mm^3 and 18,791 mm^3, respectively, and the C1 bubble volume was reduced by 6.72%; at the cavitation severe stage $NPSH_a$ = 0.054 m, the bubble volumes of the original impeller and C1 impeller during the rotation cycle were 3,42,080 and 2,52,360 mm^3, respectively, and the C1 bubble volume was reduced by 26.23%. It can be found that the tiny-blade scheme is particularly effective in suppressing cavitation during the initial and severe stages of cavitation.

8.3.2 Turbulent Kinetic Energy Distribution

Figure 11 shows the distribution of turbulent kinetic energy in the middle section of the impeller. The magnitude of the turbulent kinetic energy represents the turbulent intensity. As shown in **Figures 7**, **11**, at the initial and developing stages of cavitation, cavitation is mainly generated near the inlet of the impeller. The arrangement of tiny blades can increase the turbulent energy near the inlet, and in the low-turbulent kinetic energy region, which also increases its turbulent intensity, the increased turbulent energy is still small. Moreover, the turbulent flow has the characteristics of pressure and velocity pulsation as well as the characteristics of high momentum and fast transfer, thus suppressing the initial and developmental stages of cavitation. When the cavitation develops to the severe stage, the turbulent kinetic energy on the pressure surface of the main blade in front of the tiny blade increases slightly, and the high-turbulent kinetic energy area behind the tiny blade near the outlet position decreases significantly. The turbulent dissipation loss decreases, and the hydraulic performance improves, as shown in **Figure 10**, when $NPSH_a$ = 0.054 m.

8.3.3 Flow Field Structure

Figure 12 depicts the streamline distribution in the middle section of the impeller at different cavitation margins. It can be seen from **Figures 8**, **12** that the longer tiny blades of scheme B3 weaken the strength and scale of the vortices in the flow channel during the cavitation initial and development stages. However, after the

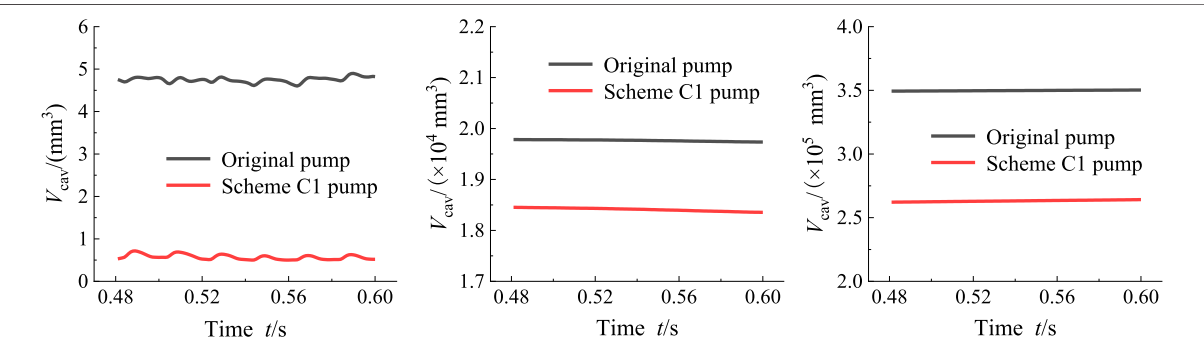

FIGURE 10 | Cavitation volume under different $NPSH_a$.

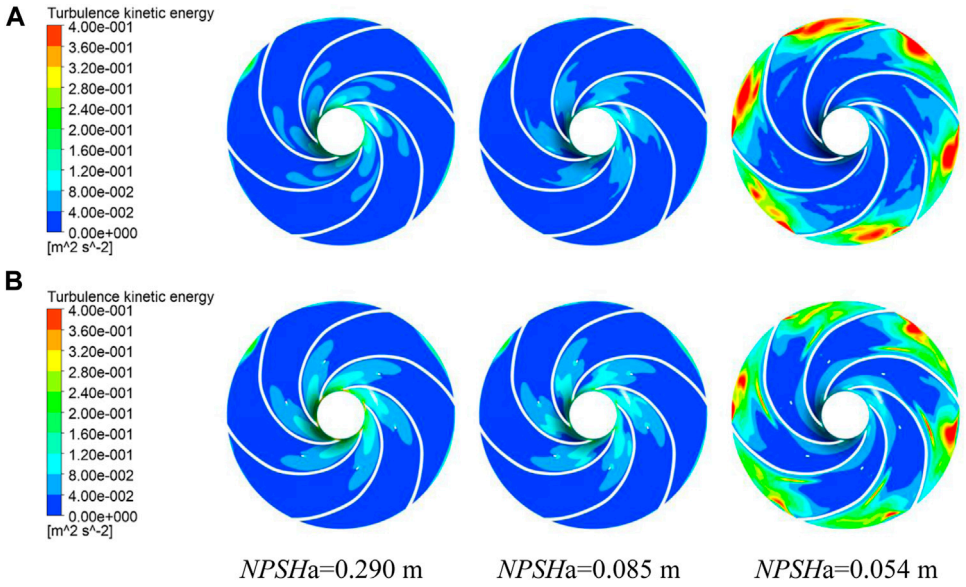

FIGURE 11 | Turbulent kinetic energy distribution in the middle section of the impeller: **(A)** original impeller and **(B)** B3 impeller.

shortening of the tiny blade, compared with the original impeller, the length of the tiny blade of scheme C1 is only 5 mm, and its ability to confine and comb the fluid is weakened, so the intensity and scale of the vortex in the impeller of scheme C1 have less change compared with the original impeller but have a slight tendency to enhance, indicating that the shorter tiny blade has a certain disturbing effect on the flow field structure, especially near the blade inlet. However, it can be seen from **Figure 10** that the shorter, tiny blade scheme C1 still significantly reduces the volume of cavitation in the impeller. In the severe cavitation stage, the vortex intensity in the impeller is significantly weaker in scheme C1 compared to the flow field structure of scheme B3 but slightly enhanced compared to the original impeller flow field structure. This is due to the reduced work capacity of the flowing fluid after the shortening of the small

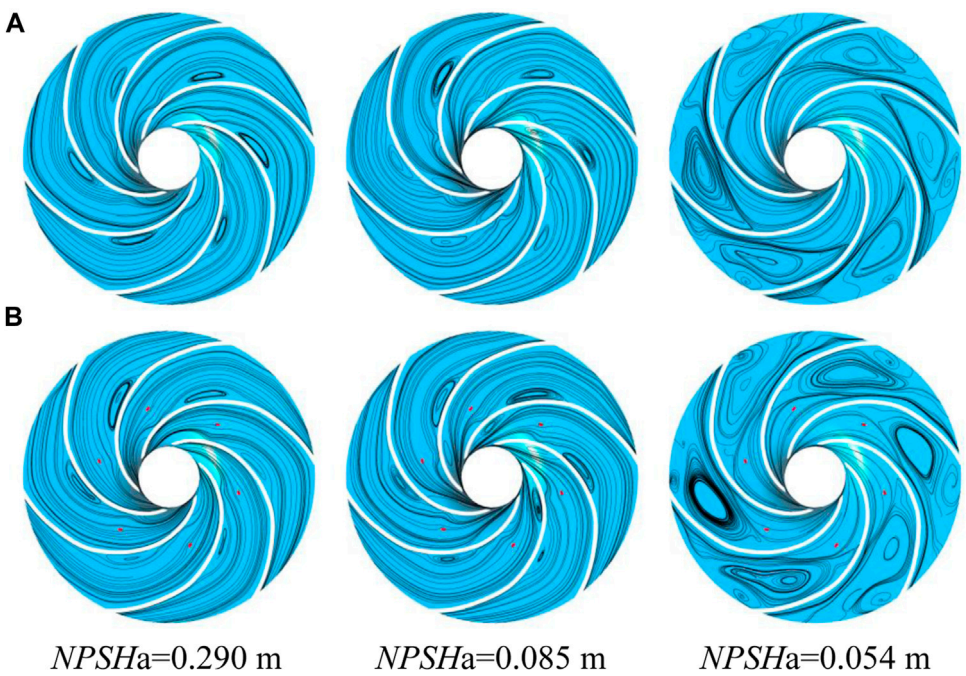

FIGURE 12 | Distribution of streamline: **(A)** original impeller and **(B)** B3 impeller.

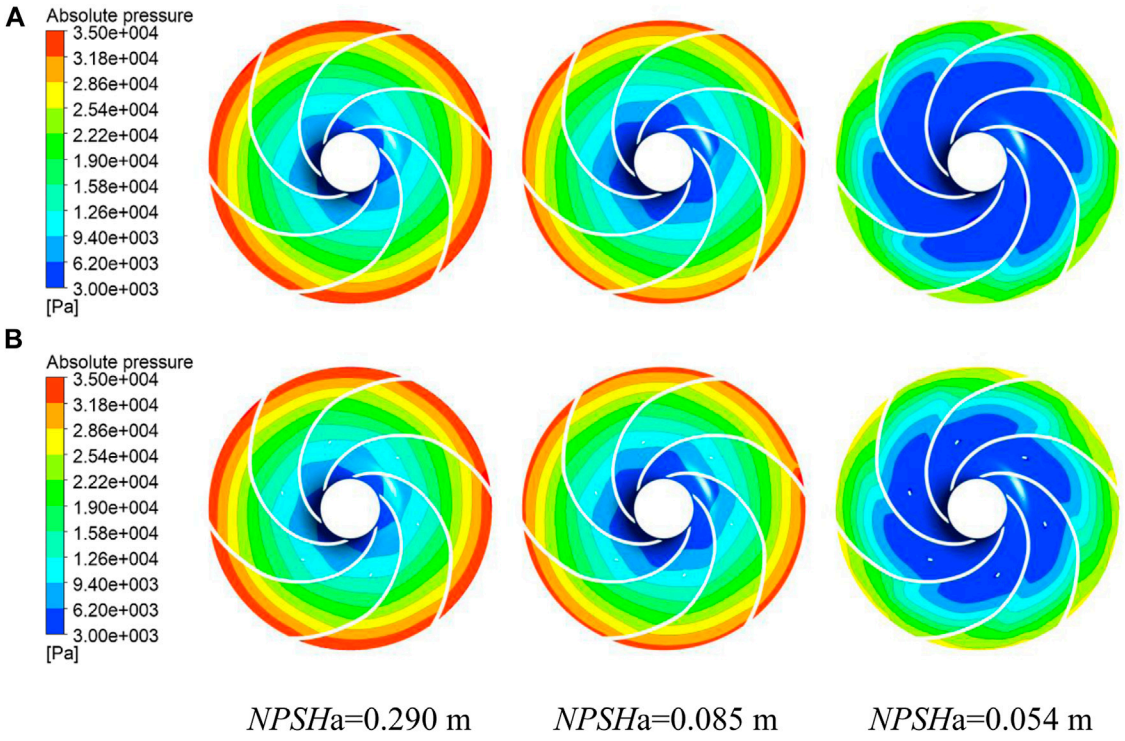

FIGURE 13 | Pressure distribution in the middle section of the impeller: **(A)** original impeller and **(B)** B3 impeller.

blades; the kinetic energy obtained by the flowing fluid is reduced, and the vortex promotion effect is relatively weaker.

8.3.4 Pressure Distribution

Figure 13 shows the absolute pressure contour distribution in the middle section of the impeller. The cavitation in the impeller is caused by the pressure at the location of the cavitation falling below the saturated vapor pressure. With the development of cavitation, the low-pressure area in the impeller first appears at the inlet of the impeller, so the bubble also first appears at the inlet of the blade. With the cavitation margin reduced, the low-pressure area spreads from the inlet of the blade to the outlet, and the cavitation also spreads from the inlet to the outlet. The distribution change of the bubble volume fraction is consistent with the distribution change of the low-pressure area, as shown in **Figures 7**, **13**. After cavitation occurs, with the gradual reduction of the cavitation margin, the existence of tiny blades induces the relative high pressure near the impeller inlet. The pressure change is an important factor in inhibiting the diffusion of low-pressure areas in the impeller to the outlet, which in turn suppresses the expansion of the volume of the bubble. As shown in **Figure 13**, when *NPSH*a = 0.054 m, it can also be seen that the pressure gradient near the impeller outlet is larger, and the head after breaking is also higher, which improves the hydraulic performance during cavitation.

8.3.5 Pulsation Amplitude Analysis

In order to better analyze the transient frequency characteristics of the flow field, six absolute pressure-monitoring points, such as P1-P5 and V1, are set in the middle of the impeller flow channel and at the position of the volute, as shown in **Figure 14**.

Figure 15 depicts the main frequency amplitude of pressure pulsation obtained by a fast Fourier transform (FFT) of the absolute pressure at each monitoring point, and *A* is the main frequency amplitude. From **Figure 15**, it can be obtained that at each stage of cavitation, compared with the original impeller, the C1 impeller has a decreasing trend in the amplitude of pressure

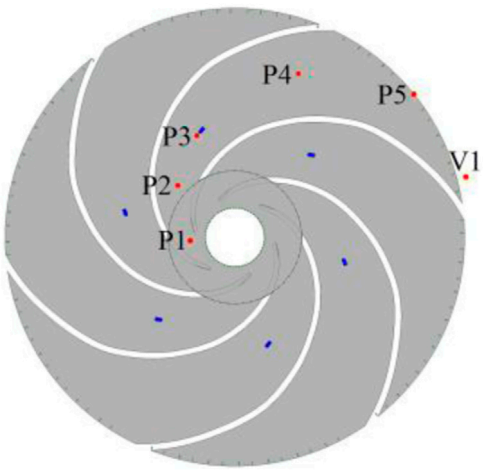

FIGURE14 | Monitoring points in the impeller middle plane.

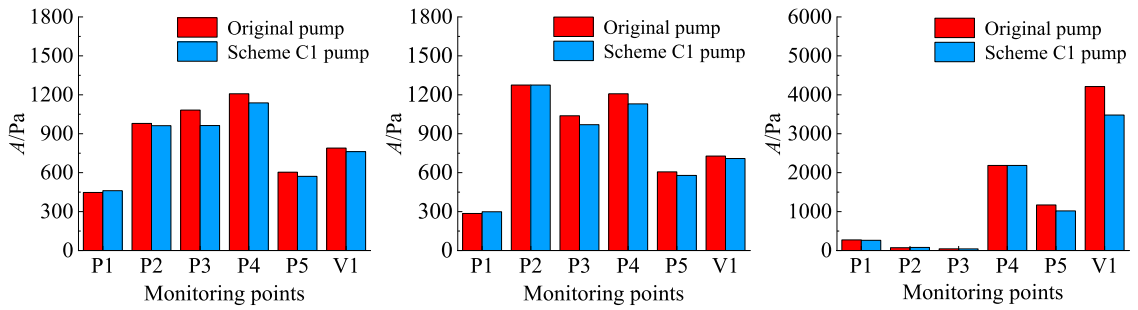

FIGURE15 | Amplitude of main frequency of pressure.

pulsation at all monitoring points, except for a slight increase in pressure pulsation at two points, P1 and P2, near the inlet, which is consistent with the results of the turbulence energy analysis in **Figure 11**. This indicates that the existence of the tiny blades will indeed produce a small disturbance to its front impeller inlet position and produce an optimization effect on the flow field behind it. In general, the addition of tiny blades can reduce the overall pressure pulsation in the pump, which then also reduces the noise and vibration generated by the operation of the centrifugal pump.

9 CONCLUSION

In this study, the effects of adding non-connected tiny blades with different radial positions, widths, and length parameters to the shroud of a low-specific speed centrifugal pump impeller on the cavitation performance were investigated by combining numerical simulation and experiments, and the cavitation volume, flow field structure, turbulence energy, pressure distribution, and pressure pulsation amplitude were comparatively analyzed. On the basis of comparison and analysis, the conclusions are as follows:

1) Compared with the original pump, after adding tiny blades with different radial positions, widths, and lengths to the shroud of the impeller, the effect on the head and efficiency of the centrifugal pump under each working condition is small, and the relative change rate is within ±1.0%. Adding tiny blades near the inlet of the shroud of the impeller has a suppressive effect on the initial stage of cavitation and a facilitating effect on the development and severe stages of cavitation. The addition of tiny blades in the middle and backward positions of the impeller radius produced inhibitory effects in all stages of cavitation, especially in the initial and severe stages of cavitation.
2) There is an optimal width of the tiny blade to achieve the best cavitation suppression effect, and when the width of the tiny blade is equal to 3/4 of the width of the main blade, the cavitation performance of the centrifugal pump is optimal. The tiny blade length parameter has little effect on the cavitation performance.
3) The tiny blades slightly increase the turbulent energy near the blade inlet, inducing a relatively high pressure near the inlet and reducing the turbulent energy in the high-turbulent energy region near the impeller outlet. At the same time, it reduces the overall pressure pulsation in the pump, which in turn reduces noise and vibration and makes its cavitation operation more stable.

DATA AVAILABILITY STATEMENT

The original contributions presented in the study are included in the article/Supplementary Material, further inquiries can be directed to the corresponding author.

AUTHOR CONTRIBUTIONS

ZZ completed the writing, the experiment part and the data processing. WZ provided theoretical guidance and shared in writing, and revising the paper.

FUNDING

This work was supported by the National Natural Science Foundation of China (No. 52169018) and the Industrial Support Plan Project of Gansu Provincial Education Department (2021CYZC-27).

REFERENCES

Acosta, A. J. (1958). "An Experimental Study of Cavitating Inducers," in *Second Symposium on Naval Hydrodynamics: Hydrodynamic Noise Cavity Flow* (Washington, D.C.: Office of Naval Research - Department of the Navy), 533–557.

Brennen, C. E. (1994). *Hydrodynamics of Pumps*. Norwich, VT, USA: Concepts ETI Inc.

Brujan, E.-A., and Matsumoto, Y. (2012). Collapse of Micrometer-Sized Cavitation Bubbles Near a Rigid Boundary. *Microfluid Nanofluid* 13, 957–966. doi:10.1007/s10404-012-1015-6

Chudina, M. (2003). Noise as an Indicator of Cavitation in a Centrifugal Pump. *Acoust. Phys.* 49 (4), 463–474. doi:10.1134/1.1591303

Coutier-Delgosha, O., Fortes-Patella, R., and Reboud, J. L. (2003). Evaluation of the Turbulence Model Influence on the Numerical Simulations of Unsteady Cavitation. *J. Fluids Eng.* 125 (1), 38–45. doi:10.1115/1.1524584

Cui, B., Zhu, K., Zhang, Y., and Lin, P. (2019). Experimental and Numerical Study of the Performance and Cavitation Flow of Centrifugal Pump with Jetting Device. *J. Mech. Sci. Technol.* 33 (10), 4843–4853. doi:10.1007/s12206-019-0925-6

Dular, M., Požar, T., Zevnik, J., and Petkovšek, R. (2019). High Speed Observation of Damage Created by a Collapse of a Single Cavitation Bubble. *Wear* 418-419, 13–23. doi:10.1016/j.wear.2018.11.004

Guan, X. F. (2011). *Modern Pumps Theory and Design*. Beijing, CHN: China Space Navigation Press.

He, Y., Yuan, S., Guo, X., Yuan, J., Chong, X., and Huang, L. (2006). Numerical Simulation for 3-D Incompressible Turbulent Flow in the Impeller with Splitting Vanes of Centrifugal Pump. *Chin. J. Mech. Eng.* 40 (11), 153–157. doi:10.3901/JME.2004.11.153

Ji, B., Luo, X., Arndt, R. E. A., and Wu, Y. (2014). Numerical Simulation of Three Dimensional Cavitation Shedding Dynamics with Special Emphasis on Cavitation-Vortex Interaction. *Ocean Eng.* 87, 64–77. doi:10.1016/j.oceaneng.2014.05.005

Ji, B., Luo, X., Wu, Y., Peng, X., and Duan, Y. (2013). Numerical Analysis of Unsteady Cavitating Turbulent Flow and Shedding Horse-Shoe Vortex Structure Around a Twisted Hydrofoil. *Int. J. Multiphase Flow* 51, 33–43. doi:10.1016/j.ijmultiphaseflow.2012.11.008

Kurokawa, J. (2011). J-Groove Technique for Suppressing Various Anomalous Flow Phenomena in Turbomachines. *Int. J. Fluid Machinery Syst.* 4 (1), 1–13. doi:10.5293/ijfms.2011.4.1.001

Li, X., Yuan, S., Pan, Z., Li, Y., and Yang, J. (2012). Realization and Application Evaluation of Near-Wall Mesh in Centrifugal Pumps. *Trans. Chin. Soc. Agric. Eng.* 28 (20), 67–72. doi:10.3969/j.issn.1002-6819.2012.20.009

Li, Y., Feng, G., Li, X., Si, Q., and Zhu, Z. (2018). An Experimental Study on the Cavitation Vibration Characteristics of a Centrifugal Pump at normal Flow Rate. *J. Mech. Sci. Technol.* 32 (10), 4711–4720. doi:10.1007/s12206-018-0918-x

Luo, X., Zhang, Y., Peng, J., Xu, H., and Yu, W. (2008). Impeller Inlet Geometry Effect on Performance Improvement for Centrifugal Pumps. *J. Mech. Sci. Technol.* 22 (10), 1971–1976. doi:10.1007/s12206-008-0741-x

Menter, F. R. (1994). Two-Equation Eddy-Viscosity Turbulence Models for Engineering Applications. *AIAA J.* 32 (8), 1598–1605. doi:10.2514/3.12149

Pei, J., Yin, T., Yuan, S., Wang, W., and Wang, J. (2017). Cavitation Optimization for a Centrifugal Pump Impeller by Using Orthogonal Design of experiment. *Chin. J. Mech. Eng.* 30 (1), 103–109. doi:10.3901/CJME.2016.1024.125

Reboud, J. L., and Dellanoy, Y. (1994). "Two-Phase Flow Modelling of Unsteady Cavitation," in Proc. Second Intl Symp. on Cavitation, Tokyo, Japan, 39–44.

Wei, Z., Tao, R., Xiao, R., and Hu, H. (2021). Hydrodynamic Improvement by Adding Inlet Baffles on Centrifugal Pump for Reducing Cavitation Instabilities. *J. Vibration Control.*, 1–12. doi:10.1177/10775463211047401

Wijngaarden, L. (2016). Mechanics of Collapsing Cavitation Bubbles. *Ultrason. Sonochem.* 29, 524–527. doi:10.1016/j.ultsonch.2015.04.006

Wong, G. S., Macgregor, C. A., and Hoshide, R. K. (1965). Suppression of Cavitation and Unstable Flow in Throttled Turbopumps. *J. Spacecraft Rockets* 2 (1), 73–80. doi:10.2514/3.28124

Yuan, S. Q., Zhang, J. F., Yuan, J. P., and Fu, Y. D. (2008). Orthogonal Experimental Study Effect of Main Geometry Factors of Splitter Blades on Pump Performance. *J. Drainage Irrigation Machinery* 26 (2), 1–5. doi:10.3969/j.issn.1674-8530.2008.02.001

Zhang, Y. L., Yuan, S. Q., Zhang, J. F., Feng, Y. N., and Lu, J. X. (2014). Numerical Investigation of the Effects of Splitter Blades on the Cavitation Performance of a Centrifugal Pump. *IOP Conf. Ser. Earth Environ. Sci.* 22 (5), 052003. doi:10.1088/1755-1315/22/5/052003

Zhang, Y., Yuan, S., Zhang, J. F., Peng, Y., and Mao, J. (2015). Numerical Analysis on Effects of Splitter Blades on Cavitation Performance in a Centrifugal Pump. *J. Drainage Irrigation Machinery Eng.* 33 (10), 846–852. doi:10.3969/j.issn.1674-8530.14.0142

Zhao, W. G., Lu, J. J., and Zhao, F. R. (2020). Cavitation Control of Centrifugal Pump Based on gap Jet Principle. *J. ZheJiang Univ. (Engineering Science)* 54 (9), 1785–1794. doi:10.3785/j.issn.1008-973X.2020.09.015

Zhao, W. G., Zhai, L. J., Xia, T., and Li, S. S. (2018). Numerical Simulation of Slotted Blade in Centrifugal Pump on Cavitation Suppression. *Trans. Chin. Soc. Agric. Mach* 49, 157–164. doi:10.6041/j.issn.1000-1298.2018.12.019

Zhao, W., and Zhao, G. (2017). An Active Method to Control Cavitation in a Centrifugal Pump by Obstacles. *Adv. Mech. Eng.* 9 (11), 168781401773294. doi:10.1177/1687814017732940

Zheng, X. B., Liu, L. L., Guo, P. C., and Hong, F. (2018). Numerical Investigation of Three-Dimensional Cavitating Performance of NACA66 Hydrofoil Base on Different Cavitation Models. *Chin. J. Hydrodynamics* 33 (2), 199–206. doi:10.16076/j.cnki.cjhd.2018.02.008

Zhu, B., and Chen, H.-x. (2012). Cavitating Suppression of Low Specific Speed Centrifugal Pump with gap Drainage Blades. *J. Hydrodyn* 24 (5), 729–736. doi:10.1016/S1001-6058(11)60297-7

Zwart, P. J., Gerber, A. G., and Belamri, T. (2004). "A Two-Phase Flow Model for Predicting Cavitation Dynamics," in Fifth international conference on multiphase flow, Yokohama, Japan, May 30-June 3, 2004, 152.

Conflict of Interest: The authors declare that the research was conducted in the absence of any commercial or financial relationships that could be construed as a potential conflict of interest.

Publisher's Note: All claims expressed in this article are solely those of the authors and do not necessarily represent those of their affiliated organizations or those of the publisher, the editors, and the reviewers. Any product that may be evaluated in this article or claim that may be made by its manufacturer is not guaranteed or endorsed by the publisher.

frontiers | Frontiers in Energy Research

ORIGINAL RESEARCH
published: 12 April 2022
doi: 10.3389/fenrg.2022.854529

Research on Damping Contribution Rate of Key Parameters of Valve-Controlled Damping Adjustable Damper

Fangwei Xie [1,2], Xiuwei Shi [1], Jinxin Cao [3], Zhiwen Ding [1], Chengcheng Yu [1] and Yonghua Gao [1]*

[1]School of Mechatronic Engineering, China University of Mining and Technology, Xuzhou, China, [2]Jiangsu Province and Education Ministry Co-sponsored Collaborative Innovation Center of Intelligent Mining Equipment, China University of Mining and Technology, Xuzhou, China, [3]School of Mechanical Engineering, Jiangsu University, Zhenjiang, China

Valve-controlled damping adjustable damper has the characteristics of simple structure and adjustable damping, and it has always been a hot research topic. This paper establishes a mathematical model of damping characteristics of the valve-controlled damping adjustable damper and designs the experiment of the damping characteristics of the compression stroke and the recovery stroke. Through simulation and experiment, the accuracy of the mathematical model is verified, and the damping contribution rate of different key parameters under different excitation speeds is analyzed. The results show that the mathematical model of the damping characteristics can well describe the working state of the damper. The damping contribution rate of key parameters under different excitation speeds is obtained. The damping contribution of the constant through-hole diameter decreases gradually after the valve is opened for the first time. With the increase of the excitation speed, the valve plate equivalent thickness and the valve plate maximum limit clearance of the check valve gradually play a major role in the damping contribution rate. The research results can screen out the key parameters, improve the development efficiency of the damper, and provide guidance for the damper design and optimization.

Keywords: damping contribution rate, key parameter, valve-controlled, damping characteristics, damper

OPEN ACCESS

Edited by:
Jin-Hyuk Kim,
Korea Institute of Industrial Technology, South Korea

Reviewed by:
Hemantha Kumar,
National Institute of Technology, India
Wenai Shen,
Huazhong University of Science and Technology, China
Hongwei Cui,
Taiyuan University of Technology, China

****Correspondence:***
Fangwei Xie
xiefangwei@cumt.edu.cn

Specialty section:
This article was submitted to Process and Energy Systems Engineering, a section of the journal Frontiers in Energy Research

Received: *14 January 2022*
Accepted: *25 March 2022*
Published: *12 April 2022*

Citation:
Xie F, Shi X, Cao J, Ding Z, Yu C and Gao Y (2022) Research on Damping Contribution Rate of Key Parameters of Valve-Controlled Damping Adjustable Damper. Front. Energy Res. 10:854529. doi: 10.3389/fenrg.2022.854529

INTRODUCTION

As a key component of a semi-active suspension system, the valve-controlled damper is always a research hotspot (Wang, 2016; Yang et al., 2019; Cao, 2020). The damper belongs to the damping multi-state switching damper. Different damping oil circuits are designed by using multiple superimposed valve groups, the oil circuit is switched by an electromagnetic start-stop valve to realize damping adjustment, the adjustable damping damper controlled by the valve has great stability and good promotion perspective. Researchers at home and abroad have studied damper for more than one hundred years and achieved a series of results (Lindler et al., 2000; Liu et al., 2019).

Maemor et al. (2003) proposed an optimization method for the semi-active damper and optimized the area of the compensation hole of the damper with the minimum vertical acceleration as the optimization objective. The results show that the optimized damper can better cope with the change of aircraft mass than the original damper. Causemann (2003) developed a continuously variable damper. The external pilot relief valve can continuously

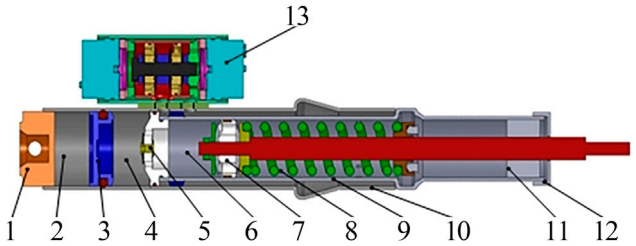

FIGURE 1 | Structure of the valve-controlled damping adjustable damper. Note: 1. Mounting Base; 2. Nitrogen cavity; 3. Floating Piston; 4. Oil storage cavity; 5. Bottom Valve; 6. Compression Cavity; 7. Piston Valve; 8. Recovery Cavity; 9. Inner Cylinder; 10. Outer Cylinder; 11. Guide; 12. End Cap; 13. Damping Control Valve.

adjust the damping force of the damper in real-time by collecting road spectrum and body posture information. Farjoud et al. (2012) established a nonlinear model of the damper, studied the influence of the parameters of the superposition valve on the damping characteristics, and verified the correctness of the mathematical model through experiments. Luczko and Ferdek (2019) designed a damping adjustable hydraulic damper with an additional inner cylinder. The purpose of changing the damping characteristics according to the road conditions is realized by selecting the appropriate structural parameters.

Zhou and Ren (2009) studied the optimal damping matching of automobile suspension and optimized the thickness of the throttle valve plate of the damper by using the design method of optimal curve fitting. Chen et al. (2013) designed a valve-controlled multi-state switching damper and analyzed the relationship between the damping force of the damper and the stroke and frequency. The experimental results show that the mathematical model has high accuracy. Xuan (2016) designed a four gear valve-controlled adjustable damper, deduced the mathematical model of damping force in the working process, and developed a prototype of the damper. The experimental results show that the valve-controlled adjustable damper can meet the application requirements. Ding et al. (2018) designed an ADS (Adjuster Damping Control) damper, established mathematical models of damping characteristics in different gears, and the influence of geometric parameters of ADS valve damping characteristics are studied. Xie et al. (2018) used Matlab to deduce the analytic expressions of deflection deformation of the single valve plate and the superimposed valve plate and analyzed the influence of geometric parameters of annular valve plate on the deflection of the valve plate. The research has a certain guiding significance for parametric modeling and the optimal design of the damper. Wang et al. (2018) took the maximum adjustment range of MRF (Magnetorheological Fluid) damper as the goal and optimized the effective length of working cylinder, piston rod diameter, and piston diameter by using the Matlab optimization toolbox. The results show that the method is accurate and reliable. Ma (2018) established an RSM (Response Surface Methodology) model of multi-point force damper, selected ten design variables, optimized the design with the indicator characteristics under multiple speed conditions proposed by the cooperative enterprise, which guided the similar engineering. Zhang et al. (2019) established a fluid-structure coupling model of the damper with ADINA, analyzed the influence of different elastic modulus and viscosity on the damping stiffness. Huang et al. (2020) established a simulation model of electro-hydraulic pneumatic coupling damper by AMESim, studied the indicator characteristics and velocity characteristics under different current and external excitation conditions, in addition, explored the influence of different structural parameters of the damper damping characteristics.

At present, many mathematicians have carried out a lot of research on the influence of different structural parameters on the damping characteristics of the damper, and have achieved some results, but most of these researches focus on qualitative analysis and the influence weight of each parameter is not given. To improve the performance of the damper, researchers use different optimization methods to optimize the design of the single tube, double tube, and magnetorheological fluid dampers (Fu, 2016). However, there are few studies on the optimization design of the valve-controlled adjustable damper. At present, the development of the damper still has to carry out the cycle "design, experimentation, evaluation, improvement". Designers spend a lot of time and energy on repetitive work. At the same time, most adjustment of parameters still depends on experience, which has the disadvantages of low development efficiency and long cycle. With the wide application of the valve-controlled adjustable damper, the demand for the optimal design of this type of damper is more and more intense.

This paper establishes the mathematical model of damping characteristics of the valve-controlled damping adjustable damper and designs the experiment of damping characteristics of the compression stroke and the recovery stroke. Through simulation and experiment, the accuracy of the mathematical model is verified, and the damping contribution rate of key parameters of the valve-controlled damping adjustable damper

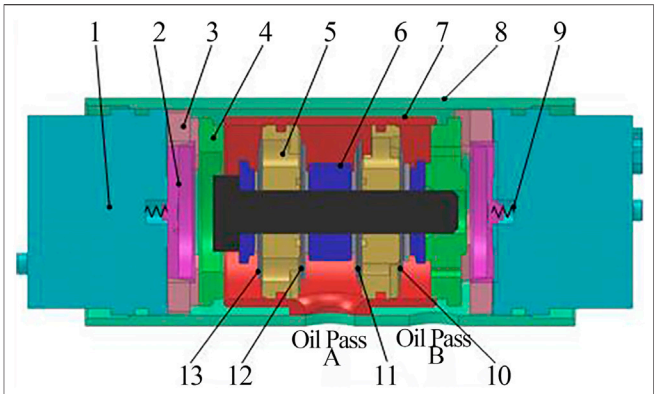

FIGURE 2 | Structure of the damping control valve. Note: 1. Electromagnet; 2. Flapper valve spool; 3. Flapper valve body; 4. Transparent Cover; 5. Check valve; 6. Locate ring; 7. Inner cylinder; 8. Outer cylinder; 9. Reset spring; 10. Check Valve "d"; 11. Check Valve "c"; 12. Check Valve "b"; 13. Check Valve "a".

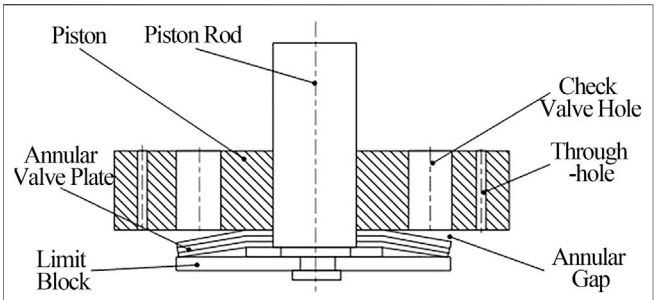

FIGURE 3 | Structure of the check valve.

under different excitation speeds is analyzed. The research results can screen out the key parameters, improve the development efficiency of the damper, and provide guidance for the damper design and optimization.

STRUCTURE AND WORKING PRINCIPLE OF VALVE-CONTROLLED ADJUSTABLE DAMPER

Structure of Valve-Controlled Adjustable Damper

Compared with the structure of the double tube damper, the valve-controlled damping adjustable damper adds a damping control valve on the outside, and the rest of the overall structure is similar to that of the double tube damper, **Figures 1–3** show the structural diagram of the damping control valve and check valve, respectively.

Damper Adopts a Double Tube Structure

The valve-controlled adjustable damper consists of two parts: the main damper and the damping control valve. The main damper adopts the double tube structure, which is used as the oil channel to guide the oil in the recovery cavity and the compression cavity to the damping control valve. The piston valve of the damper reciprocates in the inner cylinder. The upper end of the inner cylinder realizes the movement guide and seal functions of the piston rod. The lower part of the inner cylinder has a bottom valve, and the lower part of the outer cylinder also has a floating piston. The floating piston can move in the lower part of the outer cylinder, and the mounting base is installed in the lower part of the outer cylinder, which is mainly used to connect with the outside.

Piston Valve of Damper Divides Inner Cylinder Into Two Parts: Recovery Cavity and Compression Cavity

The floating piston divides the bottom part of the outer cylinder into an oil storage cavity and nitrogen cavity. The bottom valve serves as the oil channel between the compression cavity and the oil storage cavity. The upper

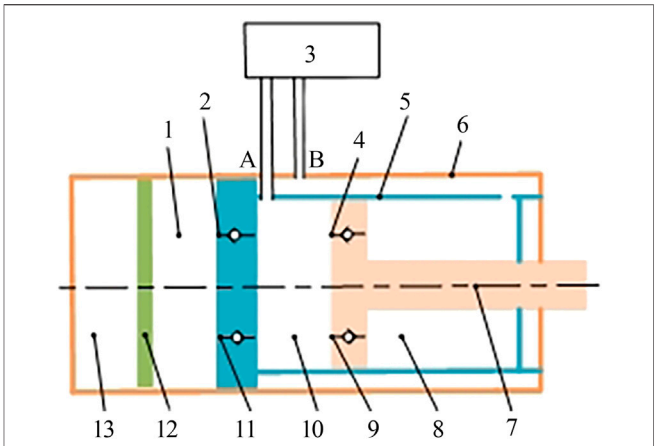

FIGURE 4 | Working principle of valve-controlled damping adjustable damper. Note: 1. Oil storage cavity; 2. Compensate valve; 3. Damping control valve; 4. Flow valve; 5. Inner cylinder; 6. Outer cylinder; 7. Piston rod; 8. Recovery cavity; 9. Recovery valve; 10. Compression cavity; 11. Compression valve; 12. Float piston; 13. Nitrogen cavity.

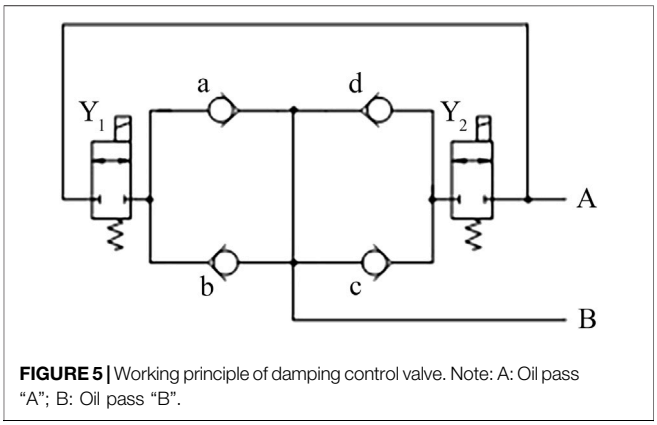

FIGURE 5 | Working principle of damping control valve. Note: A: Oil pass "A"; B: Oil pass "B".

part of the inner cylinder has an oil hole, which can lead the oil in the recovery cavity into the clearance between the inner and outer cylinders. There are also two oil holes near the bottom valve of the outer cylinder. One oil hole penetrates the inner cylinder and is connected with the compression cavity, and the other oil hole is connected with the recovery cavity through the gap between the inner and outer cylinders. The damping control valve installed on the outer cylinder connects two oil holes, through the adjustment of the damping control valve, different damping forces are produced.

Working Principle of Valve-Controlled Adjustable Damper

Figure 4 shows the working principle of the valve-controlled adjustable damper, and its working process can be divided into two parts: compression and recovery. The bottom valve consists of a compression valve and a compensation valve, the piston valve consists of a recovery valve and a flow valve. The oil flows between the damping control valve, the compression cavity, the recovery

cavity, and the oil storage cavity through the piston valve and the bottom valve.

Oil Flow Path in Compression Stroke

During the compression stroke, the piston moves towards the bottom valve and the oil pressure in the compression cavity increases. There are three ways for the oil to flow from the compression cavity to the recovery cavity: the first one flows through the damping control valve; The second one flows through the flow valve; The third one flows through the compression valve. The oil in the oil storage cavity increases and the floating piston moves downward. The recovery stroke is similar to the compression stroke.

Regulating Step

Figure 5 shows the working principle of the damping control valve. The step regulation of damping is mainly through the damping control valve. "Y_1" and "Y_2" are solenoid valves. "a", "b", "c" and "d" are check valves. When the solenoid valve is powered on, the oil circuit is opened. The solenoid valve loses power and the oil circuit is closed. During the compression stroke, the oil flows in through port "A" and out through port "B", and the recovery stroke is the opposite.

Compression stroke: after the oil enters through port "A", if both solenoid valve "Y_1" and solenoid valve "Y_2" are powered on, the oil can pass through check valve "a" and check valve "d", and exit through port "B"; If the solenoid valve "Y_1" is energized and the solenoid valve "Y_2" is de-energized, the oil flows through the check valve "a" and out of the oil outlet "B"; If the solenoid valve "Y_1" is de-energized and the solenoid valve "Y_2" is energized, the oil flows through the check valve "d" and out of the oil outlet "B".

ESTABLISHMENT OF MATHEMATICAL MODEL OF VALVE-CONTROLLED ADJUSTABLE DAMPER

Model Simplification and Hypothesis

Many factors affect the damping characteristics of the damper, such as the structural parameters of each valve system, the friction between the piston and the inner cylinder of the damper, the oil viscosity, the working temperature, and so on. Among them, the structural parameters of each valve system have a great influence on the damping characteristics, such as the constant through-hole diameter, the thickness of the valve plate, the limit clearance of the valve plate, and so on. To avoid the mathematical model being too complex and inconvenient for the subsequent simulation analysis and optimal design, it is necessary to simplify and assume the working process of the damper in the mathematical modeling. The simplification and assumption are as follows.

(a) The internal leakage of the damping control valve and the external leakage of the damper are ignored.
(b) It is assumed that the temperature of the damper is constant and the viscosity of the damper oil is constant.
(c) It is assumed that the damper oil is not compressible and the bubble phenomenon is not considered.
(d) The oil pressure of the recovery cavity and compression cavity is equal to the air pressure of the nitrogen cavity everywhere.
(e) It is assumed that there is no elastic deformation of the parts of the damper, such as the working cylinder and piston rod, except the annular valve plate.

The Damping Force

The working principle of the damper compression stroke and recovery stroke is similar. This paper analyzes the compression stroke of the valve-controlled damping adjustable damper.

When the valve-controlled adjustable damper is on the compression stroke, the piston rod moves downward, the pressure of the compression cavity increases and the pressure of the recovery cavity decreases. Under the action of the piston, the oil in the damper flows from the compression cavity to the recovery cavity through the damping control valve. The pressure of the recovery cavity, compression cavity, and nitrogen cavity are P_1, P_2, and P_3, respectively.

The piston separates the oil from the nitrogen gas. The pressure of the compression cavity and nitrogen cavity are equal. During the compression stroke, as the piston moves down, the pressure in the nitrogen cavity will also increase. According to the gas isothermal state equation:

$$P_3\left(V_0 - A_d x_q\right)^r = P_2\left(V_0 - A_d x_q\right)^r = P_0 V_0^r \tag{1}$$

Where P0 is the initial pressure of the nitrogen cavity (Pa); V0 is the initial volume of the nitrogen cavity (m3); xq is the nitrogen cavity piston displacement (m); r is the temperature index (r = 1.4).

In the compression stroke, the damping force is mainly caused by the pressure difference between the two ends of the piston and the friction between the piston and the working cavity:

$$F_c = A_d P_2 - (A_d - A_r)P_1 + F_f sgn(v) \tag{2}$$

Where F_c is the compression stroke damping force of the valve-controlled adjustable damper (N); A_d is the working cylinder area (m^2); A_r is the piston rod area (m^2); P_1 is the oil pressure of the recovery cavity (Pa); P_2 is the oil pressure of the compression cavity (Pa); F_f is the friction between the piston and the working cylinder during compression stroke (N); v is the piston movement speed (m/s); $sng(v)$ is step function of v.

$$F_f = \frac{1.33 \times 10^{-6}\sqrt{4\pi A_b}\left(H_r + s_p\right)p_n}{1 + \sqrt{\frac{\rho\delta}{1000u_t}}v_k} \tag{3}$$

Where F_f is the friction force between the piston and the working cylinder during the compression stroke (N); H_r is the contact width between the piston and the working cylinder (m); P_n is the radial pressure on piston (Pa); ρ is the hydraulic oil density (kg/m^3); δ is the oil film thickness (m); v_k is the initial valve opening speed (m/s); u_t is the dynamic viscosity of the oil (N·s/m^2); A_b is the contact area between the piston and the working cylinder (m^2); s_p is the displacement of the piston after the valve is opened (m).

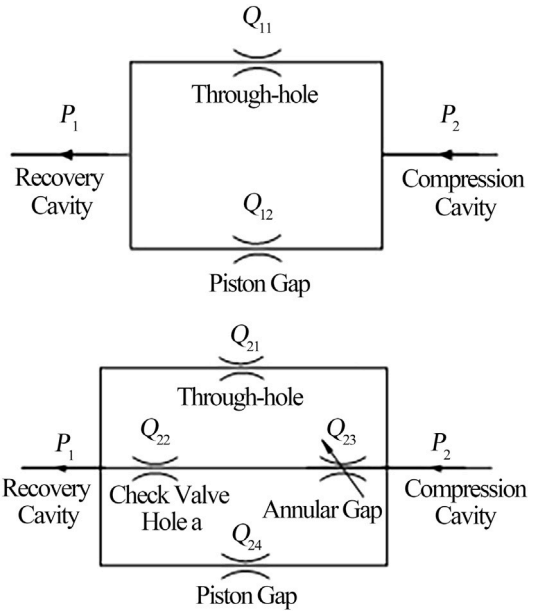

FIGURE 6 | Oil circuit diagram of the compression stroke. Note: **(A)** Before opening the valve for the first time; **(B)** After opening the valve for the first time.

Analysis of Valve Opening State of Valve-Controlled Adjustable Damper

For the valve-controlled damper, the mechanical model of the piston valve system or the damper control valve system can simplify the mechanical model of the annular thin plate. The throttling gap of the ring valve divides three stages: before the first opening, after the first opening, and after the second opening. The size of the throttling gap, that is, the deflection of the valve plate is determined by the oil hydraulic pressure difference between the two ends of the valve system. The deflection of the valve plate is zero before the first opening, and the size of the throttling gap after the first opening is determined by the oil hydraulic pressure difference between the two ends of the valve system, the deflection of the annular valve plate is fixed after the second opening, which is equal to the maximum deflection after the first opening. Therefore, it is necessary to model the two states before and after opening the valve, respectively. The oil circuit diagram of the two cases is shown in **Figure 6**.

Before Opening Valve for the First Time

Figure 6A shows a schematic diagram of the oil circuit before opening the valve for the first time. When the vibration speed is small, the oil pressure is less than the valve plate pre-tightening force (Ma et al., 2013), that is, before the initial opening of the valve, the oil in the damper flows through the constant through-hole of the damping control valve and the piston gap.

The constant through-hole is a small hole with a thick wall:

$$Q_{11} = C_t N_t A_t \sqrt{\frac{2\Delta P_{21}}{\rho}} \tag{4}$$

Where ΔP_{21} is the pressure difference between the compression cavity and the recovery cavity (MPa); C_t is the flow coefficient of the constant through-hole; N_t is the number of the constant through-hole; A_t is the flow area of the constant through-hole (m^2); ρ is the oil density (kg/m^3).

The piston gap is an eccentric annular gap, and the flow through the piston gap can be expressed as:

$$Q_{12} = \frac{\Delta P_{21}\pi d\delta^3\left(1 + 1.5e^2\right)}{12u_t l} \tag{5}$$

Where ΔP_{21} is the pressure difference between the compression cavity and the recovery cavity (MPa); d is the inner diameter of the working cylinder (m); δ is the oil film thickness (m); e is the eccentricity; l is the gap length (m).

The constant through-hole is connected in parallel to the piston gap, and the total flow is:

$$Q_1 = Q_{11} + Q_{12} = (A_d - A_r)v_{c1} \tag{6}$$

Where v_{c1} is the piston movement speed of the compression stroke (m/s).

The pressure difference between the compression cavity and the recovery cavity can be obtained by **Eq. 6**. The final compression stroke is as follows:

$$\begin{aligned} F_{c1} = {} & A_d \frac{P_0 V_0^{1.4}}{(V_0 - A_r x)^{1.4}} - \\ & (A_d - A_r)\left[\frac{P_0 V_0^{1.4}}{(V_0 - A_r x)^{1.4}} - \Delta P_{21}\right] + \\ & \frac{1.33 \times 10^{-6}\sqrt{4\pi A_b}\left(H_r + s_p\right)p_n}{1 + \sqrt{\frac{\rho\delta}{1000u_t}v_k}} sgn(v_{c1}) \end{aligned} \tag{7}$$

After Opening Valve for the First Time

Figure 6B shows the schematic diagram of the oil circuit after opening the valve for the first time. When the vibration speed increases, the oil pressure is greater than the valve plate pre-tightening force, that is, after the initial opening of the valve, the oil in the damper flows through the constant through-hole, throttle gap, and the piston gap, the throttle gap includes valve hole of check valve "a" and annular gap.

When the annular disc is open and the opening is f_a, the throttle gap can be regarded as an annular plane gap, and the flow rate is expressed as:

$$Q_{23} = \frac{\pi f_a^3 \Delta P_{31}}{6u_t \ln \frac{r_{c1}}{r_{c2}}} \tag{8}$$

Where f_a is the maximum deflection of the annular disc of the check valve "a" (m); ΔP_{31} is the pressure difference at both ends of the check valve "a" (MPa); r_{c1} is the inner circle radius of the annular disc of the check valve "a" (m); r_{c2} is the outer circle radius of the annular disc of the check valve "a" (m).

Similar to **Eq. 6**, the throttle gap of the check valve "a" is connected in series with the hole of the check valve "a", so the flow

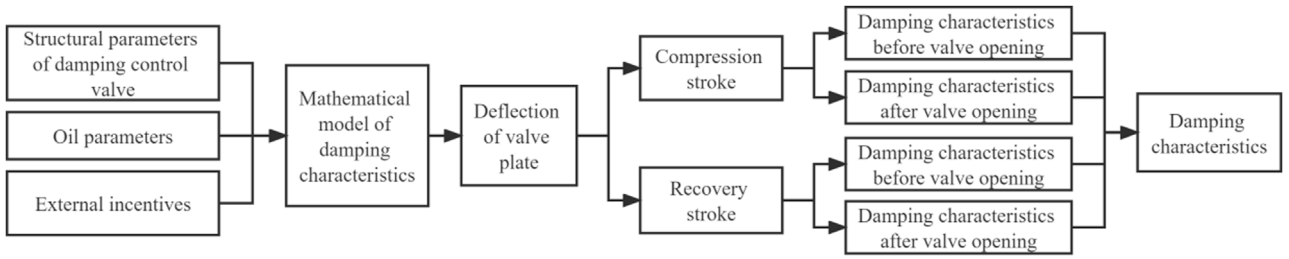

FIGURE 7 | Simulation process of the adjustable damper.

of the two is equal. The constant through-hole, throttling gap, and piston gap are parallel. The total flow after the opening of the valve can be obtained by adding the three flow rates. According to the above two groups of relationships, the total flow after the first opening of the valve is:

$$\left\{ \begin{array}{l} Q_2 = Q_{21} + Q_{23} + Q_{24} \\ = (A_d - A_r)v_{c2} \\ Q_{22} = Q_{23} \end{array} \right\} \tag{9}$$

Where v_{c2} is the velocity of the piston movement after the initial valve opening of the compression stroke (m/s); Q_{21} is the flow of the through-hole (L/min); Q_{22} is the flow of the through-hole of check valve "a" (L/min); Q_{23} is the flow of the through the annular gap (L/min); Q_{24} is the flow of the through piston gap (L/min).

The flow calculation of "Q_{21}" and "Q_{24}" is similar to that of "Q_{11}" and "Q_{12}" before opening the valve for the first time. The pressure difference between the compression cavity and the recovery cavity can be obtained by **Eq. 9**. Finally, the damping force of the compressed stroke after opening the valve is:

$$\begin{aligned} F_{c2} = {} & (A_d - A_r)\left[\frac{P_0 V_0^{1.4}}{(V_0 - A_r x)^{1.4}} + \Delta P_{21}\right] \\ & - A_d \frac{P_0 V_0^{1.4}}{(V_0 - A_r x)^{1.4}} \\ & + \frac{\Delta P_{21} \pi d \delta^3 \left(1 + 1.5e^2\right)}{12 u_t l} sgn(v_{c2}) \end{aligned} \tag{10}$$

COMPARATIVE ANALYSIS ON SIMULATION EXPERIMENT OF VALVE-CONTROLLED ADJUSTABLE DAMPER

Simulation Analysis of Damping Characteristics

The simulation analysis of damping characteristics of the valve-controlled adjustable damper can reduce the prototype experiment, evaluate the performance of the damper and improve the development efficiency.

Simulation Experiment and Key Parameters Design

Based on the mathematical model of the valve-controlled adjustable damper, the damping characteristic model of the valve-controlled adjustable damper is built by using Matlab software, and the damping characteristic is simulated and analyzed. **Figure 7** shows the simulation flow chart of the adjustable damper.

The structural parameters and oil parameters of the damping control valve are internal parameters, and the external excitation is the external parameter. Combined with the mathematical model of damping characteristics, the damping characteristics of the compression stroke before and after opening the valve and the recovery stroke before and after opening the valve are solved, respectively, and the damping characteristic curve of the whole damper is drawn finally. According to the test requirements of damping characteristics of the damper, the external excitation signal is set as a sinusoidal signal with an amplitude of 50 mm.

The vibration speed of the damper are 0.05, 0.13, 0.26 0.39 and 0.52 m/s, the corresponding excitation frequencies are set at 0.16, 0.42, 0.83, 1.24 and 1.66 Hz, respectively. To improve the simulation efficiency, we choose the second gear of the damping valve as the simulated target, and **Table 1** shows the main structural parameters of the damper under this target.

As shown in **Figure 8**, the indicated power characteristic curve of the valve-controlled adjustable damper can obtain by substituting the set parameters into the simulation program.

Indicator Characteristics

As shown in **Figure 8**, when the excitation speed is 0.05, 0.13, 0.26, 0.39, and 0.52 m/s, the maximum compression damping force is 431 N, 909 N, 1268 N, 1690 N, and 2047 N, respectively, and the maximum recovery damping force is 780 N, 1638 N, 2348 N, 3099 N, and 3935 N, respectively. With the increase of the excitation speed, the damping force also increases and the maximum damping force appears in the stroke center of the damper. During the compression stroke, when the displacement is −20–20 mm, the damping force is basically unchanged. The damping force change rate gradually decreases from the maximum stroke to the stroke center, the curve is smooth, and the damping force is not distorted.

TABLE 1 | Key structural parameters of the valve-controlled damping adjustable damper.

Parameters	Value	Unit
Inner diameter of the working cylinder (d_d)	36	mm
Diameter of the piston rod (d_r)	15	mm
Number of the constant through-hole (n)	4	-
Diameter of the constant through-hole (d_t)	4	mm
Number of the check valve "a" (n_a)	4	-
Vale hole diameter of the check valve "a" (d_{ay})	8	mm
Valve plate equivalent thickness of the check valve "a" (h_{ae})	0.4	mm
Valve plate pre-tightening force of the check valve "a" (F_a)	200	N
Valve plate maximum limit clearance of the check valve "a" valve plate (δ_a)	0.3	mm
Number of the check valve "a" (n_b)	4	-
Vale hole diameter of the check valve "b" (d_{bf})	7	mm
Valve plate equivalent thickness of the check valve "b" (h_{be})	0.9	mm
Valve plate pre-tightening force of the check valve "b" (F_b)	450	N
Valve plate maximum limit clearance of the check valve "b" (δ_b)	0.2	mm

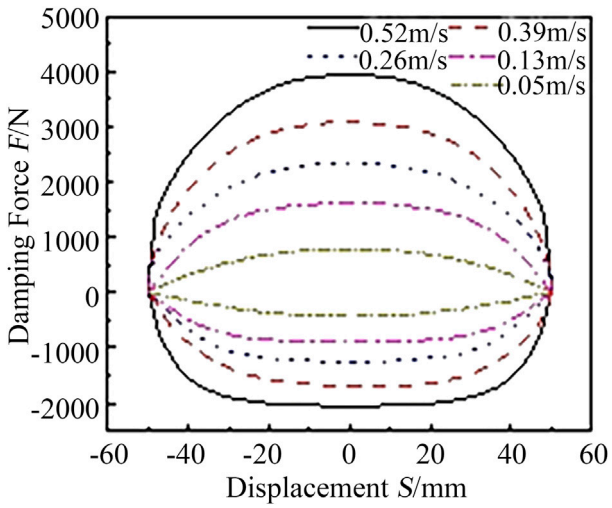

FIGURE 8 | Indicator diagram of the damper.

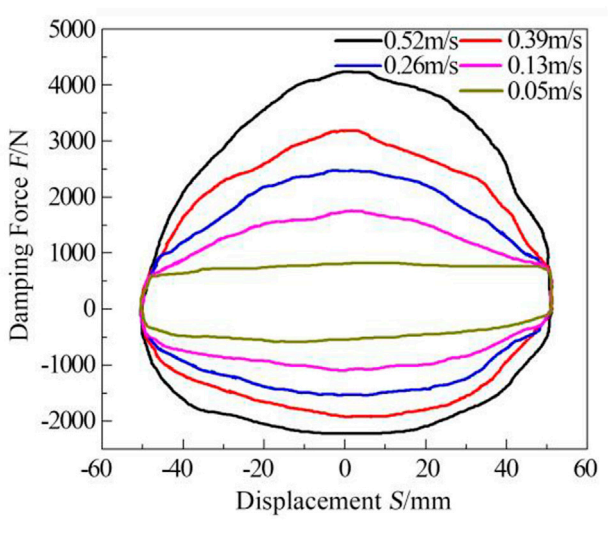

FIGURE 10 | Indicator diagram of the damper.

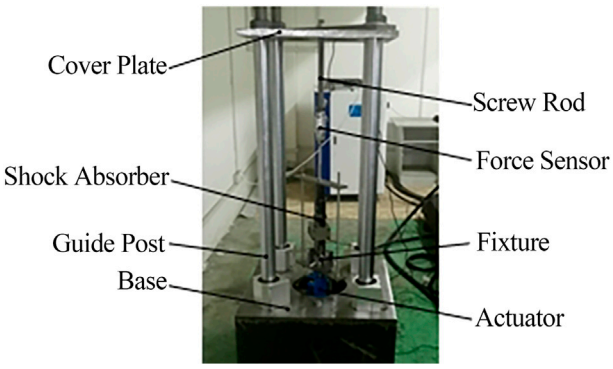

FIGURE 9 | Picture of the experimental bench.

Experimental Study on Damping Characteristics

To ensure the accuracy and reliability of contribution rate analysis and damper parameter optimization results, it is necessary to verify the accuracy of the mathematical model of damping characteristics. Therefore, an experimental study on the valve-controlled adjustable damper is carried out.

Experimental Design

Figure 9 shows a test bench for the valve-controlled adjustable damper. The test bench mainly consists of three parts: mechanical system, hydraulic system, and measurement and control system. The mechanical part is mainly composed of the bench and damper fixtures. The hydraulic part mainly includes a hydraulic pump station, electro-hydraulic servo valve, actuator, and other hydraulic auxiliary components. The measurement and

TABLE 2 | Comparison of damping peak values of the simulation and test.

Speed (m/s)	Compression stroke		
	Experimental peak (N)	Simulation peak (N)	Error (%)
0.05	481	431	11.6
0.13	987	909	8.6
0.26	1,402	1,268	10.4
0.39	1819	1,690	7.6
0.52	2,232	2047	9.1
Speed (m/s)	**Recovery stroke**		
	Experimental peak (N)	**Simulation peak (N)**	**Error (%)**
0.05	862	780	10.5
0.13	1807	1,638	10.3
0.26	2,556	2,348	8.9
0.39	3,327	3,099	7.4
0.52	4,203	3,911	7.5

control system mainly includes a monitoring computer, displacement sensor, force sensor, servo amplifier, etc.

During the experiment, it is necessary to ensure the vertical installation of the damper. The lower lug of the damper is connected to the actuator through a clamp, and the upper end of the damper is connected to a force sensor to adjust the gear of the damper. The test method of fixed stroke and variable frequency is adopted.

According to the vibration speed of the damper, the excitation frequencies of the corresponding actuators are set at 0.16, 0.42, 0.83, 1.24, and 1.66 Hz, respectively (Xie et al., 2015). After three to five working cycles, according to the damping force and displacement signals collected by the acquisition card, the characteristic curves of the indicator diagram under each excitation frequency are drawn, as shown in **Figure 10** and **Table 2**.

Indicator Characteristics

Comparing **Figures 8** and **10**, there are found that the experimental curve does not have distortion, and the contour of the indicator diagram is similar to the simulation curve. With the increase of the excitation speed, the damping force also increases. The maximum damping force appears at the stroke center of the damper. At the same time, the absolute value of the recovery damping force is greater than the compression damping force, and the damping force is not distorted. As shown in **Table 2**, under the five experimental speeds, the maximum error between the experimental peak and the simulation peak is 11.6%, and the average error of the peak is 9.15%, which indicates that the established mathematical model can better describe the working state of the damper.

RESEARCH ON DAMPLING CONTRIBUTION RATE OF KEY PARAMETERS

Design of experiments (DOE) is a structured mathematical-statistical method (Montgomery, 2009). Through small-scale experiments and experimental data analysis, the influence of different control parameters on one or more target functions can be compared, and the key experimental factors can be identified. Through the experimental design, the influence of various design variables on damping characteristics can be explored, and the key design variables can be selected to reduce the design cost.

The damping contribution rate reflects the percentage of damping force of different parameters in the damping work process. The key design parameters are initially screened, the upper and lower limits of each parameter are given, the cumulative damping force of each key parameter is calculated, and the damping contribution rate of different parameters is obtained.

Experimental Design of Key Parameters of Valve System

DOE is essentially a mathematical model, which aims to find the relationship between factors and response. It is generally divided into three stages: experiment plan, experiment execution, and experiment result in analysis.

Determination of Experimental Factors

Many factors affect the damping characteristics of the valve-controlled adjustable damper. To improve the efficiency of experimental design, the key parameters such as the constant

TABLE 3 | Parameter level values of influencing factors of damping characteristics.

Parameters	Lower limit	Upper limit	Unit
Vale hole diameter of the check valve "a" (d_{ay})	4	12	mm
Valve plate equivalent thickness of the check valve "a" (h_{ae})	0.2	0.6	mm
Valve plate pre-tightening force of the check valve "a" (F_a)	100	300	N
Valve plate maximum limit clearance of the check valve a valve plate (δ_a)	0.15	0.45	mm
Vale hole diameter of the check valve "b" (d_{bf})	3.5	10.5	mm
Valve plate equivalent thickness of the check valve "b" (h_{be})	0.45	1.35	mm
Valve plate pre-tightening force of the check valve "b" (F_b)	225	675	N
Valve plate maximum limit clearance of the check valve "b" (δ_b)	0.1	0.3	mm
Diameter of the constant through-hole (d_t)	2	6	mm
Piston clearance (δ)	0.03	0.09	mm
Dynamic viscosity (u_t)	15	25	N·s/m^2

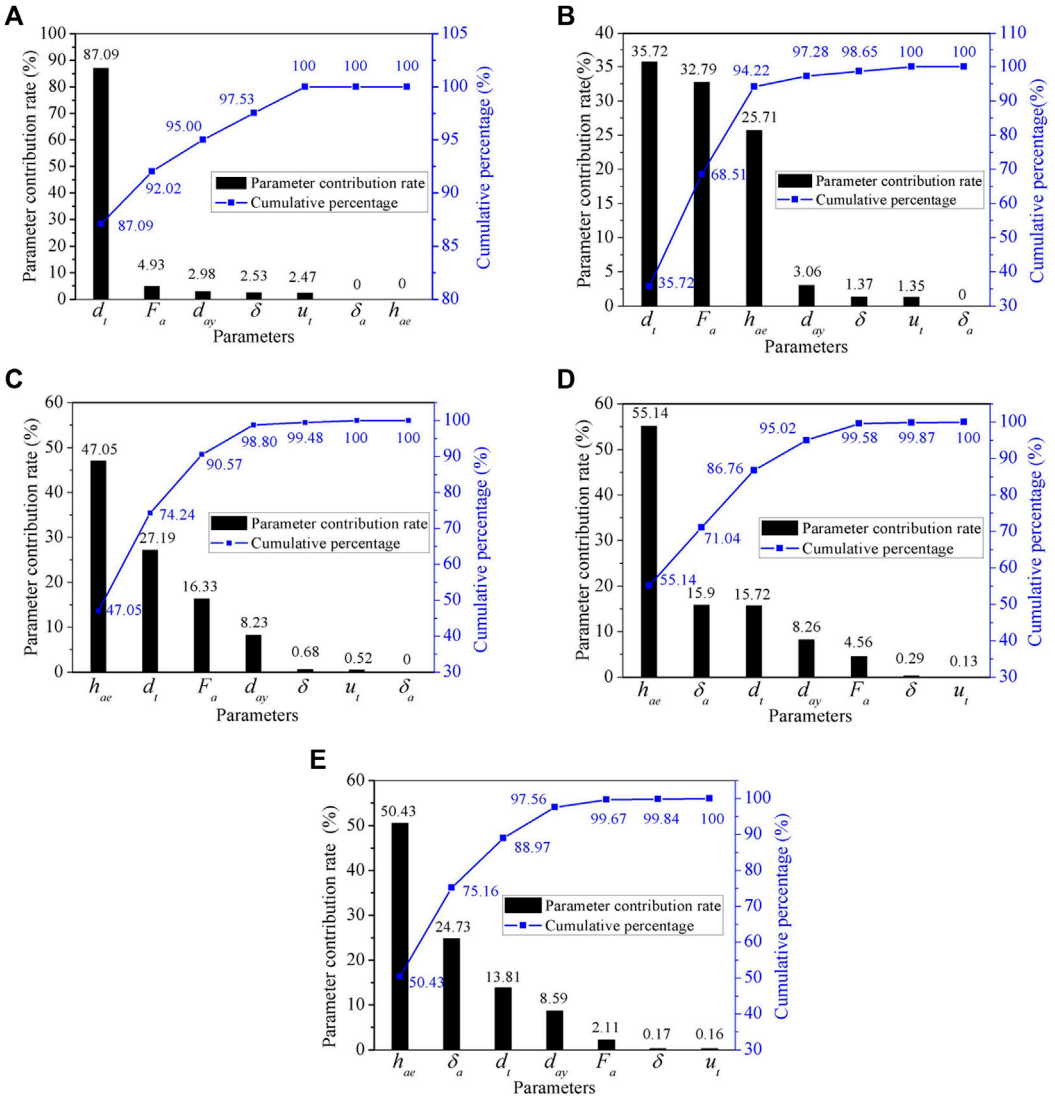

FIGURE 11 | The damping contribution rate of each parameter to the compression stroke under different excitation speeds (%). Note: Excitation speeds: **(A)** 0.05 m/s **(B)** 0.13 m/s **(C)** 0.26 m/s **(D)** 0.52 m/s **(E)** 1 m/s.

through-hole diameter, the valve plate equivalent thickness and the valve plate pre-tightening force of the two check valves "a" and "b" are selected as DOE experimental factors. **Table 3** shows the selected experimental factors and their level values.

Determine Design Matrix, Factor Level, and Response

According to the research purpose, the damping work of the compression stroke is determined as the response under different excitation speeds of 0.05, 0.13, 0.26, 0.52, and 1 m/s.

Experimental Plan

In ISIGHT, DOE components in-process components and Matlab interface components in application components are used to build the simulation process. The structural parameters and oil parameters of the damping control valve are internal parameters, and the external excitation is external parameters. The experiment includes two strokes of restoration and compression, five excitation speeds for each stroke, seven factors for each stroke, and two levels for each factor, run ISIGHT, and get the final result after calculation.

Discussion of Key Parameters of Valve System

Figure 11 shows the damping contribution rate of each parameter in the compression stroke under different excitation speeds. In the figure, the left axis represents the

damping contribution rate of the parameter, and the right axis represents the cumulative percentage of the parameter.

Figure 11A shows that when the excitation speed is 0.05 m/s, the damping contribution rate of the constant through-hole diameter is the largest, reaching 87.09%; Other parameters such as the valve plate pre-tightening force of the check valve "a" and the valve hole diameter of the check valve "a" contribute less than 5%. This is because when the excitation speed is 0.05 m/s, the check valve "a" is in the state before the first opening, and the damping force is basically generated by the constant through-hole at this stage, and other parameters have little influence on the damping work of the whole compression stroke.

Figure 11B shows that when the excitation speed is 0.13 m/s, the damping contribution rate of the constant through-hole diameter, the valve plate pre-tightening force of the check valve "a", and the valve plate equivalent thickness of the check valve "a" are larger, and the cumulative contribution rate of the three reaches 94.22%. The damping contribution rate of the constant through-hole diameter decreased. This is because when the valve is opened for the first time, the damping force is mainly provided by the through-hole and the annular gap.

Figure 11C shows that when the excitation speed is 0.26 m/s, the damping contribution rate of the valve plate equivalent thickness, the constant through-hole diameter, and the valve plate pre-tightening force of the check valve "a" are in the top three respectively, and their cumulative contribution rate reaches 90.57%. The damping contribution rate of the valve plate equivalent thickness of the check valve "a" increases, while the valve plate pre-tightening force of the check valve "a" decreases, and the damping contribution rate of the constant through-hole diameter further decreases. The reason is that the influence of the stage between the first opening and the second opening on the damping characteristics is mainly determined by the annular gap caused by the deformation of the valve plate.

Figure 11D shows that when the excitation speed is 0.52 m/s, the parameter with the largest damping contribution rate is the valve plate equivalent thickness of the check valve "a", reaching 55.14%; The damping contribution rate of the valve plate maximum limit clearance of the check valve "a" increased from the seventh to the second, accounting for 15.9%. The damping contribution rate of the constant through-hole diameter and the valve plate pre-tightening force of the check valve "a" further decreased. This is because when the valve is opened in the second stage, the value of the valve plate maximum limit clearance of the check valve "a" directly determines the flow area of the annular gap. The reason for the decrease of the damping contribution rate of the constant through-hole diameter and the valve plate pre-tightening force of the check valve is similar to that when the excitation speed is 0.26 m/s, so it will not be repeated.

Figure 11E shows that when the excitation speed is 1 m/s, the parameters with the largest damping contribution rate are the valve plate equivalent thickness of the check valve "a" and the valve plate maximum limit clearance of check valve "a", and the cumulative contribution rate of both is 75.16%.

The damping contribution of the constant through-hole diameter decreases gradually after the valve is opened for the first time. With the increase of the excitation speed, the valve plate equivalent thickness and the valve plate maximum limit clearance of the check valve gradually play a major role in the damping contribution rate. The mathematical modeling of the compression stroke and the recovery stroke is similar to the experimental design process. The discussion of the damping contribution rate of the key parameters in the recovery stroke is similar to that of the compression stroke, so it will not be repeated.

CONCLUSION

A valve-controlled damper with adjustable damping is developed and its damping characteristics are studied. The mathematical model of the damping characteristics of the valve-controlled adjustable damper before and after the opening valve is established, and the damping contribution rate of each parameter of the damping control valve is obtained. Detailed conclusions are presented below.

(a) The peak error of experiment and simulation is within the acceptable range, the damping force has no distortion, and the mathematical model of damping characteristics before and after opening the valve can better describe the working state of the damper.

(b) The simulation obtains the damping contribution rate of each parameter of the compression stroke damping control valve. When the excitation speed is 0.05 m/s, the damping contribution rate of the constant through-hole diameter is 87.09%; When the excitation speed is 0.13 and 0.26 m/s, the damping contribution rate of the constant through-hole diameter, valve plate pre-tightening force of the check valve "a", and the valve plate equivalent thickness of the check valve "a" are larger, and the cumulative contribution rate of the three is 94.22 and 90.57%, respectively; When the excitation speed is 0.52 m/s, the parameter with the largest damping contribution rate is the valve plate equivalent thickness of the check valve "a", reaching 55.14%. When the excitation speed is 1 m/s, the parameters with the largest damping contribution rate are the valve plate equivalent thickness of the check valve "a" and the valve plate maximum limit clearance of the check valve "a", and their cumulative contribution rate reaches 75.16%.

(c) The damping contribution of the constant through-hole diameter decreases gradually after the valve is opened for the first time. With the increase of the excitation speed, the valve plate equivalent thickness and the valve plate maximum limit clearance of the check valve "a" gradually play a major role in the damping contribution rate.

(d) The research results of this paper can screen out the key design variables, improve the development efficiency of the damper, and provide reference and guidance for the damper design and optimization.

DATA AVAILABILITY STATEMENT

The original contributions presented in the study are included in the article/Supplementary Material, further inquiries can be directed to the corresponding author.

AUTHOR CONTRIBUTIONS

FX and XS carried out conceptualization, writing the original manuscript, and revising. JC and ZD did methodology development, model design, and data collection. CY participated in the experiments and manuscript revision. YG did results discussion and language polish.

FUNDING

FX was supported by the Fundamental Research Funds for the Central Universities (2020ZDPYMS20).

ACKNOWLEDGMENTS

The author(s) disclosed receipt of the following financial support for the research, authorship, and/or publication of this article: The authors would like to acknowledge the financial supports given by the Fundamental Research Funds for the Central Universities (2020ZDPYMS20).

REFERENCES

Cao, J. X. (2020). *Parameter Optimization of Valve-Controlled Damping Adjustable Shock Absorber Based on Vehicle Ride Comfort*. Master's Dissertation. Zhenjiang, China: Jiangsu University. doi:10.27170/d.cnki.gjsuu.2020.000403

Causemann, P. (2003). Modern Vibration Damping Systems. *ATZ Worldw* 105 (11), 10–13. doi:10.1007/BF03225190

Chen, L., Yu, L., and Cui, X. L. (2013). Performance Simulation and experiment of Damping Multi-State Switching Shock Absorber. *J. Jiangsu Univ. (Natural Sci. Edition)* 34 (3), 6–10. doi:10.3969/j.issn.1671-7775.2013.03.001

Ding, E., Xie, F., Dai, H., Gao, Q., Zhang, J., Feng, Y., et al. (2018). Fluid Flow Modeling of a Four-Stage Damping Adjustable Shock Absorber and its Experimental Research. *Int. J. Struct. Integrity* 9 (1), 17–26. doi:10.1108/IJSI-03-2017-0016

Farjoud, A., Ahmadian, M., Craft, M., and Burke, W. (2012). Nonlinear Modeling and Experimental Characterization of Hydraulic Dampers: Effects of Shim Stack and Orifice Parameters on Damper Performance. *Nonlinear Dyn.* 67 (3), 1437–1456. doi:10.1007/s11071-011-0079-2

Fu, X. (2016). Research on Valve-Controlled Adjustable Damping Shock Absorber and Damping Characteristics. *Glob. Market Inf. Herald* 37, 129. CNKI:SUN:HQXX.0.2016-37-102.

Huang, Y. M., Hou, S. J., Qin, D. C., and Wang, T. T. (2020). Theoretical Modeling and Key Parameter Impact Analysis of Built-In Valve-Controlled Damping Adjustable Shock Absorber. *Automobile Tech.* 532 (1), 37–43. doi:10.19620/j.cnki.1000-3703.20191046

Lindler, J. E., Dimock, G. A., and Wereley, N. M. (2000). Design of a Magnetorheological Automotive Shock Absorber. *Proc. SPIE–the Int. Soc. Opt. Eng.* 3985, 426–437. doi:10.1117/12.388845

Liu, Z. T., Miao, Y. Y., Zhang, S. B., You, J., and Wei, J. R. (2019). The Development and Research Status of the Shock Absorber Industry in the Automobile Industry. *Jiangsu Sci. Tech. Inf.* 36 (10), 80–85. doi:10.3969/j.issn.1004-7530.2019.10.024

Łuczko, J., and Ferdek, U. (2019). Non-linear Analysis of a Quarter-Car Model with Stroke-dependent Twin-Tube Shock Absorber. *Mech. Syst. Signal Process.* 115, 450–468. doi:10.1016/j.ymssp.2018.06.008

Ma, T., Cui, Z. F., and Zhang, M. M. (2013). Modeling and Simulating of the Gas-Precharged Dual-Sleeve Shock Absorber with Multiple Valve Plates Using AMESim. *J. Mech. Eng.* 49 (12), 123–130. doi:10.3901/JME.2013.12.123

Ma, Y. F. (2018). *Design and Research of Multi-point Force Value Vehicle Shock Absorber Based on Multi-Objective Optimization*. Master's Dissertation. Chengdu, China: Southwest Jiaotong University. CNKI:CDMD:2.1018.709778.

Maemor, K., Tanigawa, N., Koganei, R., and Morihara, T. (2003). Optimization of a Semi-active Shock Absorber for Aircraft landing Gear, ASME 2003 International Design Engineering Technical Conferences and Computers and Information in Engineering Conference, Chicago, United states, September 2003. New York, NY: ASME, 597–603. doi:10.1115/detc2003/dac-48765

Montgomery, D. C. (2009). *Experimental Design and Analysis*. Beijing: China Statistics Press. 978-7-115-19234-9.

Wang, T., Zhou, J., Meng, F. X., and Ji, W. T. (2018). A Structural Optimization Design Method for Train Vertical MR Damper. *Mech. manufacturing automation* 47 (1), 101–104. doi:10.19344/j.cnki.issn1671-5276.2018.01.029

Wang, Z. Q. (2016). Discussion on the Present Situation and Development of Automobile Shock Absorbers. *Tech. Innovation Appl.* 159 (11), 151. CNKI:SUN:CXYY.0.2016-11-129.

Xie, F., Ding, E., Xuan, R., Zhang, X., Feng, Y., and Zhu, J. (2018). Influence Rules of Geometric Parameters on Deformation of Valve Slices in Valve-Controlled Adjustable Damping Shock Absorber. *Int. J. Struct. Integrity* 9 (1), 107–118. doi:10.1108/IJSI-04-2017-0025

Xie, F. W., Xuan, R., and Zhang, B. (2015). Design and Experimental Study of Test Bench for Damping Adjustable Shock Absorber Based on xPC. *Automobile Tech.* 483 (12), 44–48. doi:10.3969/j.issn.1000-3703.2015.12.011

Xuan, R. (2016). *Research on Valve-Controlled Adjustable Damping Shock Absorber and its Damping Characteristics*. Master's Dissertation. Zhenjiang, China: Jiangsu University. doi:10.7666/d.D823375

Yang, M. J., Yu, J. Q., and Guo, Y. B. (2019). Present Situation and Development Tendency of Shock Absorbers in Vehicle Suspensions. *ENGINEERING TEST.* 59 (2), 97–100. doi:10.3969/j.issn.1674-3407.2019.02.036

Zhang, W. L., Mei, Y. H., and Liu, L. Y. (2019). Research on Optimization of Hydraulic Double Cavity Damping Stiffness Based on Finite Element Method. *Mod. manufacturing Technol. equipment* 277 (12), 86–89. doi:10.16107/j.cnki.mmte.2019.1210

Zhou, C. C., and Ren, C. B. (2009). Optimum Design of Throttle Slice Thickness and its Characteristic Test for Telescopic Damper with Damping Matching. *J. Vibration Eng.* 01, 54–59. doi:10.16385/j.cnki.issn.1004-4523.2009.01.008

Conflict of Interest: The authors declare that the research was conducted in the absence of any commercial or financial relationships that could be construed as a potential conflict of interest.

Publisher's Note: All claims expressed in this article are solely those of the authors and do not necessarily represent those of their affiliated organizations, or those of the publisher, the editors and the reviewers. Any product that may be evaluated in this article, or claim that may be made by its manufacturer, is not guaranteed or endorsed by the publisher.

NOMENCLATURE

Fc valve-controlled damping adjustable damper compression stroke damping force, N

F_f friction between the piston and the working cylinder during the compression stroke, N

F_a valve plate pre-tightening force of the check valve "a", N

F_b valve plate pre-tightening force of the check valve "b", N

l gap length, m

A_d working cylinder area, m^2

A_r piston rod area, m^2

A_b contact area between the piston and the working cylinder, m^2

A_t flow area of the constant through-hole, m^2

P_n radial pressure on piston, Pa

P_0 initial pressure of the nitrogen cavity, Pa

P_1 oil pressure of recovery cavity, Pa

P_2 oil pressure of compression cavity, Pa

P_3 pressure of nitrogen cavity, Pa

ΔP_{21} pressure difference between the compression cavity and the recovery cavity, MPa

ΔP_{31} pressure difference at both ends of the check valve "a", MPa

V_0 initial volume of the nitrogen cavity, m^3

v_{c1} piston movement speed of the compression stroke, m/s

v_{c2} velocity of piston movement after initial valve opening of the compression stroke, m/s

r_{c1} inner circle radius of the annular disc of the check valve "a", m

r_{c2} outer circle radius of the annular disc of the check valve "a", m

δ_a valve plate maximum limit clearance of the check valve "a", mm

δ_b valve plate maximum limit clearance of the check valve "b", mm

d_d inner diameter of the working cylinder, mm

d_r diameter of the piston rod, mm

d_t diameter of the constant through-hole, mm

d_{ay} valve hole diameter of the check valve "a", mm

d_{bf} valve hole diameter of the check valve "b", mm

N_t number of the normal through-hole, -

n number of the normal through-hole, -

n_a number of the check valve "a" hole, -

n_b number of the check valve "b" hole, -

H_r contact width between the piston and the working cylinder, m

h_{ae} valve plate equivalent thickness of the check valve "a", mm

h_{be} valve plate equivalent thickness of the check valve "b", mm

C_t flow coefficient of the constant through-hole

P oil density, kg/m^3

Δ oil film thickness, m

e eccentricity, -

δ piston clearance, mm

x_q the nitrogen cavity piston displacement, m

r the temperature index, 1.4

s_p the displacement of the piston after the valve is opened, m

frontiers | Frontiers in Energy Research

ORIGINAL RESEARCH
published: 28 April 2022
doi: 10.3389/fenrg.2022.880338

Flow Characteristic Analysis of the Self-Priming Pump Based on the Population Balance Model

Hao Chang[1,2], Shiming Hong[1], Dehui Yu[3], Guangjie Peng[1], Jialin Du[1] and Shouqi Yuan[1]**

[1]Research Center of Fluid Machinery Engineering and Technology, Jiangsu University, Zhenjiang, China, [2]International Shipping Research Institute, Gong Qing Institute of Science and Technology, Jiujiang, China, [3]Chongqing Pump Industry Co. Ltd., Chongqing, China

Self-priming pumps, as important two-phase fluid machinery, are widely used in disaster relief and emergency fields. The flow characteristics of the air–liquid two-phase fluid play an essential role in the self-priming pump performance. However, the traditional simulation employed the single-diameter bubbles for analysis, which cannot reflect the internal flow field characteristics. Therefore, in this article, the Population Balance Model (PBM) is employed, which divides the bubble into different diameter groups, and the collision and coalescence between the bubble are considered in the calculation to investigate the influence of different air voids and flow conditions on the performance self-priming centrifugal pumps. The result shows that the frequency of bubble coalescence at the shroud is higher, which is conducive to the formation of large-sized bubbles. Meanwhile, the increment of flow conditions has a significant effect on reducing the pressure pulsation of the gas–liquid two-phase flow, while the improvement of the air voids not only destroys the instability and asymmetry of the internal flow of the two-phase flow but also aggravates the amplitude of pressure pulsation, increasing the surface loading of the blade and radial force. Therefore, this article can provide a certain theoretical reference for the study of air–liquid two-phase flow characteristics of self-priming centrifugal pumps.

Keywords: population balance model, self-priming pump, flow characteristics, blade surface loading, pressure fluctuation

OPEN ACCESS

Edited by:
Lei Tan,
Tsinghua University, China

Reviewed by:
Daqing Zhou,
Hohai University, China
Xiao Ruofu,
China Agricultural University, China

****Correspondence:***
Guangjie Peng
pgj@ujs.edu.cn
Shouqi Yuan
shouqiy@ujs.edu.cn

Specialty section:
This article was submitted to Process and Energy Systems Engineering, a section of the journal Frontiers in Energy Research

Received: *21 February 2022*
Accepted: *18 March 2022*
Published: *28 April 2022*

Citation:
Chang H, Hong S, Yu D, Peng G, Du J and Yuan S (2022) Flow Characteristic Analysis of the Self-Priming Pump Based on the Population Balance Model. Front. Energy Res. 10:880338. doi: 10.3389/fenrg.2022.880338

INTRODUCTION

Self-priming pump plays an essential role in disaster relief and emergency fields, and many scholars pay attention to the flow characteristic of the air–liquid two-phase flow of the self-priming pump. Wang et al. (2019a) and Wang et al. (2019b) simulated the air–liquid two-phase basis of the four-stage self-priming pump and found that the self-priming procession consisted of three parts, and the middle self-priming part has an important effect on the self-priming performance. Qian et al. (2020) and Qian et al. (2021) employed the Euler–Euler multiphase model and SST k-omega turbulence model to investigate the two-phase flow patterns of the self-priming process. The results present the air–liquid mixing and separation regulation, and the experiments are carried out to improve the accuracy of the analysis. Huang et al. (2014) studied the transient gas–liquid flow of the start-up stage based on a vertical self-priming pump, and the self-priming time and performance can be predicted by numerical calculations. Zhou et al. (2019) analyzed the influence of reflux holes on the transient flow characteristics of the self-priming sewage centrifugal pump, and the unsymmetrical vortex flow structures are found in the flow field, which aggravates the pressure fluctuation amplitude. Zhang

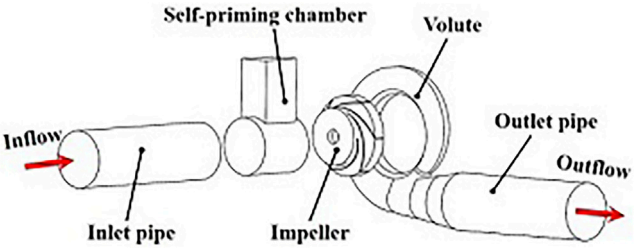

FIGURE 1 | The calculation model of the self-priming pump.

et al. (2021) compared the rapid and slow starting periods of the self-priming pump by experiment, and the similarities and differences between the different start methods were investigated in detail. Chang et al. (2020) and Chang et al. (2021) combined the orthogonal design and grey-correlational method to analyze the influence of geometrical parameters of self-priming equipment on the self-priming performance, and the effect law of the self-priming time is obtained.

Zhang et al. (2016) conducted the visualization experiment based on a three-stage pump with gas and water as the medium and found that the inlet part of the impeller is a bubbly flow, and the average bubble diameter increases with the increase in gas content but decreases with the increase in speed. Ganat et al. (2015) proposed a novel flow calculation method to improve the error caused by the previous measurement based on the traditional method of measuring gas flow. Barrios and Prado (2011) found that the bubble behavior is related to the sudden drop of the head, which is accompanied by the cavitation at the inlet of the pump based on the visual experiment. Yonggang et al. (2019) studied the flow mechanism of the reactor system cooling pump in a gas–liquid two-phase mixed operation state and used the CFX numerical calculation method to analyze the internal gas–liquid distribution of the reactor cooling pump under the four flow conditions with different gas content. Murakami and Minemura (1974) studied the effect of the number of impeller blades on the performance of centrifugal pumps under the aeration conditions and found that the hydraulic loss caused by the bubble flow resistance reduces the total head. Monte Verde et al. (2017) studied the gas–liquid two-phase flow in an electric pump through high-speed photography, and the results show that the appearance of cavitation was the cause of the deterioration of the pump performance. Müller et al. (2015) analyzed the gas–liquid flow characteristics in the centrifugal pump based on the Euler–Euler two-fluid model. Meanwhile, the bubbles and water are regarded as incompressible media, and the interphase force only considers the drag force calculated by the Schiller–Norman model throughout the simulation process. Wu et al. (2017) proposed to use the high-pressure gas generated in the system evaporator to drive a multi-stage gas–liquid booster instead of an electrical working fluid pump which can improve the performance of the organic Rankine cycle system. Zhang et al. (2017) conducted an experimental study on the internal flow characteristics of the side-channel pump under the gas–liquid two-phase flow conditions and analyzed the influence of the blade suction angle on the head and efficiency under different inlet air volume fractions. Musakaev and Borodin (2016) established a two-phase flow model based on a centrifugal pump located in a permafrost zone, which is used to predict the flow field parameters of the two-phase flow inside the centrifugal pump, and added the influence of temperature on the gas–liquid two-phase flow.

Although the researchers have carried out a lot of research on the air–liquid two-phase flow in the centrifugal pumps, the air–liquid two-phase flow simulations were conducted based on the single-diameter bubbles for the analysis. However, in actual operation, due to the interaction between the bubbles and the internal flow field, the collision and coalescence of the bubble are generated, namely, the small bubbles will collide to form large bubbles, and the large bubbles will break into the small bubbles. Therefore, there is a certain deviation in the simulation of the air–liquid two-phase flow with a single-diameter bubble. In this article, the Population Balance Model (PBM) was employed, which divides the bubble into different diameter groups, and the collision and coalescence of the bubble are considered in the calculation to investigate the influence of different air voids and flow conditions on the performance self-priming centrifugal pumps under the part-load flow conditions, which provides a certain theoretical reference for the study of the air–liquid two-phase flow characteristics of the self-priming centrifugal pumps.

CALCULATION METHOD AND MODEL

In this article, the SST k-ω turbulence model is used for the transient numerical calculation, and the total calculation time is 0.2 s. The numerical analysis medium uses 25°C clear water and air as the two-phase flow. By adopting the Euler–Euler model to load the group balance model, the internal flow characteristics of different air voids under the part-load flow conditions are analyzed. The calculation of the self-priming pump consists of five parts: inlet pipe, outlet pipe, self-priming chamber, impeller, and volute. In order to reduce the influence of the inlet and outlet pipe on the analysis results, the inlet and outlet pipe are extended

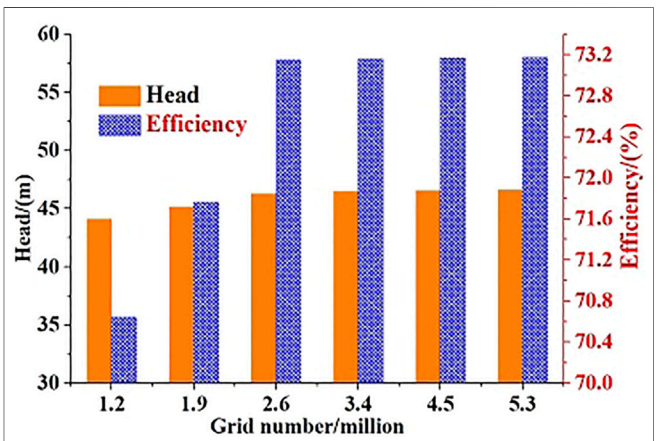

FIGURE 2 | Grid sensitive analysis.

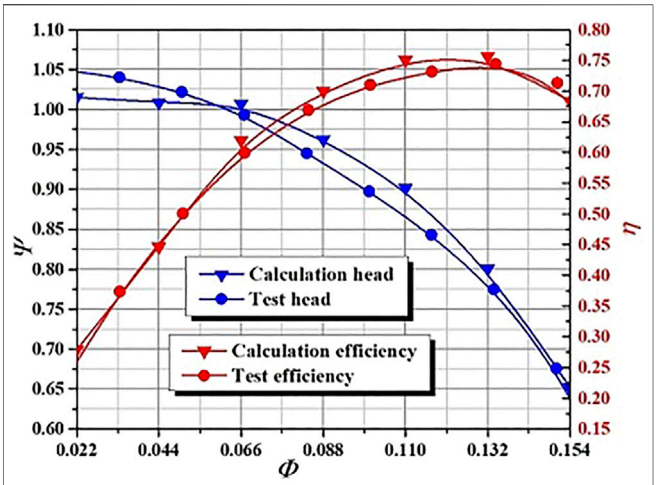

FIGURE 3 | Investigation of the calculation and experiment.

TABLE 1 | Selection of schemes.

	Scheme 1	Scheme 2	Scheme 3	Scheme 4
Flow rate (m^3/h)	100	100	300	300
Air voids (%)	2	6	2	6

TABLE 2 | Groups of different bubble sizes.

	Group 1	Group 2	Group 3	Group 4	Group 5
Bubble size (mm)	1	2	3	4	5
	Group 6	Group 7	Group 8	Group 9	Group 10
Bubble size (mm)	6	7	8	9	10

5 times of the impeller inlet diameter, and the calculation model is shown in **Figure 1**.

In order to decrease the investigation period, the structured grids are applied on the calculation models by ANSYS ICEM, the grids of the blade leading edge and volute tongue is conducted as a local encryption part. Meanwhile, the optimal flow condition is 500 m^3/h, the rotation speed is 2,200 r/m, and the design head is 45 m. Considering the influence of the grid number on the self-priming pump performance, the grid sensitive analysis is conducted. Grid numbers of 5.3×10^6, 4.5×10^6, 3.4×10^6, 2.6×10^6, 1.9×10^6, and 1.2×10^6 are selected. It is found that the deviation of the hydraulic performance is less than 1% when the grid number reaches 2×10^6, and the investigation results are shown in **Figure 2**. In addition, to ensure the analysis accuracy, the hydraulic experiments are carried out to validate the calculation result, as shown in **Figure 3**. The result presents that the deviation between the experiment and calculation is below 3%, which are the results from the volumetric loss without considering the numerical calculation. Thus, the calculation method is reliable for further investigation.

Meanwhile, four schemes under the part-load flow conditions are proposed, as shown in **Table 1**. According to the previous analysis, the bubbles size distribution is divided into 10 groups. The bubble groups and sizes are shown in **Table 2**. In the calculation process, the drag force and the virtual mass force are added as the interphase force, and the Schiller–Naumann model is set as the drag coefficient. At the same time, the breakage and coalescence between the bubbles are considered, and the Luo–Svendsen coalescence and breakage models are added in the calculation.

ANALYSIS OF INTERNAL FLOW FIELD

In this article, the group balance model is applied to analyze the influence of air voids and flow conditions on the internal flow characteristics. **Figure 4** presents the distribution of 10 different sized bubbles on the circumferential surface of the rear cover (Span 0). **Figure 4A** shows the distribution of the bubbles with the 1 mm diameter. It can be seen that the bubble distribution of each scheme has obvious similarities. Meanwhile, a small number of bubbles with 1 mm were found on the leading edge of the blades in scheme 1. However, by increasing the air voids under the same flow condition, the strength and area of the bubble distribution are slightly increased in scheme 2. When the flow conditions improve to 300 m^3/h, it can be found that a small amount of 1 mm bubbles are generated at the leading edge in scheme 3. Although the distribution area is smaller than that in scheme 2, the strength is significantly enhanced. At the same time, it can be found that the 1 mm bubbles are also generated in the impeller flow passages, but the area is significantly smaller than the leading edge of the blade. By further increasing the air voids based on scheme 3, each impeller flow channel of scheme 4 is distributed with the first size group of the bubbles, and the distribution area is significantly larger than scheme 3.

As shown in **Figure 4B**, the distribution of the bubbles with 2 mm on Span 0 has a similar variation trend with the 1 mm bubbles, but the area and intensity are significantly enhanced. Compared with the other three schemes, the distribution area of 2 mm bubbles in scheme 1 is the smallest. When the air voids are increased from 3 to 6%, the bubble distribution near the leading edge of the blade is significantly increased. The main reason for this phenomenon is that the improvement of air voids aggravates the collision frequency between the small-sized bubbles and the coalescence ability of the bubble groups improves continuously. When the flow rate reaches 300 m^3/h and the air voids are 3%, it is found that the bubbles are generated at the leading edge of the blade and the impeller flow channel. Subsequently, by increasing the air voids to 6%, the distribution of the 2 mm bubbles at the leading edge of the blade and the impeller flow channel is further enhanced. Therefore, by comparing the distribution of the first two groups of size bubbles, it can be found that the bubble

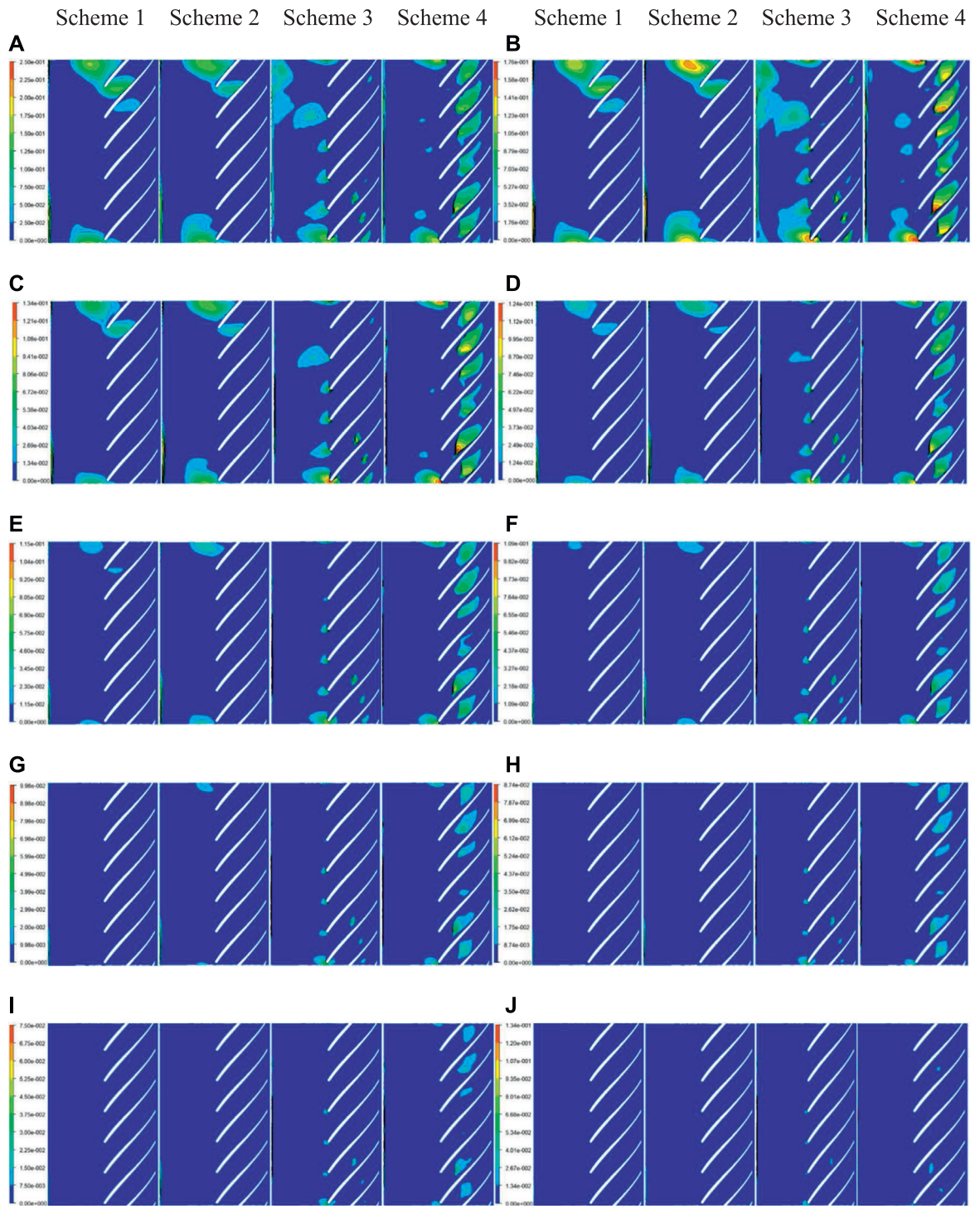

FIGURE 4 | Distribution of different sizes bubbles on the Span 0. **(A)** The distribution of 1 mm bubbles. **(B)** The distribution of 2 mm bubbles. **(C)** The distribution of 3 mm bubbles. **(D)** The distribution of 4 mm bubbles. **(E)** The distribution of 5 mm bubbles. **(F)** The distribution of 6 mm bubbles. **(G)** The distribution of 5 mm bubbles. **(H)** The distribution of 6 mm bubbles. **(I)** The distribution of 5 mm bubbles. **(J)** The distribution of 6 mm bubbles.

distribution shows an increasing trend as the bubble size improves. However, in **Figure 4C**, the distribution area and the intensity of the 3 mm bubbles are slightly reduced compared to the 2 mm bubbles. When the size bubbles improve from 3 to 10 mm, the corresponding size bubble distribution is continuously reduced. As the bubble size

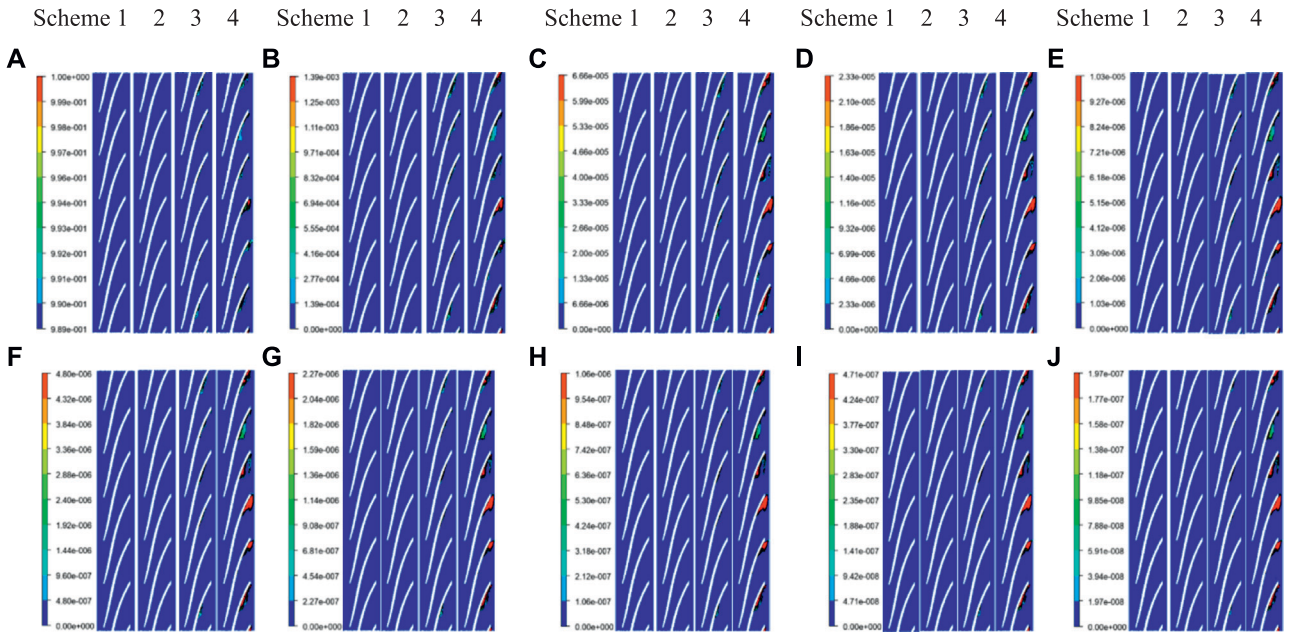

FIGURE 5 | Distribution of different sizes bubbles on the Span 1. **(A)** 1 mm bubbles. **(B)** 2 mm bubbles. **(C)** 3 mm bubbles. **(D)** 4 mm bubbles. **(E)** 5 mm bubbles. **(F)** 6 mm bubbles. **(G)** 7 mm bubbles. **(H)** 8 mm bubbles. **(I)** 9 mm bubbles. **(J)** 10 mm bubbles.

increases to 7 mm, no bubble can be found in scheme 1. Meanwhile, when the bubble size increases to 10 mm, only a small amount of the 10 mm bubbles is generated in scheme 4. Therefore, it can be found that as the bubble size increases from 3 to 10 mm, the coalescence ability of the bubbles of the corresponding size is continuously weakened.

However, the overall variation of the bubble distribution on the rear cover (Span 1) is relatively small. **Figure 5A** presents the distribution of the bubbles with 1 mm. It can be seen from the figure that only a small number of bubbles were generated on the trailing edge of the blade in scheme 4. By comparing the 2 mm bubble distribution diagrams, it can be found that there are a few bubbles generated in schemes 1 and 2. **Figures 5C–J** present the distributions from the 3 mm to the 10 mm bubbles. Through comparison, it is found that the distribution of the last eight groups of bubbles shows the same variation trend. There are no large-sized bubbles generated in schemes 1 and 2, but a small number of the large-sized bubbles are generated in scheme 3, and the bubble distribution on the pressure surface of scheme 4 is larger than the other schemes, and the bubble distribution between the adjacent blades is quite different. Furthermore, a large number of bubbles are formed on the trailing edge of the pressure surface near the tongue. As the position of the blade gradually moves away from the tongue, the distribution area gradually decreases. This is mainly due to the continuous collision of the bubbles in the flow field at the shroud, which leads to the generation and gathering of the large-sized bubbles. Therefore, by comparing the bubbles distribution on the shroud and rear cover, it can be found that more large-sized bubbles are formed on the shroud, while the small-size bubbles are generated on the rear cover. The main reason for this phenomenon is that the trailing edge vortex is formed at the outlet of the impeller when the self-priming centrifugal pump operates the under part-load flow conditions. According to the previous analysis (Chang et al., 2019), it can be seen that the vortex is mainly formed near the rear cover, thus the violent collision of the bubble group is formed near the rear cover, which results in the coalescence of the large-sized bubbles. In contrast, the frequency of the bubble coalescence at the shroud is higher, which is conducive to the formation of the large-sized bubbles.

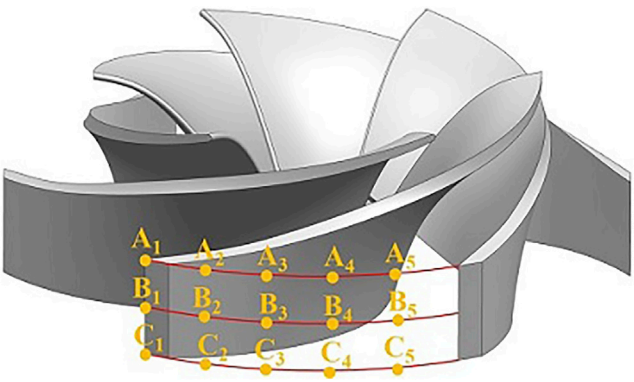

FIGURE 6 | The location diagram of the pressure monitoring points.

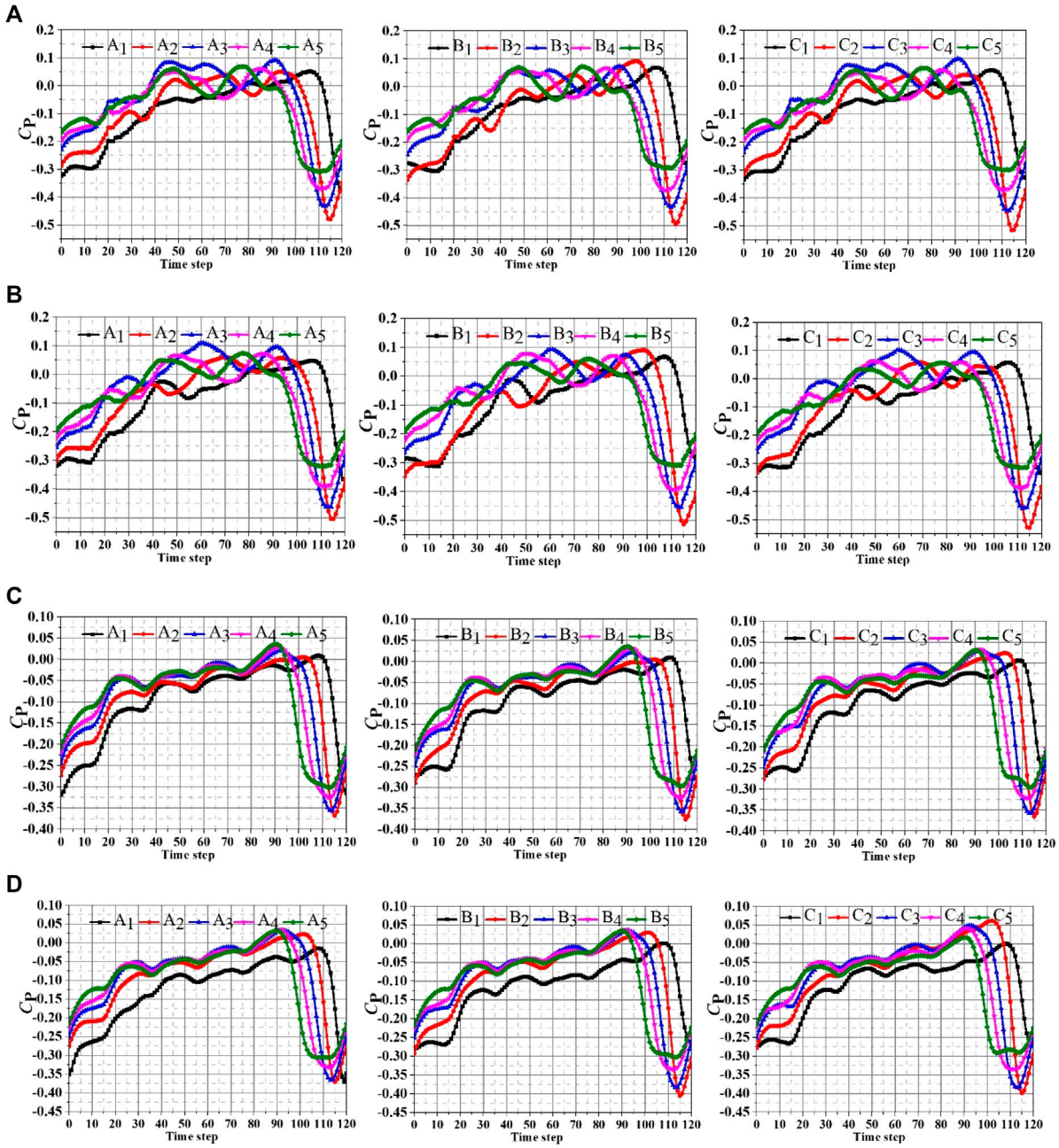

FIGURE 7 | The pressure fluctuations distribution of different schemes. **(A)** The pressure pulsation distribution of scheme 1. **(B)** The pressure pulsation distribution of scheme 2. **(C)** The pressure pulsation distribution of scheme 3. **(D)** The pressure pulsation distribution of scheme 4.

ANALYSIS OF PRESSURE PULSATION CHARACTERISTICS

In order to ensure the smooth operation of the self-priming pump under the air–liquid two-phase flow conditions, the pressure pulsation characteristics under the different air voids and flow conditions were analyzed in this section. Considering the wrap angle of the impeller to be 60°, the pressure pulsation monitoring points are set on Span 0, Span 0.5, and Span 1 circumference surface every 10°, namely, the monitoring points C_1, C_2, C_3, C_4, and C_5 on the circumference of Span 0, the monitoring points B_1, B_2, B_3, B_4, and B_5 on the circumference of Span 0.5, and the monitoring points A_1, A_2, A_3, A_4, and A_5 on the circumference of Span 1, as shown in **Figure 6**.

Considering the accuracy of the investigation, the data of pressure pulsation are expressed by the dimensionless format, and only the pressure pulsation of the last rotation period is

employed. The dimensionless pressure fluctuation data can be obtained by **formula (1)**. At the same time, the density is the mixed density of the air–liquid two-phase flow. For the density of different air voids, the density can be calculated by **formula (2)** and **3**, respectively.

$$C_{\mathrm{p}} = \frac{\sqrt{\frac{1}{N}\sum_{j=0}^{N-1}\tilde{p}^{2}\left(node, t+\Delta t\right)}}{\frac{1}{2}\rho_{\mathrm{Mix}}\mu_{2}^{2}}, \tag{1}$$

$$\rho_{\mathrm{Mix2\%}} = 98\%\rho_{l} + 2\%\rho_{a}, \tag{2}$$

$$\rho_{\mathrm{Mix6\%}} = 94\%\rho_{l} + 6\%\rho_{a}, \tag{3}$$

where, ρ_{Mix} is the mixed density of the air–liquid two-phase flow, ρ_{l} is the density of the liquid, and ρ_{a} is the density of air.

Figure 7 shows the distribution of pressure pulsation at the impeller outlet, it found that the pressure pulsation under the air–liquid two-phase flow is more complicated. There are multiple secondary peaks within a rotation period, and the pressure pulsation amplitude of each monitoring point is quite different. At the same time, due to the position difference of the monitoring points, the phase difference of the pressure pulsation peaks is generated at each point, and the No. 5 monitoring points sweep the tongue firstly. Therefore, the earliest pressure pulsation peak appeared at the monitoring point 5, and the pressure pulsation peaks of the monitoring points 4, 3, 2, and 1 are lagging behind point 5, respectively. However, the multiple peaks of pressure pulsation are found on the different monitoring points. This phenomenon is attributed to the violent collision of bubbles in the air–liquid two-phase flow, which results in the continuous breakage of large bubbles and the coalescence of small bubbles, the internal flow field is relatively turbulent, thus the multiple peaks of pressure pulsation are generated at each monitoring point.

As shown in **Figure 7**, the pressure pulsation amplitude increased continuously when the monitoring points moved from the shroud to the rear cover in scheme 1. The negative amplitude of pressure pulsation of each monitoring point is greater than the positive amplitude. While the positive amplitude difference of the monitoring points on the same circumferential surface is slightly different, the negative amplitude is quite different. Among them, the order of the magnitude of the negative amplitude of each monitoring point is 2 > 3> 4 > 5> 1, namely, the negative amplitude of position 2 is the largest. As the air voids increase to 6%, it can be found that the negative amplitude of the pressure pulsation at each monitoring point in scheme 2 is still greater than the positive amplitude, and the magnitude of the negative amplitude is significantly improved compared to scheme 1. Meanwhile, the pulsation amplitude of the monitoring points on the rear cover is also greater than the pressure pulsation amplitude on the shroud. Furthermore, by comparing the monitoring points on the same circumferential surface, it can be found that the order of the negative amplitudes of the monitoring points remain unchanged. When the flow conditions are further increased, it can be found that the pressure pulsation amplitude of scheme 3 is significantly reduced, which is consistent with the internal flow law of the clear water state. The speed of the fluid flowing out of the impeller continues to increase, which collides with the fluid in the volute. Due to the large difference in speed and direction of the fluid between the impeller and volute, a large impact loss and severe pressure pulsation are formed. With the increase of the flow conditions, the speed difference between the impeller and the volute continues to decrease, the unstable characteristics of the internal flow field are effectively improved, and the pressure fluctuation waveforms at each monitoring point tend to be consistent. At the same time, when the flow rate reaches 300 m^3/h, and the air voids are increased from 2 to 6%, it can be found that the pressure pulsation amplitude of each monitoring point in scheme 4 has a significant increase. More importantly, the amplitude of the monitoring points on the rear cover is still greater than that of the shroud, which results from the increase of the air voids enhancing the frequency of collisions between the bubbles in the two-phase flow and aggravating the instability of the internal flow. The breakage and coalescence of the bubbles at the rear cover are more significant, thus making the pressure fluctuations more severe. Therefore, in this section, the pressure pulsation characteristic of the air–liquid two-phase flow is analyzed by increasing the flow condition and the air voids. It can be found that the two methods have opposite mechanisms of pressure pulsation. The increase in flow conditions has a significant effect on reducing the pressure pulsation of the gas–liquid two-phase flow, and the improvement of the air voids not only destroys the stability of the internal flow of the two-phase flow but also aggravates the amplitude of pressure pulsation.

ANALYSIS OF BLADE SURFACE LOADING

Figure 8 presents the blade surface loading distribution on the two circumferential surfaces of the shroud and the rear cover. It can be found that the surface loading of the blade is mainly composed of the two upper and lower curves, and the difference between the two curves presents the surface loading of the blade. By comparing the blade surface loading of the four schemes, it can be found that the pressure on the pressure surface and the suction surface presents the increment trend from the leading edge to the trailing edge, and there are three zero-load points that are generated on the blade, namely. The pressure on the pressure surface and suction surface has the same value.

The pressure curve on the pressure surface of the blade first drops sharply near the leading edge and then rises at a constant speed to intersect with the pressure curve of the suction surface, that is, there is a point where the pressure on the pressure surface of the blade is equal to the suction surface of the blade, and the first zero load point is generated at the blade relative streamline position of 0.25. This phenomenon is attributed to the collision between the leading edge of the blade and the incoming flow of the inlet pipe, the sudden changes of the liquid speed direction under the action of the

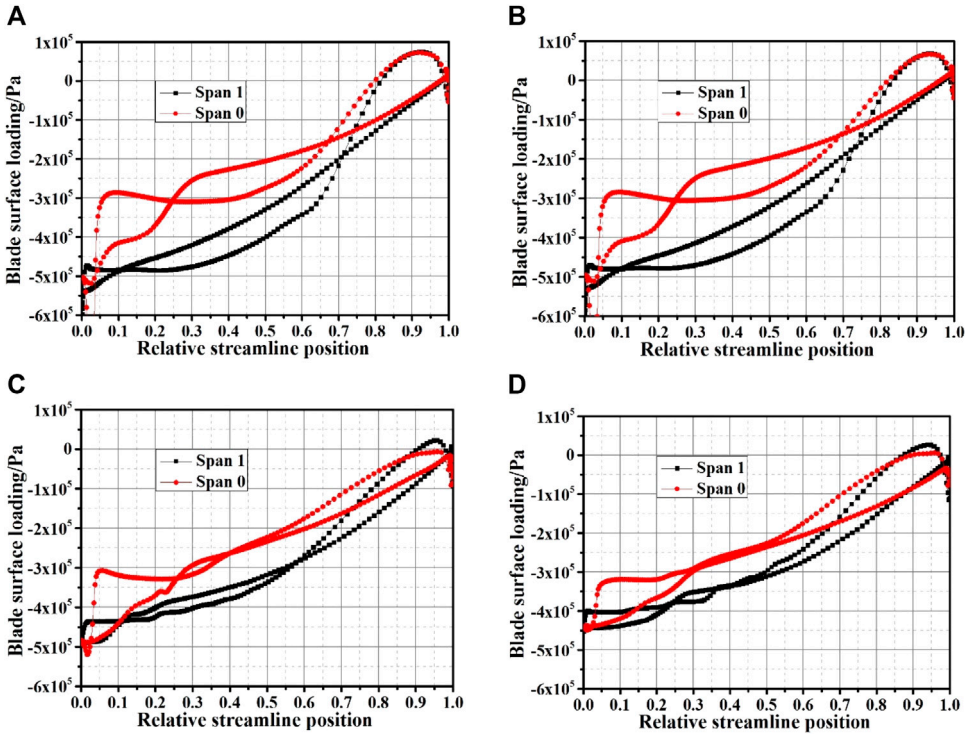

FIGURE 8 | The blade loading with different schemes. **(A)** Scheme 1. **(B)** Scheme 2. **(C)** Scheme 3. **(D)** Scheme 4.

blade, which results in the pressure on the pressure surface and the suction surface changes sharply. At the same time, when the relative streamline position passes through the first zero load point, the pressure on the pressure and suction surface still maintains the upward trend, but the pressure growth rate on the suction surface continues to increase and gradually exceeds the growth rate of the pressure surface. At this time, due to the continuous collision of large bubbles and the coalescence of small bubbles, the pressure on the pressure and suction surface of the blade improves progressively. When the pressure caused by the collision and coalescence of the bubble on the suction and pressure surface keep the same value, the second zero load point is formed. In addition, the formation of the third zero-load point is mainly due to the influence of the stator–rotor interaction between the tongue and blade. By comparing the blade surface loading distribution of different schemes, it can be found that due to the violent collision of bubbles at the rear cover, the pressure on the pressure surface and suction is significantly larger than that at the shroud. The surface loading of the rear cover is larger than the shroud. After increasing the air voids based on scheme 1, the blade surface loading increased slightly. However, as the flow rate increases, the blade surface loading decreases effectively. By comparing scheme 3 and scheme 4, the result shows that the blade surface loading has also been improved. Therefore, the effect of air voids and flow rate on the blade surface loading is obtained, two factors have opposite effects on the blade loading. The increment of the flow rates improves the internal flow law and greatly reduces the surface load of the blade, while the improvement of the air voids enhances the collision between the bubbles, which aggravates the instability in the flow field, and increases the surface loading of the blade.

DISTRIBUTION OF RADIAL FORCE

The pump with a spiral volute will lead to the radial force on the impeller during operation, which will cause the shaft to be subjected to alternating stress, resulting in a directional disturbance and affecting the service life of the pump. This phenomenon is attributed to the asymmetry structure of spiral volute is design basis of optimal flow condition, the velocity, and pressure of the liquid in the volute around the impeller are uniform and axisymmetric, without force is pushed on the impeller at the radial direction. However, the break of the radial pressure balance under the nonoptimal flow rates results in the generation of the radial force. In order to ensure the precision of the radial force analysis, we perform a dimensionless processing on the radial force to obtain the radial force coefficient C_F. The calculation formula is

$$C_F = \frac{2F_R}{\rho_{Mix}\mu_2^2 D_2 b_2}. \tag{4}$$

At this time, the density is the mixed density of the air–liquid two-phase flow. Therefore, the density of different air voids can be solved by **Eqs 2**, **3** separately.

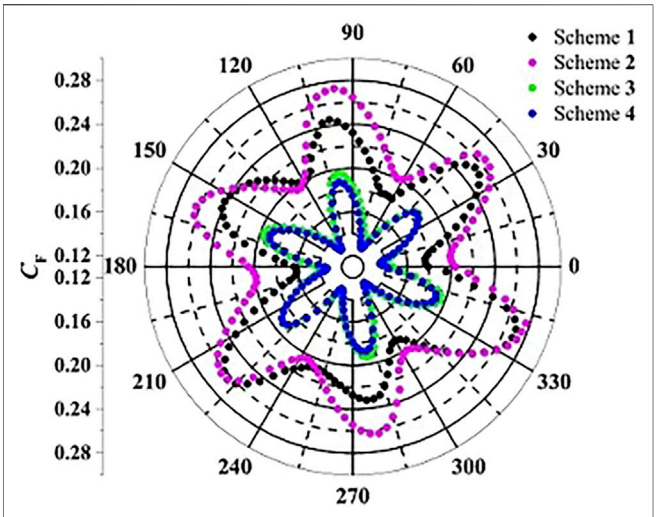

FIGURE 9 | Radial force distribution of each scheme.

Figure 9 shows the radial force polar coordinate distribution of different schemes. It can be seen from the figure that the direction and magnitude of the radial force upon the impeller during the rotation process are always changing. Meanwhile, each group of schemes has the similar transformation law, and there is a consistent waveform in each rotation cycle. With the rotation of the impeller, six wave peaks and six wave troughs can be found in the radial force distribution of each scheme, which is equal to the number of impeller blades, and the wave peaks and troughs have the same angle under the different flow conditions. However, by comparing the four schemes, it can be found that the radial force amplitude of scheme 1 and scheme 2 is large, and the obvious eccentricity is generated. With the increase in flow conditions, the radial force amplitude of scheme 3 and scheme 4 decreases significantly. At the same time, the eccentricity phenomenon is effectively improved. The main reason for this phenomenon is that the velocity in the flow field of the volute is inconsistent with the velocity and direction at the outlet of the impeller, and an obvious collision is created, which results in an uneven distribution of the velocity at the exit of the impeller. The velocity in each flow passage of the impeller is relatively turbulent, which results in a larger radial force amplitude. At the same time, according to the internal flow field analysis, it can be seen that there are continuous bubble collisions in the impeller, a lot of large bubbles are generated, and these bubbles are not evenly distributed in each impeller flow channel, which promotes the formation of local blockages in the individual flow channels. Furthermore, the flow direction in the flow field is changed, which intensifies the asymmetry of the velocity at the impeller outlet. Therefore, the eccentricity of the radial force distribution in schemes 1 and 2 is generated. Moreover, due to the air voids continuously improving from scheme 1 to scheme 2, the collision frequency of the bubbles in the flow field is increased, which leads to the eccentricity phenomenon being more obvious. With the increase of the flow conditions, the velocity difference between the volute and the impeller in the flow field gradually decreases, and the internal flow field becomes smoother. Hence, the radial force amplitude is significantly reduced, and the eccentricity phenomenon is effectively improved.

Therefore, the influence of the flow conditions and the air voids on the radial force of the impeller was investigated in this section. It can be found that the increase in the flow condition effectively improves the internal flow law and greatly reduces the radial force of the impeller. While the increment of air voids enhances the collision between the bubbles, aggravating the asymmetry in the flow field intensifies the eccentricity of the radial force.

CONCLUSION

(1) By comparing the bubble distribution on the shroud and rear cover, it can be found that larger-sized bubbles are formed on the shroud, while the smaller-sized bubbles are generated on the rear cover. Because of this, the trailing edge vortex is formed at the outlet of the impeller when the self-priming centrifugal pump operates under the part-load flow conditions. The vortex is mainly formed near the rear cover; thus, the violent collision of the bubble group is formed near the rear cover, which results in the difficulty in coalescence of the large-sized bubbles. In contrast, the frequency of the bubble coalescence at the shroud is higher, which is conducive to the formation of the large-sized bubbles.

(2) The pressure pulsation characteristic of the air–liquid two-phase flow is analyzed by increasing the flow condition and the air voids. It can be found that the two methods have opposite mechanisms of pressure pulsation. The increase in the flow conditions has a significant effect on reducing the pressure pulsation of the gas–liquid two-phase flow, and the improvement of the air voids not only destroys the stability of the internal flow of the two-phase flow, but also aggravates the amplitude of pressure pulsation. Meanwhile, the multiple peaks of pressure pulsation are found on different monitoring points, considering the violent collision of the bubbles in the air–liquid two-phase flow, which results in the continuous breakage of the large bubbles and the coalescence of small bubbles, the internal flow field is relatively turbulent. Thus, the multiple peaks of pressure pulsation are generated at each monitoring point.

(3) According to the analysis of the blade surface loading and the radial force distribution, it can be found that the pressure on the pressure surface and the suction surface presents the increment trend from the leading edge to the trailing edge, and the three zero load points are generated on the blade. Meanwhile, the pressure on the pressure and suction surface is significantly larger than that at the shroud, and the effect of air voids and flow rate on the blade surface loading is obtained. The increment of the flow rates improves the internal flow law and greatly reduces the surface load of the blade, while the improvement of the air voids enhances the collision

between bubbles, which aggravates the instability and asymmetry in the flow field, increasing the surface loading of the blade and radial force.

DATA AVAILABILITY STATEMENT

The raw data supporting the conclusion of this article will be made available by the authors, without undue reservation.

AUTHOR CONTRIBUTIONS

This is a joint work, and the authors were in charge of their expertise and capability: HC was in charge of investigation, analysis, writing, and revision; JD and SH were in charge of methodology and revision; GP was in charge of validation and revision; DY was in charge of data analysis; and SY was in charge of manuscript revision.

FUNDING

The authors gratefully acknowledge the support from Open Research Subject of Key Laboratory of Fluid Machinery and Engineering (Xihua University), grant number LTJX 2021-003; Open Research Subject of Hubei Key Laboratory of Hydroelectric Machinery Design and Maintenance (China Three Gorges University), grant number 2020KJX07; the 69th batch of general funding from the China Postdoctoral Science Foundation, grant number 2021M691298; and Natural Science Research Project of Jiangsu Province Colleges and Universities: 21KJB570004, Priority Academic Program Development of Jiangsu Higher Education Institutions (PAPD).

REFERENCES

Barrios, L., and Prado, M. G. (2011). Modeling Two-Phase Flow Inside an Electrical Submersible Pump Stage. *J. Energ. Resour. Technol.* 133 (4), 042902. doi:10.1115/1.4004967

Chang, H., Agarwal, R. K., Li, W., Zhou, L., and Shi, W. (2019). Numerical and Experimental Study of a Vortex Structure and Energy Loss in a Novel Self-Priming Pump. *Processes* 7 (10), 701. doi:10.3390/pr7100701

Chang, H., Hong, S., Yu, D., Peng, G., Ye, D., Liu, J., et al. (2021). Experimental Optimization of Self-Priming Pump Based on the Full Factor Test. *Mechanics* 27 (5), 429–434. doi:10.5755/j02.mech.29931

Chang, H., Shi, W., Li, W., Wang, C., Zhou, L., Liu, J., et al. (2020). Experimental Optimization of Jet Self-Priming Centrifugal Pump Based on Orthogonal Design and Grey-Correlational Method. *J. Therm. Sci.* 29 (1), 241–250. doi:10.1007/s11630-019-1160-2

Ganat, T. A., Hrairi, M., Hawlader, M. N. A., and Farj, O. (2015). Development of a Novel Method to Estimate Fluid Flow Rate in Oil wells Using Electrical Submersible Pump. *J. Pet. Sci. Eng.* 135, 466–475. doi:10.1016/j.petrol.2015.09.029

Huang, S., Su, X., Guo, J., and Yue, L. (2014). Unsteady Numerical Simulation for Gas-Liquid Two-Phase Flow in Self-Priming Process of Centrifugal Pump. *Energ. Convers. Manag.* 85, 694–700. doi:10.1016/j.enconman.2014.03.023

Monte Verde, W., Biazussi, J. L., Sassim, N. A., and Bannwart, A. C. (2017). Experimental Study of Gas-Liquid Two-Phase Flow Patterns within Centrifugal Pumps Impellers. *Exp. Therm. Fluid Sci.* 85, 37–51. doi:10.1016/j.expthermflusci.2017.02.019

Müller, T., Limbach, P., and Skoda, R. (2015). "Numerical 3D RANS Simulation of Gas-Liquid Flow in a Centrifugal Pump with an Euler-Euler Two-phase Model and a Dispersed Phase Distribution[C]," in 11th European Conference on Turbomachinery Fluid dynamics & Thermodynamics, Madrid, Spain, March 23, 2015 (European Turbomachinery Society).

Murakami, M., and Minemura, K. (1974). Effects of Entrained Air on the Performance of Centrifugal Pumps : 2nd Report, Effects of Number of Blades. *Bull. JSME* 17 (112), 1286–1295. doi:10.1299/jsme1958.17.1286

Musakaev, N. G., and Borodin, S. L. (2016). Mathematical Model of the Two-Phase Flow in a Vertical Well with an Electric Centrifugal Pump Located in the Permafrost Region. *Heat Mass. Transfer* 52 (5), 981–991. doi:10.1007/s00231-015-1614-3

Qian, H., Mou, J., Ren, Y., Zhu, Z., Liu, N., Zheng, S., et al. (2021). Investigation of Self-Priming Process of a Centrifugal Pump with Double Blades. *J. Therm. Sci.* 30 (3), 849–858. doi:10.1007/s11630-020-1370-7

Qian, H., Mou, J., Wu, D., Ren, Y., Zheng, S., and Zhu, Z. (2020). Experimental Investigation on the Gas-Liquid Flow Patterns in a Centrifugal Pump during Self-Priming Process. *AIP Adv.* 10 (1), 015136. doi:10.1063/1.5139240

Wang, C., He, X., Zhang, D., Hu, B., and Shi, W. (2019). Numerical and Experimental Study of the Self-priming Process of a Multistage Self-priming Centrifugal Pump. *Int. J. Energ. Res* 43 (9), 4074–4092. doi:10.1002/er.4497

Wang, C., Hu, B., Zhu, Y., Wang, X., Luo, C., and Cheng, L. (2019). Numerical Study on the Gas-Water Two-phase Flow in the Self-Priming Process of Self-Priming Centrifugal Pump. *Processes* 7 (6), 330. doi:10.3390/pr7060330

Wu, T., Liu, J., Zhang, L., and Xu, X. (2017). Experimental Study on Multi-Stage Gas-Liquid Booster Pump for Working Fluid Pressurization. *Appl. Therm. Eng.* 126, 9–16. doi:10.1016/j.applthermaleng.2017.07.159

Yonggang, L., Rongsheng, Z., Xiuli, W., Yang, W., Qiang, F., and Daoxing, Y. (2019). Study on the Complete Rotational Characteristic of Coolant Pump in the Gas-Liquid Two-Phase Operating Condition. *Ann. Nucl. Energ.* 123, 180–189. doi:10.1016/j.anucene.2018.09.030

Zhang, F., Böhle, M., and Yuan, S. (2017). Experimental Investigation on the Performance of a Side Channel Pump under Gas-Liquid Two-Phase Flow Operating Condition. *Proc. Inst. Mech. Eng. A: J. Power Energ.* 231 (7), 645–653. doi:10.1177/0957650917713090

Zhang, J., Cai, S., Li, Y., Zhu, H., and Zhang, Y. (2016). Visualization Study of Gas-Liquid Two-Phase Flow Patterns inside a Three-Stage Rotodynamic Multiphase Pump. *Exp. Therm. Fluid Sci.* 70, 125–138. doi:10.1016/j.expthermflusci.2015.08.013

Zhang, Y.-L., Zhu, Z.-C., Zhao, Y.-J., Wu, J., and Zhou, F.-L. (2021). Comparative Experiments on a Self-Priming Pump Delivering Water Medium during Rapid and Slow Starting Periods. *Iran J. Sci. Technol. Trans. Mech. Eng.* 45 (4), 1007–1019. doi:10.1007/s40997-020-00342-z

Zhou, P., Wu, Z., Mou, J., Wu, D., Zheng, S., and Gu, Y. (2019). Effect of Reflux Hole on the Transient Flow Characteristics of the Self-Priming Sewage Centrifugal Pump. *J. Appl. Fluid Mech.* 12 (3), 689–699. doi:10.29252/jafm.12.03.29207

Conflict of Interest: DY was employed by Chongqing Pump Industry Co., Ltd.

The remaining authors declare that the research was conducted in the absence of any commercial or financial relationships that could be construed as a potential conflict of interest.

Publisher's Note: All claims expressed in this article are solely those of the authors and do not necessarily represent those of their affiliated organizations, or those of the publisher, the editors, and the reviewers. Any product that may be evaluated in this article, or claim that may be made by its manufacturer, is not guaranteed or endorsed by the publisher.

frontiers | Frontiers in Energy Research

ORIGINAL RESEARCH
published: 04 May 2022
doi: 10.3389/fenrg.2022.884571

Flow Field and Particle Flow of Two-Stage Deep-Sea Lifting Pump Based on DEM-CFD

Li Yuanwen[1], *Guo Zhiming*[1], *Shaojun Liu*[2,3] *and Hu Xiaozhou*[2,3]*

[1]College of Mechanical and Electrical Engineering, Changsha University, Changsha, China, [2]College of Mechanical and Electrical Engineering, Central South University, Changsha, China, [3]Shenzhen Research Institute of Central South University, Shenzhen, China

Through discrete element method-computational fluid dynamics, the internal flow field and particle motion law of a two-stage deep-sea lifting pump at different rotational speeds were analyzed in this work. In addition, the physical phenomena, such as flow field velocity, secondary flow, and particle flow, were studied. The relationship between the rotational speed of the lifting pump and solid–liquid two-phase flow was investigated. An experiment on the hydraulic performance of the lift pump showed that the resulting lift and efficiency were consistent with the numerical simulation data. When the rotational speed was 1,450 rpm, the particles can obtain a higher kinetic energy from the flow field, the flow was more stable, and particle deposition was reduced.

Keywords: DEM-CFD, deep-sea mining, pump, particle, solid-liquid two phase

OPEN ACCESS

Edited by:
Ling Zhou,
Jiangsu University, China

Reviewed by:
Hao Yan,
Hefei University of Technology, China
Xianghui Su,
Zhejiang Sci-Tech University, China

***Correspondence:**
Hu Xiaozhou
csu_huxiaozhou@163.com

Specialty section:
This article was submitted to Process and Energy Systems Engineering, a section of the journal Frontiers in Energy Research

Received: *26 February 2022*
Accepted: *19 April 2022*
Published: *04 May 2022*

Citation:
Yuanwen L, Zhiming G, Liu S and Xiaozhou H (2022) Flow Field and Particle Flow of Two-Stage Deep-Sea Lifting Pump Based on DEM-CFD. Front. Energy Res. 10:884571. doi: 10.3389/fenrg.2022.884571

INTRODUCTION

Oceans contain many resources, including rich deep-sea mineral resources. For example, the total rare earth reserves in the North Central Pacific and Southeast Pacific Oceans are approximately 88 billion tons, which is more than 800 times the total rare earth resources on land (approximately 110 million tons) (Kato et al., 2011). In deep sea mining, lift pumps are key pieces of equipment for ore transportation. The performance (Chen, 2019) and safety of the lifting pump are important aspects of the operating efficiency of the entire deep-sea mining system. Zou et al. (2013) studied the lifting problem of electric transmission pumps and proposed a two-phase flow model of a homogeneous slurry. Dong et al. (2018) used a two-phase flow model of a homogeneous slurry to divide the solid particle size, thereby promoting the research on solid–liquid two-phase flow in deep-sea mining. However, their research utilized the traditional discrete phase model, whereby the mixture of fine particles and seawater was considered a homogeneous slurry, and the particle size ratio, and collision and aggregation between the particles were ignored. Furthermore, the interaction between the particles and fluid was not considered. He et al. (2018) proposed discrete element method-computational fluid dynamics (DEM-CFD) to study the gas–solid two-phase flow. Ebrahimi and Crapper (2017) studied the dynamic principle of DEM-CFD on a solid–liquid two-phase fluid flow. Hu et al. (2021) studied the internal flow of the pump through DEM-CFD coupling simulation and obtained the results for deep-sea pumps in extreme cases, such as surpassing the rated concentration, transportation of extremely large particles, deviation from the rated flow, and return flow of the slurry in the event of a power failure. For investigating the flow characteristics, Li et al. (2019) studied the external characteristics of the pump at different speeds and return flow rates of the pump based on DEM-CFD. These reports results provide favorable support for

the study of solid–liquid two-phase flow in deep-sea mining. Wang et al. (2021) studied the influence of the particle migration characteristics on the pump flow and wear. Yang et al. (2014) analyzed the influence of the rotational speed on the solid–liquid two-phase flow, and pointed out that the volume distribution of the particles on the surface of the space guide vane is less affected by the rotational speed. Hu et al. (2020) used DEM-CFD to study the particle transport problem in Y-shaped elbows, and discussed the flow process of particles and fluids at different transport speeds. Liu et al. (2020) studied the effect of particle volume fraction on the performance of deep-sea electric pumps based on the DEM-CFD method. However, these previous studies ignored the interaction between particles. Moreover, the calculation process assumed that no slip exists between the particles and wall. Although this assumption is rational when the particles are smaller, large particle sizes have stronger interparticle interactions. In addition, the relative slip between the particles and wall affects the flow field and interaction between the particles.

Thus, in deep-sea mining, the solid–liquid two-phase flow in the flow channel of the lifting pump is complicated, which is reflected in the random collisions between particles, interactions between the particles and walls, turbulence of the fluid and particles, and interactions between fluids (Chen et al., 2021). In the exploration of deep-sea lifting pumps, computational fluid dynamics (CFD) methods have been widely used to simulate pumps in clean water conditions. However, CFD methods can only calculate the properties of the fluid. Discrete phase model addresses the dynamics of small particles in liquids. This model ignores the particle volume, reduces the particles to Lagrangian particles, and ignores the collisions between the particles (Safaei et al., 2014); thus, it is not suitable for large-diameter particle dynamics (Rashidi et al., 2017). The DEM involves coupled calculations of CFD and DEM realized by the soft sphere method, inter-particle collision, and particle volume fraction. This approach can obtain the fluid and particle properties of a solid–liquid two-phase flow with high accuracy, which is useful in mud transportation simulation. Chen et al. (2020) used the DEM-CFD coupling method to simulate the working conditions of different shapes and concentrations of horizontal pipeline transportation, and obtained the relationship between the effects of the particle characteristics on the efficiency of slurry transportation and flow characteristics. In this study, the DEM-CFD method was employed to investigate the movement of the fluid and particles in a two-stage pump flow path at different speeds.

Numerical Simulations

Particles move independently from each other, and interactions occur when the particles collide with each other and with the walls. The lifting motion of the particles in the fluid is affected by the drag force, which is calculated as

$$f_{d,i} = \frac{1}{8}\pi C_D \rho_f d_i^2 \left(u_f - u_p\right)\left|u_f - u_p\right|. \tag{1}$$

C_D is the drag coefficient, expressed as

$$C_D = \begin{cases} \frac{24}{\mathrm{Re}_p}\left(1 + 0.15\mathrm{Re}_p^{0.687}\right), & \mathrm{Re}_p \le 10^3 \\ 0.44, & \mathrm{Re}_p > 10^3 \end{cases} \quad \mathrm{Re}_p = \frac{\rho_f \left|u_f - u_p\right| d_i}{\mu_f}, \tag{2}$$

where Re_p is the Reynolds number, ρ_f is the solid–liquid two-phase flow density (kg/m^3), μ_f is the solid–liquid two-phase flow viscosity (Pa·s), d_i is the particle diameter (m), u_f is the fluid velocity (m/s), and u_p is the particle velocity (m/s).

The pressure gradient force is expressed as

$$f_{\nabla p,i} = -\frac{1}{6}\pi d_i^3 \frac{\partial p}{\partial x}. \tag{3}$$

The additional mass force is expressed as

$$f_{vm,i} = \frac{1}{12}\pi \rho_f d_i^3 \frac{d\left(u_f - u_p\right)}{dt}. \tag{4}$$

The Basset force is expressed as

$$f_{B,i} = \frac{3}{2} d_i^2 \sqrt{\pi \rho_f \mu_f} \int_{t_0}^{t} \frac{d\left(u_f - u_p\right)}{dt} \frac{d\tau}{\sqrt{t-\tau}}. \tag{5}$$

The Saffman force is expressed as

$$f_{saff,i} = 1.615 d_i^2 \left(u_f - u_p\right) \sqrt{\mu_f \rho_f \frac{du_f}{dt}}. \tag{6}$$

The Magnus force is expressed as

$$f_{Mag,i} = \frac{1}{8}\pi \rho_f d_p^3 \left(u_f - u_p\right)\omega, \tag{7}$$

where ω is the angular velocity of the particles (rad/s) and d_p is the particle diameter (m).

A frictional force is developed owing to the difference between the speeds of the solid particles and liquid phase; the frictional force of the liquid phase flow is given by

$$f_f = \frac{1}{2} C_D a_s \rho_f \Delta V_r^2 \tag{8}$$

The interaction between the particles and fluid is expressed as

$$f_{fp,i} = f_{d,i} + f_{\nabla p,i} + f_{vm,i} + f_{B,i} + f_{saff,i} + f_{Mag,i} + f_f. \tag{9}$$

The equation for the dynamic movement of the particles can be obtained using the collision relationship between the particles, and interaction between the fluid and particles, as follows:

$$m_i \frac{dv_i}{dt} = \sum f, \tag{10}$$

$$I_i \frac{d\omega_i}{dt} = \sum M, \tag{11}$$

where F is the resultant force of the normal and tangential contact forces, and M is the resultant moment of the particle tangential and rolling frictional moments.

At present, the Verlet and Euler methods are often used to solve the dynamic equation of a particle, and the position,

TABLE 1 | Contact interaction settings in the EDEM.

Interaction	Coefficient of Restitution	Coefficient of Static Friction	Coefficient of Rolling Friction
Particle–particle	0.45	0.28	0.01
Particle–pump	0.48	0.10	0.01

TABLE 2 | Impeller parameters of the deep-sea lifting pump.

Parameter	Value
Inlet diameter	235 mm
Maximum outer diameter of outlet	425 mm
Minimum outer diameter of outlet	395 mm
Import placement angle	35°
Exit placement angle	32.5°
Blade wrap angle	105°
Exit width	60 mm
Number of blades Blade thickness	416 mm

velocity, and acceleration of the particle are superimposed and calculated by Taylor series expansion (Childs, 1991).

The Verlet algorithm was proposed by Loup Verlet in the 1860s. This method is widely used in the field of molecular dynamics and has gradually been applied to solve the Newtonian equations of motion of particles (Gonzalez et al., 2006).

In DEM-CFD, the fluid and particles are considered separately in the coupling calculation. First, the flow field is calculated in Fluent. After the flow field iteration is completed, the data are transmitted to the EDEM solver. The particles are used as discrete phases in EDEM to calculate the flow field information. Parenteau (2010) conducted numerical simulations of a solid–liquid two-phase flow in deep-sea mining using the CFD and DEM-CFD coupling calculation methods. The CFD method did not calculate the interaction between the particles and wall, and the simulation results are different from the experimental results. Meanwhile, the DEM-CFD method considers the interaction between the particles and walls, and has greater calculation accuracy than the CFD method. Thus, the DEM-CFD method has significant advantages in the analysis of a solid–liquid two-phase flow. Compared with the traditional CFD method, the particle movement in the pump can be accurately analyzed.

As a rotating fluid machine, the lifting pump adopts a rotating coordinate system based on the axial direction of the impeller rotating shaft. Under this coordinate system, the continuity equation and Navier–Stokes equation of the relative velocity of the liquid phase are

$$\frac{\partial}{\partial x_j}\left(\rho_f u_{fj}\right) = 0, \tag{12}$$

$$\frac{\partial}{\partial t}\left(\rho_f u_{fi}\right) + \frac{\partial}{\partial x_j}\left(\rho_f u_{fi} u_{fj}\right) = -\frac{\partial}{\partial x_i}\left[(1 - C_{vc})p - \frac{1}{2}\omega_1^2 r^2\right] + \rho_f g_{fi} + \frac{\partial \tau_{fij}}{\partial x_j} + \frac{\rho_s}{t_p}\left(u_{fi} - u_{pi}\right) - 2\varepsilon_{ijk}\omega_j u_{fk}, \tag{13}$$

where u_{fj}, u_{fi}, and u_{fk} are the liquid phase velocity vectors (m/s); ω_1 is the rotational angular velocity of the impeller (rad/s); ω_j is the component of the rotational angular velocity

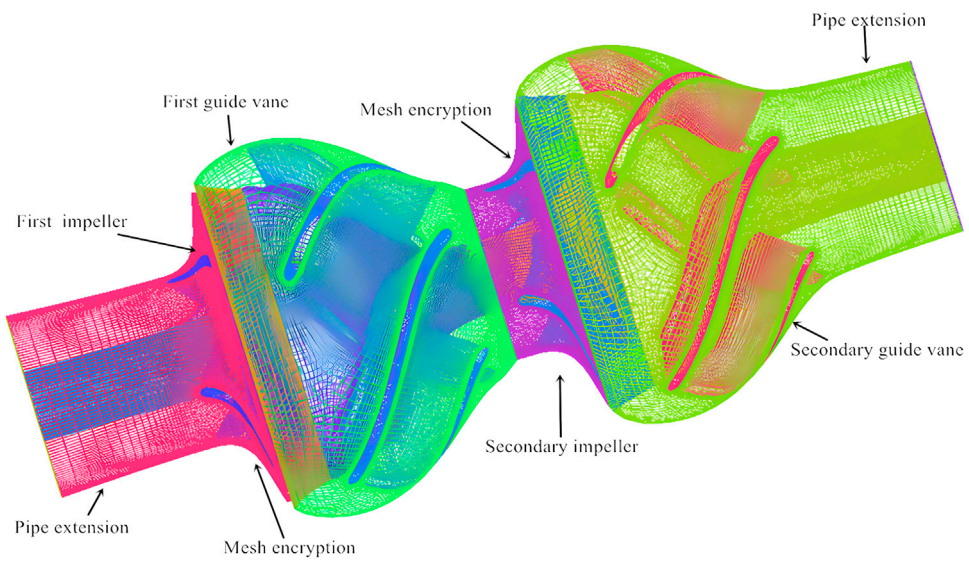

FIGURE 1 | Two-stage deep-sea lifting pump grid.

TABLE 3 | Space guide vane parameters.

Parameter	Value
Inlet placement angle	12°
Exit placement angle	85°
Wrap angle	97°
Vane length	262 mm
Number of blades	5
Inlet diameter	395 mm
Blade thickness	16 mm
Annular width	61 mm

of the impeller (rad/s); r is the linear distance to the axis of rotation (m); t_p is the relaxation time of the particles (s); ρ_s is the solid phase density (kg/m^3); ρ_f is the solid liquid density (kg/m^3); p is the equivalent pressure considering the centrifugal force (N); τ_{fij} is the pressure vector (N); C_{vc} is the concentration; and g_{fi} is the gravitational acceleration (m/s^2) (Brennen and Yong, 2010).

$$\frac{\partial}{\partial x_j}\left(\rho_s u_{pj}\right) = 0, \tag{14}$$

TABLE 4 | Grid-independence simulation test.

Simulation Conditions	Grids Number	Total Head (m)	Error Compared to the Test (%)
Pump model at 1,450 rpm; particle mass concentration of 6%	712564	89.72	7.42
	963456	88.24	5.63
	1375459	86.39	3.41
	1947618	85.24	2.04
	2306471	84.63	1.31
Experiment	–	83.54	–

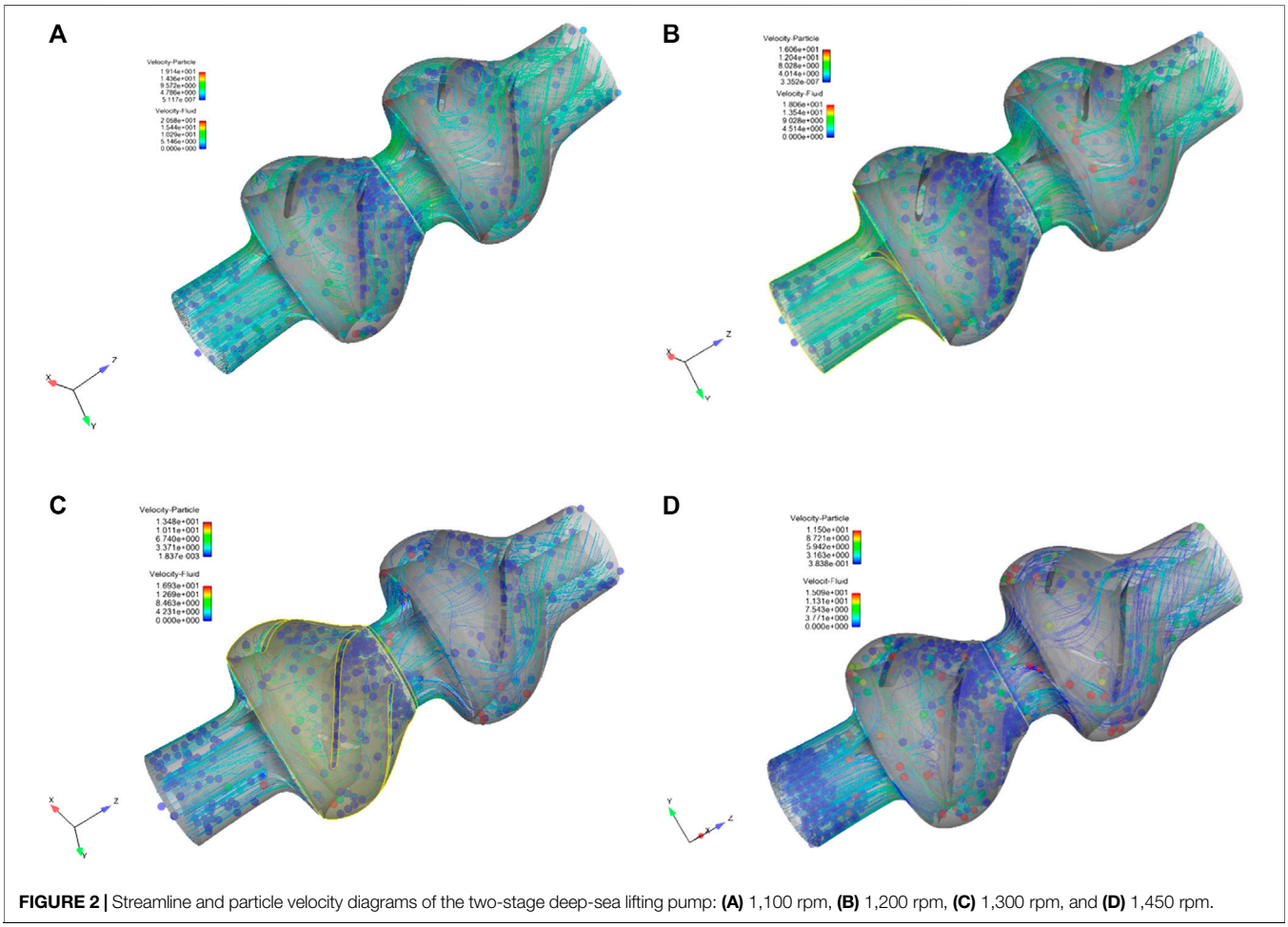

FIGURE 2 | Streamline and particle velocity diagrams of the two-stage deep-sea lifting pump: **(A)** 1,100 rpm, **(B)** 1,200 rpm, **(C)** 1,300 rpm, and **(D)** 1,450 rpm.

$$\frac{\partial}{\partial t}\left(\rho_s u_{pi}\right)+\frac{\partial}{\partial x_j}\left(\rho_s u_{pi}u_{pj}\right)=-\frac{\partial}{\partial x_i}\left(C_{vc}p-\frac{1}{2}\omega_1^2 r^2\right)$$
$$+\rho_s g_{pi}+\frac{\partial \tau_{pij}}{\partial x_j}+\frac{\rho_s}{t_p}\left(u_{pi}-u_{fi}\right)-2\varepsilon_{ijk}\omega_j u_{pk}, \quad (15)$$

where u_{pi} is the solid phase velocity vector.

3D Model and Meshing

In this study, the production capacity of the mining system was set to 30 t/h. The particle volume concentration was set to 6%. The maximum particle size was 20 mm, and the flow rate was 420 m^3/h. In the simulation, a single particle size of 20 mm was used according to the project requirements, and the particle concentration was controlled with the mass flow rate of 14 kg/s.

The DEM-CFD coupling was based on the Euler–Lagrange method and implemented on the FLUENT-EDEM platform. The flow field information of the fluid in the computational domain was first computed in Fluent for a time step. When the convergence conditions were reached, the drag and lift forces of the particles were calculated, and the information was transmitted to the EDEM. EDEM calculated the particle position, velocity, volume, etc., and passed this information back to Fluent. Thus, the particle and flow field information for the next time step was cyclically updated.

The impeller and diffuser of the multi-stage pump are composed of duplex stainless steel with a density of 7,850 kg/m^3, Poisson's ratio of 0.33, and shear modulus of 7.744 $10^{+10.}$ The contact force of the particles was calculated by the Hertz–Mindlin no-slip model. The lift model adopted the Saffman and Magnus lift models, and the particle–particle and particle–pump interaction settings are shown in **Table 1**.

As the consistency of the EDEM and Fluent data at the inlet and outlet promotes stabilization and convergence, it is preferable to use the predefined pressure outlet and velocity inlet as the boundary conditions for the Fluent data. The EDEM particle factory was set to an infinite number model, thereby randomly generating particles on the same inlet plane as that of the Fluent based on the particle mass flow, and setting equal velocities for the particles and fluid. The data between different sub-computing domains were passed through interfaces. The physical properties of water were set to a temperature of 20°C, density of 0.9982 g/cm^3, and viscosity of 1.003 × 10^{-3} Pa·s. Renormalization group *k*–ε was chosen as the turbulence model for the refinement of the swirl effect under turbulence. This refinement enhanced the accuracy of the swirling flow in deep-sea lifting pumps. The standard wall treatment, which can effectively handle most industrial flow at y+ of 15–100 near the solid wall, was set as the wall function.

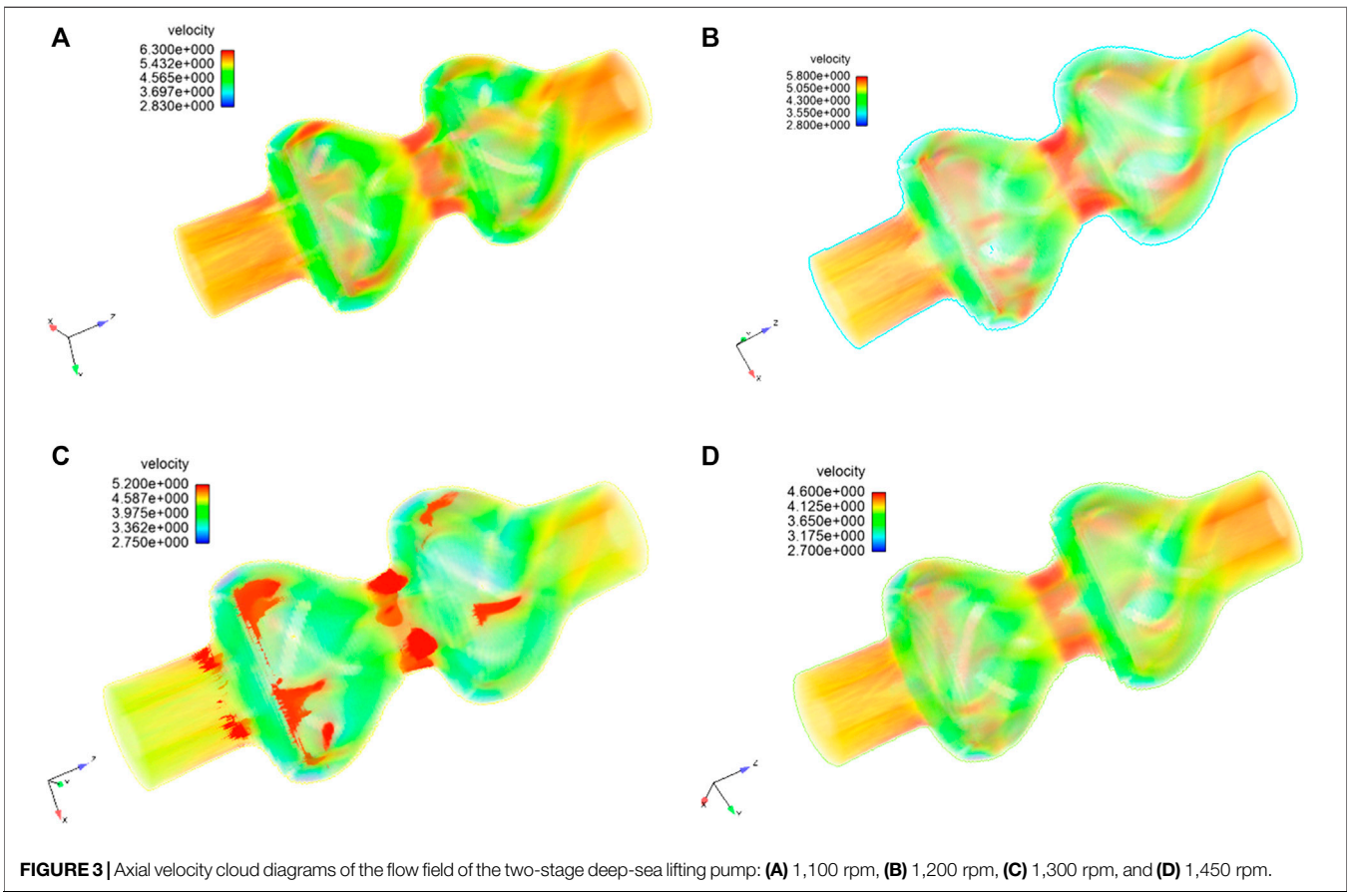

FIGURE 3 | Axial velocity cloud diagrams of the flow field of the two-stage deep-sea lifting pump: **(A)** 1,100 rpm, **(B)** 1,200 rpm, **(C)** 1,300 rpm, and **(D)** 1,450 rpm.

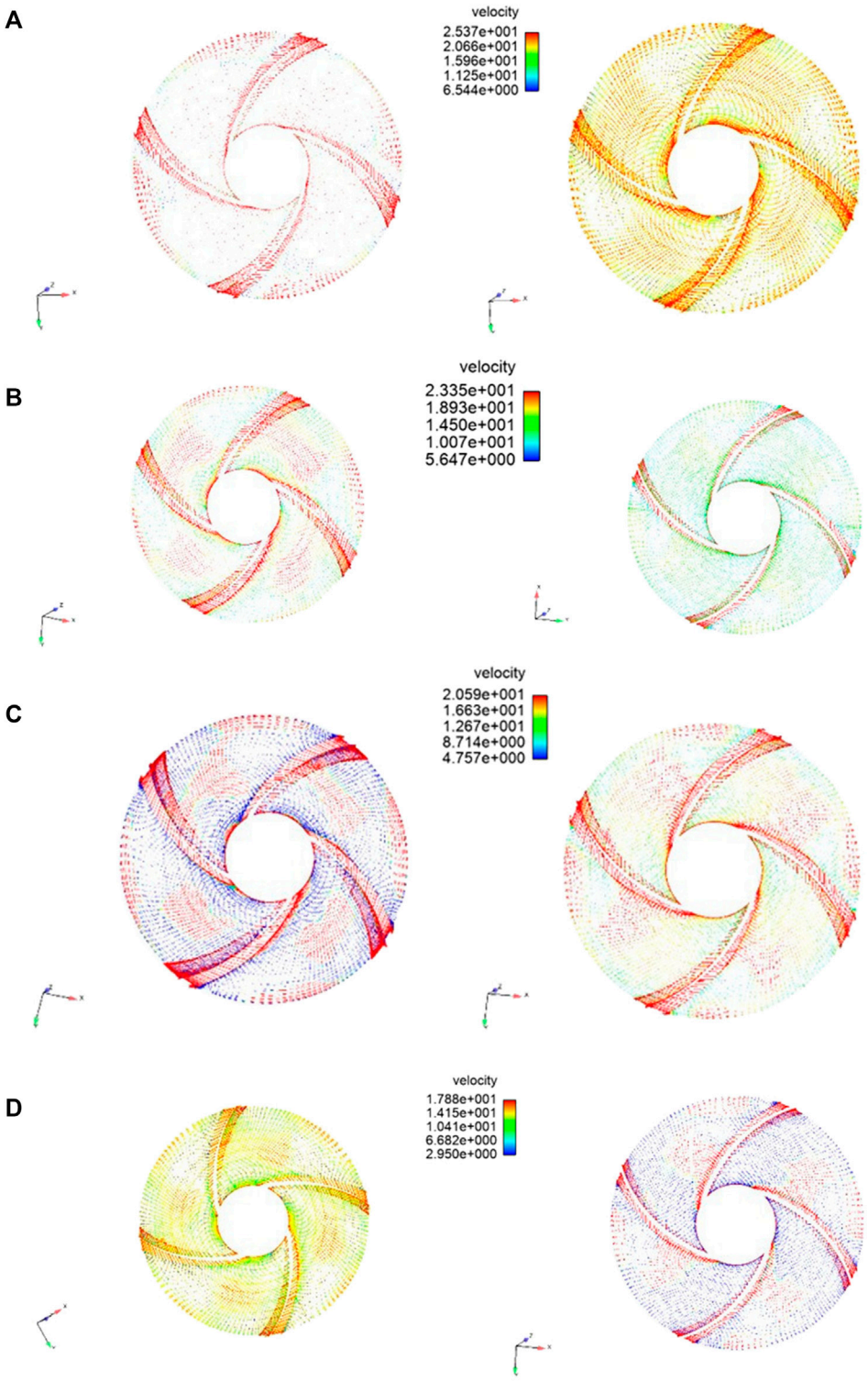

FIGURE 4 | Flow velocity vector diagrams of the impeller section: **(A)** 1,100 rpm, **(B)** 1,200 rpm, **(C)** 1,300 rpm, and **(D)** 1,450 rpm.

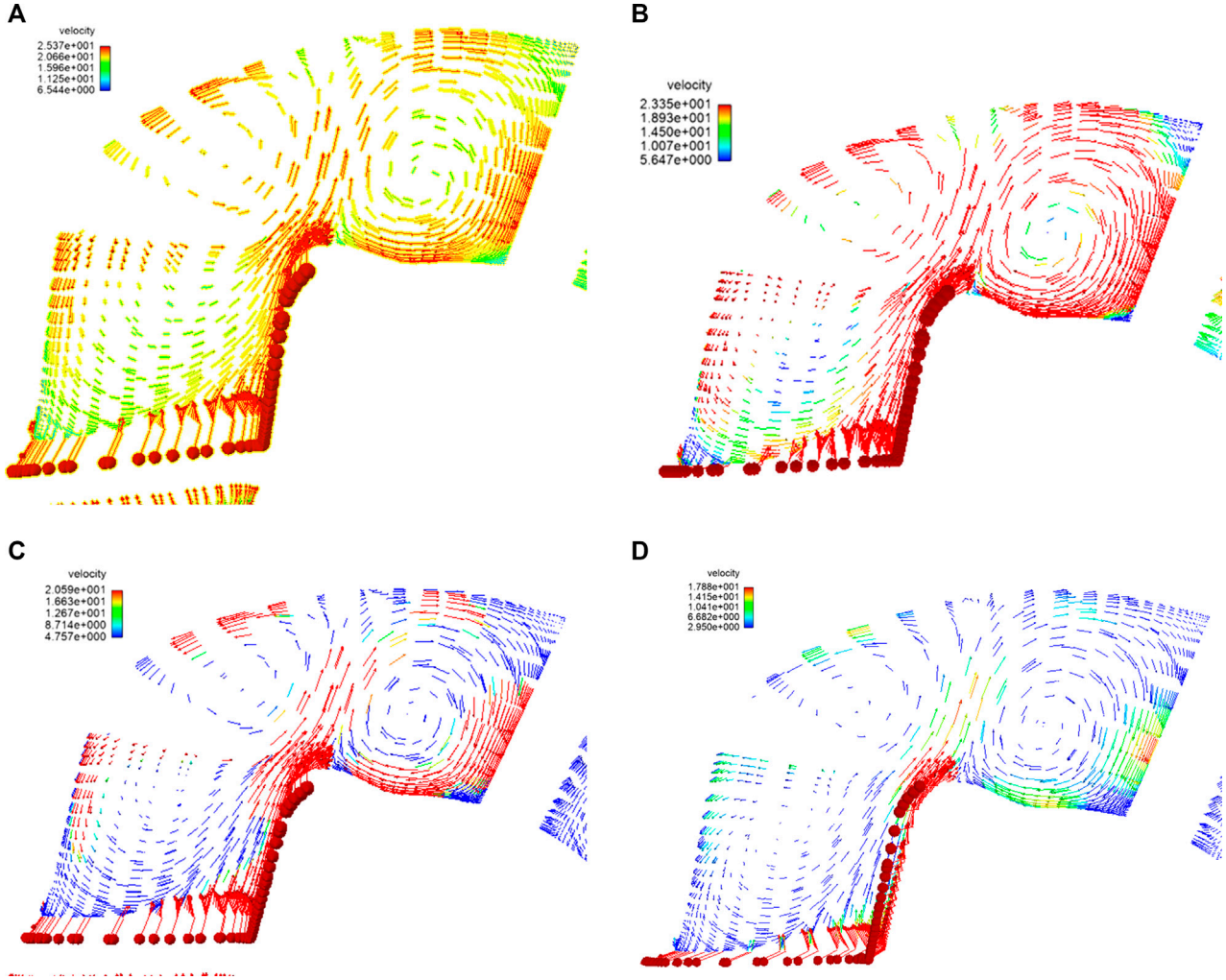

FIGURE 5 | Distribution of the secondary flow in the link between the impeller and space guide vane: **(A)** 1,100 rpm, **(B)** 1,200 rpm, **(C)** 1,300 rpm, and **(D)** 1,450 rpm.

SIMPLEC was used for the pressure–velocity coupling method, which increased the moment, turbulent kinetic energy, and turbulent dissipation rate to the second-order upwind to improve the accuracy of the simulation. The time step was fixed as the elapsed time per 4° of pump rotation: 4.6×10^{-4} s for 1,450 rpm, 5.442×10^{-4} for 1,300 rpm, 6.123×10^{-4}s for 1,100 rpm, and 6.9074×10^{-4} s for 1,000 rpm. The convergence rule for all residuals was set to 1×10^{-4}.

The parameters of the impeller are listed in **Table 2**. **Table 3** shows the space guide vane parameters of the deep-sea lifting pump. **Figure 1** shows a grid diagram of the two-stage deep-sea lifting pump. The inlet section of the first-stage impeller and outlet section of the second-stage space guide vane were lengthened for the smooth entry of the flow field. The grid was dense at the turning points of the first-stage and second-stage impellers, which was beneficial for the calculation of the flow field. The computational domain model was divided into five unstructured meshes with different grid qualities in ICEM. The simulation results are shown in **Table 4**. The grid-independence simulation test showed that a satisfactory result could be guaranteed for 2300000 grids.

NUMERICAL CALCULATIONS

The inlet velocity of the fluid and particles were both set to 3.16 m/s. The coarse-grained ore has spherical particles with a volume fraction of 6% for the 20-mm particles. The impeller speed was set to 1,100, 1200,1300, and 1,450 rpm, according to China's key R&D program—Deep Sea Polymetallic Combined Mining and Test Engineering.

Figure 2 shows the flow lines and particle velocity diagrams of the two-stage deep-sea lifting pump. The velocity of the particles is lower than the velocity of the fluid, indicating that there is no advance phenomenon during the lifting process. The maximum

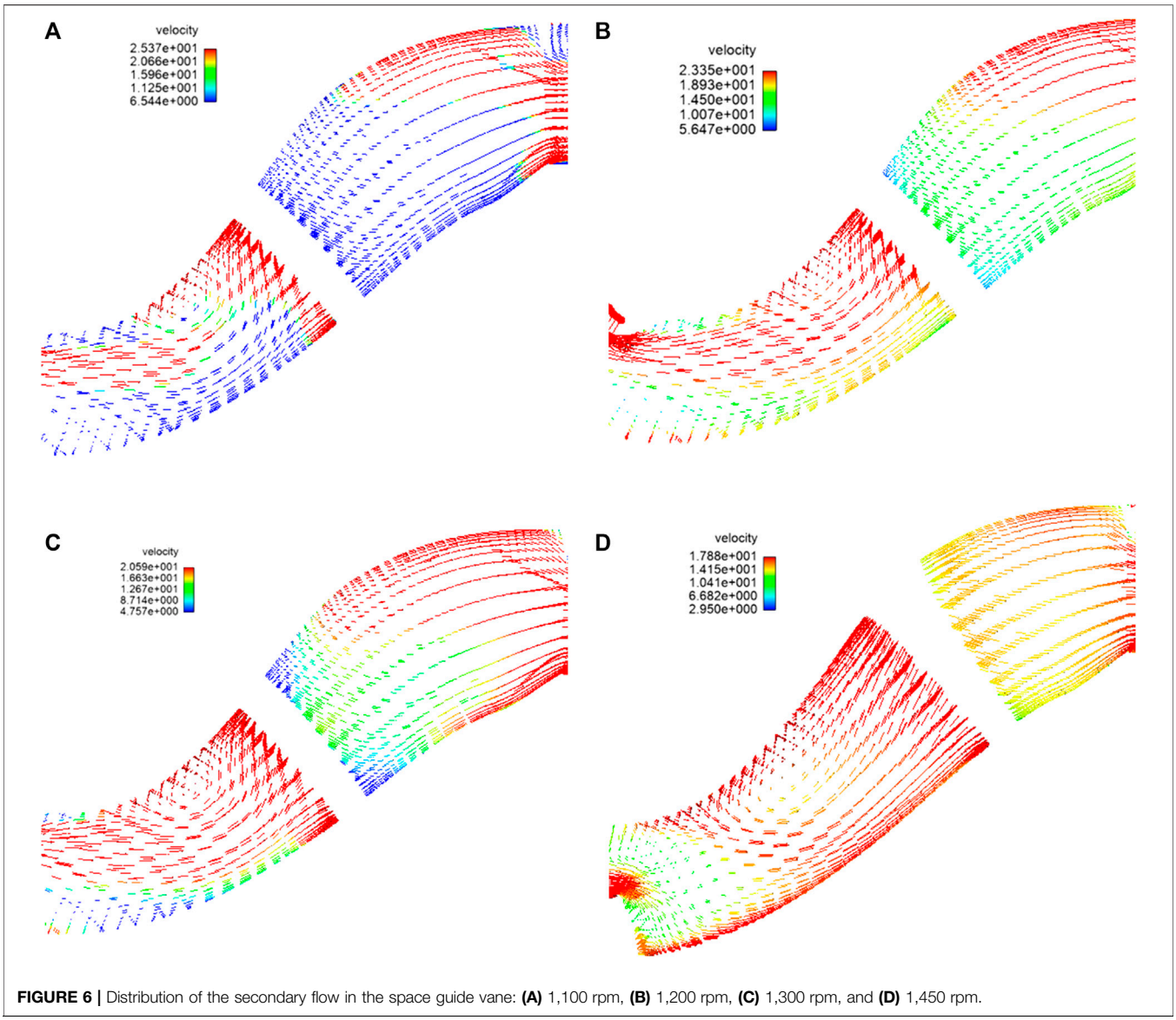

FIGURE 6 | Distribution of the secondary flow in the space guide vane: **(A)** 1,100 rpm, **(B)** 1,200 rpm, **(C)** 1,300 rpm, and **(D)** 1,450 rpm.

TABLE 5 | Particle volume concentration distribution under different speed conditions.

Rotational Speed (rpm)	First-Stage Impeller (%)	First-Stage Space Guide Vane (%)	Second-Stage Impeller (%)	Second-Stage Space Guide Vane (%)
1,100	3.48	6.67	3.39	5.62
1,200	3.12	6.59	2.96	5.42
1,300	2.94	6.42	2.85	5.15
1,450	2.63	6.31	2.57	4.92

velocity of the particles and streamlines occurred at the end of the blade. At a speed of 1,100 rpm, the maximum velocity of the particles is 10.2 m/s. As the rotational speed increased, the velocity of the particles and fluid increased. As shown in **Figure 2D**, the particle velocity reached 19.1 m/s. The blade accelerated the particles well, facilitating their easy passage through the deep-sea lifting pump. After the blade accelerated the particles, they entered the space guide vane. When the particles are thrown from the blade, they hit the outer shell of the space guide vane, resulting in substantial energy loss. The

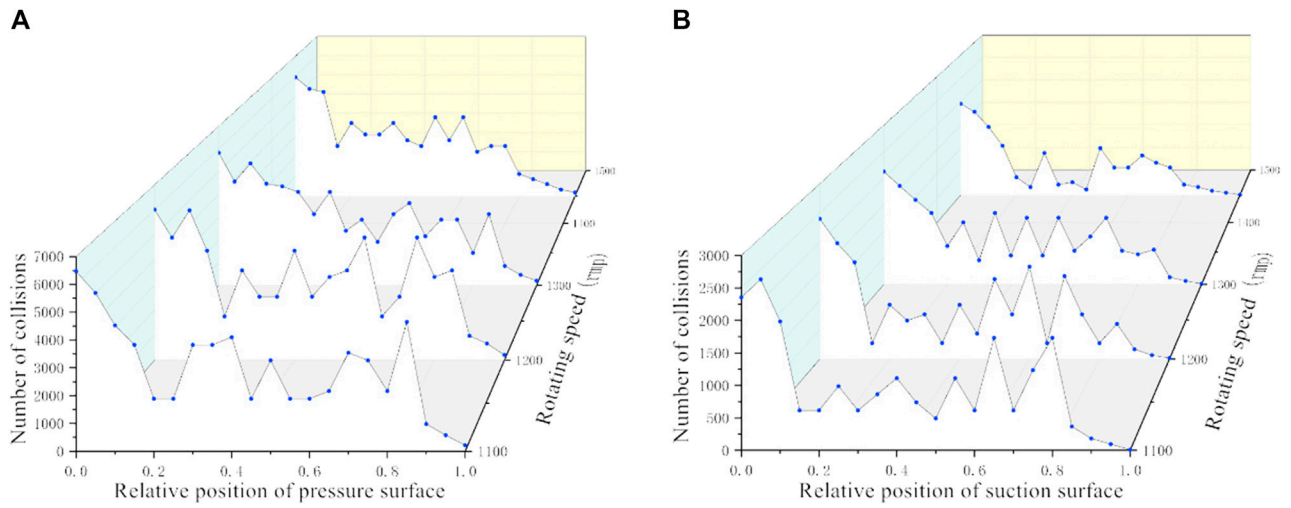

FIGURE 7 | Number of particle collisions on the pressure and suction surfaces of the impeller blade.

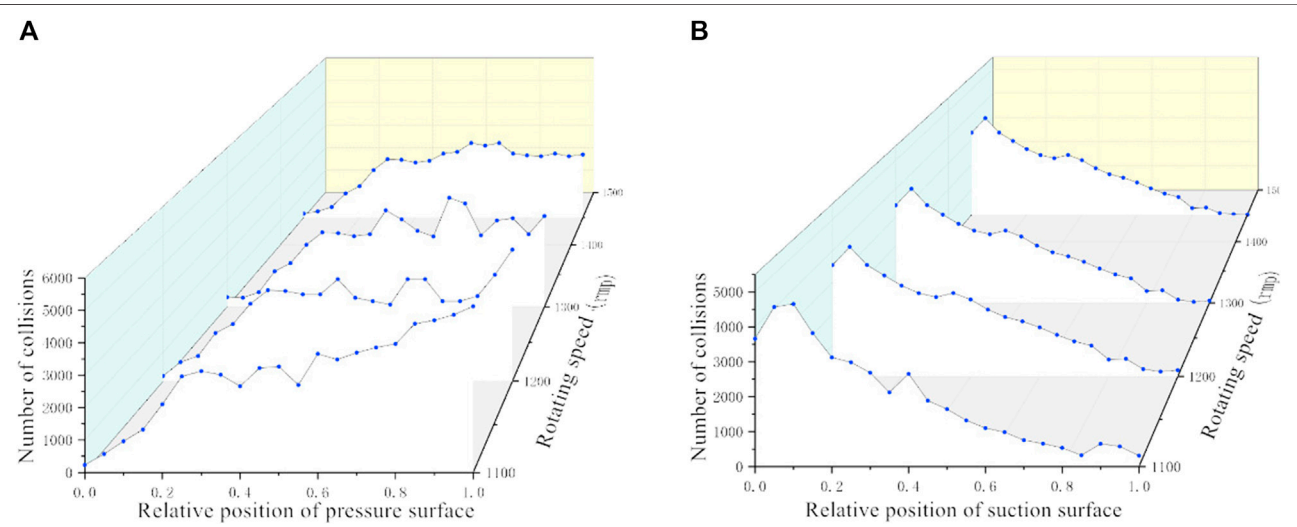

FIGURE 8 | Number of particle collisions on the pressure and suction surfaces of the space guide vane blade.

pressure surface of the space guide vane is in contact with the suction surface. As shown in **Figure 2**, the particles on the pressure surface of the space guide vane are larger than those on the suction surface. Therefore, the pressure surface of the space guide vane will undergo more collisions, and its wear will exceed that of the suction surface. In the two-stage deep-sea lifting pump, the number of particles in the first-stage pump is greater than that in the second-stage pump because of the numerous particles that suddenly entered the pump body, resulting in excessive particle concentration at the junction. With the increase in speed, the number of particles in the first-stage pump decreased, resulting in the significant improvement of the flow capacity. In the deep-sea lifting pump, there is a high possibility of blockage of the first-stage pump.

The fluid moved spirally along the direction of rotation of the impeller blade and reached the maximum speed at the end of the blade. The maximum speed reaches 14.4 m/s (**Figure 2A**) and 20.5 m/s (**Figure 2D**). The fluid flows smoothly in the impeller and space guide vanes, indicating the reasonable design of the impeller and space guide vane, and improved pump efficiency. After the fluid enters the space guide vane, the kinetic energy is gradually converted into pressure, thereby decreasing the speed. Local agglomeration occurred at low speeds and decreased as the speed increased. At a higher rotational speed, the uneven transmission of the particles are weakened, thereby stabilizing

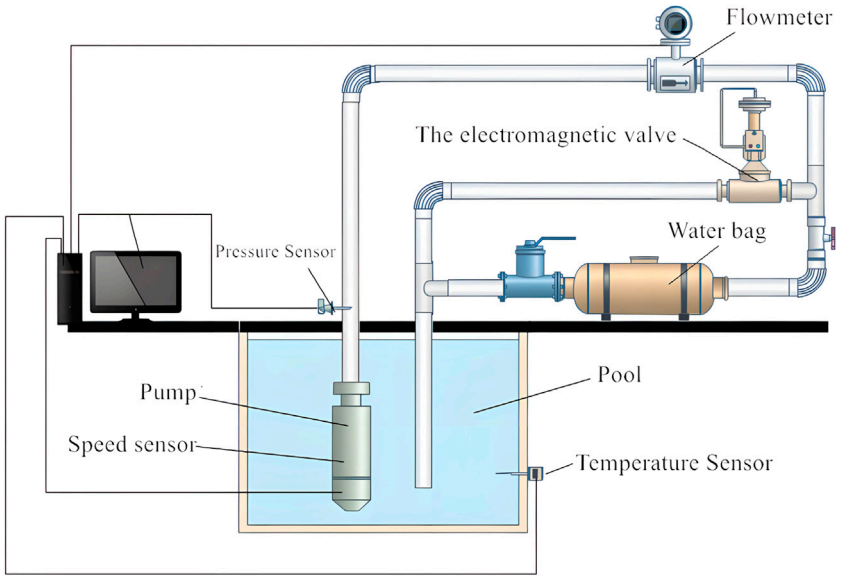

FIGURE 9 | Schematic of the test loop.

the particle transmission, and improving the efficiency and head of the pump.

When the rotational speed increased, the acceleration effect of the impeller on the solid–liquid two-phase flow increased, and the movement of the solid–liquid two-phase flow in the impeller and space guide vane stabilized. This is conducive to the transportation of solid–liquid two-phase flows.

Figure 3 shows the axial velocity cloud diagram of the flow field of the two-stage deep-sea lifting pump. As the deep-sea lifting pump is used for lifting solid particles, the axial velocity directly determines the improvement in the solid–liquid two-phase flow. As shown in **Figure 3**, the axial velocity at the inlet of the impeller is relatively higher than that at the impeller blades. The speed is relatively small because the rotation of the fluid through the blades changes the direction of the fluid velocity from axial to radial. After flowing out of the impeller, the fluid enters the space guide vane, which turns and stabilizes the flow. Consequently, the axial velocity of the fluid increases, and it enters the second-stage impeller with higher stability. As the speed increases, the axial velocity of the fluid at the outlet of the second-stage space guide vane increases from 4.6 m/s to 6.3 m/s. This also indicates the further increase of the lifting capacity of the deep-sea lifting pump for a solid–liquid two-phase flow.

Figure 4 shows the fluid velocity vector diagram of the impeller section at different speeds. A high-speed area, called the "jet area," appears near the pressure surface of the impeller blade, and a low-speed area, called the "wake area," is formed near the suction surface of the impeller blade. As shown in **Figure 4D**, the relative speed in the impeller channel is higher, which suppressed the separation of the boundary layer; thus, no vortex is formed. At the exit of the impeller, the maximum velocity of the jet and wake areas are 25.3 and 20.66 m/s, respectively, and the relative velocity gradient of the jet wake is small.

At low rotational speeds, the vortex range increased, thereby reducing the hydraulic efficiency, increasing the squeezing effect of the impeller blades, and weakening the flow capacity of the particles. As shown in **Figure 4A**, the maximum velocity of the jet and wake area are 17.8 and 2.95 m/s, respectively. The relative velocity gradient of the jet wake is large. A larger jet wake structure increased the hydraulic loss of the lifting pump. The jet wake velocity gradient at the first-stage impeller is larger than that at the second-stage impeller because the former has more particles. As the rotating speed of the impeller blades increases, the speed of the fluid on the blades increases, which is beneficial for fluid transportation and reducing the generation of vortices.

FIGURE 10 | Pump test bench.

FIGURE 11 | Two-stage lifting pump on the test bench.

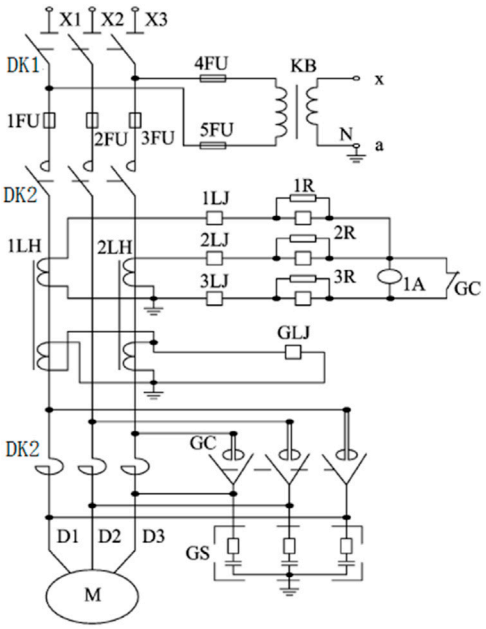

FIGURE 12 | Control main circuit.

The secondary flow is an important parameter for studying the flow field in a flow channel. The generation of a secondary flow has a significant influence on the efficiency of deep-sea pumps. Thus, the secondary flow in the flow channel was studied, and a vector diagram was created. **Figures 5**, **6** show the distribution of the secondary flow in the connection between the impeller and space guide vane, and that in the space guide vane, respectively.

When the fluid enters the inlet of the space guide vane from the outlet of the impeller, the velocity changes from radial to axial, and the pressure direction changes. The junction between the impeller and space guide vane has a large curve, where the fluid impacts the impeller and space guide vane. A secondary flow appears in the guide vane shell, forming a pair of vortices in the opposite directions, which are called "basic vortices." As the rotational speed increases, the outlet flow rate increases, which increases the basic vortex and hydraulic loss. However, from the perspective of the entire lifting process of the deep-sea lifting pump, a speed increase is beneficial to the hydraulic efficiency of the pump. The bend of the runner has a significant influence on the appearance of the basic vortex. In the deep-sea lifting pump, the basic vortex occupies the majority of the flow channel and causes the accumulation of particles.

After the fluid enters the space guide vane, the basic vortex begins to flow to the outer shell of the space guide vane to form a new vortex, called the "curvature vortex," which gradually became smaller. As the speed of the main flow in the flow channel of the space guide vane increases, the pressure gradient decreases, the curvature vortex begins to decrease, and the flow begins to stabilize, which is conducive to the transportation of the solid–liquid two-phase flow.

The volume concentrations of the particles are listed in **Table 5**. The particle volume concentration at the first-stage impeller space guide vane is higher than that at the second-stage impeller space guide vane. Owing to its high-speed rotation, the particle volume concentration in the first-stage impeller is slightly lower than that in the second-stage impeller. This is because when the particles enter the first-stage impeller from the extension section of the inlet, the stagnation effect of the particles is stronger, resulting in a higher particle volume concentration. After entering the space guide vane, the particles maintained a high speed. With the turning of the space guide vane and under the effect of steady flow, the kinetic energy of the particles in the space guide vane continuously decreases. When the particles enter the second-stage impeller from the first-stage space guide vane, the collision between the particles increases owing to the gradual narrowing of the vane channel. This results in increased friction between the particles and energy loss. The particle flow is obstructed, resulting in increased volume concentration at the exit of the first-stage space guide vane. This effect increases with decreasing speed.

When the speed is increased from 1,100 to 1,450 rpm, the volume concentrations at the first-stage and second-stage impellers reduced by 0.85 and 0.82%, respectively. The change in the concentration has minimal effect. The volume concentration at the first-stage guide vane is less than 0.36%, whereas that at the second stage is less than 0.7%. The influence of the second-stage space guide vane is higher than that of the first-stage space guide vane. Meanwhile, for the particles at 1,450 rpm, the volume concentrations at the first-stage space guide vane and second-stage impeller are similar; however, the volume concentrations at the first- and second-stage space guide vanes are significantly different, which indicates that the influence of the rotational speed of the latter is greater than that of the former.

TABLE 6 | Test and simulation results.

	Rotational Speed (rpm)	Head (m)	Efficiency (%)
Test	1,100	73.26	40.68
Simulation	1,100	74.31	41.81
Test	1,200	77.33	43.98
Simulation	1,200	79.01	44.94
Test	1,300	80.08	45.81
Simulation	1,300	81.67	47.32
Test	1,450	83.54	46.13
Simulation	1,450	84.63	48.04

As the rotational speed increases, the relative velocity between the particles and fluid decreases, the followability of the particles improves, and the particles can pass through the flow channel easier. Therefore, selecting the optimal operating speed of the pump can ensure efficiency and flow capacity. There may be extensive particle siltation on the blades at the outlet of the first-stage space guide vane and inlet of the second-stage impeller.

The particle distribution and wear were studied through the particle collisions on the impeller and space guide vane. **Figure 7** shows the statistics of the particle collisions on the pressure and suction surfaces of the impeller blade. As the collision between the first-stage and second-stage impellers is similar, the erosion position can be predicted by analyzing the collision of the first-stage impeller.

As the particles in the deep-sea lifting pump are driven by the high-speed rotation of the impeller, they hit the pressure and suction surfaces of the blade, causing erosion and wear of the blade wall. As shown in **Figure 7** (1.0 on the horizontal axis denotes the end of the blade), the numbers of particle collision at different speeds are approximately constant. The number of collisions on the pressure surface of the blade is higher than that on the suction surface, indicating that the wear of the pressure surface is stronger than that of the suction surface. When the relative position is less than 0.2, the number of particle collisions on the pressure surface of the blade increases, which intensifies its wear. With the increase in speed, the number of particle collisions gradually decreases, indicating that the flow of the particles tends to stabilize.

Figure 8 shows the statistics of the effect of the particles on the pressure and suction surfaces of the space guide vane blade, where 1.0 on the horizontal axis denotes the end of the space guide vane blade. When the relative position is less than 0.4, the collision of the particles on the suction surface of the space guide vane blade increases. With the movement of the particles in the flow channel, the relative position exceeds 0.6. The pressure surface of the space guide vane has more collisions, indicating that the particles gradually approached this surface during their flow. The rotational speed has minimal effect on the number of particle collisions on the pressure and suction surfaces of the space guide vane.

Experiment

The phenomenon of inter-stage matching occurs during the lifting process of the multi-stage pumps. Therefore, to ensure the smooth progress of the sea trial of the deep-sea lifting pump and verify the numerical simulation model developed in this study, a two-stage deep-sea lifting pump was used in the experimental test. The solid–liquid two-phase fluid concentration was equal to 6% in the test. The particles are manganese nodules with a diameter of 20 mm and flow rate of 420 m^3/h. The speeds of 1,000, 1,100, 1,200, 1,300, and 1,450 rpm were selected. The two-phase flow tests were done under the aforementioned condition.

The two-stage pump tests was conducted at Tianjin Bailiyitong Electric Pump Co., Ltd. The company has an advanced high-pressure platform for conducting diving tests. The pump test system included a test pump well with a depth of 9 m in the test pool, pipelines, and valves. The schematic of the test loop is shown in **Figure 9**. The pump test field is shown in **Figures 10**, **11**. The test instruments include the pump inlet and outlet pressure sensors, electromagnetic flow meters, pump speed sensors, current, voltage, and power factor measuring instruments, as shown in **Figure 11**. The test parameters were consistent with the simulation parameters.

The test steps include the test preparation and testing. The test preparation was carried out as follows:

1) The structural parameters of the pump under test were verified to ensure that they are within the design error;
2) The surface roughness of the overcurrent parts of the pump under test was recorded;
3) The pump under test was installed, and the pump shaft by hand was tested;
4) The normal rotation of each rotating part without interference was ensured;
5) All sensors were checked;

FIGURE 13 | Measurement and control systems.

6) The status of each valve in the required position was checked.

The test process was conducted as follows:

1) The main control power switch (leakage micro-break) of the submersible low-voltage test bench and DK1 main power switch were turned on;
2) The isolating switch of the SD4 cabinet was adjusted to a high voltage;
3) The combination switch of the diving high-pressure table was turned to the T1 (high-pressure table) position;
4) The submersible high-voltage test bench master control power switch (leakage micro-break) was turned on;
5) The high-pressure test bench DK2.VS.1 was turned on;
6) The low-pressure test bench DK4 was turned on;
7) The boost button T1 of the diving high-voltage test bench was pressed to increase the voltage until the monitoring voltmeter showed that KV was approximately 40% of the rated voltage. The motor was started, and the value of the ammeter KA was observed and monitored, as was whether the current was balanced. The voltage was increased, the starting current was observed until the motor turned up, and the rated voltage was adjusted to test according to the test item;
8) The computer was turned on to enter the relevant acquisition program, and the test points were adjusted to collect the relevant data.

Figure 12 shows the control main circuit. **Figure 13** shows images of the measurement and control system.

According to **Eqs 16**, **17**, the head H and efficiency η can be calculated, respectively:

$$H = \frac{p_2}{\rho g} + \frac{v_2^2}{2g} - \left(\frac{p_1}{\rho g} + \frac{v_1^2}{2g}\right) + z_2 - z_1, \tag{16}$$

where p_1 and p_2 are the static pressures at the inlet and outlet of the deep-sea lifting pump, respectively; v_1 and v_2 are the average speeds of the inlet and outlet, respectively; and z_1 and z_2 are the shaft heights;

$$\eta = \frac{\rho g Q H}{\omega_3 M}, \tag{17}$$

where ω_3 is the rotational speed and M is the impeller torque; both of which can be obtained in the post-processing of the numerical simulation.

$$\rho = \rho_p c_{vc} + \rho_f (1 - c_{vc}), \tag{18}$$

where ρ_p is the solid phase density (kg/m^3), ρ_f is the fluid density (kg/m^3).

Table 6 lists the test and simulation results. The simulation results are significantly close to the experimental results. The simulated head and efficiency are the same as those in the experiment. The maximum errors of the head and efficiency are 2.14 and 3.12%, respectively, which proves that the numerical simulation model used in this study can reflect the actual situation.

Figure 14 shows a comparison of the flow field velocities obtained using the numerical simulation and experiment. The maximum speed error is 7.61%. With the increase in the rotational speed, the velocity of the flow field increases, indicating that the particles can obtain more kinetic energy from the flow field to sustain their movement, thereby reducing their deposition on the surfaces. The errors between both methods are less than 10%, which can be attributed to the standard spherical particles used in the simulation, even with the existence of other particle shapes in the experiment. The consistency between the experimental and numerical simulation results verifies the credibility of the numerical simulation.

From the experiment, the head and efficiency can satisfy the design requirements. With the deep-sea lifting pump speed of 1,450 rpm, the largest lift, efficiency, and fluid velocity are obtained, indicating that the particles can obtain more energy from the flow field. This confirms that the design of the flow channel is reasonable, which ensures the transportation of particles.

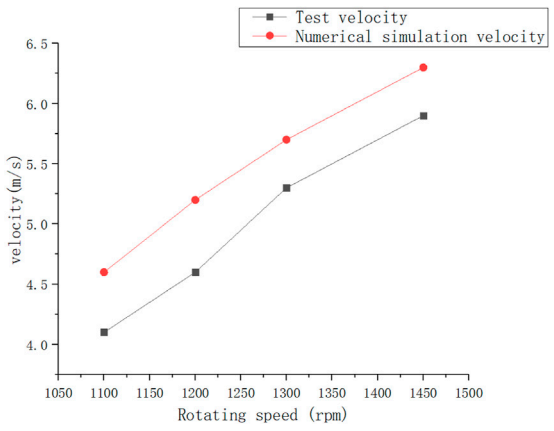

FIGURE 14 | Comparison of the flow field velocities.

CONCLUSION

The operation of a deep-sea lifting pump was numerically simulated through DEM-CFD. The results of the model were verified experimentally. The following conclusions were obtained:

1) The test and simulation results were consistent, and the design requirements were met, indicating the excellent slurry transport performance of the pump. Thus, DEM-CFD can accurately predict the head and efficiency of multi-stage centrifugal pumps conveying coarse particle slurry.
2) As the speed increased, the accelerating effect of the impeller on the solid–liquid two-phase flow increased, and the movement of the solid–liquid two-phase flow in the impeller and space guide vane became more stable, which is conducive to the transportation of solid–liquid two-phase flows.

3) At low rotational speeds, the vortex range increased, thereby reducing the hydraulic efficiency. In addition, the squeezing effect of the blades increased, which weakened the flow capacity of the particles. A large jet wake structure increased the hydraulic loss of the lifting pump. Generally, the jet wake velocity gradient at the first-stage impeller was larger than that at the second-stage impeller owing to the presence of numerous particles in the former. When the rotational speed was 1,450 rpm, the outlet flow rate increased, and the hydraulic efficiency of the deep-sea lifting pump became more favorable. As the speed of the main flow in the space guide vane channel increased, the pressure gradient decreased, the curvature vortex began to decrease, and the flow stabilized, which is conducive to the transportation of the solid–liquid two-phase flow.
4) Based on the particle movements, the particle volume concentration at the first-stage impeller space guide vane was higher than that at the second-stage impeller space guide vane. The particles in the deep-sea lifting pump were driven by the high-speed rotation of the impeller, and hit the blades with pressure. The surface and suction surfaces caused the erosion and wear of the blade wall. As the rotational speed increased, the number of particle collisions gradually decreased, indicating the stabilization of the particle flow.

5) Through the experiments and numerical simulations, with the increase in the lift, the efficiency of the core pump and velocity of the flow field increased simultaneously, indicating that the particles can obtain more kinetic energy from the flow field. At a rotational speed of 1,450 rpm, the movement of the particles was ensured, thereby reducing their deposition. The results of the experiment and numerical simulation were consistent, indicating the credibility of the numerical simulation results.

In this study, spherical particles were mainly used to investigate the hydraulic lifting of the solid–liquid two-phase flow. In actual deep-sea mining, the particles crushed by the crusher are expected to have various shapes. Therefore, the influence of the particle shape on the hydraulic lifting should be further explored, and the theory proposed in this article should be further examined.

DATA AVAILABILITY STATEMENT

The original contributions presented in the study are included in the article/Supplementary Material, further inquiries can be directed to the corresponding author.

AUTHOR CONTRIBUTIONS

All authors listed have made a substantial, direct, and intellectual contribution to the work and approved it for publication.

FUNDING

This work was supported by the National Key R&D Program of China: Development and Test of Lifting Pump for Deep Sea Mining Test Project (2016YFC0304103-4) and a fund from the National Natural Science Foundation of China: Research on deformation bifurcation and instability mechanism of hyperelastic bilayer circular tube under complex Load (12002067).

REFERENCES

Brennen, C. E., and Yong, O. L. (2010). Multi-phase Flow Foundations. *Rev. Foreign Sci. Tech. Books.* 11, 21–22. doi:10.1080/14616701003638418

Chen, H., Liu, W., Chen, Z., and Zheng, Z. (2021). A Numerical Study on the Sedimentation of Adhesive Particles in Viscous Fluids Using LBM-LES-DEM. *Powder Technol.* 391, 467–478. doi:10.1016/j.powtec.2021.06.031

Chen, Q., Xiong, T., Zhang, X., and Jiang, P. (2020). Study of the Hydraulic Transport of Non-spherical Particles in a Pipeline Based on the CFD-DEM. *Eng. Appl. Comput. Fluid Mech.* 14, 53–69. doi:10.1080/19942060.2019.1683075

Chen, Y. (2019). Sea Trials of the Deep-Sea Mining Program. *World Sci.* 05, 41

Childs, D. W. (1991). Fluid-structure Interaction Forces at Pump-Impeller-Shroud Surfaces for Axial Vibration Analysis. *J. Vib. Acoust.* 113, 108–115. doi:10.1115/1.2930144

Dong, Z., Liu, S., and Hu, X. (2018). Study on Calculation Method of Coarse Particle Two-Phase Flow. *Mar. Eng.* 36, 110.

Ebrahimi, M., and Crapper, M. (2017). CFD-DEM Simulation of Turbulence Modulation in Horizontal Pneumatic Conveying. *Particuology* 31, 15–24. doi:10.1016/j.partic.2016.05.012

González, J., Parrondo, J., Santolaria, C., and Blanco, E. (2006). Steady and Unsteady Radial Forces for a Centrifugal Pump with Impeller to Tongue Gap Variation. *J. Fluids Eng.* 128, 454–462. doi:10.1115/1.2173294

He, Y., Bayly, A. E., and Hassanpour, A. (2018). Coupling CFD-DEM with Dynamic Meshing: A New Approach for Fluid-Structure Interaction in Particle-Fluid Flows. *Powder Technol.* 325, 620–631. doi:10.1016/j.powtec.2017.11.045

Hu, Q., Chen, J., Deng, L., and Liu, S. (2021). CFD-DEM Coupling Simulation and Experimental Research on Deep Sea Lifting Pump under Extreme Conditions. *Chin. J. Nonferrous Met.* 9, 1–16. doi:10.3390/jmse9090987

Hu, Q., Zou, L., Lv, T., Guan, Y., and Sun, T. (2020). Experimental and Numerical Investigation on the Transport Characteristics of Particle-Fluid Mixture in Y-Shaped Elbow. *J. Marine. Sci. Engineer.* 8, 675. doi:10.3390/jmse8090675

Kato, Y., Fujinaga, K., Nakamura, K., Takaya, Y., Kitamura, K., Ohta, J., et al. (2011). Deep-sea Mud in the Pacific Ocean as a Potential Resource for Rare-Earth Elements. *Nat. Geosci.* 4, 535–539. doi:10.1038/ngeo1185

Li, Y.-w., Liu, S.-j., and Hu, X.-z. (2019). Research on Rotating Speed's Influence on Performance of Deep-Sea Lifting Motor Pump Based on DEM-CFD. *Mar. Georesources Geotechnol.* 37, 979–988. doi:10.1080/1064119x.2018.1514550

Liu, S., Li, Y., and Hu, X. (2020). Effect of Particle Volume Fraction on the Performance of Deep-Sea Mining Electric Lifting Pump Based on DEM-CFD. *J. Mech. Eng.* 56, 257

Parenteau, T. (2010). "Flow Assurance for Deepwater Mining." in Proceedings of the 29th International Conference on Ocean, Offshore and Arctic Engineering, 49118. Shanghai, China: ASME, 11–21. doi:10.1115/omae2010-20185

Rashidi, S., Esfahani, J., and Ellahi, R. (2017). Convective Heat Transfer and Particle Motion in an Obstructed Duct with Two Side by Side Obstacles by Means of DPM Model. *Appl. Sci.* 7, 431. doi:10.3390/app7040431

Safaei, M. R., Mahian, O., Garoosi, F., Hooman, K., Karimipour, A., Kazi, S. N., et al. (2014). Investigation of Micro- and Nanosized Particle Erosion in a 90°

Pipe Bend Using a Two-phase Discrete Phase Model. *ScientificWorldJournal* 2014, 740578–740590. doi:10.1155/2014/740578

Wang, R., Guan, Y., Jin, X., Tang, Z., Zhu, Z., and Su, X. (2021). Impact of Particle Sizes on Flow Characteristics of Slurry Pump for Deep-Sea Mining. *Shock Vib.* 9, 88–97. doi:10.1155/2021/6684944

Yang, F., Chen, Q., and Zeng, Y. (2014). Research on the Design Method of Deep-Sea Mining Slurry Pump. *J. Hefei Univ. Technol.* 12, 1413.

Zou, W., Lu, Y., and Li, Z. (2013). Numerical Simulation Analysis of Lifting Pump in Deep-Sea Mining. *J. Hunan Univ.* 40, 59

Conflict of Interest: The authors declare that the research was conducted in the absence of any commercial or financial relationships that could be construed as a potential conflict of interest.

Publisher's Note: All claims expressed in this article are solely those of the authors and do not necessarily represent those of their affiliated organizations, or those of the publisher, the editors and the reviewers. Any product that may be evaluated in this article, or claim that may be made by its manufacturer, is not guaranteed or endorsed by the publisher.

frontiers | Frontiers in Energy Research

ORIGINAL RESEARCH
published: 09 May 2022
doi: 10.3389/fenrg.2022.881811

Influence of Hole Geometry on Performance of a Rotational Hydrodynamic Cavitation Reactor

Wei Zhang[1], *Chao Xie*[1], *Honggang Fan*[1]* *and Bing Liu*[2]*

[1]State Key Laboratory of Hydroscience and Engineering, Department of Energy and Power Engineering, Tsinghua University, Beijing, China, [2]College of Mechanical and Electronic Engineering, Shandong University of Science and Technology, Qingdao, China

Cavitation is a common phenomenon in hydraulic power industry, ship propulsion, pump station and other industrial fields. In the present work, a high-speed camera is used to visualize the flow field in a rotational hydrodynamic cavitation reactor (RHCR) in a closed cycle test rig, and the numerical simulation is carried out based on the RNG k-ε turbulence model and the Zwart-Gerber-Belamri (ZGB) cavitation model. Influence of hole diameter, hole height and hole cone bottom length on performance of RHCR are comprehensively investigated. The results show that the numerical results are in good agreement with the experimental data, which verifies the accuracy and reliability of the numerical method. The hole diameter mainly influences the water vapor exchange boundary, the hole height mainly influences the cavitation area and intensity, and the cone bottom length mainly influences the vortex number and intensity. Under different hole diameters, the dominant frequent of pressure fluctuation in hole is 24 f_i corresponding to the hole number along the circumferential direction, and the maximum amplitude appears near the hole top due to the small gap between the hole top and the side wall of the rotor. When the hole diameter increases from 11 to 17 mm, the pressure fluctuation amplitude increases by 1.65 times for each increase of 2 mm.

Keywords: hydrodynamic cavitation reactor, hole geometry, numerical simulation, vortex, pressure fluctuation

OPEN ACCESS

Edited by:
Ling Zhou,
Jiangsu University, China

Reviewed by:
Changchang Wang,
Beijing Institute of Technology, China
Yuchuan Wang,
Northwest A&F University, China

***Correspondence:**
Honggang Fan
fanhonggang@tsinghua.org.cn
Bing Liu
metrc@sdust.edu.cn

Specialty section:
This article was submitted to Process and Energy Systems Engineering, a section of the journal Frontiers in Energy Research

Received: *23 February 2022*
Accepted: *08 March 2022*
Published: *09 May 2022*

Citation:
Zhang W, Xie C, Fan H and Liu B (2022) Influence of Hole Geometry on Performance of a Rotational Hydrodynamic Cavitation Reactor. Front. Energy Res. 10:881811. doi: 10.3389/fenrg.2022.881811

INTRODUCTION

Cavitation is an unsteady and multiphase turbulent flow phenomenon involving mass transfer between vapor and liquid phases (Liu et al., 2018; Liu et al., 2019a; Liu et al., 2019b). Cavitation flow is accompanied by the formation, development and collapse of cavitation, as well as the mass and energy transfer of two phases (Prasad et al., 2018; Sun and Lei, 2020). During this process, the collapse of the bubble can generate a local hot spot of 2,000–6,000 K and induce 10^{10} K/s heat transfer within 1 ms (Hart et al., 1990; Flint and Suslick, 1991; Didenko et al., 1999a; Didenko et al., 1999b; Rae et al., 2005). Meanwhile, in this extreme environment, water molecules can undergo splitting reactions and chain reactions to produce H and OH radicals (Gostisa et al., 2021). It can accelerate chemical reaction (Sun et al., 2018a), sewage treatment (Sun et al., 2021a), organic matter decomposition (Sun et al., 2021b), sterilization and deactivation (Pegu and Arya, 2021), biodiesel synthesis (Innocenzi and Prisciandaro, 2021) and other engineering applications. Therefore, it has a promising potential application in industry and shares a broad prospect in many disciplines.

According to the flow physics of cavitation generation, cavitation can be generally classified into acoustic cavitation (AC) (Gholami et al., 2020), hydrodynamic cavitation (HC) (Wang et al., 2021),

optical cavitation (OC) (Gogate, 2007) and particle cavitation (PC) (Sun et al., 2020a). Among them, the first two categories are more widely studied. With the development and popularization of ultrasonic equipment, the researches on ultrasonic cavitation have experienced a significant increase, and its applications involve many aspects such as medicine (Qian et al., 2020), material processing (Zhao et al., 2020), biochemistry (Patil et al., 2021) and food processing (Krasnikova et al., 2020). However, due to the disadvantages of high energy consumption, small cavitation area and high equipment cost, ultrasonic cavitation has some drawbacks in its further industrialization and practical application (Burzio et al., 2019). On the contrary, hydrodynamic cavitation has the advantages of simple design, low price and high efficiency, so it is widely used in industry (Kwon and Yoon, 2013). In the past, hydrodynamic cavitation is usually generated by orifice plate (Angele, 2021), venturi tube cavitation reactor (Bimestre et al., 2020) and so on. Kuldeep et al. (Kuldeep and Kumar, 2016) numerically simulated flow field inside the venturi cavitation reactor, and the results show that the ratio 1:1 of throat height/diameter to length and 6.5° of divergence angle can be an optimal geometry for best cavitation activity. Alister et al. (Simpson and Ranade, 2018) quantitatively discussed the influence of some key geometric parameters such as the orifice plate thickness, orifice inlet sharpness and wall angle on cavitation behaviors. Keiji et al. (Yasuda and Ako, 2019) studied the influence of venturi shape on the hydrodynamic cavitation reaction rate. Alves et al. (2019) investigated the hydrodynamic cavitation efficiency in removing chemical oxygen demand (COD) from sucrose solution and from effluent generated by the soft drink industry. However, because these two types of cavitation generators induce cavitation through cross-sectional area change, the water flow is severely restricted and the pressure loss is large (Šarc et al., 2018). In addition, their effectiveness was found to be unsatisfactory with high expenses (Sun et al., 2020b). Therefore, more efficient designs need to be developed that can replace the traditional cavitation generator.

Recently, a rotational hydrodynamic cavitation reactor that is composed of rotor and stator is used to generate cavitation. The cavitation mechanism of the structure cavitation reactor is composed of various forces in the complex flow field (mainly shear force and centrifugal force). It gets rid of the traditional cavitation generation mode, and can generate group cavitation in the cavitation reactor with high cavitation intensity and high cavitation efficiency. PetkovsEk et al. (2013) and Badve et al. (2013) studied the ability of rotational structure reactor to treat sewage and industrial wastewater. Kim et al. (2019) carried out the experiment of sludge treatment by rotational cavitation reactor. Milly et al. (2008) used a rotational structure reactor to sterilize fluid food. Sun et al. (2018b) studied the thermal performance of a new type of rotational hydrodynamic cavitation reactor through experiments. Thaiyasuit et al. (2021) studied the optimal production conditions for biodiesel production in a rotating cavitation reactor with uneven rotor surface. Janez et al. (Kosel et al., 2019) used a rotational cavitation reactor to refine pulp samples and found that the device could generate strong shear force and multiple cavitation regions. All of the above researches are based on the applicability test of RHCR, but the mechanism research of RHCRs and the influence of its own structure on the cavitation effect are very limited. Moreover, the hole in the rotor and its geometrical structure is vital for the cavitation generation, and there is still a significant vacancy in quantitatively investigating its effects and underlying mechanics.

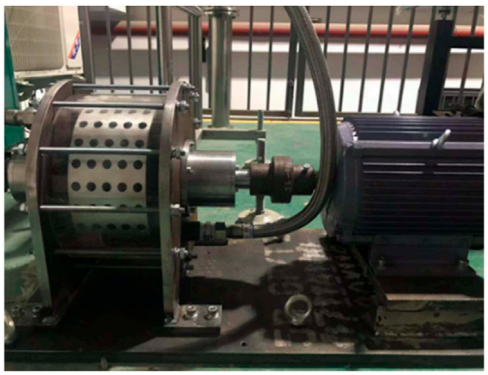

FIGURE 1 | Tested rotational hydrodynamic cavitation reactor.

In order to address the above problems, the high-speed photographic measuring and the numerical simulation were both employed to study the cavitating flow pattern and pressure fluctuation characteristics inside the RHCR. Subsequently, the correlation between the hole diameter, height and cone bottom length and cavitation characteristics were analyzed, which contributes to the optimal design of RHCR.

EXPERIMENTAL AND NUMERICAL METHODOLOGY

Research Object

As shown in **Figure 1**, the RHCR is mainly composed of a rotor and a stator. The rotor is a solid cylinder with a diameter of 264 mm. 24 rows of inner holes are evenly distributed on the rotor surface along the circumferential direction, and the angle between any two adjacent rows of inner holes is 15°. There are 5 columns of inner holes evenly distributed on the rotor surface along the axial direction, and the distance between two adjacent rows of inner holes is 22.5 mm. The height of each hole is 55 mm and the diameter is 15 mm. The clearance between the rotor and the stator is fixed at 8 mm. The rotor rotates under the drive of the motor and generates cavitation in the inner hole. The motor can be controlled by the inverter by setting different rotation speeds. The rotation speed in the present work is set as 1,200 r/min.

In order to reveal the influence of the inner hole structure on the performance of the RHCR, this study analyzed three geometric factors of the inner hole structure. Case 1 keep the hole height 55 mm and the cone bottom length 5 mm unchanged, and select five kinds of diameters, 11, 13, 15, 17 and 19 mm

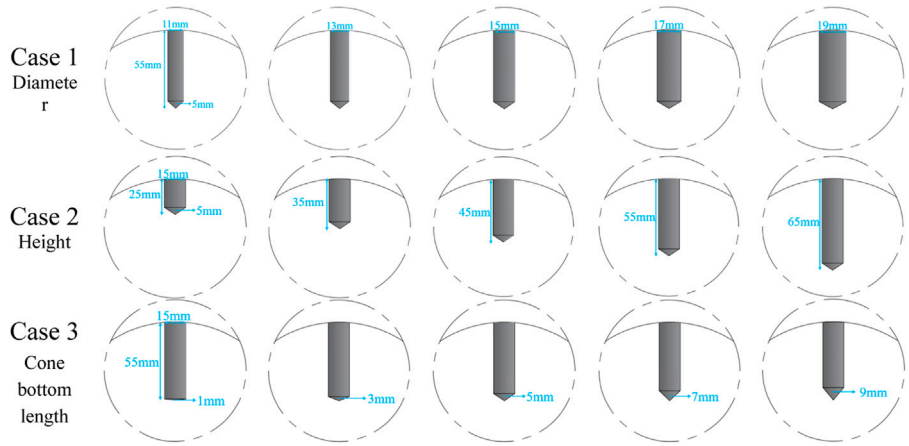

FIGURE 2 | Various geometrical factors of the hole.

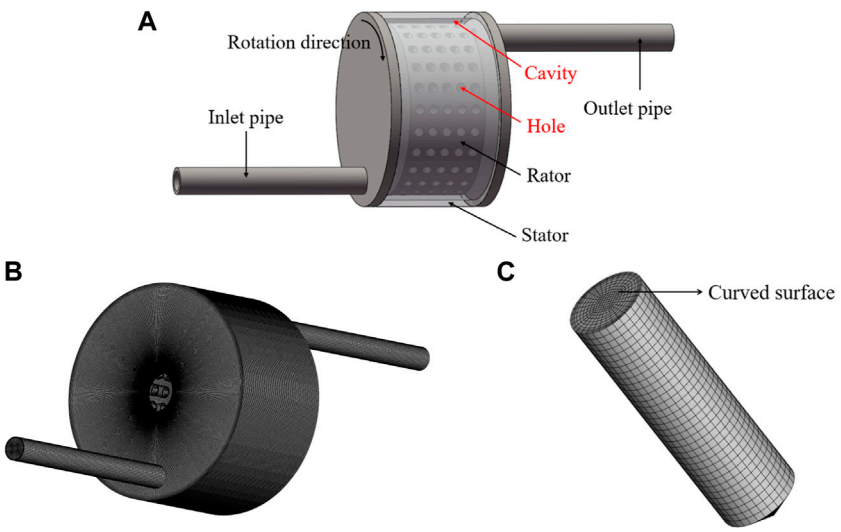

FIGURE 3 | The model and mesh of RHCR: **(A)** Schematic diagram of the RHCR, **(B)** Computing domain mesh, and **(C)** Single hole mesh.

respectively. Case 2 keep the hole diameter 15 mm and the cone bottom length 5 mm unchanged, and select five kinds of heights, 25, 35, 45, 55, and 65 mm respectively. Case 3 keep the hole diameter 15 mm and the height 55 mm unchanged, and select five kinds of cone bottom lengths, 1, 3, 5, 7, and 9 mm respectively. The detailed information on the geometrical factors can be found in **Figure 2**.

Computational Domain and Meshes

As shown in **Figure 3A**, the computational domain is divided into four parts: inlet domain, cavity domain, rotor domain and outlet domain. The rotor-stator interface is employed to couple the adjacent rotary domain and stationary domain. Moreover, the fluid domain adopts a hexahedral structure mesh is applied to the whole computational domain by using ANSYS ICEM 20.0. Furthermore, mesh near the wall of the inner holes is locally refined, as shown in **Figures 3B,C**.

NUMERICAL METHOD AND SETTING

Numerical Model and Boundary Conditions

The fluid in the cavitation flow field is considered a homogeneous and compressible mixed medium of liquid and vapor. The continuity and momentum equations in the Cartesian coordinates are as follows:

$$\frac{\partial \rho}{\partial t} + \frac{\partial \left(\rho \overline{u_j}\right)}{\partial x_j} = 0 \tag{1}$$

TABLE 1 | Results of the mesh-independence test.

Resolution	Maximum Element Size (mm)	Relative to the Pressure Difference
Coarse	2	1
Medium	1.5	0.998,481
Fine	1	0.998,948

$$\rho\frac{\partial\overline{u_i}}{\partial t}+\rho\overline{u_j}\frac{\partial\overline{u_i}}{\partial x_j}=\rho F_i-\frac{\partial\bar{p}}{\partial x_i}+\mu\frac{\partial^2\overline{u_i}}{\partial x_j\partial x_j}-\rho\frac{\partial\left(\overline{u_i'u_j'}\right)}{\partial x_j} \tag{2}$$

where ρ is density, t is time, u is velocity, μ is viscosity coefficient, and F is volume force. The RNG k-ε (Liu et al., 2009) turbulence model is applied because of its advantage in predicting the flow with a high strain rate and streamline curvature.

The cavitation model proposed by Zwart is employed to simulate the cavitation flow. In this model, a transport equation with source terms based on the homogeneous flow is used to solve the interphase mass transfer between liquid and vapor phases, which is governed as follows:

$$\frac{\partial\left(\rho_v\alpha_v\right)}{\partial t}+\frac{\partial\left(\rho_v\alpha_v u_i\right)}{\partial x_i}=m^+-m^- \tag{3}$$

The mass transfer for vaporization rate m^+ and condensation rate m^- are modeled as follows:

$$m^+=C_{vap}\frac{3r_g\left(1-\alpha_v\right)\rho_v}{R_b}\sqrt{\frac{2}{3}\frac{\max\left(p_v-p,0\right)}{\rho_l}} \tag{4}$$

$$m^-=C_{cond}\frac{3\alpha_v\rho_v}{R_b}\sqrt{\frac{2}{3}\frac{\max\left(p-p_v,0\right)}{\rho_l}} \tag{5}$$

where α_v is the vapor volume fraction. ρ_v is the vapor density, and its value is 0.02308 kg/m^3 ρ_l is the liquid density, and its value is 997 kg/m^3 p_v is the water vaporization pressure that is set as 3,574 Pa in the present simulation. C_{vap} and C_{vond} are the empirical coefficients of evaporation and condensation, and their values are 50 and 0.01 respectively (Zwart et al., 2004).

In the present study, the total volume fraction of vapor, β_{total}, is defined as the ratio of total vapor volume V_{vapor} to total volume V_{total} of fluid domain.

$$\beta_{total}=\frac{V_{vapor}}{V_{total}}=\frac{\sum_{i=1}^{N}\beta_{vapor}V_i}{\sum_{i=1}^{N}V_i} \tag{6}$$

where, N is the total number of holes in the fluid domain. β_{vapor} is the volume fraction of steam in each inner hole, V_i is the volume of each inner hole.

The commercial software ANSYS-CFX 20.0 are employed in the present work to simulate the internal flow of the RHCR. The flow conditions of the numerical simulation are consistent with those in the experiment test. The total inlet pressure is 90,000 Pa. The liquid volume fraction is 1, and the gas volume fraction is 0. The outlet mass flow is set to 2.5 kg/s.

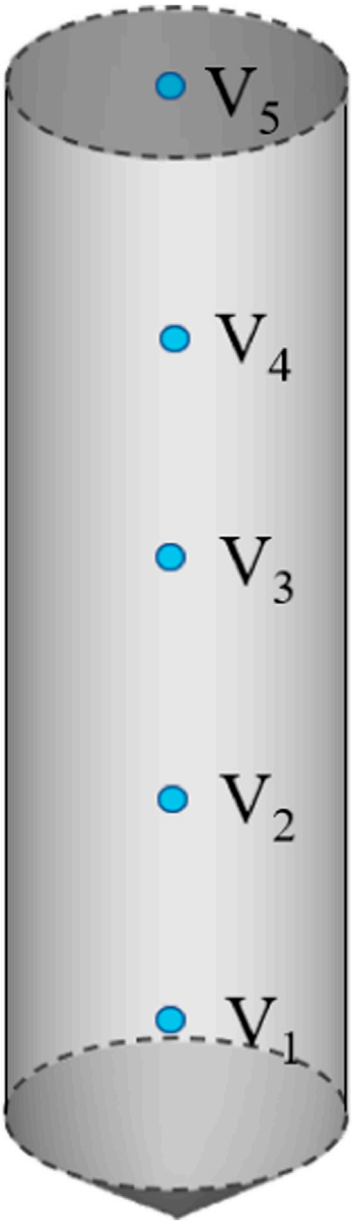

FIGURE 4 | Monitoring points in hole.

Non slip wall condition is applied on all the solid walls of the RHCR. In transient calculation, the results of steady calculation were ultilized as the initial flow field.

Independence Test of Mesh Density and Time Step

Because the geometrical models for each case were not identical, the maximum element size was chosen as the index of the mesh resolution, instead of using the total cell number. **Table 1** presents the results of the mesh-independence test for three mesh resolutions of the original

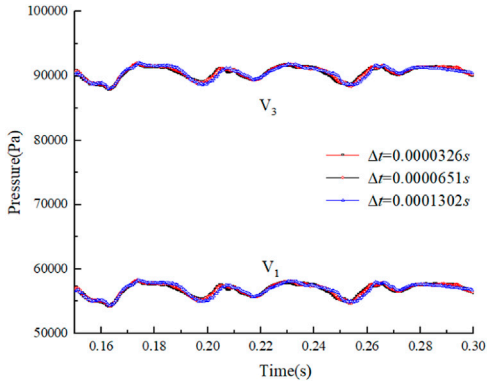

FIGURE 5 | Time-step independence verification.

model: coarse, medium, and fine. Because the relative pressure difference between the medium and fine mesh was negligible. Considering the computational resources and mesh sensitivity, this paper adopts a medium mesh resolution to predict the simulation results.

In the transient calculation, in order to verify the time independence, the time step Δt is taken as 1/16, 1/32 and 1/64 of the time interval between two adjacent inner holes at the same position. These three times steps are corresponding to $T/24/16$ = 0.0001302s, $T/24/32$ = 0.0000651s, $T/24/64$ = 0.0000326s, where T is the rotating period of the RHCR. As shown in **Figure 4**, a monitoring point is set up every 11 mm from the bottom of the hole, and a total of 5 monitoring points are V_1, V_2, V_3, V_4, and V_5 respectively.

The calculation results of the three times steps are shown in **Figure 5**, the difference between the simulation results under three times steps is very small. Considering the calculation cost, this paper takes the Δt = 0.0001302s.

In order to verify the accuracy of numerical simulation, the fully developed cavitation patterns obtained by the experiment shown in **Figure 6B** and the simulation shown in **Figure 6C** is compared. The results show that the numerical simulation agrees well with the experimental observation, which shows that the employed numerical method is reliable and accurate to predict the cavitating flow field inside the RHCR.

RESULTS AND ANALYSIS

Based on the previous methods, a systematic investigation on the influence of hole diameter, hole height and cone bottom length on the cavitation patter has been carried out. The pressure fluctuation characteristics of RHCR are further analyzed with consideration of the most influential parameter.

Effect of Diameter

Figure 7 shows the vapor phase distribution under different hole diameters varying from 11 to 19 mm. It is found that the increase of hole diameter results in the increase of cavitation intensity and area. As demonstrated in **Figure 7**, when the hole diameter increases from 11 to 19 mm, the cavitation extends from the hole bottom to the top. The vapor volume fractions β_{total} are 10% of D_1 = 11 mm, 22% of D_2 = 13 mm, 55% of D_3 = 15 mm, 75% of D_4 = 17 mm, and 85% of D_5 = 19 mm, respectively. For a small hole diameter, the cavitation intensity is suppressed due to the rotor centrifugal force. With the hole diameter increasing, the water-vapor exchange boundary shifts towards the hole top, which leads to a stronger exchange with the water in the actor. Consequently, the hole diameter plays a significant role on cavitation intensity and area in the RHCR.

Effect of Height

Figure 8 shows the vapor phase distribution under different hole height varying from 25 to 65 mm. The results show there is none cavitation under hole height of H_1 = 25 mm, and when the hole height increases to H_2 = 35 mm the cavitation appears. The vapor volume fractions are 0% of H_1 = 25 mm, 18% of H_2 = 35 mm, 55% of H_3 = 45 mm, 75% of H_4 = 55 mm, and 85% of H_5 = 65 mm, respectively.

Figure 9 shows the pressure and streamline in the hole of different height. when the height of the hole is less than 25 mm, the water in the hole can sufficiently exchange with the outer water despite of the centrifugal force generated by the rotation of the rotor, and the pressure in the hole bottom is not below the saturated vapor pressure. Therefore, the cavitation does not occur under hole height of H_1 = 25 mm. When the height of the hole is greater than 25 mm, the streamlines are complex in the hole with the heights of 35, 45, and 55 mm in **Figure 9**. Due to the increase of the hole height, the water in the hole cannot flow into the hole completely because of the centrifugal force, the water reduces the pressure inside the hole, thus creating cavitation. For the hole height structures from 35 to 55 mm,

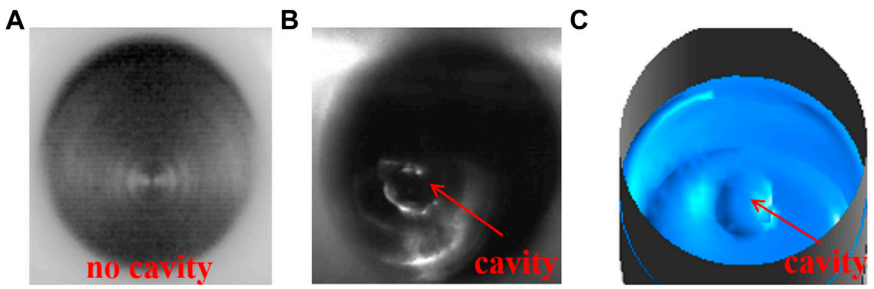

FIGURE 6 | Comparison of experiment and simulation: **(A)** no cavity of experiment diagram, **(B)** cavity of experiment diagram, and **(C)** cavity of simulation diagram.

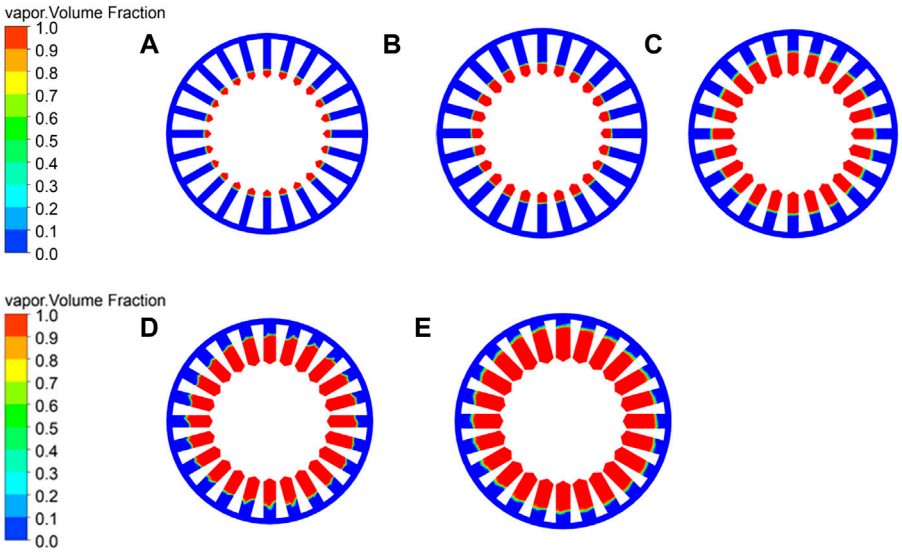

FIGURE 7 | Vapor phase distribution with different diameters: **(A)** D_1 = 11 mm, **(B)** D_2 = 13 mm, **(C)** D_3 = 15 mm, **(D)** D_4 = 17 mm, and **(E)** D_5 = 19 mm.

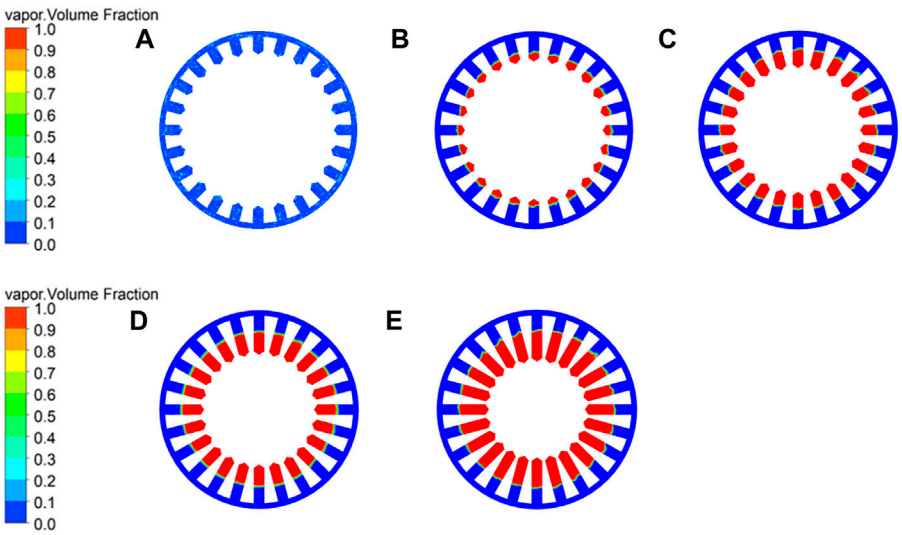

FIGURE 8 | :Vapor phase distribution with different heights: **(A)** H_1 = 25 mm, **(B)** H_2 = 35 mm, **(C)** H_3 = 45 mm, **(D)** H_4 = 55 mm, and **(E)** H_5 = 65 mm.

the center of the vortex is just on the boundary of the low pressure region in the hole, which is just about 25 mm. This better explains why cavitation occurs in the region below 25 mm hole height.

In summary, for different hole heights, the water-vapor exchange boundary is nearly the same position. The reason is that the centrifugal force is related to the radius of a circle. With the increase of the hole height, the cavitation intensity and area increase.

Effect of Cone Bottom Length

Figure 10 shows the vapor phase distribution under different cone bottom lengths varying from 1 to 9 mm. The results show that the increase of length for the cone bottom leads to a decrease of cavitation intensity and area. The vapor volume fractions are 64% of L_1 = 1 mm, 58% of L_2 = 3 mm, 55% of L_3 = 5 mm, 40% of L_4 = 7 mm and 34% of L_5 = 9 mm, respectively.

Figure 11 shows the pressure and streamline in the hole. There are several vortexes in the hole close to the top and bottom, respectively. The vortex formation mechanism is that the water in hole interacts with the outer water and then induces the shear force near the hole outlet interface. For different cone bottom lengths, the vortex shape near the hole top is similar due to the similar shear force, while the vortex number and intensity are different near the hole bottom due to the different cone bottom length.

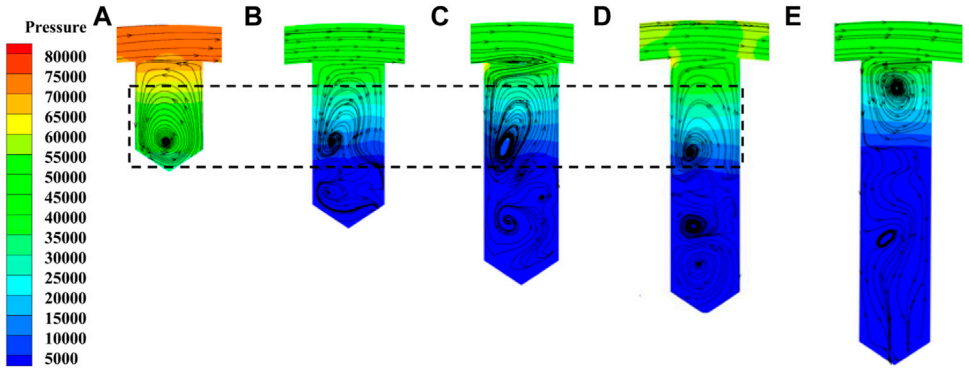

FIGURE 9 | Streamline distribution in hole of different hole height: **(A)** H_1 = 25 mm, **(B)** H_2 = 35 mm, **(C)** H_3 = 45 mm, **(D)** H_4 = 55 mm, and **(E)** H_5 = 65 mm.

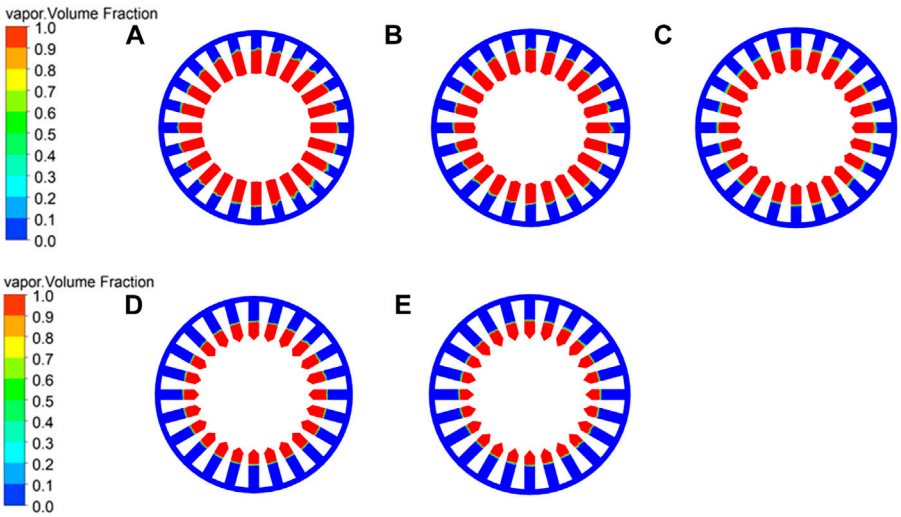

FIGURE 10 | Vapor phase distribution with different cone bottom lengths: **(A)** L_1 = 1 mm, **(B)** L_2 = 3 mm, **(C)** L_3 = 5 mm, **(D)** L_4 = 7 mm, and **(E)** L_5 = 9 mm.

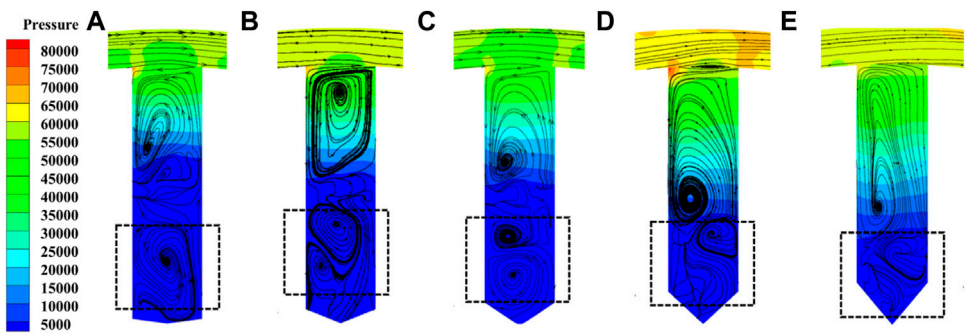

FIGURE 11 | Streamline distribution in hole: **(A)** L_1 = 1 mm, **(B)** L_2 = 3 mm, **(C)** L_3 = 5 mm, **(D)** L_4 = 7 mm, and **(E)** L_5 = 9 mm.

With the increase of the cone bottom length, the low-pressure region reduces, and the vortex intensity near the hole bottom also weakens. The vortex number varies under different cone bottom lengths, and the reason may be that the shear force, the centrifugal force and pressure gradient interact in the hole. Therefore, the cone bottom length mainly

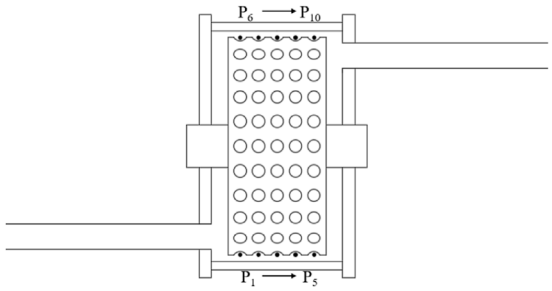

FIGURE 12 | Monitoring points for pressure.

influences the pressure distribution and vortex near the hole bottom, which affects the cavitation intensity and area in the hole.

Therefore, based on the simulation calculation results of the RHCR in this study and the limitation of its structure, the optimal combination of structural parameters in this paper are selected as 17 mm hole diameter, 55 mm hole height and 1 mm cone bottom length under the experimental working conditions.

Spectrum Analysis of Pressure Fluctuation

Figure 12 shows monitoring points of pressure in the rotor, which are used to investigate the influence of hole diameter on

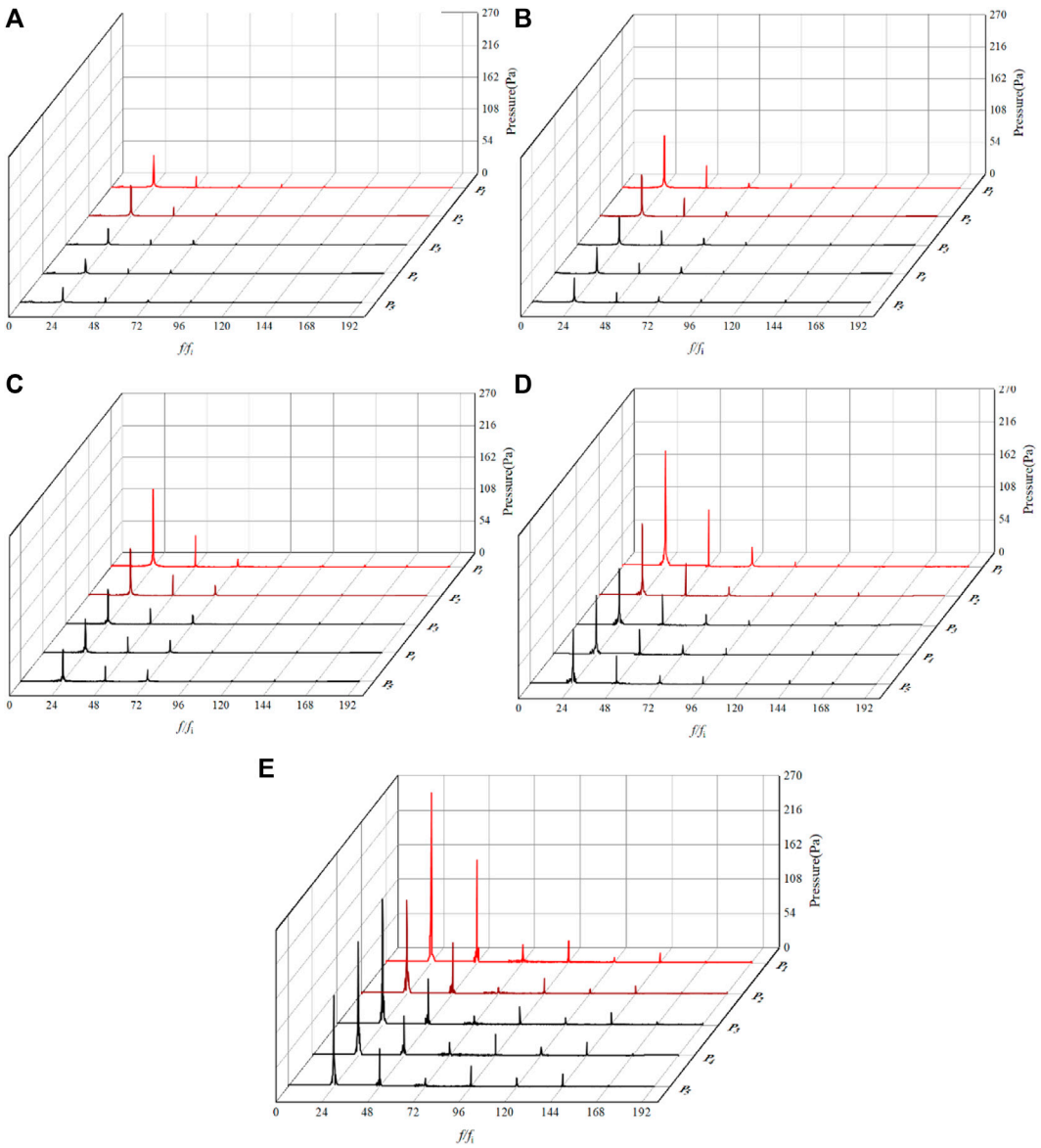

FIGURE 13 | Pressure fluctuation spectrum of P_1-P_5 with different hole diameters: **(A)** D_1 = 11 mm, **(B)** D_2 = 13 mm, **(C)** D_3 = 15 mm, **(D)** D_4 = 17 mm, and **(E)** D_5 = 19 mm.

TABLE 2 | Pressure pulsation at inlet side.

Monitoring Point	Maximum Amplitudes of Pressure Fluctuation (Pa)				
	11 mm	13 mm	15 mm	17 mm	19 mm
P_1	54.1	89.1	132.1	191.6	267.1
P_2	51.6	70.9	79.0	120.1	147.2
P_3	27.4	47.4	58.6	94.5	198.2
P_4	25.0	44.7	57.4	98.8	178.5
P_5	24.8	41.5	54.7	92.1	137.9

the pressure fluctuation of cavitation reactor. Total 10 points are set in the rotor, and P_1- P_5 are set at the reactor bottom along the flow direction, and P_6- P_{10} are set at the reactor top along the flow direction.

The total time for transient calculation is twenty rotor rotation cycles,and the pressure fluctuation data of the 8th to 16th cycle is taken to obtain the spectral characteristics of the pressure fluctuation by the method of Fast Fourier Transform.

Figure 13 shows the frequency domain of pressure fluctuation of points P_1-P_5 for different hole diameters in the RHCR. The dominant frequency of pressure fluctuation at each monitoring point is 24 f_i, and f_i = 20 Hz is the rotor frequency due to the rotor speed of 1,200 r/min. Generally, the amplitude of pressure fluctuation decreases for the harmonic frequency, and the amplitudes of pressure fluctuation at P_1 and P_2 monitoring points are stronger than that at P_3, P_4 and P_5.

Table 2 shows the maximum amplitude of pressure fluctuation points of P_1-P_5 for different hole diameters in the RHCR. The maximum pressure fluctuations of different hole diameters are all located at P_1 close to the hole top, and the amplitudes are 54.1, 89.1, 132.1, 191.6, and 267.1 Pa, respectively. Along the direction of P_1-P_5, the pressure fluctuation amplitude presents a decreasing trend. From P_3 to P_5, the pressure fluctuation amplitude becomes stable, and the reason is that the flow impact is mainly induced at the reactor inlet near the P_1 and P_2.

Figure 14 shows the pressure distribution in the RHCR. Due to the small gap between the inlet and the side wall of the rotor, the water impacts on the side wall of the rotor and form a high-pressure zone in region 1, which induces the strong pressure fluctuation amplitude near point 1. In addition, the relative motion between the rotor and the stable wall results in the rotor-stator interaction, which also induces the strong pressure fluctuation amplitude near point 1. Therefore, in order to reduce the pressure fluctuation amplitude, the distance between the rotor and reactor wall should be considered in the optimized design of the RHCR.

As shown in **Figure 14** the pressure distribution on the outlet side of the RHCR in **Figure 14A** and the pressure distribution on both sides of the RHCR in **Figure 14B** are more stable compared to the inlet side, and there is no interference from the water flow hitting the rotor. Therefore, five monitoring points on the outlet side were selected to analyze the influence of inner hole diameter on the pressure fluctuation of RHCR.

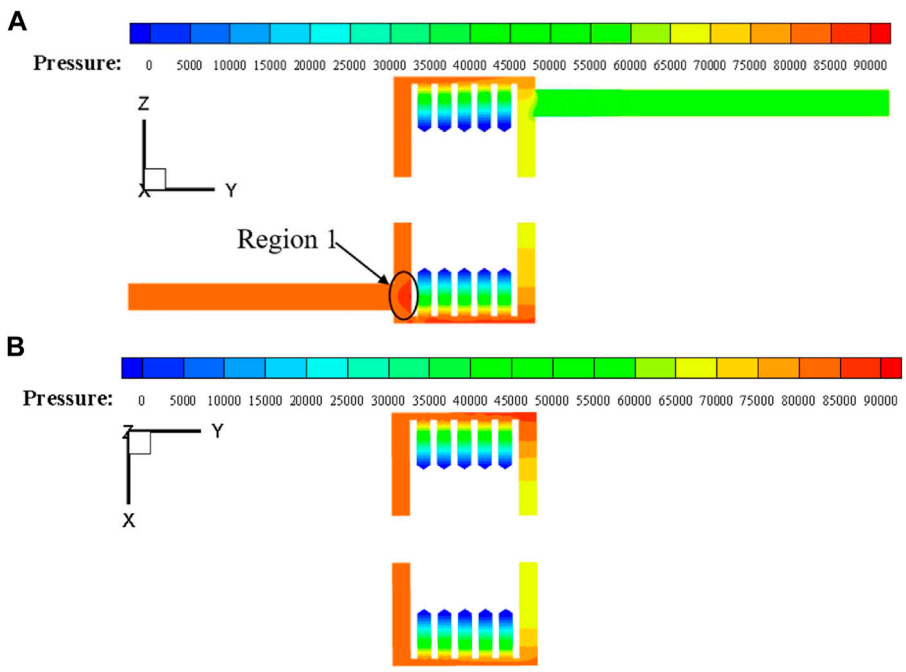

FIGURE 14 | Pressure distribution in RHCR: **(A)** pressure distribution at YZ cross-section, and **(B)** pressure distribution at YX cross-section.

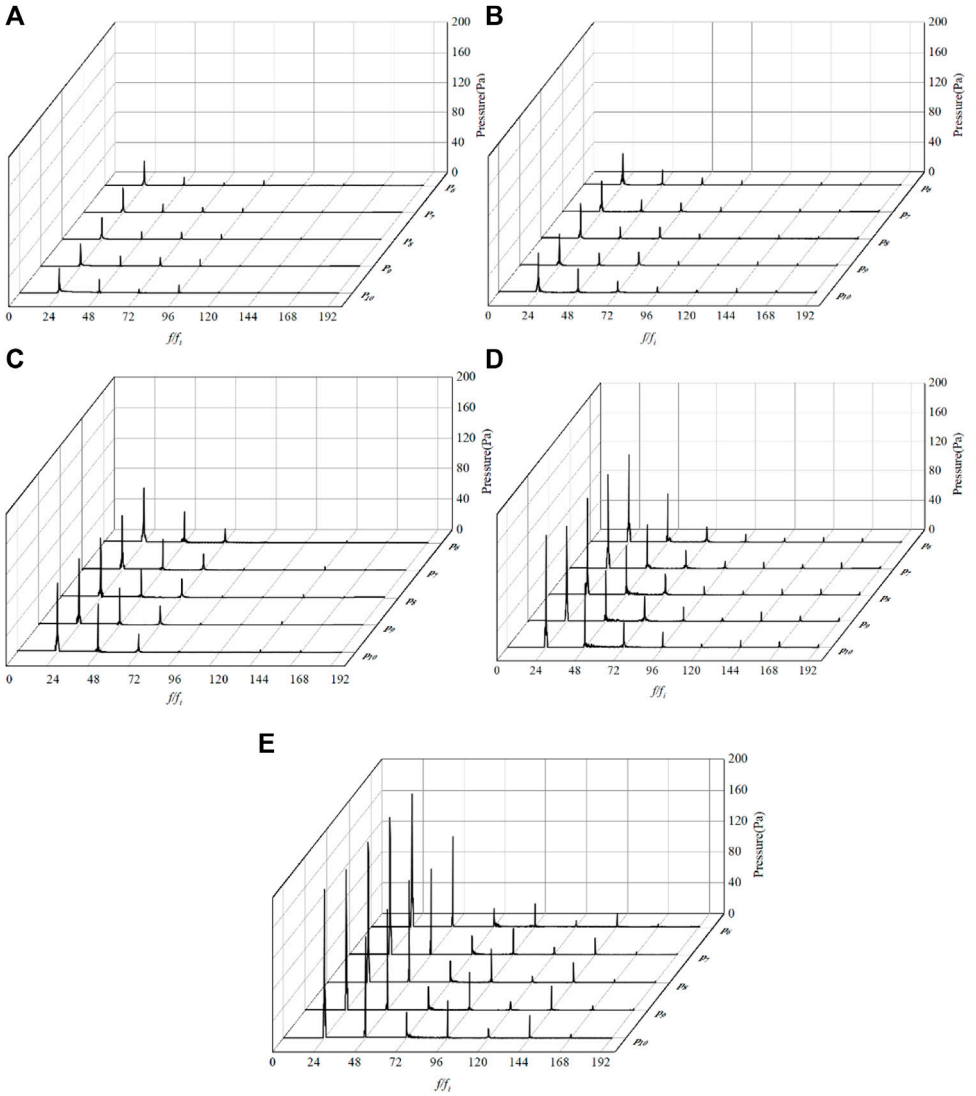

FIGURE 15 | Pressure fluctuation spectrum of P_6-P_{10} with different hole diameters: **(A)** D_1 = 11 mm, **(B)** D_2 = 13 mm, **(C)** D_3 = 15 mm, **(D)** D_4 = 17 mm, and **(E)** D_5 =19 mm.

Figure 15 shows the frequency domain of pressure fluctuation of points P_6-P_{10} for different hole diameters in the RHCR. As shown in **Figures 15A–E**, the pressure fluctuation amplitudes of points P_6-P_{10} are relatively uniform for different hole diameters, and the dominant frequency of pressure fluctuation at each monitoring point is 24 f_i.

Figure 16 shows the frequency domain of pressure fluctuation at the same point of P_8 for different hole diameters. With the increase of the hole diameter, the amplitude of pressure fluctuation obviously increases. When the diameter increases from 11 to 13 mm, the fluctuation amplitude increases about 1.65 times. When the diameter increases from 17 to 19 mm, the fluctuation amplitude increases by 1.37 times. The reason is that the larger hole diameter has stronger effect on the flow field, especially on the interface between hole top and main stream.

CONCLUSION

In the present work, a high-speed camera is used to observe the internal flow pattern in the RHCR, and the numerical simulation is used to calculate the three-dimensional cavitating turbulent flow. Effects of hole diameter, hole height and hole cone bottom length on performance of RHCR are comprehensively investigated, and the main conclusions are as follows:

1) The numerical simulation data agrees well with the experiment result, which validates that the numerical model and method are reliable and accurate.
2) The hole geometry of diameter, height and cone bottom length will influence the water-vapor exchange boundary, cavitation area and intensity, vortex number and intensity. The optimal

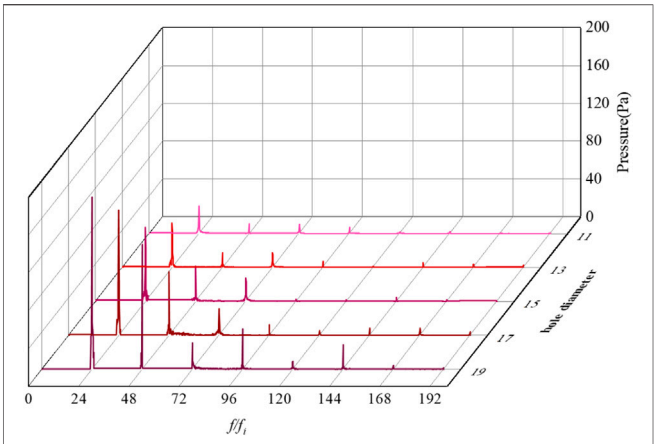

FIGURE 16 | Pressure fluctuation spectrum of P_8 with different hole diameters.

structural parameters of the RHCR were taken as 17 mm hole diameter, 55 mm hole height and 1 mm cone bottom length.

3) The dominant frequent of pressure fluctuation in hole is 24 f_i corresponding to the hole number along the circumferential direction, and the maximum amplitude appears near the hole top due to the small gap between the hole top and the side wall of the rotor.

DATA AVAILABILITY STATEMENT

The original contributions presented in the study are included in the article/Supplementary Material, further inquiries can be directed to the corresponding authors.

AUTHOR CONTRIBUTIONS

WZ, HF, and BL contributed to conception and design of the study. CX and WZ finished the experiment and numerical simulation. WZ performed the statistical analysis. CX wrote the first draft of the manuscript. WZ, HF, and BL wrote sections of the manuscript. All authors contributed to manuscript revision, read, and approved the submitted version.

FUNDING

This work was supported by the National Natural Science Foundation of China (51879140), the State Key Laboratory of Hydroscience and Engineering (2021-KY-04), Tsinghua-Foshan Innovation Special Fund (TFISF) 2021THFS0209, the Creative Seed Fund of Shanxi Research Institute for Clean Energy, Tsinghua University.

REFERENCES

Alves, P., Silva, P., Ferreira, D. C., and de Souza Inácio Gonçalves, J. C. (2019). COD Removal from Sucrose Solution Using Hydrodynamic Cavitation and Hydrogen Peroxide: a Comparison between Venturi Device and Orifice Plate. *Rbrh* 24. doi:10.1590/2318-0331.241920180147

Angele, K. (2021). Prediction of Cavitation in Orifice Plates-A Novel and Simple Rule-Of-Thumb. *Exp. Comput. Multiph. Flow* 3 (1), 68–76. doi:10.1007/s42757-020-0059-1

Badve, M., Gogate, P., Pandit, A., and Csoka, L. (2013). Hydrodynamic Cavitation as a Novel Approach for Wastewater Treatment in wood Finishing Industry. *Separat. Purif. Techn.* 106 (Complete), 15–21. doi:10.1016/j.seppur.2012.12.029

Bimestre, T. A., Júnior, J. A. M., Botura, C. A., Canettieri, E., and Tuna, C. E. (2020). Theoretical Modeling and Experimental Validation of Hydrodynamic Cavitation Reactor with a Venturi Tube for Sugarcane Bagasse Pretreatment. *Bioresour. Techn.* 311, 123540. doi:10.1016/j.biortech.2020.123540

Burzio, E., Bersani, F., Caridi, G. C. A., Vesipa, R., Ridolfi, L., and Manes, C. (2019). Water Disinfection by Orifice-Induced Hydrodynamic Cavitation. *Ultrason. Sonochem.* 60, 104740. doi:10.1016/j.ultsonch.2019.104740

Didenko, Y. T., McNamara, W. B., and Suslick, K. S. (1999b). Hot Spot Conditions during Cavitation in Water. *J. Am. Chem. Soc.* 121 (24), 5817–5818. doi:10.1021/ja9844635

Didenko, Y. T., McNamara, W. B., and Suslick, K. S. (1999a). Temperature of Multibubble Sonoluminescence in Water. *J. Phys. Chem. A.* 103 (50), 10783–10788. doi:10.1021/jp991524s

Flint, E. B., and Suslick, K. S. (1991). The Temperature of Cavitation. *Science* 253 (5026), 1397–1399. doi:10.1126/science.253.5026.1397

Gholami, A., Pourfayaz, F., and Maleki, A. (2020). Techno-economic Assessment of Biodiesel Production from Canola Oil through Ultrasonic Cavitation. *Energ. Rep.* 7, 266–277. doi:10.1016/j.egyr.2020.12.022

Gogate, P. R. (2007). Application of Cavitational Reactors for Water Disinfection: Current Status and Path Forward. *J. Environ. Manage.* 85 (4), 801–815. doi:10.1016/j.jenvman.2007.07.001

Gostisa, J., Širok, B., Repinc, S. K., Levstek, M., Stražar, M., Bizjan, B., et al. (2021). Performance Evaluation of a Novel Pilot-Scale Pinned Disc Rotating Generator of Hydrodynamic Cavitation. *Ultrason. Sonochem.* 72 (3), 105431. doi:10.1016/j.ultsonch.2020.105431

Hart, E. J., Fischer, C.-H., and Henglein, A. (1990). Sonolysis of Hydrocarbons in Aqueous Solution. *Int. J. Radiat. Appl. Instrumentation. C. Radiat. Phys. Chem.* 36 (4), 511–516. doi:10.1016/1359-0197(90)90198-q

Innocenzi, V., and Prisciandaro, M. (2021). Technical Feasibility of Biodiesel Production from virgin Oil and Waste Cooking Oil: Comparison between Traditional and Innovative Process Based on Hydrodynamic Cavitation. *Waste Manage.* 122, 15–25. doi:10.1016/j.wasman.2020.12.034

Kim, H., Sun, X., Koo, B., and Yoon, J. Y. (2019). Experimental Investigation of Sludge Treatment Using a Rotor-Stator Type Hydrodynamic Cavitation Reactor and an Ultrasonic Bath. *Processes* 7 (11), 790. doi:10.3390/pr7110790

Kosel, J., Šinkovec, A., and Dular, M. (2019). A Novel Rotation Generator of Hydrodynamic Cavitation for the Fibrillation of Long conifer Fibers in Paper Production. *Ultrason. Sonochem.* 59, 104721. doi:10.1016/j.ultsonch.2019.104721

Krasnikova, E. S., Morgunova, N. L., Krasnikov, A. V., Akchurin, S. V., and Akchurina, I. V. (2020). Physical and Chemical Effects of Ultrasonic Cavitation on the Grain of Meat when Lamb Salting. *J. Phys. Conf. Ser.* 1679, 022001. doi:10.1088/1742-6596/1679/2/022001

Kuldeep, V., and Kumar, S. (2016). Computational Study of Different Venturi and Orifice Type Hydrodynamic Cavitating Devices. *J. Hydrodynamics* 28 (02), 293–305. doi:10.1016/s1001-6058(16)60631-5

Kwon, W. C., and Yoon, J. Y. (2013). Experimental Study of a Cavitation Heat Generator. *Proc. Inst. Mech. Eng. E: J. Process Mech. Eng.* 227 (1), 67–73. doi:10.1177/0954408912451535

Liu, M., Tan, L., and Cao, S. (2019a). Cavitation-Vortex-Turbulence Interaction and One-Dimensional Model Prediction of Pressure for Hydrofoil ALE 15 by Large Eddy Simulation. *J. Fluids Eng.* 141 (2), 021103. doi:10.1115/1.4040502

Liu, M., Tan, L., and Cao, S. (2019b). Dynamic Mode Decomposition of Cavitating Flow Around ALE 15 Hydrofoil. *Renew. Energ.* 139, 214–227. doi:10.1016/j.renene.2019.02.055

Liu, M., Tan, L., Liu, Y., Xu, Y., and Cao, S. (2018). Large Eddy Simulation of Cavitation Vortex Interaction and Pressure Fluctuation Around Hydrofoil ALE 15. *Ocean Eng.* 163, 264–274. doi:10.1016/j.oceaneng.2018.06.005

Liu, S., Li, S., and Wu, Y. (2009). Pressure Fluctuation Prediction of a Model Kaplan Turbine by Unsteady Turbulent Flow Simulation. *J. Fluids Eng.* 131 (10), 101102. doi:10.1115/1.3184025

Milly, P. J., Toledo, R. T., Harrison, M. A., and Armstead, D. (2008). Inactivation of Food Spoilage Microorganisms by Hydrodynamic Cavitation to Achieve Pasteurization and Sterilization of Fluid Foods. *J. Food Sci.* 73 (2), VII. doi:10.1111/j.1750-3841.2008.00827.x

Patil, P. B., Raut-Jadhav, S., and Pandit, A. B. (2021). Effect of Intensifying Additives on the Degradation of Thiamethoxam Using Ultrasound Cavitation. *Ultrason. Sonochem.* 70, 105310. doi:10.1016/j.ultsonch.2020.105310

Pegu, K., and Arya, S. S. (2021). Comparative Assessment of HTST, Hydrodynamic Cavitation and Ultrasonication on Physico-Chemical Properties, Microstructure, Microbial and Enzyme Inactivation of Raw Milk. *Innovative Food Sci. Emerging Tech.* 69 (3), 102640. doi:10.1016/j.ifset.2021.102640

PetkovsEk, M., Zupanc, M., Dular, M., Kosjek, T., Heath, E., Kompare, B., et al. (2013). Rotation Generator of Hydrodynamic Cavitation for Water Treatment. *Separat. Purif. Techn.* 118 (Complete), 415–423. doi:10.1016/j.seppur.2013.07.029

Prasad, S. V., Thomas, S. A., and Vinayak, R. V. (2018). Modelling of Vortex Based Hydrodynamic Cavitation Reactors. *Chem. Eng. J.* 377, 119639. doi:10.1016/j.cej.2018.08.025

Qian, X., Wang, Y., Xu, Y., Ma, L., Xue, N., Jiang, Z., et al. (2020). Active Targeting Nano-Scale Bubbles Enhanced Ultrasound Cavitation Chemotherapy in Y1 Receptor-Overexpressed Breast Cancer. *J. Mater. Chem. B* 8 (31), 6837–6844. doi:10.1039/d0tb00556h

Rae, J., Ashokkumar, M., Eulaerts, O., von Sonntag, C., Reisse, J., and Grieser, F. (2005). Estimation of Ultrasound Induced Cavitation Bubble Temperatures in Aqueous Solutions. *Ultrason. Sonochem.* 12 (5), 325–329. doi:10.1016/j.ultsonch.2004.06.007

Šarc, A., Kosel, J., Stopar, D., Oder, M., and Dular, M. (2018). Removal of Bacteria *Legionella pneumophila*, Escherichia coli, and Bacillus Subtilis by (Super)cavitation. *Ultrason. Sonochem.* 42, 228–236. doi:10.1016/j.ultsonch.2017.11.004

Simpson, A., and Ranade, V. V. (2018). Modelling of Hydrodynamic Cavitation with Orifice: Influence of Different Orifice Designs. *Chem. Eng. Res. Des.* 136, 689–711. doi:10.1016/j.cherd.2018.06.014

Sun, W., and Lei, T. (2020). Cavitation-Vortex-Pressure Fluctuation Interaction in a Centrifugal Pump Using Bubble Rotation Modified Cavitation Model under Partial Load. *J. Fluids Eng.* 142, 051206. doi:10.1115/1.4045615

Sun, X., Jia, X., Liu, J., Wang, G., Zhao, S., Ji, L., et al. (2020b). Investigation on the Characteristics of an Advanced Rotational Hydrodynamic Cavitation Reactor for Water Treatment. *Separat. Purif. Techn.* 251, 117252. doi:10.1016/j.seppur.2020.117252

Sun, X., Kang, C. H., Park, J. J., Kim, H. S., Om, A. S., and Yoon, J. Y. (2018b). An Experimental Study on the thermal Performance of a Novel Hydrodynamic Cavitation Reactor. *Exp. Therm. Fluid Sci.* 99, 200–210. doi:10.1016/j.expthermflusci.2018.02.034

Sun, X., Liu, J., Ji, L., Wang, G., Zhao, S., Yoon, J. Y., et al. (2020a). A Review on Hydrodynamic Cavitation Disinfection: The Current State of Knowledge. *Sci. Total Environ.* 737, 139606. doi:10.1016/j.scitotenv.2020.139606

Sun, X., Park, J. J., Kim, H. S., Lee, S. H., Seong, S. J., Om, A. S., et al. (2018a). Experimental Investigation of the Thermal and Disinfection Performances of a Novel Hydrodynamic Cavitation Reactor. *Ultrason. Sonochem.* 49, 13–23. doi:10.1016/j.ultsonch.2018.02.039

Sun, X., Wang, Z., Xuan, X., Ji, L., Li, X., Tao, Y., et al. (2021b). Disinfection Characteristics of an Advanced Rotational Hydrodynamic Cavitation Reactor in Pilot Scale. *Ultrason. Sonochem.* 73 (3), 105543. doi:10.1016/j.ultsonch.2021.105543

Sun, X., Xuan, X., Song, Y., Jia, X., Ji, L., Zhao, S., et al. (2021a). Experimental and Numerical Studies on the Cavitation in an Advanced Rotational Hydrodynamic Cavitation Reactor for Water Treatment. *Ultrason. Sonochem.* 70, 105311. doi:10.1016/j.ultsonch.2020.105311

Thaiyasuit, P., Khiowthong, W., and Seehanam, W. (2021). Investigation on Continuous FAME Production Using Rotor Reactor with Bumpy Number Variation under Theoretical Methanol to Oil Molar Ratio Condition. *IOP Conf. Ser. Mater. Sci. Eng.* 1137 (1), 012007. (10pp). doi:10.1088/1757-899x/1137/1/012007

Wang, B., Su, H., and Zhang, B. (2021). Hydrodynamic Cavitation as a Promising Route for Wastewater Treatment - A Review. *Chem. Eng. J.* 412 (3-4), 128685. doi:10.1016/j.cej.2021.128685

Yasuda, K., and Ako, D. (2019). Effect of Venturi Tube Shape on Reaction Performance by Hydrodynamic Cavitation. *J. Chem. Eng. Jpn./JCEJ* 52 (3), 280–282. doi:10.1252/jcej.18we183

Zhao, J., Jiang, Z., Zhu, J., Zhang, J., and Li, Y. (2020). Investigation on Ultrasonic Cavitation Erosion Behaviors of Al and Al-5Ti Alloys in the Distilled Water. *Metals* 10 (12), 1631. doi:10.3390/met10121631

Zwart, P. J., Gerber, A. G., and Belamri, T. A. (2004). "A Two-phase Model for Predicting Cavitation Dynamics," in Proceedings of the 5th International Conference on Multiphase Flow (ICMF) (Yokohama, Japan.

Conflict of Interest: The authors declare that the research was conducted in the absence of any commercial or financial relationships that could be construed as a potential conflict of interest.

Publisher's Note: All claims expressed in this article are solely those of the authors and do not necessarily represent those of their affiliated organizations, or those of the publisher, the editors and the reviewers. Any product that may be evaluated in this article, or claim that may be made by its manufacturer, is not guaranteed or endorsed by the publisher.

frontiers | Frontiers in Energy Research

ORIGINAL RESEARCH
published: 12 May 2022
doi: 10.3389/fenrg.2022.885634

Startup Process Optimization of Hydropower Unit Based on Stress Measurement of Francis Turbine Runner

Ye Zhou[1]*, *Jianfeng Ma*[2], *Dengfeng Cao*[1] and *Lielong Wu*[2]

[1]Institute of Hydraulic Machinery, Department of Operation Support, China Institute of Water Resources and Hydropower Research, Beijing, China, [2]Institute of Mechanical and Electrical Product Reliability Engineering, Zhejiang Sci-Tech University, Hangzhou, China

The energy efficiency characteristics of the turbine, cavitation performance of the runner, and operation stability of the unit are the three major concerns of a hydropower field, the latter two factors leading to the units' cavitation and stability problems under some operation conditions and fatigue failure of the runner blades, which are the main causes of structural and mechanical failure for the hydropower units. In this article, three conventional unit startup processes are introduced, and combined with the optimal impulse control strategy, an optimized unit startup method is proposed. As the optimal guide vane opening adjustment setting value is obtained by solving the planned startup control strategy, 3D modeling and CFD simulation are carried out, then the equivalent stress characteristics are obtained by finite element calculation when the unit is running from startup to no load at a rated speed on three different startup modes. At last, the dynamic stress tests of the runner blade are performed at the hydropower station by using wireless acquisition and transmission technology, and the peak value and characteristics of the dynamic and static stresses of the blade under different startup processes are obtained. In this, the validity of the model analysis is proved by the comparison between the simulation calculation and the measured results, and the effectiveness of the startup control strategy is proved by combining the runner blade dynamic stress simulation, calculation, and the field dynamic stress test results. The optimization method of the startup process proposed in the article can alleviate the abnormal vibration of the unit and provide a basis for long-term stable operation of the hydropower unit.

Keywords: Francis turbine, stress measurement, startup process, hydropower unit, optimal impulse control

OPEN ACCESS

Edited by:
Ling Zhou,
Jiangsu University, China

Reviewed by:
Yongxue Zhang,
China University of Petroleum, China
Liu Demin,
Dongfang Electric Machinery Co., Ltd., China
Weiguo Zhao,
Lanzhou University of Technology, China

***Correspondence:**
Ye Zhou
zhouye@foxmail.com

Specialty section:
This article was submitted to Process and Energy Systems Engineering, a section of the journal Frontiers in Energy Research

Received: *28 February 2022*
Accepted: *24 March 2022*
Published: *12 May 2022*

Citation:
Zhou Y, Ma J, Cao D and Wu L (2022) Startup Process Optimization of Hydropower Unit Based on Stress Measurement of Francis Turbine Runner. Front. Energy Res. 10:885634. doi: 10.3389/fenrg.2022.885634

INTRODUCTION

With the development of the design, manufacture, and installation technology of hydropower units, the capacity and size of the turbine are getting larger and larger, and the development and application of conventional turbines, especially the reaction turbines, are becoming more and more extensive. Due to the increase in size and capacity of the unit, the specific speed of the turbine is also increased accordingly, the rigidity of the runner structure is relatively reduced, and the turbine blades of some units develop cracks and breaks; furthermore, some hydropower units built, both domestic and

abroad, have problems such as runner cracks. So, in addition to the efficiency and cavitation characteristics, the stability of the hydropower unit is gaining more and more attention.

Currently, more and more scholars, both domestic and abroad, conduct finite element analysis on turbine models and prototypes, predict the operation characteristics of turbines, and carry out optimal design research to achieve better design results. In this article, three conventional unit startup processes are introduced, and combined with the optimal impulse control strategy, an optimized unit startup method is proposed. As the optimal guide vane opening adjustment setting value is being obtained by solving the planned startup control strategy, the 3D modeling and CFD simulation are carried out, then the equivalent stress characteristics are obtained by finite element calculation, when the unit is running from startup to no load at a rated speed on three different startup modes. At last, the dynamic stress tests of the runner blade are performed at the hydropower station by using the wireless acquisition and transmission technology, and the peak value and characteristics of the dynamic and static stress of the blade under different startup processes are obtained. In this, the validity of the model analysis is proved with the comparison between the simulation calculation and measured results, and the effectiveness of the startup control strategy is proved by combining the runner blade dynamic stress simulation, calculation, and the field dynamic stress test results. The optimization method of the startup process proposed in the article can alleviate the abnormal vibration of the unit and provide a basis for the long-term stable operation of the hydropower unit.

STARTUP PROCESS OF HYDROPOWER UNIT

Common Startup Processes

The common startup control methods of the hydropower units include open-loop control, closed-loop tracking control, and open–closed loop–combined control (Lei et al., 2021).

An open-loop control mainly means that after the governor receives the power-on command, the guide vane will be opened to the preset opening at the maximum opening speed, and the opening will remain unchanged. When the frequency rises to the preset value, the guide vane will be opened again. close to the predetermined no-load opening, such that the unit quickly rises to rated speed and stabilizes.

Closed-loop tracking control means that the governor is always in a closed-loop adjustment state during the startup process, tracking the frequency given curve to 50 Hz.

Open and closed loop joint control means that when the governor receives the start command, it is set in the opening control mode first, the given value of the opening is set as the start opening, the frequency is set to a certain setting value less than 50 Hz, and then the opening is quickly increased to the start opening. When the frequency is increased to the set value, the PID adjustment is automatically activated, and the set frequency value is automatically increased to 50 Hz (Chen et al., 2019; Hou et al., 2019).

The dynamic characteristics of the turbine are obviously nonlinear because the water diversion system has the water hammer effect and the inertia of the turbine unit is large. Therefore, it is difficult to use the typical linear feedback method to control effectively. The traditional PID control and the derived feedback control are usually simulated and calculated by the simple linearized approximate model of the system, and it is difficult to effectively control the real turbine control and operation system.

Therefore, in this article, the optimal guide vane opening adjustment setting value is obtained by solving the planned startup control strategy, and the effectiveness of the startup control strategy is proved by combining the runner blade dynamic stress simulation, calculation, and the field dynamic stress test results.

According to the requirements of the planned startup control strategy, the best control method is to make the guide vane opening act according to the time curve shown in **Figure 1**, that is, the operating speed of the guide vane is started, and after reaching a certain opening, it is closed to the no-load opening at the maximum allowable operating speed.

Startup Process Optimization

According to the characteristics of hydraulic flow energy, when the startup process ends, the water energy used by the turbine is exactly equal to the energy consumed by overcoming various resistances during the startup process and the kinetic energy required for increasing the rotor speed; this is the basic principle of the optimal impulse control strategy (Sun et al., 2018; Wang et al., 2019). The common change process of the guide vane opening for hydropower unit is shown in **Figure 1**.

In **Figure 1**, f is the percent of unit frequency against 50 Hz, y is the percent of guide vane opening, and the top point of the guide vane opening curve is the peak value $y_{\max}$. The value y_{no_load} corresponding to the last straight section of the guide vane opening curve is the stable opening of the unit at a given speed with no load. In order to determine the maximum guide vane opening $y_{\max}$ during startup and the stable opening y_{no_load} during the no-load running, the solution can be solved according to the principle of optimal energy balance.

The theoretical formula for turbine flow is:

$$q = y\sqrt{1+\zeta},$$

where q is the flow discharge of the turbine, y is the guide vane opening, and ζ is the water pressure change rate of the turbine, which can be calculated by measuring the pressure difference at the spiral case inlet and draft tube outlet, and then obtaining the change of turbine work head.

The input power N of turbine is:

$$N = y\sqrt{(1+\zeta)^3}.$$

Therefore, the sum of the power due to the water flow of the turbine can be obtained by integrating the power N. The kinetic energy stored by the rotor at the current speed is:

$$E = J\omega^2/2,$$

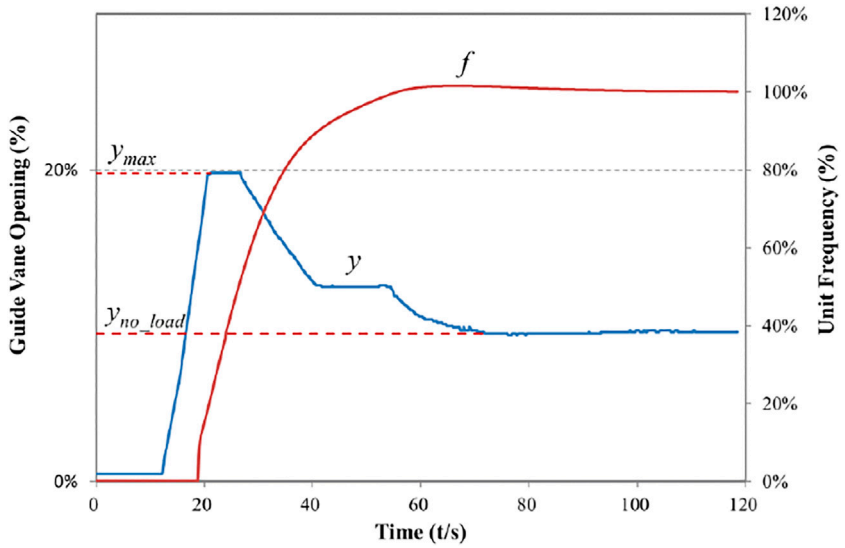

FIGURE 1 | The common change process of the guide vane opening for hydropower unit.

where J is inertia of the unit, and ω is the rotational speed.

According to the optimal impulse control strategy, the unit reaches the speed ω at time of t_d, and so we can get the power loss s each time before t_d.

$$s_i = \int_{i-1}^{i} N dt - J\left(\omega_i^2 - \omega_{i-1}^2\right) \Big/ 2,$$

where s_i is the power loss at time i, and ω_i is the speed at time i.

Then, we can calculate with the formula:

$$s = s_\omega(\omega)$$

When $\omega = \omega_n$—here ω_n is the rated speed—the guide vane opening y_{no_load} at no load can be obtained by calculations. Similarly, through the power loss formula, the relationship between t and ω after time t_d can be calculated, and the y_{max} value that meets the requirements is obtained by iterative calculations (Tan and Islam, 2004).

Therefore, we can use the effective impulse principle in the startup process to obtain the curve y of the guide vane opening and formulate the control strategy of the startup process according to the prediction model of the guide vane opening.

SIMULATION OF RUNNER BLADE DYNAMIC STRESS

Numerical Calculation Model

The three-dimensional incompressible unsteady Navier–Stokes equation is used for the time-averaged method, and the Reynolds average method is performed to obtain the control equation in the time-averaged form (Hong et al., 2015; Xing and Xu, 2015):

$$\frac{\partial \rho}{\partial t} + \nabla(\rho u) = 0.$$

The momentum equation is:

$$\frac{\partial u}{\partial t} + u \cdot \nabla u - f + \frac{\nabla p}{\rho} - \nu \nabla^2 u = 0,$$

where $\partial u/\partial t$ is the fluid acceleration; f is the body force per unit mass of fluid, usually $f = g$ (g is the gravity acceleration); $\nabla p/\rho$ is the resultant force of pressure p received on the surface of the fluid per unit mass; ρ is the fluid density; ∇ represents the divergence; ν is the viscosity coefficient; and u is the fluid velocity.

The turbulence model adopts the SST model, which has great advantages in predicting the turbulent scale of near-wall flow or flow with adverse pressure gradient. Therefore, the model is selected when solving the unsteady turbulent flows in the draft tube. The turbulent kinetic energy equation and turbulent dissipation rate equation of the SST model are, respectively (Kang et al., 2016; Tiwari et al., 2020):

$$\frac{\partial \rho k}{\partial t} + \frac{\partial \rho C_j k}{\partial x_j} = \frac{\partial}{\partial x_j}\left(\Gamma_k \frac{\partial k}{\partial x_j}\right) + G_k + Y_k,$$

$$\frac{\partial \rho \omega}{\partial t} + \frac{\partial \rho C_j \omega}{\partial x_j} = \frac{\partial}{\partial x_j}\left(\Gamma_\omega \frac{\partial \omega}{\partial x_j}\right) + G_\omega - Y_\omega + D_\omega.$$

The calculation uses the discrete method of the finite volume method. The finite volume method is also called the control volume method (Bai et al., 2012). Its basic principle is to divide the computational domain into tiny control volumes corresponding to the grid nodes, one to one. Each control volume does not repeat each other. The equations are integrated to obtain a set of discrete equations. In order to give the integral form of the control volume, assumptions are made about the convective flux at the nodes of the control volume grid, such that different forms of discrete equations can be derived.

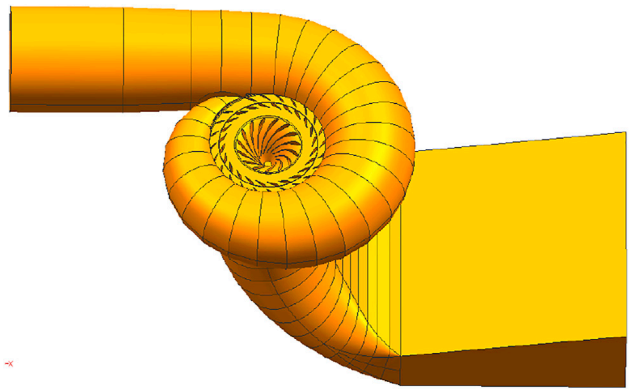

FIGURE 2 | The geometric model of the overall computational domain.

Computational Domain Model

As the geometry of each part of the turbine flow passage is relatively complex, to accurately simulate the flow channel shape of the real turbine during the modeling process, Siemens NX software is used to geometrically model the entire flow channel of the turbine. The entire calculation area includes spiral case, static vanes, guide vanes, runners, and draft tubes. The overall computational domain geometric model is shown in **Figure 2**. To accurately simulate the internal flow of the flow components of the turbine and minimize the error in the numerical calculation, high-precision hexahedral meshes are used to mesh the flow components.

The object of the numerical analysis is the model hydraulic turbine, and its overall geometric modeling is completed by the Siemens NX software platform. All the flow parts are divided into high-precision hexahedral meshes by the ANSYS ICEM-CFD software to make field analysis calculations. Through the analysis, the flow field calculation of the runner and other flow components is obtained as the load of the structure field calculation.

For the calculation of the flow field in the Francis turbine and the calculation of the structure field of the runner, the three-dimensional geometric models for the calculation of the flow field and the structure field are established, respectively. **Figure 3** shows the models for flow field calculation, structure field calculation, and the fluid–structure interaction surface.

The calculation object of the structure field is the Francis turbine runner, and the constraint condition is a fixed constraint given on the connecting surface of the upper crown of the runner and the main shaft flange. The load on the runner includes inertial force and surface force. The inertial force includes the force caused by the runner's gravity and rotation. The surface force is mainly the water pressure on the fluid–solid interface caused by the fluid flow, which is obtained from the results of the runner flow field calculation.

The total pressure at the inlet of the spiral case and its velocity direction are used as the inlet conditions, and the average static pressure at the draft tube outlet is used as the outlet conditions for the flow field calculation. Through the CFD calculation of the overall flow channel, the calculated inner flow field is more accurate, and a more accurate blade surface pressure load is provided for the subsequent structural field calculation.

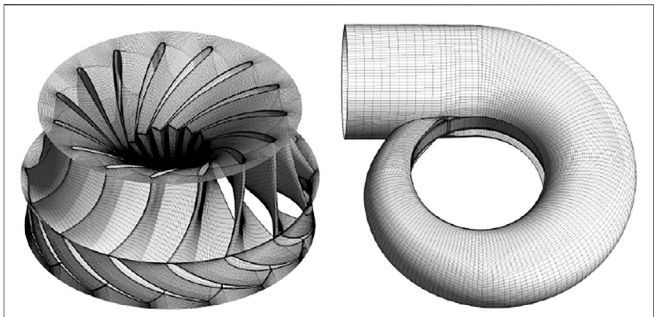

FIGURE 3 | The geometric models of Francis runner and spiral case.

MEASUREMENT OF RUNNER BLADE STRESS

To compare the force of the runner under different startup modes, the dynamic stress test of the runner blade was carried out, that is, the strain gauge was pasted on the runner blade, the data were collected and stored by wireless transmission, and the relationship between the static stress and the dynamic stress with the guide vane opening was analyzed. The layout of the strain gauge is shown in **Figure 4**.

The photos of the strain gauge fixing and protection are shown in **Figures 5** and **6**.

The cables are led from the large hollow shaft to the accessories of the top air supply valve, and the test instruments and equipment are fixed by bolts and welding to ensure that the equipment does not detach or is not thrown out when the unit rotates at high speed. All measurement signals are stored offline in the acquisition instrument and transmitted to the engineer's computer synchronously. The photos of data acquisition equipment are shown in **Figure 7**.

RESULT OF STRESS MEASUREMENT FOR DIFFERENT STARTUP PROCESSES

Conventional Control Methods

Two conventional control methods were carried out on-site, and the guide vane opening process and speed rise curve were recorded, that is, after the governor received the starting command, the guide vane was opened to the set opening at the fastest speed, then kept unchanged. When the frequency rises to the set value, the opening of the guide vane servomotor was adjusted to the set value of no load, then the servomotor control mode was turned to PID adjustment mode.

Here, we select the strain–stress point at BV3 shown in **Figure 4**, where the previous runner crack appeared as the characteristic parameter, and analyze the stress change at this location under different startup processes.

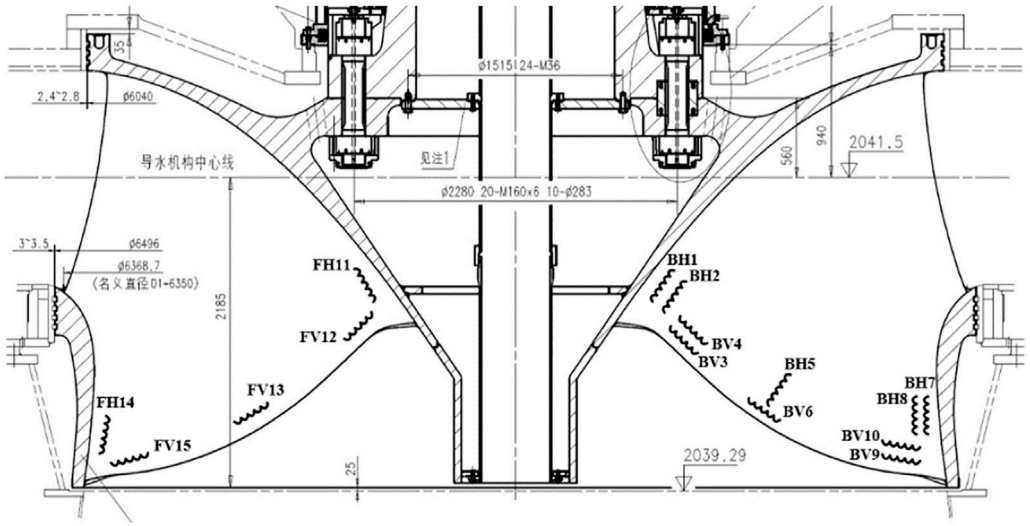

FIGURE 4 | The layout of the strain gauges for Francis turbine runner.

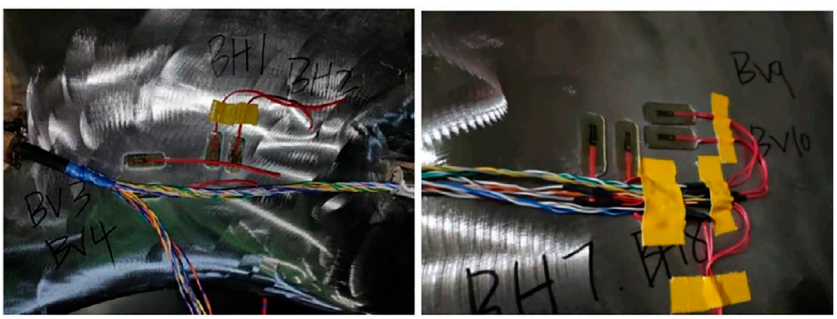

FIGURE 5 | The photos of fixing the strain gauges by special glue.

FIGURE 6 | The photos of protection of the strain gauges by metal protective coating.

The sampling rate of the stress signal is 1,200 Hz, and the static stress and dynamic stress are calculated by sliding for the period of 1 s. The average value of the static stress is calculated, and the peak-to-peak value of the dynamic stress is calculated.

For the first time, the single stage acceleration adjustment was adopted, the guide vane opening process and speed rise curve are shown in **Figures 8–10**.

As the guide vane is directly opened to the no-load opening degree in this adjustment method, the dynamic stress in the

FIGURE 7 | The photos of data acquisition equipment fixed by bolts and welding.

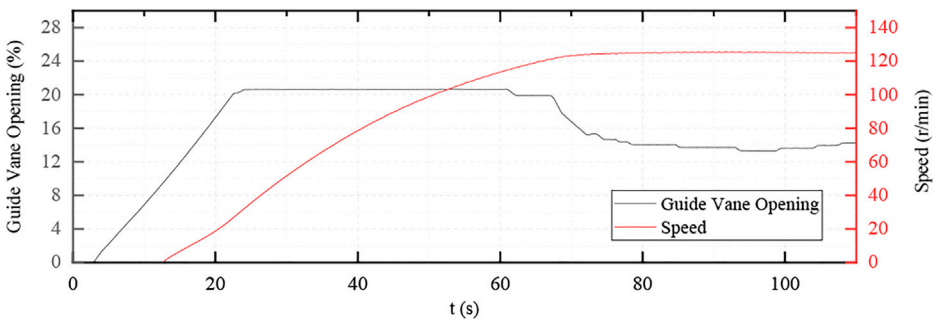

FIGURE 8 | The curve of the guide vane opening and the speed (single-stage acceleration).

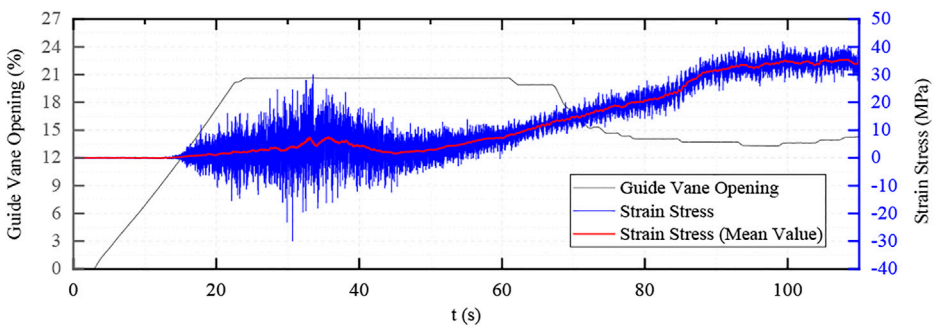

FIGURE 9 | The stress curve of the blade back in the direction of vertical water flow (single stage acceleration).

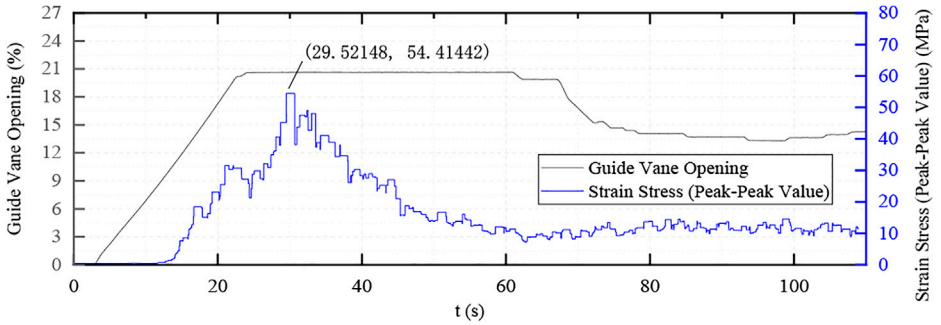

FIGURE 10 | The dynamic strain–stress curve with the guide vane opening (single-stage acceleration).

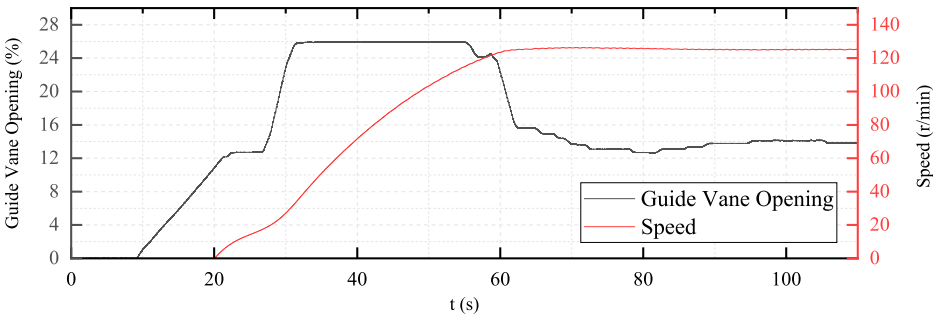

FIGURE 11 | The curve of the guide vane opening and the speed (two-stage acceleration).

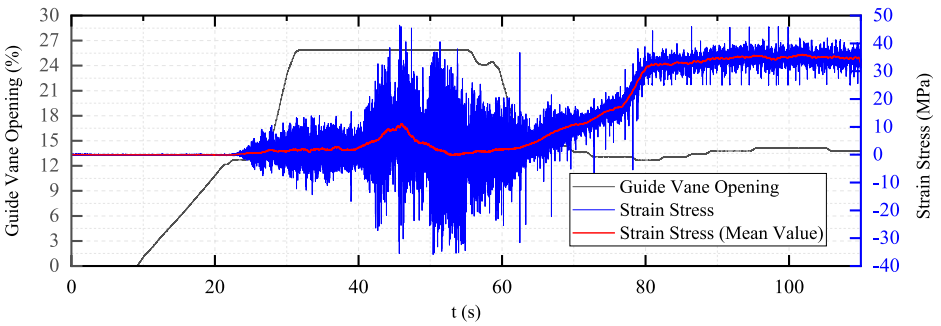

FIGURE 12 | The stress curve of the blade back in the direction of vertical water flow (two-stage acceleration).

process is relatively large and the maximum dynamic stress is about 55 MPa, but the duration is short, about 2–4 s.

Then the second conventional adjustment mode test is carried out, but the guide vane adjustment mode is two-stage acceleration, and the adjustment curves and typical dynamic stress curves are shown in **Figures 11**–**13**.

In the two-stage adjustment process, the accelerated opening time of the second stage of the guide vane is relatively long, and the static and dynamic stress of the vane increases significantly. The maximum dynamic stress was about 82 MPa, which exceeds the maximum dynamic stress of the first test.

Optimized Control Method

Combined with the effective impulse principle and two-stage startup strategy, an over adjustment mode is added to optimize the control mode. The calculation results in $y_{\max} = 21.5\%$, $y_{no\_load} = 13.5\%$, and the startup curve are as in **Figures 14**–**16**.

It can be seen from **Figure 16** that in the process of accelerating the speed of the unit from zero to 100 r/min, the blade is subjected to a large dynamic stress, and the maximum dynamic stress is about 44 MPa. Compared with the single-stage startup, the guide vanes are opened in two stages during the optimized startup process, and the maximum

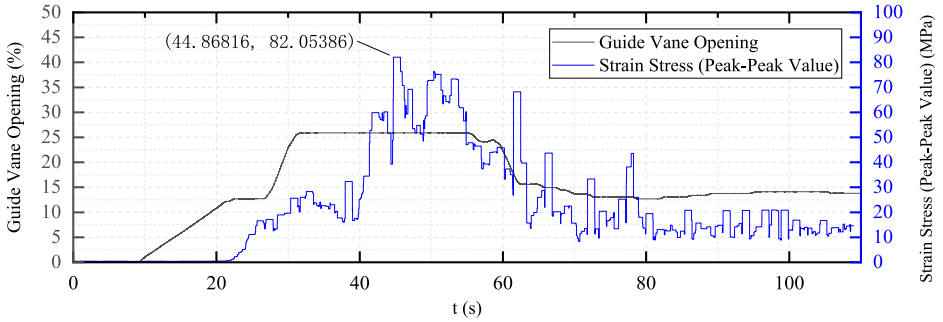

FIGURE 13 | The dynamic strain–stress curve with the guide vane opening (two-stage acceleration).

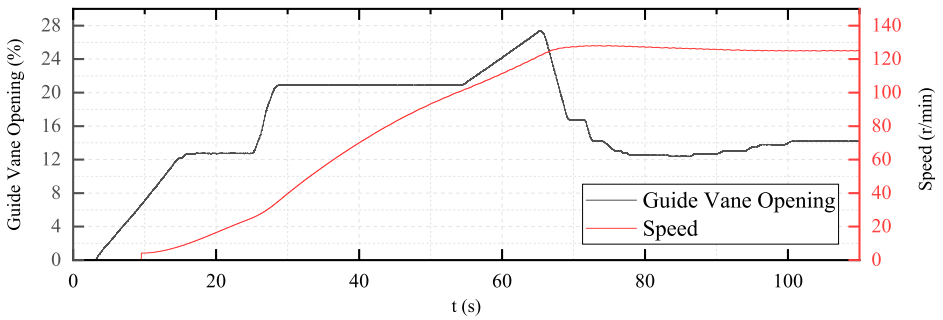

FIGURE 14 | The curve of the guide vane opening and the speed (optimized control mode).

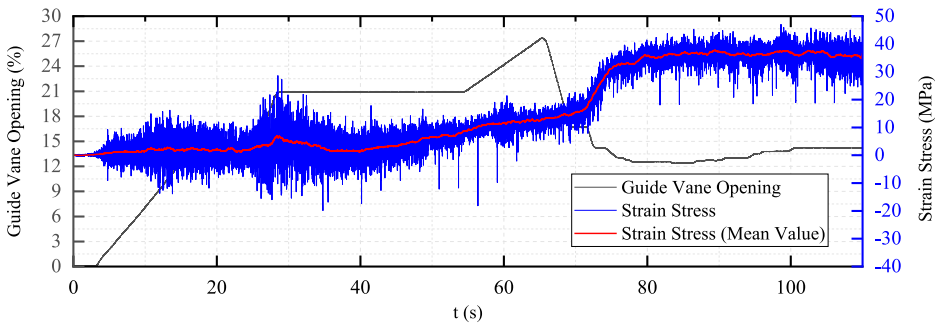

FIGURE 15 | The stress curve of the blade back in the direction of vertical water flow (optimized control mode).

dynamic stress is greatly reduced, but the duration of the dynamic stress is increased.

Data Analysis and Comparison

As the SST and k-ε turbulence model are used to simulate the internal flow of each flow-through component of the turbine, and the error is minimized in the numerical calculation, all flow-through components are divided into high-precision hexahedral meshes by the ANSYS ICEM-CFD software. The ANSYS runner structure finite element calculation model has 853,000 mesh elements and 1,233,000 nodes, as shown in **Figure 17**.

The blade surface pressure is changed with time, and the hydrodynamic pressure load is carried out according to the following steps:

1) According to the results of the unsteady flow analysis, the water pressure values at each node on the blade surface of the finite element model at each moment are taken out, and the water pressure load file at each moment is established after processing.
2) In the finite element preprocessing file, the water pressure load array is established, and the water pressure load array is

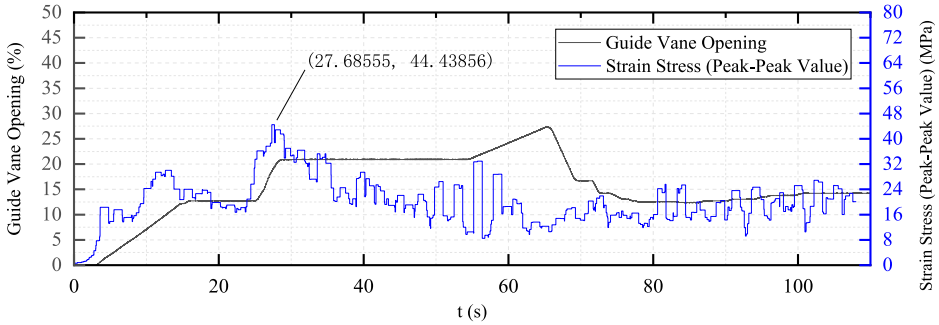

FIGURE 16 | The dynamic strain–stress curve with the guide vane opening (optimized control mode).

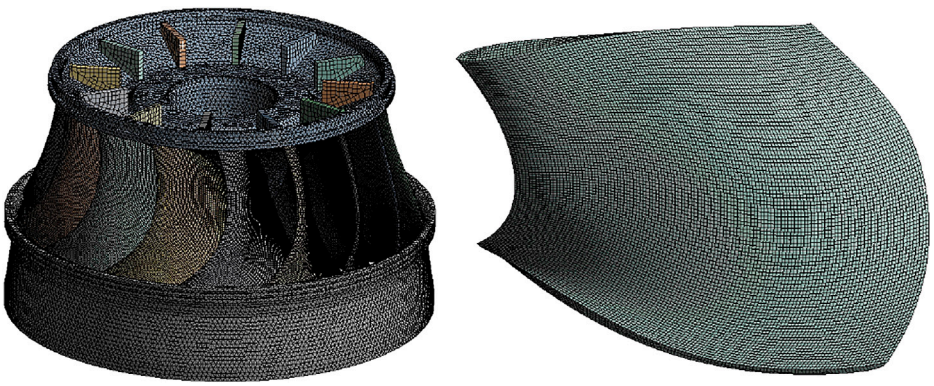

FIGURE 17 | The structure finite element calculation model of the runner and blade.

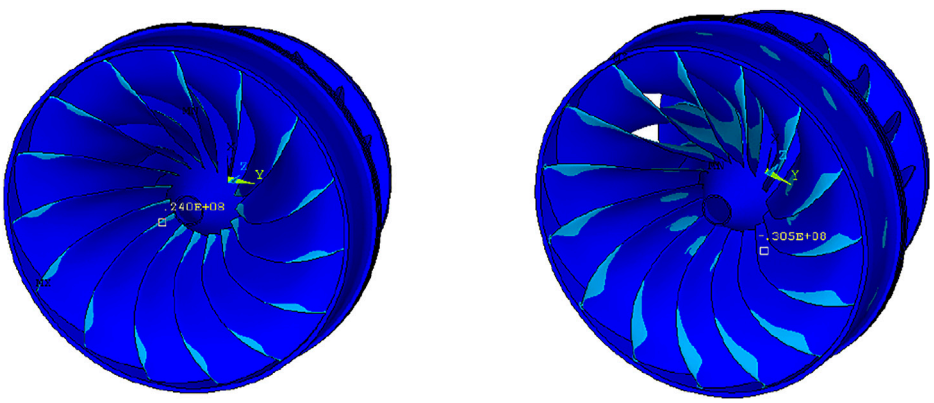

FIGURE 18 | The stress cloud diagram for the runner and blade (single-stage acceleration).

assigned values through the water pressure load file at each moment.

3) At different times, the blade pressure is loaded on the nodes of the computing network, and the time load step file is written.

According to the parameters of the three startup processes, the CFD simulation of the turbine fluid is carried out. When the unit reaches no load, the simulation results of the force cloud diagram of the blade are shown in **Figures 18–20**:

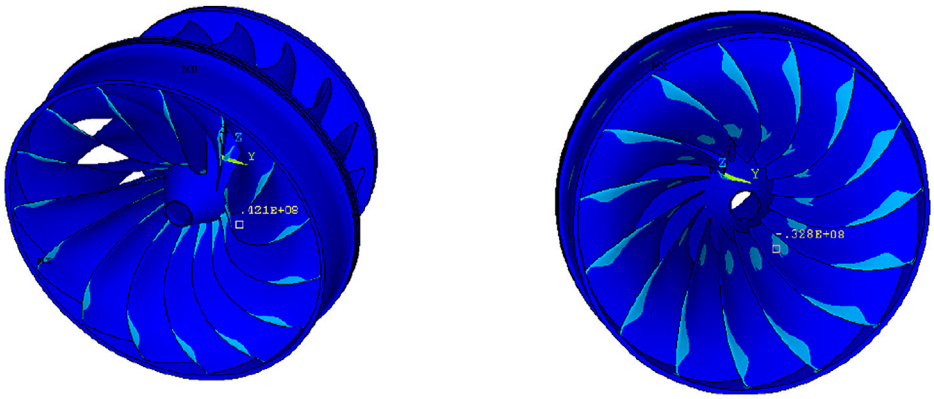

FIGURE 19 | The stress cloud diagram for the runner and blade (two-stage acceleration).

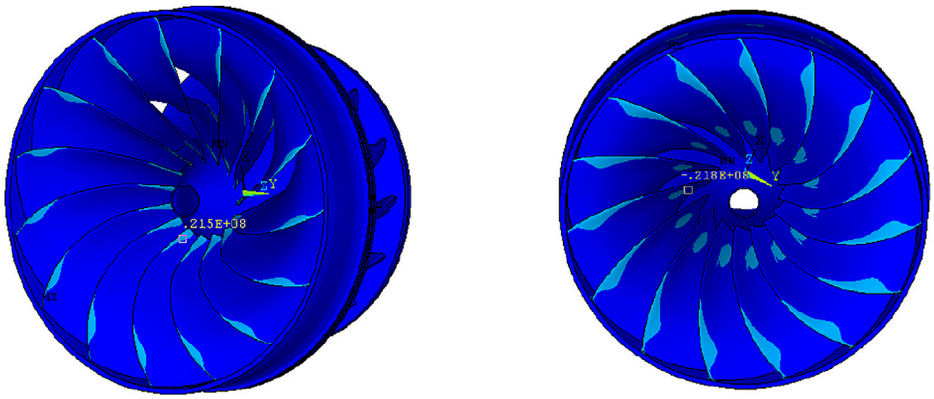

FIGURE 20 | The stress cloud diagram for the runner and blade (optimized control mode).

TABLE 1 | The governor parameter, max. dynamic stress test, and simulation results.

Unit startup mode	Opening of acceleration (%)	Opening limit at no load (%)	Max. dynamic stress (MPa)	Time of max. dynamic stress (s)	Simulate max. dynamic stress (MPa)
Single-stage acceleration	21.5	21.5	54.41	29.52	54.5
Two-stage acceleration	13.5	26.5	82.05	44.87	73.9
Optimized control mode	13.5	21.5	44.44	27.69	43.3

The governor parameter setting, maximum dynamic stress test, and simulation results are shown in **Table 1**:

CONCLUSION

1) The dynamic stress test of the rotating parts for the hydraulic machinery, especially the turbine runner, is currently difficult in field testing, and many key technologies have to be paid attention to. The metal repair agent currently used for the protective layer on the surface of the strain gauge may affect the stress measurement, and further verification and analysis are required. The protective steel pipe of the strain gauge transmission cable is welded on the surface of the runner cone, and then the wire is combined with a steel rope from the large hollow shaft to the top, which may also have a certain impact on the flow state of the runner outlet. However, these two methods ensure that the strain gauge can work effectively during the long-term startup, shutdown, and load changing processes of the unit and that it will not peel off or fail to work. Most runner dynamic

stress tests in the past failed due to the loss of strain gauge signal or sensor detachment in a short period of time (Huang et al., 2014; Unterluggauer et al., 2019).

2) From the test and simulation results, it can be seen that when the optimal pulse control strategy is adopted, the best parameters of the unit adjustment process can be obtained, such as the opening acceleration and the no-load opening limit and other data. The maximum dynamic stress on the runner blades when the unit starts up on the optimized control mode is only 81.6% the maximum dynamic stress on the single-stage control mode and 54.2% of the maximum dynamic stress on the two-stage acceleration control mode—almost only about half of it. Therefore, it can be verified that the optimal pulse control strategy can achieve a very good optimization effect.
3) Through the CFD simulation and calculation, with the guide vane opening, flow rate, and pressure data at the moment of maximum dynamic stress under the condition of no load on the runner, it can be seen that the difference between the simulation results and the actual measurement results under the three adjustment processes of the runner blade is 54.41, 82.05, and 44.44 MPa and proves that the CFD calculation can play a guiding and correcting effect in the common test of different startup modes of the unit.
4) The current dynamic stress test only analyzes the whole process data from the startup to 100% rated speed and then to the no-load of the unit. In fact, the whole dynamic stress test covers the load changing process, startup, and shutdown process of the unit, and the displacement, vibration, and pressure pulsation data of the unit's operation are measured synchronously. If further analysis can be carried out under these operating conditions, it can provide further guidance for the optimization and zoning of the operating load of the unit.

DATA AVAILABILITY STATEMENT

The original contributions presented in the study are included in the article/Supplementary Material, and further inquiries can be directed to the corresponding author.

AUTHOR CONTRIBUTIONS

YZ, JM, and DC contributed to the conception and design of the study. DC organized the database. YZ and JM performed the statistical analysis. YZ wrote the first draft of the manuscript. LW performed the infinite element calculation. All authors contributed to manuscript revision, and read and approved the submitted version.

REFERENCES

Bai, B., Zhang, L., Guo, T., and Liu, C. (2012). Analysis of Dynamic Characteristics of the Main Shaft System in a Hydro-Turbine Based on ANSYS. *Proced. Eng.* 31, 654–658. doi:10.1016/j.proeng.2012.01.1081

Chen, S., Li, G., Wang, D., Wang, X., Zhang, J., and Yu, X. (2019). Impact of Tail Water Fluctuation on Turbine Start-Up and Optimized Regulation. *Energies* 12 (15), 2883. doi:10.3390/en12152883

Hong, H., Yong-Zhong, Z., Hui-Yan, W., Shun-Bing, O., Zhi-Zhong, Z., and Xiao-Bing, L. (2015). Numerical Analysis of Solid-liquidtwo-phase Turbulent Flow in Francis Turbine Runner with Splitter Bladesin sandy Water. *Adv. Mech. Eng.* 7 (3), 168781401557382. doi:10.1177/1687814015573821

Hou, J., Li, C., Guo, W., and Fu, W. (2019). Optimal Successive Start-Up Strategy of Two Hydraulic Coupling Pumped Storage Units Based on Multi-Objective Control. *Int. J. Electr. Power Energ. Syst.* 111, 398–410. doi:10.1016/j.ijepes.2019.04.033

Huang, X., Oram, C., and Sick, M. (2014). Static and Dynamic Stress Analyses of the Prototype High Head Francis Runner Based on Site Measurement. *IOP Conf. Ser. Earth Environ. Sci.* 22 (3), 032052. doi:10.1088/1755-1315/22/3/032052

Kang, M.-W., Park, N., and Suh, S.-H. (2016). Numerical Study on Sediment Erosion of Francis Turbine with Different Operating Conditions and Sediment Inflow Rates. *Proced. Eng.* 157, 457–464. doi:10.1016/j.proeng.2016.08.389

Lei, L., Li, F., Kheav, K., Jiang, W., Luo, X., Patelli, E., et al. (2021). A Start-Up Optimization Strategy of a Hydroelectric Generating System: From a Symmetrical Structure to Asymmetric Structure on Diversion Pipes. *Renew. Energ.* 180, 1148–1165. doi:10.1016/j.renene.2021.09.010

Sun, Y., Cao, L., and Zhou, H. (2018). "Research on Closed-Loop Start-Up Process of Hydraulic Turbine Based on Adaptive Variable Parameters of Water Head" in IOP Conference Series Materials Science and Engineering (IOP Publishing), 452, 1–6. doi:10.1088/1757-899x/452/4/042007

Tan, K., and Islam, S. (2004). Optimum Control Strategies in Energy Conversion of PMSG Wind Turbine System without Mechanical Sensors. *IEEE Trans. Energ. Convers.* 19 (2), 392–399. doi:10.1109/tec.2004.827038

Tiwari, G., Kumar, J., Prasad, V., and Patel, V. K. (2020). Utility of CFD in the Design and Performance Analysis of Hydraulic Turbines - A Review. *Energ. Rep.* 6, 2410–2429. doi:10.1016/j.egyr.2020.09.004

Unterluggauer, J., Doujak, E., and Bauer, C. (2019). Fatigue Analysis of a Prototype Francis Turbine Based on Strain Gauge Measurements. *Wasser Wirt Schaft* 109 (1), 66–71. doi:10.1007/s35147-019-0238-9

Wang, X., Zhang, J., Yu, X., Lv, J., and Zhang, X. (2019). Multi-objective Intelligent Start-Up Strategy for Small Hydropower Plants Based on Adaptive Variable Parameters of Water Head. *J. Renew. Sustainable Energ.* 11 (1), 014703. doi:10.1063/1.5043368

Xing, X. Y., and Xu, Y. J. (2015). Numerical and Experimental Research on Solid-Liquid Two-phase Flow Pattern in the PID. *Adv. Pet. Exploration Development.* 9 (2), 111–116. doi:10.3968/7104

Conflict of Interest: The authors declare that the research was conducted in the absence of any commercial or financial relationships that could be construed as a potential conflict of interest.

Publisher's Note: All claims expressed in this article are solely those of the authors and do not necessarily represent those of their affiliated organizations, or those of the publisher, the editors, and the reviewers. Any product that may be evaluated in this article, or claim that may be made by its manufacturer, is not guaranteed or endorsed by the publisher.

frontiers | Frontiers in Energy Research

METHODS
published: 01 July 2022
doi: 10.3389/fenrg.2022.811690

The Cavitation Characteristics of High Speed Centrifugal Pumps With Different Impeller Types

Wen-xiong Chao[1,2]*, *Bao-lu Shi*[3], *Hui Ruan*[1,2] and *Wei Dong*[4]

[1]Xi'an Aeronautical University, Shaanxi, China, [2]National Joint Engineering Research Center of Special Pump System Technology, Shaanxi, China, [3]Astronaut Center of China, Shaanxi, China, [4]Northwest A&F University, Shaanxi, China

Addressing the cavitation prevention requirements for a longer service life of the high-speed centrifugal pump in the temperature control system of aerospace, the effect of blade inlet width on cavitation performance is studied on the premise of consistency of impeller outlet diameter D_2, impeller outlet width b_2, volute inlet diameter D_3, pump interface and other structural parameters. Therefore, the corrected coefficient k_1 of blade inlet exclusion coefficient is introduced; four groups of centrifugal impellers with inlets of different geometric structures blades are put forward. To begin with, based on the D# pump performance test and Pumplinx simulation, the cavitation performance of high-speed pump with four different groups of impellers is studied under five working conditions of negative inlet pressure (P_j=(–20, –30, –40, –50, –60)kPa) on the premise that energy characteristics agree well with cavitation performance. According to the results, when P_j drops from –50 kPa to –60 kPa, the cavitation perform changes the most significantly. This indicates that the method of twisting the centrifugal impeller of the suspended forward-extended blade shows a significant effect in preventing cavitation performance under such working conditions of high speed and negative pressure. Its application in aerospace power systems can effectively reduce the impact of low pressure in the system and significantly improve the cavitation performance.

Keywords: impeller type, twisted overhung forward-extended, high-speed centrifugal pump, cavitation, ethylene glycol aqueous solution, numerical simulation CLC number: TH137, TH311 document code: A 0 preface

OPEN ACCESS

Edited by:
Ling Zhou,
Jiangsu University, China

Reviewed by:
Baoling Cui,
Zhejiang Sci-Tech University, China
Weiguo Zhao,
Lanzhou University of Technology, China

***Correspondence:**
Wen-xiong Chao
cwx3860605@126.com

Specialty section:
This article was submitted to Process and Energy Systems Engineering, a section of the journal Frontiers in Energy Research

Received: *09 November 2021*
Accepted: *07 March 2022*
Published: *01 July 2022*

Citation:
Chao W-x, Shi B-l, Ruan H and Dong W (2022) The Cavitation Characteristics of High Speed Centrifugal Pumps With Different Impeller Types. Front. Energy Res. 10:811690. doi: 10.3389/fenrg.2022.811690

PREFACE

Aerospace systems often require miniaturized high speed centrifugal pumps, which are prone to cavitation, a phenomenon degrading the hydraulic performance of pumps, especially at the blade inlet areas (Guan, 1995; Wang, 2004). Under continuous high-frequency and high-pressure blow by the cavitation bubble, the metal surfaces of flow passage components such as volute casing could sustain metal damage that shortens their service life. Therefore, cavitation prevention in high-speed pumps became an urgent requirement. However, conventional analysis of civil or industrial centrifugal pumps is mainly conducted with clean water or at low speed. No research have been conducted on the different types of impellers with overhung forward-extended blades at high speed in ethylene glycol aqueous solution. Research on the cavitation characteristics of high-speed centrifugal pumps in ethylene glycol aqueous solution is rare. Thus, this study focused on the cavitation under high-speed operation with multi-component non-Newtonian ethylene glycol aqueous solution to address the urgent need for analyzing the effect of impeller

TABLE 1 | Geometrical parameters of the pump.

Parameters	*Value*/Mm
Width of blade inlet	2(A); 3(B) 4(C); 6.4(D)
Width of blade outlet	3
Diameter of the impeller inlet	14
Short-blades initial diameter	24
Diameter of the impeller outlet	35
Axial width of volute	3.2
Discharge angle	29(A); 36(B) 29(C); 36(D)
Long-blade wrap angle	217(A); 93(B) 217(C); 93(D)
Short-blade wrap angle	64(A); 26(B) 26(C); 93(D)

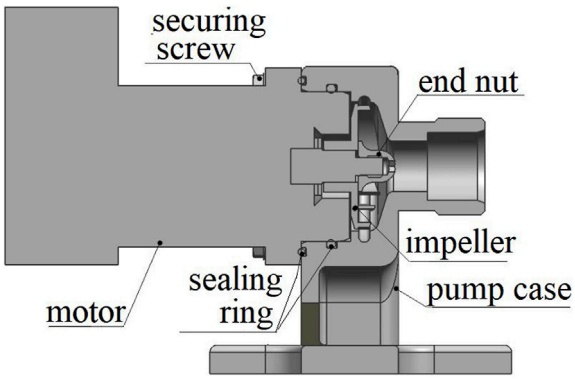

FIGURE 1 | Structure of centrifugal pump.

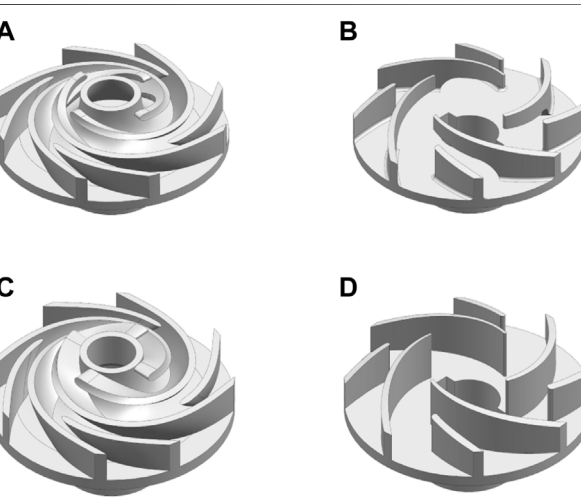

FIGURE 2 | Structure diagrams of four types of centrifugal impellers.

shapes on cavitation characteristics of high-speed centrifugal pumps for aerospace temperature control systems in special media.

Cavitation characteristics of centrifugal pumps have been extensively studied. Zhang et al., Feng, and Chao et al. (Feng, 2016; Zhang et al., 2017; Chao and Wang, 2019) investigated the influence of impeller type on cavitation (splitter blade and composite impeller). Zhao et al. and Wang et al. (Wang and Xie, 2016; Zhao and Zhao, 2017) studied the influence of blade adjustment (obstacle arrangement and slotting) on cavitation. Wei et al., Fu et al., and Chao et al. (Fu and Shen, 2016; Wei and Song, 2016; Chao and Wang, 2018) explored the centrifugal pump inlet backflow cavitation characteristics under different working conditions. Hu et al. (Hu and Song, 2017) studied the cavitation characteristics of micro-pump under low flow. Pei et al. (Pei and Yin, 2017) examined the influence of impeller geometric parameters on cavitation performance with the orthogonal experimental design based on Computational Fluid Dynamics (CFD).

Current cavitation prevention measures, such as changing the pump inlet structure and adopting a front inducer, are not applicable to aerospace systems due to their internal structure, shapes, and dimensions. Measures such as reducing the flow resistance of the pipeline and increasing the medium pressure in front of the pump are not applicable due to pipeline structure and pressure specification in the aerospace system. Measures such as using anti-cavitation materials are restricted by the anti-redundancy requirements.

Under the promise that existing cavitation and hydraulic tests conform well to the Pumplinx three-dimensional full flow channel vapor-liquid two-phase numerical simulation, we conducted numerical simulation and explored the internal cavitation characteristics of high-speed centrifugal pumps with four different types of impellers in ethylene glycol aqueous solution (Zindani et al., 2016; Yao and Luo, 2019; Han et al., 2021; Liao and Wuruikang, 2021; Tang et al., 2021) and obtained the influence of different geometric shapes of the blade on the external characteristics and cavitation flow characteristics of high-speed centrifugal pumps. This study could provide a theoretical basis for the better application of high-speed centrifugal pumps in aerospace systems.

DESIGN PARAMETERS AND MODEL

Design Parameters

Parameters of the research object are follows: the rated flow Q_v = 400 L/h, the boost value ΔP = 170 kPa, the rated speed n = 9,400 r/min, and the impellers are four Long and four short blade semi-open compound type. **Table 1** shows the geometrical parameters of the pump, and **Figures 1**, **2** presents the structure diagrams of four centrifugal impeller types.

Design Mode

The fluid passing through the impeller follows the velocity triangle. The axial plane component velocity v_m is the component of the fluid flowing out of the impeller along the axis and is related to the fluid flow passing through the impeller. With the same fluid flow, a larger flow area means smaller velocity and minimal energy loss.

With consistent outlet diameters and outlet widths of volute and impeller, we designed four groups of impellers, namely, twisted overhung forward-extended backswept composite

TABLE 2 | Verification of grid independence.

The Number of Grids/Ten Thousand	≈150	≈204	≈230	≈260	≈290	≈320
Pressure gain ΔP/kPa	173.59	173.37	173.32	173.21	173.21	172.31

impeller (A), cylindrical overhung forward-extended backswept composite impeller (B), twisted backswept composite impeller (C) and cylindrical backswept composite impeller (D), respectively, using four long blades and four short blades, as shown in **Figure 2**.

$$\begin{cases} V = \dfrac{Q}{\eta_v F_1 k_1} \\ k_1 = 1 - \dfrac{ZS_{u1}}{D_1 \pi}\delta_b \\ k = 1 - \dfrac{ZS_{u1}}{D_1 \pi} \\ \delta_b = \dfrac{b'}{b} \end{cases} \tag{1}$$

When designing the twisted overhung forward-extended backswept composite impeller (A) with four short blades and four long blades, the corrected blade excretion coefficient k_1 was introduced (**Eq. (1)**). The conventional calculation method for blade inlet velocity of centrifugal pump only considers the blade thickness and ignores the blade width b. This paper proposed to consider both the thickness (k in **Eq. 1**) and width of the blade when calculating the blade excretion coefficient.

The revise corrected coefficient k_1 takes into account the thickness and width of the blade,So K_1 is smaller than K.Reduce the blade inlet working face, increase the opening area and flow capacity of the inlet between blades, According to the Bernoulli Equation,The flow rate decreases, the pressure increases,So as to improve the anti cavitation performance.

Formula:F_1 is the discharge section area of the calculation point, k is the blade excretion coefficient at the calculation point, k_1 is the corrected blade excretion coefficient at the calculation point, D_1 is the diameter of the diameter at the calculation point, S_{u1} is the circumferential thickness of the blade at the calculation point, ?$_v$ is the volumetric efficiency, b is the width of the blade at the calculation point, b' is the width of the forward-extended blade at the calculation point, δ_b is the width coefficient, Z is the number of blades, and V is the inlet velocity at the calculation point.

CALCULATION METHOD AND MESHING

Governing Equation

The motion of the ethylene glycol aqueous solution in the high-speed centrifugal pump is an unsteady three-dimensional complex turbulent flow with the following Reynolds time-averaged N-S equations:

$$\begin{cases} \nabla \bullet u = 0 \\ \rho \dfrac{du}{dt} = \rho F - \nabla P + \mu \nabla^2 u \end{cases} \tag{2}$$

Formula: ∇ is the vector operator in the Cartesian coordinate system, u is the velocity vector of the fluid; P is the fluid pressure; F is the force vector per unit mass; ρ, μ are the density and molecular viscosity of the fluid, respectively.

Cavitation Phase Transition Model

Pumplinx numerical simulation software operates with the Singhal full cavitation model "Cavitation" based on the idea of the two-phase flow model. The "Cavitation" model solves the dynamic process of the phase transition of the cavitation bubble with the bubble dynamics Rayleigh-plesset equation and introduces the concept of mixing density, which integrates the non-condensable gas, evaporation condensation processes and the compressibility of liquids (Wen et al., 2018; Ma and Pan, 2020; Bai and Ma, 2021). This model has also been tested and verified by a large number of engineering projects.

The Singhal full cavitation model and the N-S equation were combined, and the RNG k-ε turbulence model was adopted to solve the equation. By combining the Singhal model with the continuity equation, the relationship between the changing rates of density and vapor phase volume fraction was obtained as follows:

$$\frac{D\rho_m}{Dt} = -\left(\rho_l - \rho_v\right)\frac{D\alpha_v}{Dt} \tag{3}$$

where vapor volume fraction α_v is related to cavitation bubble number density and cavitation bubble diameter R_B:

$$\alpha_v = n\left(\frac{4}{3}\pi R_B^3\right) \tag{4}$$

Singhal model is based on the Rayleigh-Plesset bubble dynamics equation:

$$\frac{Pv - P\infty}{\rho_l} = R_B\frac{d^2R_B}{dt^2} + \frac{3}{2}\left(\frac{dR_B}{dt}\right)^2 + 4\frac{v}{R}\frac{dR_B}{dt} + 2\frac{\sigma}{\rho R_B} \tag{5}$$

The expression for the phase transition rate is obtained by neglecting the viscosity and surface tension effects and combining the continuity equation of each phase:

$$R = \frac{3\alpha_v}{R_B}\frac{\rho_v\rho_l}{\rho_m}\left(\frac{2}{3}\frac{p_B - p}{\rho_l}\right)^{1/2} \tag{6}$$

Where: P_B is the saturation vapor pressure, σ is the surface tension coefficient.

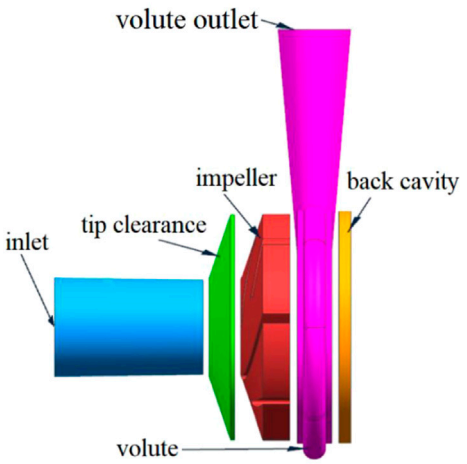

FIGURE 3 | Computational domain of Centrifugal Pump.

In the simulation of internal flow cavitation of centrifugal pump, the phase change rate is related to vapor phase density, liquid density and mixture density. The Singhal model takes into account the effects of turbulence and non-condensable gas. The Singhal vapor phase mass fraction transport equation is as follows:

$$R = \frac{3\alpha_v}{R_B}\frac{\rho_v\rho_l}{\rho_m}\left(\frac{2}{3}\frac{p_B - p}{\rho_l}\right)^{1/2} \tag{7}$$

Where: ρ_V are vapor phase density and volume fraction and $\overline{v_V}$ is the average vapor phase velocity; *Re* and *Rc* are the phase change rates of vaporization and condensation, respectively, and their expressions are:

$$\begin{cases} \mathrm{Re} = 3\dfrac{\rho_V\rho_1}{\rho_m}.\dfrac{\alpha_v(1-\varphi_V)}{R_b}\sqrt{\dfrac{2}{3}.\dfrac{p_V - p}{\rho_1}}; if\ p < P_V \\ \mathrm{Re} = 3\dfrac{\rho_V\rho_1}{\rho_m}.\dfrac{\alpha_v(1-\varphi_V)}{R_b}\sqrt{\dfrac{2}{3}.\dfrac{p - p_V}{\rho_1}}; if\ p > P_V \end{cases} \tag{8}$$

$$R_b = \{3\alpha_v/[4\pi n(1-\alpha_v)]\}^{1/3}$$

Calculation Method

The flow in the centrifugal pump is mainly three-dimensional viscous and incompressible unsteady turbulent flow. Reynolds time averaged N-S equations, RNG K-andepsi; two-side turbulence model and SIMPLE algorithm are selected, Singhal full Cavitation model. The first phase is the ethylene glycol aqueous solution, and the second phase is the bubble. The saturated vapor pressure of ethylene glycol aqueous solution is 1.41 kPa.

During the calculation, the speed of centrifugal pump impeller n = 9,400 r/min and volute outlet volume flow rate Q_v = 400 L/h(0.000111 m^3/s)and inlet pressure (P_j=(−20, −30, −40, −50, −60)kPa). During the numerical calculation, the NPSH of the pump is changed by gradually decreasing the inlet pressure from 0 Pa to control the cavitation degree in the pump.

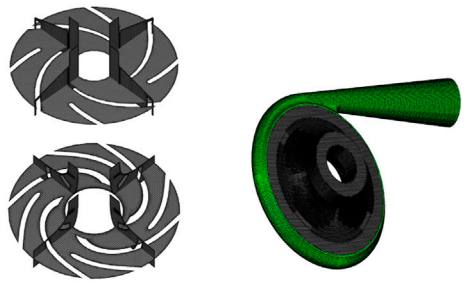

FIGURE 4 | Computation grid of the centrifugal pump.

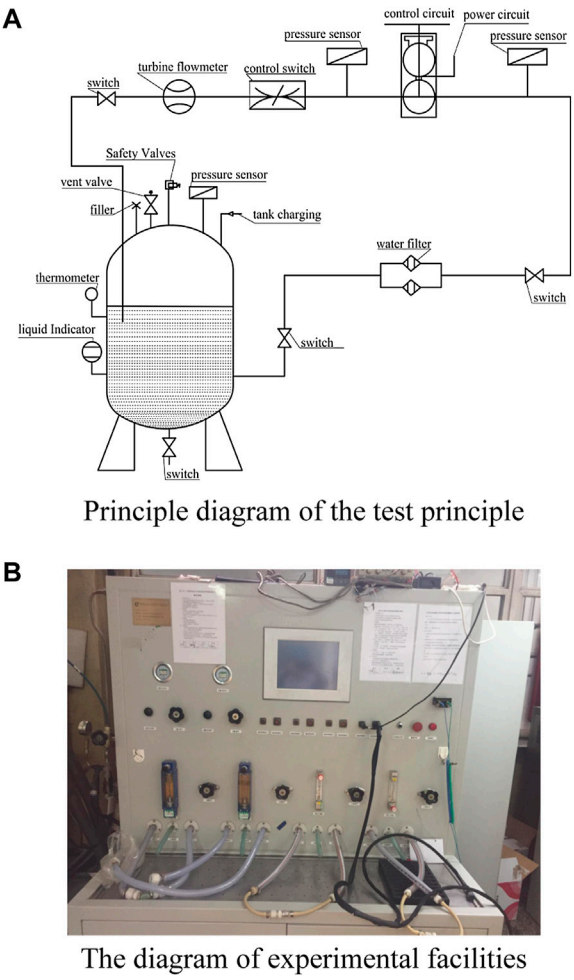

FIGURE 5 | The centrifugal pump experimental facilities.

Meshing

The quality of the fluid domain grid is decisive for the accuracy of the numerical simulation results. PumpLinx

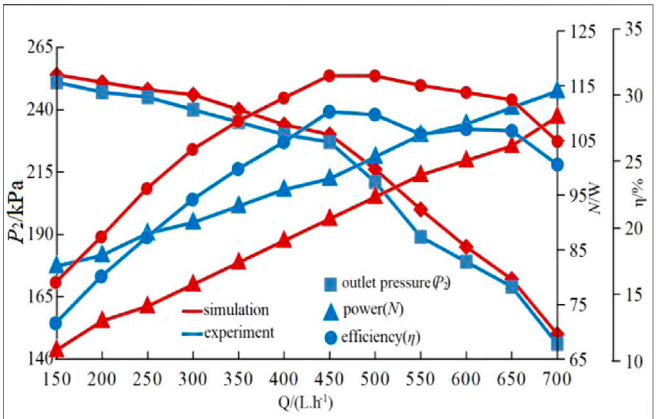

FIGURE 6 | Performance curves under different working conditions.

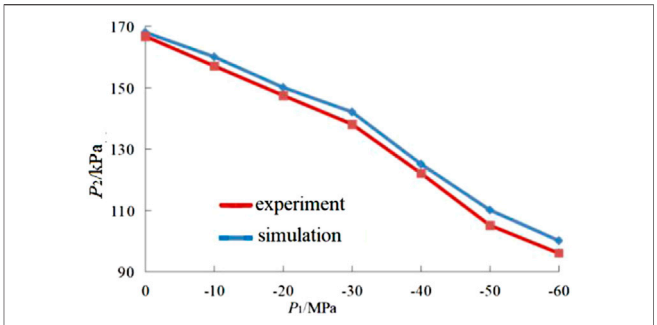

FIGURE 7 | Cavitation characteristics curves under different conditions.

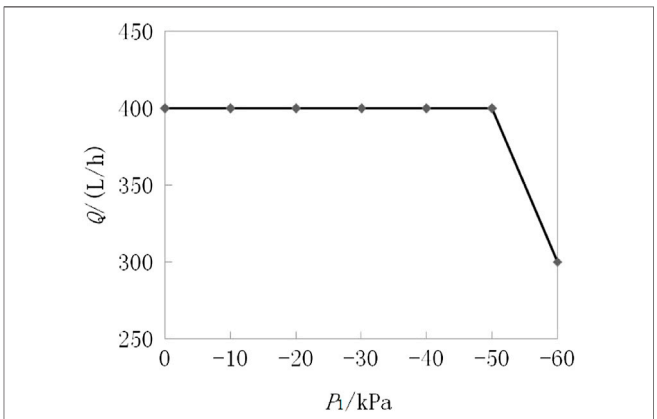

FIGURE 8 | The change of outlet flow rate with inlet negative pressure.

uses the finite volume method for CFD simulation solution, that is, the unstructured grid. PumpLinx grid generator uses a proprietary CAB geometric equirectangular height adaptive binary tree Cartesian coordinate algorithm and a more regular Cartesian hexahedral mesh, which can generate body-fitted grid near wall surfaces. The CAB algorithm can automatically adjust the grid size to fit the geometric surfaces and geometric boundary lines by continuously splitting the grid. Adaptive algorithm was also incorporated when generating grids for automatic encrypted resolution of the geometry of complex details. At the same accuracy level, the proprietary grid generation algorithm has a smaller grid number than the tetrahedral mesh.

Figure 3 shows the three-dimensional diagram of the flow channel of the flow passage component, and **Figure 4** shows the grid diagram of the impeller, where the computational domain consists of the impeller, the volute, and the tip clearance layer of the impeller. Since this study focuses on the cavitation characteristics of high-speed centrifugal pumps, the grid topology, number of grids, and the grid aspect ratio are controlled to ensure a relatively smaller size difference between adjacent grid nodes and more accurate numerical simulation results. Following the grid independence verification, the total number of grids in the computational domain is finally determined to be approximately 2.6 million considering the computer capability and efficiency. **Table 2** verification of grid independence.

VERIFICATION OF HYDRAULIC CHARACTERISTICS TEST

In this paper, the hydraulic performance characteristics of a semi-open composite impeller low-specific speed centrifugal pump used for cryogenic circulation in a certain space station with a shrinkage coefficient of one were tested on the AECC Xi'an Engine Control Co. Ltd. open test bench, of which glass rotameter type: LZB-20D, 60–600 L/h, class 2.5 level, sensor type: MPM 480, 0–0.6 MPa, class 0.25 level.as shown in **Figure 5**. The working medium of the test was low-temperature glycol aqueous solution.

The cavitation test was carried out on a hydraulic test bench with a four Long and four short blade composite centrifugal pump according to the test standard GB/T3216-2005. The ethylene glycol aqueous solution density ρ = 1,030 kg/m^3, the temperature t = 7.6°C, and the flow rate Q_V = 400 L/h. The initial inlet pressure P_j = 0 kPa. The inlet pressure of the pump was gradually reduced by adjusting the inlet valve until the decreased value of inlet and outlet pressure difference was 3% of the rated inlet and outlet pressure difference. At this time, the critical cavitation margin was reached. The cavitation test results were compared with the numerical simulation results to verify the accuracy of the numerical simulation. The test setup is shown in **Figure 5**.

Figure 6 shows the error between the experimental performance value and the performance parameter predicted by the numerical simulation of the cylindrical backswept compound impeller (D) at the design operation point under the non-cavitation condition. It can be seen that the errors between the head value and the test value are all below 5%, indicating that the numerical calculation simulation can simulate the internal flow field of the centrifugal pump at the design operation point and the numerical simulation results in this paper are accurate. Although the power error did not exceed 10%, the error is still large because the mechanical friction loss of various

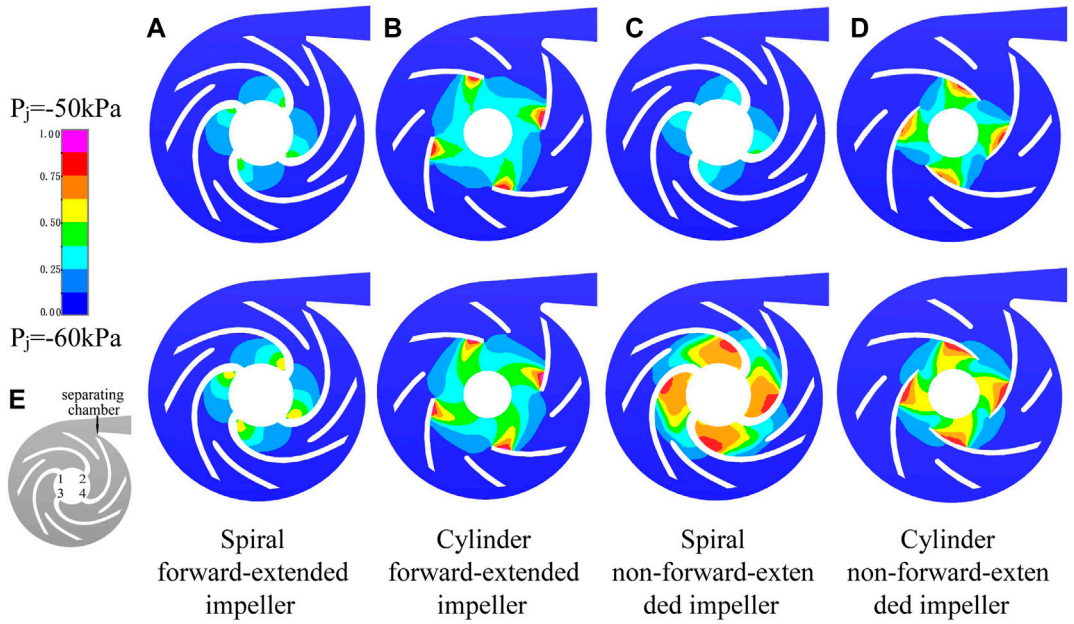

FIGURE 9 | The cavitation bubble volume distribution diagrams of the midsections of the pumps.

bearings and friction pairs in the operation of the centrifugal pump is not considered in the numerical simulation process.

Figure 7 shows the error between the experimental performance value and the performance parameter predicted by the numerical simulation of the cylindrical backswept compound impeller (D) under the cavitation condition. It can be seen that the errors between the head value and the test value are all less than 5%, indicating that the numerical calculation simulation can simulate the internal flow field of the centrifugal pump at the design operation point and numerical simulation results in this paper are accurate. When the inlet negative pressure P_j = −50 kPa, the inlet and outlet pressure difference Δp = 155 kPa and is close to 3% of the rated pressure difference. At this time, the pump outlet pressure P_2 = 105 kPa, which is critical cavitation outlet pressure.

Figure 8 shows that when the inlet negative pressure is −50 kPa, the pump outlet flow rate remains at 400 L/h, but when the inlet negative pressure is −60 kPa, the outlet flow rate decrease to 300 L/h, indicating that a large amount of steam has been generated in the centrifugal pump at this time, with the largest volume of steam in the blade and the most intense bubble activity.

CAVITATION CALCULATION RESULTS AND ANALYSIS

Cavitation Analysis of the Midsection at Unequal Inlet Negative Pressure Is Unequal

Figure 9 shows the cavitation bubble volume distribution diagrams of the midsections of the four types of pumps when the inlet negative pressure (P_j = −50 kPa; P_j = −60 kPa) and the design flowrate. In general, cavitation regions of the four types of pumps show a similar pattern. They all appear at the inlets of impellers and are mainly concentrated on the blade back (non-working surface). However, the cavitation regions vary due to the difference in impeller type. When P_j = −50 kPa, the cavitation regions of type A and type C are round, the volume fractions are both below 0.5; the cavitation regions of type B and type D are rectangular, the volume fractions are both below 0.875. The cavitation severity is ranked as B > D > A > C. When P_j = −60 kPa, the cavitation regions of the four types of impellers expand from the back of the blade to the working surface of the blade and gradually expand from the low-pressure area of the blade to the flow channel. The cavitation strength is obviously deepened, especially for type C, whose volume fraction increases from a level below 0.5 to 0.875. The cavitation regions of type A and type C are still round, and the volume fraction of type A is below 0.625. The cavitation regions of type B and type D gradually turn into round, and the volume fractions are still within the range of below 0.875. The cavitation severity ranking becomes C > D > B > A. Therefore, the non-forward-extended blade has a weaker cavitation resistance than the forward-extended blade.

Due to the asymmetry of the volutes of the centrifugal pumps, the pressure and velocity at the dynamic and static coupling are non-uniformly distributed. In addition, the blades are arranged in a 4 × 4 staggered layout, resulting in the asymmetry distribution of the cavitation region. The most serious cavitation is at four in Figure E, followed by that at 3 and 2, and the lightest at 1, forming a reciprocating 4, 3, 1, two cavitation bubble cycle. As the inlet negative pressure of the high-speed centrifugal pump increases from P_j = −50 kPa (critical point) to P_j = −60 kPa, the distribution area of cavitation bubbles on the blade surface gradually expands.

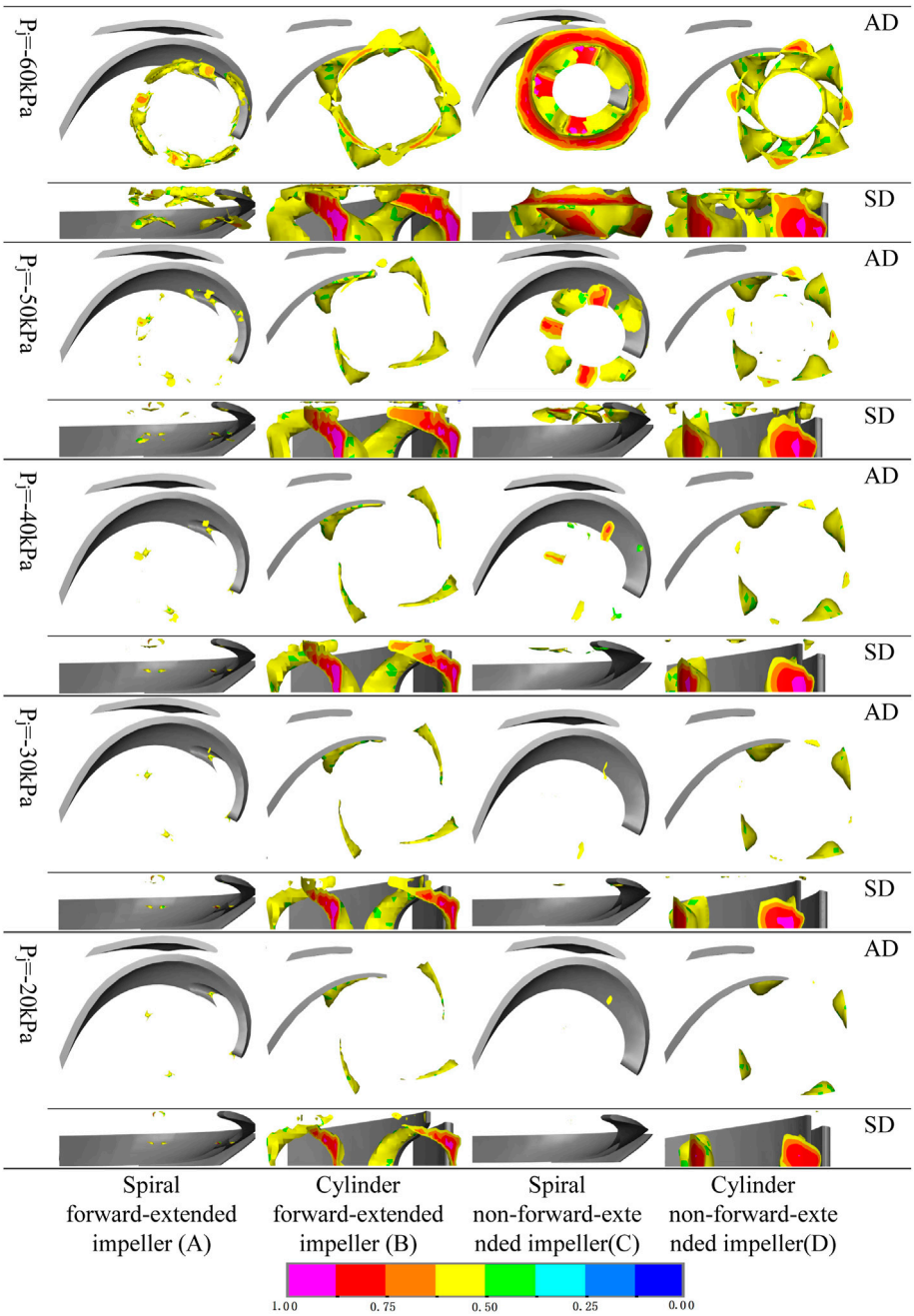

FIGURE 10 | The distribution cloud diagrams of gas-phase volume fractions of different types of pumps at different inlet negative pressures under the design flow. **(A)** Spiral forward-extended impeller **(B)** Cylinder forward-extended impeller **(C)** Spiral non-forward-extended impeller **(D)** Cylinder non-forward-extended impeller.

The Analysis of Cavitation Bubble in the Pump at Unequal Inlet Negative Pressure

To analyze the cavitation evolution process in different types of impellers, the cavitation region with the volume fraction larger or equal to the 0.5 iso-surface in impeller axial view and the lateral view is extracted under the rated operating condition with the same speed and different inlet negative pressure values Taking a pair of blades in **Figure 10** as an example. In **Figure 10**, the cavitation characteristics of the high-speed.

centrifugal pump can be divided into three processes:1) Cavitation bubble first appears at the head of the suction surface of the blade and at the rear of the blade inlet. The distribution of cavitation bubbles at the four blades is different. This is the initial stage of the cavitation bubble, except the cavitation bubbles at type A blade suction surface, which are few and sporadic-dot-shaped and initially occur everywhere except the contact between the blade and

the back shroud. 2) As the inlet negative pressure continues to increase, the cavitation bubbles gradually grow and increase, and there is no obvious sharp increase. At this time, the performance of the pump does not change. The number of cavitation bubbles at the suction surface of the type A blade increases more uniformly, the increase is small. The cavitation bubbles of the type A blade are sporadic spot-shaped. The lateral view shows that cavitation bubbles appear at the area from the blade inlet to the middle of the blade. When the inlet negative pressure reaches P_j = −50 kPa, the increase becomes significant, and the cavitation bubbles are star-shot-shaped. The cavitation bubble with a strength level of 0.875 does not occur until the negative inlet pressure reaches this level. Type B cavitation bubbles are tadpole-shaped and opposite to the direction of rotation of the impeller. Four tadpole shapes form a ring shape attached to the forward-extended section of the blade in the lateral view. With the increase of inlet negative pressure, the tadpole-shaped cavitation bubbles become longer and wider, the cavitation strength deepens, and the ring gradually closes. When P_j = −20 kPa, type B has the cavitation bubble with a strength level of 0.875, and when P_j = −40 kPa, the cavitation bubble with a strength level of one appears. Type C cavitation bubbles occur at the inlet of the blade. When P_j = −20 kPa, there is almost no cavitation bubble; when P_j = −40 kPa, cavitation bubbles increase, and the ring-type cavitation bubbles are more obvious; when P_j = -50 kPa, eight cavitation bubble rounds are presented, each having two rounds, underside of the blade tip has one round, and the rear of the blade tip at the suction surface has one round. The two cavitation bubbles are laterally zygomorphic at 45°; when P_j = −40 kPa, the cavitation bubble with a strength level of 0.875 appears. Type D cavitation bubbles present four lentil shapes, forming a ring. When P_j = −30 kPa, small cavitation bubbles of different sizes appear in the middle of the four lentil shapes in the axial view. In the lateral view, the four lentil shapes are at the root of the blade, and small cavitation bubbles are at the tip of the blade. With the increase of the inlet negative pressure, the tadpole-like cavitation bubbles become longer and wider, the cavitation strength deepens, and the ring is closed. Type D blade has the cavitation bubble with a strength level of 0.87 when P_j = −20 kPa, and when P_j = −40 kPa, the cavitation bubble with a strength level of one appears. Cavitation bubble volume change of type C impeller is more significant than cavitation bubble volume changes of other types of impellers before P_j = −50 kPa. Type B and type D impellers have larger cavitation volumes than type A and type C impellers. This stage is called the development of cavitation. (3) When P_j = −60 kPa, the cavitation bubble volumes of the four types of impellers increase suddenly, forming complete cavitation or severe cavitation. The sudden increments are ranked as C > D > B > A. The bottom layers of type B and type D cavitation bubbles become thickened, and the cavitation bubble trails at the outlet of the impeller completely block the outflow of the liquid flow. The bottom layers of type C cavitation bubbles become thickened, and the cavitation bubble trail at the inlet of the impeller completely blocks the outflow of the liquid flow. The outflow blocked by the three types of cavitation bubbles accounts for 3/4 of the impeller flow. At this time, the performance of the centrifugal pump is severely degraded. Although type A cavitation bubbles have a sudden increase, the increase is one order of magnitude less than the increases of the other three types.

It can be seen from **Figure 7** and **Figure 8** that when the inlet negative pressure is reduced from P_j = −20 kPa to P_j = −60 kPa, type A and type C impellers reduce the impact loss of the blade on the medium with the impact changing from the axial direction to the radial direction, and reduce the energy loss at the inlet, improving the fuel flow characteristics. The forward-extended sections of type A and type B blades occupy a smaller inlet space and have a smaller excretion towards the medium compared to those of type C and type D blades, which makes the inlet velocity small. In conventional inlet velocity calculation, the excretion coefficient, such as coefficient k in **Eq. (1)**, is calculated by considering only the blade thickness and ignoring the blade width. In this paper, the corrected inlet excretion coefficient, such as the coefficient k_1 in **Eq. (1)**, is proposed after considering the blade width.

In general, impellers with forward-extended blades (type A and type B) have less variation in cavitation strength and cavitation region compared to those without forward-extended blades (type C and type D), indicating that impellers with forward-extended blades (type A and type B) have stronger cavitation resistance.

CONCLUSION

Under the condition that the design parameters, such as the outlet diameter of the volute and the impeller and the specific speed, remain unchanged, we designed four sets of impellers with different blade forms and studied the anti-cavitation characteristics of the high-speed centrifugal pump using ethylene glycol aqueous solution as the medium in the aerospace temperature control system under different inlet negative pressures. The following conclusions are drawn:

(1) For the design of blades in the centrifugal pump, while ensuring the blade thickness and taking into account the blade inlet width, the corrected coefficient k_1 of the blade was introduced to obtain the twisted, overhung and forward-extended blade beyond the conventional design.
(2) When the inlet negative pressure decreased from P_j = −50 kPa to P_j = −60 kPa, the volume fraction of type A was below 0.625, and the volume fractions of other types were increased to 0.875. The cavitation severity changed from B > D > A > C to C > D > B > A.
(3) When the inlet negative pressure decreased from P_j = −20 kPa to P_j = −60 kPa, type A had the smallest cavitation area and cavitation strength. The shape, size, and position of the cavitation regions of the four types of impellers varied significantly. The change of type C subject to inlet negative pressure gradient was the most sensitive. Type B and type D both had cavitation bubbles with the strength level of 0.875 when P_j = −20 kPa and cavitation bubbles with the strength level of one when P_j = −40 kPa.
(4) The width of the blade inlet was reduced so that the excretion strength of the blade inlet to the medium was weakened, the

inlet energy loss of the blade was improved, and the flow loss at the blade inlet was reduced, improving the anti-cavitation characteristics, especially when $P_j = -60$ kPa.

Chao Wenxiong (1985-), male, postgraduate, associate professor, mainly engaged in the research and optimization of the int-ernal fluid drive and control of aerospace centrifugal pumps.

DATA AVAILABILITY STATEMENT

The original contributions presented in the study are included in the article/Supplementary Material, further inquiries can be directed to the corresponding author.

AUTHOR CONTRIBUTIONS

W-xC:Conceptualization, Methodology, Software, Investigation, Formal Analysis, Writing—Original Draft; B-lS:Data Curation, Writing—Original Draft; HR: Visualization, Investigation; WD: Resources, Supervision.

FUNDING

National Natural Science Foundation of China (52009114); Natural Science Foundation of Shaanxi Provincial Department of Science and Technology (2021JM-525); Xi'an Aeronautical University Foundation (2020KY1227).

REFERENCES

Bai, K., and Ma, X. (2021). Nume-rical Simulations of Internal Flow Fieldand Mass Flow Characteristic of Gear Pumps in torpedo Based on Pumplinx[J]. *Ship Sci. Technology* 43 (3), 56–59.

Chao, W., and Wang, J. (2018). Hydraulic Characteristics Analysis of Centrifugal Pump with Unshrouded Composite Impeller at Different Tip Clearances[J]. *Chin. Hydraulics Pn-eumatics* (11), 89–93.

Chao, W., and Wang, J. (2019). Numerical Simulation and Experimental Analysis for Cavitation in Compos-Ite Centrifugal Pump. *[J].Chinese SpaceScience and Technolongy.* 39 (3), 64–70. doi:10.16708/j.cnki.1000-758X.2019.0020

Feng, J. (2016). Numerical Analysis of Unsteady Flow Field of Centrifugal Pump under Different Impeller Type[J]. *China Pet. Chem. Stand-ard Qual.* 36 (11), 9–11.

Fu, Y., and Shen, C. (2016). Cav-itation Characteristic Induced by Inlet Back Flow in a Centrifugal Pump[J]. *J. Drainage Irrigation Machinery Eng.* (10), 841–846. doi:10.3969/j.issn.1674-8530.15.0183

Guan, X. (1995). *Modern Pumps Tech-Nical Manuals*. Beijing: Astronautic Publishing House.

Han, Y., Zhou, L., Bai, L., Shi, W., and Agarwal, R. (2021). Comparison and Validation of Various Turbulence Models for U-bend Flow with a Magnetic Resonance Velocimetry experiment. *Phys. Fluids* 33, 125117. doi:10.1063/5.0073910

Hu, S., and Song, W. (2017). Numerical Analysis of Cavitation Characteristics of High Speed Micro-pump in Low Flow[J]. *J. Eng. Therm. Energ. Power* 32 (8), 100–106. doi:10.16146/j.cnki.rndlgc.2017.08.0016

Liao, W., and Wuruikang, F. (2021). The Hydraulic Design and Opt-Imization for Ultra-thin Centrifugal Micropump[J]. *J. Eng. Thermophys.* 42 (5), 1251–1256.

Ma, H., and Pan, Y. (2020). Research on Influence of Blade Outlet Angle on Int-Ernal and External Performance of Centrifugal Pump Based on Pumplinx[J]. *Coal Mine Machinery* 41 (05), 60–63. doi:10.13436/j.mkjx.202005020

Pei, J., and Yin, T. (2017). Cavitation Optimization for a Centrifugal Pump Impeller by Using Orthogonal Designof Experiment[J]. *Chin. J. Mech. Eng.* 30 (01), 103–109. doi:10.3901/cjme.2016.1024.125

Tang, S., Zhu, Y., and Yuan, S. (2021). An Improved Convolutional Neural Network with an Adaptable Learning Rate towards Multi-Signal Fault Diagnosis of Hydraulic Piston Pump. *Adv. Eng. Inform.* 50, 101406. doi:10.1016/j.aei.2021.101406

Wang, F. (2004). *Computational Fluid Dy-Namics Analysis-CFD Software Princip-Le and application[M]*. Beijing: TsinghuaUniversity Press.

Wang, Y., and Xie, S. (2016). Nu-merical Simulation of Cavitation Performance of Low Specific Speed Centrifu-Gal Pump with Slotted Blades[J]. *Journ-al Drainage Irrigation Machin-ery Eng.* 34 (3), 210–215. doi:10.3969/j.issn.1674-8530.15.0009

Wei, L., and Song, W. (2016). Num-erical Simulation and Analysis of the Flow at the Inlet of a High Speed Centrifugal Pump Based on the Soft ware CFD[J]. *J. Eng. Therm. Energ. Power* 31 (7), 103–109. doi:10.16146/j.cnki.rndlgc.2016.07.017

Wen, C., Zhang, C., and Li, Y. (2018). Simulation of Internal Flow Field of Gear Pump Based on Pump-Linx[J]. *J. Chengdu Univ.* 37 (3), 307–312.

Yao, W., and Luo, J. (2019). A Novel Bezier Method for Continuous Thrust Maneuver Orbit Optimal Design[J]. *Jour-nalof Astronautics* 40 (11), 1274–1285.

Zhang, X., Lai, X., and Liao, J. (2017). Analysis of Influence of Splitter Bladeon Unsteady Cavitation Flow Character-Istics of Centrifugal Pump[J]. *J. Eng. Therm. Energ. Power* 32 (4), 109–114. doi:10.16146/j.cnki.rndlgc.2017.04.017

Zhao, W., and Zhao, G. (2017). Numerical Simulation and Experi-Mentof Obstacle Arrangement on Centrifugalpump Blade to Suppress Cavitation[J]. *Trans. Chin. Soc. Agric. Machinery* 48 (9), 111–120. doi:10.6041/j.issn.1000-1298.2017.09.014

Zindani, D., Roy, A. K., and Kumar, K. (2016). Design of Blade of Mixed Flow Pump Impeller Using Mean Stream Line Method. *Proced. Technology* 23, 464–471. doi:10.1016/j.protcy.2016.03.051

Conflict of Interest: The authors declare that the research was conducted in the absence of any commercial or financial relationships that could be construed as a potential conflict of interest.

Publisher's Note: All claims expressed in this article are solely those of the authors and do not necessarily represent those of their affiliated organizations, or those of the publisher, the editors and the reviewers. Any product that may be evaluated in this article, or claim that may be made by its manufacturer, is not guaranteed or endorsed by the publisher.

Advantages of publishing in Frontiers

OPEN ACCESS
Articles are free to read for greatest visibility and readership

FAST PUBLICATION
Around 90 days from submission to decision

HIGH QUALITY PEER-REVIEW
Rigorous, collaborative, and constructive peer-review

TRANSPARENT PEER-REVIEW
Editors and reviewers acknowledged by name on published articles

Frontiers
Avenue du Tribunal-Fédéral 34
1005 Lausanne | Switzerland

Visit us: www.frontiersin.org
Contact us: frontiersin.org/about/contact

REPRODUCIBILITY OF RESEARCH
Support open data and methods to enhance research reproducibility

DIGITAL PUBLISHING
Articles designed for optimal readership across devices

FOLLOW US
@frontiersin

IMPACT METRICS
Advanced article metrics track visibility across digital media

EXTENSIVE PROMOTION
Marketing and promotion of impactful research

LOOP RESEARCH NETWORK
Our network increases your article's readership